

PARAGENESIS, GEOCHEMISTRY AND METALLOGENY OF THE DUBLIN GULCH INTRUSION-RELATED AU DEPOSIT, YUKON TERRITORY, CANADA.

by

© Fraser Andrew Kirk, B.Sc. (Hons).

A Thesis submitted to the

School of Graduate Studies

in partial fulfilment of the requirements for the degree of

Master of Science

Department of Earth Science

Memorial University of Newfoundland

May, 2016

St. John's, Newfoundland and Labrador

Abstract

This study concerns the Dublin Gulch intrusion-related gold system, Yukon Territory, Canada. Located 85 km, north northwest of the town of Mayo, YT, the property hosts a 3.3 M oz Au deposit associated with a mid-Cretaceous pluton. A detailed, 8 stage, hydrothermal paragenesis has been constructed for the deposit. At least two discrete fluids are responsible for sulfide mineralization at Dublin Gulch. The latter of the two hydrothermal fluids is responsible for the majority of Au endowment on the property. Geochemical signatures of mineralization support this finding, displaying distinct populations of arsenopyrite compositions and sulfur isotopes for each fluid. Lead isotopes from sulfosalts associated with the second fluid suggest hydrothermal scavenging from country rocks. Geochronology and petrogenetic studies show that a short lived intrusive event c. 93-94 Ma took place at Dublin Gulch and that the main Au mineralising fluid may be linked to a yet unseen intrusion at depth.

Acknowledgements

This thesis has benefitted from the support and influence of a number of people. First and foremost I would like to thank my supervisor, Dr. Graham D. Layne for his unwavering support, guidance and enthusiasm. His scientific curiosity is unrivalled and his willingness to have countless scientific discussions, many at great length, has undoubtedly contributed to a vast improvement in the quality of this study.

Secondly, I would like to thank my supervisory committee member Dr. George Jenner for his daily support, jokes, lunchtime discussions and cribbage games. His knowledge of igneous petrology has been invaluable in construction of a petrogenetic model for this study.

I would like to thank a number of others: Dr. Greg Dunning obtained the U-Pb geochronology dates using TIMS; Glenn Piercey provided great assistance in the acquisition and processing of S and Pb isotopes using SIMS; Pam King helped with sample crushing and processing; Sherri Strong performed the Sm/Nd and Sr isotope analyses; Michael Shaffer provided SEM guidance.

This study has been funded by Victoria Gold Corporation who own the Dublin Gulch Deposit and through an NSERC Collaborative Research and Development Grant (CRDPJ 421812 - 2011) to Dr. Graham D. Layne. I would like to thank Dr. Vanessa Bennett and Dr. Bill Keats who were instrumental in the conception of this project. The management and staff at Victoria Gold Corporation were incredibly hospitable and welcoming in their support of my time at Dublin Gulch and in their support of sharing this research to the wider scientific community. In particular I would like to thank Dr. Joanna (Ettliger) Hodge for her mentoring and advice during summer 2012 and beyond. Mark Ayranto, Paul Gray, and Helena Kuikka of Victoria

Gold Corp are thanked for their ongoing support and input during the concluding stages of this project.

I would also like to thank John and Jane Leendertse for allowing me to live in their home during the later stages of this research. I thank my friends in St. John's, Scotland, and in various locations around the world for providing relief during the more stressful periods of this research and in their help with settling in a new country. I thank my parents, John and Patricia, for supporting my academic career, for their unwavering belief in me and for affording me the opportunity to achieve my goals. My sister, Laura, has been a constant source of laughter and support. Finally, I would like to thank my partner, Nikki Leendertse, for her constant love and support.

Table of Contents

Abstract.....	ii
Acknowledgements.....	iii
Table of Contents.....	v
List of Figures.....	x
List of Tables.....	xiii
Co-Authorship Statement.....	xv
Chapter 1 Introduction.....	1-1
1.1 Rationale for Study.....	1-2
1.2 An Overview of Intrusion-Related Gold Deposits.....	1-3
1.3 Objective of Study.....	1-4
1.4 Methodology.....	1-5
1.4.1 Logging and Field Sampling.....	1-5
1.4.2 Petrography.....	1-6
1.4.3 Geostatistics.....	1-6
1.4.4 Geochemistry.....	1-7
1.4.5 Arsenopyrite Geothermometry.....	1-7
1.4.6 S Isotopes.....	1-7
1.4.7 Pb Isotopes.....	1-8
1.4.8 Nd and Sr Isotopes.....	1-8
1.4.9 U/Pb Geochronology.....	1-8
1.5 Thesis Structure.....	1-8
References.....	1-11
Chapter 2 Paragenesis and Timing of Gold Mineralization in the Potato Hills Trend, Dublin Gulch, Yukon Territory, Canada.....	2-1
2.1 Introduction.....	2-2
2.1.1 Location and Zone Distribution.....	2-2
2.1.2 Nomenclature.....	2-2
2.1.3 Regional Geology.....	2-3
2.1.4 Local Geological Setting.....	2-9
2.1.5 Zones of the Deposit.....	2-12
2.1.6 Previous Work.....	2-13

2.1.7	Scope and Aims of this Study.....	2-15
2.2	Paragenesis.....	2-20
2.2.1	Introduction.....	2-20
2.2.2	Stage 1: Contact Metamorphism.....	2-21
2.2.3	Stage 2: Skarn.....	2-23
2.2.4	Stage 3: Quartz- K-feldspar Partially Aligned Stockwork Veins.....	2-23
2.2.5	Stage 4: Quartz- Carbonate- Chlorite Veins.....	2-30
2.2.6	Stage 5a: Arsenopyrite-rich Veins.....	2-37
2.2.7	Stage 5b: Au-rich Stage.....	2-40
2.2.8	Stage 6: Pyrite-Sulfosalt Veins.....	2-46
2.2.9	Stage 7: Late Stage Carbonate Veins.....	2-46
2.2.10	Stage 8: Supergene Alteration.....	2-50
2.2.11	Brief Discussion of Rex Peso Veins.....	2-50
2.3	Geostatistical Analysis of Assay Data.....	2-53
2.3.1	Introduction.....	2-53
2.3.2	Element Correlations.....	2-55
2.3.3	Correlations Results.....	2-58
2.3.4	Stacked Histograms.....	2-59
2.4	Principal Component Analysis (PCA).....	2-64
2.4.1	Introduction.....	2-64
2.4.2	PCA Results.....	2-64
2.4.3	Discussion.....	2-67
2.5	Discussion.....	2-71
2.5.1	Wider Applications of this Study to (R)IRGS and Other Models.....	2-73
2.6	Conclusions.....	2-76
	References.....	2-78
Chapter 3	Geothermometry and Isotopic Characteristics of the Ore Mineralization of the Dublin Gulch Au Deposit, YT, Canada.....	3-1
3.1	Introduction.....	3-3
3.1.1	Location and Zone Distribution.....	3-3
3.1.2	Deposit Type.....	3-3
3.1.3	Previous Work.....	3-4

3.1.4 Scope of Study.....	3-5
3.2 Geologic Setting.....	3-6
3.2.1 Regional Setting.....	3-6
3.2.2 Local Geological Setting.....	3-10
3.3 Paragenetic Stages of Hydrothermal Mineralization.....	3-14
3.4 Arsenopyrite Composition and Geothermometry.....	3-20
3.4.1 Introduction.....	3-20
3.4.2 Analytical Approach.....	3-21
3.4.3 Results.....	3-22
3.4.4 Compositional Zoning.....	3-24
3.5 Sulfur Isotopes.....	3-26
3.5.1 Introduction.....	3-26
3.5.2 Sample Selection.....	3-27
3.5.3 Methodology.....	3-27
3.5.4 Results.....	3-27
3.6 Lead isotopes.....	3-31
3.6.1 Introduction.....	3-31
3.6.2 Methodology.....	3-31
3.6.3 Results.....	3-31
3.7 Discussion.....	3-35
3.7.1 Temperature Estimates from Arsenopyrite Composition.....	3-35
3.7.2 Sulfur Isotopes.....	3-45
3.7.3 Lead Isotope Systematics.....	3-56
3.8 Genetic Model and Implications for Exploration.....	3-68
3.8.1 Genetic Model.....	3-68
3.8.2 Implications for Exploration.....	3-71
References.....	3-73
Chapter 4 Magmatism and Metallogeny of the Dublin Gulch area, YT, Canada: Insights from Nd and Sr Isotopes, and U-Pb Geochronology.....	4-1
4.1 Introduction.....	4-2
4.1.1 Scope of Study.....	4-3
4.2 Geological Setting.....	4-5

4.2.1 Regional Geology.....	4-5
4.2.2 Local Geology.....	4-9
4.3 Sample Description.....	4-11
4.3.1 Sample Collection and Locations.....	4-11
4.3.2 Group 1: Dublin Gulch Stock from Eagle Zone.....	4-11
4.3.3 Group 2: Equigranular to porphyritic dykes from Platinum and Potato Hills Zones.....	4-12
4.3.4 Group 3: Porphyritic dykes from Peso Zone.....	4-13
4.4 Analytical Methods.....	4-14
4.4.1 U-Pb Geochronology.....	4-14
4.4.2 Whole Rock Geochemistry.....	4-15
4.4.3 Nd and Sr Isotopes.....	4-16
4.5 U-Pb Geochronology Results.....	4-16
4.6 Lithochemistry Results.....	4-17
4.6.1 Major Elements.....	4-17
4.6.2 Trace Elements.....	4-25
4.6.3 Nd and Sr Isotopes.....	4-30
4.6.4 Summary.....	4-33
4.7 Comparison with other IRGS.....	4-36
4.7.1 Geological Setting.....	4-37
4.7.2 Major Elements.....	4-39
4.7.3 Trace Elements.....	4-49
4.7.4 Nd and Sr Isotopes.....	4-56
4.8 Discussion.....	4-57
4.9 Petrogenetic Model for Dublin Gulch and Affiliated Plutonic Rocks...	4-63
4.10 Conclusions.....	4-67
References.....	4-70
Chapter 5 Summary and Conclusions.....	5-1
5.1 Summary of Significant Findings.....	5-2
5.1.1 Deposit Paragenesis and the Timing of Gold Deposition.....	5-2
5.1.2 Geothermometry and Fluid Sources.....	5-2
5.1.3 Characteristics of Associated Plutonic Rocks.....	5-5
5.2 Implications for IRGS exploration.....	5-5

5.2.1 Mineralization.....	5-5
5.2.2 Host Pluton.....	5-7
5.3 Recommendations for Future Work.....	5-8
5.3.1 Infrared Fluid Inclusion Microthermometry.....	5-8
5.3.2 Detailed Study of the Rex and Peso Zones.....	5-9
5.3.3 IRGS beyond the Tombstone Tintina Gold Belt.....	5-10
References.....	5-11
Appendices.....	A-1
Appendix A: Sample Locations.....	A-2
Appendix B: Mineralization Textures Library.....	A-7
B.1 Native Gold Textures.....	A-8
B.2 Paragenetic Textures.....	A-11
Appendix C: Limits of Detection for geochemical analyses.....	A-20
C.1 Limits of detection for Chapter 2 Geostatistics and PCA.....	A-21
C.2 Limits of detection for Chapter 4 whole rock geochemistry.....	A-22
Appendix D: Arsenopyrite EPMA Data.....	A-23
D.1 EPMA Arsenopyrite Data.....	A-24
D.2 EPMA Arsenopyrite Analysis Spot Images.....	A-28
Appendix E: Sulfur Isotope Data.....	A-36
E.1 Arsenopyrite Sulfur Isotope Data.....	A-37
E.2 Pyrite Sulfur Isotope Data.....	A-48
E.3 Pyrrhotite Sulfur Isotope Data.....	A-54
Appendix F: Lead Isotope Data.....	A-64
F.1 SIMS Lead Isotope Method.....	A-65
F.2 Lead Isotope Data.....	A-67
F.3 SIMS Lead Isotope Analysis Spot Images.....	A-69
Appendix G – U-Pb Geochronology Data.....	A-73
Appendix H – Whole Rock Geochemistry Data used in Chapter 4.....	A-75
H.1 Table of sample names for Dublin Gulch samples in Chapter 4....	A-76
H.2 Data for Dublin Gulch, Scheelite Dome and Brewery Creek.....	A-77
Appendix I – Strontium and Neodymium Isotope Method.....	A-84

List of Figures

Figure 2.1	Stratigraphy and thrust stacking of the Selwyn Basin, modified from Murphy (1997).....	2-5
Figure 2.2	Map of the Tintina Gold Province (TGP) within the Yukon and Alaska.	2-8
Figure 2.3	Map of the exposed granitoid rocks of the DGS with the currently perceived outline of the PHT overlain.	2-11
Figure 2.4	Paragenetic stages for Dublin Gulch.....	2-16
Figure 2.5	Hand specimen and photomicrograph textures of Stage 1 mineralization.	2-22
Figure 2.6	Field relations and hand specimen textures of Stage 2 mineralization.....	2-24
Figure 2.7	Field relations of Stage 3 mineralization.....	2-25
Figure 2.8	Hand specimen textures of Stage 3 mineralization.....	2-27
Figure 2.9	Photomicrographs of Stage 3 mineralization textures.....	2-28
Figure 2.10	Hand specimen textures of Stage 4 mineralization.....	2-31
Figure 2.11	Photomicrographs of Stage 4 mineralization textures.....	2-32
Figure 2.12	Surface exposure of Stage 5a veins.....	2-35
Figure 2.13	Hand specimen textures of Stage 5 mineralization.....	2-36
Figure 2.14	Photomicrographs of Stages 5 & 6 mineralization textures.....	2-38
Figure 2.15	Photomicrographs of Stages 5b & 6 native gold textures.....	2-42
Figure 2.16	Hand specimen textures of Stage 6 mineralization.....	2-47
Figure 2.17	Photomicrographs and back-scattered electron images of Stage 6 mineralization textures.	2-48
Figure 2.18	Example of the most common supergene alteration of sulfide minerals at Dublin Gulch - the replacement of arsenopyrite by apple-green coloured scorodite.....	2-52
Figure 2.19	Stacked histograms comparing As, Au and Bi concentrations.....	2-61
Figure 2.20	Principal Component Analysis of alteration set elements for Dublin Gulch, YT.....	2-66
Figure 2.21	Principal Component Analysis of ore mineralization set elements for Dublin Gulch, YT.....	2-69
Figure 3.1	Stratigraphy of the Selwyn Basin and thrust stacking, modified from Murphy (1997).....	3-7

Figure 3.2	Map of the Tintina Gold Province (TGP) within the Yukon and Alaska.....	3-9
Figure 3.3	Map of the exposed granitoid rocks of the DGS with the currently perceived outline of the Potato Hills Trend (PHT) overlain.....	3-12
Figure 3.4	Paragenetic stages for Dublin Gulch.....	3-18
Figure 3.5	Box and whiskers plot of ranges in arsenopyrite compositions at Dublin Gulch, grouped by paragenetic stage.....	3-23
Figure 3.6	Images of compositional zoning in arsenopyrite grains suggesting prolonged periods of precipitation and mineral growth.....	3-25
Figure 3.7	Box & whiskers plot of SIMS sulfur isotope data for Dublin Gulch samples, grouped by sulfide mineral.....	3-30
Figure 3.8	Pb isotope values for sulfosalt phases at Dublin Gulch plotted as $^{207}\text{Pb}/^{204}\text{Pb}$ vs $^{206}\text{Pb}/^{204}\text{Pb}$	3-34
Figure 3.9	T- fS ₂ stability fields for each vein stage.....	3-36
Figure 3.10	Arsenopyrite compositions (at. % As) with sulfur isotope ($\delta^{34}\text{S}$) values superimposed, for sample FK-099 (Eagle Zone).....	3-45
Figure 3.11	Box plot of sulfur isotope data for Scheelite Dome, grouped by sulfide mineral.....	3-50
Figure 3.12	Sulfur isotope data for the Clear Creek deposit.....	3-51
Figure 3.13	Proposed Pb isotope growth curves for intrusion-related Selwyn Basin ore deposits (Layne, unpublished data).....	3-58
Figure 3.14	Pb isotope data for Dublin Gulch deposits, Hyland Au deposit (SE Yukon) and several Ag-Pb-Zn vein deposits within the greater Selwyn Basin Province/Tombstone-(Tintina-) Gold Belt (TTGB) area.....	3-61
Figure 3.15	Map of deposits included in Pb isotope discussion.....	3-62
Figure 3.16	Pb isotope data for feldspar separates from Tombstone Plutonic Suite and Mayo Plutonic Suite granitoid samples.....	3-64
Figure 4.1	Simplified geological map showing the distribution of geochronology samples, the Dublin Gulch Stock and Au-Ag prospects.....	4-4
Figure 4.2	Summary of plutonic suite classification schemes for the northern Cordillera.....	4-8
Figure 4.3	Cathodoluminescence (CL) images of zircon crystals with igneous growth zoning from sample Eagle 6-1.....	4-15
Figure 4.4	U-Pb Concordia of zircons for representative sample of each rock type.....	4-17
Figure 4.5	Harker plots for select major elements at Dublin Gulch.....	4-23

Figure 4.6	Major element plots for samples at Dublin Gulch.....	4-24
Figure 4.7	Trace element vs. SiO ₂ plots for samples at Dublin Gulch.....	4-28
Figure 4.8	REE and extended REE plots for samples at Dublin Gulch.....	4-29
Figure 4.9	Tectonic discrimination plots for samples at Dublin Gulch.....	4-29
Figure 4.10	⁸⁷ Sr/ ⁸⁶ Sr _(i) vs. εNd _(i) for 5 samples at Dublin Gulch.....	4-32
Figure 4.11	Map showing plutonism within the central Yukon Territory.....	4-36
Figure 4.12	Geological map of the Scheelite Dome igneous complex.....	4-38
Figure 4.13	Summary geologic map of the Brewery Creek area.....	4-39
Figure 4.14	Modified alkali-lime index plot after Frost and Frost (2008).....	4-44
Figure 4.15	Harker plots for selected major elements at Brewery Creek, Dublin Gulch and Scheelite Dome.....	4-46
Figure 4.16	Major element plots for rocks at Brewery Creek, Dublin Gulch and Scheelite Dome.....	4-47
Figure 4.17	Trace element vs. SiO ₂ plots for samples at Dublin Gulch, Scheelite Dome and Brewery Creek.....	4-53
Figure 4.18	REE plots for rocks from Dublin Gulch and Scheelite Dome.....	4-54
Figure 4.19	REE plots for rocks from Dublin Gulch and Scheelite Dome. Average values for each MALI grouping.....	4-55
Figure 4.20	Tectonic discrimination diagrams for rocks at Dublin Gulch and Scheelite Dome.....	4-55
Figure 4.21	εNd _(i) vs. ⁸⁷ Sr/ ⁸⁶ Sr _(i) diagram for Dublin Gulch and comparable intrusive rocks related to IRGS.....	4-56
Figure 4.22	Geochemical discrimination diagrams for the Iberian Variscan Belt...	4-66

List of Tables

Table 2.1	Legend for Figure 2.4.....	2-18
Table 2.2	Chemical formulae of minerals at Dublin Gulch.....	2-19
Table 2.3	Table showing geochemical analysis of individual vein samples of Stage 5 vein material from various locations around the Dublin Gulch deposit.....	2-45
Table 2.4	Legend for data transformations performed on individual elements for statistical analyses.....	2-56
Table 2.5	Pearson Product-moment Correlation Coefficient and Spearman's Rank Correlation Coefficients for detected elemental concentrations at Dublin Gulch.....	2-57
Table 2.6	Principal component scores for alteration group of elements.....	2-65
Table 2.7	Principal component scores for mineralization set of elements at Dublin Gulch.....	2-68
Table 3.1	Legend for Figure 3.4.....	3-19
Table 3.2	Summary of Electron Probe Micro-Analysis (EPMA) results for arsenopyrite grains at Dublin Gulch.....	3-21
Table 3.3	Stated values for standards used for EPMA from Kretschmar and Scott (1976).....	3-22
Table 3.4	Pb isotope values for Dublin Gulch.....	3-32
Table 3.5	Temperature estimates of arsenopyrite using the method of Kretschmar and Scott (1976) from this study.....	3-37
Table 3.6	Summary of Baker and Lang (2001) fluid inclusion types, properties and temperatures recorded by these types at Dublin Gulch.....	3-42
Table 3.7	Lead isotopes of feldspar minerals from plutons within the Selwyn Basin Terrane.....	3-66
Table 4.1	Locations of Dublin Gulch samples analysed in this study.....	4-11
Table 4.2	Major and trace element data for samples analysed in this study.....	4-20
Table 4.3	Geochemical classification based on major element data.....	4-22
Table 4.4	Sr and Nd isotope data and REE ratios for samples at Dublin Gulch.....	4-31
Table 4.5	Comparison of selected trace elements at Dublin Gulch to examples of I-type (Whalen et al. 1987) and Shoshonitic (Jiang et al. 2002) series rocks.....	4-34
Table 4.6	Summary of MALI classification of rock types at Brewery Creek, Dublin Gulch and Scheelite Dome.....	4-45

Table 4.7	Mean values for MALI groupings.....	4-48
Table 4.8	Overview of age and rock type associations in the Mayo and Tombstone plutonic suites.....	4-61

Co-Authorship Statement

This master's thesis and the research papers presented here (Chapter 2–4) have been prepared predominantly by the thesis author, with guidance from my supervisor Dr. Graham D. Layne and supervisory committee member Dr George A. Jenner. Some of the SIMS analyses were conducted by Glenn Piercey in 2013. Pam King helped in the preparation of samples for U-Pb geochronology. Dr Greg. R. Dunning conducted U-Pb geochronology analyses in 2014. Sherri Furey conducted Sr and Nd isotope analyses in 2014. Beside these contributions, the design of the research proposal, the field work and sample collection, preparation, and processing, the analytical work, the data collection, and interpretation, as well as the manuscript preparation was conducted exclusively by the thesis author.

This work was funded by a grant from the NSERC Collaborative Research and Development (CRD) Program, which included both financial and field support from Victoria Gold Corporation.

CHAPTER 1

Introduction

1.1 Rationale for Study

The Dublin Gulch property is located approximately 85 km north northwest of the town of Mayo, Yukon Territory, Canada. The deposit is hosted almost entirely (>90%) within the upper portion of a mid-Cretaceous granodiorite pluton, the Dublin Gulch Stock (DGS). The remainder is hosted within hanging wall metasedimentary rocks of the Neoproterozoic-Cambrian Hyland Group of the Selwyn Basin Province. There are a number of recognized auriferous zones at Dublin Gulch, the most notable of which is the 3.3 Moz Eagle Zone (3.0 Moz – 134 Mt @ 0.69 g/t Au indicated; 0.3 Moz – 0.2 Mt @ 0.56 g/t Au inferred: Tetra Tech, 2015), which includes a 2.3 Moz (92 Mt @ 0.78 g/t Au) proven and probable Au reserve (Tetra Tech, 2015). A number of additional significant mineral occurrences lie along an extended (>13 km-long) belt of Au-As-Bi-Sb and Ag-Pb-Zn mineralization known as the Potato Hills Trend (PHT), which also incorporates both the DGS and the Eagle Zone.

The style of mineralization at Dublin Gulch has led to it being considered representative of a class of ore deposit termed “Intrusion-Related Gold Systems” (IRGS) (e.g., Thompson et al. 1999; Baker and Lang, 2001). This classification has subsequently been further refined by some authors to “Reduced Intrusion-Related Gold Systems” (RIRGS; e.g., Thompson and Newberry, 2000). This latter classification is almost exclusively based on deposits found within the Tintina Gold Province (TGP) of Yukon and Alaska. Hart (2007) echoed the advice of Thompson and Newberry (2000) and Lang and Baker (2001) who called for more detailed studies of individual “RIRGS” deposits in order to better understand the processes that formed them. Lang and Baker (2001) stated that the study of this type of deposit was still “in its infancy”. This study was initiated in response to this need for more detailed studies of individual exemplar deposits within the Northern Cordillera.

1.2 An Overview of Intrusion-Related Gold Deposits

Gold deposits closely associated with plutonism have been assigned a number of names and classifications, which oft reflect their genetic models. Hart (2005) gives a summary of the different terms used by previous authors (e.g., Hollister, 1992; Thompson et al., 1999; Lang and Baker, 2001) to describe the type of deposit at Dublin Gulch. This study shall use the generalized term “Intrusion-Related Gold Systems” (IRGS) to refer to deposits that could be reasonably included in the same broad genetic model as Dublin Gulch.

Hart (2005) lists the following as the most common characteristics for Reduced Intrusion-Related Gold Systems:

1. Parent intrusions are metaluminous, subalkalic intrusions of intermediate to felsic composition that are transitional between ilmenite and magnetite series;
2. Carbonic hydrothermal fluids were responsible for mineralization;
3. A metal association that variably combines gold with elevated Bi, W, As, Mo, Te, and/or Sb, and low concentrations of base metals;
4. A low average sulphide mineral content, generally <5 vol. %, and a relatively reduced ore mineral assemblage that typically comprises arsenopyrite, pyrrhotite, and pyrite, and lacks magnetite or hematite;
5. Spatially restricted, usually weak, hydrothermal alteration;
6. A tectonic setting well inboard of inferred or recognized convergent plate boundaries;
7. Found in magmatic provinces best or formerly known for tungsten and/or tin deposits.

Newberry and Solie (1995) recognised a significant variation in the bulk sulfur content among intrusion-related gold deposits in Alaska, and coined the term “Porphyry As” deposits for the relatively sulfur-rich arsenic-rich examples, reflecting the fact that a vein stage dominated by arsenopyrite was a common feature in this sub-type of deposit. As will be discussed below, Dublin Gulch would fall within this sub-type. Here we shall use “As-rich IRGS” in place of “Porphyry As” for these deposits. Further, we shall use the term “As-poor IRGS” to refer to deposits with sulfur contents below 2 modal %, and no distinct arsenopyrite-bearing stage (e.g., Fort Knox).

1.3 Objective of Study

Based on existing published research, and further to the desire to inform the ongoing exploration effort at Dublin Gulch, several key scientific questions were addressed in this study:

1: Is the paragenesis of alteration and mineralization (originally proposed by Maloof et al. (2001), and greatly enlarged by our new study) observed for the Eagle Zone common to other zones of mineralization along the Potato Hills Trend (PHT)? Can these paragenetic stages be tied to the same hydrothermal fluid event(s) throughout the PHT?

2: Does the implied evolution of hydrothermal fluid composition at Eagle Zone result from the gradual evolution of a single magmatic fluid emanating from the Dublin Gulch Stock (DGS)? Alternatively, do the observations require a more episodic release of fluids from the DGS proper – or from subsequently emplaced granitic intrusions or intrusive phases that may crosscut or intrude the DGS at depth?

3: Is the close association of Au and Bi mineralization persistent throughout the PHT? And can it be correlated with a later stage fluid that is hotter and more saline than those detected in quartz-hosted fluid inclusions in earlier studies?

4: Proximity to known W mineralization is a common theme for IRGS within the Tintina Gold Province. What is the detailed relationship between early W mineralization and later Au mineralization in the Dublin Gulch deposits? What is the relationship between roof-pendant hosted W mineralization at Wolf/Mar/Ray Gulch and the common occurrence of W within the sheeted quartz vein-hosted Au mineralization to the west?

5: Did a non-magmatic fluid component (or sulfur source) play an important role in Au mineralization at Dublin Gulch?

A more global objective of the study was to improve models for IRGS/RIRGS deposits in general, and to facilitate more efficient methods of exploration for this deposit type, both in the Northern Cordillera and globally.

1.4 Methodology

1.4.1 Logging and Field Sampling

Drill core logging of four drill holes and re-logging of eight historical drill holes was conducted over two field seasons in 2011 and 2012. Drill core logging was focussed primarily on areas of mineralisation, with care taken to also gain a representative view of non-mineralised areas in order to understand fresh host lithologies. In total, 364 samples of drill core from across the Dublin Gulch deposit were taken as a representative sample of mineralisation and intrusive lithologies. A further 24 drill core samples for the Rex-Peso prospect were taken to assess the

affinity of this prospect with the main zones of auriferous mineralization. An additional 52 samples were extracted from outcrops, particularly in areas of high gold grade veining and intrusive complexity where no drilling had yet taken place. A large subset of these samples were subsequently selected and made into thin sections and/or cut as reference hand specimens.

1.4.2 Petrography

Polished thin sections of 100 samples were fabricated by Texas Petrographics, Inc. Samples were selected to provide an overview of the mineralization and alteration assemblages present in paragenetic stages initially identified during logging and field sampling. Thin sections were examined using reflected and transmitted light microscopy in order to describe textures and mineralogy. Terraspec™ shortwave infra-red (SWIR) spectroscopy was used to characterize alteration suites in areas of the most pervasive alteration. Petrographic studies were supplemented by scanning electron microscopy-energy dispersive X-ray spectroscopy (SEM-EDS), especially for identification of sulfosalt mineral species and characterization of native gold deportment.

1.4.3 Geostatistics

Element correlations using both the Pearson (1896) and Spearman (1904) methods were conducted on data from the multi-element assay database of Victoria Gold Corp for the Dublin Gulch deposits. Stacked Histograms were used to perform qualitative element correlations with As in lieu of an appropriate statistical method, due to limitations caused by maximum limits of detection for this element. A principal component analysis (PCA) was conducted using the same data set, in order to identify element vectors and the relationships between elements that were not

highlighted by linear correlations. The findings of this approach were integrated with the petrographic study and used to further verify the paragenetic sequence at Dublin Gulch.

1.4.4 Geochemistry

Two sets of samples were sent out for detailed geochemical analysis. The first set comprised 12 samples from outcrop of high grade gold veins. Analyses of these samples were conducted using the 32 element assay package selected by Victoria Gold Corp at ALS Minerals, Vancouver, Canada. Eight samples of igneous rocks were sent to Actlabs (Ancaster, Ontario) for detailed whole rock analysis of major, trace, and rare earth elements in support of a geochronological and petrogenetic examination of the mid-Cretaceous plutonic and volcanic rocks in the Dublin Gulch area.

1.4.5 Arsenopyrite Geothermometry

Fourteen polished thin sections were selected for EPMA (Electron Probe Microanalysis) at Carleton University in 2013. These contained arsenopyrite grains from multiple paragenetic stages, which were analysed for major (Fe-As-S) and trace metal contents. The atomic percentage of As in arsenopyrite was used to make temperature estimates for these stages, based on the arsenopyrite geothermometer method of Kretschmar and Scott (1976).

1.4.6 S Isotopes

Sulfur isotope microanalysis was performed on arsenopyrite (eight samples), pyrite (six samples) and pyrrhotite (14 samples) using Secondary Ion Mass Spectrometry (SIMS). Samples were selected to highlight important paragenetic stages from a range of auriferous zones across the deposit. The purpose of the S isotope study was to assess the sources of sulfur for mineralisation

at Dublin Gulch and, in particular, to determine if a non-magmatic sulfur signature could be identified for any of the stages.

1.4.7 Pb Isotopes

Lead isotope microanalysis was performed on six samples of sulfosalts, from paragenetic stages associated with native gold, also using SIMS. These analyses were designed to test the hypothesis that if all fluids were totally consanguineous, and purely magmatic – in which case the Pb isotope signature of sulfide minerals would be expected to be homogeneous both within and between mineralized zones.

1.4.8 Nd and Sr Isotopes

Nd and Sr isotopes were determined by TIMS on six samples of igneous rocks from the DGS, and proximal volcanic lithologies, to constrain the nature of the source materials and subsequent processes that may have occurred as the parent magma for the deposits ascended through the crust during emplacement.

1.4.9 U/Pb Geochronology

U-Pb zircon geochronology was undertaken on five samples of igneous rocks from the DGS, and proximal volcanic lithologies, to complement the Nd –Sm and Sr isotope determinations.

1.5 Thesis Structure

This thesis consists of five chapters and several supplemental appendices.

Chapter 1 provides a brief rationale for the thesis project; and a brief overview of the location, deposit type, previous studies, research objectives, and methodology.

Chapters 2, 3, and 4 are presented in the form of manuscripts intended for publication in scientific journals. As such, significant repetition or overlap of introductory and geological setting information is present in the beginning sections of these chapters.

Chapter 2 presents a detailed paragenesis, defining eight distinct stages. A key focus of the paragenetic study was the characterization of the auriferous stages, and the deportment of native gold. It also provides an essential framework for the design and interpretation of the techniques applied in the subsequent parts of the study. Statistical correlations and a Principal Component Analysis (PCA) of elemental concentrations are also used to provide geochemical evidence to verify the paragenetic sequence.

Chapter 3 presents arsenopyrite geothermometry of vein stages, and microanalytical S and Pb isotopic studies of sulphide mineralisation. These observations are used to describe the geochemical conditions of mineralisation and the processes that operated to produce the deposit.

Chapter 4 is a deposit scale study of the petrogenetic and magmatic history of the Dublin Gulch pluton and related intrusive rocks. Major and trace element geochemistry, Nd and Sr isotopes and U-Pb geochronology are used to better define the magmatic system at Dublin Gulch and to propose a more detailed model for the relationship between magmatism and mineralisation.

Chapter 5 is a summary chapter that draws together the themes from the preceding three chapters to highlight the most pertinent findings of the research. In addition, suggestions for the direction of future research are provided.

Appendices provide supplemental data including a library of images of textural and mineralogical interest, geochemical limits, and full data sets and spot locations of isotopic measurements (see Table of Contents).

References

- Baker, T., and Lang, J.R., 2001, Fluid inclusion characteristics of intrusion-related gold mineralization, Tombstone-Tungsten magmatic belt, Yukon Territory Canada: *Mineralium Deposita*, v. 36, p. 563–582.
- Hart, C.J.R., 2005, Classifying, distinguishing and exploring for intrusion-related gold systems: The Gangu: Newsletter of the Geological Association of Canada Mineral Deposits Division, v. 87, p. 1, 4–9.
- Hart, C.J.R., 2007, Reduced intrusion-related gold systems, In: Goodfellow, W.D., (ed.), *Mineral deposits of Canada: A Synthesis of Major Deposit Types, District Metallogeny, the Evolution of Geological Provinces, and Exploration Methods*: Geological Association of Canada, Mineral Deposits Division, Special Publication No. 5, p. 95-112.
- Hollister, V.F., 1992, On a proposed plutonic porphyry gold deposit model: *Nonrenewable Resources*, v. 1, p. 293–302.
- Kretschmar, U. and Scott, S.D., 1976, Phase relations involving arsenopyrite in the system Fe-As-S and their application: *Canadian Mineralogist*, v. 14, p. 364-386.
- Lang, J.R. and Baker, T., 2001, Intrusion-related gold systems: the present level of understanding: *Mineralium Deposita*, vol. 36, no. 6, p. 477-489.
- Maloof, T.L., Baker, T., and Thompson, J.F.H., 2001, The Dublin Gulch intrusion-hosted deposit, Tombstone Plutonic Suite, Yukon Territory, Canada: *Mineralium Deposita*, v. 36, p. 583–593.
- Newberry, R.J., and Solie, D.N., 1995, Data for plutonic rocks and associated gold deposits in Interior Alaska: Alaska Division of Geological and Geophysical Surveys, Public Data File 95-25, 61 p.
- Pearson, K., 1896, Mathematical contributions to the theory of evolution. III. Regression, heredity, and panmixia: *Philosophical Transactions of the Royal Society A*, v. 187, p. 253–318.
- Spearman, C.E., 1904, The proof and measurement of association between two things: *American Journal of Psychology*, v. 15, p. 72-101.
- Tetra Tech, 2015, Prepared for Victoria Gold Corp., Technical Report – Feasibility Study, Eagle Gold Project, Yukon: NI 43-101 Technical Report, dated May 29, 2015, 411 p.
- Thompson, J.F.H., and Newberry, R.J., 2000, Gold deposits related to reduced granitic intrusions, In: S.G., Hagemann and P.E., Brown (eds.), *Gold in 2000: Society of Economic Geologists, Reviews in Economic Geology*, v. 13, p. 377–400.

Thompson, J.F.H., Sillitoe, R.H., Baker, T., Lang, J.R., and Mortensen, J.K., 1999, Intrusion-related gold deposits associated with tungsten-tin provinces: *Mineralium Deposita*, v. 34, p. 323–334.

CHAPTER 2

Paragenesis and Timing of Gold Mineralization in the Potato Hills Trend, Dublin Gulch, YT, Canada.

FRASER A. KIRK AND GRAHAM D. LAYNE.

Department of Earth Sciences, Memorial University, 300 Prince Philip Drive, St John's, Newfoundland, A1B 3X5, Canada

Abstract

The Dublin Gulch property is located approximately 85 km north-northwest of the town of Mayo, Yukon Territory, Canada. The granodioritic, mid-Cretaceous Dublin Gulch Stock (DGS) hosts an Intrusion-related Gold System (IRGS) that comprises a number of auriferous zones, the most notable of which is the 3.3 Moz Eagle Zone. A number of additional significant Au occurrences lie along an extended (>13 km-long) belt of Au-As-Bi-Sb and Ag-Pb-Zn mineralization known as the Potato Hills Trend (PHT), which includes the Eagle Zone, as well as the exposed length of the DGS.

A detailed paragenetic sequence for Dublin Gulch IRGS has been developed, implying two apparent fluid pulses from the DGS. The first pulse was responsible for the formation of the Wolf W skarn, and quartz-dominated stockwork veins within the upper portion of the DGS. The second fluid pulse formed a series of more widely-spaced arsenopyrite and pyrite veins. Most native gold is genetically related to the second hydrothermal fluid pulse and displays two textural styles/stages; the first associated with arsenopyrite-rich veins, and the second with bismuthinite and sulfosalt minerals. Geostatistical analysis of drill core assay data corroborates the association of gold with specific paragenetic stages.

2.1 Introduction

2.1.1 Location and Zone Distribution

The Dublin Gulch property is located approximately 85 km north-northwest of the town of Mayo, Yukon Territory, Canada. The deposit is hosted almost entirely (>90%) within the upper portion of a mid-Cretaceous granodiorite pluton, the Dublin Gulch Stock (DGS). The remainder is hosted within hanging wall metasedimentary rocks of the Hyland Group, Selwyn Basin Province. There are a number of recognized auriferous zones at Dublin Gulch, the most notable of which is the 3.3 M oz Eagle Zone (3.0 M oz – 134 Mt @ 0.69 g/T Au indicated; 0.3 Moz – 0.2 Mt @ 0.56 g/T Au inferred: Tetra Tech, 2015), which includes a 2.3 Moz (92 Mt @ 0.78 g/T Au) proven and probable Au reserve (Tetra Tech, 2015). A number of additional significant metal occurrences lie along an extended (>13 km-long) belt of Au-As-Bi-Sb and Ag-Pb-Zn mineralization known as the Potato Hills Trend (PHT), which transits the DGS, and includes the Eagle Zone.

2.1.2 Nomenclature

Deposit Type: Gold deposits associated with (granitoid) intrusives have been assigned a number of names and classifications consequent to specific genetic models. Hart (2005) gives a summary of the different terms used by previous authors (e.g., Hollister, 1992; Thompson et al., 1999; Lang and Baker, 2001) to describe this general class of deposit. Here we shall use the generalized term “Intrusion-related Gold Systems” (IRGS) to refer to deposits that could be reasonably included in the same genetic model as Dublin Gulch.

Deposit Sub-Classes: Newberry and Solie (1995) recognised a significant variation in the bulk sulfur content of many intrusion-related gold deposits in Alaska, and coined the term “Porphyry

As” deposits for the relatively sulfur-rich deposits, reflecting the fact that a vein stage dominated by arsenopyrite was a common feature in this sub-type of deposit. Here we shall use “As-rich IRGS” in place of “Porphyry As” and “As-poor IRGS” to refer to deposits with sulfur contents below 2 modal %, and no distinct arsenopyrite-bearing stage (e.g., Fort Knox).

“Partially Aligned Stockwork”: Previous literature describing IRGS (e.g., Hart, 2007) has termed the common feature of an array of partially aligned quartz veins as “sheeted veins”. The author finds the term “partially aligned stockwork” more agreeable as it is more in keeping with porphyry deposit nomenclature and allows a more obvious comparison to processes which operate in porphyry systems for this class of deposit. Further, it avoids confusion with the geometry of some later stage gold-bearing arsenopyrite veins in the Dublin Gulch system, which are more widely spaced, sub-vertical vein sets, and actually conform more closely to the traditional use of the term “sheeted veins”.

The Ray Gulch – Mar – Wolf Tungsten skarn: A W-skarn deposit at Dublin Gulch was historically referred to as the “Ray Gulch” skarn (Brown et al., 2002), and subsequently the “Mar” skarn (SRK Consulting, 2008). The name currently used by Victoria Gold Corp., the “Wolf” skarn, is adopted throughout this paper.

2.1.3 Regional Geology

Stratigraphy: The DGS was emplaced into the Yusezyu Formation of the Hyland Group in the Selwyn Basin Province of the Northern Cordillera during the Middle Cretaceous. Rocks of the Selwyn Basin (see Fig. 2.1 for stratigraphy), a passive margin sequence, were deposited as sediments on the north-western margins of North America during the late Precambrian (Neoproterozoic) to Middle Jurassic (Abbott et al., 1986; Gordey and Anderson, 1993). The

Hyland Group is composed of coarse-grained sandstones inter-bedded with shales, which largely formed as turbidite flows during the latest Precambrian to Early Cambrian (Fritz et al., 1983, 1991; Gordey and Anderson, 1993). The Yusezyu Formation is a series of coarse, gritty sandstones and pebbly conglomerates interbedded with shales and siltstones. The upper parts of the formation are variably calcareous, with minor limestone horizons. The Yusezyu Formation records the earliest sedimentation within the Selwyn Basin, and its deposition ceased before the end of the Neoproterozoic (Murphy, 1997).

Deformation: The Tombstone Thrust and the Robert Service Thrust sheets disrupted the stratigraphy of the Selwyn Basin by creating a number of thrust stacks (Fig. 2.1) during the Jurassic (Mair et al., 2006). The DGS is located close to the Tombstone Strain Zone associated with the Tombstone Thrust. These thrust stacks potentially formed structural conduits for the migration of magma upwards in the crust of the Selwyn Basin, and may, in fact, have been the dominant tectonic controls of magma ascent in the Dublin Gulch area (S. Craggs, pers. comm., 2013). The DGS was intruded into the hinge zone of the Dublin Gulch Antiform (Stephens, 2003), and this zone appears to provide a key structural control and explanation of the elongate ridge geometry of the pluton.

Metamorphism within the Selwyn Basin is typically of lower greenschist facies. The Tombstone High Strain Zone reached a higher metamorphic grade. The maximum depth of burial for the Hyland Group is estimated at less than 10 km, suggesting pressures of around 2.8 kb (McInnes, 2007).

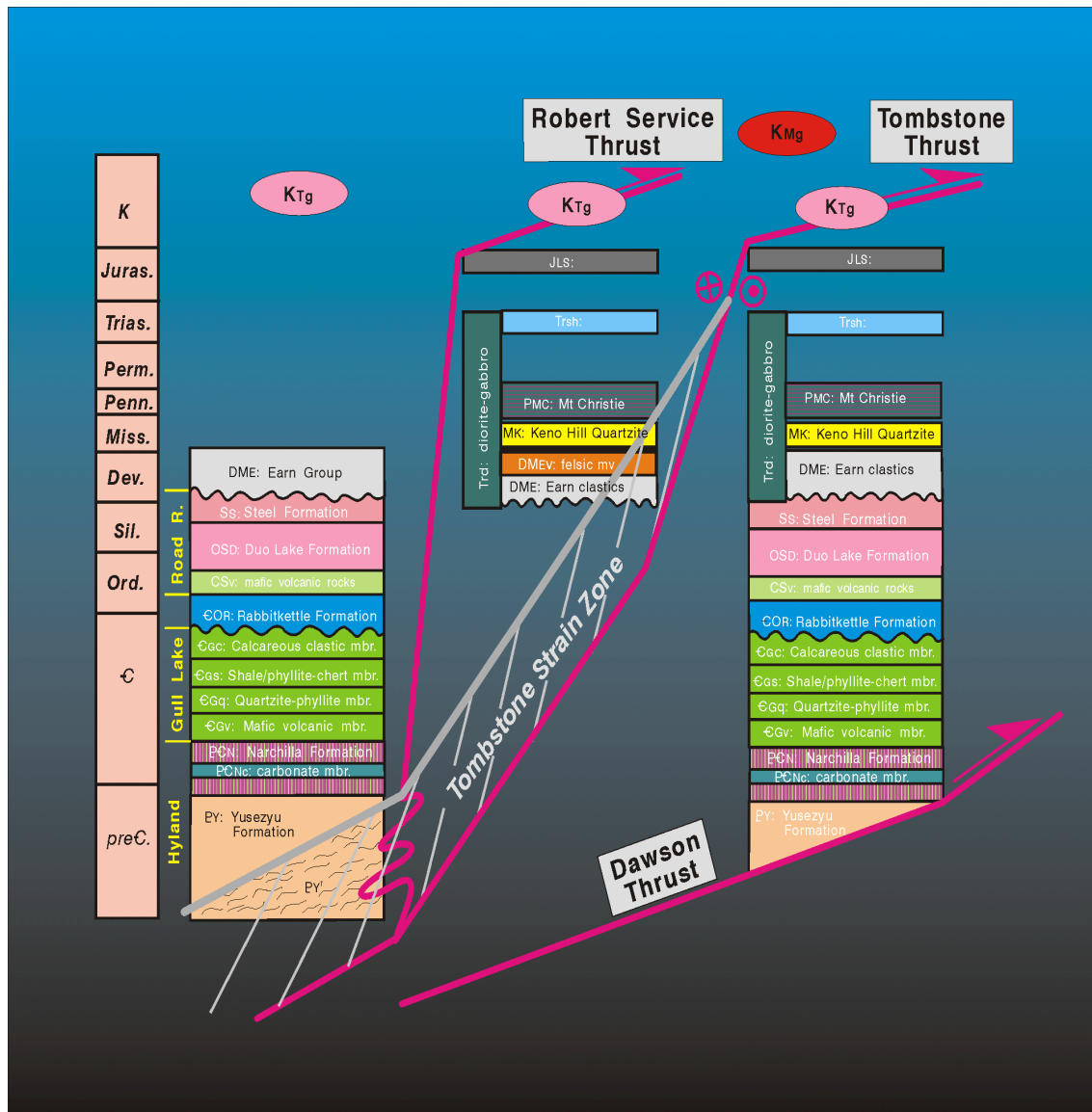


FIGURE 2.1. Stratigraphy and thrust stacking of the Selwyn Basin, modified from Murphy (1997). Dublin Gulch is hosted by the Yusezyu Formation, a series of coarse, gritty sandstones and pebbly conglomerates interbedded with shales and siltstones, which forms the base of the Hyland Group. The DGS was intruded outside - but proximal to (<10 km from) - the Tombstone Strain Zone.

Magmatism: The DGS is one of a series of Cretaceous plutons that have been included within the Tintina Gold Province (TGP) (see Fig. 2.2). The TGP (e.g., Hart, 2004) is a belt of gold deposits in the Northern Cordillera of Yukon and Alaska that are bounded by two dextral transpressional fault systems - the Denali Fault (southern limit) and the Tintina Fault (northern limit). The belt also extends beyond the northern tip of the Tintina Fault, into the Selwyn Basin in the Yukon, and into the western-most NWT.

Within the TGP a series of highly prospective IRGS deposits form the Tombstone Gold Belt (TGB), the most significant known district for IRGS globally. A series of previous nomenclature systems for plutonic suites in Yukon and Alaska had been proposed by various authors (e.g., Anderson, 1983, 1988; Woodsworth et al., 1991). The name TGB was first used by Mortensen et al. (1995) and Murphy (1997), who designated two distinct suites of plutons within the belt. They designated the series of plutons on the northern margins of the Selwyn Basin, which trend roughly east-west, as the Tombstone Suite. The series of plutons that trend broadly north-south along the YT-NWT border was termed the Tungsten Plutonic Suite by Mortensen et al. (1995, 2000). It should be noted that this division included only small plutons around 94 Ma. Mortensen et al. (1995, 2000) included the DGS as a member of the Tombstone Suite.

Hart et al. (2004a, b) subsequently defined plutonic provinces for the entirety of Alaska and the Yukon based on geochemical affinities, age and morphology. Hart et al. (2004b) revised the terminology for plutonic suites within the Yukon, subdividing the Tombstone Suite into the Tombstone and Mayo suites, and widening the parameters of inclusion for the Tungsten Suite. These subdivisions were made on the basis of geographical location, pluton size, rock types, geochemistry, and morphology. The Tombstone Suite, as defined by Hart et al. (2004b), features 10-80 km², concentrically zoned plutons in the north-western-most portion of the Selwyn Basin,

which are alkalic and largely composed of syenite. The Mayo Suite features plutons trending east-west along the northern margin of the Selwyn Basin, 1-5 km² (western portion)/ 20-80 km² (eastern portion), single phase to weakly composite, and which are alkalic-calcic to calcic and chiefly composed of quartz monzonite. The Tungsten Suite is comprised of ~15 km², gradationally zoned plutons, which are peraluminous, alkalic-calcic to calcic and feature quartz monzonite to monzogranite compositions. Hart et al. (2004b) defined age ranges for the respective suites as: Tungsten Suite (97 Ma – 94 Ma), Mayo Suite (95 Ma – 92 Ma), and Tombstone Suite (92 Ma – 90 Ma). Rasmussen (2013) refined these ranges to: Tungsten Suite (98 Ma – 94 Ma), Mayo Suite (96 Ma – 93 Ma), and Tombstone Suite (94 Ma – 89 Ma). The Dublin Gulch Pluton was designated by Hart et al. (2004b) as a member of the Mayo Suite, rather than the Tombstone Suite.



FIGURE 2.2. Map of the Tintina Gold Province (TGP) within the Yukon and Alaska. Deposits are shown by a large circle; occurrences are shown by a small circle. Those deposits which are marked in red can arguably be considered under the same genetic model as Dublin Gulch. Those deposits marked in black are not of the same genetic origin as Dublin Gulch, or are ambiguous in origin. Those deposits marked in purple are skarn deposits associated with intrusions similar to those that form IRGS in the TGP. Within the TGP is the Tombstone Gold Belt (marked in pink), which is the predominant host to IRGS in the Yukon and Alaska. Mair et al. (2006) suggests that the presence of IRGS along a continuing trend of the TGB in the Fairbanks district, is consequent to a post-depositional 450 km offset along the Tintina Fault. Population centres marked are Whitehorse (W), Mayo (M), Dawson (D), and Fairbanks (F). Map after Hart (2007).

2.1.4 Local Geological Setting

The DGS (Fig. 2.3), as exposed in the study area, is a single phase granodiorite intrusion (Murphy, 1997). The intrusion forms an elongate ridge (approx. 6 km x 2 km) that trends at 070°. The DGS displays a generally equigranular, medium-grained texture throughout the main body - with a strongly developed porphyritic texture within 10 m of contact margins. Although the intrusion appears single phase, there are areas of compositional heterogeneity where it could be classified as quartz monzonite rather than granodiorite. Mafic enclaves are present in the main granodiorite, and show very little deformation, suggesting passive intrusion under little to no tectonic stress.

A series of narrow (usually cm-scale) aplite dykes cross-cut both the skarn and the DGS in the Wolf Skarn area. Later stage dykes of andesite to dacite composition, which vary between porphyritic (Hyland Group hosted) and equigranular to porphyritic (DGS hosted) textures, crosscut the main intrusive and partially aligned stockwork veins of early mineralization. The relationship between these late stage dykes, and vein stages later than partially aligned stockwork veins of paragenetic Stage 3 (see below), remains enigmatic in the absence of observable examples of cross-cutting relationships.

Published U-Pb ages for the crystallization of the DGS are 92.8 ± 0.5 Ma (titanite; n=2) and $93.5 +5.8/-0.5$ (zircon; Murphy, 1997), 94.0 ± 0.3 Ma (zircon; Selby et al., 2003) and 94.1 ± 0.3 Ma (zircon; Chapter 4). Andesitic and dacitic dykes sampled from the Dublin Gulch area appear contemporaneous with the DGS (Chapter 4).

A Re-Os date for molybdenite (Selby et al., 2003) suggests a date of 93.2 ± 0.3 Ma for the hydrothermal activity that precipitated this specific phase of mineralization. This would be

closely linked to emplacement of the DGS, given the overlap with the age estimates above, and likely affiliated with our paragenetic Stage 3. The paragenesis of this study places molybdenite in the earliest vein stages, preceding native gold, so this age may not be exactly simultaneous with (nor resolvable from) main gold endowment at Dublin Gulch.

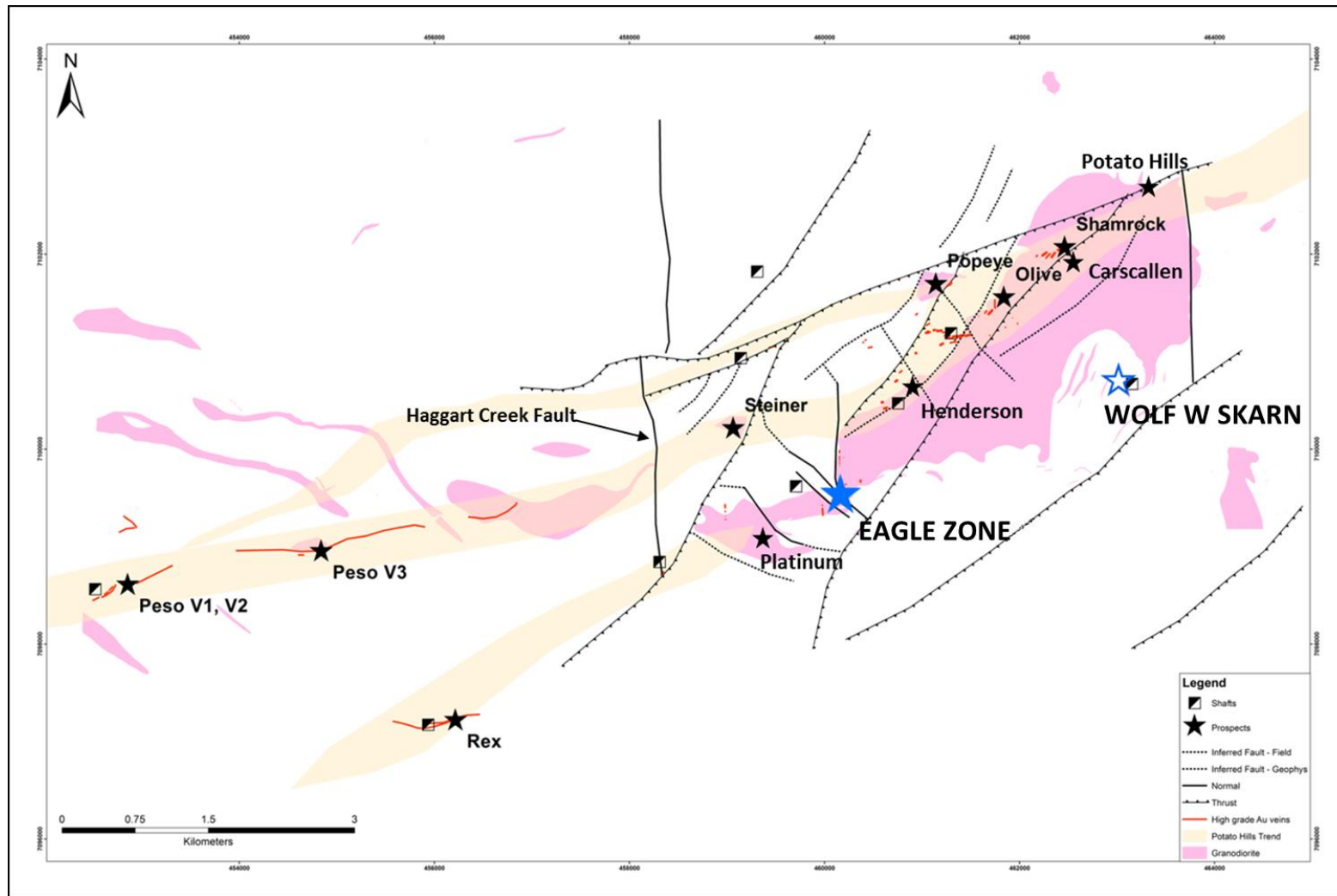


FIGURE 2.3. Map of the exposed granitoid rocks of the DGS (pink) with the currently perceived outline of the PHT (tan/peach) overlain. The Eagle Zone deposit is shown with solid blue star. The Wolf Tungsten Skarn is shown with an outlined blue star. Major prospects are shown with a black star symbol. The structural framework of the deposits is highlighted by a series of normal and thrust faults. There is a clear pattern of major prospects occurring along the stretch of the PHT, particularly where it intersects the DGS. Recognized high grade Au occurrences occur almost exclusively along the PHT with the exception of those in Eagle Zone, which has not been included as part of the trend in previous literature due to a distinct deposit model being proposed for its genesis. Map adapted from Victoria Gold Corporation.

2.1.5 Zones of the Deposit

With the exception of the Wolf W Skarn, mineralization at Dublin Gulch is almost exclusively vein-bound, occurring in a variety of zones and prospects across the Dublin Gulch property (see Fig. 2.3). Auriferous mineralization is chiefly hosted within the DGS, with the remainder (<10%) hosted by the intruded, Yusezyu Formation metasedimentary rocks.

The Eagle Zone sits within a ~5 km long ridge of exposed granodiorite of the DGS (Fig 2.3). The Platinum Zone is located along this same ridge, on the topographical rise out of the Haggart Creek Valley towards the Eagle Zone. The Haggart Creek Valley is punctuated geologically by the Haggart Creek Fault, which forms a topographic low. The DGS ridge rises toward the Potato Hills, which are located at the far northeastern end of the granodiorite ridge. The Olive and Shamrock zones are the most prominent zones in this far northeastern part of the trend. Both are exposed by a series of creeks and gulches, which are likely the surface manifestations of NNW-trending faults.

The Rex and Peso zones (“Rex-Peso” Veins) lie on the opposite (west) side of the Haggart Creek Fault to the majority of known DGS-hosted mineralization, and are situated on the hills rising westward out of the Haggart Creek Valley. The Wolf W Skarn (hosted by a roof pendant of Hyland Group limestone within the DGS) lies on the southeastern edge of the Dublin Gulch ridge, often forming cliffs and vertical rock faces. There is a uniformly steep drop off in the topography progressing south off the Dublin Gulch ridge, into a wide valley immediately below.

Clusters of porphyry-style partially aligned stockwork veins occur throughout the pluton; Eagle and Olive zones contain the most extensive clusters of mineralised stockwork veins, and consequently the most graduated Au grades in the deposit. The Shamrock Zone contains

arsenopyrite-rich veins with up to 118 g/T Au in individual grab samples, but these veins appear more volumetrically restricted than in Eagle or Olive. Shamrock shows the strongest disparity in Au grade between Au-rich arsenopyrite veins and largely barren stockwork quartz - K-feldspar veins. In the more distal zones, e.g., Platinum, Steiner, and Popeye, mineralization occurs in the same style as in the more prominent zones but, as currently exposed, appears lower, and more sporadic, in Au content. In general, auriferous mineralization in the vicinity of the DGS typically appears to extend no more than 10 m (upwards) into the surrounding metasedimentary rocks of the Yusezyu Formation.

The greater Potato Hills Trend refers to a >13 km long belt of mineralization (outlined in Fig. 2.3), which extends from the Peso (Vein) Zone in the South West towards the Shamrock Zone, and then beyond the Potato Hills to the northeast. The Rex Zone is currently included in the Potato Hills Trend, as it appears consanguineous with the Peso Zone veins, but is represented as a small spur of the Trend to the south-southeast in Figure 2.3. Of note is that, in both Rex and Peso zones, high grade Au veins appear much more continuous laterally, as opposed to the more laterally discontinuous vein geometries described above for the Olive and Shamrock zones.

2.1.6 Previous Work

A report by Thompson (1945) highlighted cassiterite occurrences at Dublin Gulch (Tin Dome), which have not been described in any detail in subsequent literature. Subsequently, Lennan (1983) first described W-bearing skarn mineralization at Dublin Gulch (Wolf Skarn). Hitchins and Orssich (1995) provided the first focused study on the auriferous Eagle Zone. Murphy (1997) mapped the regional geology surrounding Dublin Gulch in the most detail to date, as part of a survey of the Northern McQuesten and Mayo map area.

Hollister (1992) proposed the porphyry gold model as applicable to auriferous mineralization at Dublin Gulch. Sillitoe and Thompson (1998) highlighted the difficulty of distinguishing certain styles of intrusion-related Au mineralization from orogenic gold mineralization. However, Thompson et al. (1999) subsequently ascribed Dublin Gulch to the intrusion-related class of mineral deposits, based on the association with the Wolf Skarn, ore metal associations, and tectono-magmatic setting. Thompson and Newberry (2000) highlighted the apparent link between this style of mineralization and what appeared to be moderately reduced granitoid intrusive rocks in the region. The term “Reduced Intrusion-Related Gold Systems” (RIRGS) arose from the work of Thompson et al. (1999), Thompson and Newberry (2000), and Lang et al. (2000). Hart (2005, 2007) further developed the RIRGS model, highlighting metal zonation patterns and element correlations with a strong emphasis on deposits in the Northern Cordillera, Yukon and Alaska. In fact, the Dublin Gulch and Fort Knox (Alaska) deposits represent the holotypes for his proposed RIRGS classification.

Maloof et al. (2001) presented a paragenesis for Dublin Gulch that showed native gold occurring during a single stage, in association with arsenopyrite veins. They attributed this event to the evolution of a single hydrothermal fluid from the DGS, which cooled with time and distance. Baker and Lang (2001) studied fluid inclusions in quartz, recognising that early quartz was likely not in equilibrium with gold mineralization; however, they stated that the relationship of fluid inclusions to gold mineralization was difficult to resolve texturally. Lang and Baker (2001) present a process-driven model for intrusion-related Au deposits in general, and a synthesis of global examples into a single overall deposit type. They suggested a temperature range of roughly 350 to 150°C for hydrothermal activity in this class of deposits.

Brown et al. (2002) presented the most detailed study of the Wolf Skarn to date, including a mineral paragenesis for the skarn - which has been adopted for this study. Stephens (2003) showed that quartz veins at Dublin Gulch possess structural features that are consistent with early mineralization being genetically linked to the emplacement and evolution of the Dublin Gulch granodiorite.

Recent NI 43-101 technical reports for the Wolf Skarn (SRK Consulting, 2008), and the Eagle Zone (Wardrop Engineering Inc., 2009, 2011a, 2011b, 2012; Scott Wilson Mining, 2010; Tetra Tech, 2015) have been focussed on providing compliant resource estimates.

2.1.7 Scope and Aims of this Study

The aims of this study were to assess the consanguinity of the various styles of mineralization along the PHT, the temporal and spatial distribution of Au within the PHT, and the possibility of multiple discrete hydrothermal fluid events related to the DGS. Of key interest was to assess the relationship of auriferous mineralization in the Eagle Zone to that along the greater PHT. This paper presents a detailed paragenesis for the mineralization at Dublin Gulch, with particular emphasis on the timing of Au delivery. The paper contains two main sections, the first addresses mineralogy and textures and presents a detailed paragenesis, based mainly on petrography and textural analysis - supplemented with SEM-EDS and semi-quantitative EPMA analyses to confirm the identity of some less abundant mineral phases. The second section presents statistical element correlations and principal component analyses (PCA) of an extensive drill core assay database, to further elucidate the timing of Au mineralization.

Minerals	Stages										
	1	2a	2b	2c	3	4	5a	5b	6	7	8
	Contact Metamorphism	Skarn			Qtz-K-spar Veins	Qtz-Chl-Carb Veins	Arspy-Rich Veins	Au-rich Stage	Pyrite-Sulfosalt Veins	Carbonate Veins	Supergene Alteration
Pyrrhotite	█										
Chalcopyrite	█										
Quartz		█	█	█	█	█	█				
Wollastonite		█									
Scheelite											
Garnet (Grossular)			█								
Pyroxene (Hedenbergite)			█								
Calcite								█		█	
Chlorite				█		█					
Actinolite				█							
Biotite											
K-Feldspar					█	█					
Albite					█						
Pvrite									█		
Nickel-(Iron)-Sulfides											
Epidote											
Molybdenite											
Ankerite Dolomite										█	
Arsenopyrite							█				
Arsenopyrite											
Sphalerite									█		
Galena											
Tennantite											
Cobaltite*											
Gersdorffite*											
Marcasite											
Muscovite-Phengite											
Dickite								█			
Kaolinite								█			
Pyrophyllite*								█			
Native Au											
Electrum											
Ullmannite*											
Bismuthinite											
Tetradymite											
Stibnite											
Jamesonite								█			
Boulangerite								█			
Bournonite*								█			
Freibergite-Tetrahedrite*								█			
Madocite*											
Native Bi											█
Scorodite											█
As-Bi Alloy											█
Fe-O-OH Oxides											█

FIGURE 2.4. Paragenetic stages for Dublin Gulch. Stage 2 (skarn) stages are adapted from Brown et al. (2002). Minerals marked with an asterisk (*) were not observed during this study, but were identified by ALS Minerals (2011) - their paragenetic placement was determined by the author on the basis of the textural descriptions and chemistry from that report. Symbol descriptions are shown in Table 2.1.

TABLE 2.1. Legend for FIGURE 2.4

Symbol	Description
█	Characteristic or dominant mineral in a vein stage – generally comprises >25% of the vein.
▬	Major mineral in a vein stage – generally comprises 10 – 25 % of the vein.
—	Minor mineral in a vein stage – generally comprises 2 – 10 % of the vein.
- - - - -	Uncommon mineral in a vein stage – generally comprises <2% of the vein.
.....	Trace to Rare mineral in a vein stage – Detectable only with microscope
	Definitive paragenetic stage transition marked by distinct cross-cutting relationships in all cases.
	Gradational stage transition marked by ambiguous or absence of cross-cutting relationships.

TABLE 2.2. Chemical formulae of minerals at Dublin Gulch.

Mineral	Formula	Mineral	Formula	Mineral	Formula
Actinolite	$\text{Ca}_2(\text{Mg,Fe})_5\text{Si}_8\text{O}_{22}(\text{OH})_2$	Epidote	$\text{Ca}_2\text{Al}_2(\text{Fe,Al})(\text{SiO}_4)(\text{Si}_2\text{O}_7)\text{O}(\text{OH})$	Pyrite	FeS_2
Albite	$\text{NaAlSi}_3\text{O}_8$	Freibergite-Tetrahedrite	$(\text{Ag,Cu,Fe})_{12}(\text{Sb,As})_4\text{S}_{13} - (\text{Cu,Fe})_{12}\text{Sb}_4\text{S}_{13}$	Pyrophyllite	$\text{Al}_2\text{Si}_4\text{O}_{10}(\text{OH})_2$
Ankerite-Dolomite	$\text{Ca}(\text{Fe,Mg,Mn})(\text{CO}_3)_2 - (\text{Ca,Mg})(\text{CO}_3)_2$	Galena	PbS	Pyroxene (Hedenbergite)	$\text{CaFeSi}_2\text{O}_6$
Arsenopyrite	FeAsS	Garnet (Grossular)	$\text{Ca}_3\text{Al}_2(\text{SiO}_4)_3$	Pyrrhotite	$\text{Fe}_{(1-x)}\text{S}$ (x = 0 to 0.2)
Biotite	$\text{K}(\text{Mg,Fe})_3(\text{AlSi}_3\text{O}_{10})(\text{F,OH})_2$	Gersdorffite	NiAsS	Quartz	SiO_2
Bismuthinite	Bi_2S_3	Jamesonite	$\text{Pb}_4\text{FeSb}_6\text{S}_{14}$	Scheelite	CaWO_4
Boulangerite	$\text{Pb}_5\text{Sb}_4\text{S}_{11}$	K-feldspar	KAlSi_3O_8	Scorodite	$\text{FeAsO}_4 \cdot 2\text{H}_2\text{O}$
Bournonite	PbCuSbS_3	Kaolinite	$\text{Al}_2\text{Si}_2\text{O}_5(\text{OH})_4$	Sphalerite	$(\text{Zn,Fe})\text{S}$
Calcite	CaCO_3	Madocite	$\text{Pb}_{17}(\text{Sb,As})_{16}\text{S}_{41}$	Stibnite	Sb_2S_3
Chalcopyrite	CuFeS_2	Marcasite	FeS_2	Tennantite	$\text{Cu}_6[\text{Cu}_4(\text{Fe,Zn})_2]\text{As}_4\text{S}_{13}$
Chlorite	$(\text{Mg,Fe})_3(\text{Si,Al})_4\text{O}_{10}$	Molybdenite	MoS_2	Tetradymite	$\text{Bi}_2\text{Te}_2\text{S}$
Cobaltite	CoAsS	Muscovite - Phengite	$\text{KAl}_2(\text{AlSi}_3\text{O}_{10})(\text{F,OH})_2 - \text{K}(\text{AlMg})_2(\text{OH})_2(\text{SiAl})_4\text{O}_{10}$	Ullmannite	NiSbS
Dickite	$\text{Al}_2\text{Si}_2\text{O}_5(\text{OH})_4$	Nickel-(Iron)-Sulfides	Ni-(Fe)-S	Wollastonite	CaSiO_3

2.2 Paragenesis

2.2.1 Introduction

As discussed above, the majority of sulfide-bearing mineralization at Dublin Gulch is hosted within the main phase granodiorite pluton, and hydrothermal activity appears to have been heavily controlled by the intrusion and crystallization of the DGS. The paragenesis of mineralization at Dublin Gulch is summarized in Figure 2.4 - and each stage is described in detail below. The chemical formulae of all minerals listed in Figure 2.4 are presented in Table 2.2. Intrusion of the DGS produced a contact aureole that caused phase transformation of syn-sedimentary iron sulfides in the Hyland Group metapelites during emplacement (Stage 1). Penecontemporaneously, the Wolf W Skarn (Stage 2) replaced a large roof pendant of an adjoining carbonate horizon within the Hyland Group, appearing to predate a series of vein-bound stages at Dublin Gulch. A network of partially aligned, closely-spaced quartz- K-feldspar veins (Stage 3) are the first expression of brittle-fracture hydrothermal activity, followed by a series of less strongly aligned quartz-chlorite-calcite veins (Stage 4).

Higher grade “sheeted” auriferous veins (Stage 5a) – averaging 5-50 cm in width and spaced 30-50 meters apart - cross-cut and replace Stage 3 and 4 veins. Stage 5a veins are dominated by arsenopyrite. Intense wallrock alteration (muscovite/phengite-dickite-kaolinite-pyrophyllite with calcite) is the most characteristic feature of Stage 5b – which hosts the bulk of gold mineralization. Stage 5b veins contain Pb-Fe-Bi-Sb-As- sulfosalts, bismuth minerals, native gold and electrum. Pyrite, sphalerite, jamesonite, and boulangerite, with minor native gold and electrum, comprise Stage 6, which cross-cuts Stage 5. The final veining event at Dublin Gulch is represented by numerous carbonate crack-seal veins (Stage 7), which are observed to cross-cut

all earlier vein stages and rock types. Supergene alteration and/or shallow weathering (Stage 8), causing oxidation of host rocks and ore minerals, is restricted to 50 m from present surface.

Paragenetic stages were identified through a combination of field observations, petrography, Secondary Electron Microscopy – Energy Dispersive X-Ray Analysis (SEM-EDS) and Electron Probe Microanalysis (EPMA). Clay alteration minerals were identified using a TerraSpec™ Short Wave Infrared (SWIR) instrument. Supplemental textural images are available in Appendix B: Mineralization Textures Library.

2.2.2 Stage 1: Contact Metamorphism

Metapelites within the Hyland Group locally contain pyrite-rich horizons which, within the contact metamorphic aureole of the DGS (~2 km radius, Maloof et al., 2001), display contact metamorphism to pyrrhotite (see Fig. 2.5). Where the pyrite was sufficiently rich in Cu, minor chalcopyrite is intergrown with pyrrhotite within the hornfelsed zone. This texture is most prominent in the immediate roof zone above the pluton, but does occur wherever pyrite-rich horizons have been contact metamorphosed. The deportment of the pyrrhotite and chalcopyrite still mimics the deformed sedimentary layering of their host metapelite.

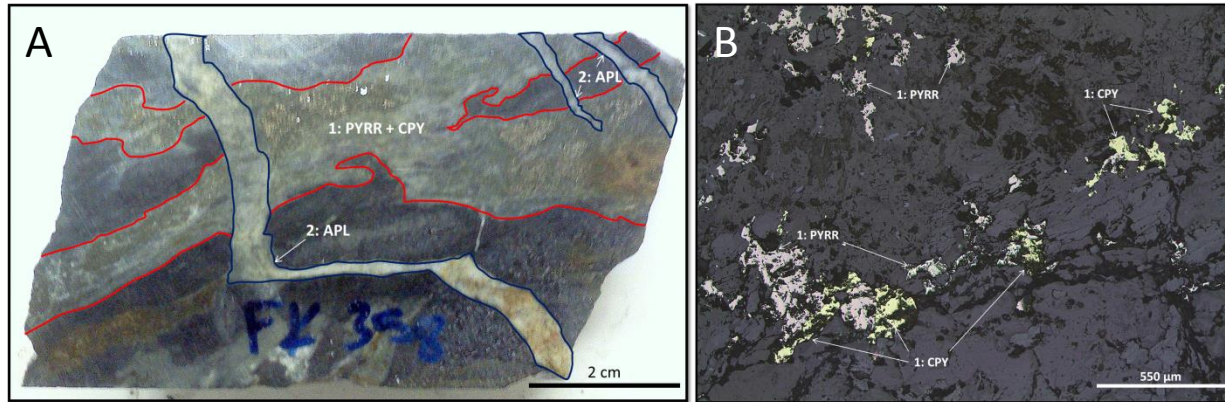


FIGURE 2.5. Hand specimen and photomicrograph textures of Stage 1 mineralization. A: Expression of contact metamorphism within the Yusezyu Formation (Hyland Group) around Dublin Gulch. Reaction of pyrite to pyrrhotite and chalcopyrite is shown above and is restricted to distinct bands (green coloured), which were originally more pelitic. The darker coloured rock type is highly silicified pelite. Aplite veinlets/dykelets, veins and small dykes are common in the hornfelsed zone around the DGS. Sample FK-358 (DDH DG10-407C, 45.50 m, Eagle Zone). B: Photomicrograph of contact metamorphic pyrrhotite (peach-brown) and chalcopyrite (yellow) intergrown, hosted within metapelite of the Hyland Group. Sample FK-358 (DDH DG10-407C, 45.50 m, Eagle Zone). APL = Aplite, CPY = Chalcopyrite, PYRR = Pyrrhotite.

2.2.3 Stage 2: Skarn

Stage 2 is differentiated from Stage 1 due to the fact that heat from the thermal aureole and fluid release from the DGS was required for the formation of Stage 2, while Stage 1 was formed by the thermal aureole alone. During intrusion of the DGS a carbonate roof pendant fell into contact with the partially crystallised magma chamber. The roof pendant contained a limestone horizon, which was reactive with hydrothermal fluids in the uppermost part of the crystallising magma chamber (Fig. 2.6). This event produced a prograde garnet-pyroxene (grossularite-hedenbergite) skarn containing scheelite and minor pyrrhotite. The prograde skarn is locally overprinted by later quartz-actinolite-chlorite-calcite. The skarn has been described in detail by Brown et al. (2002) and this description has been incorporated into the paragenesis presented here. Tungsten in the form of scheelite provides an indicated resource of 12.7 Mt at a grade of 0.31 wt.% WO_3 (SRK Consulting, 2008). The skarn is cross-cut by a series of aplite dykes similar to those observed within the contact metamorphic hornfels elsewhere. Within the skarn, these typically cross-cut remnant bedding and lenses (Fig. 2.6). Previous examinations of the Wolf Zone skarn (Brown et al., 2002; SRK Consulting, 2008) have not recognized any significant gold resource within this zone.

2.2.4 Stage 3: Quartz- K-feldspar Partially Aligned Stockwork Veins

Vein Morphology: Stage 3 veins are the most widespread of any vein type at Dublin Gulch, and formed preferentially in the roof and northern shoulder of the DGS ridge. Veins are concentrated preferentially along the long axis of the pluton ($\sim 070^\circ$). Veins dip steeply to the south-east in an approximate range of $70\text{-}85^\circ$. Stage 3 veins are typically 10-20 mm thick and often occur together in clusters with similar orientation (Fig. 2.7).

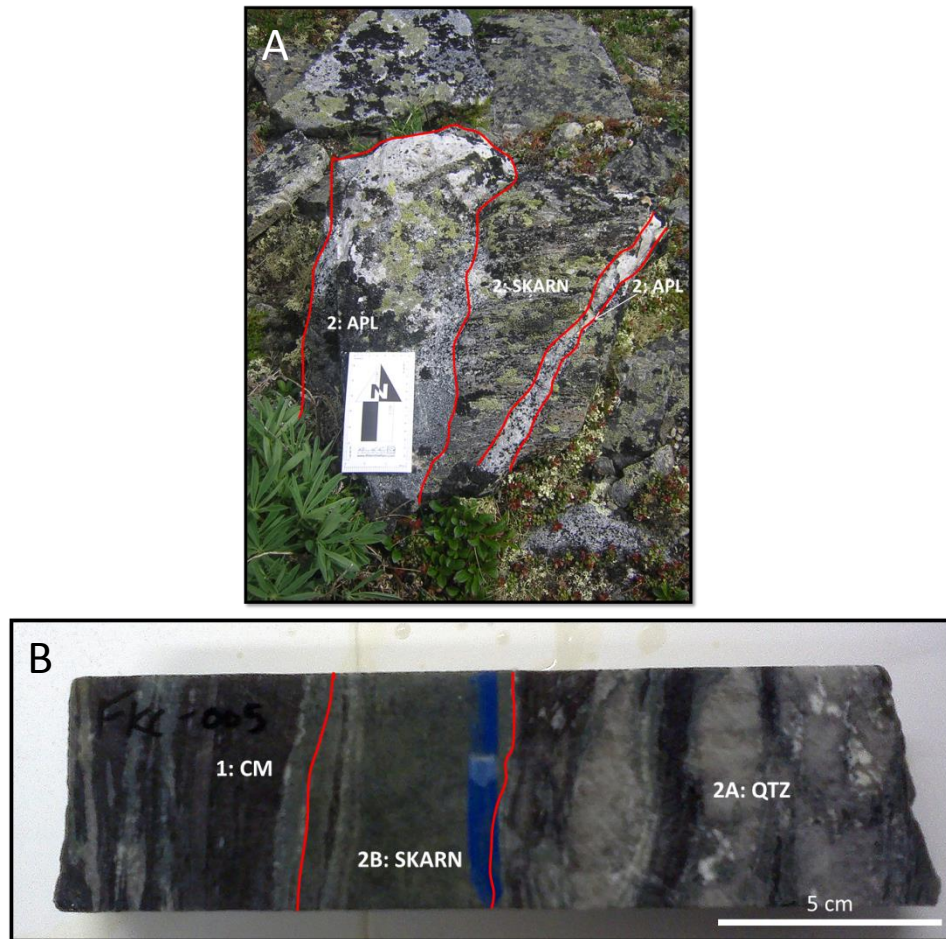


FIGURE 2.6. Field relations and hand specimen textures of Stage 2 mineralization. A: Outcrop of the Wolf Skarn being cross-cut by two aplite dykes (contained within the red boundary lines). Skarn is the lower relief rock type and has a darker (green) hue reflecting the presence of diopside. Scale card is 15 cm long. Location: NAD83 7100502 N 4633780 E, Wolf Skarn Zone. B: Expression of skarn mineralization in diamond drill core, garnet-pyroxene replacement of limestone horizons is the locus for W mineralization as scheelite (2B: green band in core). There is extensive silicification of the metasedimentary rock sequences surrounding the skarn as evidenced by numerous quartz lenses in the diamond drill core. Sample FK-005 (DDH MT08-006, 32.70 m, Wolf Zone). CM = Contact Metamorphosed Yusezyu Formation, QTZ = Quartz, SKARN = Stage 2B Garnet-Pyroxene skarn.



FIGURE 2.7. Field relations of Stage 3 mineralization. A: Outcrop of Stage 3 partially aligned stockwork veins. Veins are typically 1 – 2 cm in width with alteration selvages of 1 – 2 cm on either side of the vein. Veins are spaced ~5 – 10 cm apart and can form in sets of multiple veins over several meters. The example shown is from the oxidized upper 50 m of the DGS, and has potassic alteration selvages. Scale card is 15 cm in length. Location: NAD83 7101566 N 461734 E, Olive Zone. B: Outcrop of quartz and K-feldspar veins hosted by the DGS, example is taken from un-oxidized rock where potassic alteration selvages are present, but not accentuated by later near surface oxidation. Vein geometries are sub-parallel but never mutually cross-cutting in this stage. Veins trend along the long axis of the pluton (070°) and dip steeply ($70 - 85^{\circ}$) to the south east. Location: NAD83 7099754 N 460173 E, Eagle Zone. K-FELD = Potassium Feldspar, QTZ = Quartz.

Stage 3 veins are observed to crosscut the Stage 2 skarn. Stage 3 veins are also commonly the host to overprinting by minerals associated with later fluid stages and show textures of re-fracturing. These specific textures will be discussed in more detail in the sections on the later vein stages.

Gangue Mineralogy: Stage 3 veins are dominated by quartz and K-feldspar, with variable occurrence of calcite and/or siderite (Fig. 2.8). Quartz is purple/pink to colourless and is generally medium grained (0.5 - 2 mm) and euhedral. K-feldspar is white and euhedral with medium grain size. Calcite and/or siderite account for around 5% of the vein volume when they are present. Siderite is generally associated with showings at or near surface and may represent a supergene alteration of hypogene calcite.

Alteration: Alteration selvages are typically restricted to 2 – 20 mm on either side of the veins. Alteration is variable within this vein type from early albitic (in which white albite flanks each vein) to late potassic (in which pink K-feldspar flanks the vein). Potassic selvages are more recognizable in areas where there is greater oxidation, which gives them a rich pink appearance. Supergene oxidation of the veins and pluton is restricted to around 50 m depth from surface for all areas at Dublin Gulch (this is distinct from the Fort Knox property in Alaska, which is oxidized to currently drilled depths (>450 m); A. Bakke, pers. comm. 2013). Generally, albitic selvages are narrower than potassic selvages, averaging 2 – 5 mm versus 5 – 20 mm widths, respectively. Alteration is typically not intense enough to cause destruction of biotite within the host granodiorite, which is deemed typical of “normal” potassic alteration in the porphyry environment (Beane, 1974). The presence of amphibole in Stage 3 veins is unique to those hosted within the skarn.

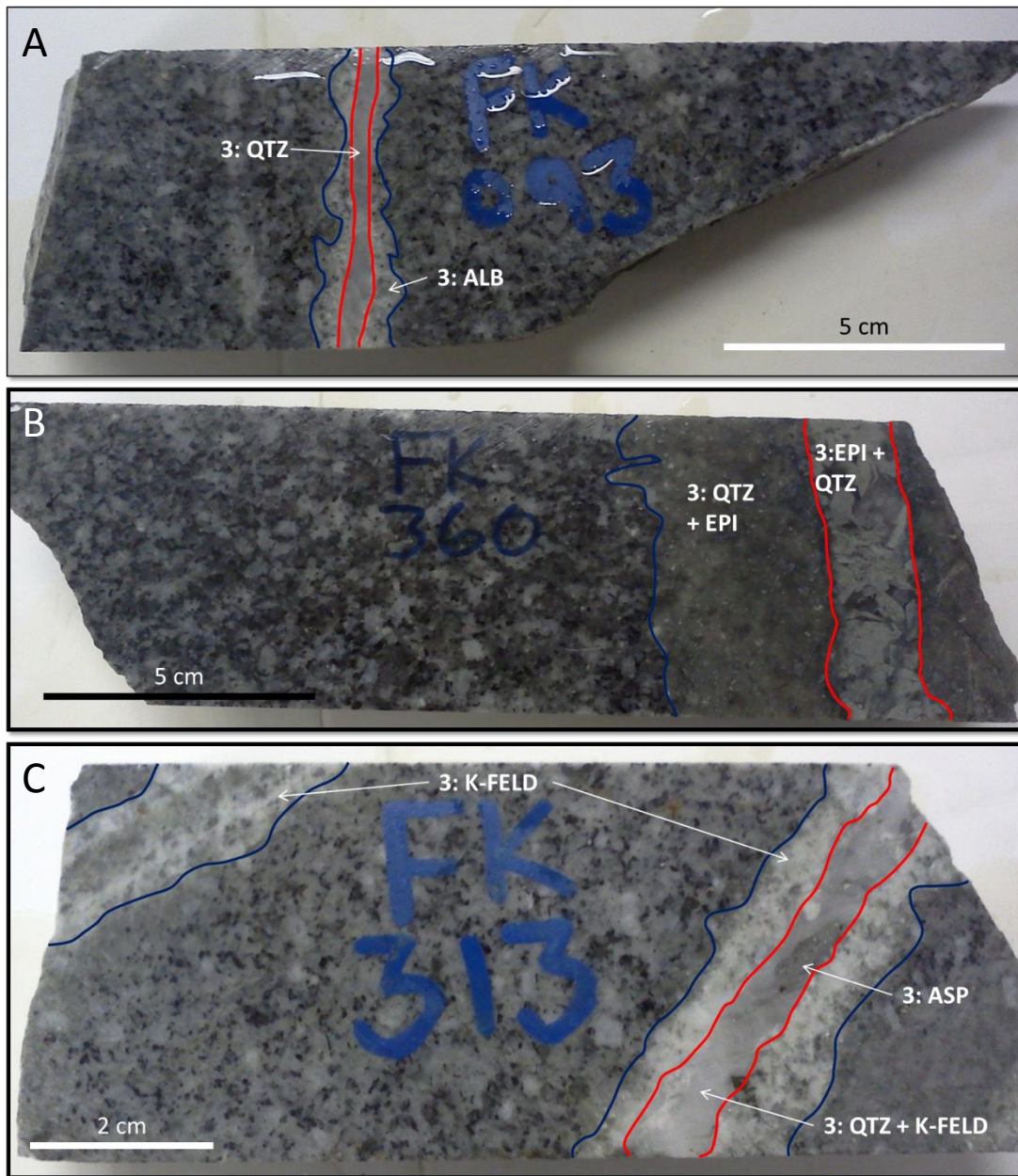
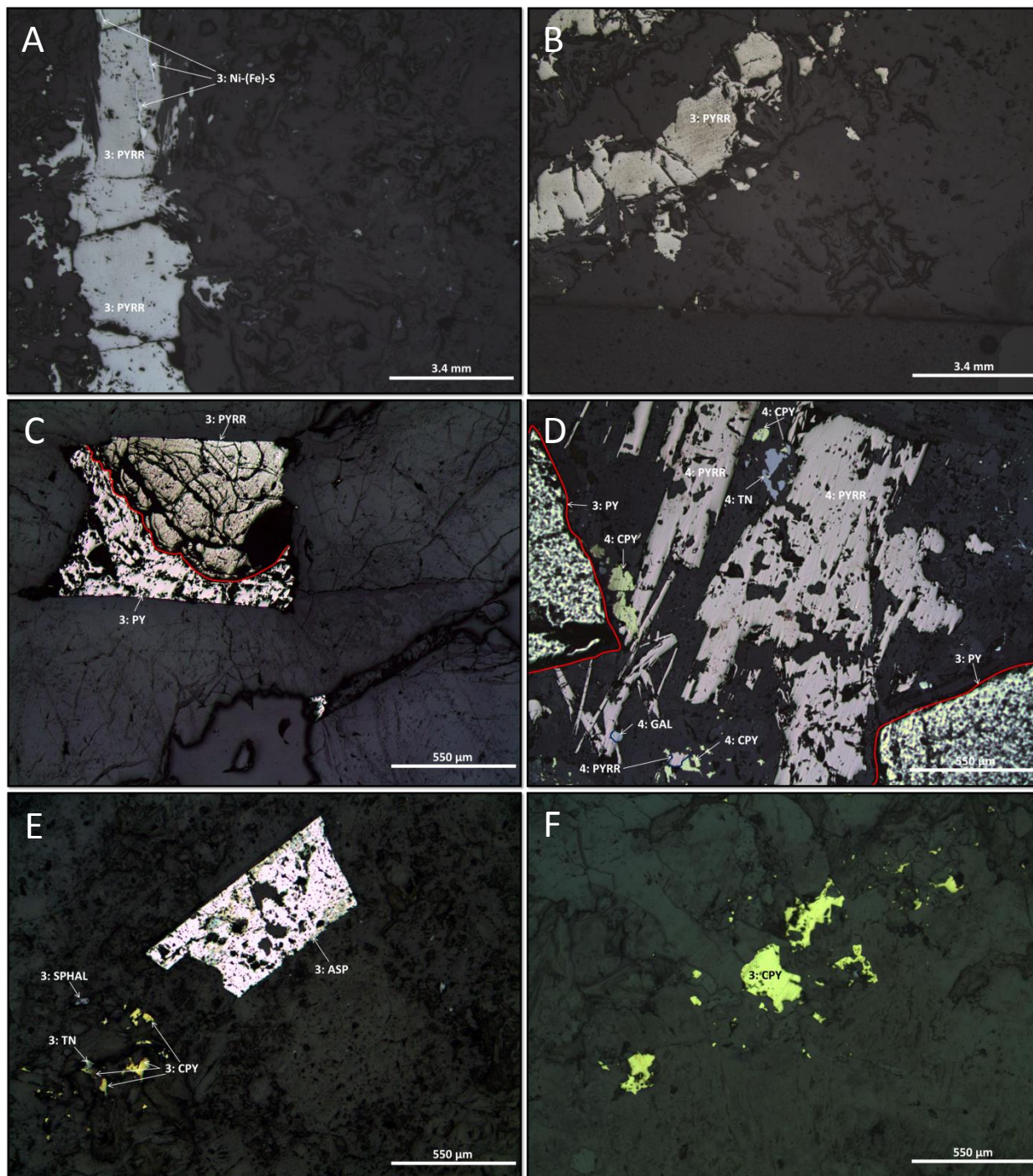


FIGURE 2.8. Hand specimen textures of Stage 3 mineralization. A: Drill core showing an example of a Stage 3 vein dominated by quartz with a restricted albite alteration selvage. Sample FK-093 (DDH DG10-405C, 143.14 m, Eagle Zone). B: Example of uncommon quartz and epidote vein with quartz with minor epidote alteration selvages. Veins of this type are relatively rare, but follow the morphology and occurrence pattern of Stage 3 veins. Sample FK-360 (DDH DG11-463C, 163.35 m, Shamrock Zone). C: Stage 3 quartz and K-feldspar vein (right) with potassic alteration selvages causing destruction of biotite in the host granodiorite. In the left portion of the sample the presence of a vein is indicated only by the alteration selvage showing at surface of cut core. Sample FK-313 (DDH DG11-435C, 210.78 m, Eagle Zone). ALB = Albite, ASP = Arsenopyrite, EPI = Epidote, K-FELD = Potassium Feldspar, QTZ = Quartz.



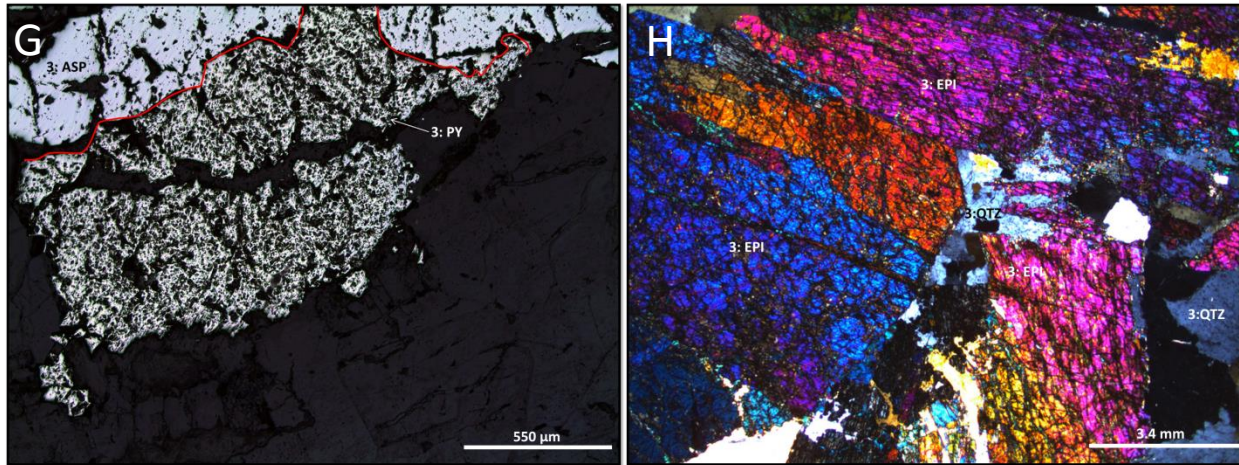


FIGURE 2.9. Photomicrographs of Stage 3 mineralization textures. A: Pyrrhotite with small inclusions of nickel-(iron)-sulfides. Sample FK-096 (DDH DG10-405C, 164.85 m, Eagle Zone) B: Stage 3 pyrrhotite is most commonly present as discrete irregular grains. Sample FK-348 (DDH DG11-435C, 440.52 m, Eagle Zone) C: Stage 3 pyrrhotite being overprinted by later Stage 3 pyrite; demonstrating variable Fe-S mineral stabilities during Stage 3 mineralization. Sample FK-313 (DDH DG11-435C, 210.78 m, Eagle Zone) D: Stage 3 pyrite in a vein which has been re-fractured and mineralised with Stage 4 chalcopyrite, galena, pyrrhotite, and tennantite. Sample FK-099 (DDH DG10-405C, 168.50 m, Eagle Zone) E: Chalcopyrite, when not closely associated with pyrrhotite, is most commonly associated with tennantite ± sphalerite in small clusters of discrete grains. Arsenopyrite is most often present as discrete grains. Sample FK-246 (DDH DG10-373C, 160.60 m, Olive Zone) F: Chalcopyrite in a grouping of discrete grains, the most common texture for all sulfides in Stage 3. Sample FK-313 (DDH DG11-435C, 210.78 m, Eagle Zone) G: Arsenopyrite and pyrite in apparent textural equilibrium. Sample FK-285 (DDH DG10-373C, 277.53 m, Olive Zone) H: Thin section photomicrograph (X-polars) of epidote and quartz from vein shown in Fig. 2.5B. Sample FK-360 (DDH DG11-463C, 163.35 m, Shamrock Zone). ASP = Arsenopyrite, CPY = Chalcopyrite, EPI = Epidote, GAL = Galena, Ni-(Fe)-S = Nickel-(Iron)-Sulfides, PY = Pyrite, PYRR = Pyrrhotite, SPHAL = Sphalerite, TN = Tennantite.

Ore Mineralogy: The sulfide content of Stage 3 veins is typically <2%, and pyrrhotite is the dominant sulfide mineral. It is very commonly intergrown with chalcopyrite, which comprises around 5% of the sulfide content of this stage (Fig. 2.9). Fine-grained scheelite is found disseminated throughout these veins. Molybdenite is also present at modal abundances as high as 2%, occurring with pyrite, or in isolation. Arsenopyrite may comprise up to 5% of some Stage 3 veins – occurring as discrete grains or in close association with pyrrhotite and pyrite. Minor sphalerite and galena (<1%) are present in this stage, typically in association with chalcopyrite (Fig. 2.9D, E). Stage 3 veins hosted within the granodiorite sometimes host native gold, but this was precipitated during later stage mineralization. However, during the course of this study there was no native gold observed within Stage 3 veins that crosscut the skarn. Scheelite is present within Stage 3 veins hosted within both the skarn and granodiorite.

2.2.5 Stage 4: Quartz- Carbonate- Chlorite Veins

Vein Morphology: Stage 4 veins show similar general orientation to Stage 3 veins, with an overall trend of 070°, and with a subsidiary conjugate vein set perpendicular to this trend (Stephens, 2003). Stage 4 veins are typically narrower (2-5 mm) and have a more anastomosing geometry than Stage 3 veins, although they can also be observed in the “partially aligned stockwork” style.

Gangue Mineralogy: Stage 4 contains quartz, chlorite, and calcite as diagnostic minerals, with variable minor amounts of K-feldspar (Fig. 2.10). Chlorite typically occurs as ‘clots’, which are closely associated with pyrrhotite and chalcopyrite (Fig. 2.10A). Calcite is also strongly associated with the clots, which routinely effervesce vigorously when treated with hydrochloric acid.

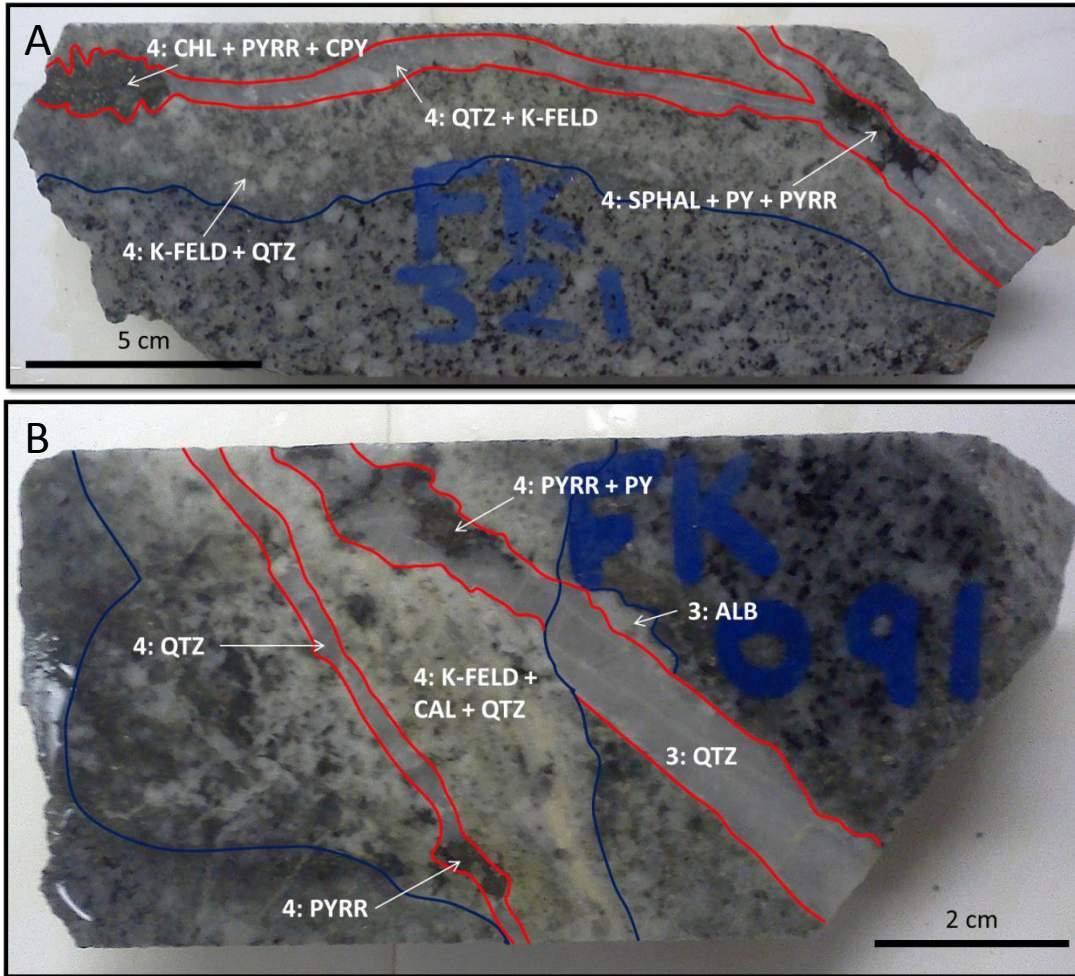
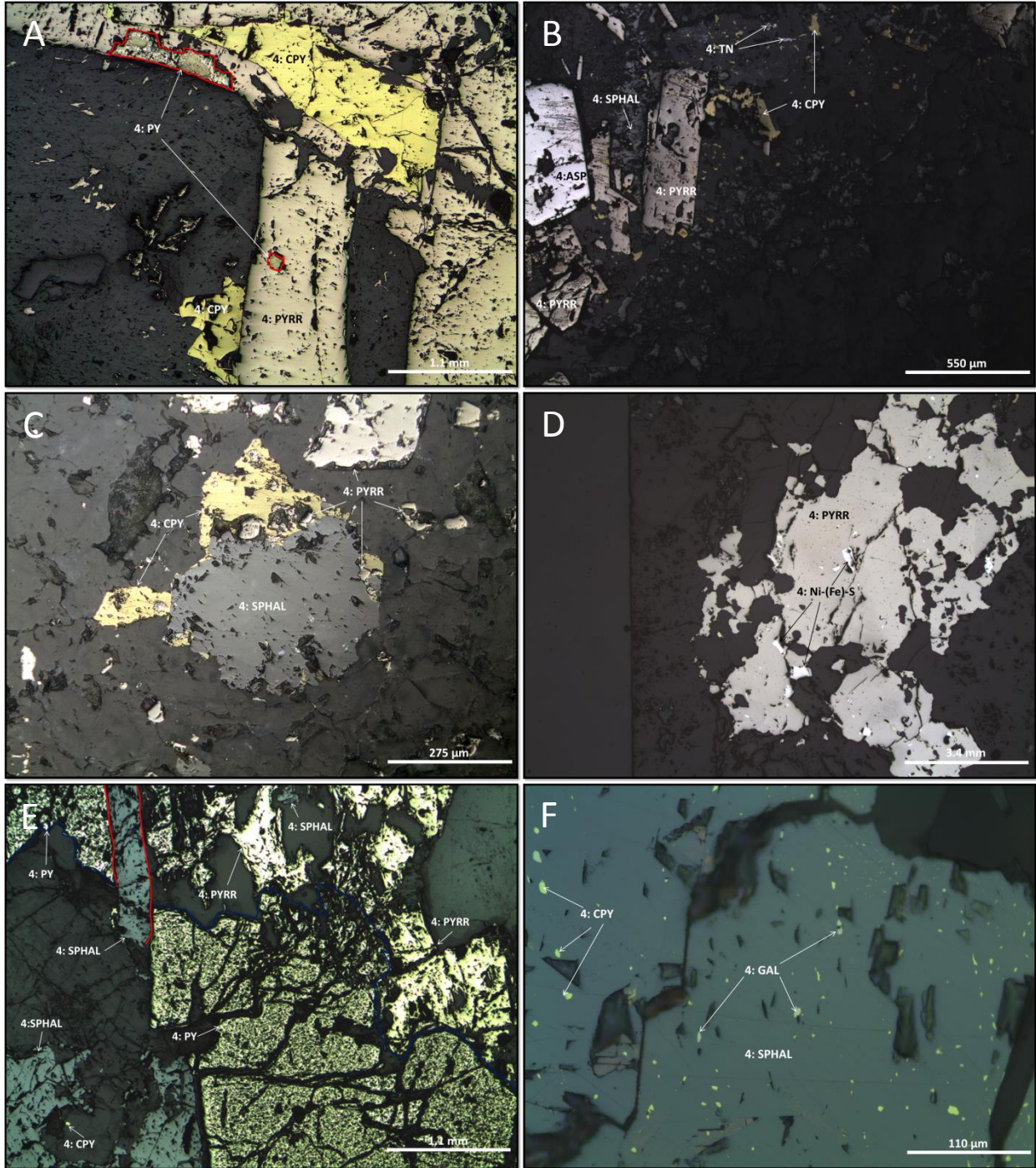


FIGURE 2.10. Hand specimen textures of Stage 4 mineralization. A: Stage 4 mineralization is often concentrated within clots of chlorite and carbonate minerals hosted in quartz and K-feldspar veins. Alteration selvages show complete destruction of biotite in the host granodiorite. Sample FK-321 (DDH DG11-435C, 235.81 m., Eagle Zone) B: Example of the more anastomosing style of Stage 4 veins relative to Stage 3 veins. The Stage 3 vein here is the thicker quartz vein with less extensive alteration selvages. Stage 4 veins exhibit carbonate-rich chlorite clots, which are also rich in sulfides and display concentration of sulfides when cross-cutting or overprinting earlier Stage 3 veins. Sample FK-091 (DDH DG10-405C, 136.93 m, Eagle Zone). ALB = Albite, CAL = Calcite, CHL = Chlorite, K-FELD = Potassium Feldspar, PYRR = Pyrrhotite, PY = Pyrite, QTZ = Quartz, SPHAL = Sphalerite.



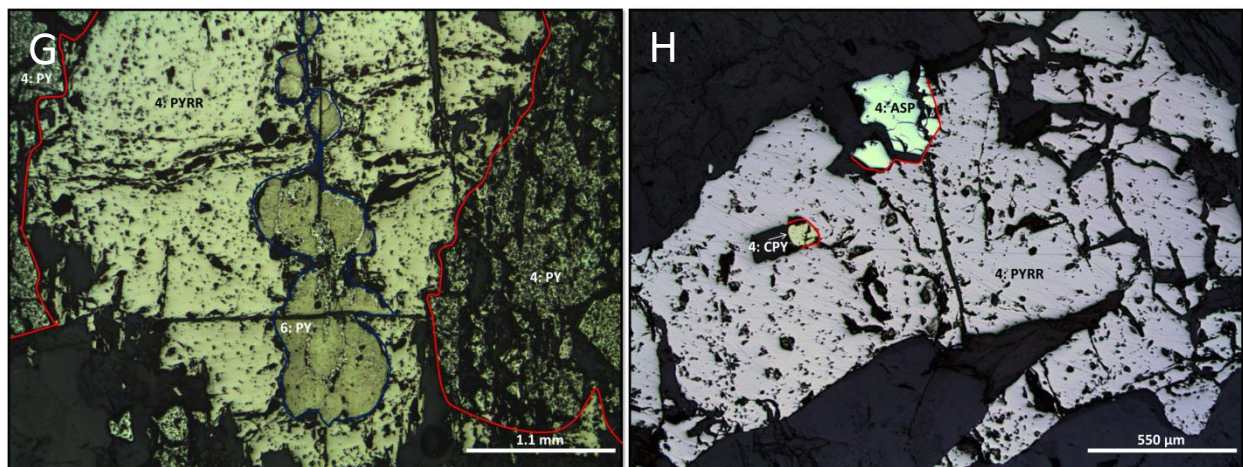


FIGURE 2.11. Photomicrographs of Stage 4 mineralization textures. A: Intergrown chalcopyrite and pyrrhotite is the most common sulfide mineral association of Stage 4 mineralization. Minor pyrite indicates that the Fe-S stability transgressed the pyrrhotite-pyrite boundary during Stage 4. Sample FK-321 (DDH DG11-435C, 235.81 m, Eagle Zone). B: Pyrrhotite with fine grained chalcopyrite and tennantite in association with arsenopyrite. Sample FK-099 (DDH DG10-405C, 168.50 m, Eagle Zone). C: Sphalerite in apparent textural equilibrium with chalcopyrite. Chalcopyrite and sphalerite commonly occur in spatial association with pyrrhotite. Sample FK-359. D: Pyrrhotite with small inclusions of nickel-(iron)-sulfides. This texture is seen in both Stages 3 and 4. Sample FK-314 (DDH DG11-435C, 212.80 m, Eagle Zone) E: Pyrite, pyrrhotite and sphalerite in apparent textural equilibrium. FK-321 (DDH DG11-435C, 235.81 m, Eagle Zone). F: “Disease-like” inclusions of chalcopyrite and galena in sphalerite are very common in Stage 4. Sample FK-321 (DDH DG11-435C, 235.81 m, Eagle Zone). G: Stage 4 pyrite and pyrrhotite, with pyrrhotite cross-cut and partially replaced by Stage 6 colloform pyrite. The refracturing and overprinting of Stage 3 and 4 veins by later veining plays an important role in Au deposition at Dublin Gulch. Sample FK-321 (DDH DG11-435C, 235.81 m, Eagle Zone). H: Pyrrhotite in apparent textural equilibrium with chalcopyrite and arsenopyrite. Sample FK-144 (DDH DG10-409C, 167.42 m, Eagle Zone). ASP = Arsenopyrite, CPY = Chalcopyrite, GAL = Galena, Ni-(Fe)-S = Nickel-(Iron)-Sulfides, PY = Pyrite, PYRR = Pyrrhotite, SPHAL = Sphalerite, TN = Tennantite.

Alteration: Alteration selvages are typically 10 – 30 mm on each side of the vein and are generally more destructive to original orthomagmatic minerals than those accompanying the Stage 3 vein phase (Fig. 2.10B). Biotite is variably altered to chlorite with accompanying K-feldspar and quartz.

Ore Mineralogy: Veins in this stage typically contain 5-10% sulfide minerals, dominated by pyrrhotite (75%) (Fig. 2.11). Chalcopyrite is the next most abundant sulfide (~10%), and is often surrounded by, or intergrown with, pyrrhotite. Where Stage 4 veins cross-cut Stage 3 veins, pyrrhotite is sometimes more prismatic than is typical (Fig. 2.9D). Minor amounts (<5%) of tennantite and chalcopyrite, as latest stage fracture fill and replacements, are present within this stage - which can cause confusion with Stage 5b mineralization vein morphologies in some examples. However, tennantite and chalcopyrite are distinct, in that they occur only in Stage 3 and 4 veins, never as part of Stage 5 or later. Pyrite and arsenopyrite are present in minor amounts (~5%) closely associated with pyrrhotite within the chlorite clots. Sphalerite, intergrown with pyrite and pyrrhotite, also occurs. Sphalerite typically has inclusions of both chalcopyrite and galena, in textures which mimic the semi-oriented “chalcopyrite disease” commonly observed in submarine volcanogenic massive sulfides, implying hydrothermal replacement of sphalerite by these phases (Fig. 2.11F). Substantial wallrock sulfidation reaction is apparent during Stage 4, as seen in examples where veins cross-cut mafic enclaves in the DGS and precipitate sulfides over the entire intersection with the enclave.

A mineralogy report by ALS Minerals (2011) identified the presence of cobaltite and gersdorffite in the Olive Zone. Based on the observed presence of both arsenopyrite and nickel-(iron)-sulfide phases at these stages, these Co-Ni-As minerals are tentatively assigned to Stages 3 and 4.



FIGURE 2.12. Surface exposure of Stage 5a veins. In less than 10% of examples the veins are hosted by metasedimentary rocks of the Yusezyu Formation, with the remaining 90% hosted by the DGS. The example shown is located east of the Potato Hills near a smaller intrusive body believed to be genetically linked to the DGS. Location: NAD83 465970 E 7102570 N, East of Potato Hills. ASP VEIN = Arsenopyrite Vein, YU FM = Yusezyu Formation.

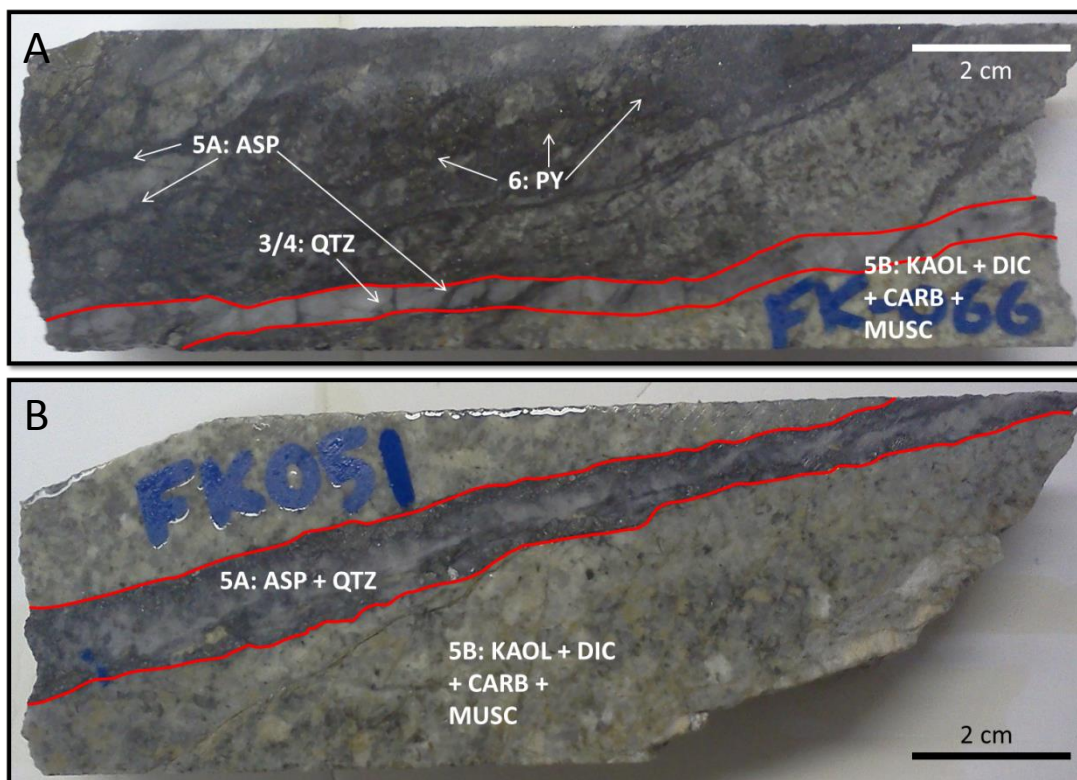


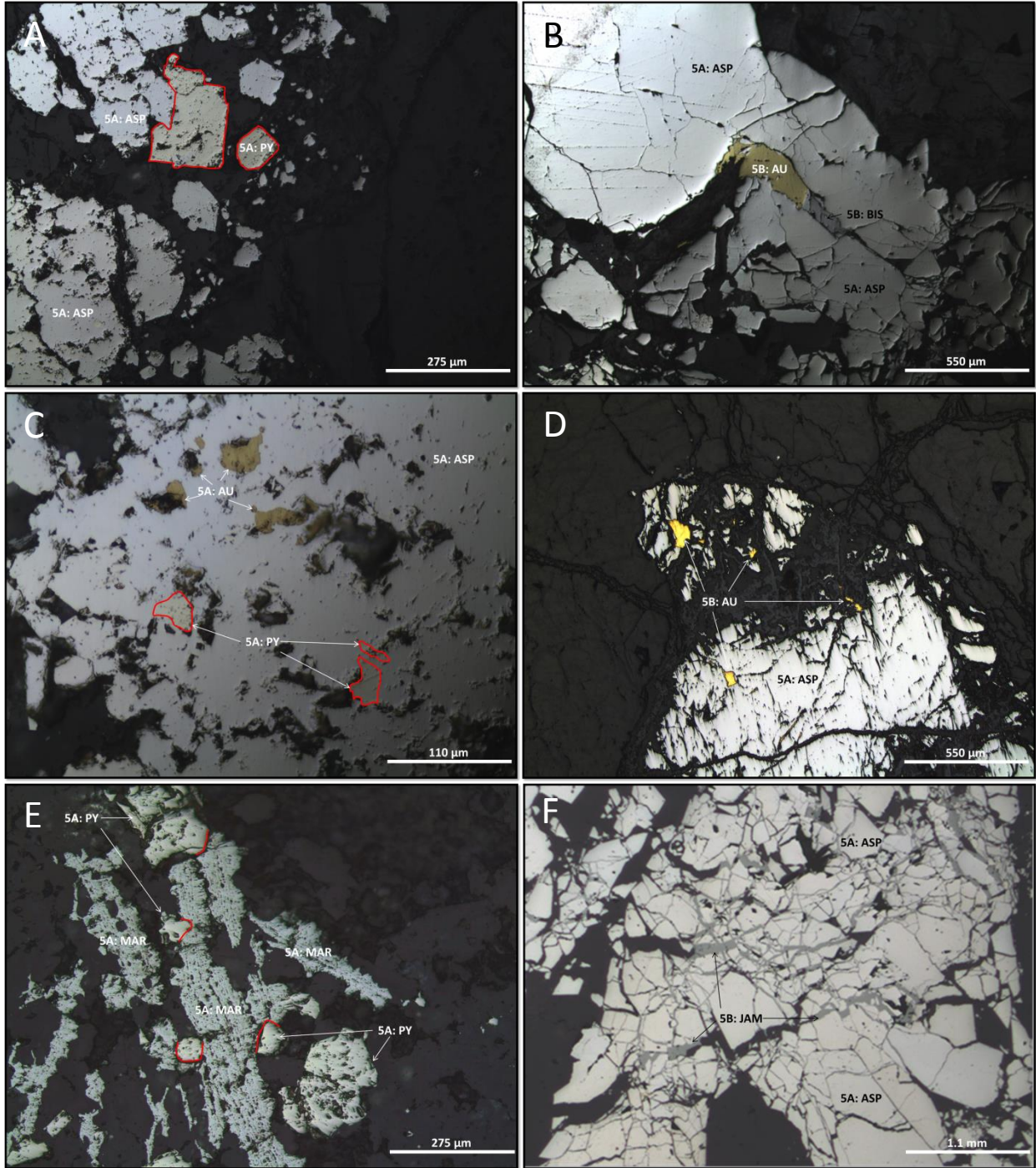
FIGURE 2.13. Hand specimen textures of Stage 5 mineralization. A: example of Stage 5a arsenopyrite vein fracturing and flooding an area of earlier Stage 3 partially aligned stockwork quartz- K-feldspar veins. Stage 3 vein margins are marked in red. Sample FK-066 (DDH DG10-377C, 199.70 m, Shamrock Zone) B: Example of less extensive flooding of Stage 5a arsenopyrite, but with more intense recrystallization of quartz from an earlier Stage 3 vein. Outer selvage is characteristic of Stage 5b type alteration. Sample FK-051 (DDH DG10-377C, 104.98 m, Shamrock Zone). ASP = Arsenopyrite, CARB = Carbonate, DIC = Dickite, KAOL = Kaolinite, MUSC = Muscovite-Phengite, QTZ = Quartz.

2.2.6 Stage 5a: Arsenopyrite-rich Veins

Vein Morphology: Stage 5 veins were first exploited during the Klondike Gold Rush of 1895 and into the early 20th Century (Wardrop Engineering Inc., 2012). Some workings and equipment from this time remain visible at Dublin Gulch. These veins show the same orientation as the preceding vein stages with an overall broad orientation of 070°. Vein fillings are dominated (up to 100%) by arsenopyrite with associated quartz (Fig. 2.12). Veins trend in a parallel nature for the entire length of the DGS and are spaced at around 30-50 m (north-south gap). They are typically 5 to 50 cm wide, with minor secondary veins 2-5 cm wide in close proximity to larger “master” veins. Micro-fractures filled with arsenopyrite and/or pyrite extend away from these larger veins. Stage 5a commonly overprints earlier veins, particularly those of Stage 3 - with examples of Stage 3 veins with a flank of arsenopyrite mineralization common (Fig. 2.13).

Gangue Mineralogy: Quartz is the only significant gangue mineral associated with this stage, occurring as a fine-grained matrix to the arsenopyrite. However, there is significant recrystallized quartz in examples, which are reoccupying and replacing earlier Stage 3 and 4 veins. This vein stage is also the predominant host to significant volumes of Stage 5b mineralization and shows Stage 5b alteration in 60-70% of examples. However, there are multiple examples of Stage 5a veins with no alteration other than quartz.

Ore Mineralogy: Arsenopyrite is the dominant sulfide in this stage, with some veins approaching 100% modally for arsenopyrite (Fig. 2.14). Arsenopyrite grains are usually highly fractured, even where it is the dominant mineral phase, and the fractures are typically filled with supergene (Stage 8) scorodite alteration of arsenopyrite. Minor pyrite and marcasite are present in the examples of this vein stage that lack Stage 5b alteration, but are texturally later than



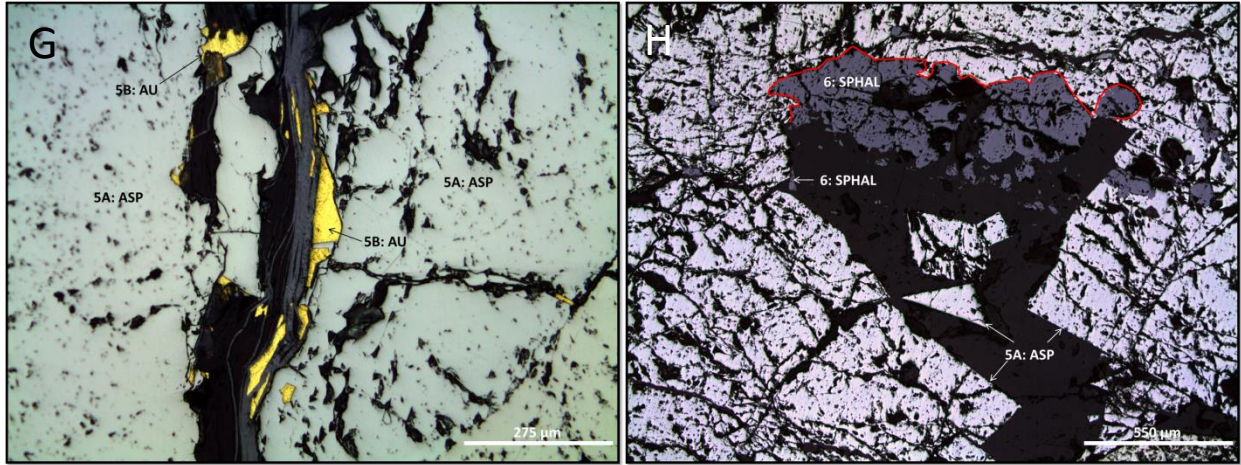


FIGURE 2.14. Photomicrographs of Stages 5 & 6 mineralization textures. A: Arsenopyrite in apparent textural equilibrium with pyrite. Sample FK-066 (DDH DG10-377C, 199.70 m, Shamrock Zone) B: Native gold and bismuthinite occupying a fracture within earlier arsenopyrite. Sample FK-051(DDH DG10-377C, 104.98 m, Shamrock Zone) C: Native gold and pyrite “locked” within arsenopyrite. Sample FK-066 (DDH DG10-377C, 199.70 m, Shamrock Zone) D: Native gold filling fractures and cavities in earlier arsenopyrite. Sample FK-TH12-41 (NAD83 460207 E 7100120 N, Eagle Zone) E: Occurrence of marcasite interpreted as a transition from pyrite stability to marcasite stability in latest Stage 5a. FK-359 (DDH DG11-465C, 172.52m, Shamrock Zone) F: Jamesonite filling fractures within earlier Stage 5a arsenopyrite. Sample FK-036 (DDH DG10-377C, 33.83 m, Shamrock Zone) G: Native gold precipitated on the margins of a fracture-filling vein in arsenopyrite. Sample FK-226 (DDH DG10-373C, 80.33 m, Olive Zone) H: Stage 6 sphalerite filling fractures and overgrowing Stage 5a arsenopyrite. Sample FK-285 (DDH DG10-373C, 277.53 m, Olive Zone). AU = Native Gold, ASP = Arsenopyrite, BIS = Bismuthinite, JAM = Jamesonite, MAR = Marcasite, PY = Pyrite, SPHAL = Sphalerite.

arsenopyrite, filling grain fractures. The morphology of pyrite and marcasite can be seen as transitional, suggesting that the conditions during precipitation transgressed the boundary between pyrite and marcasite stability (Fig. 2.14E). Arsenopyrite from this stage shows a definably different stoichiometry and trace element assemblage than arsenopyrite of Stage 3 (see Chapter 3, below), including some Stage 3 veins with Stage 5b alteration that contain later Stage 5a arsenopyrite. Micro-inclusions of galena and tetradymite within Stage 5a arsenopyrite were identified with EPMA.

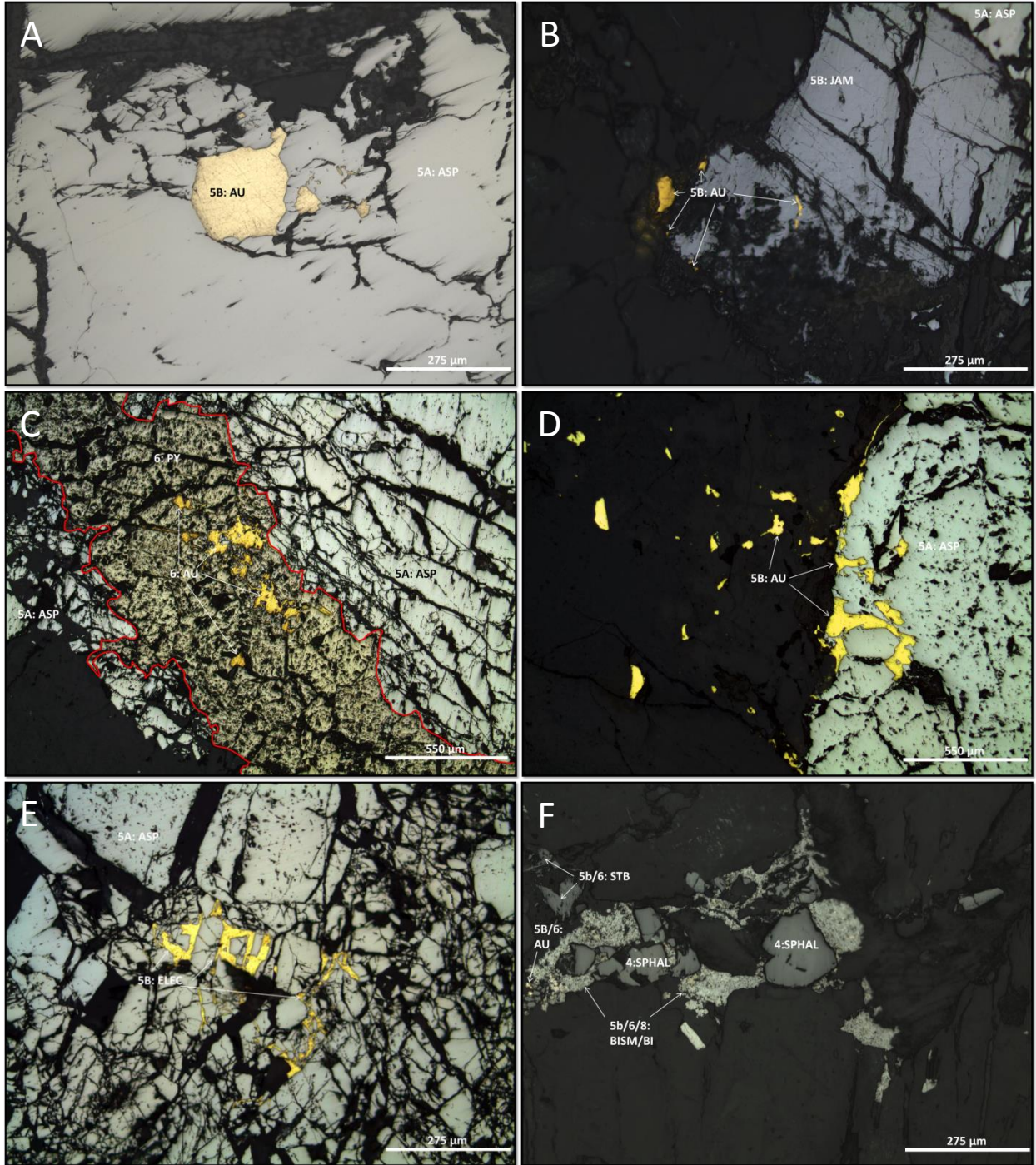
2.2.7 Stage 5b: Au-rich Stage

Vein Morphology: Examples of individual veins that contain exclusively the Stage 5b assemblage are rare. More commonly, the Stage 5b assemblage is observed replacing and overprinting minerals in earlier vein stages, which provided the necessary pre-existing plumbing for these fluids to permeate. Sulfide abundance appears to be $\leq 1\%$ in the Stage 5b assemblage, although estimation is difficult given that the assemblage is largely hosted by veins of earlier stages. Stage 5b is recognized by its associated alteration assemblage.

Alteration: Alteration associated with this stage is the most intense seen at Dublin Gulch. In core, the alteration extends from centimetres to several metres from the individual vein or vein set. Width of alteration increases as a function of vein density, suggesting that in areas of partially aligned stockwork veins (Stage 3), the fluid is reoccupying these earlier veins and causing a more widespread alteration front, rather than discrete vein selvages. In hand specimen, the alteration consists of carbonate and sericite. Petrographically, alteration minerals are typically intergrown and are pervasive, overprinting all primary magmatic and earlier hydrothermal textures. Orthomagmatic minerals are typically entirely replaced, especially feldspar minerals,

and/or recrystallized as quartz. The alteration assemblage also contains significant amounts of coarse white mica. White mica is typically interspersed with sericite and clay minerals, but does form discrete grain clusters in some places. Alteration minerals generally surround ore minerals and native gold completely. An exception to this is where ore minerals are hosted within fractured sulfides belonging to earlier vein stages. While the alteration assemblage displays a high degree of localized homogeneity, no clear pattern of mineral zoning with respect to mineralization is present. TerraSpec analysis revealed that alteration contained sericite/white mica that was variable within the muscovite-phengite series, as well as clay minerals that were transitional between dickite and kaolinite. Abundant pyrophyllite was identified in areas of intense sericitic alteration by ALS Minerals (2011), with textures broadly similar to those described above.

Ore Mineralogy: Ore mineralization associated with this stage is usually cryptic in hand specimen (aside from the associated extensive alteration) as it usually replaces existing sulfide mineralization from earlier vein stages. However, this is the stage during which the most significant Au and Bi endowment occurred at Dublin Gulch. Mineralization comprises a group of sulfosalt minerals predominated by Pb-Fe-Bi-Sb-As phases (Fig. 2.15). The most common sulfosalts present are jamesonite and boulangerite, which can be typically seen in a mutually intergrown relationship (Appendix B2.B). Bournonite, freibergite-tetrahedrite, madocite, and ullmannite are also present in the Olive and Shamrock zones (ALS Minerals, 2011). Jamesonite, boulangerite, and bournonite are sometimes observed intergrown with bismuthinite, electrum, and native gold in granular clusters, particularly when overprinting earlier vein sets (Fig. 2.15). Bismuth occurs predominantly as bismuthinite, which is variably altered to native bismuth in a



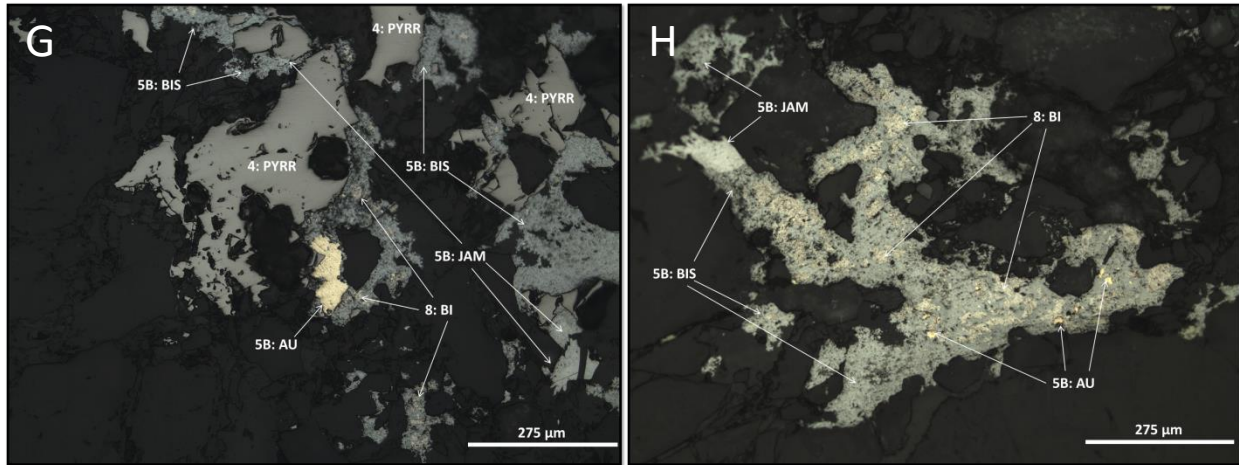


FIGURE 2.15. Photomicrographs of Stages 5b & 6 native gold textures. A: Stage 5b native gold “locked” within the edge of an arsenopyrite grain. Sample FK-TH12-41(NAD83 460207 E 7100120 N, Eagle Zone) B: Stage 5b native gold with jamesonite that overgrows earlier arsenopyrite. Sample FK-TH12-41 (NAD83 460207 E 7100120 N, Eagle Zone) C: Stage 6 native gold in association with pyrite, which is cross-cutting earlier arsenopyrite. Sample FK-025 (DDH DG10-377C, depth 9.10 m, Shamrock Zone) D: Stage 5b native gold fracture-filling and overgrowing arsenopyrite. This is the most common texture for native gold in association with arsenopyrite. Sample FK-226 (DDH DG10-373C, depth 80.33 m, Olive zone) E: Stage 5b electrum fracture-filling arsenopyrite. Sample FK-025 (DDH DG10-377C, depth 9.10 m, Shamrock Zone) F: Stage 5b native gold with native bismuth, bismuthinite, and stibnite that nucleated on earlier Stage 4 sphalerite. Sample FK-144 (DDH DG10-409C, depth 167.42 m, Eagle Zone) G: Native gold with native bismuth, bismuthinite, and jamesonite, all overgrowing earlier Stage 4 pyrrhotite. It is very common, particularly in the Eagle Zone, for native gold, which is hosted in overprinted Stage 3 and 4 veins to show this texture. Sample FK-144 (DDH DG10-409C, depth 167.42 m, Eagle zone) H: Grain cluster of native gold with native bismuth, bismuthinite, and jamesonite in an overprinted Stage 4 vein. As in 2.15 G., native bismuth commonly occurs as mottled grains within host bismuthinite. Sample FK-144 (DDH DG10-409C, depth 167.42 m, Eagle Zone). AU = Native Gold, ASP = Arsenopyrite, Bi = Native Bismuth, BIS = Bismuthinite, JAM = Jamesonite, PY = Pyrite, PYRR = Pyrrhotite.

mottled texture (Fig. 2.15H). Bismuthinite is generally texturally distinct from the sulfosalt minerals of this stage.

Native gold is observed as 1) discrete grains on the edges, or within fractures, of sulfide minerals from earlier stages - particularly Stage 5a arsenopyrite (Fig. 2.15A, D); 2) in apparent textural equilibrium with sulfosalt minerals (Fig. 2.15B); 3) associated with Stage 6 pyrite that cross-cuts Stage 5a arsenopyrite (Fig. 2.15C); and 4) associated with granular clumps of native bismuth-bismuthinite (Fig. 2.15F, G, H). Electrum (Fig. 2.15E) is more common in the paragenetically latest part of Stage 5b, and in more distal zones of the deposit. Native gold is generally found in highest concentrations as paragenetically and texturally distinct grains but, when found in association with other minerals, native gold is in highest concentrations where it is present with bismuthinite/native bismuth. Sulfide and sulfosalt minerals are relatively sparse during this stage, accounting for only 1-2 modal percent of the contents of Stage 5b veins plus selvages.

Table 2.3 shows examples of assays of Stage 5 vein material from various zones around the Dublin Gulch deposit. These imply that Au can be present in high grades with, or without, the presence of an elevation in associated elements. For example, sample N821761 contains 189.5 ppm Au with 54 ppm Bi, while sample N821757 contains 155.5 ppm Au with 3740 ppm Bi. This geochemical pattern is a consequence of the locally variable modality of mineral associations of native gold described above, and reflects the overall heterogeneity of this stage of mineralization if examined only on a sample by sample basis.

TABLE 2.3. Table showing geochemical analysis of individual vein samples of Stage 5 vein material from various locations around the Dublin Gulch deposit.

Sample	Location (NAD83)		Zone	Au ppm	Ag ppm	As ppm	Bi ppm	Cd ppm	Co ppm	Cu ppm	Fe %	Mn ppm	Mo ppm	Ni ppm	Pb ppm	S %	Sb ppm	W ppm	Zn ppm
N821751	465970	7102570	Potato Hills	5.68	0.6	>10000	149	<0.5	32	17	10.8	80	<1	3	7	4.72	62	<10	4
N821752	460207	7100120	Eagle	3.43	<0.5	>10000	<2	<0.5	33	4	10	81	<1	<1	9	4.99	43	<10	3
N821753	465970	7102570	Potato Hills	12.1	1.4	>10000	314	<0.5	54	12	18.65	51	<1	5	19	8.96	126	<10	<2
N821754	464121	7102652	Potato Hills	11.3	48.9	>10000	43	1.3	<1	298	23	13	<1	<1	7300	0.82	956	10	319
N821755	460402	7101085	Henderson	24.8	10.5	>10000	128	<0.5	1	55	14.25	102	<1	1	346	2.21	244	<10	3
N821757	462279	7101968	Shamrock	155.5	370	>10000	3740	6.7	4	72	20.7	24	<1	<1	8560	9.42	4530	20	946
N821758	462536	7102108	Shamrock	21.5	14.8	>10000	288	1.1	<1	21	5.62	69	4	2	596	0.25	343	100	59
N821759	462279	7101968	Shamrock	40.7	124	>10000	758	2	4	94	20.9	60	<1	<1	6900	>10.0	3350	40	72
N821760	461760	7101417	Olive	64	8.6	>10000	16	<0.5	1	7	17.1	50	4	<1	72	1.04	141	10	20
N821761	461759	7101530	Olive	189.5	11.4	>10000	54	<0.5	13	5	5.74	244	122	19	141	2.26	311	20	38
N821762	461759	7101530	Olive	86.8	7.9	>10000	121	<0.5	13	6	5.53	73	144	15	172	2.38	121	150	21
N821763	452637	7098513	Rex Peso	0.971	66.9	>10000	1580	15.3	3	1050	16.5	88	<1	<1	9570	1.28	6040	<10	55

Notes: Zone locations are shown in Figure 2.3. Analyses were conducted by ALS laboratories, Vancouver, Canada. All elements, except for Au, were tested using the ME-ICP61 ICP- AES Analysis Package. Au was determined using the Au-AA24 Fire Assay Fusion method for samples <10 ppm and Au-GRA22 Gravimetric Analysis for Samples >10 ppm. Samples which yielded Ag values greater than >100 ppm using the ME-ICP61 method were subsequently tested using the Me-OG62 Four Acid Digestion with Conventional ICP- AES Analysis Package. Sample numbers quoted are those used by Victoria Gold Corporation for shipment of the samples. Upper and lower limits of detection for each element and method are quoted in Appendix C.1.

2.2.8 Stage 6: Pyrite-Sulfosalt Veins

Vein Morphology: Stage 6 mineralization is dominated by pyrite, which has a nominally similar vein morphology to Stage 5a arsenopyrite, but can be seen cross-cutting Stage 5a arsenopyrite (Fig. 2.16). Veins routinely approach 100% sulfide minerals, with minor quartz in some examples – and typically occupy microfractures within earlier vein structures, or within the alteration zones surrounding earlier veins. When distinct Stage 6 veins form within the DGS granodiorite, they are generally only 10-20 mm thick. However, rare examples of this vein type are up to 75 cm thick and dominated by sulfosalts, which visibly replace pyrite (Fig. 2.17G). Alteration selvages are similar to those of Stage 5b.

Ore Mineralogy: Pyrite, sphalerite, jamesonite, and boulangerite are the dominant ore minerals associated with this stage. Native gold and electrum are also present, but in lesser abundance than Stage 5b. This vein stage has some mineral assemblage affinities with Stage 5b, but forms distinct veins that can be seen cross-cutting Stage 5a and 5b veins, giving rise to its classification as a distinct vein stage.

In the samples examined, all other Stage 6 ore minerals uniformly postdate pyrite. Figure 2.17 shows the commonly observed texture of sphalerite, jamesonite, and/or boulangerite filling fractures within earlier pyrite.

2.2.9 Stage 7: Late Stage Carbonate Veins

Late stage carbonate crack-seal veins cross-cut every other vein type at Dublin Gulch. It is unclear whether these veins are associated with continued hydrothermal activity during the cooling of the DGS or the result of hydrothermal or orogenic activity that significantly post-dated intrusion-related vein stages.

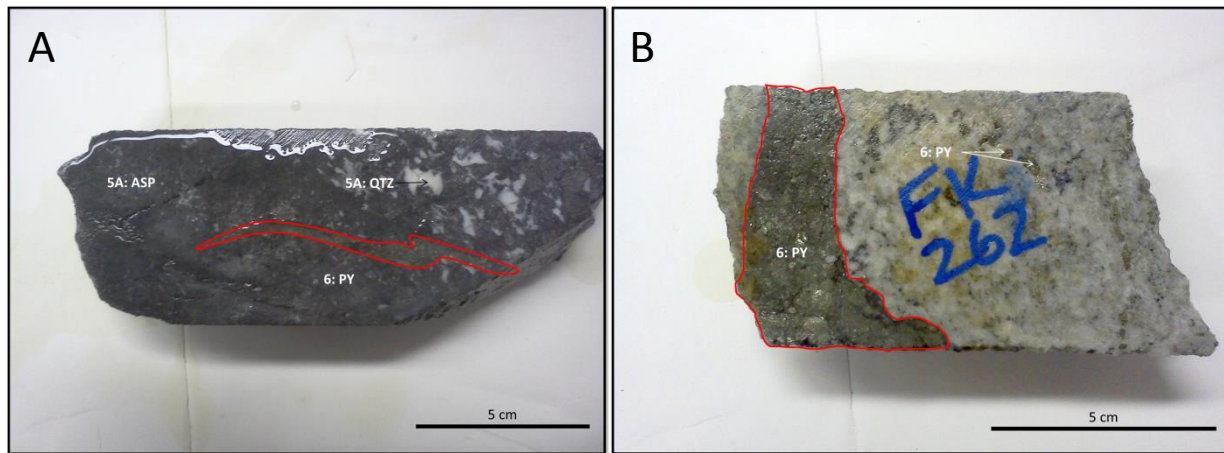
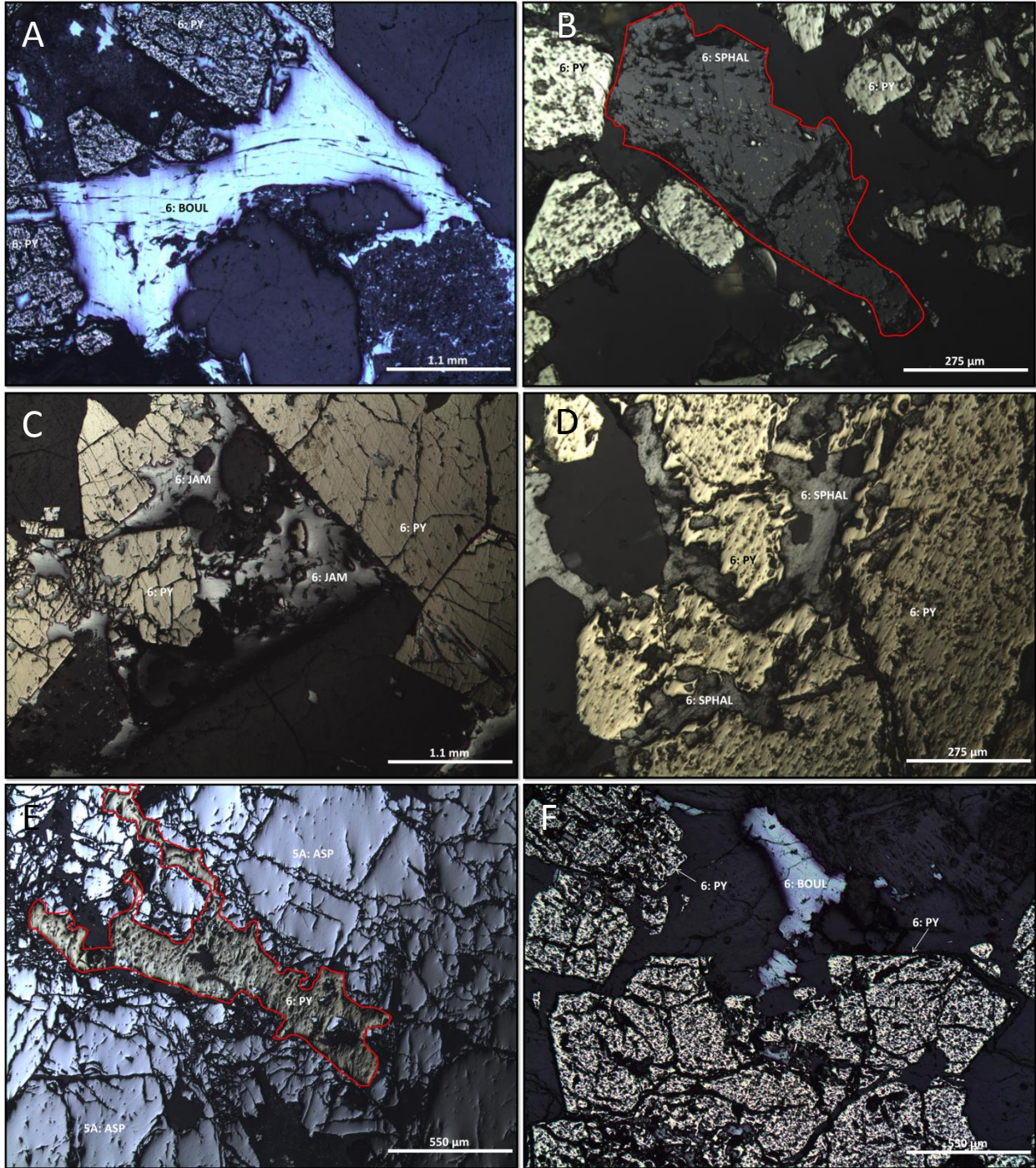


FIGURE 2.16. Hand specimen textures of Stage 6 mineralization. A: Stage 6 pyrite cross-cutting Stage 5a arsenopyrite and quartz. Sample FK-025 (DDH DG10-377C, depth 9.10 m, Shamrock Zone) B: Stage 6 pyrite cross-cutting the DGS. Alteration for Stages 5b and 6 are indistinguishable from each other and are pervasive, consisting of carbonate, clay (dickite, kaolinite, and pyrophyllite), and muscovite-phengite. Sample FK-262 (DDH DG10-373C, depth 194.75 m, Olive Zone). ASP = Arsenopyrite, PY = Pyrite, QTZ, Quartz.



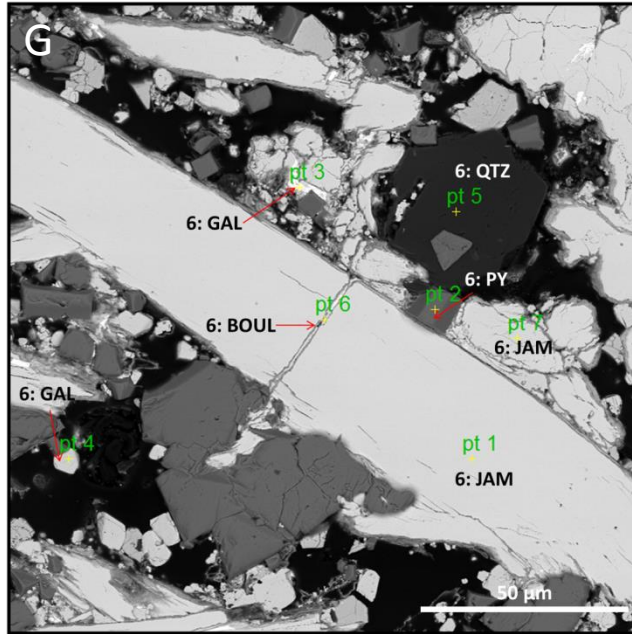


FIGURE 2.17. Photomicrographs and back-scattered electron images of Stage 6 mineralization textures. A: Boulangerite fracture-filling and overgrowing early Stage 6 pyrite grains. Sample FK-258 (DDH DG10-373C, depth 188.76m, Olive Zone) B: Pyrite, and associated sphalerite with inclusions of galena and chalcopyrite. Sample FK-TH12-49 (DDH DG12-493C, depth 351.00 m, Shamrock Zone) C: Jamesonite fracture-filling and overgrowing early Stage 6 pyrite. Sample FK-285 (DDH DG10-373C, depth 277.53 m, Olive Zone) D: Sphalerite fracture-filling early Stage 6 pyrite. Sample FK-258 (DDH DG10-373C, depth 188.76m, Olive Zone) E: Stage 6 pyrite cross-cutting earlier Stage 5a arsenopyrite. Sample FK-TH12-10 (NAD83 463325 E 7100348 N, Wolf Skarn Zone) F: Boulangerite associated with Stage 6 pyrite. Sulfosalt minerals in Stages 5b and 6 are commonly discrete grains which are proximal to earlier arsenopyrite or pyrite, respectively – but do not display mutual intergrowth or other intimate textural association. Sample FK-258 (DDH DG10-373C, depth 188.76m, Olive Zone) G: Back-scattered electron (SEM-BSE) image of jamesonite fracture-filled by boulangerite. Sample FK-TH12-03 (NAD83 458145E 7100551N, Haggart Creek). BOUL = Boulangerite, JAM = Jamesonite, QTZ = Quartz, PY = Pyrite, SPHAL = Sphalerite.

2.2.10 Stage 8: Supergene Alteration

The most economically significant supergene process was the conversion of arsenopyrite to scorodite (Fig. 2.18). The presence of scorodite provides a useful tool for prospecting, as it creates a very distinctive apple green colour gossan, making rocks containing Stage 3, 4, and 5a veins very easily identifiable in outcrop (and in core from the roof of the DGS). Combined with the knowledge that arsenopyrite is genetically associated with Stage 5 gold and is a pathfinder mineral for Stage 6 gold, this becomes an incredibly useful feature. Where supergene alteration has affected bismuth minerals a rim of As-Bi alloy has sometimes formed. Bismuthinite is also commonly altered to native bismuth, with the bismuth forming a mottled texture within the bismuthinite grain. The “oxidation” observed in the roof of the DGS – and the immediate hanging wall within the Hyland Group - is interpreted as supergene alteration as it exists pervasively within 50 m of present surface in most of the study area. The alteration of pyrite to hematite, calcite to siderite and extensive limonite/gossan weathering is also observed in this zone.

2.2.11 Brief Discussion of Rex Peso Veins

Rex-Peso is a historically recognized area of significant silver-rich mineralization immediately adjacent to the west of the DGS. The veins at Rex-Peso are hosted entirely within the Hyland Group metasediments. The Rex Zone (Fig. 2.3) was drilled by Victoria Gold Corp in 2011. However, no plutonic rock was intersected at drilled depths of up to 163 m from surface. Selected samples from 2011 drill holes showed that silver mineralization was associated with a dominantly quartz-pyrite-siderite vein type at depth. There are also minor volumes of jamesonite and boulangerite associated with these veins. The ore mineralogy of the Ag rich- veins in the

Rex and Peso zones have some affinities to Stage 6 mineralization, however, no clear link between DGS-proximal mineralization and Rex-Peso mineralization exists at this time.

The presence of distinct veining within the Hyland Group suggests that there is a concealed pluton below, which spawned hydrothermal veining to produce the Ag mineralization. Tempelman-Kluit (1964) estimated that the Haggart Creek Fault (Fig. 2.3) may represent around 1000 feet (300 m) of vertical displacement, with the eastern side being downthrown relative to the west, based on displacement of lithologies and differing foliations on either side of the fault. These observations would fit with a model in which the eastern-most extension of the DGS and associated mineralization lies at depths of over 300 m below current surface levels in the Rex-Peso Zone.

Although Rex-Peso was not evaluated in detail during this study, its general characteristics were considered in comparison to the other mineralization at Dublin Gulch in the discussion below.

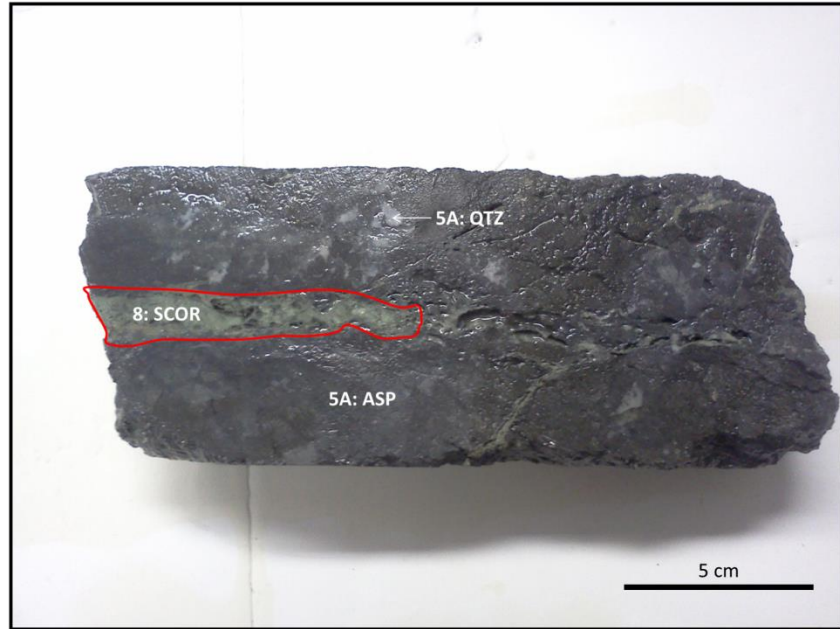


FIGURE 2.18. Example of the most common supergene alteration of sulfide minerals at Dublin Gulch - the replacement of arsenopyrite by apple-green coloured scorodite. Scorodite is a highly useful tracer mineral in surficial exploration for high grade Au veins within 50m of present surface at Dublin Gulch. Sample FK-024 (DDH DG10-377C, depth 6.96 m, Shamrock Zone). ASP = Arsenopyrite, QTZ = Quartz, SCOR = Scorodite.

2.3 Geostatistical Analysis of Assay Data

2.3.1 Introduction

Assay Database: All geostatistical analysis was performed on the current assay database of Victoria Gold Corp. consequent to exploration and development drilling at Dublin Gulch. The database comprises analyses performed since 2009 by ALS Laboratories in Vancouver, Canada for the current operator Victoria Gold Corp. - as well as historical analyses obtained by previous operators of the property. Of this historical data, only data gathered by the immediate predecessor operator Strata Gold (2004 to 2009) is of known analytical origin (also ALS Laboratories, Vancouver, Canada). Most of the remaining historical data set comprises values for Au and/or W only, and thus was not useful for geostatistical analysis. Data from ALS Laboratories, Vancouver for all elements excluding Au were tested using the ME-ICP61 ICP-AES Analysis Package. This package involved 0.25 g of the sample being digested by HNO₃, HClO₄, HF and HCl, the remaining residue was then topped up with an HCl leach and subsequently analyses using inductively coupled plasma- atomic emission spectroscopy (ICP-AES) (ALS Minerals ME-ICP61, 2009). Samples which yielded Ag values greater than >100 ppm using the ME-ICP61 method were subsequently tested using the Ag-OG62 Analysis Package, in which 0.25 g of sample is digested with HNO₃, HClO₄, HF, and HCl and then evaporated to incipient dryness. HCl and de-ionized water is then added for further digestion before being heated. The sample is cooled and transferred to a volumetric flask (100 ml) in which it is diluted to volume with de-ionized water, shaken to homogenize and then analysed using ICP-AES or atomic absorption spectroscopy (AAS) (ALS Minerals Ag-OG62, 2009). For samples with <10 ppm Au the Au-AA24 Analysis Package was used; a prepared sample is fused with a mixture of PbO, Na₂CO₃, Na₂B₄O₇•10H₂O, SiO₂ and other reagents as required,

inquarted with 6 mg of gold-free silver and then cupelled to yield a precious metal bead. The bead is digested in 0.5 ml dilute HNO₃ in the microwave oven, 0.5 ml concentrated hydrochloric acid is then added and the bead is further digested in the microwave at a lower power setting. The digested solution is cooled, diluted to a total volume of 4 ml with de-mineralized water, and analyzed by AAS against matrix-matched standards (ALS Minerals Au-AA24, 2005). For samples with >10 ppm Au, the Au-GRA22 Analysis Package was used, wherein a prepared sample is fused with a mixture of PbO, Na₂CO₃, Na₂B₄O₇•10H₂O, SiO₂ and other reagents in order to produce a lead button. The lead button containing the precious metals is cupelled to remove the lead. The remaining gold and silver bead is parted in dilute HNO₃, annealed and weighed as gold (ALS Minerals Au-GRA22, 2005). Upper and lower limits of detection for each element and method are quoted in Appendix C.

Data Transformations: Since the assay database is large, a number of quality control procedures were performed on the data to ensure that statistical techniques provide the most accurate description of elemental correlations within the deposit. The lower limits of detection for each element as cited by ALS for post-2009 results were used during this procedure as the most appropriate estimate available for minimum measurable quantities. Since it was not possible to obtain clarification of the limits of detection for values obtained while Dublin Gulch was operated by StrataGold, the limits of detection quoted for the current assay package were used for both sets of data. Values less than 2 times the stated lower detection limits were discarded from further analysis.

The frequency distribution of concentrations for each element was then tested for fit to a normal distribution, as a normal distribution is assumed for most common statistical techniques. For those elements that were not normally distributed data transformations using the square root,

log and double log of the original values were used to obtain a set of values, which were as close to normally distributed as possible. Table 2.4 lists the suffixes used to indicate which transformation has been used for each element in subsequent figures and tables.

2.3.2 Element Correlations

Element correlations are presented for the filtered and transformed data. Correlations are shown using both the Pearson Product-moment Correlation and the Spearman's Rank Correlation Coefficients (see below for brief explanation). Both techniques were used as they have complementary strengths in terms of understanding these data. The data represent 1477 individual assays from diamond drill core.

Pearson Product-moment Correlation Coefficient: The Pearson Product-moment Correlation coefficient (Pearson, 1896) is used to measure the simple linear relationship between two variables (elements), and results vary between -1 and 1. A value of 1 represents a perfect positive correlation and a value of -1 represents a perfect negative correlation.

Spearman's Rank Correlation Coefficient: The Spearman's Rank Correlation Coefficient (Spearman, 1904) ranks individual values in ascending order, giving the same rank to equal values, and then calculates a Pearson Product-moment Correlation Coefficient for the ranked values. Ranking of the values can be useful for data which, even when transformed, is not entirely normally distributed. As with the Pearson's Product Moment Correlation Coefficient, a value of 1 represents a perfect positive correlation, while a value of -1 represents a perfect negative correlation.

TABLE 2.4. Legend for data transformations performed on individual elements for statistical analyses.

Suffix	Transformation	Elements
_1	No transformation	Al, Ba, Ca, K, Mg, Na, P, Sc, Sr, Ti
_2	Square Root	Be, Cu
_3	Log	Au, As, Bi, Cd, Co, Ni, Pb, S
_4	Double Log	Ag, Cr, Fe, Mn, Mo, Sb, V, W, Zn

TABLE 2.5. Pearson Product-moment Correlation Coefficient and Spearman's Rank Correlation Coefficient for detected elemental concentrations at Dublin Gulch.

	Au_3	Ag_4	Al_1	As_3	Ba_1	Be_2	Bi_3	Ca_1	Cd_3	Co_3	Cr_4	Cu_2	Fe_4	K_1	Mg_1	Mn_4	Mo_4	Na_1	Ni_3	P_1	Pb_3	S_3	Sb_4	Sc_1	Sr_1	Ti_1	V_4	W_4	Zn_4
Au_3		0.28	-0.30	0.28	-0.07	-0.32	0.68	-0.20	-0.10	0.10	-0.23	-0.03	0.08	-0.20	-0.20	-0.18	0.13	-0.03	0.03	-0.32	0.12	0.17	0.24	-0.28	-0.03	-0.30	-0.33	0.11	-0.12
Ag_4	0.34		-0.26	0.35	-0.54	-0.23	0.28	-0.09	0.50	0.02	-0.15	0.36	0.47	-0.43	-0.12	0.41	0.13	-0.48	-0.15	-0.26	0.74	0.52	0.54	-0.12	-0.46	-0.40	-0.21	0.16	0.49
Al_1	-0.35	-0.36		-0.29	0.42	0.55	-0.25	0.07	-0.15	-0.01	0.34	-0.14	-0.05	0.53	0.26	-0.07	-0.11	0.30	0.29	0.69	-0.23	-0.28	-0.29	0.61	0.27	0.69	0.55	-0.01	-0.11
As_3	0.32	0.40	-0.37		-0.30	-0.32	0.19	-0.36	0.18	0.21	-0.25	0.26	0.41	-0.33	-0.27	0.03	0.17	-0.30	-0.11	-0.36	0.29	0.42	0.41	-0.21	-0.34	-0.42	-0.32	0.21	0.17
Ba_1	-0.12	-0.54	0.50	-0.32		0.35	-0.04	0.01	-0.56	0.05	0.18	-0.30	-0.42	0.72	0.20	-0.55	-0.05	0.80	0.29	0.42	-0.57	-0.55	-0.53	0.21	0.77	0.55	0.28	-0.06	-0.54
Be_2	-0.32	-0.30	0.66	-0.33	0.40		-0.22	0.22	-0.05	-0.05	0.13	-0.10	-0.21	0.36	0.20	-0.06	-0.17	0.33	0.16	0.44	-0.13	-0.29	-0.25	0.26	0.31	0.45	0.34	-0.18	-0.04
Bi_3	0.70	0.35	-0.30	0.21	-0.10	-0.22		-0.02	-0.13	0.29	-0.05	0.19	0.04	-0.06	-0.05	-0.18	0.11	0.05	0.00	-0.16	0.10	0.16	0.21	-0.20	0.04	-0.19	-0.15	0.01	-0.16
Ca_1	-0.17	-0.13	0.12	-0.35	0.05	0.24	0.00		0.05	0.12	0.22	-0.04	-0.19	0.11	0.45	0.29	-0.16	0.09	0.06	0.33	0.01	-0.01	-0.13	0.19	0.33	0.29	0.30	-0.19	0.05
Cd_3	-0.08	0.50	-0.17	0.19	-0.54	-0.06	-0.10	0.03		-0.03	-0.17	0.28	0.33	-0.33	-0.05	0.64	0.00	-0.63	-0.18	-0.17	0.78	0.38	0.57	-0.05	-0.57	-0.31	-0.12	-0.01	0.96
Co_3	0.17	0.09	-0.15	0.26	-0.05	-0.13	0.34	0.14	0.03		0.22	0.30	0.16	0.12	0.25	-0.01	0.01	0.08	0.27	0.12	0.01	0.16	0.03	0.15	0.12	0.16	0.20	-0.05	-0.03
Cr_4	-0.25	-0.20	0.35	-0.26	0.17	0.10	-0.08	0.19	-0.18	0.15		0.09	0.11	0.23	0.45	-0.02	-0.04	0.27	0.00	0.47	-0.18	-0.07	-0.26	0.64	0.25	0.44	0.77	0.00	-0.15
Cu_2	0.04	0.42	-0.25	0.24	-0.33	-0.14	0.25	-0.04	0.31	0.27	-0.01		0.49	-0.06	0.12	0.13	0.04	-0.22	-0.17	-0.04	0.33	0.55	0.30	0.07	-0.22	-0.23	0.08	0.05	0.24
Fe_4	0.13	0.44	-0.14	0.41	-0.39	-0.22	0.08	-0.17	0.29	0.18	0.02	0.43		-0.33	0.15	0.32	0.12	-0.33	-0.15	-0.07	0.49	0.68	0.37	0.19	-0.36	-0.25	0.07	0.17	0.33
K_1	-0.25	-0.43	0.67	-0.39	0.71	0.51	-0.12	0.18	-0.28	-0.01	0.22	-0.11	-0.28		0.24	-0.29	-0.13	0.51	0.22	0.50	-0.41	-0.41	-0.33	0.29	0.52	0.55	0.38	-0.07	-0.32
Mg_1	-0.19	-0.14	0.27	-0.26	0.17	0.18	-0.05	0.50	-0.04	0.22	0.47	0.07	0.13	0.23		0.11	-0.12	0.28	0.02	0.46	-0.07	0.07	-0.25	0.47	0.44	0.36	0.50	-0.07	-0.06
Mn_4	-0.21	0.33	0.00	0.03	-0.45	-0.02	-0.18	0.28	0.58	0.02	0.00	0.11	0.31	-0.18	0.19		-0.03	-0.61	-0.10	0.00	0.59	0.30	0.47	0.09	-0.49	-0.15	0.02	0.00	0.66
Mo_4	0.15	0.14	-0.16	0.18	-0.07	-0.18	0.13	-0.19	0.00	0.08	-0.04	0.05	0.14	-0.14	-0.14	-0.03		-0.04	-0.02	-0.15	0.08	0.06	0.08	-0.10	-0.07	-0.16	-0.14	0.20	-0.01
Na_1	-0.02	-0.45	0.32	-0.29	0.77	0.34	0.03	0.13	-0.61	0.02	0.24	-0.23	-0.27	0.45	0.27	-0.53	-0.04		0.19	0.33	-0.57	-0.41	-0.60	0.18	0.88	0.46	0.27	-0.08	-0.63
Ni_3	-0.01	-0.15	0.32	-0.10	0.24	0.10	-0.03	0.10	-0.15	0.31	0.14	-0.11	-0.02	0.22	0.22	0.01	-0.03	0.17		0.26	-0.22	-0.17	-0.15	0.12	0.21	0.41	0.08	0.01	-0.15
P_1	-0.30	-0.31	0.68	-0.36	0.43	0.46	-0.18	0.34	-0.15	-0.01	0.34	-0.12	-0.07	0.54	0.45	0.04	-0.16	0.31	0.31		-0.25	-0.20	-0.31	0.64	0.37	0.78	0.71	-0.07	-0.14
Pb_3	0.16	0.72	-0.29	0.32	-0.57	-0.18	0.16	-0.02	0.77	0.07	-0.20	0.36	0.47	-0.38	-0.06	0.54	0.09	-0.55	-0.21	-0.25		0.52	0.71	-0.10	-0.51	-0.42	-0.20	0.04	0.77
S_3	0.22	0.54	-0.39	0.45	-0.58	-0.30	0.19	0.02	0.38	0.23	-0.13	0.50	0.65	-0.41	0.08	0.26	0.08	-0.39	-0.12	-0.21	0.54		0.40	-0.08	-0.36	-0.45	-0.16	0.10	0.35
Sb_4	0.25	0.56	-0.34	0.41	-0.55	-0.28	0.24	-0.15	0.59	0.08	-0.25	0.36	0.38	-0.34	-0.21	0.46	0.08	-0.59	-0.16	-0.31	0.75	0.43		-0.20	-0.54	-0.40	-0.28	0.03	0.57
Sc_1	-0.28	-0.18	0.59	-0.23	0.18	0.18	-0.22	0.16	-0.06	0.08	0.68	-0.05	0.12	0.29	0.53	0.13	-0.11	0.12	0.35	0.47	-0.12	-0.15	-0.17		0.18	0.58	0.82	0.02	-0.01
Sr_1	-0.03	-0.43	0.32	-0.33	0.75	0.33	0.02	0.38	-0.54	0.05	0.22	-0.23	-0.29	0.49	0.44	-0.42	-0.08	0.87	0.21	0.38	-0.50	-0.34	-0.55	0.15		0.50	0.27	-0.09	-0.57
Ti_1	-0.34	-0.43	0.78	-0.47	0.55	0.44	-0.25	0.28	-0.28	0.00	0.48	-0.28	-0.22	0.59	0.41	-0.06	-0.19	0.41	0.48	0.72	-0.41	-0.48	-0.40	0.69	0.47		0.67	-0.12	-0.28
V_4	-0.36	-0.30	0.66	-0.37	0.30	0.38	-0.23	0.29	-0.13	0.04	0.74	-0.12	-0.06	0.44	0.52	0.08	-0.18	0.23	0.27	0.58	-0.23	-0.28	-0.28	0.86	0.26	0.75		-0.07	-0.09
W_4	0.10	0.16	-0.06	0.22	-0.03	-0.20	-0.01	-0.18	-0.04	-0.07	0.03	-0.02	0.15	-0.11	-0.05	0.00	0.25	-0.03	0.02	-0.08	0.03	0.09	0.00	0.02	-0.04	-0.10	-0.08		-0.01
Zn_4	-0.13	0.45	-0.09	0.17	-0.52	-0.03	-0.16	0.05	0.93	0.01	-0.13	0.24	0.30	-0.24	-0.04	0.63	-0.01	-0.63	-0.11	-0.10	0.75	0.33	0.57	0.00	-0.56	-0.21	-0.06	-0.04	

Notes: Pearson Product-moment Correlation Coefficients are shown in the lower left half and Spearman's Rank Correlation Coefficients are shown in the upper right of the diagram. Points of higher correlation (>0.59) are colour coded. The legend for colour coding is shown immediately below.

Legend	
Value	Colour Code
≤ 0.59	0.59
0.6 to 0.69	
0.7 to 0.79	
0.8 to 0.89	
0.9 to 1.0	

2.3.3. Correlations Results

Table 2.5 shows the Spearman's Rank and Pearson Product-moment Correlation Coefficients for the geochemical assay database at Dublin Gulch. The strongest elemental correlations (coefficients of >0.70 for Spearman's and/or Pearson's Correlation in Table 2.5) are interpretable based on the predominant mineral assemblages described above, and constitute five major groupings:

1. *Zn-Cd-(Mn)*: This is most readily ascribed to the extremely strong shared affinity of Zn and Cd for sphalerite. Sphalerite occurs in Stages 3, 4 and 6. Explicit analysis of Cd contents in sphalerite for each stage was not performed during this study, so it is not known whether one of these stages might predominate in governing the observed Zn-Cd correlation. Similarly, the (less pronounced) correlation of Mn with both Zn (Spearman's Rank Correlation Coefficient; 0.66) and Cd (Spearman's Rank Correlation Coefficient; 0.64) may also be a consequence of an elevated Mn content in one or more generations of sphalerite.
2. *Pb-Sb-Ag*: This correlation is a natural consequence of the Stage 5b-Stage 6 assemblage of Pb-Sb bearing sulfosalts (jamesonite, boulangerite, bournonite, madocite) associated with Ag-Sb bearing freibergite-tetrahedrite.
3. *Sc-V-(Cr)*: This is most readily ascribed to the shared affinity of these elements for Fe-Ti oxides and/or titanite, which would reside in the altered granodiorite of the host DGS. Titanite is also the dominant primary magmatic accessory mineral within the unaltered granodiorite (Hart et al., 2004b).

4. *Na-Sr-Ba (-K)*: This correlation is ascribed to the dominant residence of these elements in the albitic (and potassic) feldspars described in vein selvages in the DGS granodiorite during Stages 3 and 4.
5. *Au-Bi*: This pair also has demonstrably high correlations (Pearson's: 0.70; Spearman's: 0.68) for the database as a whole. This is ascribed to the distinct co-paragenesis of bismuthinite (and trace tetradymite) with native gold during the dominant auriferous mineralization of Stage 5b and 6.

2.3.4 Stacked Histograms

There are several paragenetic stages that contain significant arsenopyrite, and one in particular (Stage 5a) that routinely contains >50% arsenopyrite in wide veins that are closely associated with native gold. However, in the standard assay packages used at Dublin Gulch to routinely assay all diamond drill core there is an *upper* detection limit of 1 wt.% (10,000 ppm) for As – and many data are recorded simply as “>10,000 ppm As”. This presents an obstacle to using As data quantitatively in statistical analysis – despite the obvious paragenetic correlations of native gold with As-bearing minerals.

For the reasons above, traditional regressions cannot be used because the variance of the As with Au is artificially biased by this upper detection limit – essentially, As has a one-tailed distribution with a hard upper cut-off at 10,000 ppm. As an alternative for examining the correlation between As and Au, a stacked histogram plot for As-Au is presented for these two elements (Fig. 2.19A). To give a frame of reference for this diagram, a comparable stacked histogram for Bi and Au is also presented (Fig. 2.19B). Comparison to the Bi-Au histogram allows comparison to an elemental correlation that is testable, and pronounced, using traditional

regression analysis (Pearson Coefficient of 0.70 in Table 2.5). A third stacked histogram (Fig. 2.19C) is presented for As-Bi, and reflects the much weaker relationship between As and Bi (Pearson Coefficient of 0.21 in Table 2.5) than between Au and either As or Bi.

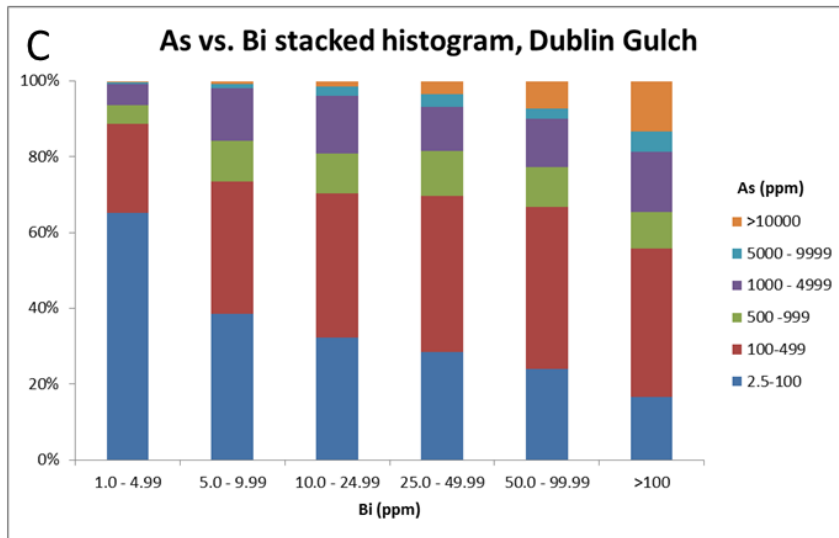
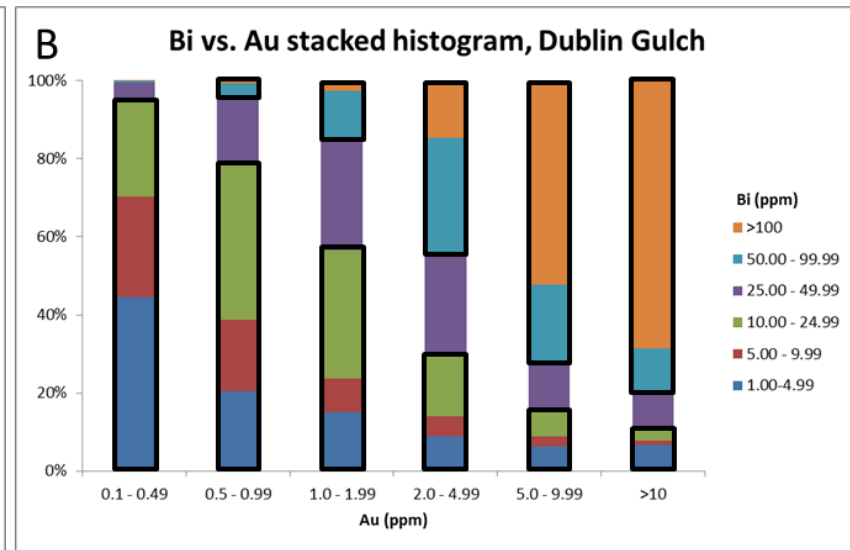
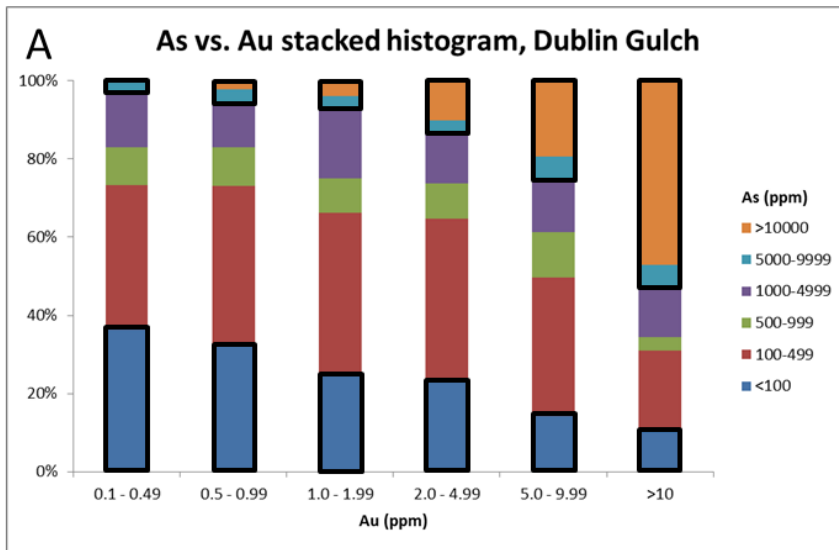


FIGURE 2.19. Stacked histograms comparing As, Au and Bi concentrations. A – Stacked histogram of As vs. Au; B – Stacked histogram of Bi vs. Au; C – Stacked histogram of As vs. Bi. The X-axis bin widths progress on a modified logarithmic scale in each graph. Black rectangles highlight upper and lower grouped bin values discussed in the text.

Histogram A in Figure 2.19 shows a pattern of gradually increasing relationship between high values for As and high values for Au. For lowest grades of Au (0.1 to 0.49 ppm) there are <2 % of As values that fall into the >10,000 ppm bin. This contrasts with the highest Au bin (>10 ppm), where >50 % of values for As fall into the >10,000 ppm bin. The increase in the proportion of high As values with increasing Au shows a broadly logarithmic progression that, given the logarithmic bin scaling, would suggest a strong positive linear correlation between Au and As. Of note is that the proportion of the middle group of As values (500 to 9999 ppm) forms a fairly constant proportion (~20 %) for all Au bins. The overall pattern is one in which the ratio of highest As values (>5000 ppm) replace the space previously filled by lowest As values (<499 ppm) as Au concentration increases. Fewer than 10% of assays with Au >10 ppm have As < 100 ppm. These patterns are consistent with Au being predominantly hosted by the arsenopyrite-rich Stage 5 veins (hosting both Stage 5a and 5b mineralization).

Histogram B in Figure 2.19 shows the strongest positive correlation of any of the histograms. Bi values greater than 50 ppm increase progressively as Au values increase. Greater than 80% of Au values >10 ppm coincide with Bi >50 ppm. Fewer than 10% of Au values >10 ppm coincide with Bi values < 10 ppm. This pattern is compatible with the explicit paragenetic coincidence of bismuthinite and native gold during Stages 5 & 6 (Fig. 2.4).

Despite the observed strong correlation of Au vs. As and Au vs. Bi, Histogram C in Figure 2.19 shows only a weak progression to higher As values with higher Bi, as expected from their weak correlations as demonstrated in Table 2.5.

Arsenopyrite compositions determined by EPMA (see Chapter 3) were used to assess the degree to which Bi might be dissolved in arsenopyrite. The highest recorded value for Bi in

arsenopyrite was 0.11 at% from a sample of Stage 5a arsenopyrite, another sample from this stage contained 0.05 at% Bi. All other samples from Stages 3, 4, and 5a contained Bi either at or below the EPMA detection limit of 0.1 at% Bi. Tetradymite is the only Bi-bearing mineral, occurring as inclusions within arsenopyrite (Stage 5a), but this texture is rare. There are several examples in which fractures in arsenopyrite are filled by bismuthinite during subsequent stages. However, Stage 5a arsenopyrite is most commonly present in isolation from other sulfides, in association with quartz or muscovite, carbonate and clay alteration.

Overall, the core explanation for the weakness of the positive correlation displayed in Figure 2.19C is likely the disparate timing of 1) the arsenopyrite-rich vein mineralization of Stage 5a, and 2) the preponderant occurrence of bismuthinite in Stage 5b. Both stages are, however, associated with discrete generations of native gold, leading to the strong correlations noted for Au-As and Au-Bi in Figures 2.19A and 2.19B.

2.4 Principal Component Analysis (PCA)

2.4.1 Introduction

The suite of elements from assay data was split into two sets, 1) an “alteration” set (Al, Ba, Be, Ca, K, Mg, Na, P, Sr, Ti), and 2) an “ore mineralization” set (Au, Ag, Bi, Cd, Co, Cu, Fe, Mn, Mo, Ni, Pb, S, Sb, W, Zn) in order to most clearly portray these complementary aspects of the sample lithologies. Data was randomly split into two subsets, for an initial analysis to test for components that were common to both splits - and then recombined for the final analysis as presented in Figure 2.20 (alteration set) and Figure 2.21 (ore mineralization set). Data used in the PCA was selected and transformed using the same criteria as for the element vs element correlations (see Section 2.3, above). The PAST software of Hammer et al. (2001) was used to carry out the PCA.

2.4.2 PCA Results

Alteration Set: Table 2.6 shows the component scores for the first three components of the alteration group of elements. Principal Component 1 (PC1) accounts for more than 47% of variation in this dataset. Principal Component 2 (PC2) represents an additional 16%, with a third component (PC3) representing 13% of the variation. Figure 2.20 shows a vector plot of PC1 vs. PC2. Based on the element vectors shown within these two components, there are 3 distinct element groupings. The first group comprises Ca, Sr, Mg, and Na. The second group comprises K, Al, P, Ti, and Be. Barium forms a separate vector, intermediate in position between Groups 1 and 2.

TABLE 2.6. Principal component scores for alteration group of elements. For each PC, left column is ranked alphabetically, right column is ranked by descending weighting. Scores above 0.350 are highlighted with boxes in the right hand columns.

PC 1				PC 2				PC 3			
Al	0.356	K	0.370	Al	-0.407	Sr	0.473	Al	0.020	Ca	0.533
Ba	0.360	Ba	0.360	Ba	0.125	Na	0.373	Ba	-0.411	Mg	0.518
Be	0.305	Al	0.356	Be	-0.199	Ca	0.362	Be	-0.063	P	0.268
Ca	0.180	Sr	0.341	Ca	0.362	Mg	0.296	Ca	0.533	Ti	0.180
K	0.370	Ti	0.334	K	-0.183	Ba	0.125	K	-0.117	Al	0.020
Mg	0.232	Na	0.318	Mg	0.296	K	-0.183	Mg	0.518	Be	-0.063
Na	0.318	P	0.313	Na	0.373	Be	-0.199	Na	-0.380	Sr	-0.106
P	0.313	Be	0.305	P	-0.288	Ti	-0.286	P	0.268	K	-0.117
Sr	0.341	Mg	0.232	Sr	0.473	P	-0.288	Sr	-0.106	Na	-0.380
Ti	0.334	Ca	0.180	Ti	-0.286	Al	-0.407	Ti	0.180	Ba	-0.411
Eigenvalue	4.7			1.6				1.3			
% variance	47.2			15.7				13.1			

Alteration PCA for Dublin Gulch

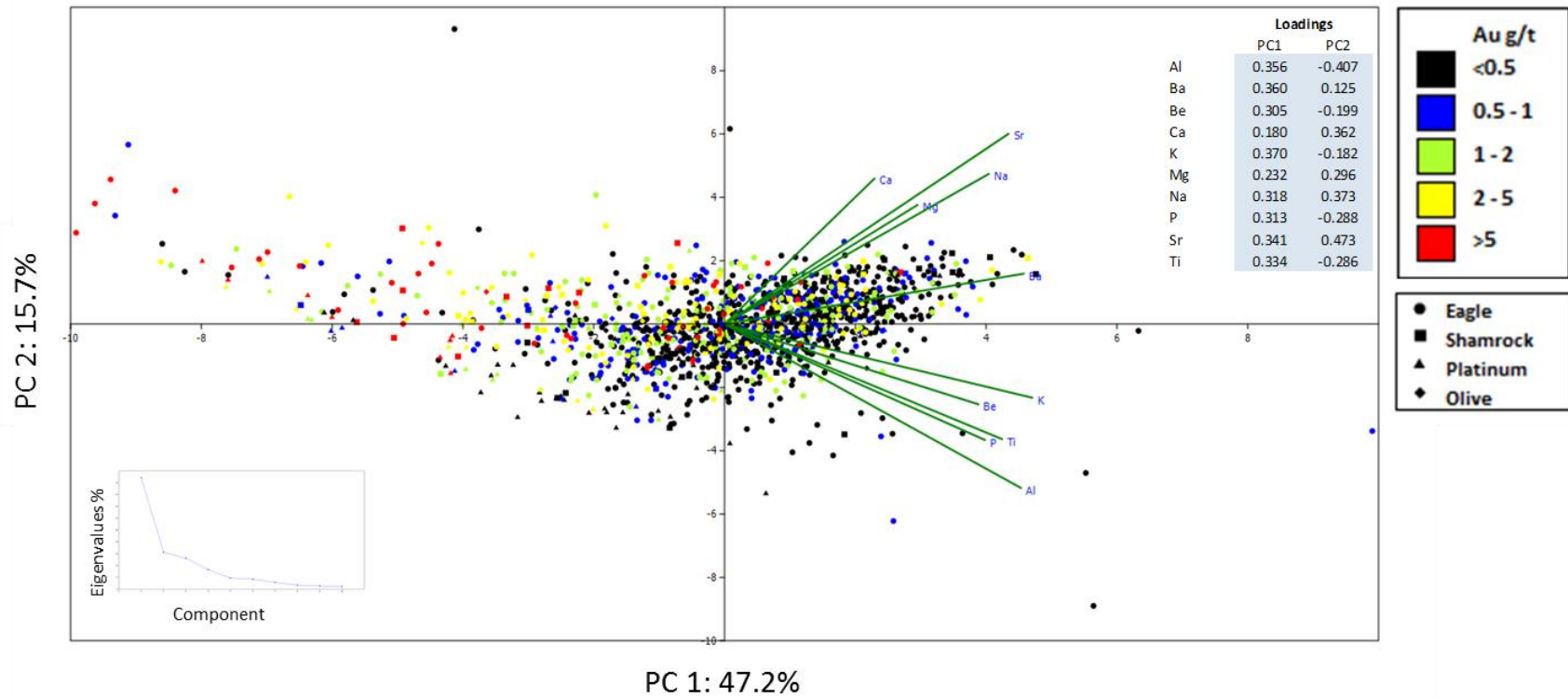


FIGURE 2.20. Principal Component Analysis of alteration set elements for Dublin Gulch, YT. The weighting vector for each element is shown with a green line. Zone within the Dublin Gulch Deposit is shown by symbol shape, Au grade is shown by colour (see attached Legend). The PAST software of Hammer et al. (2001) was used for this analysis.

Ore Mineralization Set: Table 2.7 shows the principal component scores for the mineralization suite of elements. PC1 accounts for 32 % of the variation in the data set, with components PC2 and PC3 accounting for 15 % and 10 % of variation, respectively. There are 3 dominant element groupings displayed as vectors in Figure 2.21. The first group comprises Au, Bi, Co, W, and Mo. As expected the Au vector is oriented with the same trend as individual data points with Au >5 ppm (red symbols). The second group comprises Ag, Pb, Sb, S, Fe, Cu, and P. The third group comprises Cd, Zn, and Mn and has little or no affinity with Au grades above 0.5 ppm Au.

2.4.3 Discussion

Within the Alteration dataset, the Ca-Sr-Mg-Na grouping appears correlated with sodic and propylitic alteration of granodiorite. The K-Al-P-Ti-(Be) grouping is best attributed to potassic (K-feldspar) alteration of the granodiorite, with accompanying silicification and residual P-Ti minerals.

Based on the colour encoded data points in Figure 2.20, there appears to be no significant positive correlation between either of these alteration element groupings and Au grade. In fact, Au values >0.5 ppm shows a pronounced antipathy with these alteration element vectors. This is consistent with the observations that, 1) most Au mineralization, especially in Stage 5, is concentrated with sulfide mineralization in vein fillings – while the silicate alteration minerals, such as K-feldspar and albite are located in vein selvages, and 2) the strong silicification of both the gold-bearing veins and their selvages, which may have preferentially lowered the concentrations of these other elements by effective dilution within auriferous volumes.

TABLE 2.7. Principal component scores for mineralization set of elements at Dublin Gulch. For each PC, left column is ranked alphabetically, right column is ranked by descending weighting. Scores above 0.250 are highlighted with boxes in right hand columns.

PC 1				PC 2				PC 3			
Au	0.183	Pb	0.401	Au	0.467	Bi	0.497	Au	-0.140	Ni	0.658
Ag	0.374	Ag	0.374	Ag	0.119	Au	0.467	Ag	-0.097	Co	0.584
Bi	0.168	Cd	0.341	Bi	0.497	Co	0.258	Bi	-0.044	Fe	0.191
Cd	0.341	Sb	0.341	Cd	-0.323	Mo	0.177	Cd	0.001	Mn	0.163
Co	0.086	Zn	0.318	Co	0.258	Cu	0.169	Co	0.584	Cu	0.142
Cu	0.268	S	0.302	Cu	0.169	Ag	0.119	Cu	0.142	S	0.131
Fe	0.288	Fe	0.288	Fe	0.034	W	0.112	Fe	0.191	Zn	0.039
Mn	0.197	Cu	0.268	Mn	-0.356	S	0.109	Mn	0.163	Cd	0.001
Mo	0.088	Mn	0.197	Mo	0.177	Fe	0.034	Mo	-0.203	Bi	-0.044
Ni	-0.050	Au	0.183	Ni	0.009	Ni	0.009	Ni	0.658	Ag	-0.097
Pb	0.401	Bi	0.168	Pb	-0.105	Sb	-0.019	Pb	-0.146	W	-0.108
S	0.302	Mo	0.088	S	0.109	Pb	-0.105	S	0.131	Sb	-0.136
Sb	0.341	Co	0.086	Sb	-0.019	Cd	-0.323	Sb	-0.136	Au	-0.140
W	0.031	W	0.031	W	0.112	Zn	-0.356	W	-0.108	Pb	-0.146
Zn	0.318	Ni	-0.050	Zn	-0.356	Mn	-0.356	Zn	0.039	Mo	-0.203
Eigenvalue	4.8			2.2				1.5			
% variance	32.0			14.7				9.8			

Mineralisation PCA for Dublin Gulch

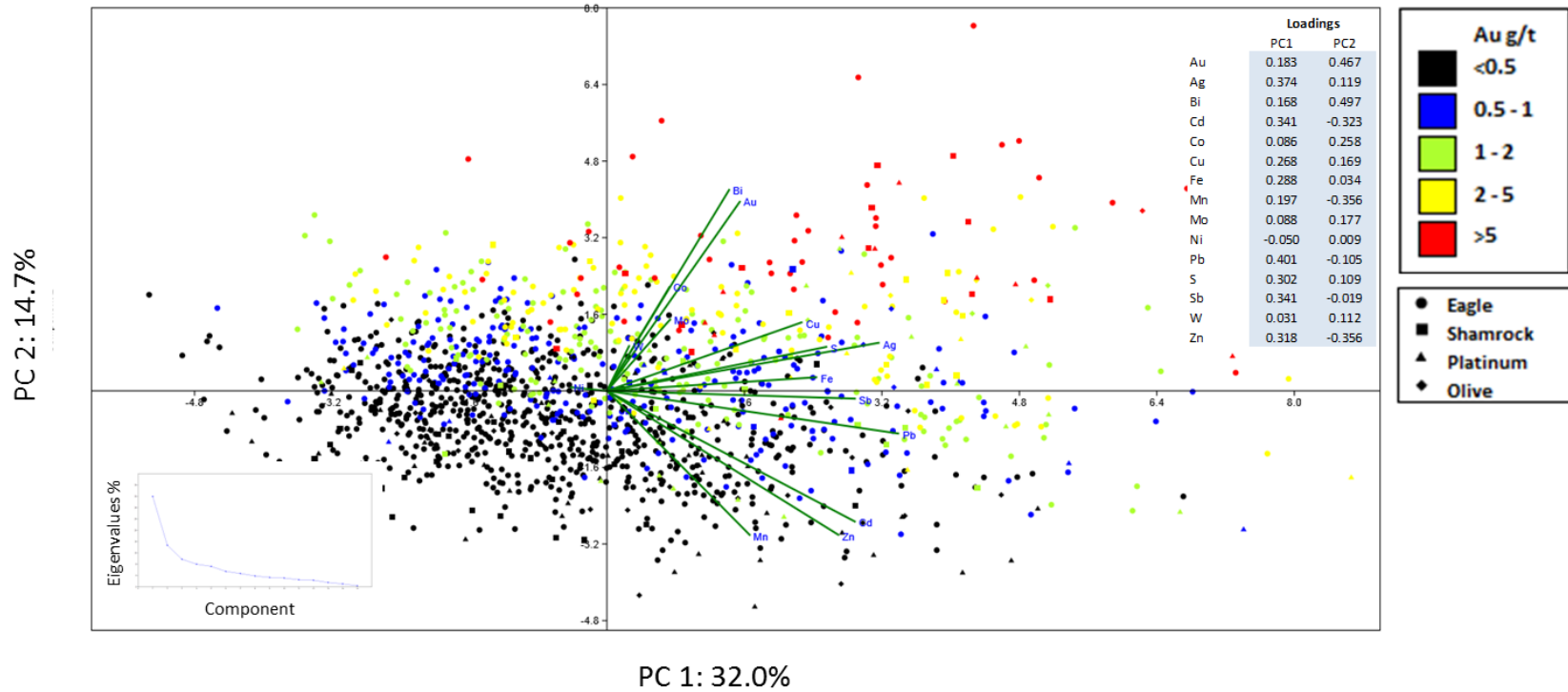


FIGURE 2.21. Principal Component Analysis of ore mineralization set elements for Dublin Gulch, YT. The weighting vector for each element is shown with a green line. Zone within the Dublin Gulch Deposit is shown by symbol shape, Au grade is shown by colour (see attached Legend). The PAST software of Hammer et al. (2001) was used for this analysis.

Within the Ore Mineralization data set, there are three pronounced element vector groupings. The first of which is Au-Bi-Co(-W-Mo). The strong correlation of Au and Bi, as discussed above, is the result of the strong textural and paragenetic association of Au with Bi minerals (especially bismuthinite) observed for Stage 5b and 6. The empirical correlation of Au and Bi was previously noted at Dublin Gulch by several authors (e.g., Hollister, 1992; Maloof et al., 2001). The association of Au and Co, however, has not been previously reported for Dublin Gulch. Interestingly, the raw correlation between Au and Co (Section 2.3) is poor, but using PCA their variance is clearly related. Cobalt occurs to some degree within arsenopyrite of all stages, but particularly in Stages 4 and 5a, in concentrations of up to 5.94% and 0.19%, respectively (see Chapter 3), and thus arsenopyrite likely represents the main mineral residence of Co at Dublin Gulch. Although Stage 5a arsenopyrite contains significantly less Co on average than Stage 4 arsenopyrite, the relative volumes of arsenopyrite (5 % in Stage 4 and >50 % Stage 5a) means that the largest overall reservoir of Co is likely Stage 5a. Cobalt therefore represents a potentially useful proxy for As, as it is not subject to the same upper detection limit problem in the routine assay data. This relationship between Au, Bi, and Co is consistent with the observed paragenesis in which Au and Bi minerals (Stage 5b) are genetically related to and hosted in the highest concentrations by arsenopyrite-rich veins (Stage 5a).

The element vector grouping of Au-Bi-Co with W-Mo is likely the result of scheelite and molybdenite mineralization within Stage 3 veins – which were subsequently reactivated and occupied by Stages 5a, 5b, and 6. Molybdenite gives the appearance of having lubricated movement along vein fractures, and thus may have actually promoted reactivation of Stage 3 veins by Stage 5 mineralization. This re-fracturing relationship, where later mineralization (our Stage 5) reactivated and fractures earlier veins (our Stage 3) was previously noted in the study of

Maloof et al. (2001). Scheelite occurs as (relict) mineral inclusions within Stage 5 arsenopyrite providing additional, textural evidence for this process. The necessity of vein reactivation to provide an Au overprint may also explain why there appears to be no substantial Au endowment within the Wolf W Skarn.

The second pronounced element vector grouping is comprised of (in descending order of length) Ag, Pb, Sb, S, Fe, and Cu, and is most easily attributed to the Fe-Pb-Sb-Cu sulfosalt assemblage of Stage 5b and 6 (jamesonite, boulangerite, bournonite, freibergite-tetrahedrite, and madocite). Freibergite is specifically an Ag-bearing phase, although Ag may potentially reside in solid solution in most of these listed minerals. Electrum (native Au-Ag) is also specific to Stages 5b and 6. Based on this element vector grouping, and vector lengths, the contribution from Stage 4 chalcopyrite (Cu-Fe) and tennantite (Cu-Fe-As) appears to have been subsidiary.

2.5 Discussion

The intrusion of the DGS granodiorite into metasedimentary rocks of the Hyland Group of the Yusezyu Formation likely utilised the structural traps formed during earlier episodes of deformation - the Dublin Gulch Antiform and the faults and fractures created by the Robert Service and Tombstone Thrusts. Contact metamorphism of sedimentary pyrite within the thermal aureole of the DGS created pyrrhotite and chalcopyrite within argillaceous units of the Yusezyu Formation, designated Stage 1 of the paragenesis.

During the initial emplacement and crystallisation of the DGS, a roof pendant of largely limestone composition fell into contact with the upper part of the magma chamber and reacted with fluids exsolving from the magma to form the Wolf W Skarn, designated Stage 2 of the paragenesis.

Brown et al. (2002) considered that later stage veins dominated by quartz within the skarn were co-incident with similar quartz veins within the DGS (Stage 3). In this study they have been merged on the basis that the same overall hydrothermal processes were operating throughout the skarn and DGS during this time. The presence of scheelite within Stage 3 veins, both in the skarn and DGS, suggests that they represent the later stages of the same fluid responsible for creating the Wolf W Skarn. The transition from initial skarn style mineralization in the Wolf Skarn Zone to vein mineralization within an extensive portion of the upper DGS was controlled by the cooling and transition of the DGS system from ductile to brittle fracture conditions. Paragenetic Stages 3 and 4 are considered as examples of the early and late expressions, respectively, of the same fluid episode - based on their morphological similarities, volumetrically coincident occurrence, and non-abrupt paragenetic transition. It should be noted that Stage 3 and 4 veins within the skarn are not a significant host to Au mineralization, while those within the DGS are. It is suggested that the process of skarnification made the roof-pendant impermeable to later hydrothermal fluids that overprinted many veins within the upper portion of the DGS.

A second episode of fluid exsolution from the DGS is considered responsible for veining during both Stages 5 and 6, based on their similarity in vein styles and metal endowment. The wide transit of this second fluid is manifested by the wide areal extent of the Potato Hills Trend (PHT) mineralization in Figure 2.3 – although mineralization west of the Haggart Creek Fault in the Rex and Peso zones remains ambiguous in its genetic relationship to the “main” PHT mineralization. The presence of Au mineralization hosted within Stage 3 and 4 veins within the granodiorite, but not within the Wolf Skarn supports the observation that most Au is delivered later than Stages 3 and 4.

Native gold was deposited during Stages 5a, 5b, and 6 – with Stage 5b appearing to be the most quantitatively important auriferous stage. Stage 5b contains a much lower modal percentage of sulfide minerals than either Stage 5a or 6, but shows a strong geochemical correlation between Au and Bi due to the co-deposition of bismuthinite with the native gold. Carbonate, muscovite/phengite, dickite, kaolinite, and pyrophyllite alteration associated with Stages 5 and 6 is the most pervasive at Dublin Gulch, and provides a key tool for recognition of Stage 3 and 4 veins that were reactivated and overprinted by later gold mineralization.

Late stage carbonate vein formation during Stage 7 may have been related to the waning stages of hydrothermal activity associated with the DGS, or possibly formed as a consequence of much later orogenic fluids. Supergene alteration (or deep weathering) of Stage 8 took place within ~50m of present surface, at an undetermined time subsequent to the formation of Stages 1 through 7, producing extensive scoroditization of arsenopyrite.

2.5.1 Wider Applications of this Study to (R)IRGS and Other Models

In the context of their Reduced Intrusion-related Gold System (RIRGS) model, several authors (e.g. Thompson and Newberry, 2000; Hart, 2007) attributed gold tenor to a single generation of partially aligned stockwork quartz veins within the DGS. Maloof et al. (2001) attributed the hydrothermal evolution of Dublin Gulch to the progressive cooling of a single fluid.

Our study shows in detail that the paragenesis of the Dublin Gulch gold mineralization is more complex than implied by these and other previous models and studies (e.g., Maloof et al., 2001; Hart, 2005). Further, our study strongly implies a sequence in which at least two discrete hydrothermal pulses occurred at Dublin Gulch – representing the most appropriate explanation for our combined textural, paragenetic, and geochemical data.

Many models (e.g., Hollister, 1991, 1992; Thompson et al., 1999; Hart, 2005, 2007) cite Dublin Gulch and Fort Knox, Alaska as closely genetically related - and as type examples of the class of Au deposit referred to as RIRGS. However, site visits and literature review (Bakke, 1995; Bakke et al., 1998; Kinross Gold Corp., 2008, 2015) for both deposits have highlighted a number of substantial differences between the two deposits:

- 1) No roof pendant skarn exists at Fort Knox
- 2) Fort Knox contains only sparse (<2%) sulfide minerals (mainly pyrite), while Dublin Gulch commonly exceeds 3- 5 modal % of a diverse suite of sulfide and sulfosalt minerals.
- 3) All major vein stages described at Fort Knox are dominated by quartz. Dublin Gulch has veins that contain up to 100% sulfide.
- 4) The Fort Knox intrusive exhibits three mappable felsic phases, and a more mafic phase. Dublin Gulch, as currently exposed and drilled, contains only one mappable felsic phase, associated with volumetrically restricted andesitic to dacitic dykes.

Notably, however, Fort Knox manifests a distinct empirical correlation between Au values and the presence of Bi mineralization. Bakke (1995) showed an Au-Bi correlation (r) of 0.86 for mineralization at Fort Knox. Minerals associated with gold at Fort Knox include native bismuth (Bi), maldonite (AuBi), bismuthinite (Bi_2S), tellurobismutite, (Be_2Te_3), bismite (Bi_2O_3), tetradymite ($\text{Bi}_2\text{Te}_2\text{S}$), and eulytite $\text{Bi}_4(\text{SiO}_4)_3$ (Bakke 1995; Bakke et al., 1998; McCoy et al., 1997; Kinross Gold Corp. 2008, 2015).

The fact that Dublin Gulch has diverse and variable sulfide phases makes it far easier to study paragenetically than Fort Knox, as there are discernible indicator sulfide minerals for each

hydrothermal stage. This allows a closer investigation of the processes that were responsible for the Au endowment at Dublin Gulch, and might be a useful proxy for Fort Knox and other mid-Cretaceous intrusion-related Au deposits of the Tintina Gold Belt, and elsewhere in the Northern Cordillera.

One explanation for the contrast in sulfide mineralogy and metal contents between Dublin Gulch and Fort Knox may lie in differences in the composition and lithology of crustal rocks through which they ascended. Mair et al. (2006) suggest that the original extent of the Selwyn Basin can be reconstructed by resolving the displacement along the Tintina Fault; this is done primarily by reconstruction of plutonic belts, but is at odds with the tectonic provinces in each area. It could be argued that the differing tectonic provinces and hence different (shallow) lithosphere are the primary reason for the differences in assimilation between Fort Knox and Dublin Gulch. However, the Golden Summit (Dolphin) prospect, which is located roughly 10 km from Fort Knox, shows a paragenesis ostensibly similar to Dublin Gulch and contains around 5% total sulfide (Abrams and Giroux, 2013). The fact that there are S-rich, As-rich intrusion-related gold deposits and S-poor, As-poor intrusion-related gold deposits in close proximity to each other suggests that the reason for differing sulfide content is most closely controlled by the local sedimentary and metasedimentary sequences into which the parent intrusions are emplaced. Those sequences that are richer in pelitic and other sulfur-rich lithologies seem more likely to form S-rich, As-rich intrusion-related gold deposits. Newberry and Solie (1995) also showed that it was possible to distinguish between high-As (described by Newberry and Solie as Porphyry As) and low-As intrusion-related gold deposits based on the Cl contents of hydrothermal biotite. High-As deposits contain biotite with a relatively higher Cl content versus low-As deposits. The differing Cl contents of hydrothermal biotite may represent a second key indicator of a difference

in fluid chemistry conditions and metal complexing. McCoy et al. (1997) state that As-rich IRGS are the predominant occurrence of this deposit type and that Fort Knox is the only major As-poor IRGS recognized in Alaska.

2.6 Conclusions

Relatively low-sulfide, porphyry-style quartz veins – as recognized within the Eagle Zone - record the first pulse of fluid from the DGS. A roof pendant scheelite-bearing skarn, localized in a reactive limestone roof pendant, appears contemporaneous with this first stage. However, a second discrete fluid pulse appears responsible for later “PHT”-type mineralization, including the bulk of gold mineralization.

Paragenetic and statistical assessments both indicate that Au was imparted to the Dublin Gulch IRGS predominantly during a second (later) hydrothermal event, rather than as an early lower-grade episode enhanced by a later higher-grade episode.

Full understanding of the shared features of gold deposits within the greater Tombstone-Tintina Gold Belt will require more detailed studies that include description of paragenetic sequences. A key point for exploration is that, whether the deposit is a high-S high-As or low-S low-As intrusion-related gold system, the presence of a network of partially aligned stockwork quartz veins related to initial pluton emplacement alone is not necessarily sufficient to produce a viable gold deposit. Episode(s) of subsequent hydrothermal and veining activity may be critical in delivering additional Au in the form of widely spaced arsenopyrite rich (high-As IRGS; e.g., Dublin Gulch) or quartz ‘shear’ (low-As IRGS) veins (e.g., Fort Knox; Bakke et al., 1998).

Modification or enhanced widths of alteration selvages may provide a useful insight into whether veins have been reactivated during later fluid events. For example, at Dublin Gulch,

multiple examples of Stage 3 veining show the subsequent overprint of alteration selvages related to the auriferous Stage 5b. Future exploration strategies for this type of deposit should look to expand known occurrences by using vein selvage alteration mapping and logging to highlight areas of potentially enhanced Au grades.

Given that the metallogenic associations and perceived hydrothermal processes which operated at Dublin Gulch show some divergence from those proposed by the RIRGS model, we tentatively propose the use of the term S-rich, As-rich intrusion-related gold deposit (SAS-IRG) for those like Dublin Gulch.

Acknowledgements

This work was funded by a grant from the NSERC Collaborative Research and Development (CRD) Program (CRDPJ 421812-2011), which included both financial and field support from Victoria Gold Corporation. We are deeply grateful to Bill Keats, Richard Eliason, Joanna (Ettliger) Hodge, and Mark Ayranto of Victoria Gold Corporation for accommodating and facilitating this research effort. Michael Shaffer (Memorial University, MAF-IIC Facility) is thanked for his expert assistance with the SEM phase of this research.

References

Abbott, J.G., Gordey, S.P., and Tempelman-Kluit, D.J., 1986, Setting of stratiform, sediment hosted lead-zinc deposits in Yukon and northeastern British Columbia, In: Morin, J.A., (Ed.), Mineral deposits of the northern Cordillera: Canadian Institute of Mining and Metallurgy Special Volume 37, p. 1–18.

Abrams and Giroux, 2013, Prepared for Freegold Ventures Ltd., and Free Gold Recovery, USA, Technical report for the Golden Summit project, Fairbanks mining district, Alaska: Technical Report dated Aug. 7, 2013, 118 p.

ALS Minerals, 2011, Prepared for Victoria Gold Corp., A mineralogical analysis of 19 core pieces from the Potato Hills Trend, Eagle Gold project – Dublin Gulch, Yukon, ALS-MV10-005, Internal Report dated Jan. 14, 2011, 53 p.

ALS Minerals AG-OG62, 2009, Ore Grade Elements by Four Acid Digestion Using Conventional ICP- AES Analysis accessed at:
http://www.alsglobal.com/~media/Files/Divisions/Minerals/Geochemistry/Geochemistry_Resources/Short_Method_Descriptions/ME-OG62_Four_Acid_Near_Total_Assay_Grade_Multi-element_Method.pdf

ALS Minerals AU-AA24, 2005, Fire Assay Fusion, AAS Finish, accessed at:
http://www.alsglobal.com/~media/Files/Divisions/Minerals/Geochemistry/Geochemistry_Resources/Short_Method_Descriptions/Au-AA23_Au-AA24_Fire_Assay_-_Atomic_Absorption_Methods.pdf

ALS Minerals AU-GRA22, 2005, Precious Metals Gravimetric Analysis Methods, accessed at:
http://www.alsglobal.com/~media/Files/Divisions/Minerals/Geochemistry/Geochemistry_Resources/Short_Method_Descriptions/Au-Ag-GRA21-GRA22_Fire_Assay_Gravimetric_Methods.pdf

ALS Minerals ME-ICP61, 2009, Trace Level Methods Using Conventional ICP- AES Analysis, accessed at:
http://www.alsglobal.com/~media/Files/Divisions/Minerals/Geochemistry/Geochemistry_Resources/Short_Method_Descriptions/ME-ICP61_Four_Acid_Near_Total_-_ICP_Multi-element_Method.pdf

Anderson, R.G., 1983, Selwyn plutonic suite and its relationship to tungsten skarn mineralization, southeastern Yukon and District of Mackenzie, In: Current research, Geological Survey of Canada, Paper 83-1B, p. 151–163.

Anderson, R.G., 1988, An overview of Mesozoic and Tertiary plutonic suites and their associated mineralization in the northern Canadian Cordillera, In: Taylor, R.P., Strong, D.F. (Eds.), Recent advances in the geology of granite-related mineral deposits: Canadian Institute of Mining and Metallurgy, p. 96–113.

Bakke, A.A., 1995, The Fort Knox “porphyry” gold deposit: Structurally controlled stockwork and shear quartz vein, sulphide-poor mineralization hosted by late Cretaceous pluton, east-central Alaska: Canadian Institute of Mining and Metallurgy, Special Volume 46, p. 795–802.

Bakke, A.A., Morrell, B., and Odden, J., 1998, The Fort Knox porphyry gold deposit, east central Alaska: Porphyry and hydrothermal copper and gold deposits: A global perspective, conference proceedings, 30 November and 1 December 1998, Perth, Australia, p. 89-98.

Baker, T., and Lang, J.R., 2001, Fluid inclusion characteristics of intrusion-related gold mineralization, Tombstone-Tungsten magmatic belt, Yukon Territory Canada: Mineralium Deposita, v. 36, p. 563–582.

Beane, R.E., 1974, Biotite stability in the porphyry copper environment: Economic Geology, v. 69, p. 241-256.

Brown, V.S., Baker, T., and Stephens, J.R., 2002, Ray Gulch tungsten skarn, Dublin Gulch, central Yukon: Gold-tungsten relationships in intrusion-related ore systems and implications for gold exploration, In: Emond, D.S., Weston, L.H., and Lewis, L.L., (eds.), Yukon exploration and geology 2001: Exploration and Geological Services Division, Yukon Region, Indian and Northern Affairs Canada, p. 259–268.

Fritz, W.H., Narbonne, G.M., and Gordey, S.P., 1983, Strata and trace fossils near the Precambrian-Cambrian boundary, Mackenzie, Selwyn, and Wernecke Mountains, Yukon and Northwest Territories, In: Current Research, Part B, Geological Survey of Canada, Paper 83-1B, p. 365-375.

Fritz, W.H., Cecile, M.P., Norford, B.S., Morrow, D., and Geldsetzer, H.H.J., 1991, Cambrian to Middle Devonian assemblages. In H. Gabrielse and C.J. Yorath (eds.), Geology of the Cordilleran Orogen in Canada, Geological Survey of Canada, Geology of Canada, no. 4, p. 151-218 (also Geological Society of America, The Geology of North America, v. G-2).

Gordey, S.P., and Anderson, R.G., 1993, Evolution of the northern Cordilleran miogeocline, Nahanni map area (105I), Yukon and Northwest Territories: Geological Survey of Canada, Memoir 248, p. 214.

Hammer, Ø, Harper, D.A.T., and Ryan, P.D., 2001, Past: Paleontological Statistics Software Package for Education and Data Analysis. Palaeontologia Electronica, v. 4, issue 1, p. 4-9, 178kb. http://palaeo-electronica.org/2001_1/past/issue1_01.htm.

Hart, C.J.R., 2004, Mid-Cretaceous magmatic evolution and intrusion-related metallogeny of the Tintina Gold Province, Yukon and Alaska: Unpubl. PhD. thesis, University of Western Australia, Perth, 188p.

Hart, C.J.R., 2005, Classifying, distinguishing and exploring for intrusion-related gold systems: The Gange: Newsletter of the Geological Association of Canada Mineral Deposits Division, v. 87, p. 1, 4–9.

Hart, C.J.R., 2007, Reduced intrusion-related gold systems, In: Goodfellow, W.D., (ed.), Mineral deposits of Canada: A Synthesis of Major Deposit Types, District Metallogeny, the Evolution of Geological Provinces, and Exploration Methods: Geological Association of Canada, Mineral Deposits Division, Special Publication No. 5, p. 95-112.

Hart, C.J.R., Goldfarb, R.J., Lewis, L.L., and Mair, J.L., 2004a, The Northern Cordillera Mid-Cretaceous Plutonic Province: Ilmenite/magnetite-series granitoids and intrusion-related mineralization: *Resource Geology*, v. 54, p. 253–280.

Hart, C.J.R., Mair, J.L., Goldfarb, R.J., and Groves, D.I., 2004b, Source and redox controls on metallogenic variations in intrusion-related ore systems, Tombstone-Tungsten belt, Yukon Territory, Canada: *Transactions of the Royal Society of Edinburgh, Earth Science*, v. 95, p. 319–337.

Hitchins, A.C., and Orssich, C.N., 1995, The Eagle zone gold-tungsten sheeted vein porphyry deposit and related mineralization, Dublin Gulch, Yukon Territory: *Canadian Institute of Mining and Metallurgy, Special Volume 46*, p. 803–810.

Hollister, V.F., 1991, Origin of placer gold in the Fairbanks, Alaska, area—A newly proposed lode source: *Economic Geology*, v. 86, p. 402-405.

Hollister, V.F., 1992, On a proposed plutonic porphyry gold deposit model: *Nonrenewable Resources*, v. 1, p. 293–302.

Kinross Gold Corp., 2008, Prepared for Kinross Gold Corp. and Fairbanks Gold Mining Inc., Technical report for the Fort Knox mine: NI 43-101 Technical Report dated Mar. 31, 2008, 79 p.

Kinross Gold Corp., 2015, Prepared for Kinross Gold Corp., Fort Knox Mine, Fairbanks North Star Borough, Alaska, USA: NI 43-101 Technical Report, dated Mar. 31 2015, 173 p.

Lang, J.R., Baker, T., Hart, C.J.R., and Mortensen, J.K., 2000, An exploration model for intrusion-related gold systems: *Society of Economic Geology Newsletter*, v. 40, p. 1, 6–15.

Lang, J.R. and Baker, T., 2001, Intrusion-related gold systems: the present level of understanding: *Mineralium Deposita*, v. 36, p. 477-489.

Lennan, W.B., 1983, Ray Gulch tungsten skarn deposit, Dublin Gulch area, central Yukon: *Canadian Institute of Mining, Metallurgy and Petroleum, Special Volume 37*, p. 245–254.

Mair, J.L., Hart, C.J.R., and Stephens, J.R., 2006, Deformation history of the western Selwyn Basin, Canada: Implications for orogen evolution and the setting of mid-Cretaceous magmatism: *Geological Society of America Bulletin*, v. 118, p. 304–323.

Maloof, T.L., Baker, T., and Thompson, J.F.H., 2001, The Dublin Gulch intrusion-hosted deposit, Tombstone Plutonic Suite, Yukon Territory, Canada: *Mineralium Deposita*, v. 36, p. 583–593.

McCoy, D., Newberry, R.J., Layer, P.W., DiMarchi, J.J., Bakke, A.A., Masterman, J.S., and Minehane, D.L., 1997, Plutonic-related gold deposits of interior Alaska: *Economic Geology*, Monograph 9, p. 191–241.

McInnes, D., 2007 (last updated), Selwyn Basin metallogeny, Yukon Geological Survey, Yukon Geological Survey website: <http://www.geology.gov.yk.ca/pdf/SelwynBasin.pdf>

Mortensen, J. K., Murphy, D. C., Hart, C. J. R., and Anderson, R. G., 1995, Timing, tectonic setting, and metallogeny of early and mid-Cretaceous magmatism in Yukon Territory: *Geological Society of America, Abstracts with Programs* 27, 65.

Mortensen, J.K., Hart, C.J.R, Murphy, D.C., and Heffernan, S., 2000, Temporal evolution of early and mid-Cretaceous magmatism in the Tintina Gold Belt, In: Tucker, T., Smith, M.J. (Eds.), *The Tintina gold belt: Concepts, exploration and discoveries: British Columbia and Yukon Chamber of Mines Special Volume 2*, p. 49–57.

Murphy, D.C., 1997, Geology of the McQuesten River region, northern McQuesten and Mayo Map Area, Yukon Territory (115P/14, 15, 16; 105M/13, 14): *Exploration and Geological Services Division, Yukon, Indian and Northern Affairs Canada Bulletin* 6, 111 p.

Newberry, R.J., and Solie, D.N., 1995, Data for plutonic rocks and associated gold deposits in Interior Alaska: *Alaska Division of Geological and Geophysical Surveys, Public Data File 95-25*, 61 p.

Pearson, K., 1896, Mathematical contributions to the theory of evolution. III. Regression, heredity, and panmixia: *Philosophical Transactions of the Royal Society A*, v. 187, p. 253–318.

Rasmussen, K.L., 2013, The timing, composition, and petrogenesis of syn- to post-accretionary magmatism in the northern Cordilleran miogeocline, eastern Yukon and southwestern Northwest Territories: Unpubl. Ph.D. Thesis, University of British Columbia, Vancouver, Canada, 810 p.

Scott Wilson Mining, 2010, Prepared for StrataGold Corp., Technical Report on the Dublin Gulch Property, Yukon Territory, Canada: NI 43-101 Technical Report dated Apr. 23, 2010, 242 p.

Selby, D., Creaser, R.A., Heaman, L.M., and Hart, C.J.R., 2003, Re–Os and U–Pb geochronology of the Clear Creek, Dublin Gulch, and Mactung deposits, Tombstone Gold Belt, Yukon, Canada: absolute timing relationships between plutonism and mineralization: *Canadian Journal of Earth Science*, v. 40, p. 1839–1852.

Sillitoe, R.H., and Thompson, J.F.H., 1998, Intrusion-related vein gold deposits: Types, tectono-magmatic settings, and difficulties of distinction from orogenic gold deposits: *Resource Geology*, v. 48, p. 237–250.

Spearman, C.E., 1904, The proof and measurement of association between two things: *American Journal of Psychology*, v. 15, p. 72-101.

SRK Consulting, 2008, Prepared for Victoria Gold Corp., NI 43-101 Preliminary Assessment Dublin Gulch Property – Mar-Tungsten Zone Mayo District, Yukon Territory, Canada: Technical Report dated Dec. 1, 2008, 161 p.

Stephens, J., 2003, Structural, mechanical and P-T evolution of intrusion-related gold mineralization at Clear Creek and Dublin Gulch, Yukon, Canada: Unpubl. Ph.D. Thesis, James Cook University of North Queensland, Townsville, Australia. 277 p.

Tempelman-Kluit, D.J., 1964, Geology of the Haggart Creek-Dublin Gulch area, Mayo District, Yukon Territory: Unpubl. M.Sc. thesis, University of British Columbia, Vancouver, Canada. 105 p.

Tetra Tech, 2015, Prepared for Victoria Gold Corp., Technical Report – Feasibility Study, Eagle Gold Project, Yukon: NI 43-101 Technical Report, dated May 29, 2015, 411 p.

Thompson, J.F.H., and Newberry, R.J., 2000, Gold deposits related to reduced granitic intrusions, In: S.G., Hagemann and P.E., Brown (eds.), *Gold in 2000: Society of Economic Geologists, Reviews in Economic Geology*, v. 13, p. 377–400.

Thompson, J.F.H., Sillitoe, R.H., Baker, T., Lang, J.R., and Mortensen, J.K., 1999, Intrusion-related gold deposits associated with tungsten-tin provinces: *Mineralium Deposita*, v. 34, p. 323–334.

Thompson, R.M., 1945, An occurrence of cassiterite at Dublin Gulch, Yukon Territory: *Economic Geology*, v. 40, p. 142-147.

Wardrop Engineering Inc., 2009, Prepared for StrataGold Corporation, Technical Report on the Dublin Gulch Property, Yukon Territory, Canada: NI 43-101 Technical Report dated February 04, 2009, 70 p.

Wardrop Engineering Inc., 2011a, Prepared for Victoria Gold Corp., Technical Report on the Eagle Zone, Dublin Gulch Property, Yukon Territory, Canada: NI 43-101 Technical Report, dated April 15, 2011, 48 p.

Wardrop Engineering Inc., 2011b, Prepared for Victoria Gold Corp., Technical Report on the Eagle Zone, Dublin Gulch Property, Yukon Territory, Canada: NI 43-101 Technical Report dated May 04, 2011, 86 p.

Wardrop Engineering Inc., 2012, Prepared for Victoria Gold Corp., Technical Report on the Eagle Zone, Dublin Gulch Property, Yukon Territory, Canada: NI 43-101 Technical Report dated April 05, 2012, 419 p.

Woodsworth, G.J., Anderson, R.G., and Armstrong, R.L., 1991, Plutonic regimes, In: Gabrielse, H., Yorath, C.J. (Eds.), Geology of the Cordilleran Orogen in Canada: Geological Survey of Canada, Geology of Canada 4, p. 491–531.

CHAPTER 3

Geothermometric, sulfur isotope and lead isotope characteristics of the ore mineralization of the Dublin Gulch Au deposit, YT, Canada.

FRASER A. KIRK, GRAHAM D. LAYNE, AND GLENN PIERCEY

Department of Earth Sciences, Memorial University, 300 Prince Phillip Drive, St John's, Newfoundland, A1B 3X5, Canada

Abstract

Victoria Gold Corporation's Dublin Gulch property, located 85 km NNE of Mayo, central Yukon, hosts the Eagle gold deposit (3.3 Moz Au indicated and inferred global resource), as well as several high-grade gold occurrences within a 13 km-long belt of Au-As-Bi-Sb and Ag-Pb-Zn mineralization. The Eagle deposit, which has been previously classified as a reduced intrusion-related gold system, hosts lower-grade gold mineralization (<1 g/T) in the form of a porphyry-style array of quartz veins. Gold mineralization elsewhere along the belt is characteristically hosted by a series of widely-spaced, sub-parallel arsenopyrite-pyrite-sulfosalt veins. Mineralization in these latter veins is generally of higher tenor than in the quartz veins within the Eagle deposit, with visible gold observed in hand specimen and >30 g/T Au returned from some grab samples.

Electron probe micro-analysis was used to characterize the compositional variations of different generations of arsenopyrite. These compositions constrain precipitation temperature to an estimated 345 to 620 °C for early quartz veins, and <300 to 490 °C for late stage arsenopyrite-pyrite-sulfosalt veins, when interpreted in the context of their associated sulfide mineral assemblages.

Microanalysis of sulfur isotopes in arsenopyrite, pyrite, and pyrrhotite revealed a range of $\delta^{34}\text{S}$ in pyrrhotite from early quartz veins of -11.7 to +2.6 ‰, and -3.9 to +2.4 ‰ from late stage arsenopyrite-pyrite(-sulfosalt) veins. Early quartz veins overprinted with late stage alteration displayed a range of -5.3 to +0.9 ‰ $\delta^{34}\text{S}$ values. The general pattern of sulfur isotope values is consistent across stable sulfide species, showing variation that is strongly controlled by the paragenetic sequence.

Microanalysis of lead isotopes in Pb-rich sulfosalts from intrusion-hosted veins yielded highly radiogenic values of 20.41 to 21.02 $^{206}\text{Pb}/^{204}\text{Pb}$, 15.89 to 16.05 $^{207}\text{Pb}/^{204}\text{Pb}$, and 40.39 to 41.11 $^{208}\text{Pb}/^{204}\text{Pb}$. Pb-rich sulfosalts from a single vein hosted by metasedimentary rocks of the Hyland Group yielded 21.70 to 21.71 $^{206}\text{Pb}/^{204}\text{Pb}$, 16.07 to 16.08 $^{207}\text{Pb}/^{204}\text{Pb}$, and 42.08 to 42.15 $^{208}\text{Pb}/^{204}\text{Pb}$. These lead isotope values are consistent with sulfide precipitation from a hydrothermal fluid initially derived from a magma that had inherited highly radiogenic Pb from its source rock, and that subsequently scavenged substantial additional radiogenic lead from the Neoproterozoic metasedimentary host and country rocks of the deposit.

Early stockwork quartz veins and late stage arsenopyrite-sulfosalt vein stages show distinct populations of both arsenopyrite composition and sulfur isotope values - suggesting two distinct, sequential mineralising events, which overlap within the Eagle deposit. The bulk of the gold was, in fact, delivered during the later stage of mineralization.

3.1 Introduction

3.1.1 Location and Zone Distribution

The Dublin Gulch property is located approximately 85 km north-northwest of the town of Mayo, Yukon Territory, Canada. The deposit is hosted almost entirely (>90%) within the upper portion of a mid-Cretaceous granodiorite pluton, the Dublin Gulch Stock (DGS). The remainder is hosted within hanging wall metasedimentary rocks of the Hyland Group, Selwyn Basin Province. There are a number of recognized auriferous zones at Dublin Gulch, the most notable of which is the 3.3 M oz Eagle Zone (3.0 M oz – 134 Mt @ 0.69 g/T Au indicated; 0.3 M oz – 0.2 Mt @ 0.56 g/T Au inferred: Tetra Tech, 2015), which includes a 2.3 M oz (92 Mt @ 0.78 g/T Au) proven and probable Au reserve (Tetra Tech, 2015). A number of additional significant metal occurrences lie along an extended (>13 km-long) belt of Au-As-Bi-Sb and Ag-Pb-Zn mineralization known as the Potato Hills Trend (PHT), which intersects the DGS, and includes the Eagle Zone.

3.1.2 Deposit Type

Gold deposits associated with (granitoid) intrusives have been assigned a number of names and classifications consequent to the creation of models to explain their genesis. Hart (2005) gives a summary of the different terms used by previous authors (e.g., Hollister, 1992; Thompson et al., 1999; Lang and Baker, 2001) to describe this general class of deposit. Here we shall use the generalized term “Intrusion-related Gold Systems” (IRGS) to refer to deposits that could be reasonably included in the same genetic model as Dublin Gulch.

3.1.3 Previous Work

A report on the Dublin Gulch area by Thompson (1945) highlighted cassiterite occurrences (Tin Dome), which have not been described in any detail in subsequent literature. Subsequently, Lennan (1983) described tungsten-bearing skarn mineralization at Dublin Gulch (Wolf W Skarn). Hitchins and Orsich (1995) provided the first focused study on the auriferous Eagle Zone. Murphy (1997) produced the most detailed map to date of the regional geology around Dublin Gulch.

Hollister (1992) proposed that the Porphyry-Au model was applicable to auriferous mineralization at Dublin Gulch. Sillitoe and Thompson (1998) highlighted the difficulty of distinguishing certain styles of intrusion-related gold mineralization from orogenic gold mineralization. However, Thompson et al. (1999) subsequently ascribed Dublin Gulch to the intrusion-related class of mineral deposits, based on the association with the Wolf W Skarn, ore metal associations and tectono-magmatic setting. Thompson and Newberry (2000) highlighted the link between this style of mineralization and what appeared to be moderately reduced granitoid intrusive rocks in this region. The term “Reduced Intrusion-related Gold Systems” (RIRGS) arose from the work of Thompson et al. (1999), Thompson and Newberry (2000), and Lang et al. (2000). Hart (2005, 2007) further developed the RIRGS model, highlighting metal zonation patterns and element correlations with a strong emphasis on deposits in the Northern Cordillera, Yukon, and Alaska. In fact, the Dublin Gulch and Fort Knox deposits represent the holotypes for his proposed RIRGS classification.

Maloof et al. (2001) presented a paragenesis for Dublin Gulch that showed native gold occurring during a single stage, in association with arsenopyrite veins. They attributed this to the evolution of a single hydrothermal fluid from the intrusion, which cooled with time and distance. Baker and Lang (2001) studied fluid inclusions in quartz, recognising that early quartz was likely not in equilibrium with gold mineralization; however, they stated that the relationship of fluid inclusions to gold mineralization was difficult to resolve texturally. Lang and Baker (2001) presented a process-driven model for intrusion-related gold deposits in general, and a synthesis of global examples into a single overall deposit type. They suggested a temperature range of approximately 350 to 150 °C for hydrothermal activity in this class of deposits.

Brown et al. (2002) presented the most detailed description of the Wolf W Skarn to date, including a paragenesis for the skarn - which has been adopted for this study. Stephens (2003) showed that quartz veins within the DGS showed structural features that were consistent with early mineralization being genetically linked to the emplacement and evolution of the Dublin Gulch Stock.

Recent NI 43-101 technical reports for the Wolf W skarn (SRK Consulting, 2008), and the Eagle Zone (Wardrop Engineering Inc., 2009, 2011a, 2011b, 2012; Scott Wilson Mining, 2010; Tetra Tech, 2015) have been focussed on providing compliant resource estimates.

3.1.4 Scope of Study

The central aim of this phase of our study was to examine geothermometric and isotopic characteristics of the mineralization in order to determine how the hydrothermal conditions evolved during sequential paragenetic stages at Dublin Gulch. This paper presents an assessment of the ore-forming processes that operated at Dublin Gulch in the context of the multi-stage

mineral paragenesis developed earlier (Chapter 2). Electron probe micro-analysis (EPMA) was used to determine the major element stoichiometry of arsenopyrite, in order to test for distinct populations of this mineral, and to gain insights into temperatures of sulfide phase precipitation. Secondary ion mass spectrometry (SIMS) was used to determine sulfur and lead isotope compositions *in situ* in sulfide and sulfosalt minerals, to gain insights into the fluid and metal sources.

3.2 Geologic Setting

3.2.1 Regional Setting

The DGS was emplaced into the Yusezyu Formation, Hyland Group in the Selwyn Basin of the Northern Cordillera during the Middle Cretaceous. The Selwyn Basin (see Fig. 3.1 for stratigraphy), a passive margin sequence, was deposited on the north-western margin of North America during the late Precambrian (Neoproterozoic) through Middle Jurassic (Abbott et al., 1986; Gordey and Anderson, 1993). The Hyland Group is mostly comprised of coarse-grained sandstones, inter-bedded with shale, that were deposited by turbidite flows during the latest Precambrian to Early Cambrian (Fritz et al., 1983, 1991; Gordey and Anderson, 1993). The Yusezyu Formation is a series of coarse, gritty sandstones and pebbly conglomerates interbedded with shales and siltstones. The upper parts of the formation are variably calcareous, with minor limestone horizons. The Yusezyu Formation records the earliest sedimentation within the Selwyn Basin, and its deposition ceased before the end of the Neoproterozoic (Murphy, 1997).

The Dawson, Tombstone, and Robert Service thrusts disrupt the stratigraphy of the Selwyn Basin and have created a number of thrust stacks (Fig. 3.1) during the Jurassic (Mair et al., 2006a). The DGS is located close to the Tombstone Strain Zone associated with the Tombstone

Thrust. These thrust stacks potentially formed structural conduits for the migration of magma upwards in the crust of the Selwyn Basin and may, in fact, have been the dominant tectonic controls of magma ascent in the Dublin Gulch area (S. Craggs, pers. comm., 2013). Empirically, the DGS was intruded into the hinge zone of the Dublin Gulch Antiform (Stephens, 2003) and this zone appears to provide a key structural control and explanation for the elongate ridge geometry of the pluton.

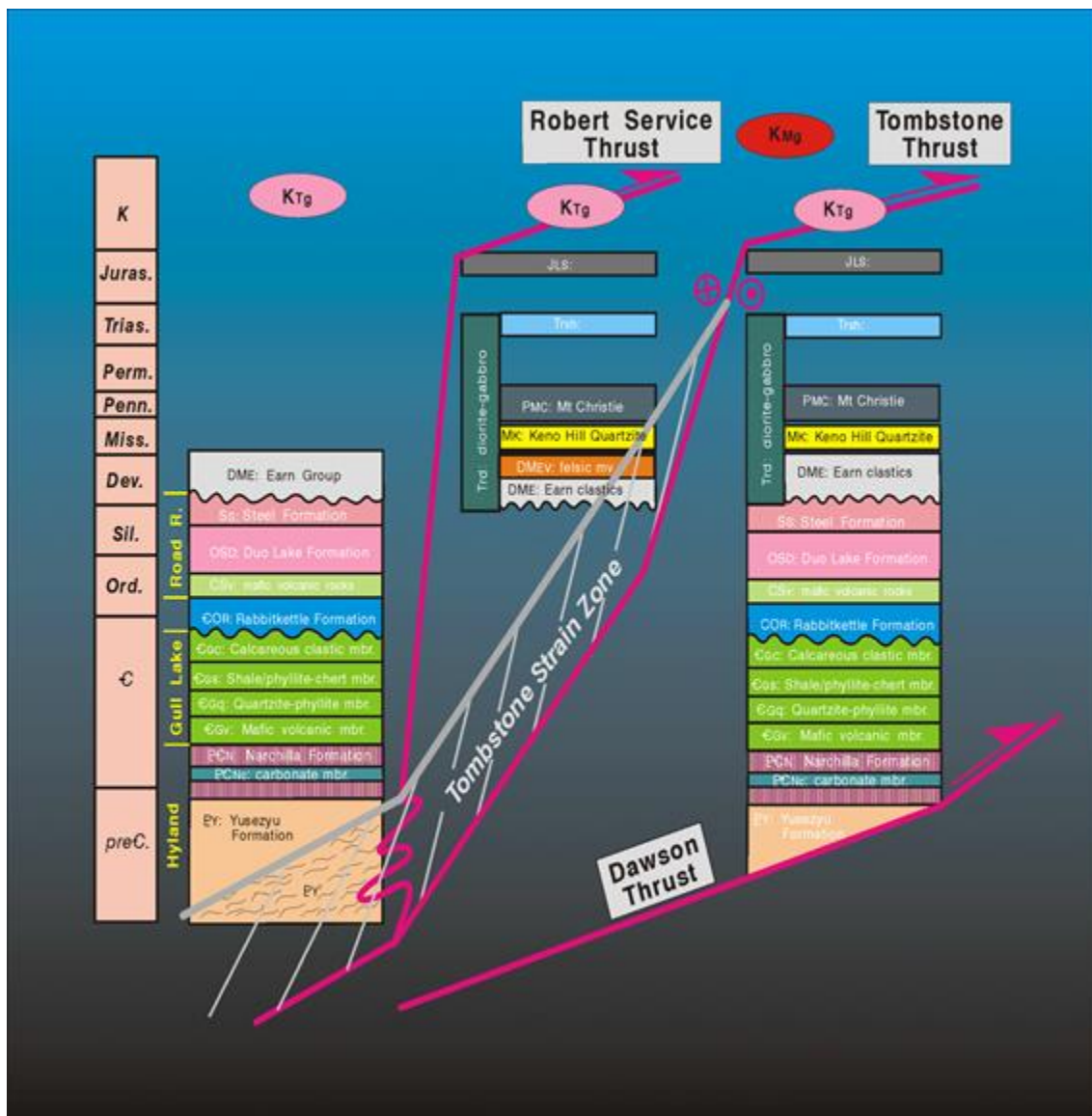


FIGURE 3.1. Stratigraphy of the Selwyn Basin and thrust stacking, modified from Murphy (1997). The DGS was intruded outside of- but proximal (<10 km) to- the Tombstone Strain Zone.

Metamorphism within the Selwyn Basin is typically of lower greenschist facies. The Tombstone Strain Zone reached a higher metamorphic grade. The maximum depth of burial for the Hyland Group is estimated at less than 10 km, suggesting pressures of around 2.8 kbars (McInnes, 2007).

The DGS is one of a series of Cretaceous plutons that have been enumerated within the Tintina Gold Province (TGP) (see Fig. 3.2). The TGP (e.g., Hart, 2004) is a belt of gold deposits in the Northern Cordillera of Yukon and Alaska that are bounded by two dextral transpressional fault systems - the Denali Fault (southern limit) and the Tintina Fault (northern limit). The belt also extends beyond the northern tip of the Tintina Fault, into the Selwyn Basin in the Yukon, and into the western-most NWT.

Within the TGP a series of highly prospective IRGS deposits form the Tombstone Gold Belt (TGB), the most significant host to IRGS globally. A series of previous nomenclature systems for plutonic suites in Yukon and Alaska was proposed by various authors (e.g. Anderson, 1983, 1988; Woodsworth et al., 1991). The name TGB was first used by Mortensen et al. (1995) and Murphy (1997), who designated two distinct suites of plutons within the belt. They designated the series of plutons on the northern margins of the Selwyn Basin, which trend roughly east-west, as the Tombstone Suite. The series of plutons that trend broadly north-south along the YT-NWT border was termed the Tungsten Plutonic Suite by Mortensen et al. (1995, 2000). It should be noted that their division included only small plutons around 94 Ma. Mortensen et al. (1995, 2000) included the DGS as a member of the Tombstone suite.



FIGURE 3.2. Map of the Tintina Gold Province (TGP) within the Yukon and Alaska. Mineral deposits are shown as large circles, mineral occurrences are shown as small circles. Gold deposits in red dots could be considered under the same IRGS genetic model as Dublin Gulch. Deposits marked in black dots are not of IRGS origin, or are ambiguous in origin. Deposits marked in purple are skarn deposits (predominantly W-bearing) associated with intrusions similar to those which form IRGS. Ray Gulch is an older name for the Wolf Skarn at Dublin Gulch. Within the TGP is the Tombstone Gold Belt (TGB; marked in pink) which is the major host to IRGS in the Yukon and Alaska. Mair et al. (2006a) suggested that the reason for the presence of IRGS in the Fairbanks district, along a projected trend of the TGB, is consequent to ~450 km of post-formation offset along the Tintina Fault. Population centres marked are Whitehorse (W), Mayo (M), Dawson (D) and Fairbanks (F). Map after Hart (2007).

Hart et al. (2004a, 2004b) subsequently defined plutonic provinces for the entirety of Alaska and the Yukon based on geochemical affinities, age, and morphology. Hart et al. (2004b) revised the terminology for plutonic suites within the Yukon, subdividing the Tombstone Suite into the Tombstone and Mayo suites, and widening the parameters of inclusion for the Tungsten Suite. This subdivision was made on the basis of geographical location, pluton size, rock types, geochemistry and morphology. The Tombstone Suite, as defined by Hart et al. (2004b), features 10-80 km², concentrically zoned plutons in the northwestern-most portion of the Selwyn Basin, which are alkalic and largely composed of syenite. The Mayo Suite features plutons trending east-west along the northern margin of the Selwyn Basin, 1-5 km² (western portion)/ 20-80 km²

(eastern portion), single phase to weakly composite, and which are alkalic-calcic to calcic and chiefly composed of quartz monzonite. The Tungsten Suite is comprised of ~15 km², gradationally zoned plutons, which are peraluminous, alkalic-calcic to calcic and feature quartz monzonite to monzogranite compositions. Hart et al. (2004b) defined age ranges for the respective suites as: Tungsten Suite (97 Ma – 94 Ma), Mayo Suite (95 Ma – 92 Ma), and Tombstone Suite (92 Ma – 90 Ma). Rasmussen (2013) refined these ranges to: Tungsten Suite (98 Ma – 94 Ma), Mayo Suite (96 Ma – 93 Ma), and Tombstone Suite (94 Ma – 89 Ma). The Dublin Gulch Pluton was designated by Hart et al. (2004b) as a member of the Mayo Suite.

3.2.2 Local Geological Setting

The DGS (Fig. 3.3), as exposed in the study area, is a single phase granodiorite intrusion (Murphy, 1997). The intrusion forms an elongate ridge (approx. 6 km x 2 km) that trends at 070°. The DGS displays a generally equigranular, medium-grained texture throughout the main body - with a strongly developed porphyritic texture (alkali feldspar phenocrysts) within 10 m of contact margins. Although the intrusion appears single phase, there are areas of compositional heterogeneity where it could be classified as quartz monzonite rather than granodiorite. Mafic enclaves are present in the main granodiorite and show very little syn-emplacement deformation, suggesting passive intrusion under little to no tectonic stress.

A series of narrow aplite dykes cross-cut both the skarn and the DGS in the Wolf W Skarn area. Late stage dykes of andesite to dacite composition, with porphyritic (within Hyland Group) to hypabyssal (within DGS) textures, crosscut the main intrusive, and the partially aligned stockwork veins of early mineralization. The relationship between these late stage dykes, and

vein stages later than partially aligned stockwork veins of paragenetic Stage 3 (see below), remains enigmatic in the absence of observable examples of cross-cutting relationships.

Published U-Pb ages for the crystallization of the DGS are 92.8 ± 0.5 Ma (titanite; n=2) and $93.5 +5.8/-0.5$ (zircon; Murphy, 1997), 94.0 ± 0.3 Ma (zircon; Selby et al., 2003) and 94.1 ± 0.3 Ma (zircon; Chapter 4). Andesitic and dacitic dykes sampled from the Dublin Gulch area appear contemporaneous with the DGS (Chapter 4).

A Re-Os date for molybdenite (Selby et al., 2003) suggested an age of 93.2 ± 0.3 Ma for the hydrothermal activity that precipitated this specific sulfide phase. This would be closely linked to emplacement of the DGS, given the overlap with the age estimates above, and likely affiliated with our paragenetic Stage 3. The paragenesis of this study places molybdenite in the earliest vein stages, preceding native gold, so this age may not be exactly simultaneous with (nor resolvable from) main gold delivery at Dublin Gulch.

With the exception of the Wolf W Skarn, mineralization at Dublin Gulch is almost exclusively vein-bound, occurring in a variety of zones and prospects across the Dublin Gulch property (see Fig. 3.3). Auriferous mineralization is chiefly hosted within the DGS, with the remainder (<10%) hosted by the intruded, Yusezyu Formation metasedimentary rocks.

The Eagle Zone sits within a ~5 km long ridge of exposed granodiorite of the DGS (Fig. 3.3). The Platinum Zone is located along this same ridge, on the topographical rise out of the Haggart Creek Valley towards the Eagle Zone. The Haggart Creek Valley is punctuated geologically by the Haggart Creek Fault, which forms a topographic low. The DGS ridge rises toward the Potato Hills, which are located at the far northeastern end of the granodiorite ridge. The Olive and Shamrock zones are the most prominent zones in this far northeastern part of the

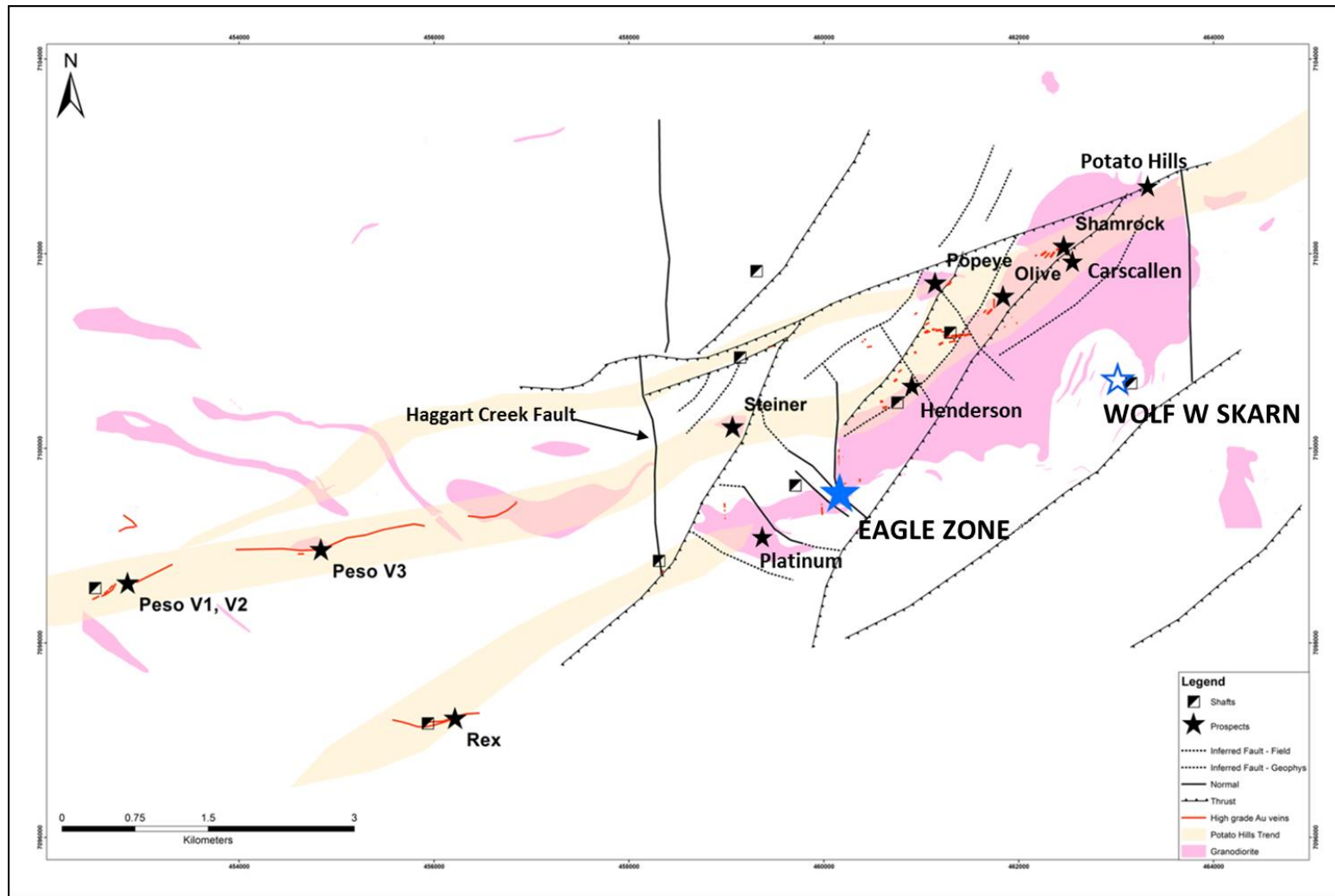


FIGURE 3.3. Map of the exposed granitoid rocks of the DGS (pink) with the currently perceived outline of the Potato Hills Trend (PHT) (tan/peach) overlain. The Eagle Zone deposit is shown as a solid blue star. The Wolf W Skarn is shown as an open blue star. Major prospects are shown with a smaller black star symbol. The structural framework of the deposits is highlighted by a series of normal and thrust faults. There is a clear pattern of major prospects occurring along the strike of the PHT (shaded yellow), particularly where it intersects the DGS. High-grade gold occurrences are shown as occurring almost exclusively along the PHT. The exception would be the Eagle Zone, which has not been historically included in the PHT, due to a distinct deposit model being proposed for its genesis.

trend. Both are exposed by a series of creeks and gulches, which are likely the surface manifestations of NNW-trending faults.

The Rex and Peso zones lie on the opposite (west) side of the Haggart Creek Fault to the majority of known DGS-hosted mineralization, and are situated on the hills rising westward out of the Haggart Creek Valley. The Wolf W Skarn (hosted by a roof pendant of Hyland Group carbonates within the DGS) lies on the southeastern edge of the Dublin Gulch ridge, often forming cliffs and vertical rock faces. There is a uniformly steep drop off in the topography progressing south off the Dublin Gulch ridge, into a wide valley immediately below.

Clusters of porphyry-style partially aligned stockwork veins occur throughout the pluton; Eagle and Olive contain the most extensive clusters of mineralised stockwork veins, and consequently the most graduated gold grades in the deposit. The Shamrock Zone contains arsenopyrite-rich veins with up to 118 g/T Au in individual grab samples, but these veins appear more volumetrically restricted than in Eagle or Olive. Shamrock shows the strongest disparity in gold grade between Au-rich arsenopyrite veins and largely barren stockwork quartz - K-feldspar veins. In the more distal zones, e.g., Platinum, Steiner, and Popeye, mineralization occurs in the same fashion as in the more prominent zones but, as currently exposed, appears lower, and more sporadic, in gold content. In general, auriferous mineralization in the vicinity of the DGS typically appears to extend no more the 10 m (upwards) into the surrounding metasedimentary rocks of the Yusezyu Formation.

The greater Potato Hills Trend refers to a >13 km long belt of mineralization (outlined in Fig. 3.3), which extends from the Peso (Vein) Zones in the southwest towards the Shamrock Zone, and then beyond the Potato Hills to the northeast. The Rex Zone is currently included in

the Potato Hills Trend, as it appears consanguineous with the Peso Zone veins, but is represented as a small spur of the Trend to the south-southeast in Figure 3.3. Of note is that, in both Rex and Peso zones, high-grade gold veins appear much more continuous, as opposed to the more laterally discontinuous vein geometries described above for the Olive and Shamrock zones.

3.3 Paragenetic Stages of Hydrothermal Mineralization

A detailed discussion of the ore and alteration paragenesis of Dublin Gulch is presented in Chapter 2 and summarized in Figure 3.4 below. A condensed version of this paragenesis is presented here, to provide context for the data to be presented below on the evolution of temperature, sulfur isotopes, and lead isotopes in the Dublin Gulch deposits.

Stage 1- Contact Metamorphism

Intrusion of the DGS into Yusezyu Formation, Hyland Group, caused formation of a contact metamorphic aureole (~2 km radius, Maloof et al., 2001). In the argillaceous horizons, original pyrite was converted to pyrrhotite and trace chalcopyrite.

Stage 2- W Skarn

A roof-pendant garnet-pyroxene-scheelite skarn in the Wolf Zone of the deposit formed as the earliest expression of ore mineralization at Dublin Gulch. The skarn is cross-cut by Stage 3 and 4 veins, but not Stages 5 or later. Previous examinations of the Wolf Zone skarn (Brown et al., 2002; SRK Consulting, 2008) have not recognized any significant gold resource within this zone.

Stage 3 – Quartz-K-feldspar Veins

An asymmetric porphyry-style stockwork (trending 070°) of 10 – 20 mm thick quartz and K-feldspar veins is the first, and most volumetrically widespread, of all the brittle-fracture vein stages. The veins are >90% hosted within the DGS, with the remainder extending into the contact metamorphic aureole. Pyrrhotite is the most common sulfide in this stage, with subsidiary pyrite, arsenopyrite, chalcopyrite, and sphalerite. Overall sulfide content in the stockworks of this vein stage is typically < 2%. Surrounding alteration of the granodiorite host rock is typically sodic (albitic), with less common potassic alteration.

Stage 4 – Quartz-Chlorite-Carbonate Veins

These veins show similar general orientation to Stage 3 veins, with an overall trend of 070° and with a subsidiary complementary vein set perpendicular to this trend. Stage 4 veins are typically narrower (2-5 mm) and have a more anastomosing geometry than Stage 3 veins. Veins are dominantly quartz, chlorite, and calcite with accessory K-feldspar. Pyrrhotite and chalcopyrite dominate the sulfide mineral assemblage. Minor sulfide minerals include pyrite, arsenopyrite, sphalerite, and tennantite. Alteration selvages for this stage are potassic.

Stage 5 – Arsenopyrite-Rich Veins

These veins were historically important at Dublin Gulch; being exploited during the Klondike gold rush of 1895 (Wardrop Engineering Inc., 2012). These veins are dominated (up to 100%) by arsenopyrite with associated quartz (Stage 5a). Late stage (Stage 5b) sulfosalts (dominantly jamesonite, boulangerite, and bournonite) are strongly associated with native gold within the veins. Pervasive calcite, muscovite/phengite, kaolinite, dickite, and pyrophyllite alteration accompanies this stage, with alteration selvages of several meters in thickness common.

These veins show the same general 070° orientation as the preceding vein stages, but are most commonly discrete subvertical sheeted veins. Veins trend in a parallel nature for the entire length of the main portion of the exposed DGS, and are characteristically spaced at around 30-50 m (north-south gap). Veins are typically 5 to 50 cm wide, with minor secondary veins 2-5 cm wide in close proximity to larger “master” veins - and micro-fractures filled with arsenopyrite and/or pyrite extending away from these largest veins. Stage 5a also commonly re-fractures earlier veins, particularly Stage 3 - with commonly observed examples of Stage 3 veins with flanking Stage 5 arsenopyrite. Stage 5 represents the majority of native gold endowment at Dublin Gulch, and is responsible for the multi-ounce values in some surface grab samples.

Stage 6 – Pyrite-Sulfosalt Veins

Stage 6 mineralization is dominated by pyrite, which has a very similar morphology to Stage 5 arsenopyrite. Stage 6 mineralization can be seen cross-cutting Stage 5 arsenopyrite. Veins contain almost exclusively sulfide minerals (pyrite, sphalerite, and sulfosalts), with minor quartz in some examples. Veins typically occupy microfractures within earlier vein structures, or within the alteration zones surrounding earlier veins. When distinct Stage 6 veins form within the granodiorite, they are generally only 10-20 mm thick. Rare examples of this vein type are up to 75 cm thick and dominated by sulfosalts that are visibly replacing earlier pyrite. Selvedge alteration from this stage is similar to that of Stage 5.

Stage 7 – Late Carbonate Veins

A series of carbonate crack-sealed micro-veins cross-cut all earlier vein styles at Dublin Gulch. It is not clear whether these veins are associated with the same event sequence, which formed the primary Au mineralization, or a later metamorphic/orogenic event.

Stage 8 – Supergene and Weathering

Oxidation of the upper 50 m from surface of the deposit is the most widespread supergene/weathering alteration observed at Dublin Gulch. An apparently supergene alteration of Stage 5 arsenopyrite to scorodite is an important tool for prospection for high-grade Au at the surface - as a distinctive green scorodite gossan characteristically makes sheeted vein mineralization from this stage more readily visible in outcrop.

Minerals	Stages										
	1	2a	2b	2c	3	4	5a	5b	6	7	8
	Contact Metamorphism	Skarn			Qtz-K-spar Veins	Qtz-Chl-Carb Veins	Arspy-Rich Veins	Au-rich Stage	Pyrite-Sulfosalt Veins	Carbonate Veins	Supergene Alteration
Pyrrhotite	█										
Chalcopyrite	█										
Quartz		█	█	█	█	█	█				
Wollastonite		█									
Scheelite											
Garnet (Grossular)			█								
Pyroxene (Hedenbergite)			█								
Calcite				█	█	█		█		█	
Chlorite				█		█					
Actinolite				█							
Biotite											
K-Feldspar					█	█					
Albite					█						
Pyrite									█		
Nickel-(Iron)-Sulfides											
Epidote											
Molybdenite											
Ankerite Dolomite										█	
Arsenopyrite							█				
Arsenopyrite											
Sphalerite									█		
Galena											
Tennantite											
Cobaltite*											
Gersdorffite*											
Marcasite											
Muscovite-Phengite									█		
Dickite								█	█		
Kaolinite								█	█		
Pyrophyllite*								█	█		
Native Au											
Electrum											
Ullmannite*											
Bismuthinite											
Tetradymite											
Stibnite											
Jamesonite									█		
Boulangerite									█		
Bournonite*									█		
Freibergite-Tetrahedrite*									█		
Madocite*											
Native Bi											█
Scorodite											█
As-Bi Alloy											█
Fe-O-OH Oxides											█

FIGURE 3.4. Paragenetic stages for Dublin Gulch. Stage 2 (Skarn) stages are adapted from Brown et al. (2002) for this study. Minerals marked with an asterisk (*) were not observed during this study but have been identified by ALS Minerals (2011), their provisional paragenetic placement was determined by the authors on the basis of the textural descriptions and chemical compositions provided by that study. Symbol descriptions are shown below in TABLE 3.1.

TABLE 3.1. Legend for FIGURE 3.4

Symbol	Description
█	Characteristic or dominant mineral in a vein stage – generally comprises >25% of the vein.
▬	Major mineral in a vein stage – generally comprises 10 – 25 % of the vein.
—	Minor mineral in a vein stage – generally comprises 2 – 10 % of the vein.
- - - - -	Uncommon mineral in a vein stage – generally comprises <2% of the vein.
.....	Trace to Rare mineral in a vein stage – Detectable only with microscope
	Definitive paragenetic stage transition marked by distinct cross-cutting relationships in all cases.
	Gradational stage transition marked by ambiguous or absence of cross-cutting relationships.

3.4 Arsenopyrite Composition and Geothermometry

3.4.1 Introduction

Arsenopyrite is present in Stages 3 through 5 at Dublin Gulch. It is one of the major sulfide phases in Stage 3, is present as a minor sulfide phase in Stage 4, and comprises up to 90% of the total mineral modality of Stage 5 veins. Since re-fracturing and overprinting of earlier vein stages is common at Dublin Gulch, it was key to identify the paragenetic stage(s) represented by each individual arsenopyrite sample selected for geothermometry. This was done by assessing textural relationships between arsenopyrite and other ore minerals, and by assessing the alteration styles associated with the vein in which the arsenopyrite was hosted - on the premise that the alteration assemblage would reflect the latest stage that occupied the vein. On this basis, only one generation of arsenopyrite was explicitly identified to be overprinting veins that were originally mineralized at an earlier stage. This was identified in a Stage 3 Olive Zone sample (FK-246, Appendix D) where Stage 5a arsenopyrite occupied Stage 3 veins, accompanied by intense Stage 5b alteration in the vein selvages. An example of a Stage 4 vein from the Eagle Zone (FK-099, Appendix D), which had been re-activated during Stage 5 mineralization and displayed the alteration assemblage of Stage 5b, contained earlier arsenopyrite, which was not re-equilibrated to Stage 5 conditions.

Arsenopyrite displays a wide range of solid solution – described as $\text{FeAs}_{1-x}\text{S}_{1+x}$, where $x \leq 0.13$ for ideal arsenopyrite (Klemm, 1965; Kretschmar and Scott, 1976; Sharp et al., 1985). Kretschmar and Scott (1976) showed, through experiments in the system Fe-As-S, that the composition of arsenopyrite is affected by the temperature and $f\text{S}_2$ at which it crystallizes. Their experimentally derived plot of mineral stabilities in T versus $f\text{S}_2$ space for this system –

contoured for atomic % As in arsenopyrite – provides the basis for arsenopyrite geothermometry of ore mineral assemblages at Dublin Gulch. Since total trace metal contents of greater than approximately 1% are perceived to significantly affect the stability fields of arsenopyrite, minor elements known to sometimes occur at substantial levels in arsenopyrite (i.e., Bi, Co, Ni, Sb, and Te) were included in our analysis.

TABLE 3.2. Summary of Electron Probe Micro-Analysis (EPMA) results for arsenopyrite grains at Dublin Gulch.

Vein Stage	Zone of deposit	As	Fe	S	Bi	Co	Ni	Sb	N
3	Eagle	34.2-35.9	33.2-33.5	30.9-32.2	-	0.0-0.1	0.0-0.1	-	10
4 with 5b Alteration	Eagle	34.2-36.5	26.7-32.3	30.3-32.6	-	0.8-5.9	0.1-0.5	-	5
5a	Proximal	31.7-33.3 (33.9)	32.2-33.7	32.6-35.2	-	-	-	-	34
	Distal	28.5-33.3 (35.9)	32.7-33.5	31.1-38.2	0.0-0.1	0.0-0.2	-	0.0-0.5	38
3 with 5b Alteration	Olive	30.7-32.5	33.1-33.5	34.7-35.3	-	0.0-0.1	0.0-0.1	0.0-0.1	5

Notes: Analyses are categorized by the paragenetic stage(s) observed in the sample in which the arsenopyrite occurred, and sub-categorized by deposit zone, with increasing distance from the Eagle Zone descending in the list. Stage 5a is cut-off at a maximum of 33.3 at. % As, based on equilibrium with associated sulfide mineral stabilities, specifically coexistence with pyrite (see discussion in text). Measured maximum values for Stage 5a, which include remnant arsenopyrite from earlier stages, are quoted in brackets. Proximal = Eagle, Henderson and Olive Zones, Distal = Carscallen, Shamrock and Potato Hills Zones. Detailed analytical data are available in Appendix D.

3.4.2 Analytical Approach

We used electron probe microanalysis (EPMA) to establish the formula and trace metal content of arsenopyrite samples from Dublin Gulch. EPMA was carried out at Carleton University using an automated four spectrometer Camebax MBX electron probe operating in wavelength-dispersive mode (WDX) at 20 kV accelerating potential with a beam current of 35 nA. Counting times were up to 50 s or 40,000 accumulated counts. The X-ray lines were chosen to minimize or eliminate elemental interferences. Raw X-ray data were converted to elemental wt.% via the

Cameca PAP matrix correction program. Procedures used were similar to those of Tuba (2014). The standards used for Fe-As-S were the synthetic ARSPY200 and ARSPY57 materials of Kretschmar and Scott (1976) (See Table 3.3). Elements are reported as weight percent (wt. %) or atomic percent (at.%). Trace elements were standardized using the values tabled for ARSPY57 in Kretschmar and Scott (1976).

3.4.3 Results

The compositions determined using EPMA for major elements Fe, As, and S - and for Bi, Co, Ni, and Sb - are illustrated in Figure 3.5 and summarized in Table 3.2. Detailed analytical data are available in Appendix D. Analyses in Table 3.2 have been arranged according to vein type, and by the zone of the deposit in which they occur. Tellurium was below detection for all EPMA analyses of arsenopyrite, and so is not reported in Table 3.2. (During EPMA analysis, a single grain of tetradymite was also identified in a sample of Stage 5a mineralization. This is the only example of a Te-bearing mineral that has been identified at Dublin Gulch to date).

TABLE 3.3. Stated values for standards used for EPMA from Kretschmar and Scott (1976). Values shown are quoted in weight percent with atomic percent quoted in brackets.

Standard	Fe	As	S	Bi	Co	Ni	Sb	Te
ARSPY200	34.51 (33.10)	44.44 (31.77)	21.03 (35.13)	N/A	N/A	N/A	N/A	N/A
ARSPY57	33.85 (33.17)	46.94 (34.28)	19.08 (32.55)	0.01	0.0042	0.0011	0.04	N/A

For most analyses, the combined Bi + Co + Ni + Sb content comprised $\ll 1.0$ at.%. The exception was arsenopyrite of Stage 4 with 5b alteration, which contained 0.8-5.9 at.% Co and 0.1-0.5 at.% Ni. As expected, these two elements appear to be substituting for Fe. Substantial Sb (up to 0.5 at.%) and Co (up to 0.2 at.%) also appeared in analyses of Stage 5a samples from Potato Hills (see Appendix D).

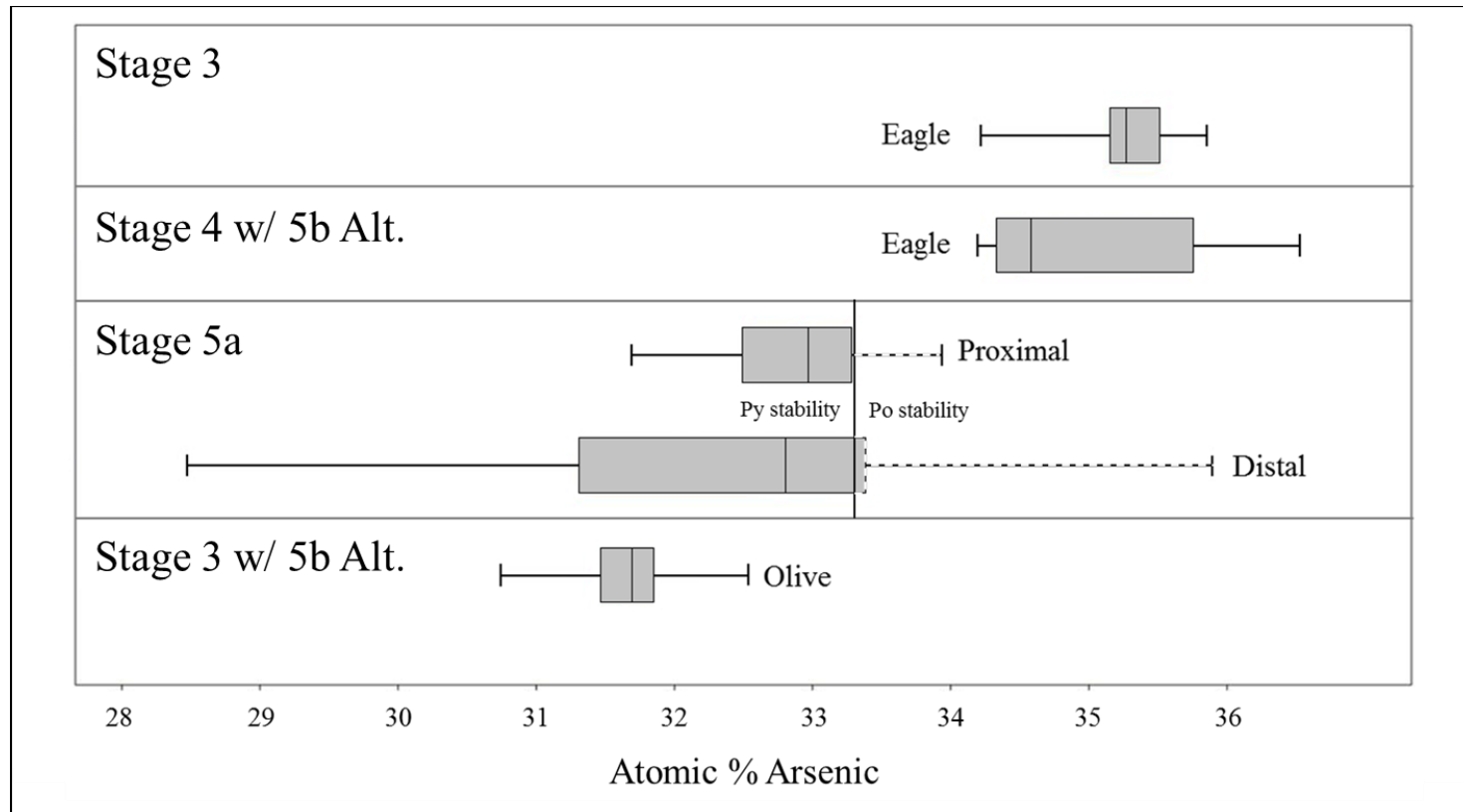


FIGURE 3.5. Box and whiskers plot of ranges in arsenopyrite compositions at Dublin Gulch, grouped by paragenetic stage. Arsenopyrites from Stage 3 and Stage 4 with Stage 5b alteration plot within a similar overall range of at.% As - from 34.2 to 36.5. Stage 5a shows a lower at.% As range - from 28.7 to 35.9 - indicating a distinctly different population. For Stage 5a the vertical line at 33.3 at. % As represents an estimate of the transition from the pyrite stability field ($\leq 33.3\%$) to the pyrrhotite stability field ($> 33.3\%$). Since Stage 5a mineralization is texturally associated with pyrite, the values above approximately 33.3 % must represent remnant arsenopyrite from earlier vein stages. The values that are considered to be from remnant arsenopyrite within Stage 5a veins are marked with dashed lines. Arsenopyrite from Stage 4 has the alteration assemblage of Stage 5b but has compositions that are more As-rich than possible for equilibrium with pyrite-bearing Stage 5 mineralization (33.3%), indicating that re-equilibration of Stage 4 arsenopyrite during Stage 5 mineralization has not taken place in the sample analysed (FK-099, Eagle Zone). Arsenopyrite from a Stage 3 vein with Stage 5b alteration (FK-024, Olive Zone; see discussion in text) has a composition suggesting re-equilibration during Stage 5a or later, further documenting the texturally implied overprinting of Stage 3 veins by later hydrothermal minerals. Plot produced using the PAST software of Hammer et al. (2001).

3.4.4 Compositional Zoning

Figure 3.6 shows examples of μm scale compositional zoning within arsenopyrite samples, as displayed in SEM-BSE images. Image brightness denotes variations in atomic % As (brightest domains have highest As content and consequently highest mean atomic weight). Intra-grain variations can exceed 6.0 at.% As (e.g., FK-TH12-61, Fig. 3.6A), which is of the same magnitude as that observed between separate paragenetic stages (Table 3.3). This suggests that some grains preserve more than one paragenetic stage of arsenopyrite. For example, samples such as that imaged in Figure 3.6A, from a nominally Stage 5a sample in the Potato Hills Zone, suggest that at least three compositionally distinct generations of arsenopyrite may be preserved in this sample. A sample of Stage 5a arsenopyrite from Olive Zone (Fig. 3.6B, C) shows evidence of more rhythmic outward “herringbone” compositional zoning, more typical of minerals formed during a single paragenetic stage in medium-to-high-temperature hydrothermal veins. A second sample from Olive Zone (Fig. 3.6D) shows what appears to be a combination of the zoning features found in the other two samples shown in Figure 3.6. Detailed assessment with SEM-EDS analysis revealed that Stage 5a arsenopyrites have sometimes overgrown cores of Stage 3 arsenopyrite (e.g., sample FK-TH12-61; Fig. 3.6E).

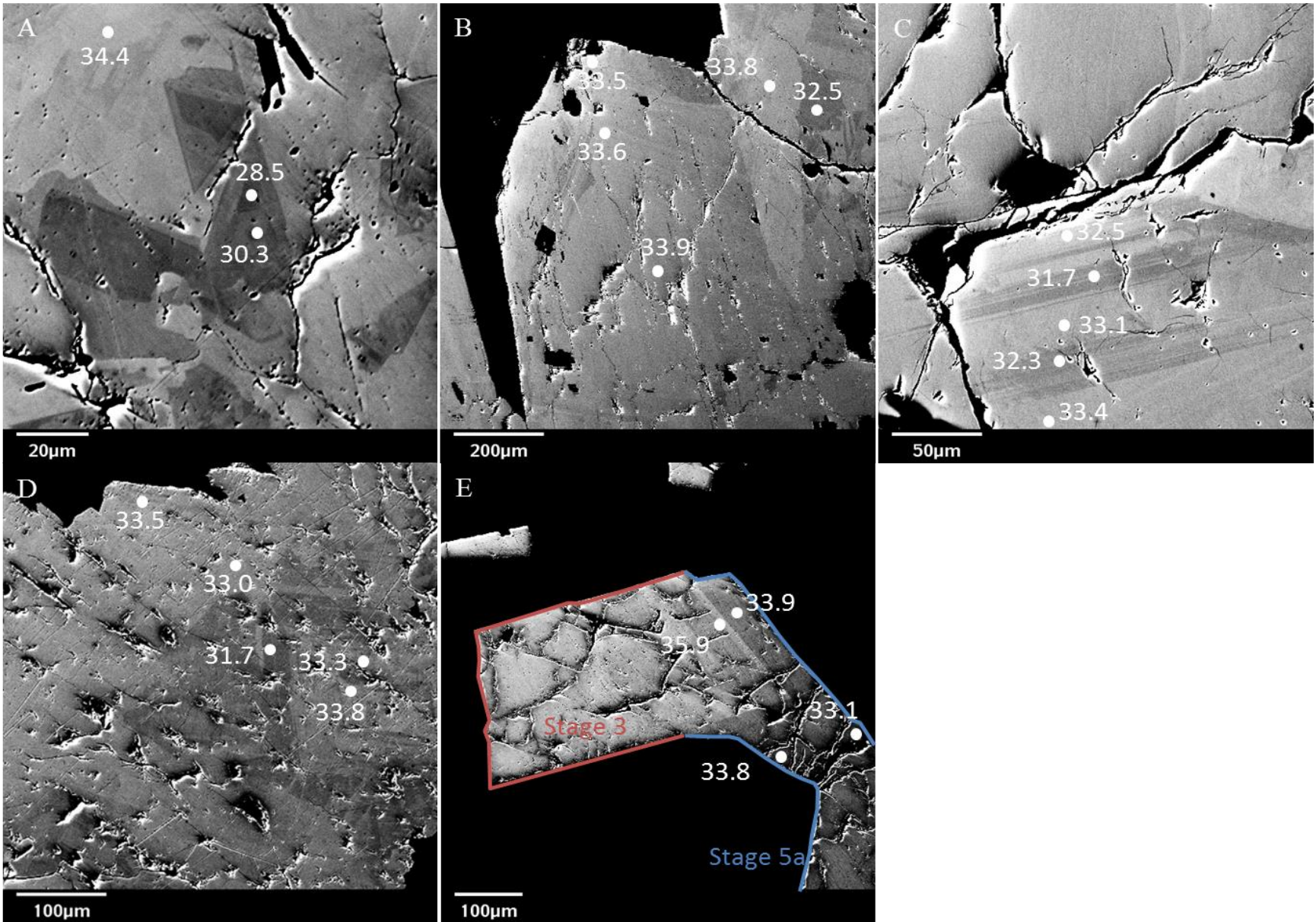


FIGURE 3.6. Images of compositional zoning in arsenopyrite grains suggesting prolonged periods of precipitation and mineral growth. Darker colour is directly correlated to lower at.% As in the grain and as a consequence, lower atomic mass. Samples: A: FK-TH12-61 (NAD83 465970 E 7102570 N, Potato Hills Zone). ; B: FK-227 (DDH DG10-373C, 81.00 m, Olive Zone); C: FK-227 (DDH DG10-373C, 81.00 m, Olive Zone); D: FK-TH12-39 (NAD83 461344 E 7101092 N, Olive Zone); E: FK-TH12-61 (NAD83 465970 E 7102570 N, Potato Hills Zone). All but one of the images, C, show values stable within both the pyrite stability field (<33.3 at.% As) and the pyrrhotite stability field (>33.3 at.% As), implying that remnants of Stage 3 or Stage 4 mineralization (pyrrhotite stability field) were commonly overgrown by Stage 5a arsenopyrite (pyrite stability field). Image E contains the most well constrained paragenetic sequence from petrography, a Stage 3 (red outline) arsenopyrite grain with Stage 5a (light blue outline) arsenopyrite overgrowth. There is a transitional boundary between true Stage 3 arsenopyrite (35.9 at.% As.) and true Stage 5a arsenopyrite (33.1 at.% As) marked by the values of 33.9 and 33.8 at.% As. These transitional values are above the values that are possible for equilibrium with the Stage 5a sulfide assemblage (pyrite stability field), but demonstrate the partial re-equilibration of Stage 3 arsenopyrite during Stage 5a mineralization.

3.5 Sulfur Isotopes

3.5.1 Introduction

Detailed sulfur isotope studies of intrusion related gold systems are relatively rare (e.g., Stephens, 2003; Marsh et al., 2003 – Clear Creek). In large part, this is due to the longstanding perception that porphyry-style systems consistently contain sulfides with $0 \pm 1\text{‰ } \delta^{34}\text{S}$ (Ohmoto and Rye, 1979), and it has been consequently inferred that other granitoid-intrusion related hydrothermal systems should give a broadly similar profile to those shown by porphyry-style systems. However, some recent studies – largely on alkalic porphyry Cu deposits in BC (Lorraine, Mount Polley, Red Chris, Galore Creek, Afton: Deyell, 2005; Deyell and Tosdal, 2005; Micko, 2010; Pass et al., 2014) - have revealed some informative variations and zoning in the $\delta^{34}\text{S}$ of ore sulfides in such systems. In this study we explored the potential variation of $\delta^{34}\text{S}$ in 24 samples of arsenopyrite, pyrite, and pyrrhotite from the Dublin Gulch Au deposit using sulfide microanalysis by Secondary Ion Mass Spectrometry (SIMS).

3.5.2 Sample Selection

Samples were selected from across the major vein stages to provide an indication of $\delta^{34}\text{S}$ variations at Dublin Gulch. The earliest sulfides present are pyrrhotite and chalcopyrite formed during contact metamorphism of the host Hyland Group metasedimentary rocks (Stage 1). Minor pyrrhotite is also present within the primary Wolf W Skarn (Stage 2). Pyrrhotite is the dominant sulfide in vein Stages 3 and 4 along with subsidiary amounts of pyrite and arsenopyrite. Arsenopyrite is the only major sulfide present in Stage 5 mineralization. Stage 6 mineralization consists of pyrite and sulfosalts – in particular, jamesonite and boulangerite. Pyrite was the only phase measured from this stage. Sulfosalt species were not measured, as appropriate microanalytical standards for these specific phases for SIMS are not currently available.

3.5.3 Methodology

Samples were cut into small slabs (20mm x 20mm or less) and mounted in 1” diameter Al rings with two-component epoxy. They were then polished using standard lapidary procedure with a Struers Tegramin system using a series of abrasive stages down to 1 μm , for a high quality metallographic finish. Sulfur isotope determinations by SIMS were carried out on pyrrhotite, pyrite and arsenopyrite at Memorial University using a Cameca IMS 4f instrument. A total of 141 spot analyses were performed using procedures similar to those of Brueckner et al. (2014).

3.5.4 Results

A box-whiskers plot (Fig. 3.7) illustrates the distribution of sulfur isotope values for each mineral phase, further subdivided by paragenetic stage. Detailed data are available in Appendix E. The most negative $\delta^{34}\text{S}$ values at Dublin Gulch occur in pyrrhotite in the hornfelsed metamorphic aureole, -12.7 to -8.7 ‰ $\delta^{34}\text{S}$. Pyrrhotite that appears as a minor phase within the

Wolf W Skarn ranges from -7.9 to -6.8 ‰ $\delta^{34}\text{S}$. Pyrrhotite from the stockwork vein stages (Stages 3 and 4) ranges from -7.4 to -4.1 ‰, and -9.6 to +2.6 ‰ $\delta^{34}\text{S}$, respectively. Pyrrhotite from quartz veins in the Rex-Peso area ranges from +2.8 to +4.9 ‰ $\delta^{34}\text{S}$, representing the most positive values observed in this study. Stages 5 and 6 contained no pyrrhotite.

Pyrite hosted in Stage 4 partially aligned stockwork veins displays a very wide range - from -6.1 to +2.6 ‰ $\delta^{34}\text{S}$. Examples of these same Stage 4 veins that also display the alteration assemblage of Stage 5b display a narrower, more negative range - from -5.3 to -3.8 ‰ $\delta^{34}\text{S}$. Late stage pyrite in Stage 5a ranges from -3.9 to +1.9 ‰ $\delta^{34}\text{S}$. Pyrite is the dominant sulfide mineral in Stage 6 mineralization, and ranges from -1.3 to 1.1 ‰ $\delta^{34}\text{S}$.

Arsenopyrite from stockwork quartz veins of Stage 3 displays very negative values, ranging from -11.7 to -7.5 ‰ $\delta^{34}\text{S}$, comparable to those of the pyrrhotite from contact metamorphosed metasedimentary rocks (Stage 1). Arsenopyrite from Stage 4 partially aligned stockwork veins that also display the alteration assemblage of Stage 5b ranges from -3.5 to +0.9 ‰ $\delta^{34}\text{S}$. Stage 5a mineralization (up to 90% arsenopyrite in individual veins) has values of -1.7 to + 2.4 ‰ $\delta^{34}\text{S}$.

A clear trend of values increasing toward ~ 0 ‰ $\delta^{34}\text{S}$ with increasing time is apparent for successive paragenetic stages. Interestingly, pyrrhotite from the Rex Zone vein shows a distinct grouping of the most positive $\delta^{34}\text{S}$ values observed in the data set. The study of Boyle et al. (1970) also included supplemental bulk sample $\delta^{34}\text{S}$ data from Dublin Gulch; pyrite from a “massive breccia zone” (-1.8 to +1.5 ‰ $\delta^{34}\text{S}$), arsenopyrite from pyrite-arsenopyrite-gold veins (0.0 to + 1.3 ‰ $\delta^{34}\text{S}$) and a single analysis of chalcopyrite from a cassiterite lode (presumably at Tin Dome prospect; -1.8 ‰ $\delta^{34}\text{S}$). Only the arsenopyrite analysis can be easily reconciled with

our paragenetic scheme, as it is reasonably similar to Stage 5 veins with Stage 6 overprinting. In this case the Boyle et al. (1970) “gold vein” sample lies within the range for Stage 5a arsenopyrite.

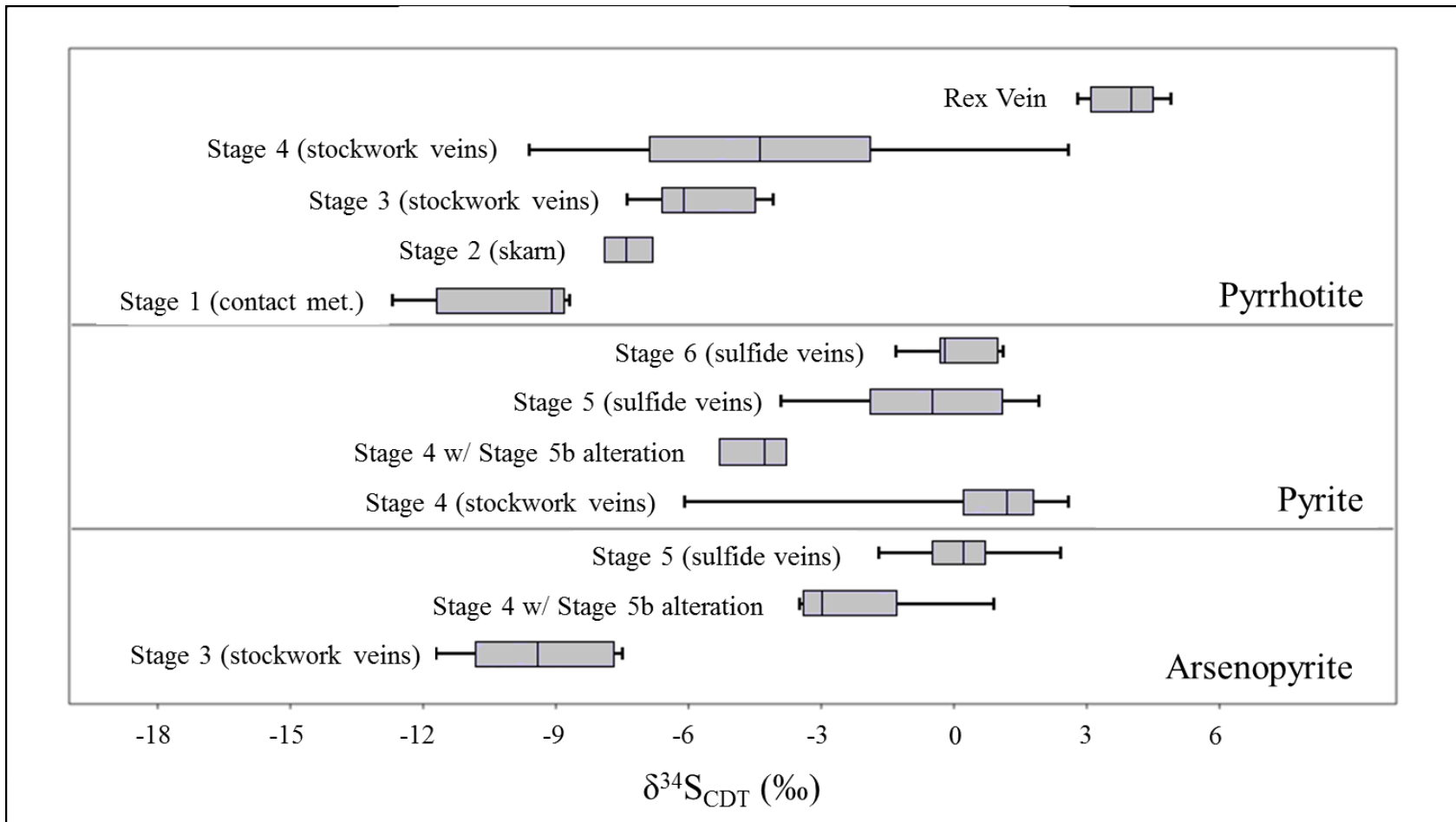


FIGURE 3.7. Box & whiskers plot of SIMS sulfur isotope data for Dublin Gulch samples, grouped by sulfide mineral. The bar section of each data set (filled in grey) represents the portion of the data that lies between the upper and lower quartiles. The mean value is marked by a line bisecting the grey area. The whiskers, which extend to the left and right of the bar, extend to the minimum and maximum observed values, respectively. Plot produced using the PAST software of Hammer et al. (2001). Detailed data are available in Appendix E. CDT = Vienna Canyon Diablo Troilite.

3.6 Lead isotopes

3.6.1 Introduction

Jamesonite and boulangerite, typically mutually intergrown, are the most abundant Pb-bearing minerals at Dublin Gulch. They occur in two successive paragenetic stages, in association with pyrite (Stages 5b and 6 – Fig. 3.4). Stages 5b and 6 are key stages for Au occurrence at Dublin Gulch, and these two sulfosalt minerals have been observed in textural equilibrium with native gold in samples containing Stage 5b and 6 mineralization. For these reasons, samples of jamesonite and boulangerite were selected for Pb isotope microanalysis by SIMS.

3.6.2 Methodology

Samples containing Pb-sulfosalt mineralization were prepared in a manner identical to those used for sulfur isotope microanalysis (Section 3.3, above). $^{208}\text{Pb}/^{207}\text{Pb}/^{206}\text{Pb}/^{204}\text{Pb}$ ratios were determined using the approach detailed in Appendix F. Two sub-areas within each of six different samples were examined, for a total of 21 individual spot analyses.

3.6.3 Results

Lead isotopes from sulfide ores in the Selwyn Basin terrane (regardless of age or genesis) uniformly display highly radiogenic ratios, with forward model ages relative to standard terrestrial Pb growth curves (e.g., Kuo and Folinsbee, 1974; Godwin and Sinclair, 1982; Heffernan et al., 2004; Hantelmann, 2013). However, the Pb isotope ratios determined here for the Dublin Gulch Stage 5b and 6 samples (Table 3.4; Appendix F) are among the most radiogenic (highest $^{206}\text{Pb}/^{204}\text{Pb}$, $^{207}\text{Pb}/^{204}\text{Pb}$) reported to date from any sulfide ore sample within the Selwyn Basin Terrane - with $^{206}\text{Pb}/^{204}\text{Pb}$ values of 20.41 to 21.71, $^{207}\text{Pb}/^{204}\text{Pb}$ of 15.89 to

TABLE 3.4. Pb isotope values for Dublin Gulch.

Sample	Description	$^{204}\text{Pb}/^{206}\text{Pb}$	SEM %	$^{207}\text{Pb}/^{206}\text{Pb}$	SEM %	$^{208}\text{Pb}/^{206}\text{Pb}$	SEM %	$^{206}\text{Pb}/^{204}\text{Pb}$	SEM %	$^{207}\text{Pb}/^{204}\text{Pb}$	SEM %	$^{208}\text{Pb}/^{204}\text{Pb}$	SEM %
FK 025 Pb1	Shamrock Zone	0.04856	0.1	0.7740	0.09	1.966	0.11	20.59	0.1	15.94	0.13	40.48	0.15
FK 025 Pb2		0.04856	0.05	0.7744	0.06	1.972	0.08	20.59	0.05	15.95	0.08	40.61	0.09
FK 025 Pb3		0.04860	0.06	0.7725	0.07	1.963	0.14	20.57	0.06	15.89	0.1	40.39	0.15
FK 025 Pb4		0.04861	0.1	0.7741	0.03	1.967	0.04	20.57	0.1	15.92	0.1	40.46	0.11
FK 025 Pb5		0.04864	0.06	0.7743	0.04	1.969	0.03	20.56	0.06	15.92	0.07	40.49	0.07
FK 036 Pb1	Shamrock Zone	0.04883	0.08	0.7802	0.04	1.982	0.05	20.48	0.08	15.98	0.09	40.58	0.10
FK 036 Pb2		0.04899	0.09	0.7805	0.04	1.983	0.04	20.41	0.09	15.93	0.10	40.49	0.10
FK 066 Pb1	Shamrock Zone	0.04805	0.1	0.7681	0.08	1.970	0.1	20.81	0.1	15.98	0.12	40.99	0.14
FK 066 Pb2		0.04797	0.07	0.7671	0.02	1.967	0.06	20.85	0.07	15.99	0.07	41.01	0.09
FK 066 Pb3		0.04784	0.11	0.7661	0.05	1.960	0.06	20.90	0.11	16.01	0.12	40.97	0.12
FK 066 Pb4		0.04758	0.1	0.7619	0.06	1.956	0.1	21.02	0.1	16.01	0.12	41.11	0.14
FK 066 Pb5		0.04792	0.09	0.7677	0.04	1.968	0.03	20.87	0.09	16.02	0.09	41.08	0.09
FK 066 Pb6		0.04812	0.16	0.7676	0.25	1.970	0.28	20.78	0.16	15.95	0.3	40.93	0.32
FK 066 Pb7		0.04795	0.06	0.7679	0.04	1.966	0.04	20.85	0.06	16.01	0.07	41.01	0.07
FK 285 Pb1	Olive Zone	0.04858	0.08	0.7754	0.03	1.988	0.02	20.58	0.08	15.96	0.08	40.92	0.08
FK 285 Pb2		0.04863	0.07	0.7770	0.04	1.992	0.02	20.56	0.07	15.98	0.08	40.96	0.08
FK 285 Pb3		0.04848	0.11	0.7781	0.08	1.993	0.16	20.63	0.11	16.05	0.14	41.11	0.19
FK 285 Pb4		0.04868	0.08	0.7781	0.03	1.995	0.04	20.54	0.08	15.98	0.08	40.99	0.09
FK TH12 03 Pb1	Haggart Creek	0.04608	0.06	0.7405	0.04	1.939	0.04	21.70	0.06	16.07	0.07	42.08	0.07
FK TH12 03 Pb2		0.04607	0.07	0.7409	0.02	1.942	0.04	21.71	0.07	16.08	0.07	42.15	0.08
FK TH12 56 Pb1	Shamrock Zone	0.04795	0.05	0.7671	0.02	1.966	0.04	20.85	0.05	16.00	0.06	40.99	0.06

16.08, and $^{208}\text{Pb}/^{204}\text{Pb}$ values of 40.39 to 42.15 ($^{204}\text{Pb}/^{206}\text{Pb}$ of 0.04607 to 0.04899, $^{207}\text{Pb}/^{206}\text{Pb}$ of 0.7405 to 0.7805 and $^{208}\text{Pb}/^{206}\text{Pb}$ of 1.939 to 1.995).

Figure 3.8 shows Pb isotope ratios for sulfosalts at Dublin Gulch plotted against standard published model Pb growth curves for terrestrial reservoirs. The Shale Curve (Godwin and Sinclair, 1982) as shown in Figure 3.8 was constructed from measurements of galena in deposits within the Cordilleran miogeocline and thus represents a more specific frame of reference for Pb isotope evolution in the Selwyn Basin.

Four other model curves, based on the “plumbotectonics model”, are also plotted in Figure 3.8. In this model, the fractionation of more radiogenic Pb into the upper crust occurs due to the preferential uptake of Pb over U in the lower crust during granulite facies metamorphism (Dickin, 2005). The Mantle Curve is a representation of the upper mantle for depths less than 500 km. The Orogene Curve is a representation of the process of orogenesis modelled at 400 Ma intervals from a starting point of 4 Ga, based on the premise that continental accretion began at that time. The contribution from the crust to the orogene in this model is from erosion of the “Upper Crust” and delamination of the “Lower Crust”. The upper crust, lower crust, and mantle are mixed and then redistributed to give values, which are used for each subsequent orogeny until the present. Starting values of the curves for 1st and 2nd versions of the model (Doe and Zartman, 1979; Zartman and Doe, 1981) use an estimated isotopic ratio starting at 4 Ga, while the 4th version (used in Fig. 3.8; Zartman and Haines, 1988) starts at 4.45 Ga, with a Pb isotope composition based on Canyon Diablo meteorite.

Sulfosalt species at Dublin Gulch plot far above the Shale Curve, displaying hypothetical forward ages. The most radiogenic sample, FK-TH12-03, is from a pyrite vein at Haggart Creek

hosted by interbedded quartzites and phyllites of the Hyland Group, and is the most distal example of mineralization relative to the DGS in the suite of samples analysed by SIMS. The remaining samples, which are hosted by the DGS (Olive and Shamrock zones; see Table 3.4), show a dispersion of values that suggests that an external very highly radiogenic Pb source mixed with the DGS reservoir to give the values obtained for distal mineralization.

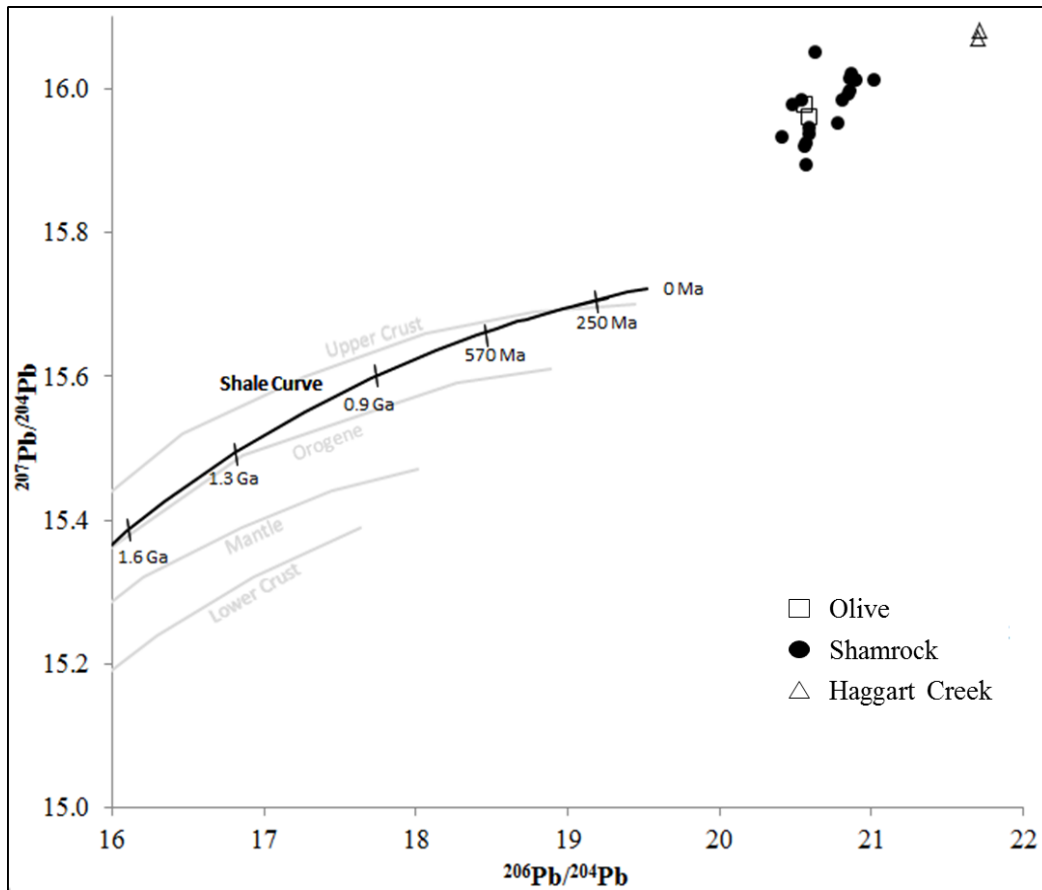


FIGURE 3.8. Pb isotope values for sulfosalts phases at Dublin Gulch plotted as $^{207}\text{Pb}/^{204}\text{Pb}$ vs $^{206}\text{Pb}/^{204}\text{Pb}$. Published growth curves are shown for reference; the Shale Curve of Godwin and Sinclair (1982) and four Pb growth curves taken from the plumbotectonics model (Doe and Zartman, 1979; Zartman and Doe, 1981; Zartman and Haines, 1988). There is no readily discernible difference between Pb isotope compositions of Stage 5b vs Stage 6 samples, and data symbols reflect mineralized zones.

3.7 Discussion

3.7.1 Temperature Estimates from Arsenopyrite Composition

Figure 3.9 shows T-fS₂ stability fields for each vein stage - based on at.% As in arsenopyrite, and the stability fields of other sulfide phases in textural equilibrium with the arsenopyrite. Constraints on maximum and minimum temperatures for arsenopyrite-bearing stages are presented in Table 3.5, as derived from the intercepts of at.% As contours of the arsenopyrite with the appropriate phase boundaries in Figure 3.9.

Stage 3 (Fig. 3.9A, in blue) and Stage 4 with 5b alteration (Fig. 3.9B, in orange) occupy similar space on the sulfur fugacity vs. temperature plot, with Stage 4 with 5b alteration ranging to somewhat higher values of at.% As. Unlike Stage 3, some Stage 4 with 5b alteration arsenopyrite contains trace metals in excess of 1 at.% - and this needs to be considered in subsequent interpretation. Kretschmar and Scott (1976) indicate that elevated trace element contents may bias the estimation of temperature from arsenopyrite stoichiometry. We note that the measurements for Stage 4 with 5b alteration that portray the highest at.% As contents, and thus increase the maximum temperature estimate above that of Stage 3 contain >6 at.% trace elements, consistent with the aforementioned effect. With these measurements eliminated, the maximum temperature estimated for Stage 4 is 560 °C.

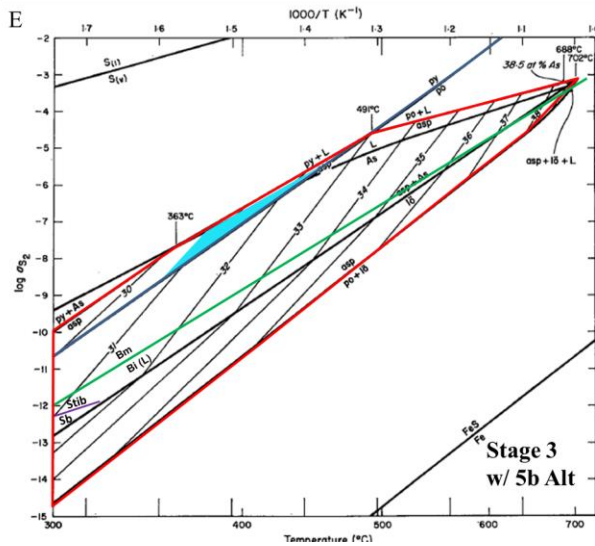
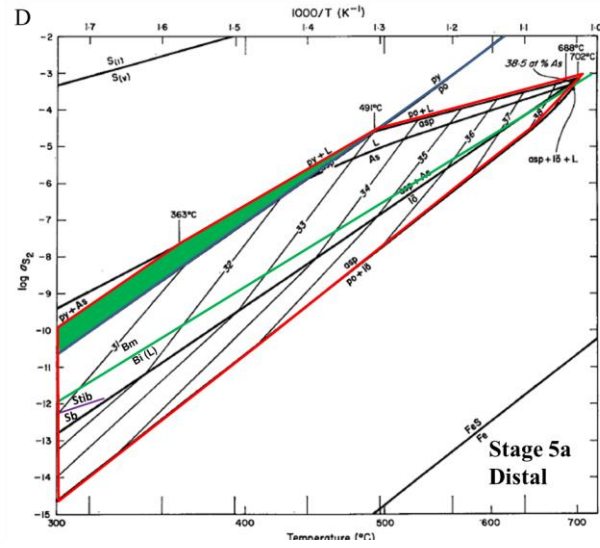
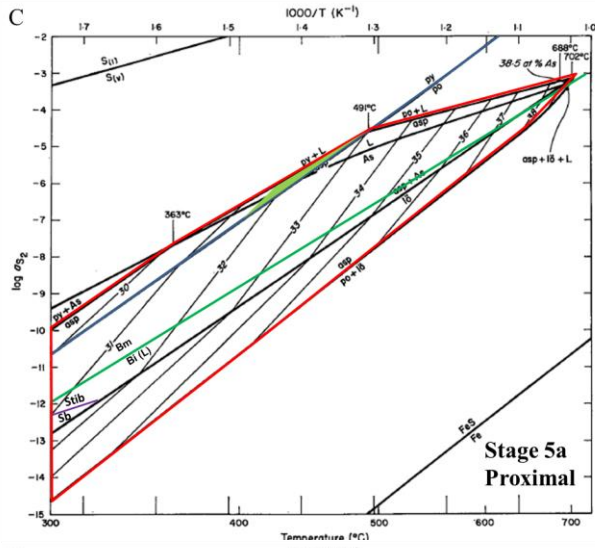
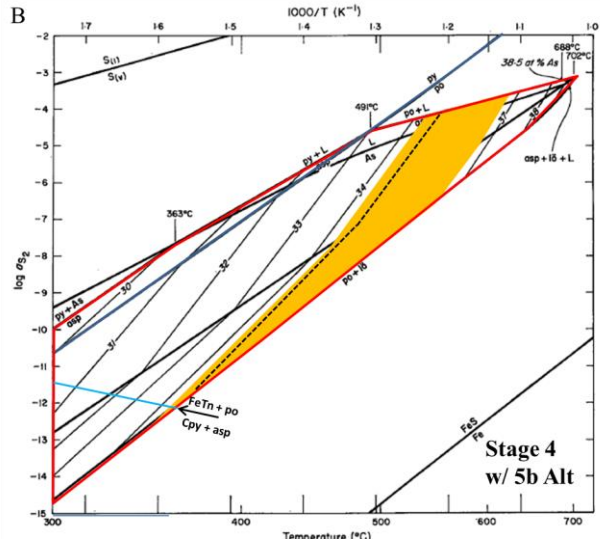
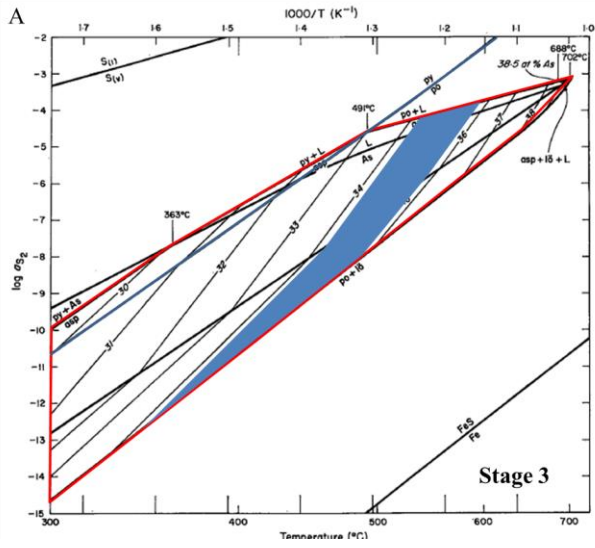


FIGURE 3.9. T-fS₂ stability fields for each vein stage. A: (Blue) Stage 3 stockwork veins. B: (Orange) Stage 4 stockwork vein with alteration mineral assemblage of Stage 5b. Dotted line indicates extent of field with samples containing high minor element contents eliminated. C: (Light Green) Stage 5a arsenopyrite veins in the proximal zones (Eagle, Henderson, Olive). D: (Green) Stage 5a arsenopyrite veins in the distal zones (Carscallen, Shamrock, Potato Hills). E: (Light Blue) Stage 3 stockwork vein with alteration mineral assemblage of Stage 5b. Red boundary shows the overall stability field of arsenopyrite (Kretschmar and Scott, 1976). Purple line highlights the Po-Py stability boundary. Light Blue line (B) highlights the breakdown of Fe-tennantite and pyrrhotite to chalcopyrite and arsenopyrite, based on the upper temperature estimate for this reaction after Tesfaye Firdu and Taskinen (2010). Green line (C, D, and E) highlights the Bismuthinite (Bm) to Bismuth Liquid (Bi (L)) transition as calculated by Bente (1982). Purple line highlights the Stibnite (Stib) to Native Antimony (Sb) transition after Einaudi et al. (2003). Overall base stability diagram after Kretschmar and Scott (1976).

TABLE 3.5. Temperature estimates of arsenopyrite using the method of Kretschmar and Scott (1976) from this study.

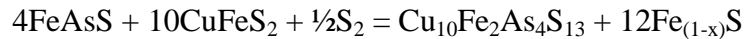
Vein Stage	Temp Range (°C)
3	350 - 595
4 w/ 5b alteration	345 - 560 (620*)
5a Proximal	405 - 490
5a Distal	<300 - 490
3 w/ 5b alteration	350 - 460

*maximum T estimate is reduced to 560 °C if samples with > 6 wt.% of minor elements are eliminated.

As a whole, Stage 5a (Fig. 3.9C, D), in which arsenopyrite is the dominant sulphide phase, displays arsenopyrite compositions that lie throughout the pyrite-arsenopyrite field of the Kretschmar and Scott (1976) diagram. Stage 5a is usefully subdivided into separate fields for the Eagle-Henderson-Olive zones (proximal, Fig. 3.9C) and the Carscallen-Shamrock-Potato Hills zones (distal, Fig. 3.9D) – with the samples from the distal zones ranging to much lower estimated temperatures (<300 °C) than the 405 to 490 °C inferred for the proximal zones. Stage 3 veins with Stage 5b alteration (Fig. 3.9E) overlap the upper part of the field for Stage 5a veins. This is compatible with other observations, discussed above, that imply that this latter generation

of arsenopyrite also formed at Stage 5b. The pattern of arsenopyrite stability fields in Figure 3.9 is consistent with our paragenetic interpretations (Chapter 2), which suggest discrete fluids for Stages 3-4 and Stages 5-6.

Given that the examples of Stage 4 arsenopyrite studied do not appear to have re-equilibrated to compositions compatible with Stage 5 T-fS₂ conditions (Figs. 3.5, 3.9), our “Stage 4 with 5b Alteration” serves as the best possible estimate of Stage 4 conditions (see below for detail). An assessment was also made as to whether any additional sulphide phase equilibria might further constrain the temperature estimates from arsenopyrite compositions. Tennantite and chalcopyrite have been observed in the nominal Stage 4 assemblage (Fig. 3.9B), implying that tennantite may have been formed by a reaction (Tesfaye Firdu and Taskinen, 2010) such as:



The line representing this reaction on Fig. 3.9B is the upper temperature boundary estimate of Tesfaye Firdu and Taskinen (2010). This reaction intersects the lower-most portion of the arsenopyrite stability diagram and suggests that Fe-tennantite will break down at below 360 °C within the pyrrhotite-arsenopyrite stability field. However, since this is an upper temperature estimate, and does not substantially further constrain the minimum temperature estimated from arsenopyrite composition, it is not used to further constrain the minimum temperature for Stage 4 in Table 3.5.

In samples of Stage 5 and 6 mineralization, native bismuth has been observed intergrown with bismuthinite. The reaction:



is plotted on Figures 3.9C, D, and E. However, the stable presence of pyrite places the Stage 5 assemblages well into the bismuthinite stability field, strongly implying that native Bi intergrowths are actually replacement textures formed during the later stage of Supergene Alteration (Fig. 3.4), along with the Bi-As alloy phase described in Chapter 1. In any case, the stable presence of bismuthinite does not additionally constrain the arsenopyrite geothermometry for the Stage 5 assemblage, since the native Bi-bismuthinite reaction lies well below the pyrite stability field.

Similarly, the reaction:



while transecting the overall stability field of arsenopyrite, also lies well below the pyrite stability field, and thus the stable presence of stibnite in Stage 5 does not further constrain the temperature range estimated for the Stage 5 assemblage.

In detail, there is a progression to lower at.% As ranges in Stage 5a as one moves NNE from the Eagle Zone. This is probably not a simple function of outward temperature zoning from a “point source” of fluid. The Dublin Gulch Stock appears ridge-like in geometry, and as one moves to the NNE one is likely sampling veins from shallower absolute emplacement depths, and larger radial distances from the ridge line that may constitute the approximate nexus of fluid emanation(s). The estimated temperature constraints for Stage 5a in Table 3.5 are thus subdivided for the more “proximal” Eagle, Henderson, and Olive zones, and the more “distal” Carscallen, Shamrock, and Potato Hills zones (Fig. 3.3).

The maximum at.% As value in some arsenopyrite from nominally Stage 5a distal veins (Appendix D) was higher than the 33.0 at.% maximum value determined experimentally for

arsenopyrite formed within the pyrite stability field (Kretschmar and Scott, 1976; Fig 3.9). In assessing nominal Stage 5a samples, any composition with >33.3 at.% As (allowing for some small analytical uncertainty in the EPMA determinations) was interpreted as belonging to remnant arsenopyrite from earlier stages where pyrrhotite was stable rather than pyrite. Textures like those in Figure 3.6E are further evidence of the ability of Stage 5a mineralization to overprint Stage 3 and 4 mineralization.

However, the pattern shown by Stage 4 arsenopyrite from veins with Stage 5b alteration selvages highlights that, while over-printing of previous stages has taken place, the re-equilibration of arsenopyrite composition is not always complete. Sample FK-099 (Eagle Zone; see Appendix B), was the sole example examined of Stage 4 with 5b alteration, and contained a single grain of arsenopyrite surrounded by pyrite. The composition of this arsenopyrite is well above 33.3 at.% As, which militates against the possibility that the arsenopyrite and pyrite formed in equilibrium. This sample, therefore, highlights a pattern in which arsenopyrite-bearing Stage 4 veins were sometimes re-activated during Stage 5, with concomitant pyrite mineralization and overprinting of Stage 4 alteration selvages by Stage 5b alteration. Although the Stage 5 fluid was able to largely overprint the existing alteration assemblage, the Stage 4 arsenopyrite was not re-equilibrated to Stage 5 composition. This same sample is assessed in more detail with respect to the relationship of arsenopyrite compositions and sulfur isotopes below (Section 3.7.1.1), along with sample FK-246 - which is an example of a Stage 3 quartz vein with Stage 5b alteration.

For the arsenopyrite sampled from Stage 3 quartz veins with Stage 5b alteration selvages there is an apparent paradox - because arsenopyrite is not recognised as a formal part of Stage 5b of our proposed paragenesis. However, in this case earlier (Stage 3) arsenopyrite has apparently

remained stable – and even wholly or partially re-equilibrated to at.% As compositions more similar to the Stage 5a arsenopyrites analysed. Stage 3 with 5b alteration samples also implicitly record Stage 5b conditions, based on the presence of this later alteration assemblage in the vein selvages.

Baker and Lang (2001) identified 6 distinct types of fluid inclusions hosted by quartz at Dublin Gulch; a summary of the characteristics of these fluid inclusion types is shown in Table 3.6. They argued that types 1B, 1C, and 2 fluid inclusions were paragenetically linked to gold mineralization based on their spatial association with Au- and Bi-bearing fractures. These stages would thus appear to conform most directly to our Stage 5b, based on Au-association and the presence of Bi minerals. The presence of quartz, however, is more closely comparable to Stage 5a. The homogenisation temperatures from fluid inclusions suggest maximum fluid temperatures of 271°C for gold mineralization (Table 3.6). This would overlap only with the very lowest estimated range from arsenopyrite of Stage 5, and Stage 3 with 5b alteration, <300 to 490 °C (Table 3.5), implying that the quartz host of these fluid inclusions may have crystallized after the bulk of the arsenopyrite.

TABLE 3.6. Summary of Baker and Lang (2001) fluid inclusion types, properties and temperatures recorded by these types at Dublin Gulch.

Type	Description	Temp Range (°C)
1A	CO ₂ -bearing inclusions; CO ₂ bubble >50% of inclusion	256 – 355
1B	CO ₂ bearing inclusions; CO ₂ bubble <50% of inclusion	205 – 271
1C	CO ₂ bearing inclusions; No visible CO ₂ bubble	150 – 212
2	H ₂ O-rich inclusions	141 – 219
3A	Halite-bearing inclusions (± Carbonate ± opaque ± unknowns)	None Reported
3B	Halite- and Sylvite-bearing inclusions (± Carbonate ± opaque ± unknowns)	None Reported

The arsenopyrite compositions presented here thus imply that cogenetic Stage 5b Au mineralization may have formed within a significantly higher temperature range than those obtained from quartz-hosted FIs. For example, the minimum temperature at which arsenopyrite with 32.0 at.% As is stable in the pyrite field is approximately 425 °C. The difficulty in directly equating the generations of quartz-hosted FIs with the detailed ore paragenesis presented in this study implies that further study of fluid inclusions tied directly to the paragenesis presented in Figure 3.4 may be helpful.

Generalized temperature constraints estimated with arsenopyrite geothermometry for the Fort Knox deposit by Newberry and Solie (1995) were >400 °C (32 at.% As) for veins with potassic alteration (most comparable to Stages 3 and 4 of this study) and <350 °C (<31 at.% As) for veins with sericitic alteration (most comparable to Stages 5 and 6 of this study). The overall ore assemblage at Fort Knox is comprised of native gold (Au), native bismuth, (Bi), maldonite (AuBi), bismuthinite (Bi₂S₃), tellurobismutite (Bi₂Te₃), bismite (Bi₂O₃), tetradymite (Bi₂Te₂S), eulytite (Bi₄(SiO₄)₃), and trace to minor amounts of pyrite (FeS₂), molybdenite (MoS₂), and

scheelite (CaWO_4) (Bakke, 1995; McCoy et al., 1997; Kinross Gold Corp., 2008). A number of other Au deposits in interior Alaska show broadly similar patterns of arsenopyrite compositions to Fort Knox (McCoy et al., 1997). However, for Fort Knox the lack of a detailed sequential mineral paragenesis, and the comparatively low sulfide contents, limit the possibilities for further constraining temperatures in that deposit using sulphide mineral stabilities. Similar patterns of arsenopyrite stoichiometry versus alteration types at Fort Knox and Dublin Gulch do suggest that, although mineralogically distinct (Fort Knox contains a much smaller proportion of sulfide phases), the two deposits might share a common two-stage hydrothermal process in their genesis.

3.7.1.1 Relationship between Arsenopyrite Composition and Sulfur Isotopes

Given that distinct populations exist for Stages 3-4 and 5-6 in terms of both arsenopyrite compositions and sulfur isotopes (see sections 3.4 and 3.5, above), it is appropriate to consider the combined variation of these two geochemical signatures. Samples containing over-printing stages provide the best possible example to observe the variation.

Sample FK-246 is an example of a Stage 3 quartz vein with Stage 5b alteration. The arsenopyrite grains measured for stoichiometry and sulfur isotopes were not identical - due to the requirements of sample preparation for each technique. Nonetheless, the arsenopyrite has a range of at.% As of 30.7 to 32.5 and sulfur isotope values of -1.3 to +0.9 ‰ $\delta^{34}\text{S}$, both of which are characteristic of Stage 5 arsenopyrite (28.5 to 33.3 at.% As and -1.7 to +0.2 ‰ $\delta^{34}\text{S}$). The agreement of these signatures for multiple arsenopyrite grains within the same sample demonstrates the propensity of Stage 5 arsenopyrite to occupy Stage 3 veins.

An example of a Stage 4 vein with 5b alteration selvages, sample FK-099, provided arsenopyrite composition and sulfur isotope measurements on the same arsenopyrite grain. The

arsenopyrite grain from this sample was bisected, and appropriate polished samples prepared from both halves. Figure 3.10 shows the sulfur isotope locations, superimposed on arsenopyrite composition measurements. A clear distinction can be made between the lighter areas (higher at.% As) and darker areas on the BSE image in Figure 3.10. Lighter areas are associated with -3.5 to -1.3 ‰ $\delta^{34}\text{S}$ and 35.8 to 36.5 at.% As. Darker areas are associated with a single sulfur isotope analysis of +0.9 ‰ $\delta^{34}\text{S}$ and arsenopyrite compositions ranging from 34.2 to 34.6 at.% As. This pattern is consistent with a commonly observed texture in hydrothermal replacement; where full re-equilibration of either at.% As or $\delta^{34}\text{S}$ of Stage 4 arsenopyrite mineralization has not been fully achieved during overprinting by Stage 5.

All of the locations in Figure 3.10 contain over 0.5 at.% combined Co and Ni. Analyses from lighter areas contain >5 at.% Co and 0.5 at.% Ni, while darker areas contain 0.8 to 0.9 at.% Co and 0.1 to 0.2 at.% Ni. The lower trace element concentration of the darker areas is also consistent with incomplete re-equilibration of original Stage 4 arsenopyrite during overprinting by Stage 5.

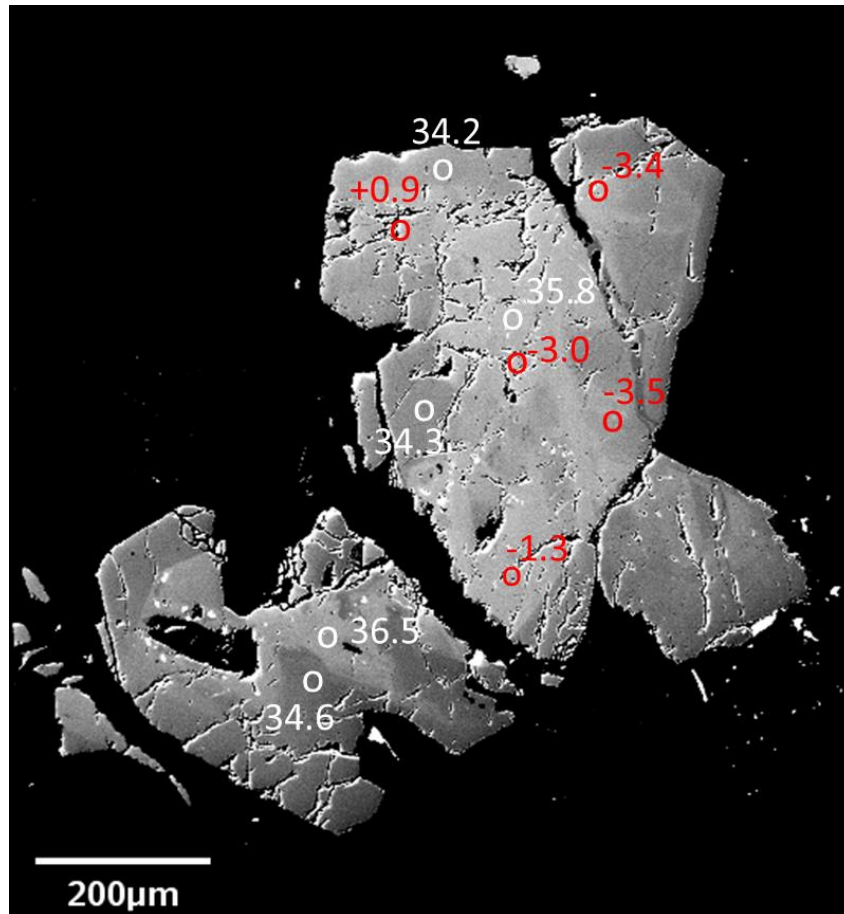


FIGURE 3.10. Arsenopyrite compositions (at.% As) with sulfur isotope ($\delta^{34}\text{S}$) values superimposed, for sample FK-099 (Eagle Zone). Arsenopyrite compositions and sulfur isotopes were measured for opposing halves of the same sample due to differing sample preparation requirements, but the morphologies of the grain halves could be matched to provide spot locations for sulfur isotopes. All spots contain elevated Co and Ni concentrations (>0.5 at.%) with the highest values, 5.9 at.% Co and 0.5 at.% Ni associated with the spot with 35.8 at.% As in a lighter area near grain centre. Compositional patterns are discussed in more detail in the text.

3.7.2 Sulfur Isotopes

For the Dublin Gulch samples, Figure 3.7 shows a clear overall trend from distinctly negative $\delta^{34}\text{S}$ in the earlier stages of the paragenesis, to values straddling 0 ‰ during the later, most auriferous hydrothermal stages.

Contact metamorphic pyrrhotite of Stage 1 has a mean value close to -9 ‰, ranges to < -12 ‰, and provides an estimate of the $\delta^{34}\text{S}$ of sulfur that was available for assimilation from the

Hyland Group country rocks by magmatic and/or hydrothermal processes during the evolution of the Dublin Gulch IRGS. The boxed ranges of pyrrhotite from Stages 2, 3, and 4 lie between -8 ‰ and -2 ‰, and show a general temporal evolution to less negative $\delta^{34}\text{S}$ across these stages.

Pyrite of Stage 4 that occurs in veins showing evidence of Stage 5b alteration in their selvages overlaps in $\delta^{34}\text{S}$ with Stage 4 stockwork vein pyrrhotite. This implies that this generation of pyrite may be genuinely pene-contemporaneous with Stage 4 pyrrhotite. However, pyrite samples from the larger population of Stage 4 stockwork veins show a range of values that also overlap Stage 4 pyrrhotite, but extend to much less negative values that - for the majority of samples - overlap with those of Stage 5 and 6 sulfides. This implies that much of the pyrite assigned on a textural basis to Stage 4 may in fact have actually been precipitated, or isotopically re-equilibrated, during Stages 5 and/or 6.

Arsenopyrite of Stage 3 closely overlaps with the range of Stage 1 contact metamorphic pyrrhotite (-11.7 to -7.5 ‰ vs -12.7 to -8.7 ‰, respectively), further implying a substantial influence of assimilated country rock sulfur during Stage 3. All samples of Stage 4 arsenopyrite tested were from veins showing some evidence of Stage 5b alteration in their selvages. Most overlap with the boxed $\delta^{34}\text{S}$ range of Stage 4 pyrrhotite, but a small population (the extended upper whisker) may actually represent replacements or overgrowths of Stage 5 arsenopyrite.

Both pyrite and arsenopyrite from Stage 5 and 6 generally have values between -2 and +2 ‰, distinctly more positive than previous stages. The pyrrhotite in Rex Zone quartz veins stands out as definitively more positive than any other Dublin Gulch samples, and this is further discussed below.

There are two broad processes that could be invoked to explain this overall sulfur isotope trend at Dublin Gulch:

1) A significant process of assimilation of lighter sulfur from country rocks into the Dublin Gulch pluton magma and/or scavenging of country rock sulfur by ore forming fluids emanating from the pluton, occurred during the earlier paragenetic stages (Stages 2 to 4). The range of sulfur isotope values for Stages 5 and 6 ($0 \pm 2 \text{ ‰}$) implies reversion to a dominantly primitive magmatic sulfur source during Stages 5 and 6; or,

2) Two stages of plutonism occurred, where an earlier intrusive phase (the Dublin Gulch Stock) assimilated light, sedimentary sulfur during ascent through the host metasedimentary rocks. This first intrusive phase would be responsible for contact metamorphism of sedimentary pyrite in the hanging wall Hyland Group, the metasomatism forming the skarn (Stage 2), and hydrothermal fluids that produced the Stage 3-4 stockwork vein systems. A second, affiliated, intrusive phase, not yet recognized in outcrop or drilling, may have then been emplaced deeper in the system, with much more limited assimilation of country rock sulfur. Fluids emanating from this second phase dominated the sulfur inventory of the fluids responsible for the auriferous veins of Stages 5 and 6, producing “magmatic” sulfur isotope signatures in the Stage 5 and 6 sulfides.

The seemingly excursive behaviour of Stage 4 partially aligned stockwork vein pyrite is attributed to the occurrence of two generations of pyrite in this nominal sample set; 1) a smaller population of pyrite genuinely belonging to Stage 4 partially aligned stockwork veins (with more negative $\delta^{34}\text{S}$, similar to the subset of pyrite sampled from the Stage 4 w/ Stage 5b alteration group); and 2) pyrite (with near-zero $\delta^{34}\text{S}$) that actually precipitated in these same vein structures during Stage 6. This interpretation is in agreement with textures that show pyrrhotite and pyrite

in close textural association in Stage 4 (Chapter 2) - suggesting that pyrite might have directly replaced pyrrhotite during the latter part of this stage, with both phases then overprinted (replaced or rimmed) by Stage 5-6 pyrite.

Pyrrhotite from the Rex Zone quartz vein stands out as the only exclusively positive sulfide $\delta^{34}\text{S}$ determined in this study. Taken in tandem with the metallogenic PCA analysis discussed in Chapter 2, this observation further implies that the Rex-Peso veins may be from a hydrothermal system distinct in space and time from the Dublin Gulch mineralization. Interestingly, Pb isotopes (see section 3.7.3, below) suggest that the Rex and Peso zones quartz veins are, in fact, distinct from each other, as well as from the sulfosalt-bearing mineralization (Stages 5 & 6) in the other zones at Dublin Gulch.

3.7.2.1 Comparison with Sulfur Isotope Compositions from Other Deposits

Other IRGS in the Tombstone-(Tintina-) Gold Belt

Scheelite Dome and Clear Creek, along with Dublin Gulch, are the most well described IRGS within the Tombstone-(Tintina-) Gold Belt (TTGB) (Stephens, 2003; Mair et al., 2006b). Since all of these plutons are hosted by metasedimentary rocks of the Hyland Group, have U-Pb ages grouped between 91.4 and 94.6 Ma (Murphy, 1997: zircon, titanite; Mair et al., 2006a: zircon) Chapter 4) and have similar lithogeochemical characteristics (Hart et al., 2004b), they provide the basis for a regional comparison of sulfur isotopes for Dublin Gulch and related IRGS.

Scheelite Dome: Sulfur isotopes at Scheelite Dome (summarized in Fig. 3.11) were determined in sulfides from four main paragenetic stages by Mair et al. (2006b); 1. Gold-(tungsten) skarn mineralization (a possible auriferous version of Stage 2 skarn at Dublin Gulch), 2. Tungsten-rich quartz veins (comparable to Stage 3 mineralization at Dublin Gulch), 3. Gold-rich veins (further sub-divided into arsenic-rich and arsenic-poor members (comparable to Stage 5 mineralization at Dublin Gulch), and 4. late-stage polymetallic Ag-Pb-Zn-Sb veins rich in sulfosalts (Comparable to Stage 6 mineralization at Dublin Gulch; or possibly the Rex-Peso veins). Tungsten-rich quartz veins are the only vein type hosted dominantly by the Scheelite Dome stock with the other, nominally more distal, vein types hosted by metasedimentary rocks of the Hyland Group.

The skarn at Scheelite dome has $\delta^{34}\text{S}$ values of -6.6 to -2.4 ‰ (arsenopyrite), -3.7 (chalcopyrite; n=1), and -7.3 to -4.5 ‰ (pyrrhotite). Arsenopyrites from tungsten-rich quartz veins have -5.8 to -5.4 ‰ $\delta^{34}\text{S}$. Arsenopyrite from Au-rich veins has values ranging from -10.9 to -7.1 ‰ $\delta^{34}\text{S}$, with the As-rich type having values of -10.9 to -9.0 ‰ $\delta^{34}\text{S}$. Stibnite from late

stage polymetallic veins have values of -10.1 to -6.8 ‰ $\delta^{34}\text{S}$, with a single analysis of sphalerite from this stage yielding -8.9 ‰ $\delta^{34}\text{S}$.

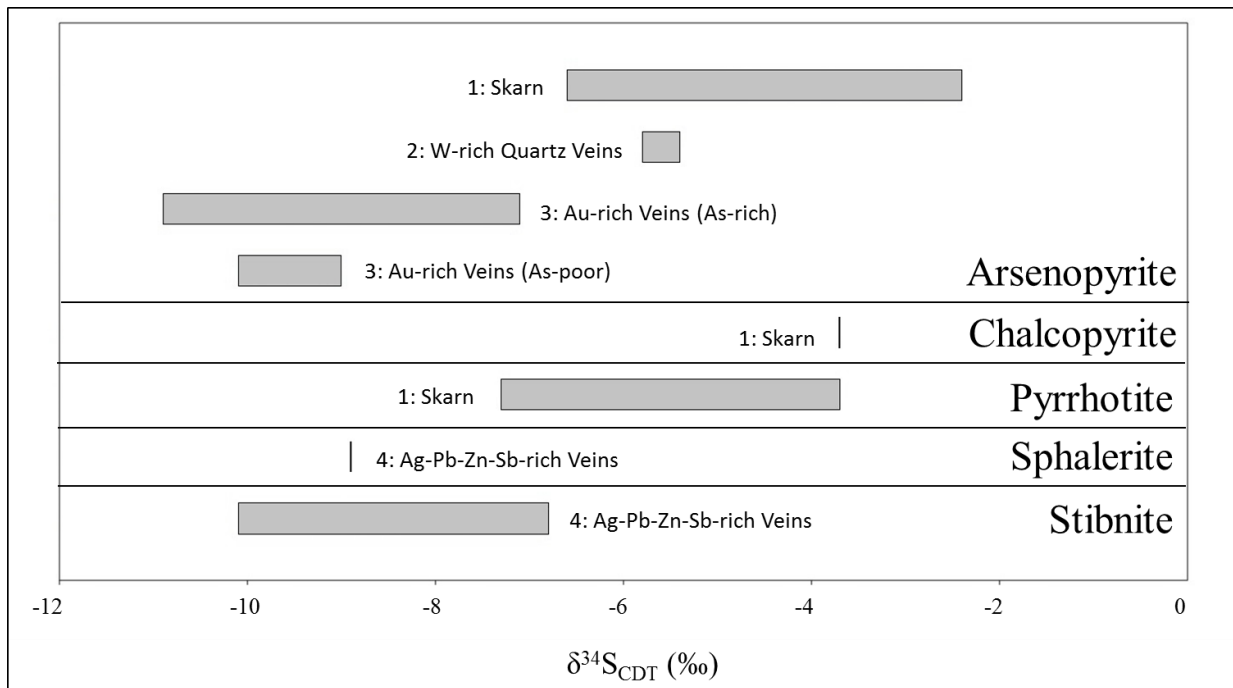


FIGURE 3.11. Box plot of sulfur isotope data for Scheelite Dome, grouped by sulfide mineral. Boxes contain the entire range of published values. Values are grouped by sulfide species and the 4 stage paragenesis outlined by Mair et al. (2006b). Data from Mair et al. (2006b). Plot produced using the PAST software of Hammer et al. (2001). CDT = Vienna Canyon Diablo Troilite.

The data of Mair et al. (2006b) are uniformly less than -2 ‰. Those in the skarn overlap the values for pyrrhotite of the Wolf W Skarn at Dublin Gulch. Vein Stages 3 and 4 at Scheelite Dome, although dominantly hosted by the Hyland Group, have mineralogical similarities to Stage 5 and 6 mineralization at Dublin Gulch. However, conversely to those at Dublin Gulch, the sulfur isotope values of these vein stages at Scheelite Dome progress towards more negative values with time, toward the general range inferred above for syn-sedimentary sulfides within the Hyland Group, (Stage 1 of the Dublin Gulch paragenesis – see Fig. 3.7). The vein stages at Scheelite Dome do not show the evolution towards heavier, near 0 ‰, sulfur values with progressive paragenetic stage evident for Dublin Gulch Stages 5 and 6. The disparity between

similar parageneses but opposing sulfur isotope patterns at Scheelite Dome and Dublin Gulch highlights a potentially variable influence of host rock sulfur reservoirs in the formation of sulfides in IRGS.

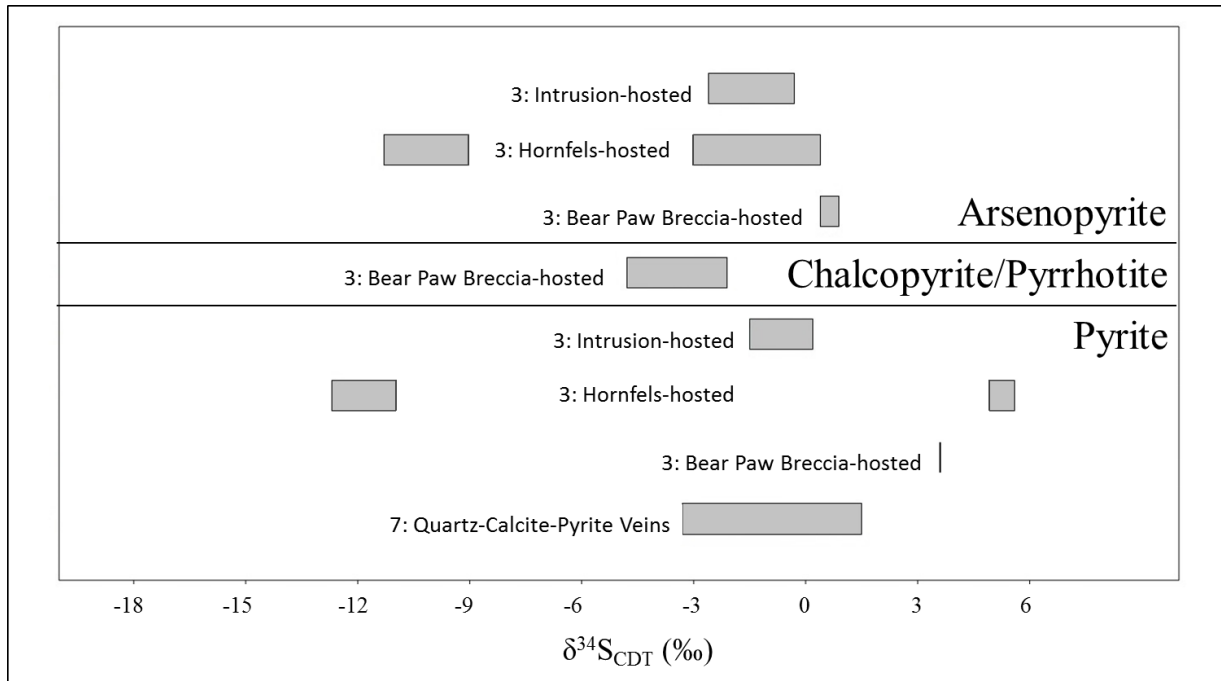


FIGURE 3.12. Sulfur isotope data for the Clear Creek deposit. Paragenetic stages are numbered here according to the seven stage paragenesis of Stephens (2003), as summarized in text. Three main hosts for Au mineralization are labelled within this scheme 1: Major intrusions (“Intrusion-hosted”) 2: The hornfelsed metamorphic halo around these intrusions (“Hornfels-hosted”) 3: The distal Bear Paw Breccia Zone in the south west of the property (“Bear Paw Breccia-hosted”). According to Stephens (2003), Stage 3 represents the main stage of Au mineralization. A broad grouping of values between -4 and $+2$ ‰ $\delta^{34}\text{S}$ is apparent for Intrusion- and Breccia-hosted Stage 3 sulfides, with larger excursions in values for Hornfels-hosted Stage 3 sulfides, particularly towards more negative values. Late stage (Stage 7) quartz-calcite-pyrite mineralization lies within a similar range to non Hornfels-hosted Stage 3 sulfides. Data from Marsh et al. (2003) and Stephens (2003). Plot produced using the PAST software of Hammer et al. (2001). CDT = Vienna Canyon Diablo Troilite.

Clear Creek: Stephens (2003) provided the most detailed paragenesis to date for the Clear Creek deposit. A seven-stage paragenesis was presented that featured, in order of occurrence; 1: Emplacement of major intrusions, 2: Emplacement of a series of dykes and dykelets, 3: Auriferous quartz-sulfide veins, 4: A hiatus in mineralization, 5: Quartz-tourmaline veins, 6: A second hiatus in mineralization and 7: Late-stage quartz-calcite-pyrite veins. Stage 3

mineralization at Clear Creek is described by Stephens (2003) as having similar vein geometry to Stages 3 and 4 at Dublin Gulch, but manifesting the alteration suite characteristic of Stages 5 and 6 at Dublin Gulch. It is not clear from the available literature if re-activation of early vein sets, as is the case at Dublin Gulch, was an important process at Clear Creek.

Sulfur isotope data for Clear Creek (Stephens, 2003; Marsh et al., 2003) are summarized in Figure 3.12, and show values that are closely grouped for subcategories of “intrusion-hosted” and “breccia-hosted” mineralization (-4 to +2 ‰ $\delta^{34}\text{S}$), with a wider range for country rock-hosted mineralization (-13 to +4 ‰ $\delta^{34}\text{S}$). A small sub-set of values for “hornfels-hosted” arsenopyrite and pyrite, lying between -13 and -10 ‰ $\delta^{34}\text{S}$, are responsible for the much wider overall ranges described by this group, and may represent metasedimentary pyrite, or its direct replacement by arsenopyrite.

The origin of this sub-set is not clear, but is most likely due to preservation or interaction with sedimentary sulfides in the Hyland Group, producing a close resemblance to the $\delta^{34}\text{S}$ values of contact metamorphosed Hyland Group rocks at Dublin Gulch. Based on the paragenesis of Stephens (2003), the majority of those sulfides most closely associated with gold mineralization (Stage 3) are included in the grouping between -4 and +2 ‰ $\delta^{34}\text{S}$ in Fig. 3.12. This is similar to the range seen at Dublin Gulch for Stage 5-6 auriferous mineralization and suggests that gold endowment at Clear Creek, and potentially other TTGB IRGS hosted chiefly within their parent pluton, was also strongly controlled by fluids with a predominantly magmatic $\delta^{34}\text{S}$ signature. Clear Creek mineralization does not appear to display earlier, “first stage” (Stages 3 and 4 at Dublin Gulch) parageneses with $\delta^{34}\text{S}$ values intermediate between the distinctly sedimentary (-13 to -10 ‰ $\delta^{34}\text{S}$) and the magmatic (-4 to +2 ‰ $\delta^{34}\text{S}$) groupings.

Keno Hill: The Keno Hill Ag-Pb-Zn deposit is located roughly 40 km south east of Dublin Gulch. It is hosted largely by the Devonian to Mississippian Earn Group, specifically the Keno Hill Quartzite. Hantelmann (2013) suggests a genetic or temporal link to the Roop Lakes Stock (92.8±0.5 Ma U-Pb on titanite; Roots, 1997), which is located 20 km to the east of Keno Hill. This suggests the possibility that Keno Hill may indeed represent a more distal style of IRGS mineralization, also related to Tintina-Tombstone plutonism, as previously proposed by Boyle et al. (1970) and others. To date, there has been no detailed study targeted at comparing the geochemical affinities of Keno Hill with those of Dublin Gulch, or other Tintina-Tombstone IRGS.

Boyle et al. (1970) presented $\delta^{34}\text{S}$ data for Keno Hill. The metasedimentary country rocks that host the deposit contain pyrite, described as syn-sedimentary biogenic in origin, which yielded values of -5.1 to +14.9 ‰ $\delta^{34}\text{S}$. Their simplified sulfide paragenesis for Keno Hill featured; 1: Early quartz veins with pyrite (-6.4 to +1.4 ‰ $\delta^{34}\text{S}$) and arsenopyrite (-3.7 to -1.1 ‰ $\delta^{34}\text{S}$), and 2: Late silver-(gold-) bearing veins with minor amounts of galena, sphalerite, jamesonite, boulangerite, and bournonite. In detail, the Stage 2 veins are comprised largely of siderite with abundant pyrite (-21.1 to +1.6 ‰ $\delta^{34}\text{S}$), galena (-12.0 to +0.7 ‰ $\delta^{34}\text{S}$), sphalerite (-3.6 to +4.4 ‰ $\delta^{34}\text{S}$), and chalcopyrite (-5.4 ‰ $\delta^{34}\text{S}$; n=1) with late minor arsenopyrite (-6.9 to -4.7 ‰ $\delta^{34}\text{S}$), as well as freibergite, boulangerite, bournonite, jamesonite, and pyrargyrite (combined, these sulfosalts ranged from -18.7 to -0.7 ‰ $\delta^{34}\text{S}$). Stage 2 was considered to be the stage of highest silver endowment. Barite was the only major sulfate identified, appearing latest in the hypogene paragenesis and yielding values of +11.4 to +16.7 ‰ $\delta^{34}\text{S}$. “Supergene” galena and mixed sulfates (gypsum, anglesite, soluble iron, and zinc sulfates) yielded ranges of -12.8 to -4.2 and -9.3 to +0.6 ‰ $\delta^{34}\text{S}$, respectively.

Boyle et al. (1970) argued, based on shared early paragenetic stages and geochemistry, that Keno Hill and Dublin Gulch represented expressions of the same type of mineralization, differing only on the basis of distance from the causative pluton (Dublin Gulch-proximal; Keno Hill-distal). This point was disputed by Tempelman-Kluit (1970) who considered Dublin Gulch and Keno Hill to be distinctly different mineralising systems, based on a distance of around 40 km between the deposits, mineralogical differences, differing tectonic positions within the Selwyn Basin, and different host rock lithologies.

Recently, Hantelmann (2013) conducted a more comprehensive sulfur isotope study, covering the main stages of his more detailed, twelve-stage paragenesis for Keno Hill. Sulfur isotopes show a complex evolution - from early arsenopyrite with $-5.9 \text{ ‰ } \delta^{34}\text{S}$, through intermediate stages of pyrite and sphalerite with approximately 0 to $+2 \text{ ‰ } \delta^{34}\text{S}$, followed by later galena and sphalerite of -1 to $-2 \text{ ‰ } \delta^{34}\text{S}$, ranging as low as $-11 \text{ ‰ } \delta^{34}\text{S}$ for distal galena-sphalerite mineralization. Stage 12 at Keno Hill contains pyrite with $+2.4$ to $+7.4 \text{ ‰ } \delta^{34}\text{S}$. Hantelmann (2013) noted a spatial zonation of $\delta^{34}\text{S}$ in galena from his Stage 8 - with values decreasing from the southeast to the north and west of the deposit. The findings of Hantelmann (2013) represent the most detailed sulfur study to date at Keno Hill and suggest that the control on sulfur sources there may be significantly different, and considerably more complex, than those at Dublin Gulch.

Alkalic Porphyry Deposits, British Columbia

Alkalic porphyry deposits of British Columbia (Lorraine, Mount Polley, Red Chris, Galore Creek, Afton: Deyell, 2005; Deyell and Tosdal, 2005; Micko, 2010; Pass et al., 2014) show trends of more negative sulfur values in the core of the deposit, with progression towards values

closer to 0 ‰ $\delta^{34}\text{S}$ with distance from the core, and with temporal evolution of the deposit. The Mount Polley deposit, the most well studied to date, will be discussed here as a proxy for other deposits of this type in British Columbia. Deyell (2005) noted an outward zonation of sulfide mineral precipitation - a bornite and chalcopyrite core, followed by a rim dominated by chalcopyrite, with pyrite and chalcopyrite on the margins of the mineralized zones. The Northeast Zone of the deposit, which has a five-stage paragenesis, shows the strongest pattern of sulfur isotope zonation. Studies yielded values from the Northeast Zone of -7.0 to -1.1 (Deyell and Tosdal, 2005) and -7.1 to +1.4 ‰ $\delta^{34}\text{S}$ (Pass et al., 2014) in sulfides, with the majority of low $\delta^{34}\text{S}$ measured in chalcopyrite. Both Deyell and Tosdal (2005) and Pass et al. (2014) noted an outward zonation from approximately -7 ‰ $\delta^{34}\text{S}$ in the core of the zone associated with high grade Cu mineralization, to approximately -1 ‰ $\delta^{34}\text{S}$ in association with more peripheral low grade Cu mineralization.

Pass et al. (2014) argued that this pattern of sulfur isotope values was inconsistent with a model of simple progressive cooling of a single homogeneous fluid source of sulfur (e.g., Ohmoto and Rye, 1979). They proposed that the oxidation state and/or the bulk S composition of the fluid must have been progressively changed during sulfide mineral precipitation. For Mount Polley, Pass et al. (2014) suggest that a process of inorganic reduction of dissolved sulfate through reaction with ferrous iron-bearing minerals in the wallrock, caused progressive change of the sulfur isotope composition of the fluid to heavier values, with concomitant hematite alteration of the wallrock. This evidence for this process having occurred includes the abundant hematite alteration of K-feldspars observed in the Northeast Zone.

However, the processes proposed for Mount Polley, and other alkalic porphyry deposits, are unlikely to have occurred at Dublin Gulch. The current model for sulfur isotope zonation in

alkalic porphyry deposits requires an oxidized hydrothermal fluid, rich in SO₂ or dissolved sulfate, in order to have formed distinctly negative $\delta^{34}\text{S}$ values in the high grade core of the deposit (Wilson et al., 2007). At Dublin Gulch the mineralogy of vein stages associated with negative $\delta^{34}\text{S}$ values show a relatively reduced mineral assemblage including arsenopyrite, pyrite and pyrrhotite, and no evidence of wallrock hematization - which would appear to preclude the presence of significant SO₂ in the hydrothermal fluids.

3.7.3 Lead Isotope Systematics

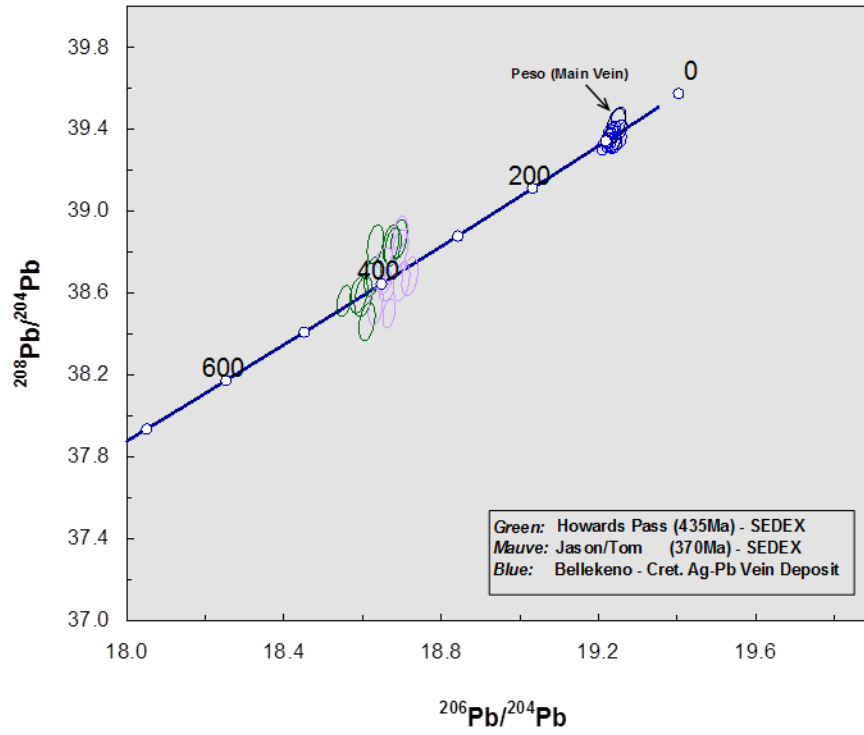
For the purposes of discussing Pb isotope systematics at Dublin Gulch, and in the TTGB as a whole, we present lead growth curves in Figure 3.13 that represent a modification of the “Shale Curve” of Godwin and Sinclair (1982). Our proposed growth curves are tied to a single, very homogeneous, example of Cretaceous Ag-Pb-Zn vein mineralization in the TTGB region – the Bellekeno deposit of the Keno Hill District - and an estimated assumed age of 95 Ma for that deposit. High precision Pb isotope data for the Bellekeno Ag-Pb-Zn vein deposit from Hantelmann (2013) are extremely homogeneous for Pb isotopes and are intersected by both our proposed curves at approximately 95 Ma, with a slight dispersion to less radiogenic ²⁰⁷Pb/²⁰⁴Pb. We note that Keno Hill District galena samples (“Yukon-Treadwell”) were also used as one reference point in the original conformable Pb model of Stanton and Russell (1959).

For reference, the proposed growth curves also intersect the data for Howards Pass and Jason/Tom SEDEX-type deposits at values reasonably close to their ages as determined by stratigraphic position (Godwin and Sinclair, 1982). This is not to suggest that the proposed intrusion-related curve is perfectly appropriate for interpreting Paleozoic SEDEX deposits in the Selwyn Basin. However, we note that these deposits are not completely homogenous for Pb

isotopes, and the observed dispersion of their Pb isotope data across any average growth curve implies that SEDEX fluids may have interacted with at least one Pb reservoir in addition to the “average” composition of their pene-contemporaneous host sediments.

The proposed growth curves of Figure 3.13 provide a useful basis for comparing available Pb isotope data for Cretaceous intrusion-related ore deposits in the greater TTGB (LEADTABLE Database of Godwin et al., 1988), and associated districts, as well as for feldspar separates from Tombstone Suite and Mayo Suite granitoids (Rasmussen, 2013).

A



B

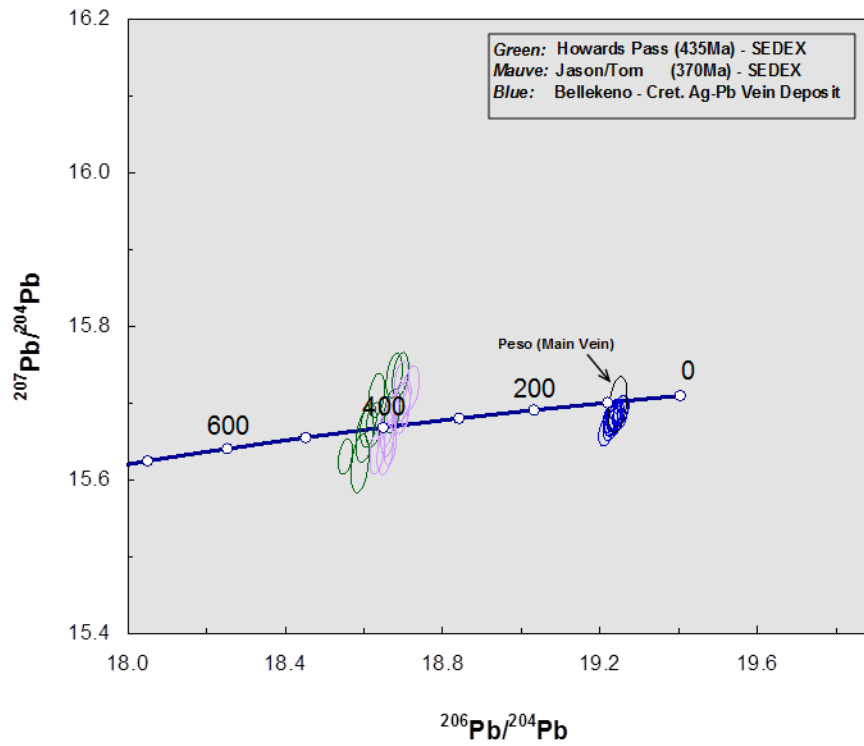


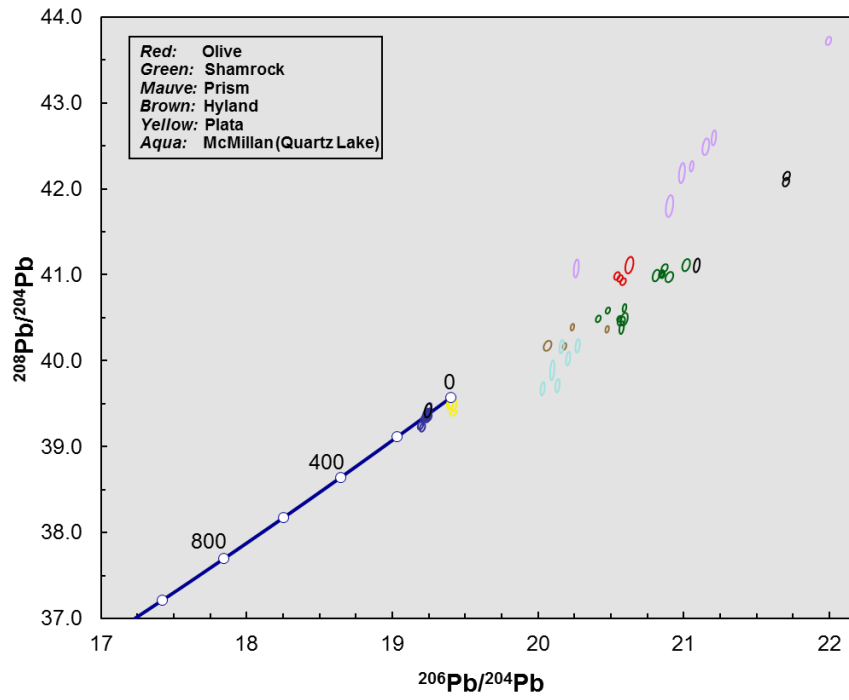
FIGURE 3.13. Proposed Pb isotope growth curves for intrusion-related Selwyn Basin ore deposits (Layne, unpublished data). A: (upper). $^{208}\text{Pb}/^{204}\text{Pb}$ vs. $^{206}\text{Pb}/^{204}\text{Pb}$. B: (lower). $^{207}\text{Pb}/^{204}\text{Pb}$ vs. $^{206}\text{Pb}/^{204}\text{Pb}$. Like the average lead isotope growth curves proposed for shale-hosted zinc-lead deposits in the Canadian Cordillera by Godwin and Sinclair (1982) – the “Shale Curve” - these curves depart the second stage of the two-stage Pb isotope growth curves of Stacey and Kramers (1975) at 1887 Ma. However, our version of these third-stage curves are calculated with lower values of both $^{238}\text{U}/^{204}\text{Pb}$ ($\mu = 11.8$ vs. 12.16) and $^{232}\text{Th}/^{204}\text{Pb}$ ($\omega = 46.5$ vs. 49.09) than the Shale Curve. Data for Howards Pass, Jason, Tom (and Tom East) are from the LEADTABLE Database (Godwin et al. 1988; and source references therein). Data for the Bellekeno deposit in the Keno Hill District are from Hantelmann (2013). A single available analysis of a sample from the Peso (Main Vein) deposit within the Dublin Gulch area (LEADTABLE) is also plotted and discussed further in the text.

Pb-sulfosalt minerals from the Olive and Shamrock zones show evidence that at least one additional highly radiogenic source of Pb was present in the ore-forming fluids of Stages 5 and 6. This is most logically attributed to interaction of the fluids with high- μ , high- ω accessory minerals in the metasediments of the Hyland Group. The Rex Vein and Haggart Creek mineralization at Dublin Gulch are displaced to even more radiogenic values. Both these latter occurrences are closely associated with black pelitic horizons of the Hyland Group, which may have contributed this even more radiogenic Pb to the mineralizing fluids.

Several other deposits in the Selwyn Basin region are plotted for comparison with the Dublin Gulch zones (Pb isotopes: Fig. 3.14; Locations: Fig. 3.15). The Hyland gold deposit in the SE Yukon is hosted by late Proterozoic rocks of the Hyland Group. The Main Zone contains structurally controlled vein-bound mineralization, with gold closely associated with pyrite-arsenopyrite veins (Armitage and Gray, 2012). Approximately 5 km west of the Hyland deposit Main Zone is the McMillan (Quartz Lake) Ag-Pb-Zn deposit, with an estimated historical resource of 1.1 million tonnes grading 8.3% Zn, 4.1% Pb, and 62 g/T Ag occurring as replacement mineralization at the sheared contact between carbonate rocks and underlying shale (INAC, 1991). This deposit is also hosted in late Proterozoic rocks of the Hyland Group.

On the Plata property, at least 6 major Ag-Pb-Zn veins, and numerous subsidiary veins, traverse both late Proterozoic and Paleozoic sedimentary rocks (Abbott, 1986). The Prism prospect contains at least 15 individual showings of Ag-Pb-Zn veining hosted in the nominally Paleozoic “Val dolomite” (Sivertz, 1985). A parent pluton has not yet been definitively identified for the Hyland, McMillan, Plata or Prism occurrences, but it is inferred that all are directly related to Cretaceous granitoid plutonism. At a minimum, their disposition on the Pb isotope diagrams of Figure 3.14 confirms an epigenetic origin.

A



B

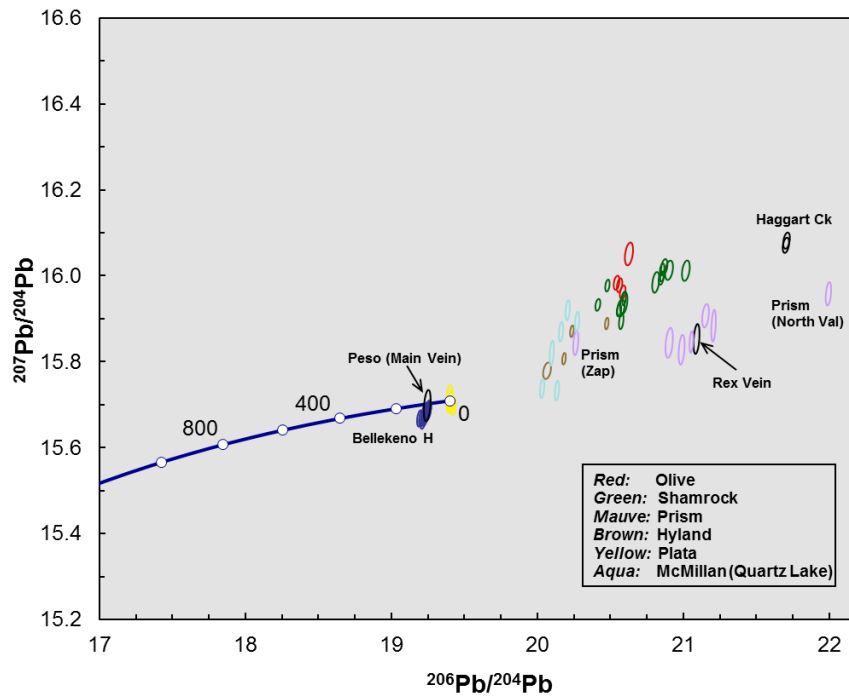


FIGURE 3.14. Pb isotope data for Dublin Gulch deposits, Hyland Au deposit (SE Yukon) and several Ag-Pb-Zn vein deposits within the greater Selwyn Basin Province/Tombstone-(Tintina-) Gold Belt (TTGB) area. A: (upper). $^{208}\text{Pb}/^{204}\text{Pb}$ vs. $^{206}\text{Pb}/^{204}\text{Pb}$. B: (lower). $^{207}\text{Pb}/^{204}\text{Pb}$ vs. $^{206}\text{Pb}/^{204}\text{Pb}$. Data for sulfosalt Pb isotopes for Olive and Shamrock Zones of Dublin Gulch are from this study (Table 3.4). Data for pyrite Pb isotopes from the Hyland deposit are from Heffernan et al. (2004). Data for galena Pb isotopes from Prism, Plata, and McMillan (Quartz Lake) deposits, and from the Peso (Main Vein) and Rex Vein at Dublin Gulch, are from the LEADTABLE database (Godwin et al., 1988). Data for Olive, Shamrock and Haggart Creek zones are the same shown in Fig. 3.8

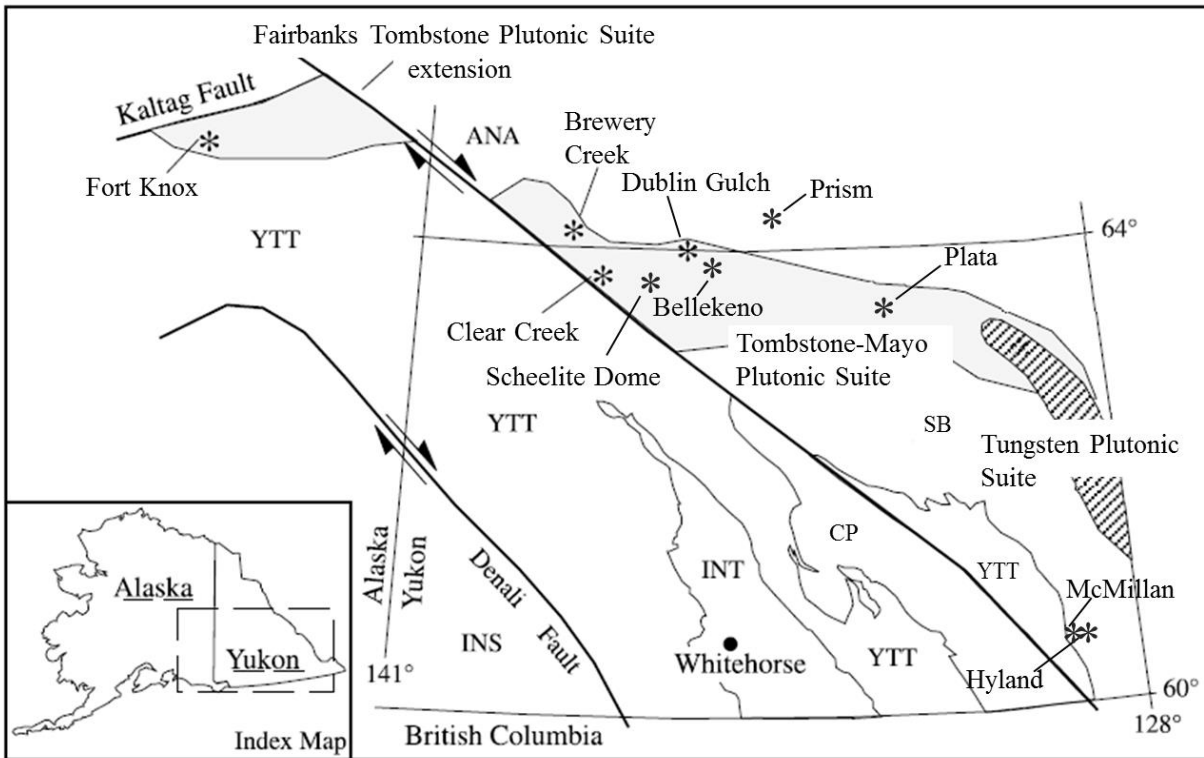


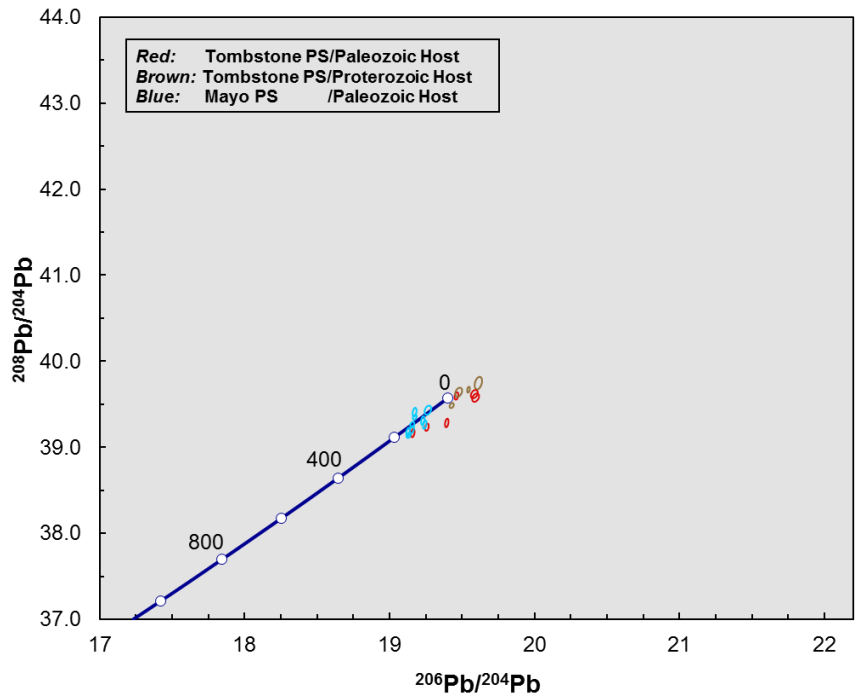
FIGURE 3.15. Map of deposits included in Pb isotope discussion. Modified after Selby et al. (2003). ANA = Ancestral North America; YTT = Yukon Tanana Terrane; CP = Cassiar Platform; INS = Insular Terrane; INT = Intermontane Terrane; SB = Selwyn Basin.

Most of the showings on the Prism prospect show values similar to those of the Rex Vein. However, the Prism (Zap) showing is more similar to the Olive-Shamrock zones, and Prism (North Val) is the most radiogenic example plotted in Figure 3.14. This is intriguing, and somewhat paradoxical, since the all the Prism veins are described as hosted by dolomitic Paleozoic metasediments (Sivertz, 1985) that would not be expected to supply a proximal source of highly radiogenic Pb.

Most of the recognized Plata property veins are highly homogeneous, and only slightly radiogenic, relative to the proposed intrusion-related gold curve, despite the presence of both Paleozoic and Proterozoic hosts rocks to the veins. However, data for the Plata #3 and #4 veins, described by Abbott (1986) as containing arsenopyrite and pyrite, and thus nominally more similar to Stages 5 and 6 of the Eagle-Olive-Shamrock zones than to Rex and Haggart Creek veins, were not available through the LEADTABLE database, but are an obvious object of curiosity for future studies.

A single sample from the Peso (Main Vein) available in LEADTABLE lies directly on the proposed growth curves at close to 95 Ma. This is an intriguing result, in distinct contrast to the extremely radiogenic Pb of the Rex Vein, with which it is traditionally grouped (“Rex-Peso vein system”). In fact, based only on Pb isotope criteria, Peso (Main Vein) most closely resembles the Bellekeno ores, and stands out as disparate from the rest of the Dublin Gulch occurrences.

A



B

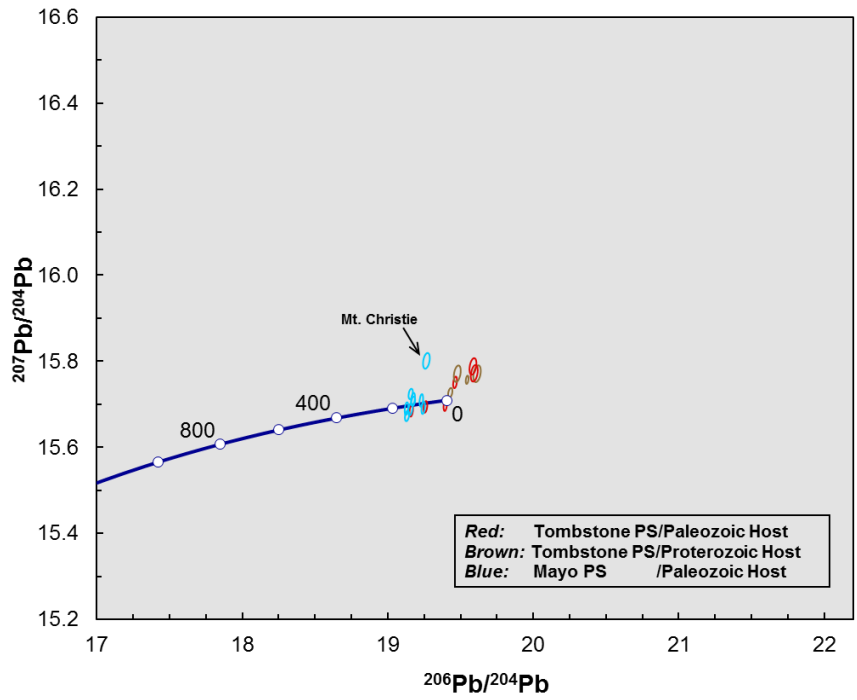


FIGURE 3.16. Pb isotope data for feldspar separates from Tombstone Plutonic Suite and Mayo Plutonic Suite granitoid samples. A: $^{208}\text{Pb}/^{204}\text{Pb}$ vs. $^{206}\text{Pb}/^{204}\text{Pb}$. B: $^{207}\text{Pb}/^{204}\text{Pb}$ vs. $^{206}\text{Pb}/^{204}\text{Pb}$. All data are from Rasmussen (2013), and Heffernan et al. (2004), and are summarized in Table 3.7.

Data for some plutons within both the Tombstone and Mayo suites is available in recent work by Heffernan et al. (2004) and Rasmussen (2013), although largely for plutons to the southeast of the main TTGB.

As shown in Figure 3.16, most Mayo Plutonic Suite samples, all of which are from plutons nominally emplaced within Paleozoic host rocks, show very little departure from the proposed growth curves. The single exception is a sample from the Mt. Christie pluton (Rasmussen, 2013). However, this sample is described as proximal to sulfide mineralization and may thus have incorporated some trace sulfides with more radiogenic Pb derived from hydrothermal fluid circulation.

Although samples from the Natla and O'Grady plutons overlap with the main grouping of Mayo Plutonic Suite samples, the other Tombstone Plutonic Suite samples, whether nominally emplaced in Proterozoic or Paleozoic host rocks, show a stronger propensity to depart to more radiogenic Pb values, in comparison to the proposed growth curves. The simplest interpretation of this latter observation is that Tombstone plutons were prone to assimilating lead by partial melting of Proterozoic crustal rocks during emplacement. It is thus possible to surmise that this assimilation may have contributed to their fertility for other metallic elements, including gold

TABLE 3.7. Lead Isotopes of feldspar minerals from plutons within the Selwyn Basin Terrane. Ages are U-Pb by LA-ICP-MS, *indicates age by $^{40}\text{Ar}/^{39}\text{Ar}$ method, Plutonic suite groupings after Heffernan et al. (2004) and Rasmussen (2013). Sample CL-06-39A could be re-classified as a member of the Tombstone suite based on the definitions of Rasmussen (2013). References ¹ = Rasmussen (2013), ² = Heffernan et al. (2004).

Sample	Plutonic Suite	Pluton/Zone	Age	Host	Host Age
CL-06-33A ¹	Tombstone	Dechen'La	93.7±0.5	Windermere Supergroup	Neoproterozoic
CL-06-34A ¹	Tombstone	Natla	92.3±0.6	Selwyn Basin	Devonian to Mississippian
CL-06-38A ¹	Tombstone	Ross River	93.0±0.9	Selwyn Basin	Devonian to Mississippian
KR-05-194 ¹	Tombstone	Coal River	92.8±0.9	Windermere Supergroup	Neoproterozoic
KR-05-198 ¹	Tombstone	Hole-in-the-Wall	91.3±2.1	Selwyn Basin	Cambrian to Devonian
KR-05-97b ¹	Tombstone	O'Grady	92.8±0.6	Selwyn Basin	Devonian to Mississippian
SH-99-06 ²	Tombstone	Coal River	92.8 ± 0.9	Windermere Supergroup	Neoproterozoic
SH-99-09 ²	Tombstone	Coal River	92.8 ± 0.9	Windermere SuperGroup	Neoproterozoic
SH-99-01 ²	Tombstone	Big Charlie	91.0 ± 0.3	Selwyn Basin	Devonian to Mississippian
98-HAS-14 ²	Tombstone	McLeod	93.9 ± 0.2	Selwyn Basin	Devonian to Mississippian
CL-06-35A ¹	Mayo	Logan	95.6 ± 1.2	Selwyn Basin	Devonian to Mississippian
CL-06-36A ¹	Mayo	Mt. Christie	96.1 ± 0.5	Selwyn Basin	Devonian to Mississippian
CL-06-37A ¹	Mayo	Mt. Christie/Christie Pass	96.7 ± 0.6	Selwyn Basin	Devonian to Mississippian
CL-06-39A ¹	Mayo	Keele River	93.3±0.4	Selwyn Basin	Devonian to Mississippian
CL-06-40A ¹	Mayo	Mile 222	96.6 ± 0.6	Selwyn Basin	Devonian to Mississippian
KR-05-113 ¹	Mayo	South Nahanni	95.8 ± 0.5*	Selwyn Basin	Cambrian to Devonian
KR-05-130 ¹	Mayo	Central Nahanni	97.1 ± 0.8	Selwyn Basin	Devonian to Mississippian
KR-05-136 ¹	Mayo	North Nahanni	96.9 ± 0.7	Selwyn Basin	Devonian to Mississippian
KR-05-621	Mayo	Mt. Christie	95.1 ± 1.2	Selwyn Basin	Mississippian to Triassic

TABLE 3.7. Cont.

Sample	$^{206}\text{Pb}/^{204}\text{Pb}$	2σ	$^{207}\text{Pb}/^{204}\text{Pb}$	2σ	$^{208}\text{Pb}/^{204}\text{Pb}$	2σ	$^{207}\text{Pb}/^{206}\text{Pb}$	$^{208}\text{Pb}/^{206}\text{Pb}$
CL-06-33A ¹	19.43	0.06	15.73	0.06	39.49	0.06	0.809	2.032
CL-06-34A ¹	19.26	0.06	15.69	0.07	39.23	0.09	0.815	2.037
CL-06-38A ¹	19.46	0.06	15.75	0.07	39.60	0.09	0.809	2.035
KR-05-194 ¹	19.61	0.11	15.77	0.10	39.75	0.15	0.804	2.026
KR-05-198 ¹	19.40	0.05	15.70	0.08	39.28	0.10	0.809	2.025
KR-05-97b ¹	19.16	0.05	15.69	0.08	39.17	0.10	0.819	2.044
SH-99-06 ²	19.48	0.10	15.77	0.10	39.64	0.11	0.810	2.035
SH-99-09 ²	19.55	0.04	15.76	0.05	39.67	0.07	0.806	2.030
SH-99-01 ²	19.59	0.10	15.79	0.10	39.62	0.10	0.806	2.023
98-HAS-14 ²	19.59	0.10	15.77	0.10	39.58	0.10	0.805	2.020
CL-06-35A ¹	19.17	0.06	15.71	0.06	39.35	0.06	0.819	2.052
CL-06-36A ¹	19.27	0.10	15.80	0.09	39.43	0.11	0.820	2.047
CL-06-37A ¹	19.16	0.06	15.72	0.06	39.26	0.07	0.821	2.050
CL-06-39A ¹	19.16	0.06	15.69	0.07	39.21	0.09	0.819	2.047
CL-06-40A ¹	19.13	0.06	15.67	0.06	39.14	0.06	0.819	2.046
KR-05-113 ¹	19.23	0.05	15.71	0.08	39.31	0.10	0.817	2.044
KR-05-130 ¹	19.24	0.05	15.69	0.08	39.26	0.10	0.815	2.040
KR-05-136 ¹	19.17	0.06	15.71	0.08	39.41	0.11	0.819	2.055
KR-05-621	19.13	0.05	15.69	0.08	39.18	0.10	0.820	2.048

3.8 Genetic Model and Implications for Exploration

3.8.1 Genetic Model

The geochemical signatures of mineralization, in combination with the paragenetic and textural studies discussed above, strongly imply two distinct fluid events in the Dublin Gulch IRGS. The first fluid was responsible for the formation of the proximal W-skarn (Wolf Skarn) and subsequent Stage 3 and 4 veining in a partially aligned stockwork hosted within the DGS. One piece of empirical evidence for this is the presence of Stage 3 and 4 veins, but the absence of Stage 5 and 6 veins, within the skarn. Brown (2001) and Stephens (2003) provided temperature estimates of 520 and ~460 °C, respectively, for the skarn based on mineral phase relationships. Geothermometry of Stage 3 and 4 arsenopyrite provided temperature estimates of 345 to 595 °C, which overlaps with these published temperature estimates for the skarn and agrees with a model in which the Stage 2 skarn, and Stage 3 and 4 veins, are formed by a single progressively cooling fluid. As noted above (Section 3.7.1) these temperature estimates are significantly higher than those obtained from fluid inclusions in quartz by Baker and Lang (2001), but there is some equivocality to assigning the quartz hosts to specific paragenetic stages within our detailed scheme.

Incorporation of sedimentary sulfur from the Hyland Group during the initial stage of plutonism caused the magma to acquire a more negative $\delta^{34}\text{S}$ inventory, and this is reflected in the composition of the mineralizing fluids of Stages 2 to 4. Corollary evidence for country rock assimilation is provided by the presence of the Wolf Skarn as a roof pendant within the DGS. During these earlier stages, the fluid also appears to have progressed from a $\delta^{34}\text{S}$ similar to the Hyland Group metasediments (especially the arsenopyrite of Stage 3 stockwork veins; Fig. 3.7) towards somewhat less negative values with time (i.e., Stage 2 to 4 pyrrhotite; Fig. 3.7). Spatially

non-uniform assimilation may have caused localized, peripheral heterogeneity in the sulfur isotope composition of the fluid that was subsequently homogenized toward more magmatic values in the uncrystallised portion of the DGS, given that the magmatic reservoir of sulfur was far larger in volume.

This model for the genesis of the first hydrothermal fluid pulse at Dublin Gulch is supported by oxygen isotope data for Clear Creek, which serves as the best proxy for Dublin Gulch in lieu of primary data. Marsh et al. (2003) and Stephens (2003) show a pattern for whole rock data in which the main stock had values of 12.5 to 13.1 ‰ $\delta^{18}\text{O}$ (fresh quartz monzonite and diorite) and 11.4 to 14.8 ‰ $\delta^{18}\text{O}$ (hydrothermally altered quartz monzonite and diorite). The Hyland Group at Clear Creek has whole rock $\delta^{18}\text{O}$ values of 11.9 to 15.9 ‰. Although these might be considered low for metasedimentary rocks, as noted by (Marsh et al., 2003), Murphy (1997) suggested that a significant volcanogenic component in the phyllites and slates of the Hyland Group may be responsible.

Quartz-hedenbergite and quartz-biotite-scheelite veins at Clear Creek (Stephens, 2003) appear to be the paragenetic equivalent of Stage 3 and 4 veins at Dublin Gulch. These veins display $\delta^{18}\text{O}$ values of ~14 – 15 ‰ and 10.2 ‰, respectively. Stephens (2003) calculated $\delta^{18}\text{O}$ (fluid) for quartz-hedenbergite veins of ~11.3 to ~12.2 for an inferred temperature range of 460 to 510 °C. These values are slightly higher than expected for a purely magmatic fluid (6 – 8 ‰ $\delta^{18}\text{O}$; Dickin, 2005) and strongly interaction with sediments of the Hyland Group, as is also suggested by the sulfur isotope systematics for Stages 1-4 at Dublin Gulch.

The second hydrothermal fluid at Dublin Gulch was related either to a second fluid pulse exsolved from the crystallizing DGS, or from an as yet unexposed second emplacement of

magma at depth. The nature of the second fluid is of critical importance to the understanding of the deposit, as the majority of Au inventory at Dublin Gulch was delivered by this fluid. Textural studies have shown clear evidence of re-fracturing and overprinting of Stage 3 and 4 veins by minerals that were precipitated during Stage 5 and 6 mineralization, and that the vein morphologies, ore assemblages and alteration assemblages produced by the two fluids vary significantly. Sulfur isotopes display distinct populations for Stage 3-4 and Stage 5-6 veins. The pattern of overprinting is also suggested by sulfides from veins with Stage 3-4 morphologies that display Stage 5b alteration selvages, and show sulfide $\delta^{34}\text{S}$ values associated with Stage 5 – 6 conditions.

Sulfur isotope values for the second fluid have a maximum range of -4 to +2.5 ‰ $\delta^{34}\text{S}$, and most are 0 ± 2 ‰, strongly suggesting a predominantly magmatic origin for the fluid. Oxygen isotopes from quartz from Au-stage veins at Clear Creek, a proxy for Stage 5 – 6 at Dublin Gulch, are 14.0 to 16.3 ‰ $\delta^{18}\text{O}$, with a small sub-set of quartz from distal mineralization at 17.9 to 18.7 ‰ $\delta^{18}\text{O}$ (Marsh et al., 2003; Stephens, 2003). Marsh et al. (2003) calculated $\delta^{18}\text{O}(\text{fluid})$ of 9 to 11 ‰ using the method of Clayton et al. (1972), and a temperature estimate of 325 °C. They hypothesized that the increased $\delta^{18}\text{O}$ for distal mineralization was a function of lower fluid temperatures due to increased distance from the heat source. Stephens (2003) refined this to 5.8 to 9.8 ‰ $\delta^{18}\text{O}(\text{fluid})$ for a temperature range of 300 to 400 °C for quartz from main Au stage veins, which is indicative of derivation from magmatic fluids.

Arsenopyrite compositions for Stage 5 suggest a temperature of precipitation of native gold of <300 to 490 °C, which is far in excess of the temperatures derived from fluid inclusions in quartz that have a more ambiguous paragenetic relationship with the main auriferous stages.

Arsenopyrite is often seen in textural equilibrium with native gold (Chapter 2), so these higher temperatures are suggested as a more realistic estimate.

Sulfosalts from Stage 6 show highly radiogenic Pb isotope values, which become even more radiogenic with distance from the pluton as a result of interaction with accessory minerals in the Hyland Group metasediments. Although sulfur isotopes suggest a dominantly magmatic source for the hydrothermal fluid at Stages 5 and 6, the Pb isotopes suggest substantial scavenging of more radiogenic Pb from the surrounding country rocks by these same fluids. This also implies that part of the Au, Ag, and/or As budget of veins in the Dublin Gulch IRGS may have been scavenged from these country rocks as well.

3.8.2 Implications for Exploration

Previous models for IRGS (e.g., Thompson et al. 1999) have focussed on early stage porphyry-style quartz veins as a key indicator that an intrusion may host auriferous mineralization. This study, however, has shown that these initial vein stages may sometimes be of secondary importance in providing the gold inventory in IRGS. At Dublin Gulch, the bulk of the gold inventory appears linked to later stage mineralization that accompanied a second fluid pulse. Further, the auriferous stages at Dublin Gulch are arsenopyrite-rich, making Dublin Gulch an example of an “As-rich” IRGS. Conversely, the Fort Knox deposit appears to represent an example of a quartz-rich, sulfide- and arsenic-poor deposit – an “As-poor” IRGS. This difference in sulfide and As concentrations relative to Au makes a direct comparison between Dublin Gulch and Fort Knox difficult using only paragenetic analysis.

At Dublin Gulch, Stage 3 and 4 veins often show re-fracturing and overprinting by late stage gold-bearing mineralization, a process that is particularly evident in their selvage

alteration assemblages. Arsenopyrite compositions and sulfur isotope signatures further support this observation; Stage 3 and 4 veins with later stage alteration assemblages also have overprinting sulfur isotope signatures that conform to the range for later stage gold-bearing mineralization.

Future exploration strategies could beneficially focus on building a potentially comparable paragenetic framework for each deposit in the TTGB – including the Scheelite Dome, Clear Creek and Brewery Creek deposits. In particular, the nature of alteration most closely associated with gold mineralization should be examined in more detail for these deposits. For example, calcite, dickite, kaolinite, muscovite/phengite or pyrophyllite alteration selvages around quartz veins may be more obvious than less volumetrically abundant Au-rich vein overprints. This would also provide insights into the level of re-fracturing and overprinting of early quartz veins, which appears beneficial in the formation of economic IRGS. The most prospective IRGS are proposed to be those that display a high density of early quartz veining, along with later stage gold-bearing mineralization that may substantially intersect the network of early quartz veins.

Acknowledgements

This work was funded by a grant from the NSERC Collaborative Research and Development (CRD) Program (CRDPJ 421812-2011), which included both financial and field support from Victoria Gold Corporation. We are deeply grateful to Bill Keats, Richard Eliason, Joanna (Ettlinger) Hodge, and Mark Ayranto of Victoria Gold Corporation for accommodating and facilitating this research effort. Michael Shaffer (Memorial University, MAF-IIC Facility) and Peter Jones (Carleton University, Dept. of Earth Sciences - Electron Microprobe Facility) are thanked for their expert assistance with the SEM and EPMA phases of this research, respectively.

References

- Abbott, J.G., 1986, Geology of the Plata-Inca property, Yukon, in *Yukon Geology*, v.1, Exploration and Geological Services Division, Yukon, Indian and Northern Affairs, Canada, p. 109-112.
- Abbott, J.G., Gordey, S.P., and Templeman-Kluit, D.J., 1986, Setting of stratiform, sediment hosted lead-zinc deposits in Yukon and northeastern British Columbia, In: Morin, J.A., (Ed.), *Mineral deposits of the northern Cordillera: Canadian Institute of Mining and Metallurgy Special Volume 37*, p. 1–18.
- ALS Minerals, 2011, A mineralogical analysis of 19 core pieces from the Potato Hills Trend, Eagle Gold project – Dublin Gulch, Yukon, ALS-MV10-005, (internal report for Victoria Gold Corp., 14 January 2011), 53 p.
- Anderson, R.G., 1983, Selwyn plutonic suite and its relationship to tungsten skarn mineralization, southeastern Yukon and District of Mackenzie, In: *Current research, Geological Survey of Canada, Paper 83-1B*, p. 151–163.
- Anderson, R.G., 1988, An overview of Mesozoic and Tertiary plutonic suites and their associated mineralization in the northern Canadian Cordillera, In: Taylor, R.P., Strong, D.F. (Eds.), *Recent advances in the geology of granite-related mineral deposits: Canadian Institute of Mining and Metallurgy*, p. 96–113.
- Armitage, A., and Gray, P.D., 2012, Prepared for Argus Metals Corp., Technical Report on the Hyland Gold Property in the Yukon Territory: technical report dated Mar, 1, 2012, 64p.
- Baker, T., and Lang, J.R., 2001, Fluid inclusion characteristics of intrusion-related gold mineralization, Tombstone-Tungsten magmatic belt, Yukon Territory Canada: *Mineralium Deposita*, v. 36, p. 563–582.
- Bakke, A.A., 1995, The Fort Knox “porphyry” gold deposit: Structurally controlled stockwork and shear quartz vein, sulphide-poor mineralization hosted by late Cretaceous pluton, east-central Alaska: *Canadian Institute of Mining and Metallurgy, Special Volume 46*, p. 795–802.
- Barton, P.B., Jr., and Skinner, B.J., 1979, Sulfide mineral stabilities, In: Barnes, H. L. (Ed.), *Geochemistry of hydrothermal ore deposits*, second edition: New York, Holt, John Wiley & Sons, p. 278-403.
- Bente, K., 1982, S-isotope investigations and geothermometric application of bismuthinites: *Mineralium Deposita*, v. 17, p. 119-132.
- Boyle, R.W., Wanless, R.K., and Stevens, R.D., 1970, Sulfur isotope investigation of the lead-zinc-silver-cadmium deposits of the Keno Hill-Galena Hill area, Yukon, Canada: *Economic Geology*, v. 65, p. 1-10.

Brown, V., 2001, The geology and genesis of the Ray Gulch tungsten skarn, Yukon Territory, Canada: Unpublished honours thesis, James Cook University, Queensland, Australia, 174 p.

Brown, V.S., Baker, T., and Stephens, J.R., 2002, Ray Gulch tungsten skarn, Dublin Gulch, central Yukon: Gold-tungsten relationships in intrusion-related ore systems and implications for gold exploration, In: Emond, D.S., Weston, L.H., Lewis, L.L. (Eds.), Yukon exploration and geology 2001, Exploration and Geological Services Division, Yukon Region, Indian and Northern Affairs Canada, p. 259–268.

Brueckner, S.B., Piercey, S.J., Layne, G.D., Piercey, G. and Sylvester, P.J., 2014, Variations of sulfur isotope signatures in sulfides from the metamorphosed Cu (-Au) volcanogenic massive sulfide Ming deposit, Newfoundland Appalachians: *Mineralium Deposita* (in press). <http://link.springer.com/article/10.1007/s00126-014-0567-7>.

Clayton, R.N., O'Neil, J.R., and Mayeda, T.K., 1972, Oxygen isotope exchange between quartz and water: *Journal of Geophysical Research*, v. 77, p. 3057–3067.

Deyell, C.L., 2005, Sulphur isotope zonation at the Mt Polley alkalic porphyry Cu-Au deposit, British Columbia, Canada: Society for Geology Applied to Mineral Deposits (SGA), 8th Biennial SGA Meeting, China, August 18–21, 2005, Proceedings, p. 373–376.

Deyell, C.L., and Tosdal, R.M., 2005, Alkalic Cu-Au deposits of British Columbia: Sulphur isotope zonation as a guide to mineral exploration: British Columbia Geological Survey Branch, Geological Fieldwork 2004, Paper 2005-1, p. 191–208.

Dickin, A.P., 2005, Radiogenic isotope geology, second edition: New York, Cambridge University Press, 512 p.

Doe, B.R., and Zartman, R.E., 1979, Plumbotectonics: The Phanerozoic. In: Barnes, H. L. (Ed.), Geochemistry of hydrothermal ore deposits, second edition: New York, Holt, John Wiley & Sons, p. 22-70.

Einaudi, M.T., Hedenquist, J.W., and Inan, E.E., 2003, Sulfidation state of fluids in active and extinct hydrothermal systems: Transitions from porphyry to epithermal environments, In: Simmons, S.F., Graham, I. (Eds.), Volcanic, geothermal, and ore-forming fluids: Rulers and witnesses of processes within the Earth: Society of Economic Geologists, Special Publication no. 10, p. 285-314.

Fritz, W.H., Narbonne, G.M., and Gordey, S.P., 1983, Strata and trace fossils near the Precambrian-Cambrian boundary, Mackenzie, Selwyn, and Wernecke Mountains, Yukon and Northwest Territories, In: Current research, Part B, Geological Survey of Canada, Paper 83-1B, p. 365-375.

Fritz, W.H., Cecile, M.P., Norford, B.S., Morrow, D., and Geldsetzer, H.H.J., 1991, Cambrian to middle Devonian assemblages, In: Gabrielse, H., Yorath, C.J. (Eds.), *Geology of the Cordilleran Orogen in Canada: Geological Survey of Canada, Geology of Canada 4*, p. 151-218 (also *Geological Society of America, The Geology of North America*, v. G-2).

Godwin, C.I., and Sinclair, A.J., 1982, Average lead isotope growth curves for shale-hosted zinc-lead deposits, *Canadian Cordillera: Economic Geology*, v. 77, p. 675–690.

Godwin, C.I., Gabites, J.E., and Andrew, A., 1988, LEADTABLE: A Galena Lead Isotope Database for the Canadian Cordillera, with a Guide to its Use by Explorationists: *British Columbia, Ministry of Energy, Mines and Petroleum Resources, Paper 1988 – 4*, 188p.

Gordey, S.P., and Anderson, R.G., 1993, Evolution of the northern Cordilleran miogeocline, Nahanni map area (105I), Yukon and Northwest Territories: *Geological Survey of Canada, Memoir 248*, 214 p.

Hammer, Ø, Harper, D.A.T., and Ryan, P.D., 2001, Past: Paleontological statistics software package for education and data analysis: *Palaeontologia Electronica*, v. 4, p. 4-9, 178kb. http://palaeo-electronica.org/2001_1/past/issue1_01.htm.

Hantelmann, J.J., 2013, The paragenesis and geochemistry of the Bellekeno Ag-Pb-Zn vein, Keno Hill district, Yukon, Canada: Unpubl. M.Sc. thesis, University of Alberta, Edmonton, Canada, 292 p.

Hart, C.J.R., 2004, Mid-Cretaceous magmatic evolution and intrusion-related metallogeny of the Tintina Gold Province, Yukon and Alaska: Unpubl. PhD. thesis, University of Western Australia, Perth, 188p.

Hart, C.J.R., 2005, Classifying, distinguishing and exploring for intrusion-related gold systems: The Gangué, *Newsletter of the Geological Association of Canada Mineral Deposits Division*, v. 87, p. 1, 4–9.

Hart, C.J.R., 2007, Reduced intrusion-related gold systems, In: Goodfellow, W.D. (Ed.), *Mineral deposits of Canada: A synthesis of major deposit types, district metallogeny, the evolution of geological provinces, and exploration methods: Geological Association of Canada, Mineral Deposits Division, Special Publication No. 5*, p. 95-112.

Hart, C.J.R., Goldfarb, R.J., Lewis, L.L., and Mair, J.L., 2004a, The Northern Cordillera Mid-Cretaceous Plutonic Province: Ilmenite/magnetite-series granitoids and intrusion-related mineralization: *Resource Geology*, v. 54, n. 3, p. 253–280.

Hart, C.J.R., Mair, J.L., Goldfarb, R.J., and Groves, D.I., 2004b, Source and redox controls on metallogenic variations in intrusion-related ore systems, Tombstone-Tungsten belt, Yukon Territory, Canada: *Transactions of the Royal Society of Edinburgh, Earth Science*, v. 95, p. 319–337.

- Heffernan, R.S., Mortensen, J.K., Gabites, J.E., and Sterenberg, V., 2004, Lead isotope signatures of Tintina Gold Province intrusions and associated mineral deposits from southeastern Yukon and southwestern Northwest Territories: Implications for exploration in the southeastern Tintina Gold Province. In: Emond, D.S., Lewis, L.L., Bradshaw, G.D. (Eds.), Yukon Exploration and Geology 2004, Yukon Geological Survey, p. 121-128.
- Hitchins, A.C., and Orssich, C.N., 1995, The Eagle zone gold-tungsten sheeted vein porphyry deposit and related mineralization, Dublin Gulch, Yukon Territory: Canadian Institute of Mining and Metallurgy, Special Volume 46, p. 803–810.
- Hollister, V.F., 1992, On a proposed plutonic porphyry gold deposit model: *Nonrenewable Resources*, v. 1, p. 293–302.
- INAC, 1991, Yukon Exploration 1990, Exploration and Geological Services division, Yukon, Indian and northern Affairs, Canada, Part C, p. 44-46.
- Kinross Gold Corporation, 2008, Technical report for the Fort Knox mine: NI 43-101 Technical Report (Prepared for Kinross Gold Corporation and Fairbanks Gold Mining Incorporated, March 31 2008), 79 p.
- Klemm, D.D., 1965, Synthesen und analysen in den dreiecksdiagrammen FeAsS-CoAsS-NiAsS und FeS₂-CoS₂-NiS₂: *Neues Jahrbuch für Mineralogie – Abhandlungen*, v. 103, p. 205-255.
- Kretschmar, U., and Scott, S.D., 1976, Phase relations involving arsenopyrite in the system Fe-As-S and their application: *Canadian Mineralogist*, v. 14, p. 364-386.
- Kuo, S., and R. E. Folinsbee, R.E., 1974, Lead isotope geology of mineral deposits spatially related to the Tintina Trench, Yukon Territory: *Economic Geology*, v. 69, p. 806-813.
- Lang, J.R., Baker, T., Hart, C.J.R., and Mortensen, J.K., 2000, An exploration model for intrusion-related gold systems: *Society of Economic Geology Newsletter*, v. 40, p. 1, 6–15.
- Lang, J.R., and Baker, T., 2001, Intrusion-related gold systems: the present level of understanding: *Mineralium Deposita*, v. 36, p. 477-489.
- Lennan, W.B., 1983, Ray Gulch tungsten skarn deposit, Dublin Gulch area, central Yukon: Canadian Institute of Mining, Metallurgy and Petroleum, Special Volume 37, p. 245–254.
- Mair, J.L., Hart, C.J.R., and Stephens, J.R., 2006a, Deformation history of the western Selwyn Basin, Canada: Implications for orogen evolution and the setting of mid-Cretaceous magmatism: *Geological Society of America Bulletin*, v. 118, p. 304–323.
- Mair, J.L., Goldfarb, R.J., Johnson, C.A., Hart, C.J.R., and Marsh, E.E., 2006b, Geochemical constraints on the genesis of the Scheelite Dome intrusion-related gold deposit, Tombstone gold belt, Yukon, Canada: *Economic Geology*, v. 101, p. 523–553.

- Maloof, T.L., Baker, T., and Thompson, J.F.H., 2001, The Dublin Gulch intrusion-hosted deposit, Tombstone plutonic suite, Yukon Territory, Canada: *Mineralium Deposita*, v. 36, p. 583–593.
- Marsh, E.E., Goldfarb, R.J., Hart, C.J.R., and Johnson, C.A., 2003, Geology and geochemistry of the Clear Creek intrusion-related gold occurrences, Tintina gold province, Yukon, Canada: *Canadian Journal of Earth Sciences*, v. 40, p. 681–699.
- McCoy, D., Newberry, R.J., Layer, P.W., DiMarchi, J.J., Bakke, A.A., Masterman, J.S., and Minehane, D.L., 1997, Plutonic-related gold deposits of interior Alaska: *Economic Geology*, Monograph 9, p. 191–241.
- McInnes, D., 2007 (last updated), Selwyn Basin metallogeny, Yukon Geological Survey, Yukon Geological Survey website: <http://www.geology.gov.yk.ca/pdf/SelwynBasin.pdf>
- Micko, J., 2010, The geology and genesis of the Central zone alkalic copper-gold porphyry deposit, Galore Creek district, northwestern British Columbia, Canada: Unpubl. Ph.D. thesis, Vancouver, Canada, University of British Columbia, 387 p.
- Mortensen, J.K., Murphy, D.C., Hart, C.J.R. and Anderson, R.G., 1995, Timing, tectonic setting, and metallogeny of early and mid-Cretaceous magmatism in Yukon Territory: *Geological Society of America, Abstracts with Programs* 27, 65.
- Mortensen, J.K., Hart, C.J.R, Murphy, D.C., and Heffernan, S., 2000, Temporal evolution of early and mid-Cretaceous magmatism in the Tintina Gold Belt, In: Tucker, T., Smith, M.J. (Eds.), *The Tintina gold belt: Concepts, exploration and discoveries: British Columbia and Yukon Chamber of Mines Special Volume 2*, p. 49–57.
- Murphy, D.C., 1997, Geology of the McQuesten River region, northern McQuesten and Mayo Map Area, Yukon Territory (115P/14, 15, 16; 105M/13, 14): Exploration and Geological Services Division, Yukon, Indian and Northern Affairs Canada Bulletin 6, 111 p.
- Newberry, R.J., and Solie, D.N., 1995, Data for plutonic rocks and associated gold deposits in Interior Alaska: Alaska Division of Geological and Geophysical Surveys, Public Data File 95-25, 61 p.
- Ohmoto, H., and Rye, R.O., 1979, Isotopes of sulfur and carbon, In: Barnes, H. L. (Ed.), *Geochemistry of hydrothermal ore deposits*, second edition: New York, Holt, John Wiley & Sons, p. 509-567.
- Pass, H.E., Cooke, D.R., Davidson, G., Maas, R., Dipple, G., Rees, C., Ferreira, L., Taylor, C., and Deyell, C.L., 2014, Isotope geochemistry of the Northeast zone, Mount Polley alkalic Cu-Au-Ag porphyry deposit, British Columbia: A case for carbonate assimilation: *Economic Geology*, v. 109, p. 859–890.

Rasmussen, K.L., 2013, The timing, composition, and petrogenesis of syn- to post-accretionary magmatism in the northern Cordilleran miogeocline, eastern Yukon and southwestern Northwest Territories: Unpubl. Ph.D. Thesis, University of British Columbia, Vancouver, Canada, 810 p.

Roots, C.F., 1997, Geology of the Mayo Map area, Yukon Territory (105M): Exploration and Geological Services Division, Yukon, Indian and Northern Affairs Canada, Bulletin 7, 82 p.

Scott Wilson Mining, 2010, Prepared for StrataGold Corp., Technical Report on the Dublin Gulch Property, Yukon Territory, Canada: NI 43-101 Technical Report dated Apr. 23, 2010, 242 p.

Selby, D., Creaser, R.A., Heaman, L.M., and Hart, C.J.R., 2003, Re–Os and U–Pb geochronology of the Clear Creek, Dublin Gulch, and Mactung deposits, Tombstone Gold Belt, Yukon, Canada: absolute timing relationships between plutonism and mineralization: Canadian Journal of Earth Science, v. 40, p. 1839–1852.

Sharp, Z.D., Essene, E.J., and Kelly, W.C., 1985, A re-examination of the arsenopyrite geothermometer: pressure considerations and applications to natural assemblages: Canadian Mineralogist, v. 23, p. 517-534.

Sillitoe, R.H., and Thompson, J.F.H., 1998, Intrusion-related vein gold deposits: Types, tectono-magmatic settings, and difficulties of distinction from orogenic gold deposits: Resource Geology, v. 48, p. 237–250.

Sivertz, G.W.G., 1985, prepared for International Prism Exploration, Summary report on the Val-Vera property, Kathleen Lakes Area, Yukon Territory: Technical Report dated Feb. 15, 1985, 35p.

SRK Consulting, 2008, Prepared for Victoria Gold Corp., NI 43-101 Preliminary Assessment Dublin Gulch Property – Mar-Tungsten Zone Mayo District, Yukon Territory, Canada: Technical Report dated Dec. 1, 2008, 161 p.

Stacey, J.S., and Kramers, J.D., 1975, Approximation of terrestrial lead isotope evolution by a two-stage model: Earth and Planetary Science Letters, v, 26, p. 207-221.

Stanton, R.L., and Russell, R.D., 1959, Anomalous leads and the emplacement of lead sulfide ores: Economic Geology, v. 54, p. 588-607.

Stephens, J.R., 2003, Structural, mechanical and P-T evolution of intrusion-related gold mineralization at Clear Creek and Dublin Gulch, Yukon, Canada: Unpubl. Ph.D. Thesis, James Cook University of North Queensland, Townsville, Australia, 277 p.

Tempelman-Kluit, D.J., 1970, Discussion of Boyle, R.W., Wanless, R.K., and Stevens, R.D., (1970) Sulfur isotope investigation of the lead-zinc-silver-cadmium deposits of the Keno Hill-Galena Hill area, Yukon, Canada: Economic Geology, v. 65, p.731.

Tesfaye Firdu, F. and Taskinen, P., 2010, Thermodynamics and phase equilibria in the (Ni, Cu, Zn)-(As, Sb, Bi)-S systems at elevated temperatures (300 – 900°C): Aalto University Publications in Materials Science and Engineering, Thermodynamics and Modelling of Metallurgical Processes, TKK-MT-216, Espoo, Finland, ISSN 1455-2329, ISBN 978-952-3273-3, 60 p.

Tetra Tech, 2015, Prepared for Victoria Gold Corp., Technical Report – Feasibility Study, Eagle Gold Project, Yukon: NI 43-101 Technical Report, dated May 29, 2015, 411 p.

Thompson, J.F.H., and Newberry, R.J., 2000, Gold deposits related to reduced granitic intrusions, In: S.G., Hagemann and P.E., Brown (eds.), Gold in 2000: Society of Economic Geologists, Reviews in Economic Geology, v. 13, p. 377–400.

Thompson, J.F.H., Sillitoe, R.H., Baker, T., Lang, J.R., and Mortensen, J.K., 1999, Intrusion-related gold deposits associated with tungsten-tin provinces: Mineralium Deposita, v. 34, p. 323–334.

Thompson, R.M., 1945, An occurrence of cassiterite at Dublin Gulch, Yukon Territory: Economic Geology, v. 40, p. 142-147.

Tuba, G., Molnár, F., Ames, D.E., Péntek, A., Watkinson, D.H., and Jones, P.C., 2014, Multi-stage hydrothermal processes involved in “low-sulfide” Cu(–Ni)–PGE mineralization in the footwall of the Sudbury Igneous Complex (Canada): Amy Lake PGE zone, East Range: Mineralium Deposita, v. 49, p. 7–47.

Wardrop Engineering Inc., 2009, Prepared for StrataGold Corporation, Technical Report on the Dublin Gulch Property, Yukon Territory, Canada: NI 43-101 Technical Report, dated February 04, 2009, 70 p.

Wardrop Engineering Inc., 2011a, Prepared for Victoria Gold Corp., Technical Report on the Eagle Zone, Dublin Gulch Property, Yukon Territory, Canada: NI 43-101 Technical Report, dated April 15, 2011, 48 p.

Wardrop Engineering Inc., 2011b, Prepared for Victoria Gold Corp., Technical Report on the Eagle Zone, Dublin Gulch Property, Yukon Territory, Canada: NI 43-101 Technical Report dated May 04, 2011, 86 p.

Wardrop Engineering Inc., 2012, Prepared for Victoria Gold Corp., Technical Report on the Eagle Zone, Dublin Gulch Property, Yukon Territory, Canada: NI 43-101 Technical Report dated April 05, 2012, 419 p.

Wilson, A.J., Cooke, D.R., Harper, B.J., and Deyell, C.L., 2007, Sulfur isotopic zonation in the Cadia district, southeastern Australia: Exploration significance and implications for the genesis of alkalic porphyry Au-Cu deposits: Mineralium Deposita, v. 42, p. 465–487.

Woodsworth, G.J., Anderson, R.G., and Armstrong, R.L., 1991, Plutonic regimes, In: Gabrielse, H., Yorath, C.J. (Eds.), *Geology of the Cordilleran Orogen in Canada: Geological Survey of Canada, Geology of Canada 4*, p. 491–531.

Zartman, R.E., and Doe, B.R., 1981, Plumbotectonics – The model: *Tectonophysics*, v. 75, p. 135-162.

Zartman, R.E., and Haines, S.M., 1988, The plumbotectonic model for Pb isotopic systematics among major terrestrial reservoirs – A case for bi-directional transport: *Geochimica et Cosmochimica Acta*, v. 53, p. 1327 – 1339.

CHAPTER 4

Magmatism and Metallogeny of the Dublin Gulch area, YT, Canada: Insights from Nd and Sr Isotopes, and U-Pb Geochronology

FRASER A. KIRK, GEORGE A. JENNER, GRAHAM D. LAYNE, AND GREG R. DUNNING

*Department of Earth Sciences, Memorial University, 300 Prince Philip Drive, St John's,
Newfoundland, A1B 3X5, Canada*

Abstract

Victoria Gold Corporation's Dublin Gulch property, located 85 km NNE of Mayo, central Yukon, hosts the Eagle gold deposit (3.3 Moz Au indicated and inferred global resource), as well as several high-grade Au occurrences within a >13 km-long belt of Au-As-Bi-Sb and Ag-Pb-Zn mineralization known as the Potato Hills Trend. Dublin Gulch is an important type example of an intrusion related gold system (IRGS). Paragenetic studies indicate that a significant portion of the gold inventory may have been linked to an intrusive phase other than the main Dublin Gulch Stock.

Three groups of intrusive rocks have been identified at Dublin Gulch based on field and spatial relationships; the main phase granodiorite of the Dublin Gulch Stock, a series of equigranular to porphyritic dacitic dykes from the Platinum and Potato Hills zones, and a series of porphyritic andesitic to dacitic dykes from the Peso Zone. U-Pb dating of zircons from these intrusive rocks suggests a short-lived igneous event at 93-94 Ma as the parent of hydrothermal mineralization. All three groups are metaluminous, and are characterized by SiO₂ of 58.6 to 65.5 wt.%; $\epsilon\text{Nd}_{(i)}$ of -14.4 to -11.6; and $^{87}\text{Sr}/^{86}\text{Sr}_{(i)}$ of 0.71362 to 0.71726.

A comparison to similar lithologies at the Scheelite Dome and Brewery Creek deposits (also considered IRGS) identified four distinct geochemical groupings of rocks, based on the modified alkali-lime index (MALI): calcic, calc-alkalic, alkali-calcic, and alkalic. All four MALI groupings exhibit remarkably similar trace element and REE compositions, and Nd and Sr isotope signatures, suggesting melt derivation from enriched sub-continental lithospheric mantle. All of the parent intrusions to significant recognized IRGS within the Selwyn Basin show characteristics consistent with emplacement in a post-collisional tectonic regime, and melt generation in response to heat flow associated with mantle upwelling following delamination.

4.1 Introduction

Intrusion related gold systems (IRGS) are now discussed as a new class of ore deposit, distinct from porphyry-associated gold (e.g., Thompson and Newberry, 2000; Hart, 2007). IRGS display a number of mineralization styles, including sheeted veins, breccias, replacements, and disseminations (Thompson et al., 1999). In many examples mineralization occurs in close genetic and spatial association with a moderately reduced ilmenite-series pluton (Thompson et al., 1999), giving rise to the term reduced intrusion-related gold systems (RIRGS) as applied by Thompson et al., (1999), Thompson and Newberry (2000), and Lang et al., (2000); and subsequently refined by Hart (2005, 2007).

The most important exemplar area for IRGS is the Tintina Gold Belt (TGB), which stretches from the southern Yukon in a westward arc into the interior of Alaska. Within the TGB a number of plutonic suites have been designated (e.g. Mortensen et al., 1995, 2000; Hart et al., 2004a, b), with a broader collection of the most prospective ones defining the Tombstone-Tintina Belt (TTB), see Figure 4.1.

Dublin Gulch is located in the Yukon Territory, Canada, approximately 85 km north northwest of the town of Mayo. This study focuses on the metallogeny and intrusive parent lithologies of the Dublin Gulch IRGS. The Eagle Zone of the Dublin Gulch deposit contains a 3.3 Moz NI43-101 compliant resource (3.0 Moz – 134 Mt @ 0.69 g/T Au indicated, 0.3 Moz – 0.2 Mt @ 0.56 g/T Au inferred; Tetra Tech, 2015), which includes a 2.3 Moz (92 Mt @ 0.78 g/T Au) proven and probable Au reserve (Tetra Tech, 2015). The deposit is hosted almost entirely (>90%) within a mid-Cretaceous granodiorite pluton, the Dublin Gulch Stock (DGS). The

remaining ~10% of the deposit is hosted within metasedimentary rocks of the surrounding Neoproterozoic Hyland Group.

The DGS has previously been designated as a member of the Mayo Plutonic Suite (MPS; Hart et al., 2004b). Deposits associated with nominal members of the MPS have been the focus of a number of recent studies (Dublin Gulch – Maloof et al., 2001; Stephens, 2003; Scheelite Dome – Mair et al., 2006a, 2011; Clear Creek – Marsh et al., 2003; Stephens, 2003). Consequently, MPS-associated deposits are the best studied collection of IRGS within the Yukon, along with Fort Knox and other deposits in the Fairbanks District of Alaska (e.g., McCoy et al., 1997, and references therein).

4.1.1 Scope of Study

The objective of this study was to address the following questions of timing and petrogenesis:

- 1) Are dykes to the west of the bounding Haggart Creek Fault (Fig 4.1) temporally related to the intrusion of the DGS?
- 2) What is the relative magnitude of the age difference between the DGS and dykes which cross-cut it?
- 3) Are dykes on either side of the Haggart Creek Fault temporally and petrogenetically related?

The samples selected for U-Pb geochronology were also analysed to determine their major and trace element geochemistry, and Nd and Sr isotope composition. The aim of the geochemical studies was to characterize the petrogenetic affinities of the rocks and to determine which were co-magmatic. The geochemical signatures obtained for our samples were also compared to published geochemical data from Dublin Gulch (Hart et al., 2004b), Scheelite Dome (Mair et al.,

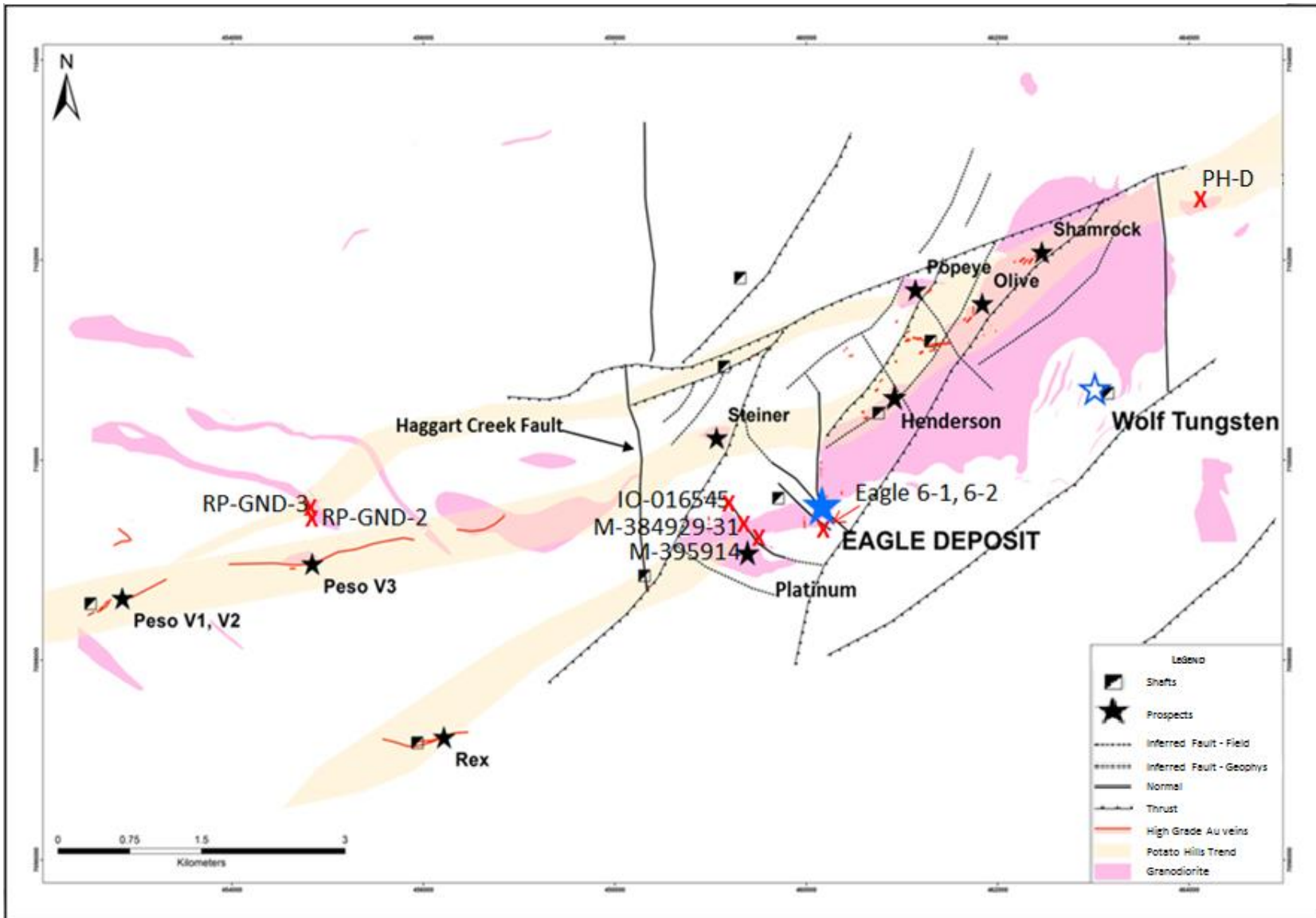


FIGURE 4.1. Simplified geological map showing the distribution of geochronology samples, the Dublin Gulch Stock and Au-Ag prospects.

2011) and Brewery Creek (Lindsay, 2006), to better establish the metallogenic signatures of IRGS in the TGB. A key goal was to link the petrogenesis and spatial distribution of geochemically distinct intrusive lithologies to significant gold occurrences.

4.2 Geological Setting

4.2.1 Regional Geology

The DGS was emplaced into the Yusezyu Formation of the Hyland Group in the Selwyn Basin of the Northern Cordillera. The Selwyn Basin, a passive margin sequence, was deposited on the North-western margins of North America during the late Precambrian to Middle Jurassic (Abbott et al., 1986; Gordey and Anderson, 1993). The Hyland Group is composed of coarse-grained sandstone, inter-bedded with shale and minor carbonate horizons, deposited by turbidite flows during the latest Precambrian to Early Cambrian. The age of deposition is based on fossils in the limestone horizons (Fritz et al., 1983, 1991; Gordey and Anderson, 1993). The Yusezyu Formation largely consists of beds of coarse sandstone, pebbly conglomerates, shale and siltstone. The upper parts of the formation are variably calcareous, with minor limestone horizons. The Yusezyu Formation records the earliest sedimentation within the Selwyn Basin, and ceased accumulating around latest Precambrian (Murphy, 1997).

The Tintina Gold Province (TGP) is a belt of Au deposits in the Northern Cordillera of Yukon and Alaska that is primarily bounded by two dextral transpressional fault systems - the Denali Fault (southern limit) and the Tintina Fault (northern limit). However, the belt extends across the Tintina Fault and into the Selwyn Basin (Fig. 3.2; Chapter 3). Mair et al. (2006b) suggest that as much as 450 km of dextral strike-slip movement may have occurred along the Tintina Fault during the late Cretaceous to Tertiary. When resolved, this movement would

account for the geochemical similarities between intrusions in the Fairbanks District, Alaska and those in the Yukon.

Within the TGP a series of highly prospective IRGS deposits form the Tombstone Gold Belt (TGB), the most significant host to IRGS globally. A series of nomenclature systems has been proposed by various authors (e.g., Anderson, 1983, 1988; Woodsworth et al., 1991) to group the intrusive/plutonic rocks in the northern Cordillera into various “suites”. The beginnings of the most current nomenclature began with Mortensen et al. (1995, 2000) and Murphy (1997). The belt of plutons on the northern margins of the Selwyn Basin, which trends roughly east-west, was designated the Tombstone Plutonic Suite; while, the series of plutons which trend broadly north-south along the YT-NWT border was termed the Tungsten Plutonic Suite (Fig. 4.2). It should be noted that this division included only small plutons with ages around 94 Ma. Hart et al. (2004a, b) defined plutonic provinces for the entirety of Alaska and the Yukon based on their geochemical affinities, age, and morphology, including a revised scheme for plutonic suites within the Yukon that split the Tombstone Suite into the Tombstone and Mayo suites, and widened the parameters for inclusion within the Tungsten Suite.

The sub-division of the original Tombstone Suite into two suites (Tombstone and Mayo) was made on the basis of geographical location, pluton size, rock types, geochemistry, and morphology. The Tombstone Suite, as defined by Hart et al. (2004b), is characterized by 10-80 km², concentrically zoned plutons, which are alkalic and largely composed of syenite, and lie within the northwestern-most portion of the Selwyn Basin. In contrast, the Mayo Suite features 1-5 km² (in western area)/ 20-80 km² (in eastern area), single phase to weakly composite plutons, which are alkalic-calcic to calcic and chiefly composed of quartz monzonite, arrayed east-west along the northern margin of the Selwyn Basin. The Tungsten Suite is comprised of ~15km²,

gradationally zoned plutons, which are peraluminous, alkalic-calcic to calcic, and feature quartz monzonite to monzogranite compositions. Hart et al. (2004b) proposed age ranges for the respective suites as: Tungsten Suite (97 – 94 Ma), Mayo Suite (95 – 92 Ma) and Tombstone Suite (92 – 90 Ma). Rasmussen (2013) refined these ranges to: Tungsten Suite (98 – 94 Ma); Mayo Suite (96 – 93 Ma); and Tombstone Suite (94 – 89 Ma). The Dublin Gulch Stock was included by Hart et al. (2004b) as a member of the Mayo Suite of intrusions.

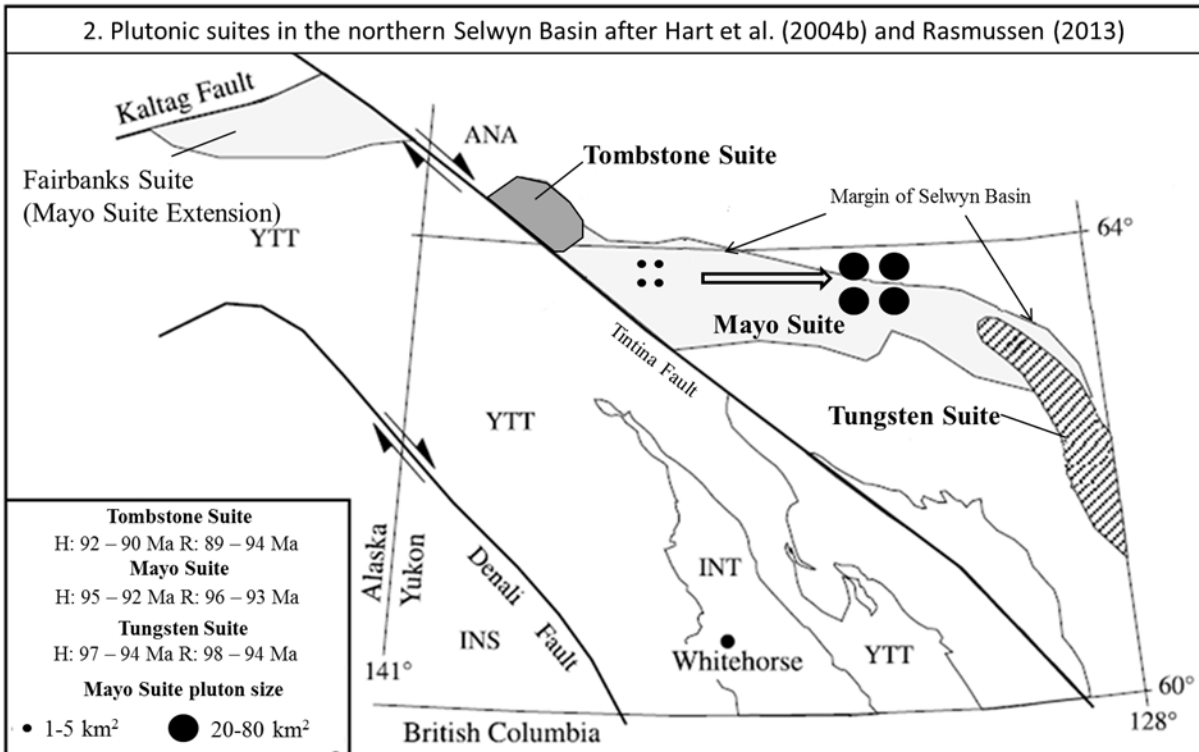
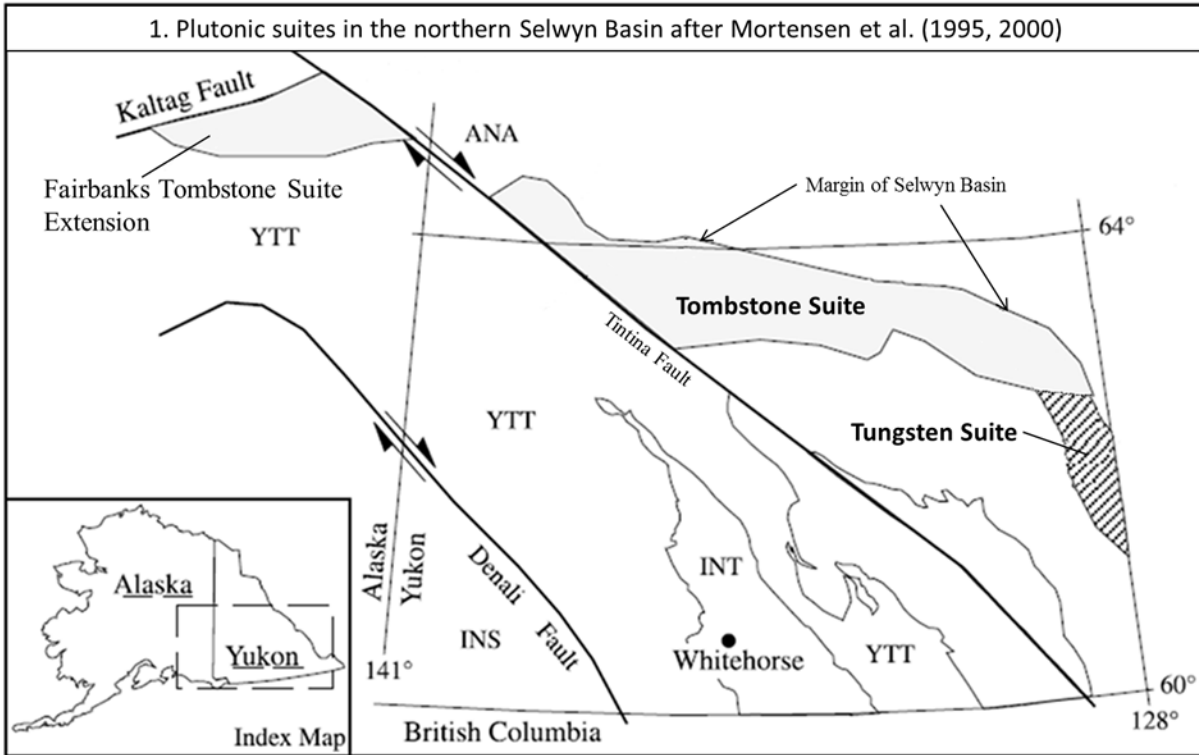


FIGURE 4.2. Summary of plutonic suite classification schemes for the northern Cordillera 1: Tombstone and Tungsten suites after Mortensen et al. (1995, 2000) 2: Tombstone, Mayo, and Tungsten suites after Hart et al. (2004b) and Rasmussen (2013).

4.2.2 Local Geology

The Dublin Gulch deposit is comprised of a number of zones and occurrences, the most notable of which is the Eagle Zone. Figure 4.1 shows the mapped exposure of the Dublin Gulch stock (DGS), and the locations of the Eagle Zone and other important zones of the deposit. The DGS, as exposed in the study area, is a granodiorite intrusion that forms an elongate ridge (approx. 6 km x 2 km) along the 070° trending axis of the Dublin Gulch antiform. The DGS displays a generally equigranular, medium-grained texture throughout its main body - with a strongly developed porphyritic texture within 10 m of contact margins. Although the intrusion appears largely compositionally homogeneous, there are volumes of compositional heterogeneity where the intrusive could be classified as a quartz monzonite rather than granodiorite. Spheroidal to oblong spheroid bodies, typically 5 to 20 cm in length, composed of hornblende, biotite, and quartz are found along the margins of the pluton. These bodies do not display remnant bedding, are never angular in shape, and are largely crystalline - suggesting that they represent magmatic enclaves rather than xenoliths. These enclaves do not show any evidence of flattening, suggesting passive intrusion under little to no tectonic stress.

A series of narrow aplite dykes cross-cut the DGS, and a roof pendant scheelite-bearing skarn, in the vicinity of the Wolf Tungsten Zone (Fig. 4.1). These aplite dykes are cross-cut by early quartz veins, implying an age of intrusion between that of skarn formation and the formation of subsequent hydrothermal veining. Late stage dykes of andesite to dacite composition, which vary between porphyritic (when hosted within Hyland Group) and equigranular to porphyritic (when hosted within DGS), crosscut the main DGS, and the aligned stockwork veins described in Chapter 3. The relationship between these late stage dykes and vein

stages later than aligned stockwork veins remains enigmatic in the absence of observable cross-cutting relationships.

Published U-Pb ages for the crystallization of the DGS are 92.8 ± 0.5 Ma (titanite; n=2) and $93.5 +5.8/-0.5$ (zircon; Murphy 1997), and 94.0 ± 0.3 Ma (zircon; Selby et al., 2003; Olive Zone). A Re-Os date for molybdenite (Selby et al., 2003) suggested 93.2 ± 0.3 Ma for hydrothermal activity, clearly linking mineralization to emplacement of the pluton. The detailed paragenesis of our study (see Chapter 2) places molybdenite in early vein stages that preceded the bulk of Au mineralization so this date may not be appropriate for the precise timing of Au delivery at Dublin Gulch.

4.3 Sample Description

4.3.1 Sample Collection and Locations

Samples were collected, during summer 2012, to assess the age and other possible inter-relationships between episodes of igneous activity at Dublin Gulch. The location and nature of the samples are given in Table 4.1 and illustrated in Figure 4.1. Three groups of intrusive rocks have been identified at Dublin Gulch, based on field relationships, petrography, and whole rock geochemistry:

Group 1: Dublin Gulch Stock (DGS) granodiorite from Eagle Zone.

Group 2: Equigranular to porphyritic dacite dykes from Platinum and Potato Hills zones.

Group 3: Porphyritic andesite to dacite dykes from Peso Zone.

TABLE 4.1. Locations of Dublin Gulch samples analysed in this study. Co-ordinates are in UTM (NAD83, Zone 8).

Sample Name	Group and Zone	Easting	Northing	Type	Depth
Eagle 6-1	1: Eagle	460182.2	7099351	Outcrop	Surface
Eagle 6-2	1: Eagle	460182.2	7099351	Outcrop	Surface
M 395914	2: Platinum	459550.0	7099300	DDH DG12-518C	113.7 m
IO-016545	2: Platinum	459187.9	7099559	DDH DG10-369C	125.0 m
M 384929-31	2: Platinum	459349.2	7099400	DDH DG12-490C	60.0 m
PH-D	2: Potato Hills	464120.5	7102652	Outcrop	Surface
RP-GND-2	3: Peso	454870.6	7099466	Outcrop	Surface
RP-GND-3	3: Peso	454857.4	7099540	Outcrop	Surface

4.3.2 Group 1: Dublin Gulch Stock from Eagle Zone.

Two samples of the main phase of the stock were taken from surface within the Eagle Zone (Eagle 6-1 and Eagle 6-2). Previous U-Pb dates for the DGS are from an unspecified location(s) (Murphy, 1997) and the Olive Zone (Selby et al., 2003). The Eagle Zone is the most economically important zone of the deposit and so these samples were selected to provide an

explicit age of the DGS there. Both samples were taken from within 10 m of the contact with surrounding metasedimentary country rocks. The pluton displays an equigranular texture, however, within 10 m of the contact it develops a porphyritic texture.

The granodiorite in the samples analysed shows a porphyritic texture with a very fine groundmass of quartz and alkali feldspar (60 %). Phenocrysts are typically medium-grained biotite (20%), and elongate to tabular amphibole (8 %) that is variably replaced by biotite, plagioclase (6%), quartz (4%), and alkali feldspar (2%). Phenocrysts show a bi-modal distribution in size with around 40% being 1-2 mm and 60 % being 0.25-0.5 mm. There is growth zonation in the plagioclase and alkali feldspar, and both commonly display resorption textures.

4.3.3 Group 2: Equigranular to porphyritic dykes from Platinum and Potato Hills Zones.

Four samples of the equigranular dykes were included in this study. Three of the samples (IO-016545, M 384929-31, and M 395914) come from diamond drill holes within the Platinum Zone. Although these holes were not drilled with oriented core barrels, Figure 4.1 shows that the samples coincide with a mapped fault and are likely part of the same dyke grouping that crosscuts the DGS. The fourth sample (PH-D) comes from an outcrop on the northern slopes of the Potato Hills and is hosted by metasedimentary rocks.

The dykes feature 1 – 2 mm phenocrysts in a 0.1 – 0.25 mm grain size groundmass. Plagioclase (20 %) is the dominant phenocryst phase. A second phenocryst phase (10 %), preserved as an eroded square shape, has been completely replaced by a fine-grained aggregate of amphibole ± mica. It is inferred to have been a calcic-clinopyroxene based on the similarity to textures at Scheelite Dome, described by Mair et al. (2003), in which diopside is variably

replaced by an amphibole aggregate. The groundmass contains fine-grained biotite (10 %), phlogopite (10 %), and amphibole (5 %). There are weak flow textures evidenced by biotite, phlogopite and amphibole that wrap around phenocrysts of plagioclase. Quartz (30 %) and alkali feldspar (10 %) are restricted to the groundmass and are entrained in some of the flow textures. The groundmass also contains minor plagioclase (5 %), and pyrite (<2 %) that is often altered to hematite. Accessory minerals present include titanite, fluorite, zircon, and trace molybdenite.

4.3.4 Group 3: Porphyritic dykes from Peso Zone.

Two of the samples in this study (RP-GND-2 and RP-GND-3) come from the Peso Zone of the Dublin Gulch deposit. This zone is peripheral to the main deposit and hosted within the Hyland Group, with no evidence of the DGS, or other plutonic phases, exposed at the surface. It is also more Ag-rich than Au-rich and is historically an area of Ag exploration. There is around 300 m of vertical displacement on the Haggart Creek Fault, which separates the Peso Zone from the main Dublin Gulch deposits (Tempelman-Kluit, 1964). Peso is within the up-thrown block, and the Dublin Gulch deposit within the down-thrown block. One of the objectives of assessing the degree to which the intrusive rocks from either side of the fault are genetically related was to assess whether the Rex-Peso veins represent a higher level of mineralization that was removed by erosion on the Dublin Gulch side of the Haggart Creek Fault. If this were the case, it would imply the potential for significant Dublin Gulch/Eagle Zone style Au mineralization at ~300-400 m depth beneath the Rex-Peso area.

Porphyritic dykes have a very fine-grained, quartz-rich groundmass (70%), and contain approximately 30% phenocrysts. The phenocrysts are quartz (12%), plagioclase (9%), hornblende (3%), biotite (5%), and phlogopite (< 2%). Phenocrysts range in size from 0.25 – 4

mm, with a normal size distribution. Quartz phenocrysts are commonly rounded, with reaction rims around 1 mm thick, implying rapid syn-emplacement crystallization. It was not possible to identify the mineral(s) product of the reaction rims. The other phenocryst phases, particularly plagioclase, are commonly altered and often show resorption textures. Pyrite is present within fractures and, as within the hypabyssal dykes of Group 2, is commonly altered to hematite.

4.4 Analytical Methods

4.4.1 U-Pb Geochronology

U-Pb geochronology was performed on zircon (Fig. 4.3) from five samples using chemical abrasion-thermal ionization mass spectrometry (CA-TIMS) at Memorial University. The CA-TIMS method is described in detail in Sparkes and Dunning (2014). The uncertainties on the isotopic ratios were calculated using an unpublished in-house program and are reported as 2σ in Appendix G. Ages are reported as the weighted average of the $^{206}\text{Pb}/^{238}\text{U}$ ages calculated using ISOPLOT, and errors are reported at the 95% confidence interval. For all samples additional zircon grains are currently being analyzed to improve the overall precision of the U-Pb dates. However, this is not expected to materially affect the discussion or conclusions presented here.

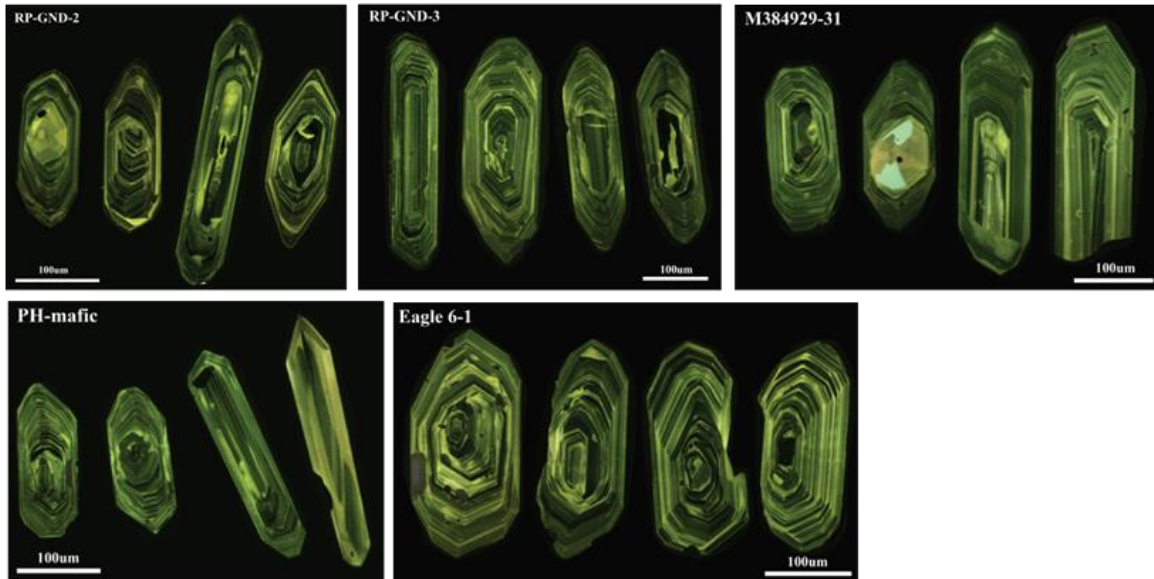


FIGURE 4.3. Cathodoluminescence (CL) images of zircon crystals with igneous growth zoning for each sample analysed. Images were taken using a FEI Quanta 400 Scanning Electron Microscope (SEM) with cathodoluminescence (CL) detector at Memorial University.

4.4.2 Whole rock geochemistry

Whole rock geochemical analysis was conducted on eight samples (Group 1: $n = 2$, Group 2: $n = 4$, Group 3: $n = 2$) by ActLabs (Ancaster, ON, Canada) using their 4Litho - lithium metaborate/tetraborate fusion ICP and ICP-MS protocol. This involves a combination of packages Code 4B (lithium metaborate/tetraborate fusion ICP whole rock) and Code 4B2 (trace element ICP-MS). Three blanks and five controls (three before sample group and two after) are analyzed per group of samples. Duplicates are fused and analysed every 15 samples. The instrument is recalibrated every 40 samples to ensure accuracy and precision of the measurements (see Litho geochemistry at www.actlabs.com). Stated limits of detection are given in Appendix C.

4.4.3 Nd and Sr isotopes

Nd and Sr isotopic compositions were determined using TIMS at Memorial University. A detailed description of the analytical methodology is presented in Appendix I.

4.5 U-Pb Geochronology Results

U-Pb concordia diagrams for samples of the three rock suites are provided in Figure 4.4. The main phase DGS granodiorite yielded an age of 94.1 ± 0.3 Ma. Since this is taken from within 10 m of the contact this age is likely to correspond with the earliest intrusion and first crystallization of the Dublin Gulch pluton. PH-D, a sample of a dyke from the Potato Hills Zone yielded an age of 94.2 ± 0.8 Ma. Sample M-384929-31 (shown as M-384-31 in Fig. 4.4) yielded an age of 94.1 ± 0.5 Ma. Porphyritic dyke samples from the Peso Zone, RP-GND-2, and RP-GND-3, yielded ages of 93.3 ± 1.5 and 94.4 ± 0.5 Ma, respectively. Based on intrusive lithologies currently recognized in the area, these ages imply that a short lived magmatic centre was responsible for igneous activity at Dublin Gulch. The results also confirm that the igneous activity in the Peso Zone is part of the same igneous episode as the DGS. Additionally, dykes that cross-cut the DGS are also part of the same overall system as the DGS and the Peso Zone. These age determinations have been used for the age correction of samples analysed for Nd and Sr isotopic compositions.

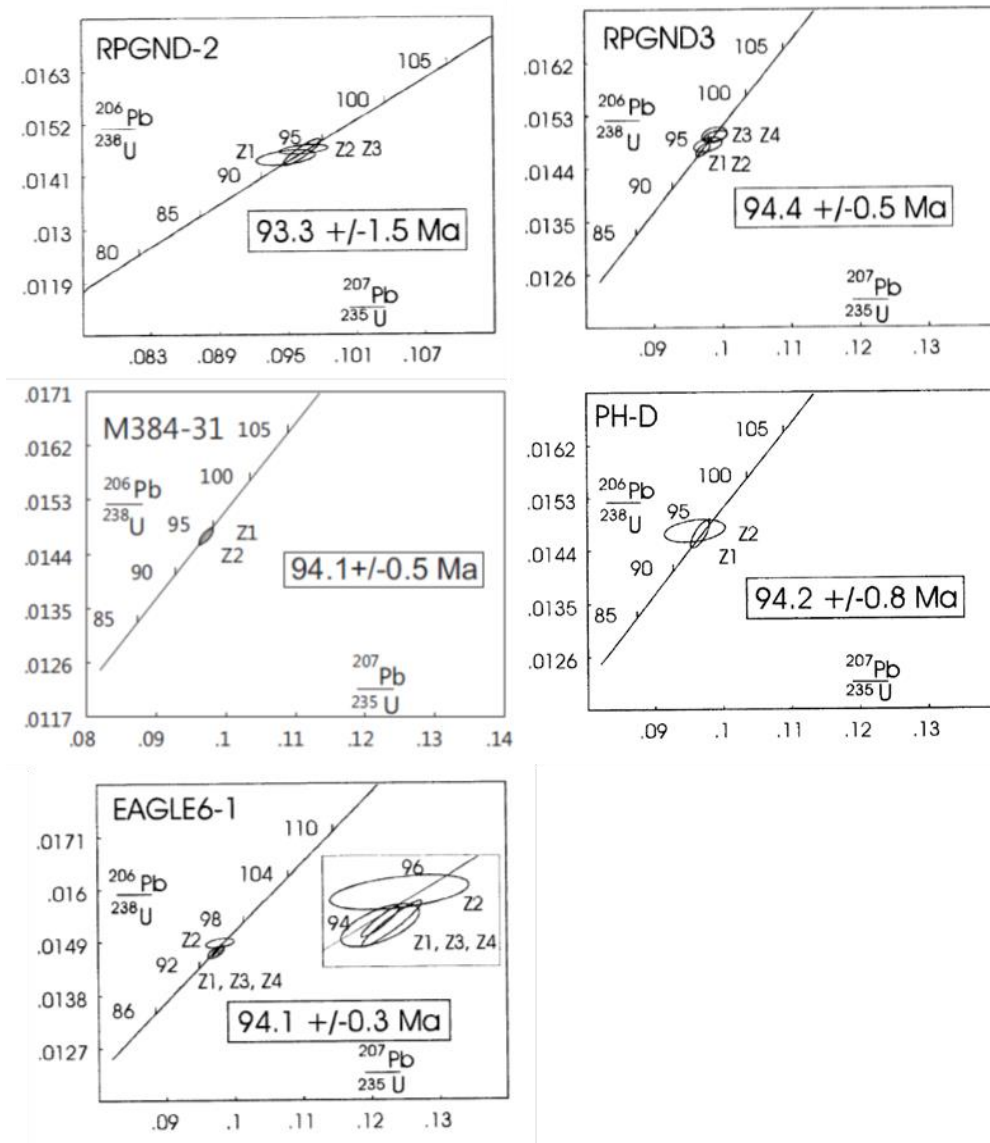


FIGURE 4.4. U-Pb Concordia of zircons for representative sample of each rock type. Ellipsoids (2σ) represent determinations for individual sub-samples of zircon separates (typically 2 to 4 grains). Group 1 = Eagle 6-1; Group 2 = M384-31 (M384929-31), PH-D; Group 3 = RP-GND-2, RP-GND-3.

4.6 Lithochemistry Results

4.6.1 Major Elements

Before discussing the results it is important to point out that we have consciously used terminology to describe their geochemical features that blends that used to describe volcanic and plutonic rocks. The field relations clearly indicate that these rocks are intrusive, but with textures

often like those exhibited in volcanic rocks. We would stress that the terms used are descriptive, and meant only to inform the reader how these rocks compare geochemically to well established norms in the literature.

All data used for comparative purposes in section 4.7 (Hart et al., 2004b; Lindsay, 2006; Mair et al., 2011) are re-calculated on a volatile-free basis and re-calculated to 100%. A compilation of the geochemical data used for these comparisons is available in Appendix H.

Major and trace element data are provided in Table 4.2. The SiO₂ concentration of the samples ranges from 62.4 to 68.1 wt.%. Harker plots for major elements (Fig 4.5) show an increase in Al₂O₃, TiO₂, K₂O, and Na₂O with increasing SiO₂ with some scatter in the data for TiO₂, K₂O, and Na₂O. MgO, FeO_(total), and CaO decrease with increasing SiO₂ with well-defined trends. MnO and P₂O₅ (not shown in Figure 4.5) do not define clear trends. A set of major element classification plots is provided in Figure 4.6. The samples, with one exception, fall in the dacite field in Figure 4.6A (LeMaitre et al., 1989) and all of the rocks are subalkaline on both this plot and that of Irvine and Baragar (1971; Fig 4.6B). The data fall in the calc-alkaline field on the AFM plot (Irvine and Baragar, 1971; Fig 4.6C), and in the high-K calc-alkaline series field of Peccerillo and Taylor (1976; Fig 4.6D). Note that all of the rocks fall in the “magnesian” field on the Fe-number vs. SiO₂ plutonic classification plot of Frost et al. (2001; Fig 4.6E).

A normative classification of each sample, and other pertinent geochemical ratios, are given in Table 4.3. Plutonic samples, Eagle 6-1 and Eagle 6-2, were characterised using the Mesonorm (Kosinowski, 1982), CIPW norm (Clarke et al., 1994), and DeBon and LeFort (1983) classification schemes for granitoids. The rock name stated in Table 4.3, granodiorite or quartz

monzonite, is that summarised from the three methods. The TAS diagram (Le Maitre et al., 1989) was used to classify Group 2 and 3 dyke samples, based on their porphyritic textures (Fig 4.6A). Group 2 and 3 dykes are classified as dacite, except for RP-GND-3 (andesite).

The aluminium saturation index (ASI) of the samples is typically less than 1.1 (Table 4.3) and shows an increase with increasing SiO₂ (Fig 4.6F). Strictly speaking, values of the ASI greater than 1 are considered peraluminous; however, since fractional crystallization of magma can drive the ASI value above this threshold, we considered ASI values ≤ 1.1 as metaluminous. RP-GND-2 has an ASI value of 1.14 (see Fig. 4.6F) and is mildly peraluminous; however, sample PH-D has a value of 1.4, which is distinctly peraluminous. The modified alkali-lime index (Frost et al., 2001) is calcic for Group 1 samples and transitional between calcic and calc-alkalic for Groups 2 and 3 (Fig. 4.6G).

TABLE 4.2. Major and trace element data for samples analysed in this study. Data are reported on a volatile-free basis, recalculated to 100%. Majors in wt.%. Trace elements in ppm. nd = not detected. * : total Fe as FeO. ** : loss on ignition (original raw data).

SAMPLE	DGp-001	DGp-002	DGv-006	DGv-004	DGv-005	DGv-001	DGv-002	DGv-003
Original Group	Eagle 6-1 1	Eagle 6-2 1	M395914 2	IO-016545 2	M384929-31 2	PH-D 2	RP-GND-2 3	RP-GND-3 3
SiO ₂	63.68	65.01	64.73	64.91	68.10	66.92	66.55	62.44
TiO ₂	0.75	0.73	0.77	0.77	0.66	0.80	0.57	0.68
Al ₂ O ₃	15.95	15.64	16.39	16.30	14.84	16.58	16.41	15.62
FeO*	5.28	5.10	5.01	4.87	4.19	4.91	4.18	5.18
MnO	0.12	0.07	0.07	0.07	0.05	0.07	0.08	0.11
MgO	3.20	3.27	2.56	2.58	2.16	2.44	2.24	4.70
CaO	5.24	4.49	4.16	4.15	3.54	2.71	3.32	5.38
Na ₂ O	2.18	1.92	2.42	2.34	2.18	1.91	2.36	2.08
K ₂ O	3.38	3.56	3.69	3.84	4.13	3.47	4.09	3.61
P ₂ O ₅	0.22	0.22	0.21	0.17	0.15	0.19	0.20	0.20
LOI**	1.26	1.34	1.63	1.19	1.07	2.18	3.02	3.59
V	97	99	126	113	93	138	65	94
Cr	72	62	103	91	71	102	52	245
Co	13	11	13	14	13	14	7	20
Ni	nd	nd	41	30	30	61	nd	85
Cu	nd	nd	10	20	41	31	10	21
Pb	14	9	30	29	26	41	32	70
Zn	62	41	124	121	71	123	73	170
Ba	1728	1680	1576	1721	1404	1889	1791	1677
Cs	8.82	13.80	15.90	11.50	13.70	6.64	4.49	7.35
Ga	22	22	21	22	20	19	21	21
Rb	155	188	187	168	205	154	162	136
Sr	587	536	513	502	414	370	581	569
Th	18.6	18.5	15.5	16.4	22.6	16.4	23.3	20.0
U	3.79	3.10	6.00	5.66	4.06	5.11	5.22	5.64
Y	17	18	23	19	14	23	14	16
Zr	169	173	187	209	191	241	184	193
Hf	4.41	4.24	4.76	5.16	4.97	6.03	4.60	4.90
Nb	15	14	16	13	12	17	19	16
Ta	1.13	1.03	0.93	1.11	1.22	0.92	1.15	1.17
La	54.5	55.6	36.9	48.8	47.3	39.4	50.6	57.4
Ce	99.7	101.0	70.8	92.5	89.3	75.4	88.6	104.0
Pr	10.05	10.2	8.11	9.55	9.35	8.84	9.42	10.45
Nd	36.1	36.3	30.0	35.4	35.4	32.0	32.0	39.1
Sm	6.36	6.10	5.79	6.27	6.59	6.33	5.54	6.60
Eu	1.45	1.34	1.38	1.43	1.17	1.42	1.20	1.47

TABLE 4.2. Cont.

SAMPLE	DGp-001	DGp-002	DGv-006	DGv-004	DGv-005	DGv-001	DGv-002	DGv-003
Original	Eagle 6-1	Eagle 6-2	M395914	IO-016545	M384929-31	PH-D	RP-GND-2	RP-GND-3
Group	1	1	2	2	2	2	3	3
Gd	5.13	4.96	5.17	5.26	4.97	5.41	3.76	5.54
Tb	0.72	0.72	0.72	0.71	0.61	0.82	0.52	0.75
Dy	3.79	3.41	4.34	3.94	2.94	4.70	2.72	3.62
Ho	0.72	0.62	0.83	0.81	0.51	0.92	0.52	0.64
Er	1.95	1.76	2.38	2.12	1.42	2.55	1.46	1.81
Tm	0.29	0.25	0.35	0.32	0.20	0.36	0.21	0.26
Yb	1.85	1.65	2.38	2.12	1.32	2.35	1.46	1.70
Lu	0.30	0.28	0.39	0.33	0.20	0.39	0.24	0.29

TABLE 4.3. Geochemical classification based on major element data. See text for discussion. Aluminium Saturation Index (ASI) after Shand (1949). Modified Alkali-Lime Index after Frost et al. (2001), C = Calcic, C-A = Calc-Alkalic.

SAMPLE	DGp-001	DGp-002	DGv-006	DGv-004	DGv-005	DGv-001	DGv-002	DGv-003
Original	Eagle 6-1	Eagle 6-2	M395914	IO-016545	M384929-31	PH-D	RP-GND-2	RP-GND-3
Group	1	1	2	2	2	2	3	3
Rock Type	Granodiorite	Quartz Monzonite	Dacite	Dacite	Dacite	Dacite	Dacite	Andesite
ASI	1.0	1.0	1.1	1.1	1.0	1.4	1.1	0.9
MALI	C	C	C/C-A	C/C-A	C/C-A	C/C-A	C/C-A	C/C-A

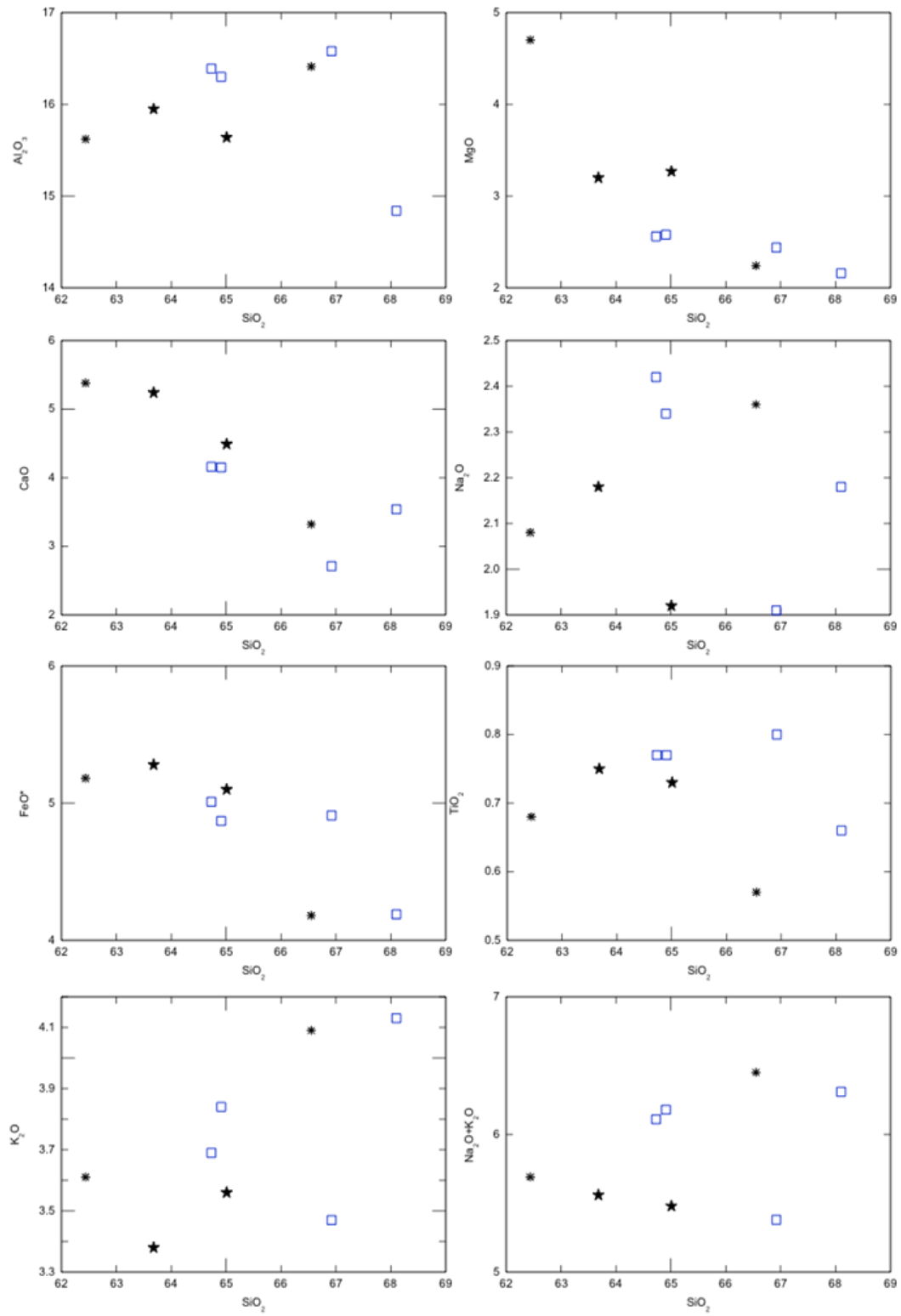


FIGURE 4.5. Harker plots for select major elements at Dublin Gulch. Group 1 = black star; Group 2 = blue square; Group 3 = black asterisk.

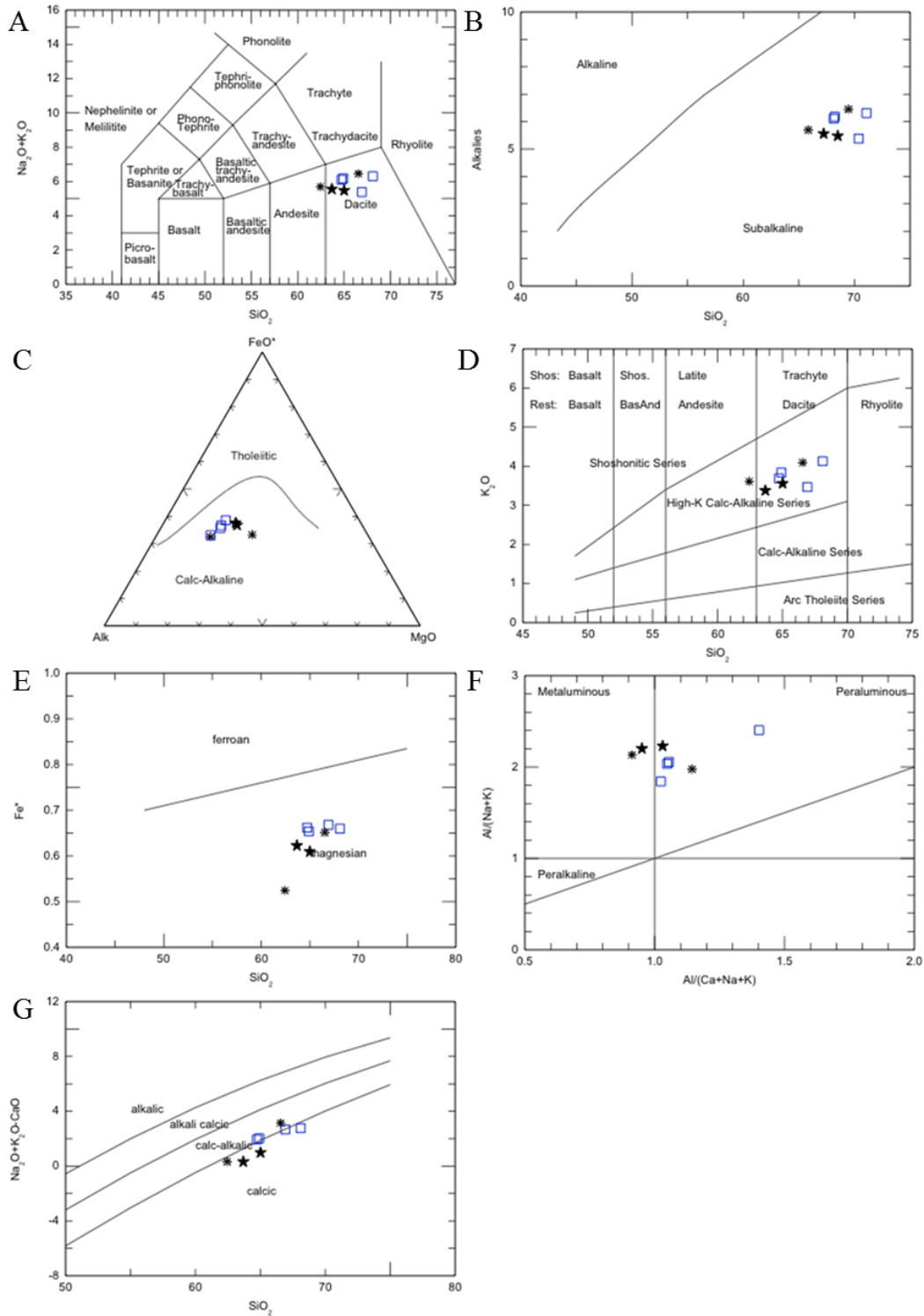


FIGURE 4.6. Major element plots for samples at Dublin Gulch. **A**: TAS plot (Le Maitre et al., 1989), **B**: alkalies vs. SiO_2 plot (Irvine and Baragar, 1971), **C**: AFM plot (Irvine and Baragar, 1971), **D**: K_2O vs. SiO_2 plot (Peccerillo and Taylor, 1976), **E**: Fe-number vs SiO_2 plot (Frost et al., 2001), **F**: ASI plot (Shand, 1949), **G**: Modified alkali-lime index plot (Frost et al., 2001).

4.6.2 Trace Elements

Variations in trace element concentrations are illustrated in plots against SiO₂ in Figure 4.7. V ranges from 65 to 138 ppm and shows no distinct pattern with increasing SiO₂. RP-GND-2 has the lowest value at 65 ppm, the rest of values are clustered between 93 and 138 ppm. Chromium ranges from 52 to 245 ppm, with the majority of samples in the range 52 to 103 ppm and a single outlier, RP-GND-3, at 245 ppm. Cobalt, Ni, Pb, and Zn mirror this pattern with ranges of 7 to 14 ppm, below detection to 61 ppm, 9 to 41 ppm, and 41 to 124 ppm, except for more enriched values for RP-GND-3 (Co: 20 ppm, Ni: 85 ppm, Pb: 70 ppm, and Zn: 170 ppm). Interestingly, RP-GND-2, also sampled from the Peso Zone, is relatively depleted (or below detection) for these elements.

We also examined variations in low field strength elements (LFSE; ionic radius/charge of >0.21) and high field strength elements (HFSE; ionic radius/charge <0.2) (excluding Y, which is conventionally included with the REE (see Saunders et al., 1980)). For the LFSE, Rb (136 to 205 ppm), Cs (4.49 to 15.9 ppm), and Ba (1404 to 1889 ppm) show incompatible behaviour, while Sr (370 to 587 ppm), Ga (19 to 22 ppm), Th (15.5 to 23.3 ppm), and U (3.1 to 6.0 ppm) show compatible behaviour. HFSE exhibit considerable scatter when plotted against SiO₂. HFSE have ranges of Y (14 to 23 ppm), Zr (169 to 241 ppm), Hf (4.24 to 6.03 ppm), Nb (12 to 19 ppm), and Ta (0.92 to 1.22 ppm).

REE and extended REE plots are shown in Figure 4.8 - with normalizations to chondrite, primitive mantle and upper crust (see also Table 4.4). All of the samples are characterized by light REE enrichment, with chondrite-normalized (n) (Sun and McDonough, 1989), (La/Sm)_n and (La/Yb)_n ratios ranging from 3.8 to 5.6 and 11.2 to 24, respectively. Chondrite-normalized

plots (Fig 4.8A) illustrate the overall pattern of LREE enrichment, slight to moderate negative Eu anomalies and a slight concave-up middle to heavy REE. While the REE patterns are enriched in the LREE, the middle and heavy REE have $(\text{Gd/Yb})_n$ values of ~ 2.2 – and chondrite-normalized abundances around 10 - and consequently we would not characterize these as HREE depleted. Group 1 and Group 3 (DGS and Peso) have almost identical REE patterns and abundances (means for both are: $(\text{La/Sm})_n = 5.5$; $(\text{La/Yb})_n = 22$). Group 2 is more variable, with $(\text{La/Sm})_n$ ranging from 3.8 to 4.8, $(\text{La/Yb})_n$ from 10.2 to 24, overall LREE abundances less than those of Groups 1 and 3, and HREE are higher. These differences lead to the REE patterns for Group 2 cutting across those of Groups 1 and 3.

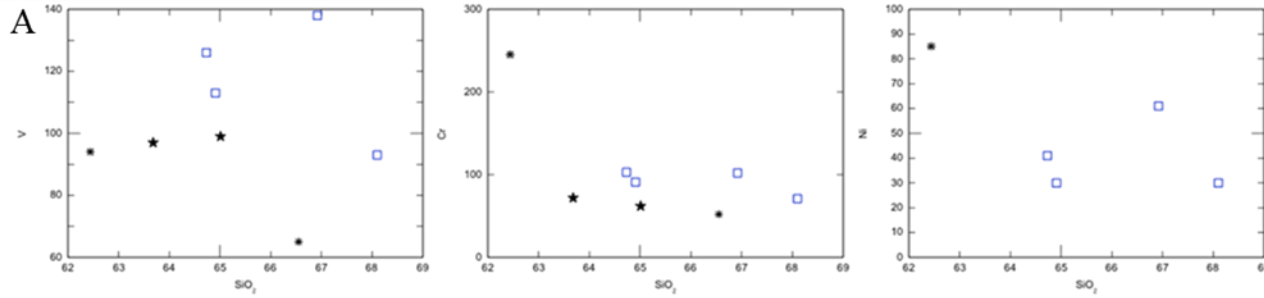
The primitive mantle-normalised plots (Fig 4.8B), incorporating LFSE, HFSE, and REE are characterized by well-developed negative Nb, Ta, P, and Ti anomalies and a strong positive Pb anomaly. Caesium is highly enriched relative to primitive mantle (PM), with normalized abundances of 500X to 2000X PM. The other LFSE, excluding Sr, generally have abundances 100X to 300X PM.

Normalized to upper crust (UC) (Fig 4.8C), the samples show a generally flat trend, with normalized abundances lying between 0.7X and 1.5X UC. A number of anomalies exist in the trend; positive Ba, Co, and Ni anomalies and negative Ta, Nb, Zr, and Hf anomalies. A mixed anomaly exists for Pb, which is strongly negative for Group 1 and positive for Groups 2 and 3.

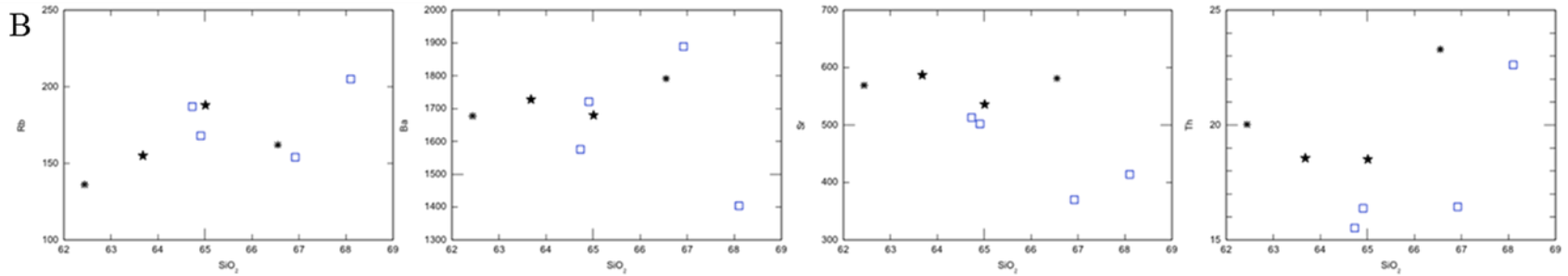
All of the samples plot within the same fields on common trace element tectonic discrimination diagrams (Fig 4.9). All samples lie within the “volcanic arc granite” field on the Rb vs. Y+Nb plot (Pearce et al., 1984) and the “volcanic arc granite and syn-collisional granite”

field on the Nb vs. Y plot (Pearce et al., 1984). Additionally, all samples fall within the “I and S type granite” field on the Zr vs. 10^4Ga/Al plot (Whalen et al., 1987).

Transition metals



LFSE



HFSE

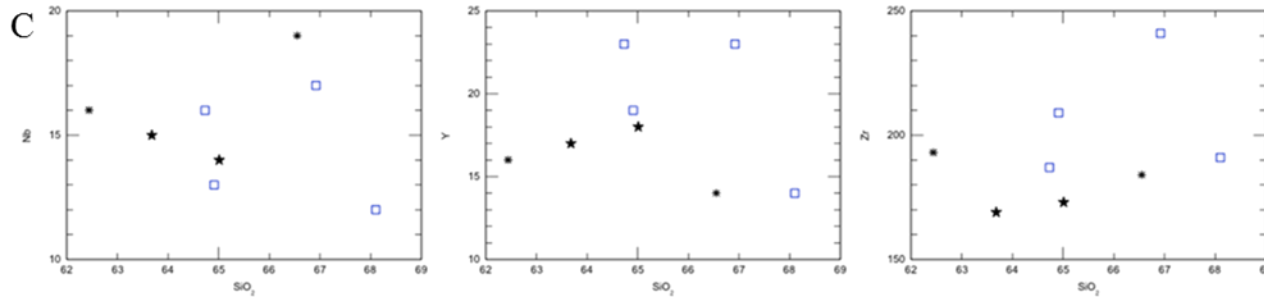


FIGURE 4.7. Trace element (ppm) vs. SiO₂ (wt.%) plots for samples at Dublin Gulch. Representative elements are shown for **A**: transition metals (V, Cr, Ni), **B**: LFSE (Rb, Ba, Sr, Th), **C**: HFSE (Nb, Y, Zr). See text for discussion. Group 1 = black star Group 2 = blue square, group 3 = black asterisk.

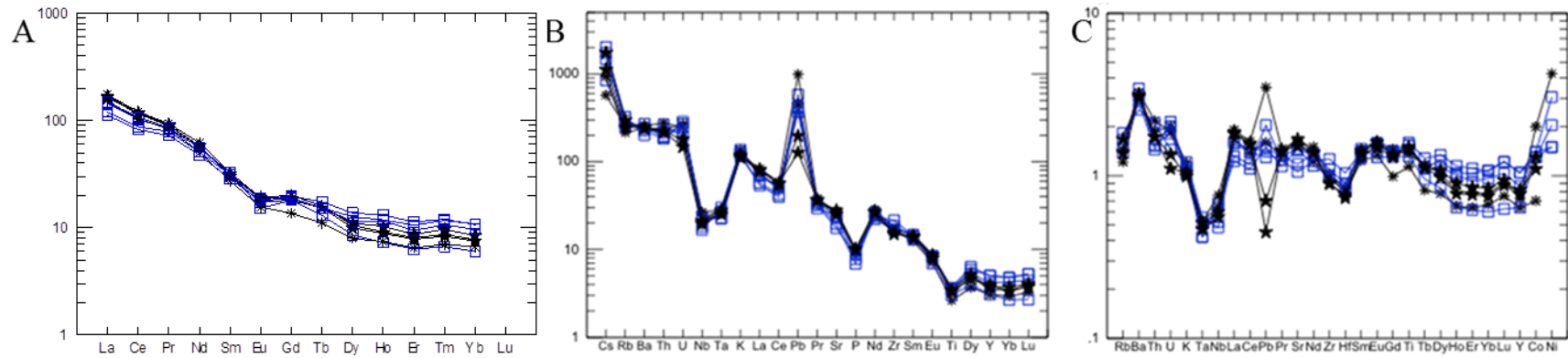


FIGURE 4.8. REE and extended REE plots for samples at Dublin Gulch. Data are normalized to **A**: chondrite (Sun and McDonough, 1989), **B**: primitive mantle (Sun and McDonough, 1989), **C**: upper crust (Rudnick and Fountain, 1995; Taylor and McLennan, 1985).

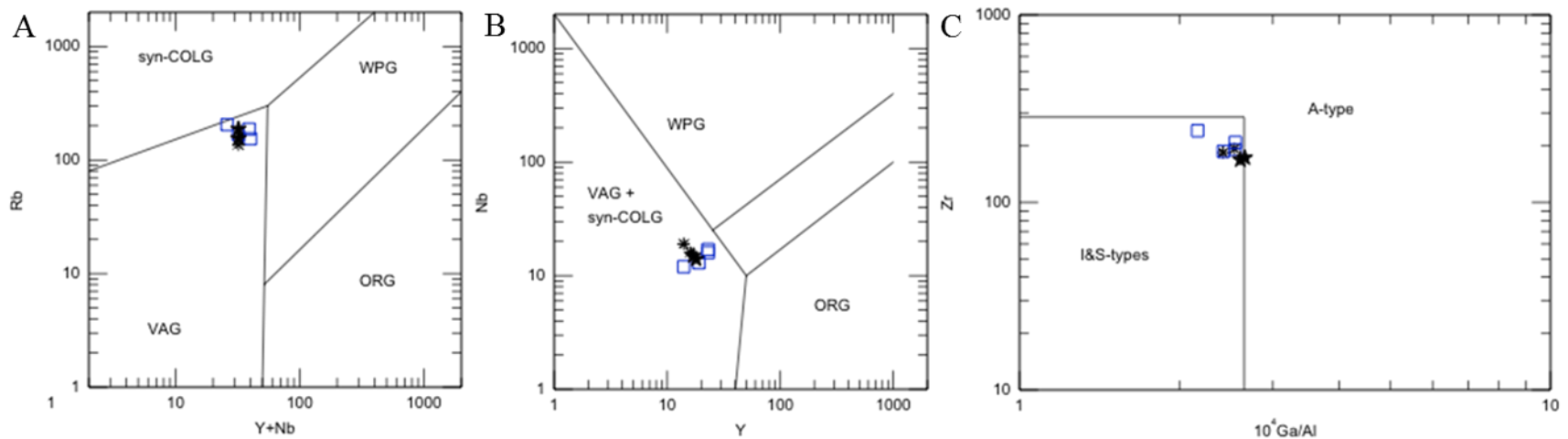


FIGURE 4.9. Tectonic discrimination plots for samples at Dublin Gulch. **A**: Rb (ppm) vs. Y+Nb (ppm) plot (Pearce et al., 1984), **B**: Nb (ppm) vs. Y (ppm) plot (Pearce et al., 1984), **C**: Zr (ppm) vs. 10^4 Ga/Al plot (Whalen et al., 1987). Syn-COLG: syn-collisional granite, VAG: volcanic arc granite, ORG: orogenic granite, WPG: within-plate granite.

4.6.3 Nd and Sr Isotopes

$^{143}\text{Nd}/^{144}\text{Nd}_{(i)}$ ranges from 0.511902 to 0.512041 (-14.4 to -11.6 $\epsilon\text{Nd}_{(i)}$), and $^{87}\text{Sr}/^{86}\text{Sr}_{(i)}$ from 0.71362 to 0.71726 (Table 4.4). The main phase DGS has $^{143}\text{Nd}/^{144}\text{Nd}_{(i)}$ of 0.511902 (-14.4 $\epsilon\text{Nd}_{(i)}$) and $^{87}\text{Sr}/^{86}\text{Sr}_{(i)}$ of 0.71661. Group 2 dykes, which cross-cut the pluton, have $^{143}\text{Nd}/^{144}\text{Nd}_{(i)}$ of 0.512029 to 0.512041 (-11.9 to -11.6 $\epsilon\text{Nd}_{(i)}$) and $^{87}\text{Sr}/^{86}\text{Sr}_{(i)}$ of 0.71362 to 0.71513. Group 3 Dykes have $^{143}\text{Nd}/^{144}\text{Nd}_{(i)}$ of 0.511962 to 0.511994 (-13.2 to -12.6 $\epsilon\text{Nd}_{(i)}$) and $^{87}\text{Sr}/^{86}\text{Sr}_{(i)}$ of 0.71525 to 0.71726. Each of the three sample groups occupies a distinct area of the $^{87}\text{Sr}/^{86}\text{Sr}_{(i)}$ vs. $\epsilon\text{Nd}_{(i)}$ plot (Fig 4.10). Group 1 has the most radiogenic Nd and Sr isotopic compositions and Group 2 are the least radiogenic, while Group 3 are intermediate in value. All three groups trend between bulk earth and published Nd and Sr isotope values for the Hyland Group (Kuran et al. 1982; Garzzone et al., 1997) (see Fig 4.20).

Neodymium ages, using the bulk earth (e.g., De Paolo and Wasserburg, 1976) and depleted mantle (T_{DM}) models (e.g., De Paolo, 1981), range from 1.25/1.39 Ga (bulk earth/depleted mantle (T_{DM})) to 1.49/1.64 (Table 4.4). The oldest model age comes from the DGS granodiorite. Group 3 samples give model ages of 1.45/1.60 Ga and 1.36/1.51 Ga. Group 2 samples give the youngest model ages, 1.44/1.61 Ga and 1.25/1.39 Ga.

TABLE 4.4. Sr and Nd isotope data and REE ratios for samples at Dublin Gulch.

SAMPLE	DGp-001	DGv-005	DGv-001	DGv-002	DGv-003
Original Group	Eagle 6-1 1	M384929-31 2	PH-D 2	RP-GND-2 3	RP-GND-3 3
Rb (ppm)	151	202	151	155	128
Sr (ppm)	573	408	362	556	534
⁸⁷ Rb/ ⁸⁶ Sr	0.76158	1.4308	1.2055	0.80567	0.69273
⁸⁷ Sr/ ⁸⁶ Sr (m)	0.717639	0.715549	0.716757	0.716325	0.718193
2σ	10	10	9	10	10
⁸⁷ Sr/ ⁸⁶ Sr (i)	0.71661	0.71362	0.71513	0.71525	0.71726
Nd (ppm)	31.9	35.8	30.2	25.5	31.8
Sm (ppm)	5.48	5.73	5.76	4.51	5.45
¹⁴⁷ Sm/ ¹⁴³ Nd	0.1035	0.09649	0.1149	0.1065	0.1031
¹⁴⁴ Nd/ ¹⁴³ Nd (m)	0.511966	0.512088	0.512112	0.512027	0.512058
2σ	7	6	6	8	7
¹⁴⁴ Nd/ ¹⁴³ Nd (i)	0.511902	0.512029	0.512041	0.511962	0.511994
εNd (m)	-13.1	-10.7	-10.3	-11.9	-11.3
εNd (i)	-14.4	-11.9	-11.6	-13.2	-12.6
T De Paolo	1491	1245	1440	1446	1361
TDM2	1641	1385	1608	1601	1509
(La/Sm)n	5.3	4.4	3.8	5.6	5.4
(La/Yb)n	19.7	24.0	11.2	23.2	22.6
(Gd/Yb)n	2.2	3.0	1.8	2.1	2.6

Initial isotopic ratios calculated using U-Pb ages reported above. A conversion factor of 2.89 (Faure and Mensing, 2005) was applied to the Rb/Sr ratio to produce the ⁸⁷Rb/⁸⁶Sr value. ⁸⁷Sr/⁸⁶Sr corrected from the deviation from NBS 987 (Accepted value=0.710240). ⁸⁷Rb/⁸⁷Sr decay constant = 1.43*10⁻¹¹ y⁻¹. A conversion factor of 0.602 (Faure and Mensing, 2005) was applied to the Sm/Nd ratio to produce the ¹⁴⁷Sm/¹⁴³Nd value. ¹⁴³Nd/¹⁴⁴Nd corrected from the deviation from JNdi-1 (Accepted value 0.512115). εNd calculated using present day bulk earth value of 0.512638. ¹⁴⁷Sm/¹⁴³Nd decay constant = 6.54 * 10⁻¹² y⁻¹. REE ratios normalised to chondritic values after Sun and McDonough (1989).

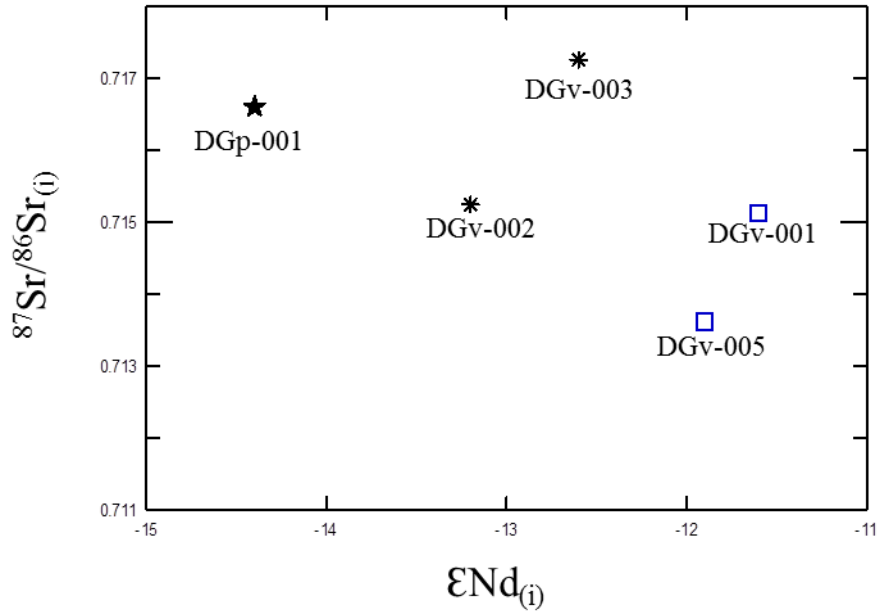


FIGURE 4.10. $^{87}Sr/^{86}Sr_{(i)}$ vs. $\epsilon Nd_{(i)}$ for 5 samples at Dublin Gulch. Group 1 = black star, group 2 = blue square, group 3 = black asterisk.

4.6.4 Summary

Three groups of rocks were initially identified at Dublin Gulch, based on field relations. U-Pb geochronology shows that these rocks can be considered as part of the same igneous event, c. 94 Ma. Normative classification of the rock types shows that Group 1 comprises granodiorite to quartz monzonite. Groups 2 and 3 are classified using the TAS diagram as dominantly dacite, with a single example of andesite (RP-GND-3). The MALI classification splits Group 1, which is calcic, from Groups 2 and 3, which are transitional between calcic to calc-alkalic. All of the rocks analysed are subalkaline, calc-alkaline, high-K, and magnesian on the associated classification plots. SiO₂ ranges between 62.4 and 68.1 wt.%. Major elements show distinct trends vs. SiO₂ that are consistent with fractional crystallisation. Trace elements that commonly substitute into major mineral phases also support this hypothesis. Strontium, which is commonly incorporated into plagioclase, decreases with increasing SiO₂, mimicking the pattern of CaO. Rubidium, commonly incorporated into potassium feldspar, increases with increasing SiO₂, mimicking the pattern of K₂O. There is an increase in the ASI with SiO₂ that is also indicative of fractional crystallisation (Zen, 1988).

Trace element geochemistry of the samples is transitional between I-type and shoshonitic when compared to representative examples from literature (Whalen et al., 1987; Jiang et al., 2002; Table 4.5). Barium and Zr are strongly enriched in the samples compared and have a strong similarity to shoshonitic series rocks. Strontium, Th, and Ce are transitional between I-type and shoshonitic compositions, while Rb does not show any distinct enrichment.

TABLE 4.5. Comparison of selected trace elements at Dublin Gulch to examples of I-type (Whalen et al., 1987) and Shoshonitic (Jiang et al., 2002) series rocks.

SAMPLE	Group 1 (mean)	Group 2 (mean)	Group 3 (mean)	I-type	Shoshonite-1	Shoshonite-2
Ba	1704	1648	1734	538	2756	1881
Rb	172	179	149	151	234	197
Sr	562	450	575	247	1020	635
Th	18.6	17.7	21.7	18	53.4	22
Zr	171	207	189	151	257	162
Ce	100	82	96	66	145	198

The ASI of the rocks is dominantly metaluminous, with a single example of a nominally strongly peraluminous sample (PH-D). However, PH-D does not contain muscovite, cordierite or almandine garnet; minerals required for a ‘true’ peraluminous rock (Zen, 1988). Zen (1988) states that rocks, which have a modal abundance of 1:3 or less of hornblende to biotite can display peraluminous compositions, since biotite has an ASI of 1.3 to 1.4, when co-existing with hornblende. This is supported by petrography of PH-D, which showed a modal abundance of hornblende to biotite of approximately 1:4. PH-D has the lowest $(La/Sm)_n$ and $(La/Yb)_n$ and the highest ϵNd value (-10.3) of the Group 2 samples. However, its overall major and trace element chemistry is consistent with that of Group 2, especially samples DGv-004 and DGv-006. While there is no doubt it is peraluminous, we do not feel that this characteristic is particularly indicative of a markedly different petrogenesis for this sample relative to other Group 2 samples, or for that matter Group 1 and 3 samples.

REE and extended REE plots for the samples are largely uniform, displaying similar anomalies for chondrite, primitive mantle, and upper crust normalisation. Tectonic discrimination diagrams show an I-type, volcanic arc granite signature for all samples. Negative anomalies for Eu, Ti, and P are consistent with plagioclase fractionation and the crystallisation of the accessory phases titanite and apatite. Negative anomalies for Nb and Ta are consistent with melt derivation in a subduction zone environment, from mantle affected by previous subduction

or by derivation or significant contamination from continental crust. However, note that the negative Nb-Ta anomaly is more strongly developed in these rocks than that characteristic of upper continental crust.

However, the pattern of highly incompatible element ratios, and variation in Nd and Sr isotope values, are not consistent with fractional crystallisation as the only process involved in generating the chemical differences between the samples. Highly incompatible elements ratios should remain constant during fractional crystallisation or partial melting. Primitive mantle normalized (Th/Nb) ratios are about 10 for all samples, consistent with fractional crystallization. However, primitive mantle-normalized (Nb/La) ratios are much more variable (0.2 to 0.4), and indicate the rocks cannot be considered purely co-genetic. The variability in the REE patterns in Group 2, and the differences in REE between this group and Groups 1 and 3, are also indicators of more complex processes taking place. It should be noted, however, that given the SiO₂ levels and relatively evolved nature of the samples, accessory mineral crystallisation may be responsible for some of the difference in the normally highly incompatible element ratios. However, variation in Nd and Sr isotopes for each of the three sample groups is most plausibly explained by source heterogeneity or, possibly, mixing between sources. Therefore, the geochemical signatures of the rocks in the sample set reflect, at a minimum, both source heterogeneity and fractional crystallisation. We did evaluate the potential for mixing to have played a role in the formation of the geochemical signatures in these rocks. However, if mixing has occurred its impacts have been obscured. We conclude this because on element-element plots there are no simple mixing (straight) lines, and on element-ratio or ratio-ratio plots the reciprocal test for mixing does not yield a straight line (Langmuir et al., 1978)

4.7 Comparison with other IRGS

The geochemical signatures of the Dublin Gulch lithologies were compared to published data for Scheelite Dome and Brewery Creek (Fig. 4.11) in order to assess any similarities between the parental intrusions for these significant IRGS. All three deposits share an intrusive history in which early, more voluminous phases gave way to less extensive phases and dykes (Mair et al., 2011 – Scheelite Dome; Lindsay, 2006 – Brewery Creek; this study – Dublin Gulch). Gold appears strongly associated with later stages within these plutonic histories, and so it is also of interest to establish if a definable geochemical difference exists between early and late igneous phases. Understanding of these signatures has obvious potential to improve regional geochemical exploration strategies for IRGS.

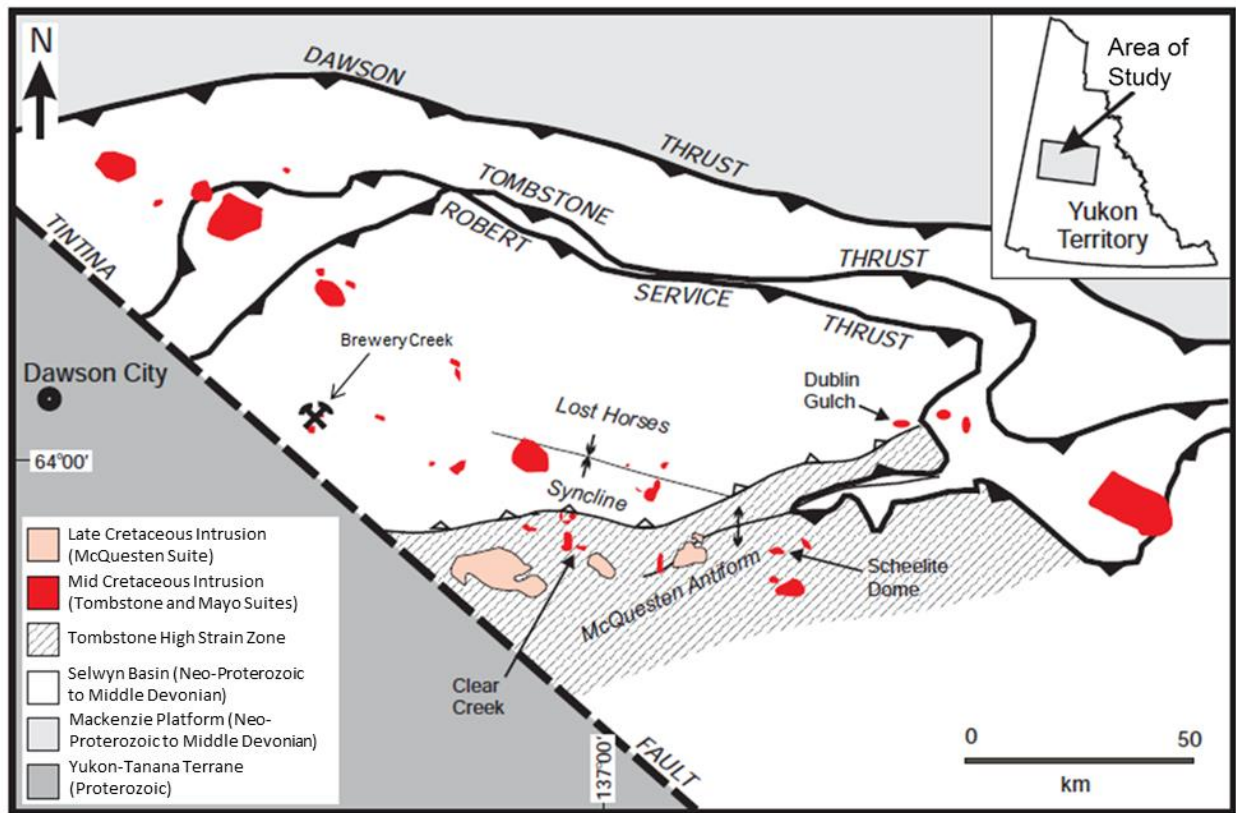


FIGURE 4.11. Map showing plutonism within the central Yukon Territory. The Brewery Creek, Dublin Gulch, and Scheelite Dome IRGS, compared below, are shown with an arrow. The Clear Creek IRGS is shown for reference but is not discussed in the text. Modified after Lindsay (2006).

4.7.1 Geological Setting

Scheelite Dome: Scheelite Dome is hosted by the Neoproterozoic Hyland Group and features two main intrusions: the 4 x 1.5 km Scheelite Dome Stock (east-west trending); and 3 x 1 km Morrison Creek Stock (north-northwest trending) (Fig. 4.12; Murphy 1997; Mair et al., 2000, 2003, 2006a, b, 2011; O’Dea et al., 2000; Stephens et al., 2004). The Morrison Creek Stock is composed of monzogranite, while the Scheelite Dome Stock features monzogranite crosscut by a series of 1-5 m wide quartz monzonite, quartz monzodiorite, and leucominette dykes. Local sedimentary rocks are intruded by dykes of granodiorite porphyry and lamprophyre (minette and spessartite) that intruded in alignment with regional metamorphic fabrics. Published U-Pb (zircon) ages for the Scheelite Dome Stock are 94.6 ± 0.9 Ma and 94.3 ± 0.95 Ma for the main monzogranite and quartz monzonite dykes, respectively (Mair et al. 2006b, 2011). Au at Scheelite Dome was shown by Mair et al. (2006a) to be strongly associated with the quartz monzonite, quartz monzodiorite and granodiorite porphyry rock types.

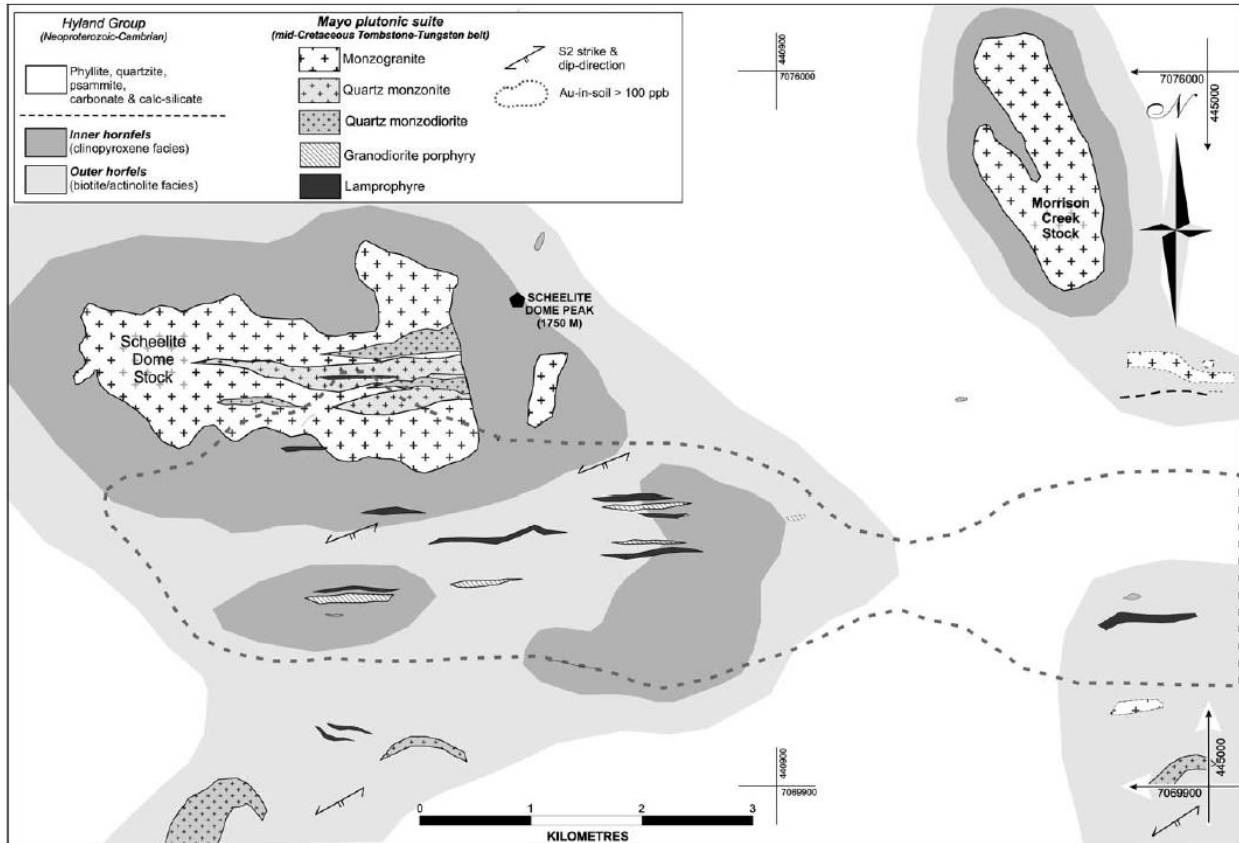


FIGURE 4.12. Geological map of the Scheelite Dome igneous complex. Taken from Mair et al. (2011).

Brewery Creek: The Brewery Creek deposit is hosted within the Siluro-Devonian Earn Group (Fig 4.13). A 12 km long trend of northwest and east-trending biotite±quartz monzonite dykes, ranging from 1 m to 1 km in width, forms the most prospective area for gold mineralization and is termed the Reserve Trend. Volumetrically restricted dykes, up to 1 m in width, composed of hornblende gabbro were present in diamond drill core from the Reserve Trend and within the Golden Pit (Fig 4.13). In the southern-most area of the property syenite is the most common intrusive rock type; exposed in the 4 km x 2 km Classic Zone that is bisected by the Classic Fault. Ages for the intrusive history of the area, from unspecified rock types, are c. 90-92 Ma (Lang, 2000) and 91.4 Ma (unpublished, GSC). A more detailed petrographic description of each rock type at Brewery Creek is available in Lindsay (2006). The Reserve Trend contains

80% of gold recognized on the property and is hosted by biotite-monzonite and quartz-biotite monzonite sills (Lindsay, 2006).

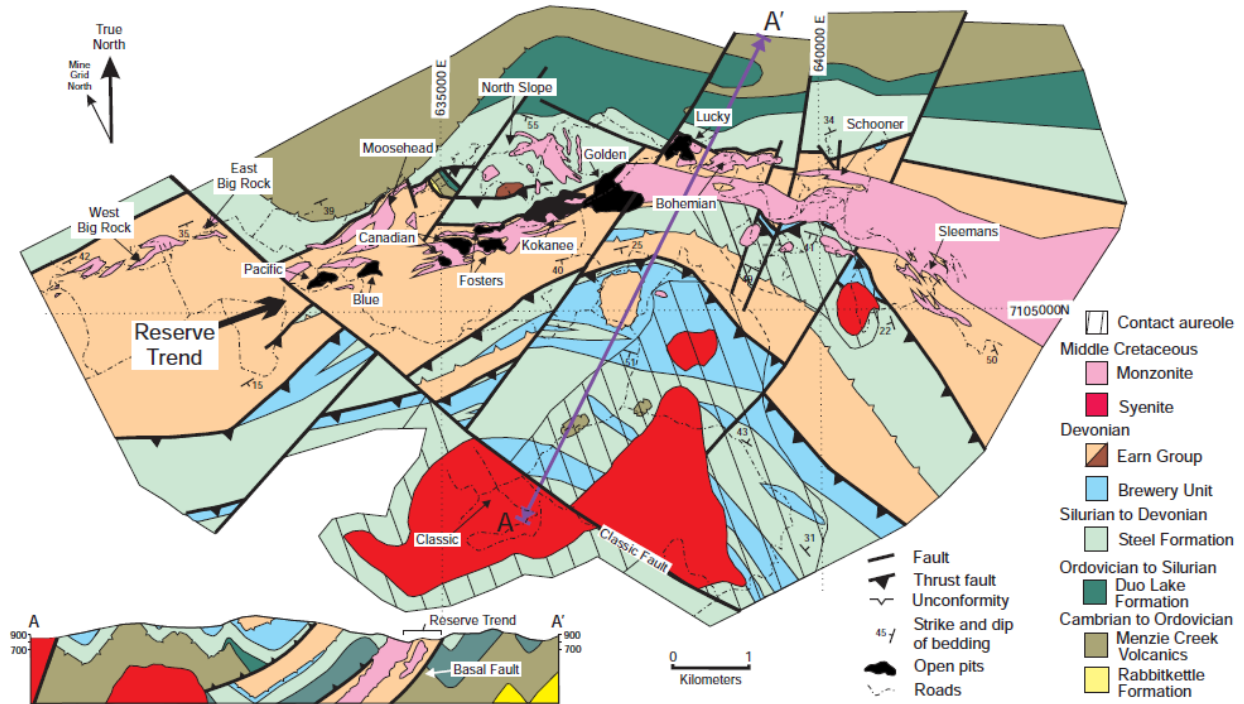


FIGURE 4.13. Summary geologic map of the Brewery Creek area. Taken from Lindsay (2006).

4.7.2 Major Elements

Major element data for the igneous rocks at Brewery Creek, Dublin Gulch, and Scheelite Dome is illustrated in a series of Harker diagrams in Figure 4.15. At Brewery Creek, SiO_2 ranges from 54 to 68 wt.%, excluding one sample at 47 wt.%, and at Scheelite Dome it ranges from 57 to 70 wt.%. SiO_2 ranges from 60 to 71 wt.% at Dublin Gulch, and represents the most evolved end of the compositional spectrum in these three IRGS, while Brewery Creek represents the least evolved. The mean SiO_2 for all three locations combined is 63.0 ± 4.7 wt.%. Titania contents in the rock suites from the 3 localities essentially overlap, with a mean of 0.71 ± 0.27 wt.%. The

more mafic samples at Scheelite Dome and Brewery Creek have higher titania, although these appear to be part of the same overall trend of decreasing TiO_2 with increasing SiO_2 ; excluding one Brewery Creek sample with ~ 2 wt.% TiO_2 . For the three deposits as a whole, Al_2O_3 ranges from 12 to 17 wt.%, with a mean of 15.1 ± 1.1 wt.%. While there is an overall trend of increasing alumina with increasing silica in the combined data set, there is also considerable scatter. Dublin Gulch is characterized by the highest Al_2O_3 contents, i.e., those between 16 and 17 wt.%. There is a well-developed negative correlation ($r = 0.90$) between FeO and SiO_2 , as illustrated in Figure 4.15. All three rock suites show considerable overlap, although as expected, those samples with lower silica from Brewery Creek and Scheelite Dome extend the range of iron contents beyond that recorded at Dublin Gulch. The mean FeO (total Fe as FeO) is 5.2 ± 1.9 wt.%. MgO also shows a negative correlation with increasing SiO_2 , and considerable overlap between the data sets from the three IRGS. The mean MgO is 3.6 ± 2.0 wt.%. All three deposits show a decrease in CaO with increasing SiO_2 , with a mean of 5.4 ± 1.8 wt.%. P_2O_5 shows a distinct trend of values that decrease with increasing SiO_2 for Brewery Creek and Scheelite Dome, with a mean of 0.31 ± 0.17 wt.%. For Dublin Gulch samples, however, P_2O_5 displays a flat trend with increasing SiO_2 and has a mean of 0.17 ± 0.04 wt.%. Na_2O has a mean value of 2.20 ± 0.45 wt.% and shows a trend of increasing values with increasing SiO_2 , but it should be noted that considerable scatter exists for these trends. K_2O exhibits different patterns for each of the three deposits; Dublin Gulch shows an increase in K_2O with increasing SiO_2 , Brewery Creek shows a decrease in K_2O with increasing SiO_2 . Scheelite Dome, however, has scattered values which could be ascribed to trends for either of the aforementioned deposits. The mean K_2O is 4.7 ± 1.7 wt.%.

Modified Alkali-Lime Index: The results of applying the classification method of Frost and Frost (2008) to all three localities is illustrated in Figure 4.14. Table 4.6 summarises the MALI groupings of rock types at Brewery Creek, Dublin Gulch and Scheelite Dome. At Dublin Gulch the samples primarily fall in the calcic and calc-alkalic fields, with one sample (a pegmatite) falling in the alkalic field. The composition of Scheelite Dome samples ranges across three of the fields - calcic, calc-alkalic, and alkali-calcic. For Brewery Creek the samples fall in the alkalic, alkali-calcic and calc-alkalic fields. In general, one would expect co-genetic rocks to fall within a single field, i.e., with an evolutionary trajectory that remained within the boundaries of a field with increasing fractionation (Frost and Frost, 2008). Taken as a whole, it is evident that the petrogenesis and evolution at each of the localities suggests at least two parent magmas evolving independently.

Table 4.7 shows average values for major and trace elements for each alkalinity grouping. The average values of trace elements for the calc-alkalic, alkali-calcic, and alkalic groupings are calculated to include the limited available data for Brewery Creek.

Calcic Group: The calcic group is composed of samples from the DGS at Dublin Gulch, as well as a mixture of andesite and dacite from Groups 2 and 3. Granodiorite, monzogranite, and spessartite lamprophyres from Scheelite Dome are also included in this grouping. All of the samples in the calcic group are subalkaline on the alkalis vs. silica plot (Irvine and Baragar, 1971; Fig 4.16C) and magnesian on the Fe-number vs. silica plot (Frost et al., 2001; Fig 4.16B). The calcic group samples follow the calc-alkaline trend on the AFM plot of (Irvine and Baragar, 1971; Fig 4.16D) and are dominantly metaluminous on the ASI plot (Shand, 1949; Fig 4.16A). Sample PH-D from Dublin Gulch is the only peraluminous sample (see above for discussion). Two groupings of samples are present on the ASI plot - the majority of samples fall within the

range 0.9 to 1.1, with a group of three samples around 0.6 to 0.7 representing spessartite lamprophyres. The samples all plot within the andesite and dacite fields on the TAS plot (Le Maitre et al., 1989; Fig 4.16E) and follow the high-K calc-alkaline series on the K_2O vs. SiO_2 plot (Peccerillo and Taylor, 1976; Fig 4.16F).

Calc-Alkalic Group: The calc-alkalic group is the only grouping that contains multiple samples from all three IRGS deposits. A single sample of the main plutonic phase at Dublin Gulch from the study of Hart et al. (2004b), and a series of andesite and dacite dykes from this study and that of Hart et al. (2004b), form the calc-alkalic grouping. A single example of a quartz monzodiorite and four samples of minette lamprophyre from Scheelite Dome fall within the calc-alkalic grouping. Two quartz biotite monzonite samples, one biotite monzonite sample and a hornblende gabbro dyke sample from Brewery Creek are also present within the group. All samples are subalkaline on the alkalis vs. silica plot (Irvine and Baragar, 1971; Fig 4.16C), two samples of minette lamprophyre from Scheelite Dome and a sample of hornblende gabbro from Brewery Creek lie on the boundary between the subalkaline and alkaline fields. Using volcanic nomenclature (TAS plot, Le Maitre et al., 1989; Fig 4.16E) calc-alkalic samples are transitional between the andesite and dacite fields (subalkaline) and the trachyandesite field (alkaline). The majority of the samples lie within the andesite and dacite fields, with a number of samples positioned on the upper margin of the fields. Samples SDv-003, SDv-007, and DGd-001 plot within the trachyandesite field, while sample BC-001 plots within the basalt field. The disparity between the classification for plutonic (alkalis vs. silica plot, Irvine and Baragar, 1971; Fig 4.16C) and volcanic (TAS plot, Le Maitre et al., 1989; Fig 4.16E) nomenclature schemes will be addressed by adopting the alkaline – subalkaline classification of Irvine and Baragar (1971), as it is more closely aligned with the patterns displayed by the MALI. The majority of samples follow

a calc-alkaline trend on the AFM plot (Irvine and Baragar, 1971; Fig 4.16D), with a single sample of hornblende gabbro from Brewery Creek plotting within the tholeiitic field. On the ASI plot (Shand, 1949; Fig 4.16A) two groupings are apparent for calc-alkalic samples, a group between 0.7 and 0.8 comprised of minette lamprophyres and quartz monzodiorite from Scheelite Dome, and two trachyandesite dykes from Dublin Gulch. This second grouping on the ASI plot lies between 0.9 and 1.1 and is comprised of Brewery Creek samples, andesite to dacite dykes from this study, and the main phase stock of Hart et al. (2004b) from Dublin Gulch. All of the calc-alkalic samples plot within the magnesian field on the Fe-number vs. silica plot (Frost et al., 2001; Fig 4.16B) and are transitional between high-K calc-alkaline and shoshonitic series on K₂O vs. SiO₂ plot (Peccerillo and Taylor, 1976; Fig 4.16F).

Alkali-Calcic Group: The alkali-calcic group is dominated by samples from Brewery Creek and Scheelite Dome. Rock types include biotite monzonite and quartz biotite monzonite from Brewery Creek and quartz monzonite, quartz monzodiorite and a granodiorite porphyry dyke from Scheelite Dome. On the alkalis vs. silica plot (Irvine and Baragar, 1971; Fig 4.16C) there is a transition from the alkaline field for lower SiO₂ to the subalkaline field with increasing SiO₂. All of the alkali-calcic samples are alkaline on the TAS plot (Le Maitre et al., 1989; Fig 4.16E). Again there is disparity in the classification of the alkalinity of samples based on the use of plutonic and volcanic nomenclature. All of the samples in this group that are subalkaline on the alkalis vs. silica plot define a calc-alkaline trend on the AFM plot (Irvine and Baragar, 1971; Fig 4.16D); alkaline samples are not plotted, as this plot requires samples to be subalkaline. On the ASI plot (Shand, 1949; Fig 4.16A) all of the samples are metaluminous, with the majority of samples in the range 0.6 to 0.9 and a single sample around 1.1 (BC-003; quartz biotite monzonite). All of the alkali-calcic samples plot within the magnesian field on the Fe-number

vs. silica plot (Frost et al., 2001; Fig 4.16B). Alkali-calcic samples typically plot within the shoshonite series on K_2O vs SiO_2 plot (Peccerillo and Taylor, 1976; Fig 4.16F), with a single sample in the high-K calc-alkaline field (BC-003; quartz-biotite monzonite).

Alkalic Group: A single example of syenite from Brewery Creek and a pegmatite from Dublin Gulch form the alkalic group. This group is alkaline on both the TAS plot (Le Maitre et al., 1989; Fig 4.16E), plotting in the trachyte field, and on the alkalis vs. silica plot (Irvine and Baragar, 1971; Fig 4.16C). Both samples are metaluminous (0.8) on the ASI plot (Shand, 1949; Fig 4.16A). BC-001 (syenite) plots within the ferroan field, while DGpeg-001 (pegmatite) plots within the magnesian field on the Fe-number vs. silica plot (Frost et al., 2001; Fig 4.16B). The high K_2O concentrations (8.3 and 10.0 wt.%) of the alkalic samples mean that they plot above the shoshonitic field on the K_2O vs. SiO_2 plot (Peccerillo and Taylor, 1976; Fig 4.16F).

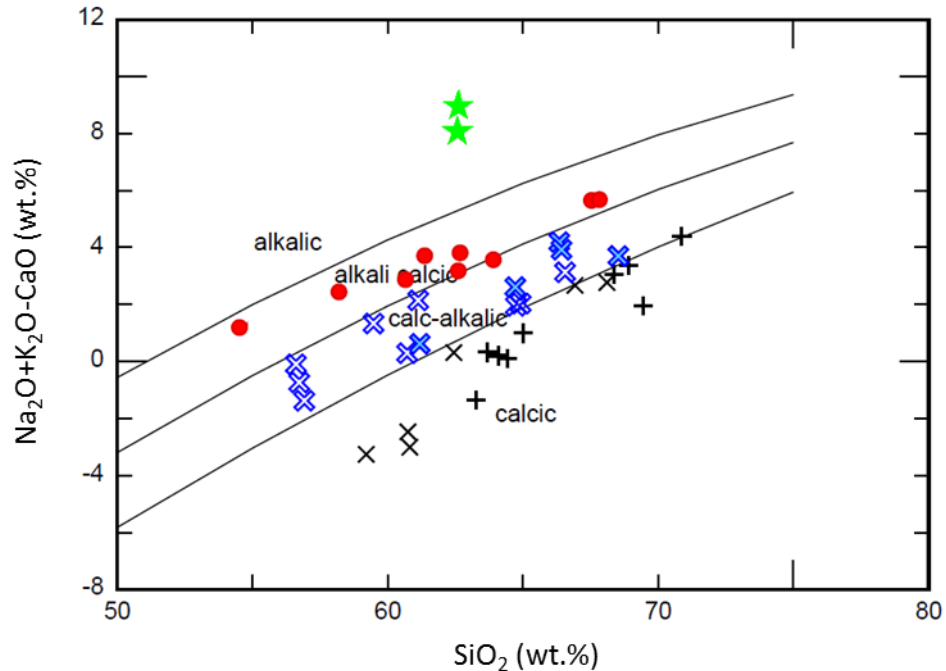


FIGURE 4.14. Modified alkali-lime index plot after Frost and Frost (2008). Black + = plutonic calcic, Black x = dykes/volcanic textured calcic, open blue x = dykes/volcanic textured calc-alkalic, filled blue x = plutonic calc-alkalic, red circles = plutonic alkali-calcic, green star = alkalic.

TABLE 4.6. Summary of MALI classification of rock types at Brewery Creek, Dublin Gulch, and Scheelite Dome.

Brewery Creek		Dublin Gulch		Scheelite Dome			
Rock Type	MALI	Rock Type	MALI	Rock Type	MALI	Rock Type	MALI
Syenite	A	Granodiorite	C	Monzogranite	C	Leucominette	C-A
Quartz biotite monzonite	C-A to A-C	Quartz syenite	C	Quartz monzonite	A-C	Minette	C-A
Biotite monzonite	C-A to A-C	Pegmatite	A	Granodiorite porphyry	C (4), A-C (1)	Spessartite	C
Hornblende gabbro	C-A	Andesite to dacite	C to C-A	Quartz monzodiorite	C-A to A-C		

C: Calcic, C-A: Calc-alkalic, A-C: Alkali-calcic, A: Alkalic

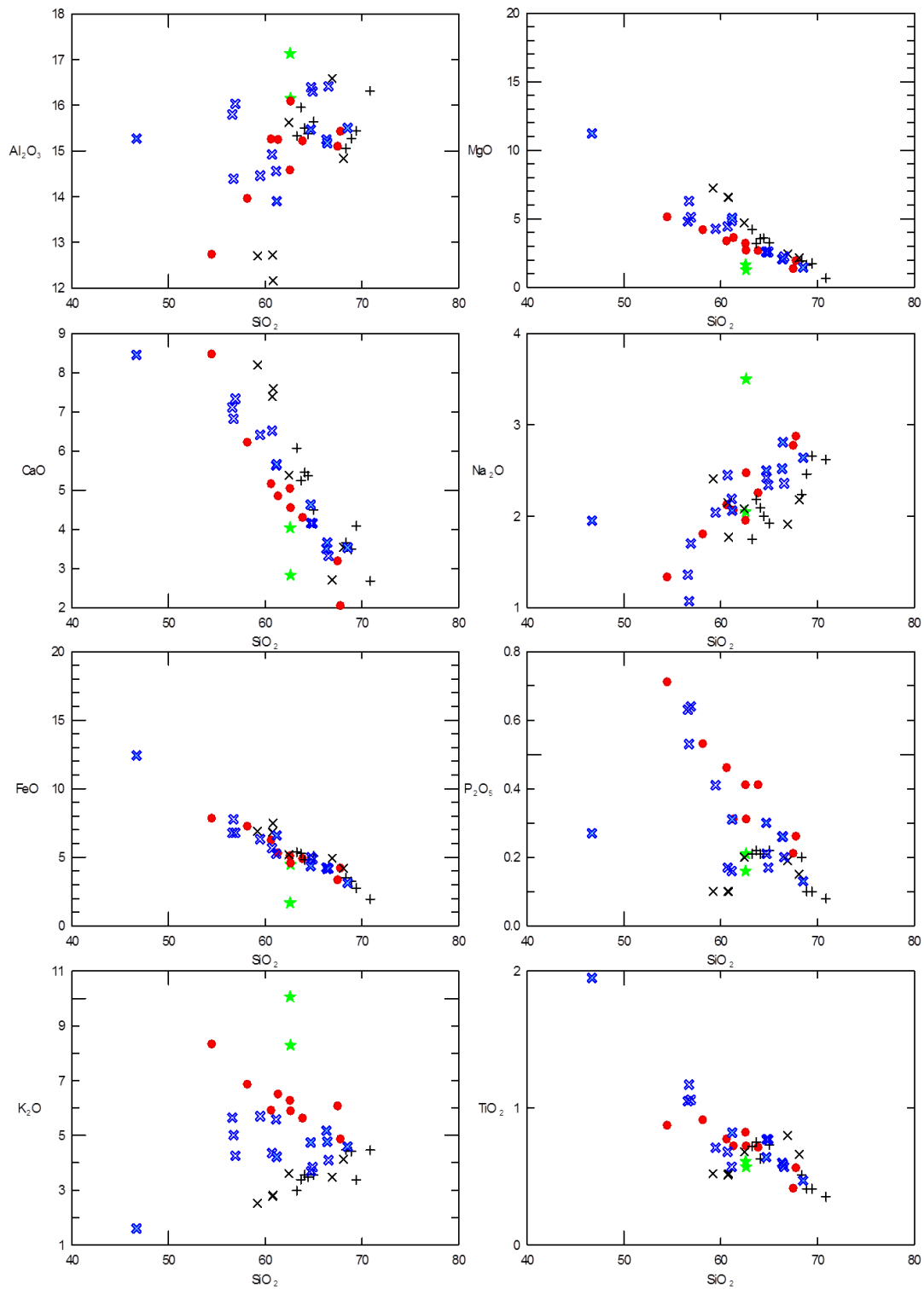


FIGURE 4.15. Harker plots (wt.%) for selected major elements at Brewery Creek, Dublin Gulch and Scheelite Dome. Black + = plutonic calcic, Black x = dykes/volcanic textured calcic, open blue x = dykes/volcanic textured calc-alkalic, filled blue x = plutonic calc-alkalic, red circles = plutonic alkali-calcic, green star = alkalic.

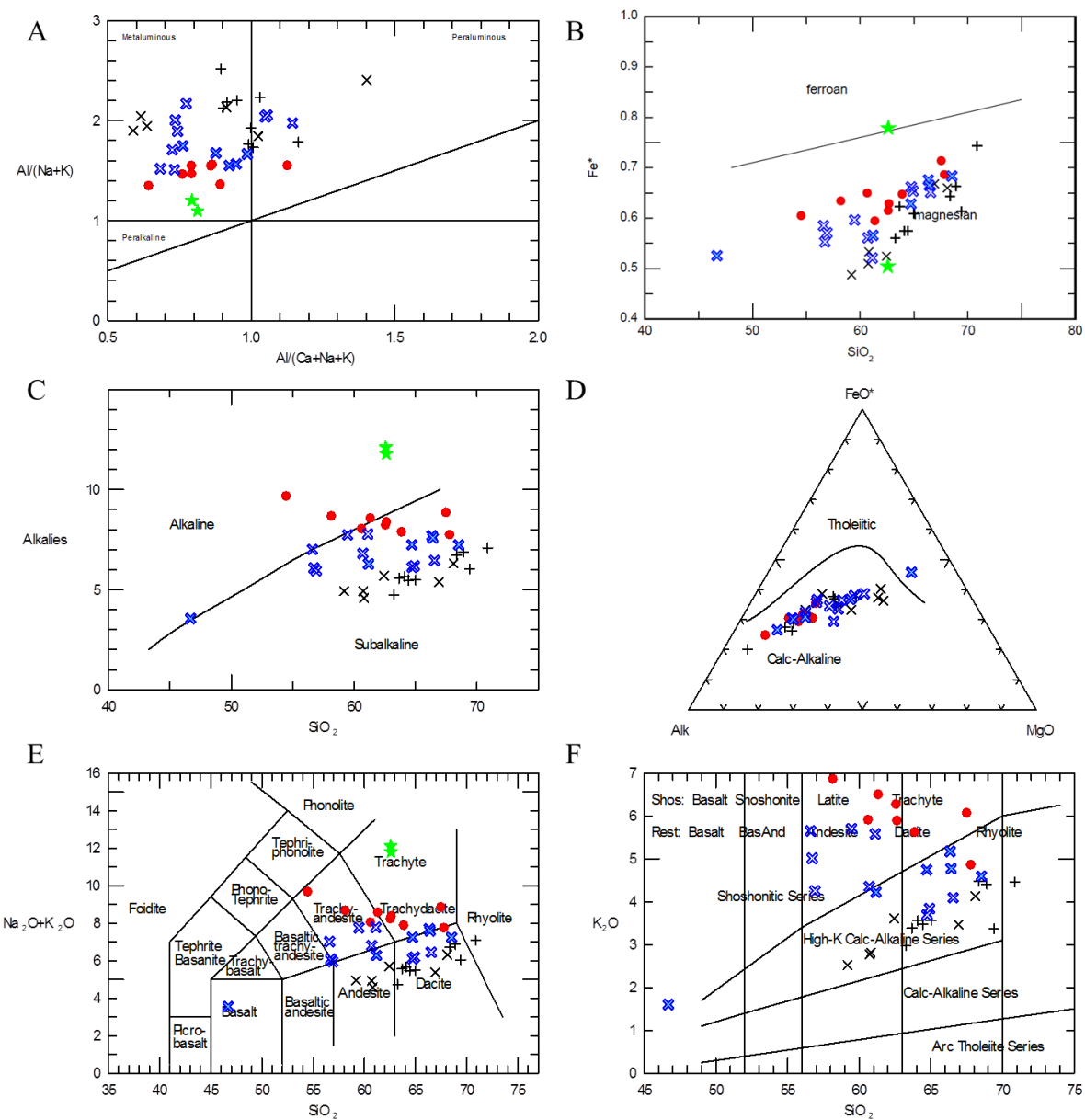


FIGURE 4.16. Major element plots for rocks at Brewery Creek, Dublin Gulch and Scheelite Dome. **A:** ASI plot (Shand, 1949), **B:** Fe-number vs SiO_2 plot (Frost et al., 2001), **C:** alkalies vs. SiO_2 plot (Irvine and Baragar, 1971), **D:** AFM plot (Irvine and Baragar, 1971), **E:** TAS plot (Le Maitre et al., 1989, **F:** K_2O vs. SiO_2 plot (Peccerillo and Taylor, 1976). Black + = plutonic calcic, Black x = dykes/volcanic textured calcic, open blue x = dykes/volcanic textured calc-alkalic, filled blue x = plutonic calc-alkalic, red circles = plutonic alkali-calcic, green star = alkalic.

TABLE 4.7. Mean values for MALI groupings

GROUP	Calcic*	S.D.	Calc-Alkalic	S.D.	Alkali-Calcic	S.D.	Alkalic**	S.D.
SiO ₂	65.08	3.42	61.43	5.46	62.14	3.97	62.59	0.02
TiO ₂	0.59	0.13	0.83	0.36	0.72	0.15	0.59	0.02
Al ₂ O ₃	14.97	1.30	15.32	0.75	14.84	0.93	16.64	0.49
FeO	4.82	1.49	5.83	2.15	5.39	1.37	3.08	1.40
MnO	0.11	0.06	0.13	0.07	0.11	0.02	0.07	0.03
MgO	3.56	1.91	4.10	2.37	3.11	1.07	1.46	0.19
CaO	5.02	1.68	5.39	1.60	4.86	1.70	3.44	0.61
Na ₂ O	2.16	0.27	2.16	0.46	2.18	0.45	2.78	0.73
K ₂ O	3.53	0.60	4.48	0.99	6.25	0.90	9.18	0.89
P ₂ O ₅	0.16	0.05	0.31	0.16	0.40	0.14	0.19	0.03
V	107	45	129	62	134	47	41	-
Cr	223	218	146	77	55	23	38	-
Co	12	6	13	3	9	2	3	-
Ni	41	19	36	15	30	7	24	-
Cu	28	10	14	4	11	-	n.d.	-
Pb	20	17	21	8	34	18	8	-
Zn	107	40	116	33	93	17	n.d.	-
Ba	2209	556	1934	528	2505	583	3877	-
Cs	14.8	7.85	13.1	10.5	22.1	6.05	8.62	-
Ga	20	2	20	2	23	1	19	-
Rb	168	26	237	62	316	18	310	-
Sr	495	72	509	48	776	118	656	-
Th	20.7	3.78	21.8	5.06	37.7	5.91	29.9	-
U	5.45	2.35	5.78	1.10	8.11	2.54	5.34	-
Y	19	6	29	11	34	6	33	-
Zr	168	35	195	18	260	34	304	-
Hf	4.51	0.82	5.27	0.52	6.98	0.91	8.62	-
Nb	15	3	16	3	24	4	23	-
Ta	1.01	0.21	1.12	0.15	1.58	0.51	1.57	-
La	47.2	9.48	48.1	9.70	87.8	14.2	63.7	-
Ce	85.9	17.0	89.1	13.9	150	27.5	113	-
Pr	9.17	1.59	9.85	1.24	16.9	2.94	12.6	-
Nd	33.3	5.61	36.4	4.74	60.4	11.7	46.1	-
Sm	6.11	0.88	7.10	1.32	10.9	2.23	9.42	-
Eu	1.36	0.18	1.55	0.30	2.32	0.44	1.65	-
Gd	4.60	0.77	5.69	1.28	7.95	1.38	6.87	-
Tb	0.73	0.11	0.95	0.29	1.21	0.22	1.16	-
Dy	3.82	0.60	5.13	1.62	5.95	1.11	5.96	-
Ho	0.73	0.12	1.02	0.34	1.11	0.23	1.14	-
Er	2.00	0.34	2.73	0.90	2.94	0.52	3.02	-
Tm	0.27	0.05	0.40	0.14	0.37	0.08	0.44	-
Yb	1.81	0.28	2.47	0.81	2.46	0.38	2.82	-
Lu	0.29	0.05	0.38	0.13	0.35	0.05	0.46	-

* REE data for DGp-004 and SDp-009 not included due to depleted patterns (see Figure 4.18).

** Major elements reported for BC-001 and DGpeg-001. Trace and rare earth elements reported for DGpeg-001.

4.7.3 Trace Elements

Trace element data for Dublin Gulch and Scheelite Dome are summarised in Table 4.7 and Harker plots in Figure 4.17. Trace element data for Brewery Creek is included where it exists. Vanadium (C: 21 to 177 ppm, CA: 33 to 285 ppm, AC: 54 to 192 ppm A: 41 ppm) and Co (C: 2 to 24 ppm, CA: 7 to 18 ppm, AC: 5 to 11 ppm, A: 3 ppm) show the most clearly defined pattern of any of the transition metals, showing compatible behaviour when plotted vs. SiO_2 . Chromium (C: 40 to 690 ppm, CA: 31 to 279 ppm, AC: 25 to 97 ppm, A: 38 ppm) shows a less well defined compatible behaviour - with an island of three samples, representing calcic spessartites from Scheelite Dome, from 560 to 690 ppm. Nickel (C: 22 to 85 ppm, CA: 21 to 66 ppm, AC: 22 to 37 ppm, A: 24 ppm), Cu (C: 14 to 44 ppm, CA: 10 to 20 ppm, AC: 11 ppm, A: n.d.), Pb (C: 3 to 70 ppm, CA: 7 to 32 ppm, AC: 16 to 66 ppm, A: 8 ppm) and Zn (C: 41 to 173 ppm, CA: 60 to 173 ppm, AC: 66 to 116 ppm, A: n.d.) do not define clear trends when plotted against SiO_2 .

LFSE show considerable scatter when plotted against SiO_2 (Fig 4.17B). Rubidium (C: 132 to 217 ppm, CA: 162 to 383 ppm, AC: 291 to 346 ppm, A: 310 ppm) shows a pattern in which there are two separate trends of incompatible behaviour when plotted against SiO_2 . These trends can be resolved to the MALI groupings (see above) in which the more enriched trend is composed of samples which are alkali-calcic and calc-alkalic, and the less enriched trend is composed of calcic and calc-alkalic samples. Strontium (C: 370 to 609 ppm, CA: 445 to 600 ppm, AC: 543 to 857 ppm, A: 656 ppm) displays considerable scatter with no apparent trend. An island of alkali-calcic samples exists between 802 and 857 ppm, represented by three examples of quartz monzonite (SDp-003, SDp-004, SDp-005) and a single example of granodiorite

porphyry (SDp-010). Barium (C: 1404 to 3620 ppm, CA: 1391 to 2938 ppm, AC: 1519 to 3068 ppm, A: 3877 ppm), Cs (C: 6.64 to 35.28 ppm, CA: 4.49 to 43.29, AC: 10.57 to 27.83 ppm, A: 8.62 ppm), Ga (C: 17 to 22 ppm, CA: 17 to 23, AC: 21 to 24 ppm, A: 19 ppm), Th (C: 13.46 to 26.85 ppm, CA: 15.39 to 32.41, AC: 26.05 to 42.48 ppm, A: 29.85 ppm) and U (C: 1.95 to 10.68 ppm, CA: 4.57 to 8.96 ppm, AC: 6.07 to 12.93 ppm, A: 5.34 ppm) define no clear division based on the MALI when plotted against SiO₂.

Harker plots of HFSE are shown in Fig 4.17C. Yttrium (C: 5 to 28 ppm, CA: 14 to 47 ppm, AC: 29 to 46 ppm, A: 33 ppm) displays the most definitive pattern for the data set, with a clear compatible behaviour for all samples. A generalised pattern of enrichment of Y for more alkalic samples over more calcic samples is present. Zirconium (C: 98 to 241 ppm, CA: 161 to 228 ppm, AC: 196 to 286 ppm, A: 304 ppm), Hf (C: 2.81 to 6.03, CA: 4.58 to 6.32 ppm, AC: 5.25 to 7.90 ppm, A: 8.62 ppm), Nb (C: 10 to 23 ppm, CA: 13 to 21 ppm, AC: 20 to 30 ppm, A: 23 ppm) and Ta (C: 0.62 to 1.33, CA: 0.85 to 1.34, AC: 1.13 to 2.57 ppm, A: 1.57 ppm) show scattered patterns when plotted against SiO₂.

Figures 4.18 and 4.19 shows chondrite-, primitive mantle- and upper crust-normalised REE plots for calcic (black), calc-alkalic (blue), alkali-calcic (red), and alkalic (green) samples. All four alkalinity groupings show very similar anomalies, which closely follow those described above in section 4.6. Chondrite-normalized plots (Figs. 4.18A; 4.19A) illustrate the overall pattern of LREE enrichment, slight to moderate negative Eu anomalies and a slight concave-up trend in the middle to heavy REE. Chondrite-normalized (n), light to middle REE (La/Sm)_n ratios range from 3.7 to 5.7, 2.8 to 5.7 and 4.6 to 5.7 for calcic, calc-alkalic, alkali-calcic groupings, respectively. The alkalic group has a (La/Sm)_n ratio of 4.2. Light to heavy REE (La/Yb)_n ratios are highest for the calcic grouping, ranging from 11.2 to 68.3. The calc-alkalic and alkali-calcic

groupings show more similar values, ranging from 6.3 to 25.9 and 20.1 to 27.05, respectively. The alkalic group has a $(La/Yb)_n$ of 15.1. While the REE patterns are enriched in the LREE, the middle and heavy REE have $(Gd/Yb)_n$ ranges of 1.6 to 5.3 (calcic), 1.5 to 2.7 (calc-alkalic) and 2.2 to 3.0 (alkali-calcic). The alkalic group has a value of 1.9. The calcic grouping is again the most enriched of any of the three MALI groupings, but we would not characterize any of the samples as HREE depleted.

The primitive mantle-normalised plots (Fig 4.18B; 4.19B), incorporating LFSE, HFSE, and the REE are characterized by well developed negative Nb, Ta, P, and Ti anomalies and a strong positive Pb anomaly for all four alkalinity groupings. Caesium is highly enriched relative to primitive mantle (PM) with normalized abundances of 500X to 2000X PM. The other LFSE, excluding Sr, generally have abundances 100X to 300X PM. Upper crust normalised plots (Figs. 4.18C; 4.19C) show a well developed Nb and Ta anomaly for all alkalinity groupings. All alkalinity groups are enriched compared to the upper crust, with a general trend of enrichment of 2X to 8X UC for the LFSE. REE are flatter, showing a ratio to the upper crust closer to 1:1.

Figure 4.20 shows tectonic discrimination plots for all of the samples from Dublin Gulch and Scheelite Dome, with Brewery Creek samples plotted where data exists. A segregation of samples based on their MALI grouping is evident on both the Rb vs. Y+Nb and Nb vs. Y plots of Pearce et al. (1984). The general trend is one in which more calcic samples plot within the upper right quadrant of the volcanic arc granite field on the Rb vs. Y+Nb plot, with a progressive shift towards the triple-point between volcanic arc granite, syn-collisional granites, and within-plate granites fields with increasing alkalinity. A similar trend is present on the Nb vs. Y plot, where calcic samples plot within the volcanic arc granite and syn-collisional granite field, with a progressive shift towards the boundary line between volcanic arc granites and syn-collisional

granites, and within-plate granites with increasing alkalinity. On the Zr vs. $10^4\text{Ga}/\text{Al}$ plot (Whalen et al., 1987) the calcic and calc-alkalic groupings lie dominantly within the “I & S type” field, while the alkali-calcic and alkalic groupings lie just outside the “I & S type” field, within the “A type” field. Spessartite lamprophyres from the calcic grouping, and a single example of quartz monzodiorite (SDp-002), also lie within the “A-type” field.

Transition metals

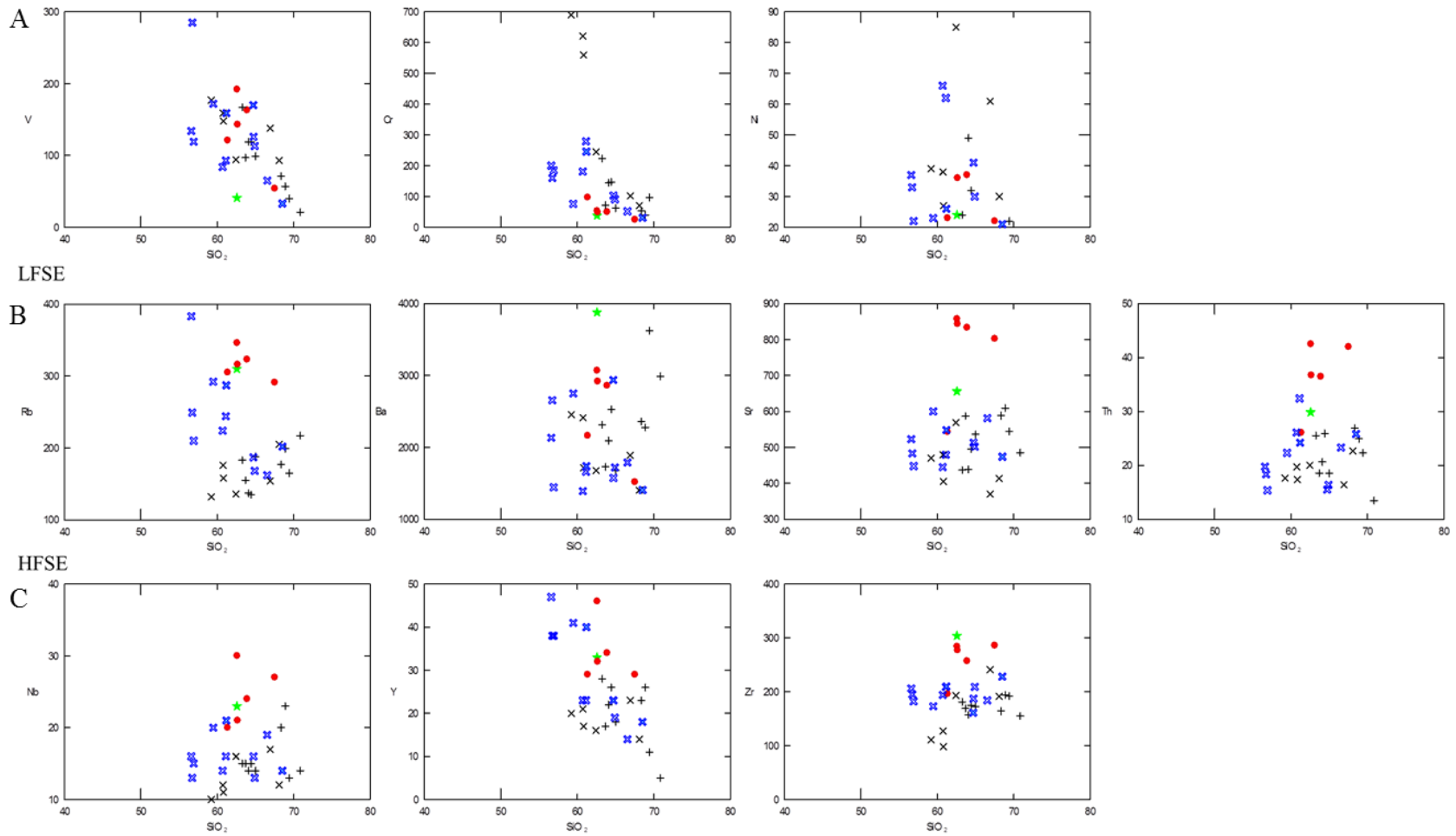


FIGURE 4.17. Trace element (ppm) vs. SiO_2 (wt.%) plots for samples at Dublin Gulch, Scheelite Dome and Brewery Creek. Representative elements are shown for **A**: transition metals (V, Cr, Ni), **B**: LFSE (Rb, Ba, Sr, Th), **C**: HFSE (Nb, Y, Zr). See text for discussion Black + = plutonic calcic, Black x = dykes/volcanic textured calcic, open blue x = dykes/volcanic textured calc-alkalic, filled blue x = plutonic calc-alkalic, red circles = plutonic alkali-calcic, green star = alkalic.

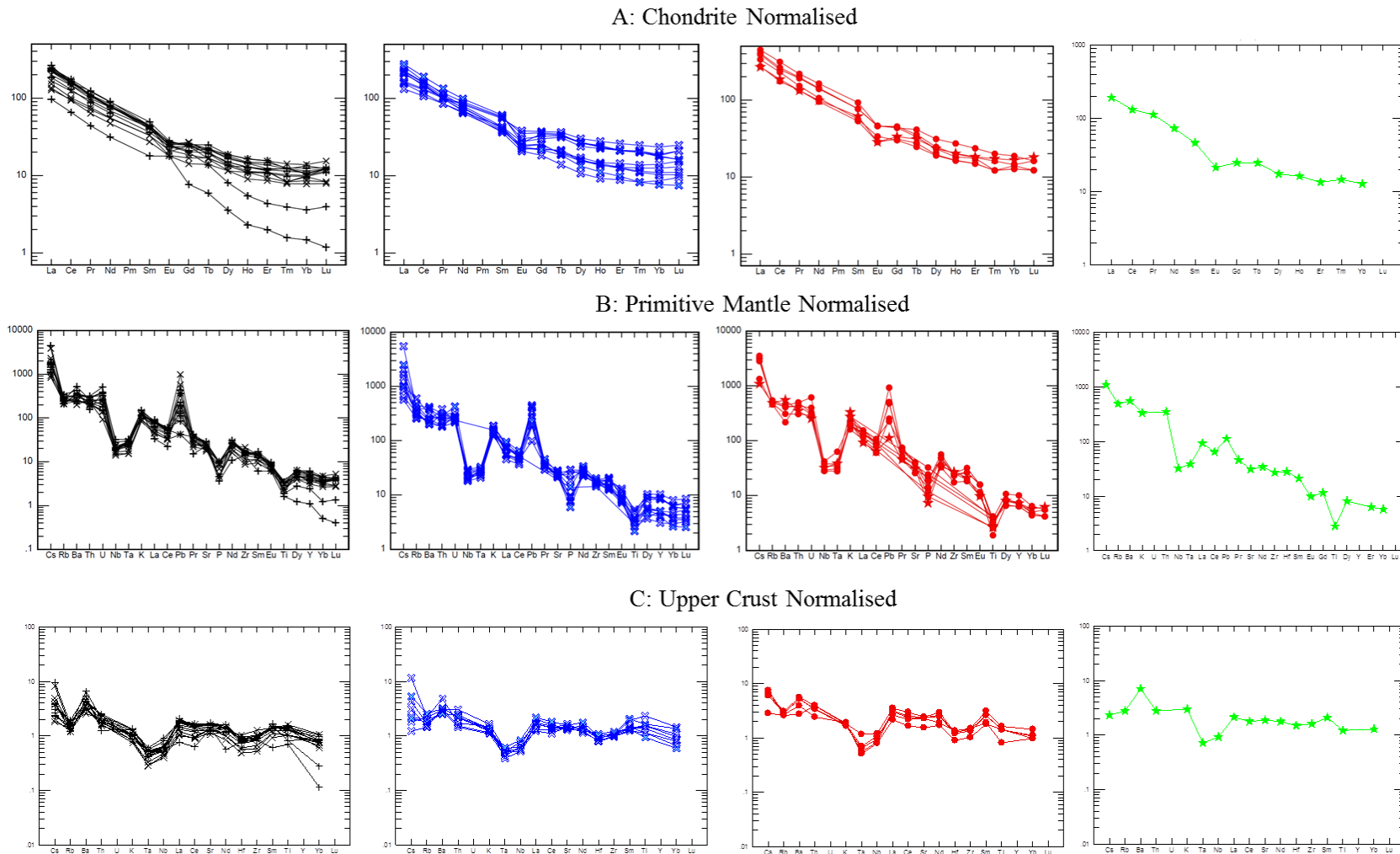


FIGURE 4.18. REE plots for rocks from Dublin Gulch and Scheelite Dome. **A:** Chondrite (Nakamura, 1974), **B:** Primitive Mantle (Sun and McDonough, 1989) and **C:** Upper Crust (Taylor and McLennan, 1985) normalisations. Black = calcic, blue = calc-alkalic, red = alkali-calcic, green = alkalic.

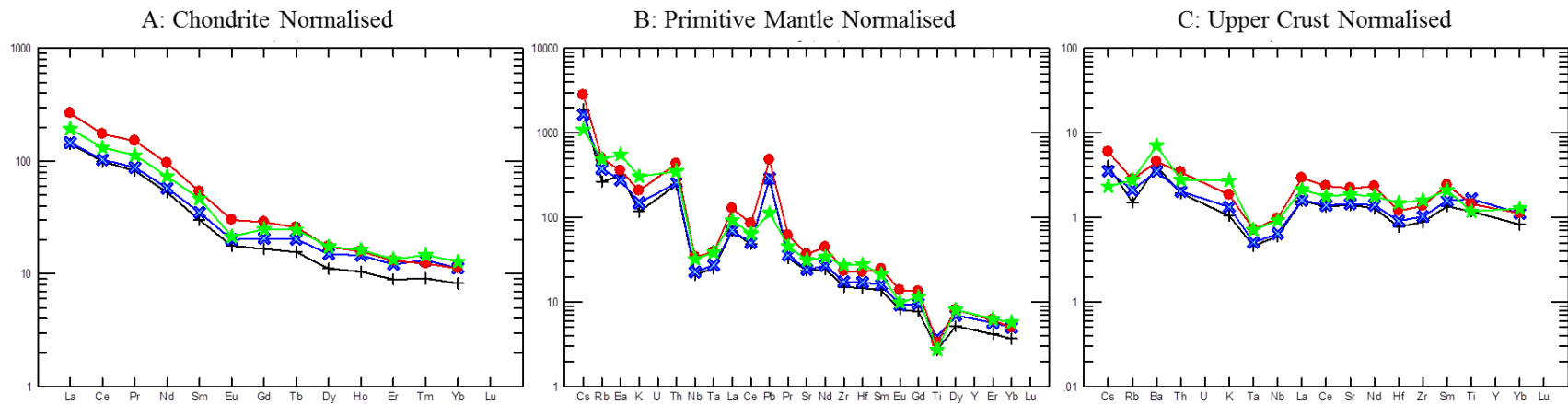


FIGURE 4.19. REE plots for rocks from Dublin Gulch and Scheelite Dome. Average values for each MALI grouping plotted against **A**: Chondrite (Nakamura, 1974), **B**: Primitive Mantle (Sun and McDonough, 1989) and **C**: Upper Crust (Taylor and McLennan, 1985) normalisations. Black = calcic, blue = calc-alkalic, red = alkali-calcic, green = alkalic.

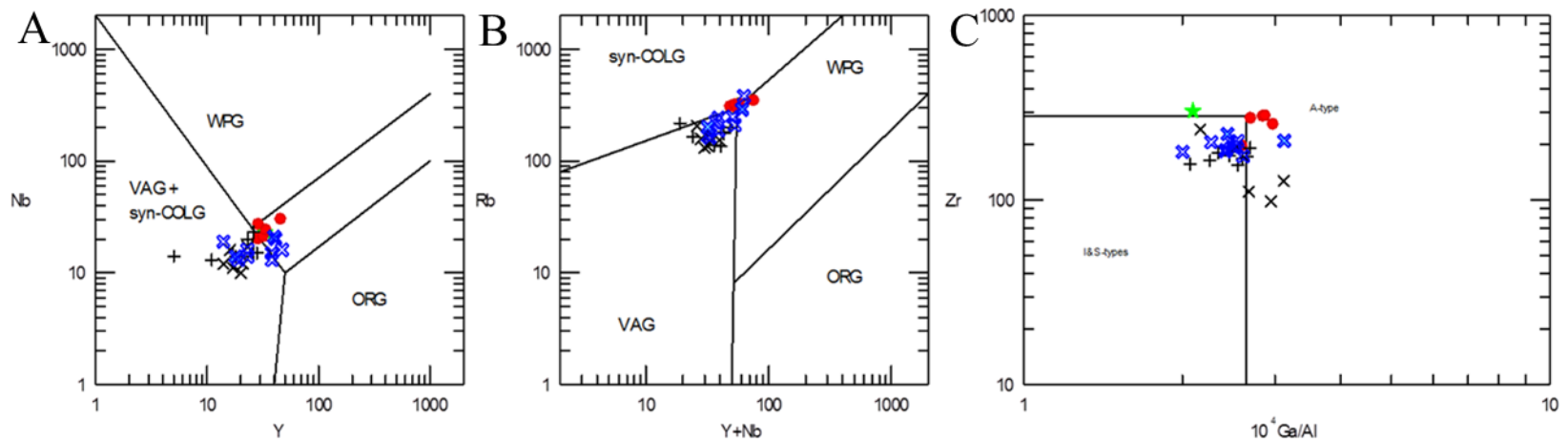


FIGURE 4.20. Tectonic discrimination diagrams for rocks at Dublin Gulch and Scheelite Dome. **A**: Rb (ppm) vs. Y+Nb (ppm) plot (Pearce et al., 1984), **B**: Nb (ppm) vs. Y (ppm) plot (Pearce et al., 1984), **C**: Zr (ppm) vs. 10^4Ga/Al plot (Whalen et al., 1987). Syn-COLG: syn-collisional granite, VAG: volcanic arc granite, ORG: orogenic granite, WPG: within-plate granite.

4.7.4 Nd and Sr Isotopes

Figure 4.21 is a $\epsilon\text{Nd}_{(i)}$ vs. $^{87}\text{Sr}/^{86}\text{Sr}_{(i)}$ plot for the Dublin Gulch samples examined in this study, as well as literature data for Scheelite Dome and Fort Knox (Fairbanks District, Alaska). Published data for rocks of the Hyland Group, the metasedimentary host to both Dublin Gulch and Scheelite Dome, plot in a more radiogenic $^{87}\text{Sr}/^{86}\text{Sr}_{(i)}$ (0.7291 to 0.7545) and more negative $\epsilon\text{Nd}_{(i)}$ (-26.2 to -21.3) space in Figure 4.21. Plutonic rocks from Scheelite Dome have relatively lower $^{87}\text{Sr}/^{86}\text{Sr}_{(i)}$ (0.7115 to 0.7142) and less negative $\epsilon\text{Nd}_{(i)}$ (-11.4 to -8.1) than Dublin Gulch. Plutonic rocks associated with the Fort Knox and nearby deposits overlap the field of Scheelite Dome rocks ($^{87}\text{Sr}/^{86}\text{Sr}_{(i)} = 0.7119$ to 0.7144 ; $\epsilon\text{Nd}_{(i)}$ -12.2 to -9.6).

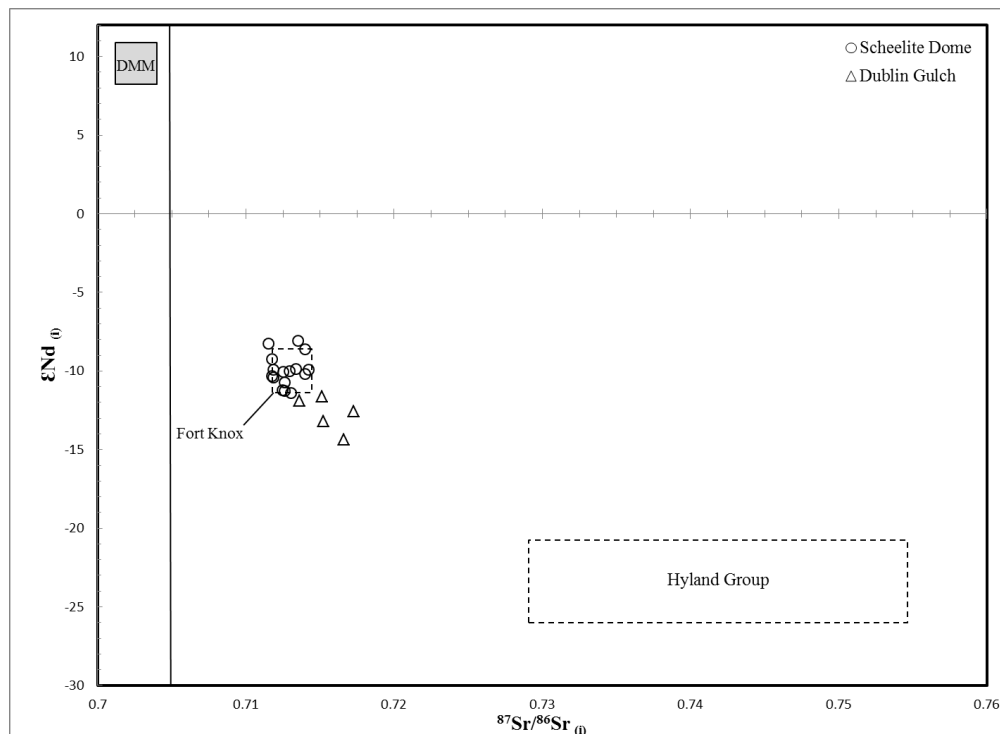


FIGURE 4.21. $\epsilon\text{Nd}_{(i)}$ vs. $^{87}\text{Sr}/^{86}\text{Sr}_{(i)}$ diagram for Dublin Gulch and comparable intrusive rocks related to IRGS. “Fort Knox” values are based on $^{87}\text{Sr}/^{86}\text{Sr}_{(i)}$ data for the Fort Knox intrusion, and $\epsilon\text{Nd}_{(i)}$ data for nearby plutons (Dolphin, Ester Dome, Gilmore Dome, Pedro Dome, Murphy Dome, Lincoln and Twin Creeks) believed related to the Fort Knox intrusion (Haynes et al., 2005). Scheelite Dome data from Mair et al. (2011). Hyland Group data, $^{87}\text{Sr}/^{86}\text{Sr}_{(i)}$ from Kuran et al. (1982) and $\epsilon\text{Nd}_{(i)}$ from Garzzone et al. (1997). DMM = Depleted MORB mantle after Zindler and Hart (1986) and Workman and Hart (2005).

4.8 Discussion

Harker plots of major elements at Dublin Gulch, Scheelite Dome, and Brewery Creek show consistent trends for all major oxides except K_2O - which is incompatible at Dublin Gulch, compatible at Brewery Creek, and a mixture of both attributes at Scheelite Dome. The MALI of samples from the three deposits combined defines four broad groupings for major rocks types; calcic, calc-alkalic, alkali-calcic, and alkalic.

As stated above, an individual magma is most likely to evolve within a single field on the MALI plot and so the observation of four distinct groupings is somewhat puzzling. Additionally, the fact that we see similar trace element, REE, and Nd and Sr isotopes for the four MALI groupings is opposite to what would be traditionally expected. The similarity in the trace and REE patterns, combined with the Nd and Sr isotopes systematics, suggests that the magma(s) that produced all four MALI groupings are from a shared, but heterogeneous, source. This naturally leads to the question: how can magmas that appear to be so closely related in terms of source signatures vary so widely in major element composition?

Mair et al. (2011) proposed a model for Scheelite Dome in which two evolving end-member magmas interacted. Samples from both proposed magma evolution paths diverge from their original MALI field and vary between MALI fields with time. Mair et al. (2011) suggest that wide variations in the modal abundances of minerals may have caused the wide differences in major and trace element geochemistry, which could explain the wide variety of MALI groupings for coeval magmas. The proposed source region for all of the rocks in the compilation is sub-continental lithospheric mantle (SCLM) (see Section 4.9 – Petrogenetic model, below) which is known to be heterogeneous (e.g., Downes, 1997), and consequently may have led to

differences in volatile element budgets between the magmas, giving rise to such varied major element compositions for such closely related magmas.

For Scheelite Dome, rock types associated with Au mineralization - namely the quartz monzonite, quartz monzodiorite and granodiorite porphyry - vary widely in their MALI classification, suggesting that the precise bulk composition of the host may not be of primary importance for IRGS genesis. Instead it is proposed that the influence of multiple magma pulses is empirically more important for IRGS generation. At Scheelite Dome, rocks associated with Au mineralization intrude later than those which show no strong association with Au, based on cross-cutting relationships.

Given that at Scheelite Dome two magma series are identifiable, and that Au mineralization is related to rock types associated with mid to late-stage intrusive activity, an important point is raised in relation to the Au mineralization at Dublin Gulch. Given that the Dublin Gulch paragenesis suggests that a second discrete hydrothermal fluid, not directly associated with the intrusion of the DGS granodiorite, is responsible for Au delivery - and that there are magmatic enclaves present that may represent a second magma - is there another later intrusive that has yet to be exposed at Dublin Gulch, which is responsible for a significant proportion of the Au endowment on the property?

Table 4.8 shows a compilation of published age data for the Tombstone and Mayo Plutonic suites within the greater Selwyn Basin. From the table it is clear that there is some overlap in age between the two suites. Dublin Gulch and Scheelite Dome are located at younger end of the age bracket for the Mayo Suite. As stated above, Hart et al. (2004b) suggested age ranges for the Mayo and Tombstone suites of 95 – 92 Ma and 92 – 90 Ma, respectively. This was

re-defined by Rasmussen (2013) as Mayo Suite: 96-93 Ma, Tombstone Suite: 93-90 Ma. Within the Mayo Suite of Hart et al. (2004b), there is a perceived size difference between the western (1-5 km²) and eastern (20-80 km²) plutons. The smaller plutons within the Mayo Suite, including Dublin Gulch, Scheelite Dome, and Clear Creek, are currently the most significant for IRGS. Brewery Creek is located within the middle of the Tombstone Belt, but is uncharacteristically small (4 x 2 km syenite with 12 km band of sills; Fig. 4.13) for the suite when compared to the reported average of 10-80 km². This suggests a link between smaller plutons within the NW Selwyn Basin and significant IRGS.

REE patterns are similar for rock types at Dublin Gulch and Scheelite Dome, including shared anomalies for all samples, suggesting a related petrogenesis. Sr and Nd isotopic compositions for rocks from Dublin Gulch (this study), Scheelite Dome (Mair et al., 2011) and inferred values for Fort Knox (Haynes et al., 2005) plot half way between depleted MORB mantle (DMM) (Zindler and Hart, 1986; Workman and Hart, 2005) and the Hyland Group metasediments (Kuran et al., 1982; Garzzone et al., 1997). Based on this pattern, it could be concluded that a simple process of assimilation of Hyland Group or similar sediments (and an isotopically similar country rock in Alaska) drove isotopic signatures towards the field of the Hyland Group. However, the intermediate SiO₂ content of the magma, I-type metaluminous character and S isotopic signatures (Chapter 3) would appear to militate against the possibility of large volumes of assimilated crust (see Section 4.9 – Petrogenetic Model, below).

Tectonic discrimination diagrams based on trace elements suggest a tectonic environment for Dublin Gulch and Scheelite Dome rocks (volcanic arc granites, syn-collisional granites; Fig. 4.20 A, B), which is inconsistent with other data for late Cretaceous magmatism in the Selwyn Basin. Although neither of these broad classification fields explicitly characterizes

the tectonic setting of magmatism, it is interesting to note that the younger intrusive rocks (based largely on cross-cutting relationships) have trace element concentrations that are more closely associated with a purely collisional environment (Pearce et al., 1984). This is contrary to the pattern that might be expected in Figure 4.20A/B, in which younger rocks plot further away from the syn-collisional granite field due to being furthest displaced in time from collision of any of the rocks in the study.

TABLE 4.8. Overview of age and rock type associations in the Mayo and Tombstone plutonic suites.

Pluton	Age (Ma)	Rock Type	Host Unit	Location	**Suite	Reference
Lost Horses/ Syenite Range	90.6 ± 0.3	Granite	Earn Group	NW Selwyn Basin	Tombstone	Murphy (1997)
Big Charlie	91 ± 0.3	Granite	Road River Group	SE Selwyn Basin	Tombstone	Heffernan (2004), Murphy (1997), Colpron & Nelson (2011)
Deadman	91 ± 1*	Syenite to Monzonite	Hyland Group	NW Selwyn Basin	Tombstone	Symons et al. (2006)
Mt. Bremner	c. 91	Syenite to Monzonite	Keno Hill Quartzite, Takhandit Fm, Road River Fm.	NW Selwyn Basin	Tombstone	Anderson (1987)
Tombstone	c. 91	Syenite to Monzonite	Keno Hill Quartzite	NW Selwyn Basin	Tombstone	Flanders et al. (2007), Anderson (1987)
Antimony Mt.	c. 91	Syenite to Monzonite	Kechika Group	NW Selwyn Basin	Tombstone	Anderson (1987)
Hole-in-the-Wall	91.3 ± 2.1	Monzogranite	Road River to Earn Group	SE Selwyn Basin	Tombstone	Rasmussen (2013), Colpron & Nelson (2011)
Brewery Creek	91.4 ± 0.2	Quartz Monzonite	Earn Group	NW Selwyn Basin	Tombstone	Diment (1996)
Lost Horses/ Syenite Range	92.1 ± 0.2	Syenite	Earn Group	NW Selwyn Basin	Tombstone	Murphy (1997)
Natla	92.3 ± 0.6	Monzogranite	Earn Group to Keno Hill Quartzite	NE Selwyn Basin	Tombstone	Rasmussen (2013)
Clear Creek	92.3 ± 0.9	Quartz Monzonite	Hyland Group	NW Selwyn Basin	Mayo	Selby et al. (2003), Marsh et al. (2003).
Roop Lakes	92.8 ± 0.5	Quartz Monzonite to Granodiorite	Keno Hill Quartzite	NW Selwyn Basin	Tombstone	Roots (1997), Lynch (2010)
O'Grady	92.8 ± 0.6	Monzonite	Hyland Group to Keno Hill Quartzite	NE Selwyn Basin	Tombstone	Rasmussen (2013)
Coal River	92.8 ± 0.9	Monzogranite	Hyland Group to Road River Group	SE Selwyn Basin	Tombstone	Rasmussen (2013), Colpron & Nelson (2011)
Ross River	93.0 ± 0.9	(Leuco)Granite	Road River to Keno Hill Quartzite.	E Central Selwyn Basin	Tombstone	Rasmussen (2013)
Keele River	93.3 ± 0.4	Monzonite	Earn Group to Keno Hill Quartzite	NE Selwyn Basin	Mayo	Rasmussen (2013)
Dechen'La	93.7 ± 0.5	Monzogranite	Hyland Group	NE Selwyn Basin	Tombstone	Rasmussen (2013)

McLeod	93.9 ± 0.2	Granite to Monzonite	Road River Group	SE Selwyn Basin	Tombstone	Heffernan (2004), Murphy(1997), Colpron & Nelson (2011).
Dublin Gulch	94.1 ± 0.3 94.0 ± 0.3	Granodiorite	Hyland Group	NW Selwyn Basin	Mayo	This study Selby et al (2003)
Scheelite Dome	94.3 ± 1.0	Quartz Monzonite	Hyland Group	NW Selwyn Basin	Mayo	Mair et al. (2006a)
Scheelite Dome	94.6 ± 0.9	Monzogranite	Hyland Group	NW Selwyn Basin	Mayo	Mair et al. (2006a)
Logan	95.6 ± 1.2	Monzodiorite	Hyland Group	NE Selwyn Basin	Mayo	Rasmussen (2013), Colpron & Nelson (2011)
Mt. Christie	96.1 ± 0.5	Monzonite	Earn Group to Keno Hill Quartzite	NE Selwyn Basin	Mayo	Rasmussen (2013)
Mile 222	96.6 ± 0.6	Monzonite	Earn Group to Keno Hill Quartzite	NE Selwyn Basin	Mayo	Rasmussen (2013)
Christie Pass	96.7 ± 0.6	Monzonite	Earn Group to Keno Hill Quartzite	NE Selwyn Basin	Mayo	Rasmussen (2013)
North Nahanni	96.9 ± 0.7	Monzogranite	Earn Group to Keno Hill Quartzite	NE Selwyn Basin	Mayo	Rasmussen (2013)
South Nahanni	c. 97	Monzogranite	Hyland Group to Gull Lake Formation	NE Selwyn Basin	Mayo	Rasmussen (2013)
Central Nahanni	97.1 ± 0.8	Granodiorite	Earn Group to Keno Hill Quartzite	NE Selwyn Basin	Mayo	Rasmussen (2013)
Mount Wilson	97.7 ± 0.8	Monzogranite	Earn Group to Keno Hill Quartzite	E Central Selwyn Basin	Mayo	Rasmussen (2013)
Pelly River	98.0 ± 1.1	Diorite	Earn Group to Keno Hill Quartzite	E Central Selwyn Basin	Mayo	Rasmussen (2013)

*age [?] variously reported as 92±1 and 91±1 in Symons et al. (2006).

** Suite as assigned by Rasmussen (2013)

4.9 Petrogenetic Model for Dublin Gulch and Affiliated Plutonic Rocks

All of the rocks considered in this study display negative Nb and Ta anomalies on incompatible element plots, which are usually interpreted to indicate derivation from subduction melting (e.g., Baier et al., 2008). However, their tectonic setting is inconsistent with plutonism directly coupled to subduction. Published $^{40}\text{Ar}/^{39}\text{Ar}$ ages for metamorphic muscovite from the Hyland Group suggest that ductile deformation ended at 104 Ma to 100 Ma (Mair et al., 2006b), implying that intrusion of Mayo Suite (96-93 Ma) and Tombstone Suite (93-90 Ma) plutons took place roughly 10 Ma after the cessation of collisional tectonics within the Canadian Cordillera. Further this magmatism took place approximately 500 km in-board of the subduction front at the time of pluton emplacement (Mair et al., 2006b). Together, these two arguments imply that a typical Andean style magmatic model is not sufficient to explain the petrogenesis of mid-Cretaceous plutons within the Selwyn Basin.

Since melting could not have been directly coupled to subduction processes, an alternative heat source for melting must be proposed. Mair et al. (2006b) suggested that the post-subduction delamination of over-thickened crust could have caused mantle upwelling and subsequent melting of metasomatized SCLM.

The ranges of Nd and Sr isotopes at Dublin Gulch and Scheelite Dome are consistent with the model proposed above, plotting half way between the mantle array and the signature of the Hyland Group. If melting of the Hyland Group had taken place to produce the magma responsible for IRGS deposit formation in the Selwyn Basin, we would expect to see a much closer alignment of Nd and Sr isotopes with those of the Hyland Group. REE patterns, which are

more enriched than typical upper crust also suggest that the Hyland Group is not the source of the magmas.

If a primitive magma derived from the mantle had assimilated crustal material to give Nd and Sr isotopes half way between DMM and the Hyland Group, it would be expected to contain much higher SiO₂, given the volume of bulk assimilation required to drive the isotopic signature in this direction. The absence of significant basaltic rock types also suggests that no primitive magma was involved in the formation of Dublin Gulch, Scheelite Dome or Brewery Creek. Magmatic enclaves are present at Dublin Gulch but contain biotite, hornblende, quartz, and alkali feldspar, which are not consistent with derivation from a primitive magma. It would also be expected that the range of Nd and Sr isotopes would disperse in a much wider range between the two end-members. $\epsilon\text{Nd}_{(i)}$ reaches a maximum of -8 for the samples in the compilation. A purely DMM-derived magma would be expected to have an $\epsilon\text{Nd}_{(i)}$ value around +10. Further, the enriched REE concentrations suggest that a more primitive magma was not involved.

Mair et al. (2011) suggest that the melting of metasomatized SCLM is the parent of igneous activity at Scheelite Dome. Given the similarity in the whole rock geochemistry, age, location, and Sm-Nd and Sr isotope data for Dublin Gulch and Scheelite Dome, the same parent source is implied for igneous activity at Dublin Gulch. Such a model, in which old SCLM with radiogenic Nd, and non-radiogenic Sr, melted after mantle upwelling consequent to delamination of the crust following orogenesis is consistent with all of the available evidence for Dublin Gulch. Shallow, localized fluid interactions with sedimentary rocks of the Hyland Group, rather than direct assimilation of crust by the magma, are responsible for early light S isotopes and the strongly radiogenic Pb isotopes of sediment hosted sulfide minerals described in Chapter 3.

Abraham et al. (2000) examined the isotopic characteristics of recent alkaline basaltic volcanism as the best available proxy for the lithospheric mantle beneath the Northern Canadian Cordillera. A single sample from Watson Lake represented the only values obtained from east of the Tintina Fault. Isotopic values for this sample were $^{87}\text{Sr}/^{86}\text{Sr}$: 0.703446 and ϵNd : +6.3, which do not suggest a strong genetic link to the source of melting at Dublin Gulch. Subsequent studies (Abraham et al., 2004; Francis et al., 2009) have focussed on assessing the nature of the lithospheric mantle beneath the accreted terranes of the Northern Canadian Cordillera. The authors are not aware of any data, obtained from recent volcanism or mantle xenoliths, which could serve as a proxy from the mantle beneath the northern Selwyn Basin.

Post-collisional magmatism of the Iberian Variscan Belt (IVB) provides a region of global comparison for the rocks of this study. Fernández-Suárez et al. (2010) considered the source for post-collisional magmatism in the IVB; concluding that meta-igneous lower crustal rocks derived from SCLM were the source of melting. A number of similarities between rocks of the IVB and those described above exist, and are summarized in Figure 4.22:

- 1) Post-collisional magmatism emplaced in the foreland thrust belt.
- 2) Rock types range from granodiorite to monzogranite.
- 3) High-K calc-alkaline to shoshonitic series rocks (Fig 4.22A).
- 4) Similar chondrite-normalized spider plots with moderate negative Eu anomaly (Fig 4.22B).
- 5) Nb vs. Y and Rb vs. Y+Nb diagrams suggesting volcanic-arc or syn-collisional origin (Fig. 4.22C and D).
- 6) Magmatic enclaves are present.
- 7) Gold mineralization associated with some plutons.

Although these similarities exist, it should be noted that there are some significant differences in magma genesis between the two regions. Fernández-Suárez et al. (2010) considered a model in which moderate assimilation of crust by magmas originating from the SCLM took place, which is supported by the presence of inherited zircons and the dominantly peraluminous nature of rocks in the IVB. Magmatism within the IVB is also much more voluminous than in the Selwyn Basin, most likely due to the fact that IVB magmatism is related to a collisional orogen that underwent extensional collapse. The rocks of our study are related to an accretionary orogen.

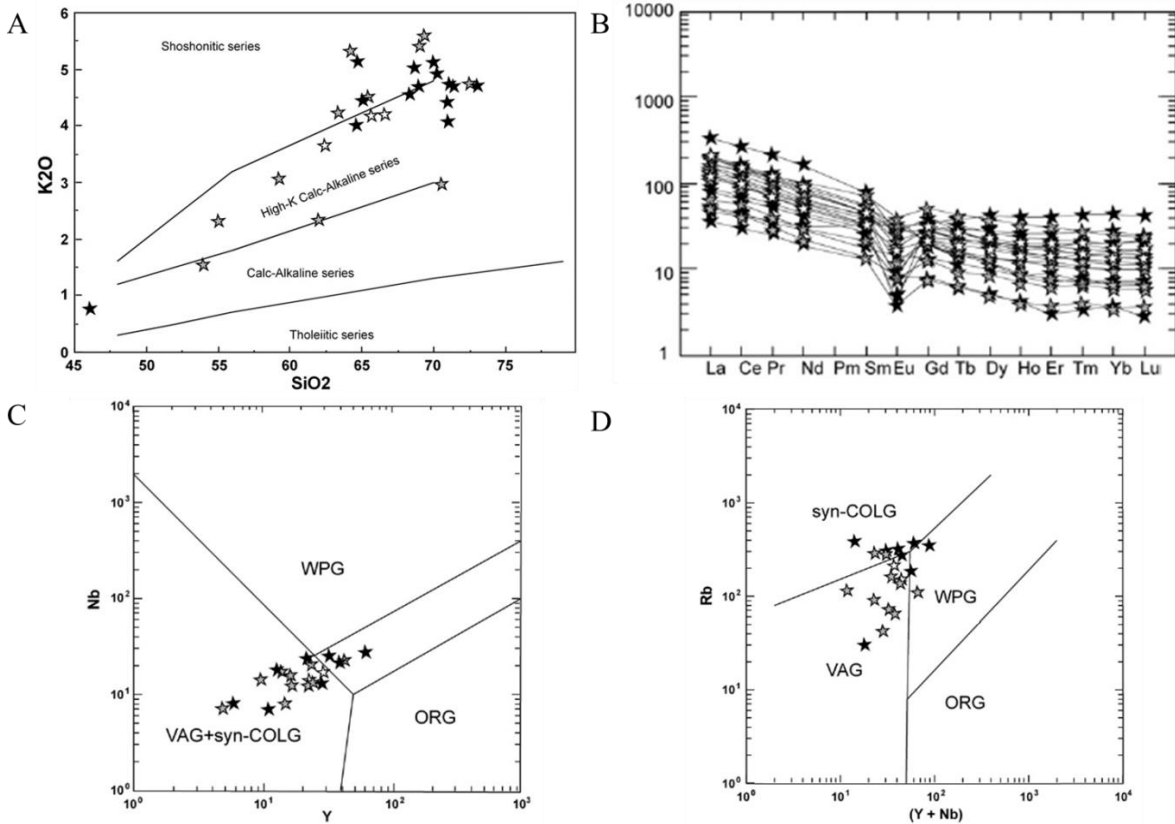


FIGURE 4.22. Geochemical discrimination diagrams for the Iberian Variscan Belt **A**: K₂O (wt.%) vs. SiO₂ (wt.%) plot (Perceirillo and Taylor, 1976), **B**: Chondrite-normalised REE plot (Sun and McDonough, 1989), **C**: Nb (ppm) vs. Y (ppm) plot (Pearce et al., 1984), **D**: Rb (ppm) vs. Y+Nb (ppm) plot (Pearce et al., 1984). All diagrams taken from Fernández-Suárez et al. (2010).

4.10 Conclusions

1. U-Pb geochronology documents a short-lived intrusive event at Dublin Gulch, and that intrusive activity on either side of the Haggart Creek fault is part of this same event. This allows for the possibility of Au endowment at depth in the Rex and Peso zones, west of the Haggart Creek fault.

2. Paragenetic studies at Dublin Gulch (Chapter 2) suggest that a second hydrothermal fluid episode is responsible for the bulk of Au delivery to the Dublin Gulch IRGS. The first hydrothermal fluid at Dublin Gulch can be directly attributed to the main phase DGS granodiorite, via the associated skarn mineralization. The second fluid episode, however, may be linked to a yet unseen later intrusive phase at depth. Although a series of andesite to dacite dykes are observed to cross-cut the DGS granodiorite, it remains unclear whether these represent plutonism coincident with the second fluid episode. Their compositional similarity to the main DGS allows for the alternative possibility that they are directly affiliated with a first magmatic phase.

3. If a second plutonic phase exists at depth it must be finitely younger than the DGS granodiorite. It is suggested therefore, that the delivery of gold may be more strongly associated with a Tombstone Suite intrusive that post-dates the main DGS granodiorite. We further propose that the other significant IRGS in the immediate area, i.e., Clear Creek, Brewery Creek and Scheelite Dome, may also be associated with intrusives that are arguably members of the Tombstone Plutonic Suite.

4. Smaller (c. 10 km²) plutons of 95-91 Ma seem to be the parents of the most significant recognized IRGS in the Tombstone Gold Belt – Dublin Gulch, Scheelite Dome, Brewery Creek,

and Clear Creek. This may in part be due to the depth of erosional exposure, and may suggest that IRGS, similarly to porphyry Cu-Mo deposits, are expected to be associated with smaller apophyses of underlying larger plutons.

5. Based on available compositional data, and allowing for some variation and diversity due to polyphase/episodic intrusion, the parent intrusions for these IRGS seem quite similar in their age and compositions, suggesting a shared source and/or melt genesis.

6. Polyphase intrusives may represent the most fertile areas of IRGS exploration in the northern Selwyn Basin. Moreover, the precise bulk composition of the intrusives seems to be of lesser importance than the presence of at least two generations of magma to drive the two stage hydrothermal activity observed in the most prospective plutons.

7. All of the parent intrusions show geochemical and isotopic characteristics consistent with emplacement in a post-collisional tectonic regime, with melt generation in response to heat flow associated with mantle upwelling following delamination of the crust.

8. Exploration strategy for IRGS in the TGB should include vigilance for later or multiple phases of plutonism that may have been beneficial in producing auriferous mineralization, particularly of the style associated with the second episode of hydrothermal activity at Dublin Gulch.

9. While significant variation in major elements is present for rock types at Dublin Gulch and Scheelite Dome, both deposits show trace elements, REE, and Nd and Sr isotopes consistent with derivation from an enriched sub-continental lithospheric mantle source. Regional exploration, rather than post discovery development of individual IRGS deposits, will benefit the most from whole rock geochemistry studies, which should focus on areas with an enriched sub-continental lithospheric mantle signature.

Acknowledgements

This work was funded by a grant from the NSERC Collaborative Research and Development (CRD) Program (CRDPJ 421812-2011), which included both financial and field support from Victoria Gold Corporation. We are deeply grateful to Bill Keats, Richard Eliason, Joanna (Ettlinger) Hodge, and Mark Ayranto of Victoria Gold Corporation for accommodating and facilitating this research effort. Sherri Furey and Pam King (Memorial University, CREAT Facility) are thanked for their expert assistance with the Sr and Nd isotope and U-Pb geochronology phases of this research, respectively.

References

- Abbott, J.G., Gordey, S.P., and Templeman-Kluit, D.J., 1986, Setting of stratiform, sediment hosted lead-zinc deposits in Yukon and northeastern British Columbia, In: Morin, J.A., (Ed.), Mineral deposits of the northern Cordillera: Canadian Institute of Mining and Metallurgy Special Volume 37, p. 1–18.
- Actlabs Catalogue, 2015, 4Litho package description, accessed at: <http://www.actlabs.com>
- Anderson, R.G., 1983, Selwyn plutonic suite and its relationship to tungsten skarn mineralization, southeastern Yukon and District of Mackenzie, In: Current Research, Geological Survey of Canada, Paper 83-1B, p. 151–163.
- Anderson, R.G., 1987, Plutonic rocks of the Dawson map area, Yukon Territory, In: Current Research, Geological Survey of Canada Paper 87-1A, p. 689-697.
- Anderson, R.G., 1988, An overview of Mesozoic and Tertiary plutonic suites and their associated mineralization in the northern Canadian Cordillera, In: Taylor, R.P., Strong, D.F. (Eds.), Recent advances in the geology of granite-related mineral deposits: Canadian Institute of Mining and Metallurgy, p. 96–113.
- Baier, J., Audétat, A., and Keppler, H., 2008, The origin of the negative niobium tantalum anomaly in subduction zone magmas: Earth and Planetary Science Letters, v. 267, p. 290-300.
- Clarke, D., Mengel, F., Coish, R. A., and Kosinowski, M. H. F., 1994, CIPW module in NewPet for DOS, version 94.01.07: St. John's: Department of Earth Sciences, Memorial University of Newfoundland.
- Colpron, M., and Nelson, J.L., 2011, A Digital Atlas of Terranes for the Northern Cordillera: BC Geofile 2011-11.
- DeBon, F., and LeFort, P., 1983, A chemical – mineralogical classification of common plutonic rocks and associations: Transactions of the Royal Society of Edinburgh, Earth Sciences, v. 73, p. 135-149.
- De Paolo, D.J., and Wasserburg, G.J., 1976, Nd isotopic variations and petrogenetic models: Geophysical Research Letters, v. 3, p. 249-252.
- De Paolo, D.J., 1981, Neodymium isotopes in the Colorado Front Range and crust–mantle evolution in the Proterozoic: Nature, v. 291, p. 193-196.
- Diment, R., 1996, Brewery Creek gold deposit, In: Yukon Exploration and Geology 1995, Exploration and geological services division, Yukon, Indian and Northern Affairs Canada, p. 57-66.

Downes, H., 1997, Shallow continental lithospheric mantle heterogeneity – petrological constraints, In: K. Fuchs (Ed.) Upper Mantle Heterogeneities from Active and Passive Seismology, Dordrecht, Kluwer Academic, p. 295-308.

Faure, G., and Mensing, T.M., 2005, *Isotopes: Principles and Applications*, 3rd edition, Hoboken, John Wiley & Sons, 897 p.

Fernández-Suárez, J., Gutierrez-Alonso, G., Johnston, S.T., Jeffries, T.E., Pastor-Galán, D., G.A. Jenner, G.A., and Murphy, J.B., 2010, Iberian late-Variscan granitoids: Some considerations on crustal sources and the significance of “mantle extraction ages”: *Lithos*, v. 123, p. 121-132.

Flanders, A.M., Harris, M.J., Kearns, L. and Hart, C.J.R., 2007. Micropetrology and mineral geochemistry of the Tombstone and Deadman plutons, Tombstone Plutonic Suite, central Yukon. In: D.S. Emond, L.L. Lewis and L.H. Weston (Eds.), *Yukon Exploration and Geology 2006*, Yukon Geological Survey, p. 149-156.

Foley, S., 1992, Vein-plus-wall-rock melting mechanisms in the lithosphere and the origin of potassic alkaline magmas: *Lithos*, v. 28, p. 435–453.

Fritz, W.H., Narbonne, G.M., and Gordey, S.P., 1983, Strata and trace fossils near the Precambrian-Cambrian boundary, Mackenzie, Selwyn, and Wernecke Mountains, Yukon and Northwest Territories: In: *Current Research, Part B*, Geological Survey of Canada, Paper 83-1B, p. 365-375.

Fritz, W.H., Cecile, M.P., Norford, B.S., Morrow, D., and Geldsetzer, H.H.J., 1991, Cambrian to Middle Devonian assemblages. In: H. Gabrielse and C.J. Yorath (eds.), *Geology of the Cordilleran Orogen in Canada*, Geological Survey of Canada, *Geology of Canada*, no. 4, p. 151-218 (also Geological Society of America, *The Geology of North America*, v. G-2).

Frost, R., Barnes, C., Collins, W., Arculus, R., Ellis, D., and Frost, C., 2001, A geochemical classification for granitic rocks: *Journal of Petrology*, v. 42, p. 2033-2048.

Frost, B.R., and Frost, C.D., 2008, A geochemical classification for feldspathic igneous rocks: *Journal of Petrology*, v. 49, p. 1955-1969.

Garzzone, C.N., Patchett, P.J., Ross, G.M., and Nelson, J., 1997, Provenance of Palaeozoic sedimentary rocks in the Canadian Cordilleran miogeocline: A Nd isotopic study: *Canadian Journal of Earth Science*, v. 34, p.1603–1618.

Gordey, S.P., and Anderson, R.G., 1993, Evolution of the northern Cordilleran miogeocline, Nahanni map area (105I), Yukon and Northwest Territories: Geological Survey of Canada, *Memoir 248*, p. 214.

Hart, C.J.R., 2005, Classifying, distinguishing and exploring for intrusion-related gold systems: The Gangee, *Newsletter of the Geological Association of Canada Mineral Deposits Division*, v. 87, p. 1, 4–9.

- Hart, C.J.R., 2007, Reduced intrusion-related gold systems, In: Goodfellow, W.D., (Ed.), Mineral deposits of Canada: A Synthesis of Major Deposit Types, District Metallogeny, the Evolution of Geological Provinces, and Exploration Methods: Geological Association of Canada, Mineral Deposits Division, Special Publication No. 5, p. 95-112.
- Hart, C.J.R., Goldfarb, R.J., Lewis, L.L., and Mair, J.L., 2004a, The Northern Cordillera Mid-Cretaceous Plutonic Province: Ilmenite/magnetite-series granitoids and intrusion-related mineralization: *Resource Geology*, v. 54, p. 253–280.
- Hart, C.J.R., Mair, J.L., Goldfarb, R.J., and Groves, D.I., 2004b, Source and redox controls on metallogenic variations in intrusion-related ore systems, Tombstone-Tungsten belt, Yukon Territory, Canada: *Transactions of the Royal Society of Edinburgh, Earth Science*, v. 95, p. 319–337.
- Haynes, E.A., Fodor, R.V., Coleman, D.S., and Jensen, P., 2005, Geochemical and isotopic compositions of the mid-Cretaceous Fort Knox and associated plutons, Fairbanks, Alaska, *Geological Society of America Abstracts with Programs*, v. 73, p. 517.
- Heffernan, R.S., 2004, Temporal, geochemical, isotopic, and metallogenic studies of mid-Cretaceous magmatism in the Tintina Gold Province, southeastern Yukon and southwestern Northwest Territories, Canada: Unpublished MSc. Thesis, University of British Columbia, Vancouver, Canada, 93 p.
- Irvine, T.N., and Baragar, W.R.A., 1971, A guide to the chemical classification of the common volcanic rocks: *Canadian Journal of Earth Sciences*, v. 8, p. 523-548.
- Jiang, Y., Jiang, S., Ling, H., Zhou, X., Rui, X., and Yang, W., 2002, Petrology and geochemistry of shoshonitic plutons from the western Kunlun orogenic belt, Xinjiang, northwestern China: implications for granitoid geneses: *Lithos*, v. 63, p. 165 – 187.
- Kosinowski, M.H.F, 1982, MSONRM, A Fortran program for the improved version of mesonorm calculation: *Computers and Geosciences*, v. 8, p. 11-20.
- Kuran, V.M., Godwin, C.I., and Armstrong, R.L., 1982, Geology and geochronometry of the Scheelite Dome tungsten-bearing skarn property, Yukon Territory: *Canadian Institute of Mining and Metallurgy Bulletin*, v. 75, p. 137–42.
- Lang, J.R., 2000, Regional and system-scale controls on the formation of copper and/or gold magmatic-hydrothermal mineralization: Final Technical Report, Mineral Deposit Research Unit 115 p.
- Lang, J.R., Baker, T., Hart, C.J.R., and Mortensen, J.K., 2000, An exploration model for intrusion-related gold systems: *Society of Economic Geology Newsletter*, v. 40, p. 1, 6–15.
- Langmuir, C., Vocke, R., Hanson, G., and Hart, S., 1978, A general mixing equation with applications to Icelandic basalts: *Earth and Planetary Science Letters*, v. 37, p. 380-392.

Le Maitre, R., Bateman, P., Dudek, A., Keller, J., Lameyre, J., Le Bas, M., Sabine, P., Schmid, R., Sorensen, H., Streckeisen, A., Woolley, A., Zanettin, B., 1989, A classification of igneous rocks and glossary of terms: Recommendations of the International Union of Geological Sciences Subcommittee on the Systematics of igneous rocks, Blackwell, Oxford, 193 p.

Lindsay, M.J., 2006, The structural and hydrothermal evolution of intrusion-related gold mineralization at the Brewery Creek mine, Yukon, Canada: Unpublished Ph.D. Thesis, James Cook University of North Queensland, Townsville, Australia, 348 p.

Lynch, G., 2010, Pressure-depth relationships of the Roop Lakes Stock and Keno Hill Ag-Pb-Zn veins, In: K.E. MacFarlane, L.H. Weston and L.R. Blackburn (Eds.), Yukon Exploration and Geology 2009, Yukon Geological Survey, p. 229-235.

Mair, J.L., Hart, C.J.R., Goldfarb, R.J., O'Dea, M., and Harris, S., 2000, Geology and metallogenic signature of gold occurrences at Scheelite Dome, Tombstone gold belt, Yukon, In: D.S., Emond, and L.H., Westen (Eds.) Yukon Exploration and Geology 1999, Exploration and Geological Services Division, Yukon, Indian and Northern Affairs Canada, p. 165–176.

Mair, J.L., Hart, C.J.R., Groves, D.I., and Goldfarb, R.J., 2003, The nature of Tombstone Plutonic Suite rocks at Scheelite Dome, Tintina Gold Province: Evidence for an enriched mantle contribution: The Ishihara Symposium: Granites and Associated Metallogenesis, Sydney, Australia, June 22-24, 2003.

Mair, J.L., Goldfarb, R.J., Johnson, C.A., Hart, C.J.R., and Marsh, E.E., 2006a, Geochemical constraints on the genesis of the Scheelite Dome intrusion-related gold deposit, Tombstone gold belt, Yukon, Canada: Economic Geology, v. 101, p. 523–553.

Mair, J.L., Hart, C.J.R., and Stephens, J.R., 2006b, Deformation history of the western Selwyn basin, Canada: Implications for orogen evolution and the setting of mid-Cretaceous magmatism: Geological Society of America Bulletin, v. 118, p. 304–323.

Mair, J.L., Farmer, G.L., Groves, D.I., Hart, C.J.R. and Goldfarb, R.J., 2011, Petrogenesis of postcollisional magmatism at Scheelite Dome, Yukon, Canada: Evidence for a lithospheric mantle source for magmas associated with intrusion-related gold systems: Economic Geology, v. 106, p. 451–480.

Maloof, T.L., Baker, T., and Thompson, J.F.H., 2001, The Dublin Gulch intrusion-hosted deposit, Tombstone Plutonic Suite, Yukon Territory, Canada: Mineralium Deposita, v. 36, p. 583–593.

Marsh, E.E., Goldfarb, R.J., Hart, C.J.R., and Johnson, C.A., 2003, Geology and geochemistry of the Clear Creek intrusion-related gold occurrences, Tintina gold province, Yukon, Canada: Canadian Journal of Earth Sciences, v. 40, p. 681–699.

- McCoy, D., Newberry, R.J., Layer, P.W., DiMarchi, J.J., Bakke, A.A., Masterman, J.S., and Minehane, D.L., 1997, Plutonic-related gold deposits of interior Alaska: *Economic Geology*, Monograph 9, p. 191–241.
- Mortensen, J.K., Murphy, D.C., Hart, C.J.R., and Anderson, R.G., 1995, Timing, tectonic setting, and metallogeny of early and mid-Cretaceous magmatism in Yukon Territory: *Geological Society of America, Abstracts with Programs* 27, 65.
- Mortensen, J.K., Hart, C.J.R., Murphy, D.C., and Heffernan, S., 2000, Temporal evolution of early and mid-Cretaceous magmatism in the Tintina Gold Belt, In: Tucker, T., Smith, M.J. (Eds.), *The Tintina gold belt: Concepts, exploration and discoveries: British Columbia and Yukon Chamber of Mines Special Volume 2*, p. 49–57.
- Murphy, D.C., 1997, Geology of the McQuesten River region, northern McQuesten and Mayo Map Area, Yukon Territory (115P/14, 15, 16; 105M/13, 14): Exploration and Geological Services Division, Yukon, Indian and Northern Affairs Canada Bulletin 6, 111 p.
- Nakamura, N., 1974, Determination of REE, Ba, Fe, Mg, Na and K in carbonaceous and ordinary chondrites: *Geochimica et Cosmochimica Acta*, v. 38, p. 757-775.
- O’Dea, M., Carlson G., Harris, S., and Fields, M., 2000, Structural and metallogenic framework for the Scheelite Dome deposit, Yukon Territory: *British Columbia and Yukon Chamber of Mines Special Volume 2*, p.115–130.
- Pearce, J.A., Harris, N.B.W., and Tindle, A.G., 1984, Trace element discrimination diagrams for the tectonic interpretation of granitic rocks: *Journal of Petrology*, v. 25, p. 956-983.
- Peccerillo, A., and Taylor, S.R., 1976, Geochemistry of Eocene calc-alkaline volcanic rocks from the Kastamonu area, Northern Turkey: *Contributions to Mineralogy and Petrology*, v. 58, p. 63-81.
- Rasmussen, K.L., 2013, The timing, composition, and petrogenesis of syn- to postaccretionary magmatism in the northern Cordilleran miogeocline, eastern Yukon and southwestern Northwest Territories: Unpublished Ph.D. Thesis, University of British Columbia, Vancouver, 810 p.
- Rock, N.M.S, 1991, *Lamprophyres: Blackie and Sons Ltd., Glasgow*, 285 p.
- Roots, C.F., 1997, Geology of the Mayo Map area, Yukon Territory (105M): Exploration and Geological Services Division, Yukon, Indian and Northern Affairs Canada, Bulletin 7, 82 p.
- Rudnick, R.L., and Fountain, D.M., 1995, Nature and composition of the continental crust: A lower crustal perspective: *Reviews of Geophysics*, v. 33, p. 267-309.

Saunders, A.D., Tarney, J., Marsh, N.G., and Wood, D.A, 1980, Ophiolites as ocean crust or marginal basin crust: a geochemical approach, In: A. Panayiotou (Ed.) Ophiolites, Proceedings International Ophiolite Symposium, Cyprus, 1979, Ministry of Agriculture and Natural Resources, Geological Survey Department, Cyprus, p. 193-204.

Selby, D., Creaser, R.A., Heaman, L.M., and Hart, C.J.R., 2003, Re–Os and U–Pb geochronology of the Clear Creek, Dublin Gulch, and Mactung deposits, Tombstone Gold Belt, Yukon, Canada: absolute timing relationships between plutonism and mineralization: Canadian Journal of Earth Science, v. 40, p. 1839–1852.

Sparkes, G.W., and Dunning, G.R., 2014, Late Neoproterozoic epithermal alteration and mineralization in the western Avalon zone: A summary of mineralogical investigations and new U/Pb geochronological results, In: Current Research, Newfoundland and Labrador Department of Natural Resources Geological Survey, Report 14-1, p. 99-128.

Shand, S.J., 1949, The Eruptive Rocks, second edition, New York, John Wiley, 444 p.

Stephens, J.R., 2003, Structural, mechanical and P-T evolution of intrusion-related gold mineralization at Clear Creek and Dublin Gulch, Yukon, Canada: Unpublished Ph.D. Thesis, James Cook University of North Queensland, Townsville, Australia, 277 p.

Stephens, J.R., Mair, J.L., Oliver, N.H.S., Hart, C.J.R., and Baker, T., 2004, Structural and mechanical controls on intrusion-related deposits of the Tombstone gold belt, Yukon, Canada: With comparisons to other vein hosted ore deposit types: Journal of Structural Geology, v. 26, p. 1025–1041.

Sun, S.S., and McDonough, W.F., 1989, Chemical and isotopic systematics of oceanic basalts: implications for mantle consumption and processes, In: Saunders, A.D., and Norry, M.J., (Eds.), Magmatism in ocean basins: Geological Society of London Special Publication, v. 42, p. 313-345.

Symons, D.T.A., Harris, M.J., Hart, C.J.R., and McCausland, P.J.A., 2006, Paleomagnetism of the ~91 Ma Deadman pluton: Post-mid-Cretaceous tectonic motion in central Yukon. In: D.S. Emond, G.D. Bradshaw, L.L. Lewis and L.H. Weston (Eds.) Yukon Exploration and Geology 2005, Yukon Geological Survey, p. 299-313.

Tanaka, T., Togashi, S., Kamioka, H., Amakawa, H., Kagami, H., Hamamoto, T., Yuhara, M., Orihashi, Y., Yoneda, S., Shimizu, H., Kunimaru, T., Takahashi, K., Yanagi, T., Nakano, T., Fujimaki, H., Shinjo, R., Asahara, Y., Tanimizu, M., and Dragusanu, C., 2000, JNdi-1: a neodymium isotopic reference in consistency with La Jolla neodymium: Chemical Geology, v. 168, p. 279-281.

Taylor, S. R., and McLennan, S. M., 1985, The continental crust: Its composition and evolution: Blackwell, Oxford, 312 p.

Tempelman-Kluit, D.J., 1964, Geology of the Haggart Creek-Dublin Gulch area, Mayo District, Yukon Territory: Unpublished M.Sc. thesis, University of British Columbia, Vancouver, Canada, 193 p.

Tetra Tech, 2015, Prepared for Victoria Gold Corp., Technical Report – Feasibility Study, Eagle Gold Project, Yukon: NI 43-101 Technical Report, dated May 29, 2015, 411 p.

Thompson, J.F.H., and Newberry, R.J., 2000, Gold deposits related to reduced granitic intrusions, In: S.G., Hagemann and P.E., Brown (eds.), Gold in 2000: Society of Economic Geologists, Reviews in Economic Geology, v. 13, p. 377–400.

Thompson, J.F.H., Sillitoe, R.H., Baker, T., Lang, J.R., and Mortensen, J.K., 1999, Intrusion-related gold deposits associated with tungsten-tin provinces: Mineralium Deposita, v. 34, p. 323–334.

Whalen, J.B., Currie, K.L., and Chappell, B.W., 1987, A-type granites: geochemical characteristics, discrimination and petrogenesis: Contributions to Mineralogy and Petrology, v. 95, p. 407-419.

Woodsworth, G.J., Anderson, R.G., and Armstrong, R.L., 1991, Plutonic regimes, In: Gabrielse, H., Yorath, C.J. (Eds.), Geology of the Cordilleran Orogen in Canada: Geological Survey of Canada, Geology of Canada 4, p. 491–531.

Workman, R.K. and Hart, S.R., 2005, Major and trace element composition of the depleted MORB mantle (DMM): Earth and Planetary Science Letters, v. 231, p. 53-72.

Zen, E., 1988, Phase relations of peraluminous granitic rocks and their petrogenetic implications: Annual Review of Earth and Planetary Sciences, v. 16, p. 21-51.

Zindler, A., and Hart, S.R., 1986, Chemical Geodynamics: Annual Reviews of Earth and Planetary Science, v. 14, p. 493-571.

CHAPTER 5

Summary and Conclusions

5.1 Summary of Significant Findings

5.1.1 Deposit Paragenesis and the Timing of Gold Deposition

A detailed 8-stage paragenetic sequence for Dublin Gulch IRGS has been developed, and implies two apparent fluid pulses from the DGS magma and/or associated plutonic episodes. Subsequent to initial contact metamorphism (Stage 1), the first pulse was responsible for the creation of the Wolf W Skarn (Stage 2), and quartz-dominated partially aligned stockwork veins within the upper portion of the DGS (Stages 3 & 4). The second fluid pulse initially formed a series of more widely-spaced arsenopyrite-pyrite veins (Stage 5a). Most native gold is genetically related to the second hydrothermal fluid pulse and displays two textural styles/stages; the first associated with the arsenopyrite-rich veins (Stage 5a & 5b), and the second with later bismuthinite and Pb-Sb-(Cu-Fe-) sulfosalt minerals (Stage 6). Geostatistical analysis of elemental associations in drill core assay data corroborates the association of gold with these specific paragenetic stages.

Although there was significant overprinting of the earlier stockwork veins by the second fluid pulse, Au inventory was predominantly delivered to the deposit during the later stages (5 & 6) of mineralization associated with this pulse.

5.1.2 Geothermometry and Fluid Sources

The geochemical signatures of mineralization, in combination with the paragenetic and textural studies discussed above, strongly imply two distinct fluid events in the Dublin Gulch IRGS. Geothermometry of Stage 3 and 4 arsenopyrite provided temperature estimates of 345 to 595°C, which overlaps with the lower range of published temperature

estimates for the skarn, and agrees with a model in which the Stage 2 skarn, and Stage 3 and 4 veins, are formed by a single progressively cooling fluid. Arsenopyrite compositions for Stage 5 represent the only estimate of the temperature of the second hydrothermal fluid and suggest a temperature of precipitation of native gold of up to 490 °C. This is far in excess of the temperatures derived from fluid inclusions in quartz, which have a more ambiguous paragenetic relationship with the main auriferous stages. Arsenopyrite is often seen in textural equilibrium with native gold, so these higher temperatures are suggested as a more realistic estimate.

Incorporation of sedimentary sulfur from the Hyland Group during the initial stage of plutonism caused the magma to acquire a more isotopically negative S inventory, and this is reflected in the $\delta^{34}\text{S}$ of the mineralizing fluids of Stages 2 to 4. Corollary evidence for country rock assimilation is provided by the presence of the Wolf Skarn as a roof pendant within the DGS. During these earlier stages, the fluid also appears to have progressed from a $\delta^{34}\text{S}$ similar to the Hyland Group metasediments (especially the arsenopyrite of Stage 3 stockwork veins) towards somewhat less negative values with time (i.e., Stage 2 to 4 pyrrhotite). Spatially non-uniform assimilation may have caused localized, peripheral heterogeneity in the sulfur isotope composition of the fluid that was subsequently homogenized toward more magmatic values in the uncrystallized portion of the DGS, given that the magmatic reservoir of sulfur was far larger in volume.

The nature of the second fluid is of critical importance to the understanding of the deposit, as the majority of Au inventory at Dublin Gulch was delivered by this fluid. Sulfur isotope values for the second fluid suggest a predominantly magmatic origin, related either to a second fluid pulse exsolved from the crystallizing DGS, or from an as

yet unexposed second emplacement of magma at depth. Textural studies have shown clear evidence of re-fracturing and overprinting of Stage 3 and 4 veins by minerals that were precipitated during Stage 5 and 6 mineralization, and that the vein morphologies, ore assemblages and alteration assemblages produced by the two fluids vary significantly. Sulfur isotopes display distinct populations for Stage 3-4 versus Stage 5-6 veins. The pattern of overprinting is also suggested by sulfides from veins with Stage 3-4 morphologies that display Stage 5b alteration selvages, and show sulfide $\delta^{34}\text{S}$ values indicative of Stage 5 – 6 fluids.

Microanalysis of lead isotopes in Pb-rich sulfosalts from DGS-hosted veins yielded highly radiogenic values - 20.41 to 21.02 $^{206}\text{Pb}/^{204}\text{Pb}$, 15.89 to 16.05 $^{207}\text{Pb}/^{204}\text{Pb}$, and 40.39 to 41.11 $^{208}\text{Pb}/^{204}\text{Pb}$. Pb-rich sulfosalts from a single vein hosted by metasedimentary rocks of the Hyland Group yielded even more radiogenic values - 21.70 to 21.71 $^{206}\text{Pb}/^{204}\text{Pb}$, 16.07 to 16.08 $^{207}\text{Pb}/^{204}\text{Pb}$, and 42.08 to 42.15 $^{208}\text{Pb}/^{204}\text{Pb}$. These lead isotope ranges are consistent with sulfide precipitation from a hydrothermal fluid initially derived from a magma that had inherited highly radiogenic Pb from its source rock, and that subsequently scavenged substantial additional radiogenic lead from the Neoproterozoic metasedimentary host and country rocks of the deposit before depositing the auriferous Stage 5b and Stage 6 mineralization.

Early quartz veins and late stage arsenopyrite-sulfosalt vein stages show definably different populations of both arsenopyrite composition and sulfur isotope values - suggesting two distinct, sequential mineralising events, which overlap within the Eagle Zone (and elsewhere within the Dublin Gulch deposit). However, the bulk of Au was, as discussed above, precipitated during the later Stage 5 and Stage 6 mineralization.

5.1.3 Characteristics of Associated Plutonic Rocks

Three groups of intrusive rocks have been identified at Dublin Gulch, 1) the main phase granodiorite Dublin Gulch Stock (DGS), 2) a series of equigranular to porphyritic dacitic dykes from the Platinum and Potato Hills zones, and 3) a series of porphyritic andesitic to dacitic dykes from the Peso Zone. U-Pb dating of zircons from these intrusive rocks suggests a short-lived igneous event at 93-94 Ma as the parent of hydrothermal mineralization. All three groups are metaluminous, and are characterized by SiO₂ of 58.6 to 65.5 wt.%; $\epsilon\text{Nd}_{(i)}$ of -14.4 to -11.6; and $^{87}\text{Sr}/^{86}\text{Sr}_{(i)}$ of 0.71362 to 0.71726.

A comparison to similar lithologies at the Scheelite Dome and Brewery Creek deposits (also considered IRGS) identified four distinct geochemical groupings of rocks, based on the modified alkali-lime index (MALI) of Frost and Frost (2008): calcic, calc-alkalic, alkali-calcic and alkalic. All four MALI groupings exhibit remarkably similar trace element and REE compositions, and Nd and Sr isotope signatures indicating a similar source region in the enriched subcontinental lithospheric mantle.

5.2 Implications for IRGS exploration

5.2.1 Mineralization

Hydrothermal Parageneses: Previous models for IRGS (e.g., Thompson et al., 1999) have focussed on early stage porphyry-style quartz veins as a key indicator that an intrusion may host auriferous mineralization. This study, however, has shown that these initial vein stages may sometimes be of secondary importance in providing the gold inventory in IRGS. At Dublin Gulch, the bulk of the gold inventory appears linked to later stage mineralization related to an identifiable second fluid pulse. Future exploration

strategies could beneficially focus on building a potentially comparable paragenetic framework for each deposit in the TTGB – including the Scheelite Dome, Clear Creek, and Brewery Creek deposits.

A key point for exploration is that, whether the deposit is a high-S high-As or low-S low-As IRGS, the presence of a network of partially aligned stockwork quartz veins related to initial pluton emplacement alone is not necessarily sufficient to produce a viable gold deposit. Episode(s) of subsequent hydrothermal and veining activity may be critical in delivering additional Au in the form of widely spaced arsenopyrite rich (high-As IRGS) or quartz ‘shear’ (low-As IRGS) veins (Bakke et al., 1998).

Alteration Studies: Future exploration strategies for this type of deposit should look to expand known occurrences by using vein selvage alteration mapping and logging to highlight areas of potentially enhanced Au grades.

For example, dickite, kaolinite and/or pyrophyllite alteration selvages around quartz veins, such as those observed for Stage 5b and Stage 6 at Dublin Gulch, may be more obvious than less volumetrically abundant ore minerals within the veins, including native gold. Alteration selvages could also potentially reveal re-fracturing and overprinting of early quartz veins, which appears significant in enriching Au contents at Dublin Gulch, i.e., modification or enhanced widths of alteration selvages may provide a useful insight into whether veins have been reactivated during later fluid events. For example, at Dublin Gulch, multiple examples of Stage 3 veining show the subsequent overprint of alteration selvages related to the auriferous Stage 5b.

Based on our research application at Dublin Gulch, the use of a hand-held or desktop short wave infra-red (SWIR) instrument, for the identification of hydrous alteration mineralogy in core or hand specimen would appear to have considerable potential application to the exploration for IRGS in general.

Nomenclature: Given that the metallogenic associations and perceived hydrothermal processes that operated at Dublin Gulch show some divergence from those proposed by the existing RIRGS model, we tentatively propose the use of the term S-rich As-rich intrusion-related gold deposit (SAS-IRG) for those like Dublin Gulch.

5.2.2 Host Pluton

Smaller (circa 10 km²) plutons of shoshonitic to high-K calc-alkaline affinity emplaced at 95-91 Ma seem to be the parents of the most significant recognized IRGS in the Tombstone Gold Belt – Dublin Gulch, Scheelite Dome, Brewery Creek, and Clear Creek. Polyphase intrusives may represent the most fertile areas of IRGS exploration in the northern Selwyn Basin. Moreover, the precise bulk composition of the intrusives seems to be of lesser importance than the presence of at least two generations of magma to drive the two stage hydrothermal activity observed in the most prospective plutons. Exploration strategies for IRGS in the TTGB should include vigilance for later or multiple phases of plutonism that may have been beneficial in producing auriferous mineralization, particularly of the style associated with the second episode of hydrothermal activity at Dublin Gulch.

The wide range of major element compositions for rocks with very similar trace element, REE, and Nd and Sr isotope compositions suggests that lithochemical

studies may be of most benefit at a regional rather than deposit scale. Regional exploration strategies would benefit from examining areas, which show the following parameters, which appear to be consistent with for all of the parent intrusions to significant IRGS within the Selwyn Basin:

- 1) Emplacement in a post-collisional tectonic regime.
- 2) Enriched subcontinental lithospheric mantle as a source of melting.
- 3) Melt generation in response to heat flow associated with mantle upwelling following delamination of the crust.

5.3 Recommendations for Future Work

5.3.1 Infrared Fluid Inclusion Microthermometry

The apparent ambiguity in the temperature estimates for mineralization from quartz-hosted fluid inclusions (Baker and Lang, 2001) versus those from arsenopyrite geothermometry (this study) is likely a consequence of the scarcity, or absence, of cogenetic quartz that we observed in the assemblages of auriferous Stages 5b and 6. Most quartz is, in fact, from earlier stages. It is therefore suggested that ore minerals transparent to infrared light might be amenable to a fluid inclusion study that is more tightly constrained to the documented auriferous stages in our more detailed paragenesis.

Some of the ore minerals present are typically opaque to visible light (0.38 μm to 0.74 μm), but become transparent when viewed using near infrared (NIR) (0.74 μm to 1.4 μm) and/or shortwave infrared (SWIR) radiation (1.4 μm to 3 μm) (Campbell et al., 1984). This allows fluid inclusions within the ore minerals themselves to be studied using microthermometric techniques. Traditional fluid inclusion studies of ore systems

necessarily use gangue minerals, such as quartz, as a proxy for metal-bearing fluids, using the assumption that gangue and ore minerals are co-genetic based on textural evidence. However, IR illuminated studies of fluid inclusions in ore minerals (e.g., Campbell and Panter, 1990) show that textural evidence linking gangue minerals to ore deposition is often ambiguous or deceptive.

Minerals in Stage 5b and Stage 6 at Dublin Gulch that are nominally amenable to IR fluid inclusion studies include: sphalerite, pyrite, tennantite, and numerous Pb-Sb-(Cu-Fe-) sulfosalt minerals (Campbell et al., 1984, Campbell and Panter, 1990; Mancano and Campbell, 1995; Bailly, 2000; Rios et al., 2006). Sulfosalt minerals in textural equilibrium with native gold provide the most obvious initial target at Dublin Gulch for this type of study.

5.3.2 Detailed Study of the Rex and Peso Zones

Preliminary lithogeochemical geostatistics, arsenopyrite geothermometry, and sulfur and lead isotopes suggest that Rex and/or Peso zones (veins) could represent a distinct mineralizing event, separate from hydrothermal activity characterized at Dublin Gulch. In fact, available lead isotope data (from this study, and from archival data in the LEADTABLE database) suggest that the Rex and Peso zones might be distinct systems from one another. A detailed study of the paragenetic sequence of both the Rex and Peso zones could address whether these two zones are related to each other, and clarify their relationship to mineralization within the DGS. Twelve diamond drill holes completed by Victoria Gold Corporation in 2011 on the Rex and Peso zones would provide well-documented intersections with which to potentially address these questions.

5.3.3 IRGS beyond the Tombstone Tintina Gold Belt

It is clear that further investigation and study of IRGS beyond the TTGB will ultimately be required in order to fully understand the key features of this deposit class globally. For the Selwyn Basin IRGS, a stronger understanding of the influence that the stratigraphic position within the host sedimentary basin has on the styles of mineralization is required. Of most direct interest is the influence of the composition of the immediate host rock sequence on the elemental associations found within individual IRGS - in particular, S-rich As-rich IRGS such as Dublin Gulch.

References

Bailly, L., Bouchot, V., Bény, C., and Milési, J.P., 2000, Fluid inclusion study of stibnite using infrared microscopy; an example from the Brouzils antimony deposit (Vendee, Armorican Massif, France): *Economic Geology*, v. 95, p. 221–226.

Baker, T., and Lang, J.R., 2001, Fluid inclusion characteristics of intrusion-related gold mineralization, Tombstone-Tungsten magmatic belt, Yukon Territory Canada: *Mineralium Deposita*, v. 36, p. 563–582.

Bakke, A.A., Morrell, B., and Odden, J., 1998, The Fort Knox porphyry gold deposit, east central Alaska: Porphyry and hydrothermal copper and gold deposits: A global perspective, conference proceedings, 30 November and 1 December 1998, Perth, Australia, p. 89-98.

Campbell, A.R., Hackbarth, C.J., Plumlee, G.S., and Petersen, U., 1984, Internal features of ore minerals seen with the infrared microscope: *Economic Geology*, v. 79, p. 1387–1392.

Campbell, A.R., and Panter, K.S., 1990, Comparison of fluid inclusions in coexisting (cogenetic?) wolframite, cassiterite, and quartz from St. Michael's Mount and Cligga Head, Cornwall, England, in: R.J., Bodnar (Ed.), *Current research on fluid inclusions*: Oxford, International, Pergamon, *Geochimica et Cosmochimica Acta*, v. 54, p. 673–681.

Frost, B.R., and Frost, C.D., 2008, A geochemical classification for feldspathic igneous rocks: *Journal of Petrology*, v. 49, p. 1955-1969.

Mancano, D.P., and Campbell, A.R., 1995, Microthermometry of enargite hosted fluid inclusions from the Lepanto, Philippines, high-sulfidation Cu-Au deposit: *Geochimica et Cosmochimica Acta*, v. 59, p. 3909–3916.

Rios, F.J., Alves, J.V., Perez, C.A., Costa, E.C., Rosiere, C.A, Fuzikawa, K., Correia Neves, J.M., Chaves, A.O., Prates, S.P., and De Barrio, R.E., 2006, Combined investigations of fluid inclusions in opaque ore minerals by NIR/SWIR microscopy and microthermometry and synchrotron radiation X-ray fluorescence: *Applied Geochemistry*, v. 21, p. 813–819.

Thompson, J.F.H., Sillitoe, R.H., Baker, T., Lang, J.R., and Mortensen, J.K., 1999, Intrusion-related gold deposits associated with tungsten-tin provinces: *Mineralium Deposita*, v. 34, p. 323–334.

APPENDICES

Appendix A: Sample Locations

Sample	Zone	Description	Easting*	Northing*	Occurrence	Depth
FK-005	Wolf Skarn	Garnet-diopside skarn in silicified Hyland Group	463048	7100995	MT08-006	32.70 m
FK-007	Wolf Skarn	Garnet-diopside skarn in silicified Hyland Group	463048	7100995	MT08-006	40.05 m
FK-024	Shamrock	Massive arsenopyrite and scorodite vein.	462468	7102090	DG10-377C	6.96 m
FK-025	Shamrock	Massive arsenopyrite and pyrite vein.	462468	7102090	DG10-377C	9.10 m
FK-036	Shamrock	Massive arsenopyrite and pyrite vein in altered granodiorite.	462468	7102090	DG10-377C	33.83 m
FK-051	Shamrock	Arsenopyrite over-printing quartz vein in altered granodiorite.	462468	7102090	DG10-377C	104.98 m
FK-066	Shamrock	Arsenopyrite and pyrite over-printing quartz veins in altered granodiorite.	462468	7102090	DG10-377C	199.70 m
FK-091	Eagle	Quartz, carbonate, chlorite, pyrrhotite vein over-printing quartz vein in altered and fresh granodiorite.	460178	7099551	DG10-405C	136.93 m
FK-093	Eagle	Quartz, pyrrhotite vein with k-spar alteration selvages in fresh granodiorite.	460178	7099551	DG10-405C	143.14 m
FK-096	Eagle	Quartz, pyrrhotite vein with k-spar alteration selvages which cross-cuts mafic enclave in fresh granodiorite.	460178	7099551	DG10-405C	164.85 m
FK-097	Eagle	Quartz, pyrrhotite veins in sericitized granodiorite.	460178	7099551	DG10-405C	164.97 m
FK-099	Eagle	Quartz, chlorite, carbonate, pyrrhotite vein with extensive alteration selvages in fresh granodiorite.	460178	7099551	DG10-405C	168.50 m
FK-105	Eagle	Quartz, chlorite, pyrrhotite vein with quartz and k-spar alteration selvages in fresh granodiorite.	460178	7099551	DG10-405C	185.82 m
FK-127	Eagle	Quartz, chlorite, pyrrhotite vein with ankerite, carbonate, k-spar alteration selvages over-printing mafic enclave in fresh granodiorite.	460135	7099412	DG10-409C	71.04 m
FK-144	Eagle	Quartz, pyrrhotite vein with albite alteration selvages in fresh granodiorite.	460135	7099412	DG10-409C	167.42 m

Sample	Zone	Description	Easting*	Northing*	Occurrence	Depth
FK-146	Eagle	Quartz, chlorite, carbonate, pyrrhotite vein in fresh granodiorite.	460135	7099412	DG10-409C	173.24 m
FK-184	Eagle	Massive arsenopyrite and pyrite vein.	460027	7099527	DG10-419C	114.86 m
FK-192	Eagle	Quartz, chlorite, pyrrhotite vein in chloritized granodiorite.	460027	7099527	DG10-419C	140.31 m
FK-223	Olive	Chlorite, pyrrhotite vein in silicified granodiorite.	461745	7101567	DG10-373C	69.19 m
FK-226	Olive	Disseminated arsenopyrite clusters in altered granodiorite.	461745	7101567	DG10-373C	80.33 m
FK-227	Olive	Disseminated arsenopyrite clusters in altered granodiorite.	461745	7101567	DG10-373C	81.00 m
FK-243	Olive	Quartz, pyrite in clay altered granodiorite.	461745	7101567	DG10-373C	148.72 m
FK-244	Olive	Quartz, K-spar, pyrite, pyrrhotite vein in sericitized, chloritized granodiorite.	461745	7101567	DG10-373C	149.27 m
FK-246	Olive	Pyrite vein in clay altered granodiorite.	461745	7101567	DG10-373C	160.60 m
FK-258	Olive	Pyrite vein in clay altered granodiorite.	461745	7101567	DG10-373C	188.76 m
FK-262	Olive	Pyrite vein in clay altered granodiorite.	461745	7101567	DG10-373C	194.75 m
FK-285	Olive	Massive arsenopyrite vein.	461745	7101567	DG10-373C	277.53 m
FK-313	Eagle	Quartz, pyrrhotite vein with K-Spar alteration selvages in silicified granodiorite.	459432	7099677	DG11-435C	210.78 m
FK-314	Eagle	Quartz, chlorite, pyrrhotite, pyrite vein in fresh granodiorite.	459432	7099677	DG11-435C	212.80 m
FK-315A	Eagle	Quartz, calcite, pyrrhotite, pyrite, arsenopyrite vein in fresh granodiorite.	459432	7099677	DG11-435C	214.28 m
FK-321	Eagle	Quartz, K-Spar, pyrrhotite, chalcopyrite, sphalerite vein with chlorite, quartz alteration selvages in fresh granodiorite.	459432	7099677	DG11-435C	235.81 m
FK-326	Eagle	Quartz, chlorite, pyrrhotite, pyrite vein in fresh granodiorite.	459432	7099677	DG11-435C	264.86 m
FK-346	Eagle	Quartz, pyrite, pyrrhotite, arsenopyrite vein in sericitized granodiorite.	459432	7099677	DG11-435C	425.21 m

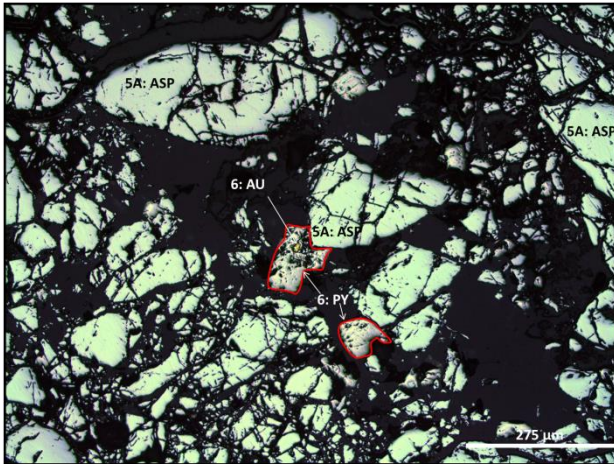
Sample	Zone	Description	Easting*	Northing*	Occurrence	Depth
FK-348	Eagle	Quartz, pyrrhotite, pyrite, arsenopyrite veins in fresh granodiorite.	459432	7099677	DG11-435C	440.52 m
FK-358	Eagle	Pyrrhotite in hornfelsed Hyland Group.	460083	7099553	DG10-407C	45.50 m
FK-359	Shamrock	Vuggy quartz, pyrrhotite vein in Hyland Group.	462136	7102068	DG11-465C	172.52 m
FK-360	Shamrock	Quartz, clinozoisite vein in fresh granodiorite.	463207	7102308	DG11-463C	163.35 m
FK-TH12-02	Henderson	Quartz, scorodite vein in Hyland Group.	460402	7101085	Outcrop	Surface
FK-TH12-03	Haggart Creek	Massive pyrite vein in Hyland Group.	458145	7100551	Outcrop	Surface
FK-TH12-10	Wolf Skarn	Garnet-diopside skarn.	463325	7100348	Outcrop	Surface
FK-TH12-29	Rex-Peso	Sphalerite, pyrite, jamesonite vein in phyllitic quartzite in Hyland Group.	455957	7097232	11RP-DH10	108.77m
FK-TH12-36	Haggart Creek	Pyrite in phyllite in Hyland Group.	458145	7100522	Outcrop	Surface
FK-TH12-39	Olive	Scorodite vein in oxidized granodiorite.	461344	7101092	Outcrop	Surface
FK-TH12-40	Olive	Scorodite vein in oxidized granodiorite.	461344	7101092	Outcrop	Surface
FK-TH12-41	Eagle	Quartz, arsenopyrite, scorodite vein in oxidized granodiorite.	460207	7100120	Outcrop	Surface
FK-TH12-49	Shamrock	Pyrite, calcite vein in altered granodiorite.	459694	7099729	DG12-493C	351.00 m
FK-TH12-52	Henderson	Quartz, scorodite vein in Hyland Group.	460402	7101085	Outcrop	Surface
FK-TH12-56	Carscallen	Massive arsenopyrite and scorodite vein.	462279	7101968	Outcrop	Surface
FK-TH12-60	Carscallen	Massive arsenopyrite and scorodite vein.	462279	7101968	Outcrop	Surface
FK-TH12-61	Potato Hills	Scorodite vein hosted in Hyland Group.	465970	7102570	Outcrop	Surface
N821751	Potato Hills	Scorodite vein hosted in Hyland Group.	465970	7102570	Outcrop	Surface
N821752	Eagle	Quartz, arsenopyrite, scorodite vein in oxidized granodiorite.	460207	7100120	Outcrop	Surface
N821753	Potato Hills	Scorodite vein hosted in Hyland Group.	465970	7102570	Outcrop	Surface
N821754	Potato Hills	Scorodite vein hosted in Hyland Group.	464121	7102652	Outcrop	Surface
N821755	Henderson	Quartz, scorodite vein in Hyland Group.	460402	7101085	Outcrop	Surface
N821757	Carscallen	Massive arsenopyrite and scorodite vein.	462279	7101968	Outcrop	Surface

Sample	Zone	Description	Easting*	Northing*	Occurrence	Depth
N821758	Shamrock	Quartz, arsenopyrite vein in altered granodiorite.	462536	7102108	Outcrop	Surface
N821759	Shamrock	Massive arsenopyrite and scorodite vein.	462279	7101968	Outcrop	Surface
N821760	Olive	Scorodite vein in oxidized granodiorite.	461760	7101417	Outcrop	Surface
N821761	Olive	Scorodite vein in oxidized granodiorite.	461759	7101530	Outcrop	Surface
N821762	Olive	Scorodite vein in oxidized granodiorite.	461759	7101530	Outcrop	Surface
N821763	Rex-Peso	Quartz, scorodite vein in Hyland Group.	452637	7098513	Outcrop	Surface
PH-D	Potato Hills	Hypabyssal dyke cross-cutting main stock.	464121	7102652	Outcrop	Surface
RP-GND-3	Rex-Peso	Andesite dyke.	454857	7099540	Outcrop	Surface
RP-GND-2	Rex-Peso	Dacite dyke.	454871	7099466	Outcrop	Surface
IO-016545	Eagle	Hypabyssal dyke cross-cutting main stock.	459188	7099559	DG10-369C	125.00 m
M 384929-31	Eagle	Hypabyssal dyke cross-cutting main stock.	459349	7099400	DG12-490C	60.00 m
M 395914	Eagle	Hypabyssal dyke cross-cutting main stock.	459550	7099300	DG12-518C	113.70 m
Eagle 6-1	Eagle	Porphyritic granodiorite.	460182	7099351	Outcrop	Surface
Eagle 6-2	Eagle	Porphyritic granodiorite.	460182	7099351	Outcrop	Surface

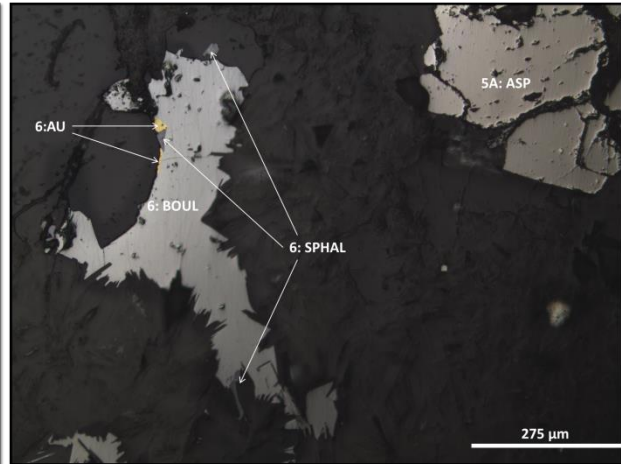
*co-ordinates are quoted in NAD83

Appendix B: Mineralization Textures Library

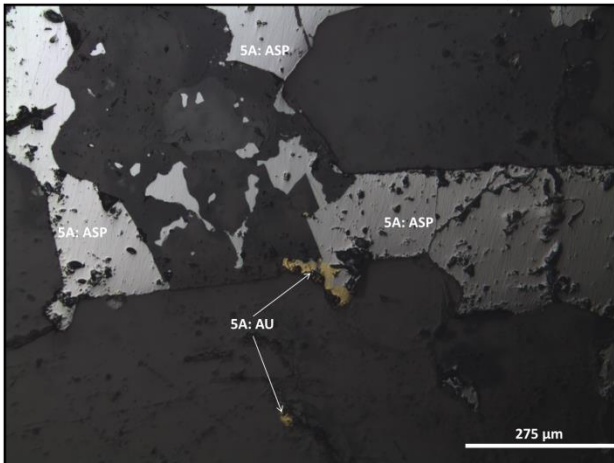
B.1 Native Gold Textures



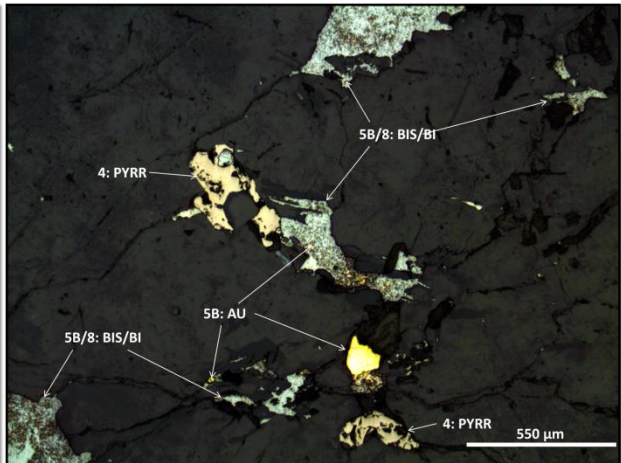
FK-024 (DDH DG10-377C, 6.96 m, Shamrock zone)



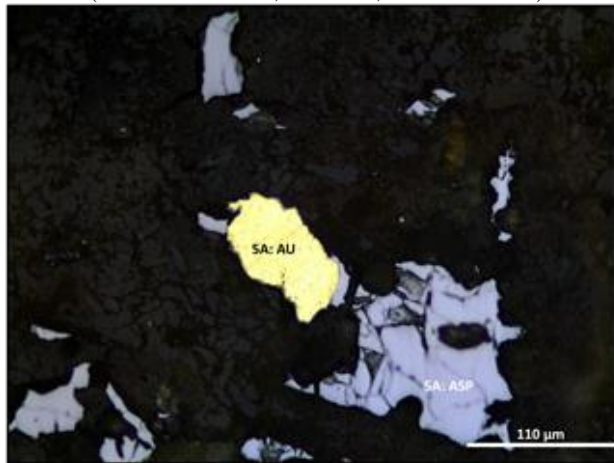
FK-066 (DDH DG10-377C, 199.70 m, Shamrock zone)



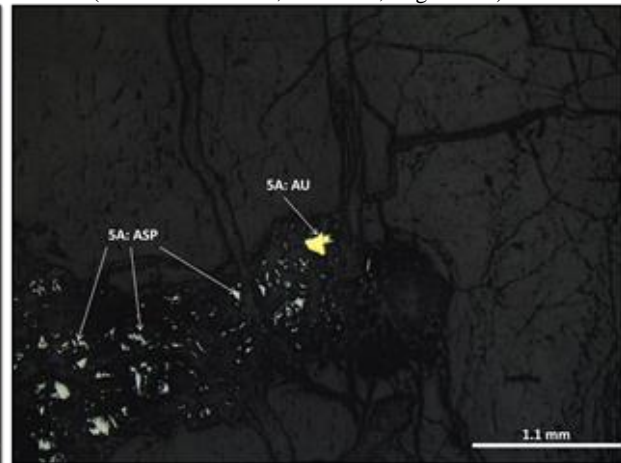
FK-066 (DDH DG10-377C, 199.70 m, Shamrock zone)



FK-144 (DDH DG10-409C, 167.42 m, Eagle zone)

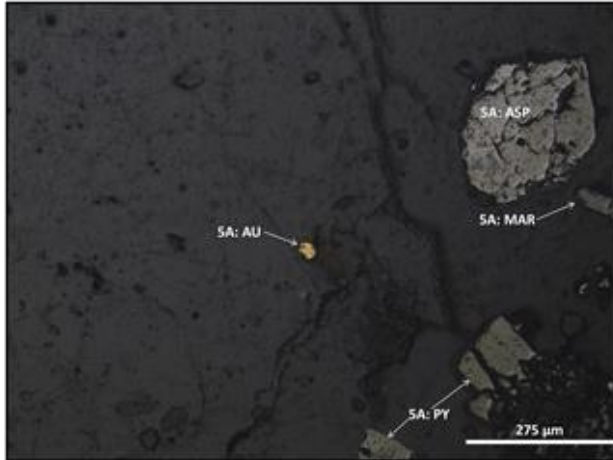


FK-TH12-02 (NAD83 460402 E 7101085N, Henderson zone)

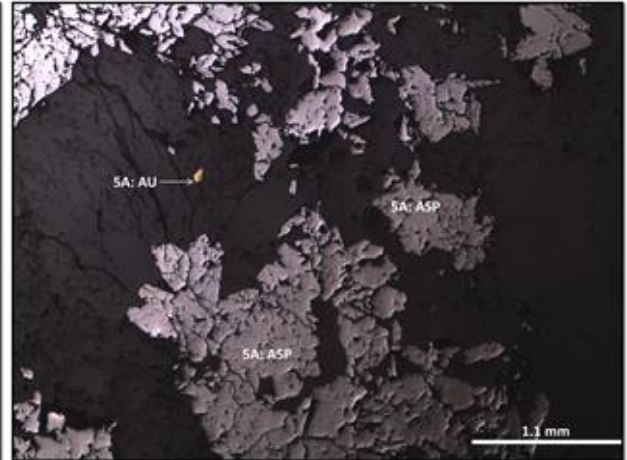


FK-TH12-02 (NAD83 460402 E 7101085N, Henderson zone)

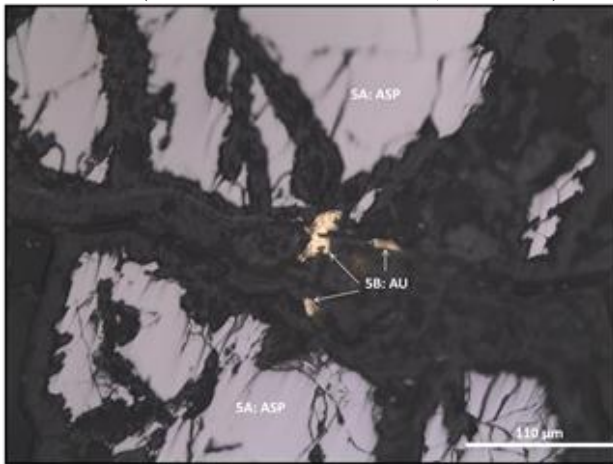
Mineral Abbreviations: ASP = Arsenopyrite, AU = Gold, BI = Bismuth, BIS = Bismuthinite, BOUL = Boulangerite, PYRR = Pyrrhotite, SPHAL = Sphalerite.



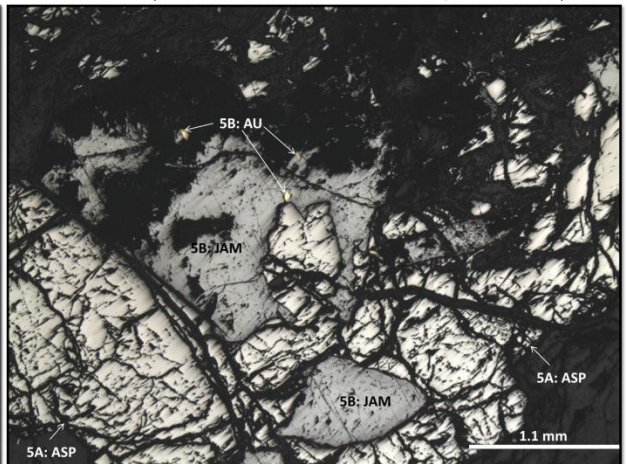
FK-TH12-39 (NAD83 461344 E 7101092 N, Olive zone)



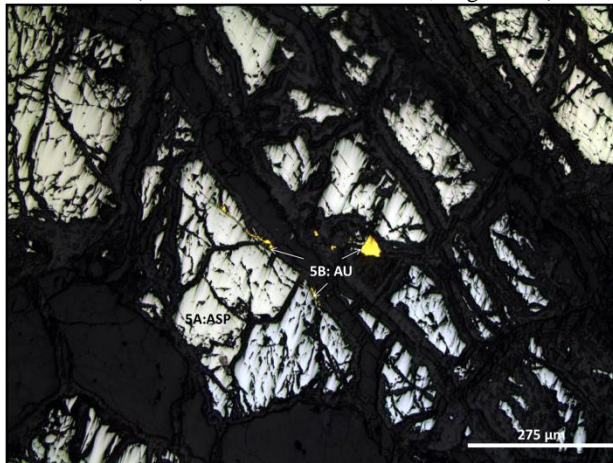
FK-TH12-40 (NAD83 461344 E 7101092 N, Olive zone)



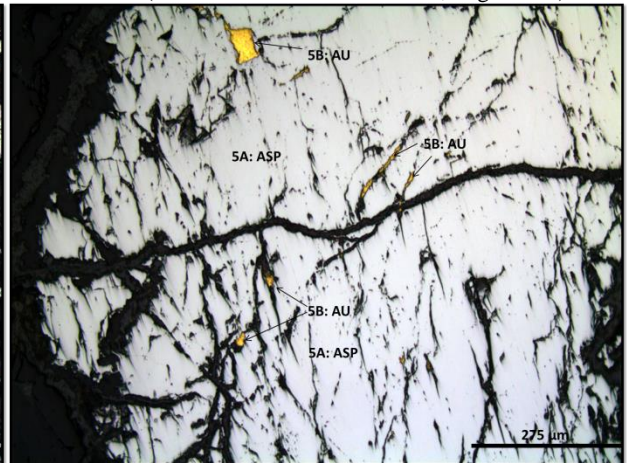
FK-TH12-41 (NAD83 460207 E 7100120 N, Eagle zone)



FK-TH12-41 (NAD83 460207 E 7100120 N, Eagle zone)

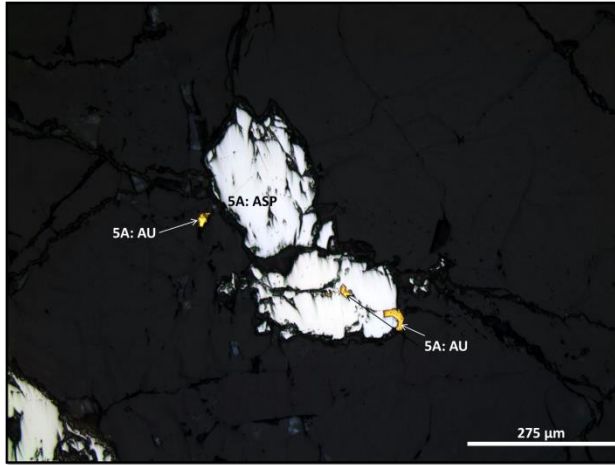


FK-TH12-41 (NAD83 460207 E 7100120 N, Eagle zone)

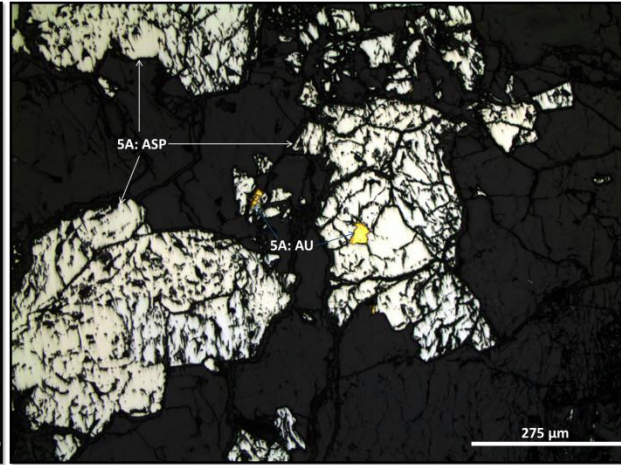


FK-TH12-41 (NAD83 460207 E 7100120 N, Eagle zone)

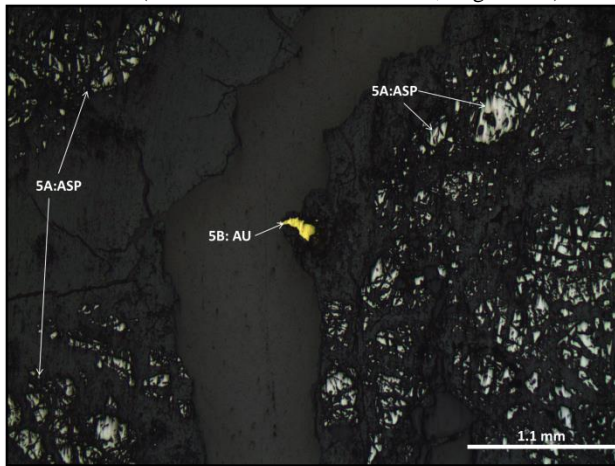
Mineral Abbreviations: ASP = Arsenopyrite, AU = Gold, JAM = Jamesonite, MAR = Marcasite, PY = Pyrite.



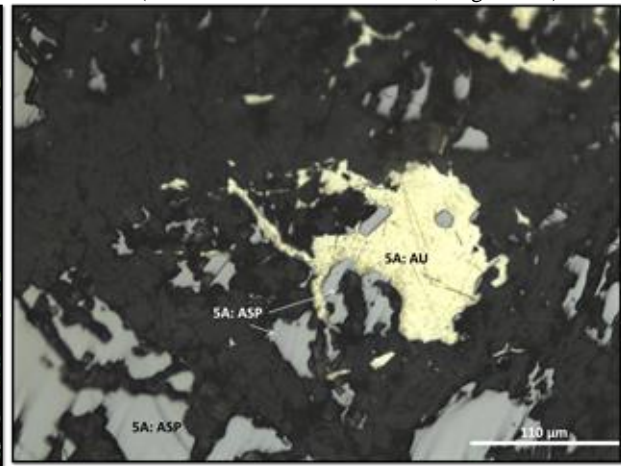
FK-TH12-41 (NAD83 460207 E 7100120 N, Eagle zone)



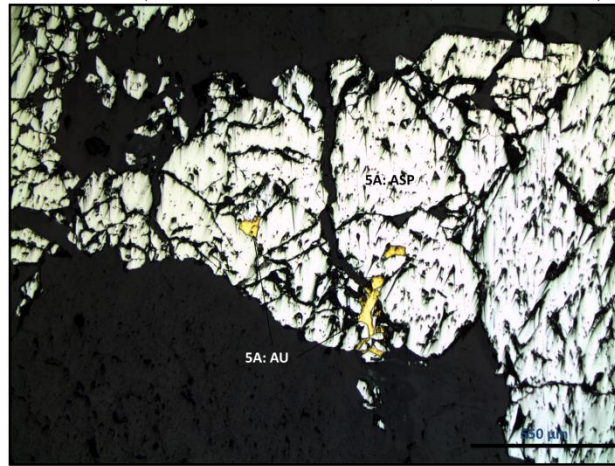
FK-TH12-41(NAD83 460207 E 7100120 N, Eagle zone)



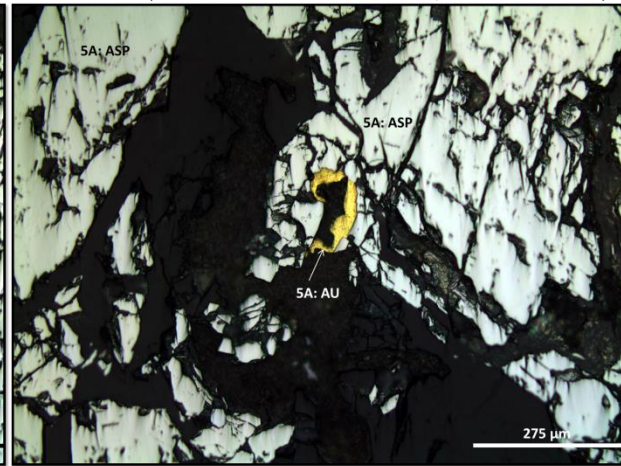
FK-TH12-52 (NAD83 460402 E 7101085N, Henderson zone)



FK-TH12-52 (NAD83 460402 E 7101085N, Henderson zone)



FK-TH12-56 (NAD83 462279 E 7101968 N, Shamrock zone)



FK-TH12-56 (NAD83 462279 E 7101968 N, Shamrock zone)

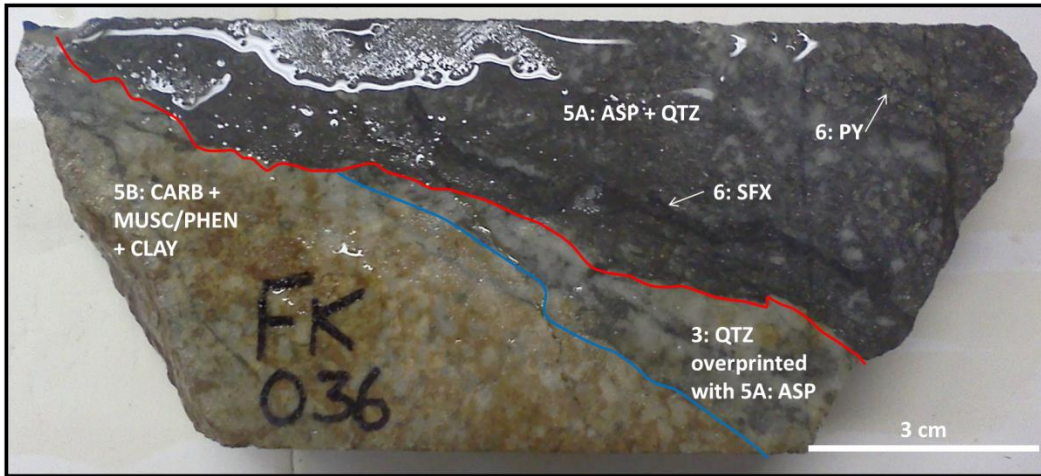
Mineral Abbreviations: ASP = Arsenopyrite, AU = Gold.

B.2 Paragenetic Textures

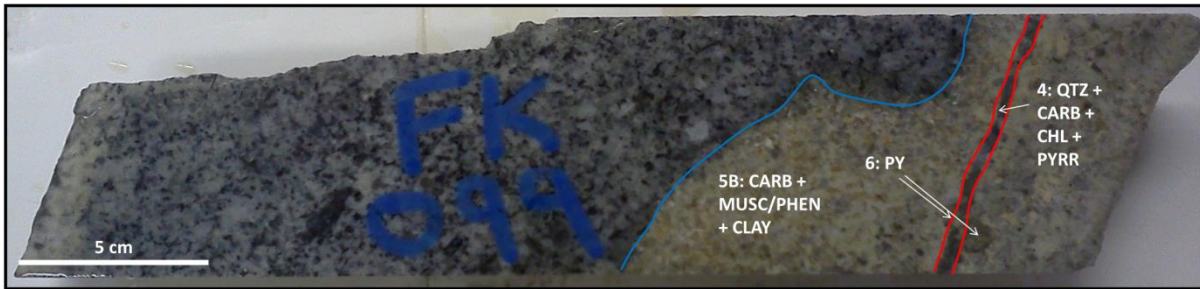
A: Core Photographs

B: Thin Section Photomicrographs

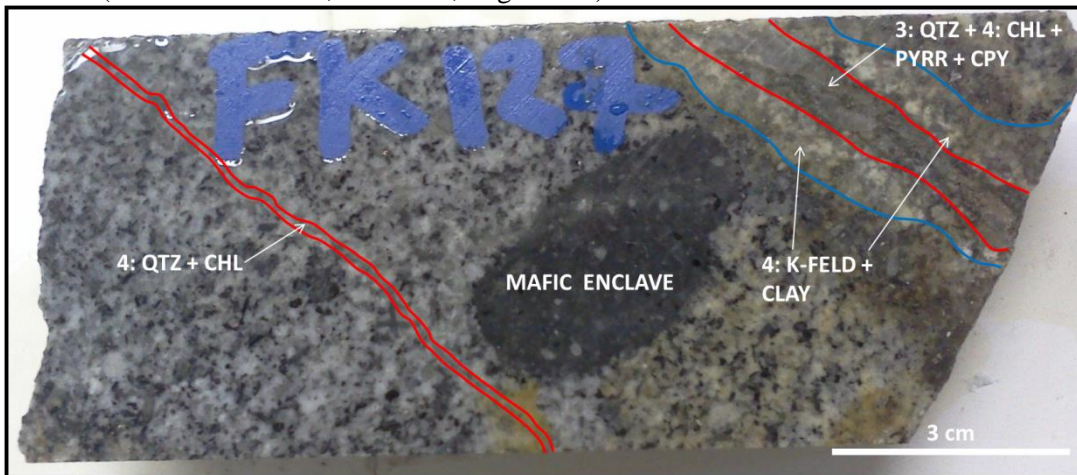
B.2.A: Core Photographs



FK-036 (DDH DG10-377C, 35.00 m, Shamrock zone)

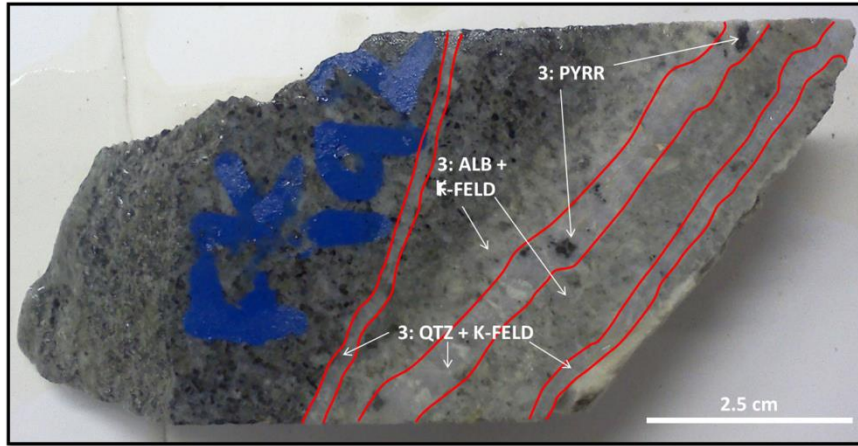


FK-099 (DDH DG10-405C, 168.50 m, Eagle zone)

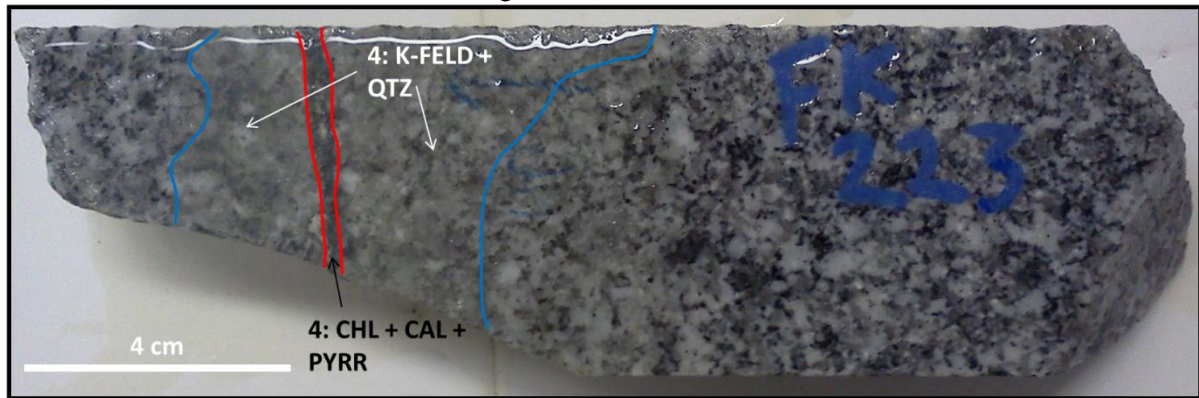


FK-127 (DDH DG10-409C, 71.04 m, Eagle zone)

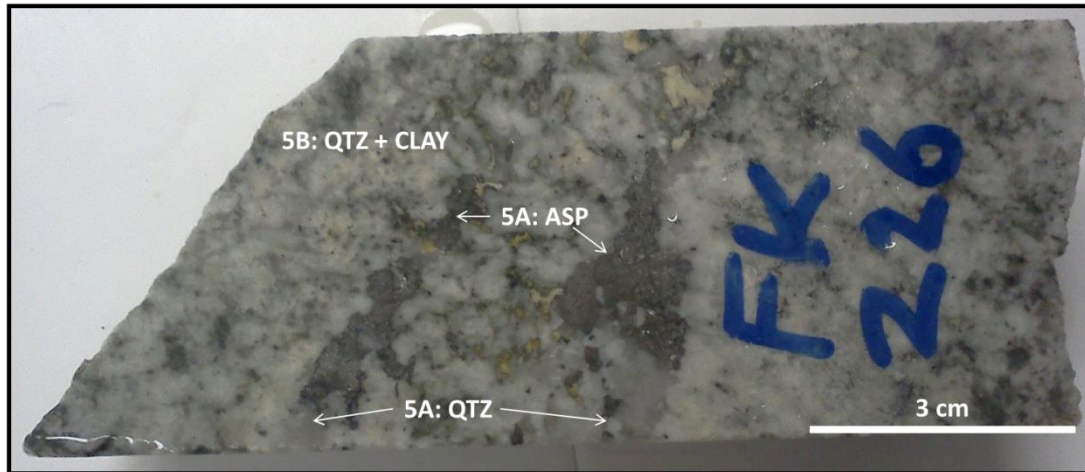
Mineral Abbreviations: ASP = Arsenopyrite, CARB = Carbonate, CHL = Chlorite, CLAY = Dickite, Kaolinite, CPY = Chalcopyrite, K-FELD = Potassium Feldspar, MUSC/PHEN = Muscovite/Phengite, PY = Pyrite, QTZ = Quartz, SFX = Sulfosalts.



FK-192 (DDH DG10-419C, 140.31 m, Eagle zone)

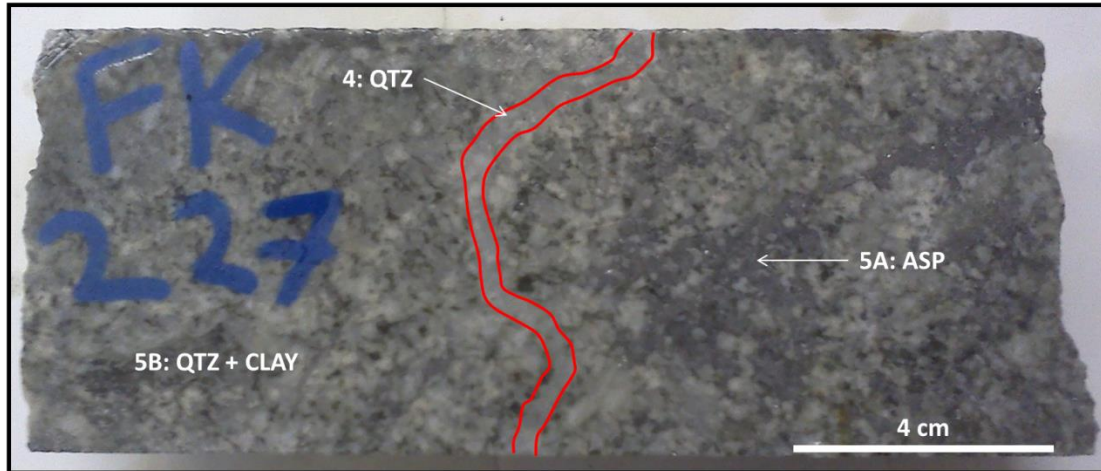


FK-223(DDH DG10-373C, 69.19 m, Olive zone)

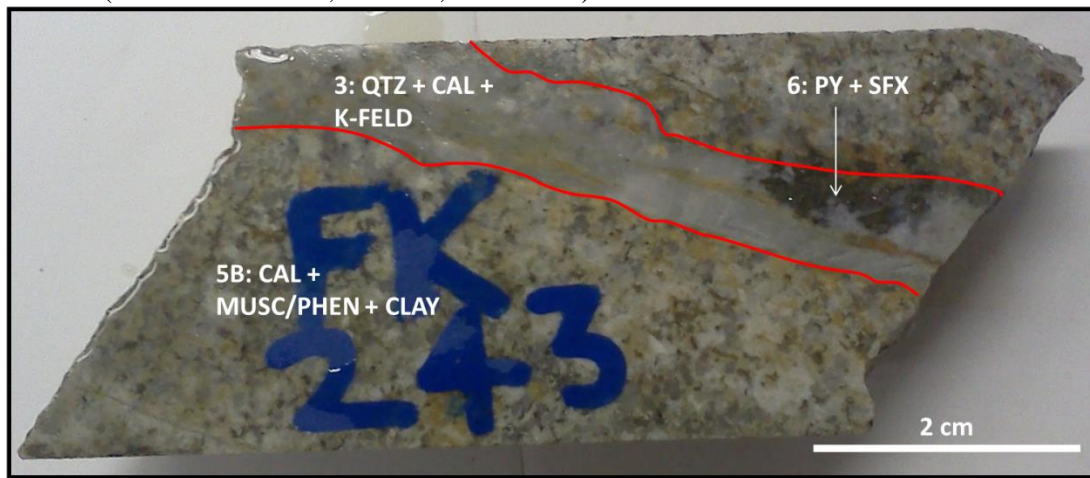


FK-226 (DDH DG10-373 C, 80.33 m, Olive zone)

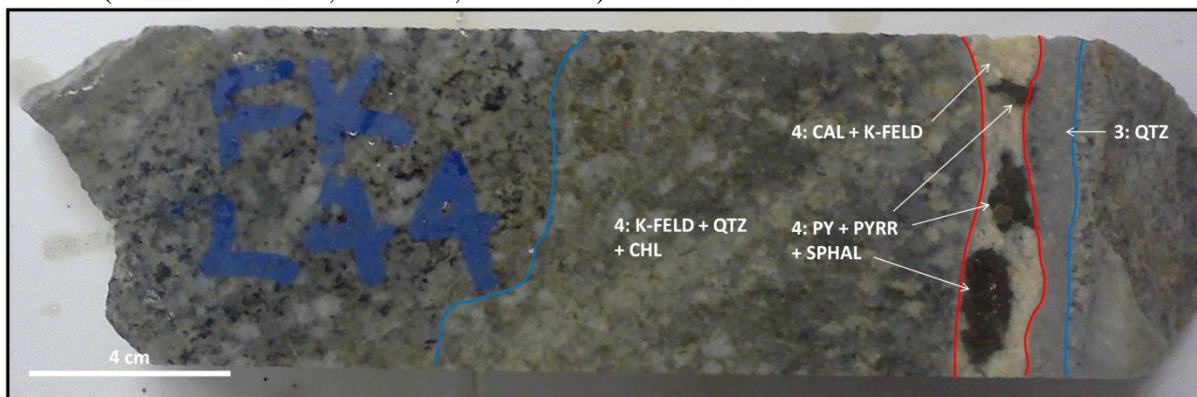
Mineral Abbreviations: ALB = Albite, ASP = Arsenopyrite, CAL = Calcite, CHL = Chlorite, CLAY = Dickite, Kaolinite, K-FELD = Potassium Feldspar, PYRR = Pyrrhotite, QTZ = Quartz.



FK-227 (DDH DG10-373C, 81.00 m, Olive zone)



FK-243 (DDH DG10-373C, 148.72 m, Olive zone)



FK-244 (DDH DG10-373C, 149.27 m, Olive zone)

Mineral Abbreviations: ASP = Arsenopyrite, CAL = Calcite, CHL = Chlorite, CLAY = Dickite, Kaolinite, K-FELD = Potassium Feldspar, MUSC/PHEN = Muscovite/Phengite, PY = Pyrite, PYRR = Pyrrhotite, QTZ = Quartz, SFX = Sulfosalts, SPHAL = Sphalerite.



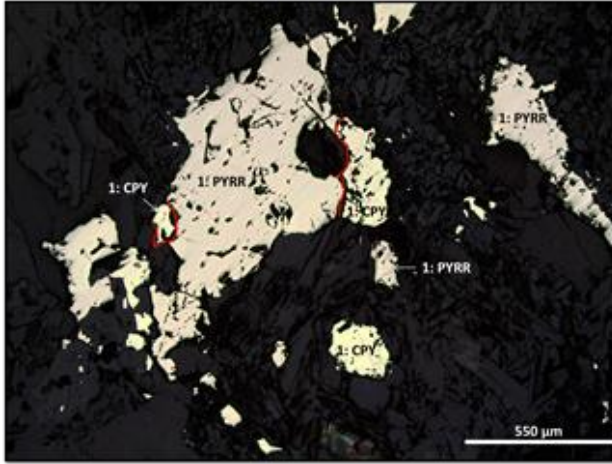
FK-246 (DDH DG10-373C, 160.60 m, Olive zone)



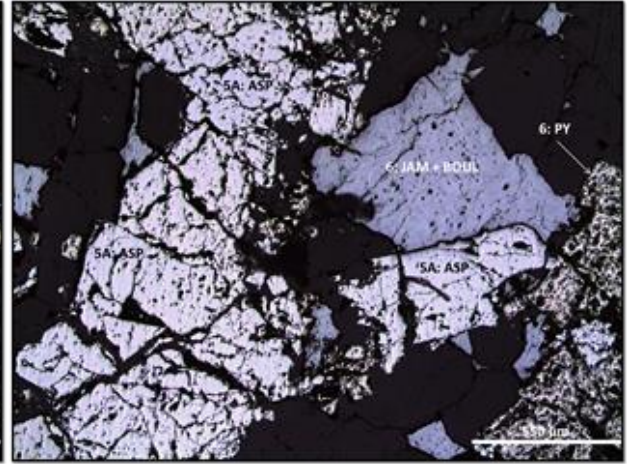
FK-258 (DDH DG10-373C, 188.76 m, Olive zone)

Mineral Abbreviations: CAL = Calcite, CARB = Carbonate, CLAY = Dickite, Kaolinite, MUSC/PHEN = Muscovite/Phengite, PY = Pyrite, QTZ = Quartz, SFX = Sulfosalts.

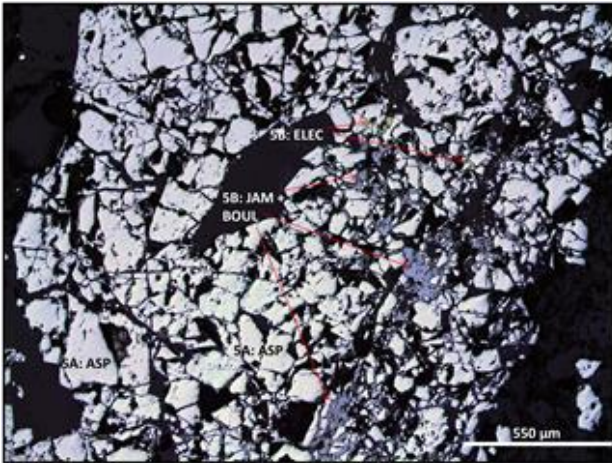
B.2.B: Thin Section Photomicrographs



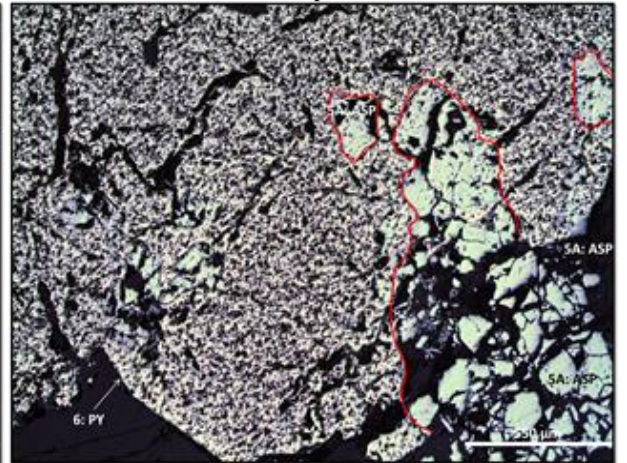
FK-007 (DDH MT08-006, 40.05 m, Wolf zone)



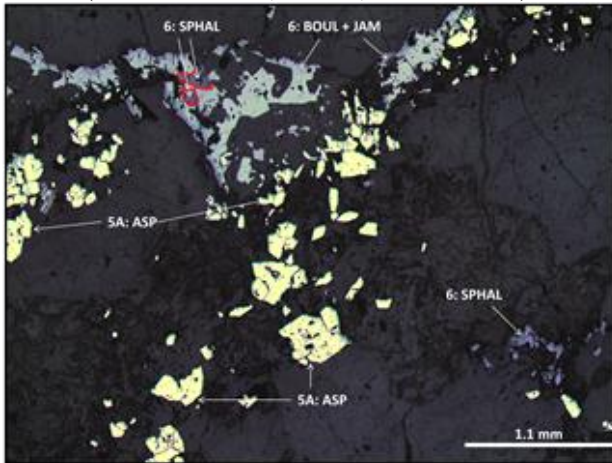
FK-025 (DDH DG10-377C, depth 9.10 m, Shamrock zone)



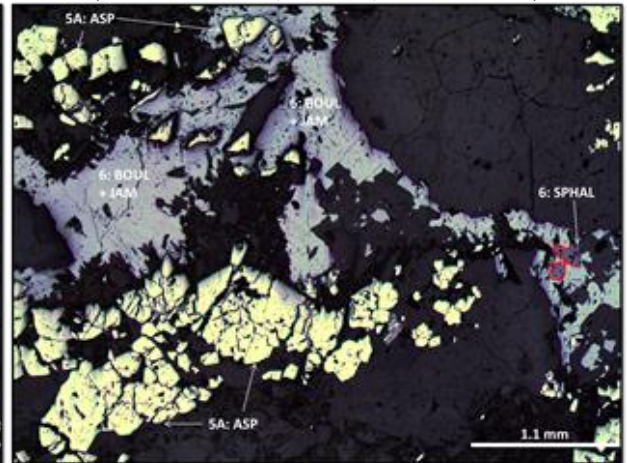
FK-036 (DDH DG10-377C, 33.83 m, Shamrock zone)



FK-066 (DDH DG10-377C, 199.70m, Shamrock zone)



FK-066 (DDH DG10-377C, 199.70m, Shamrock zone)

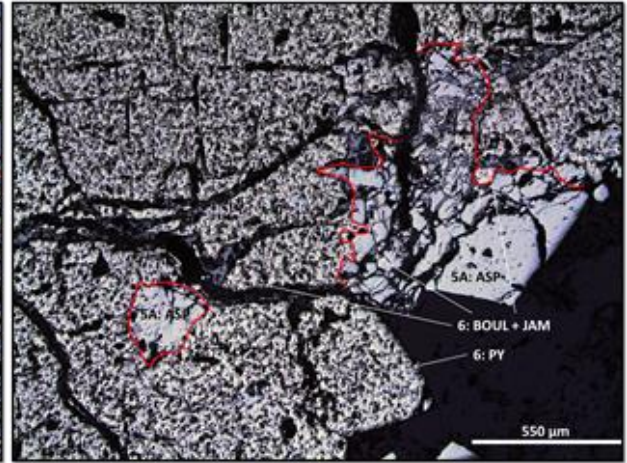


FK-066 (DDH DG10-377C, 199.70m, Shamrock zone)

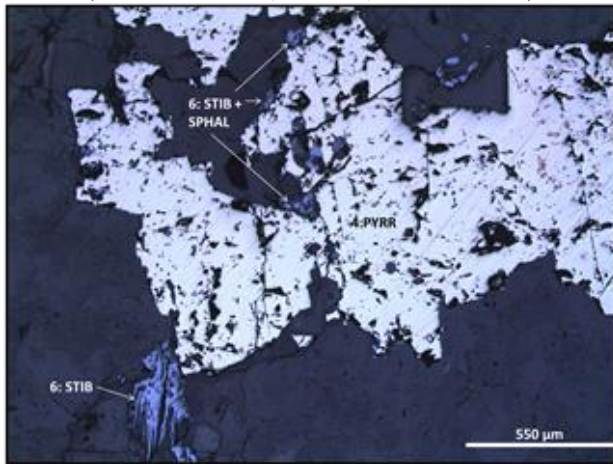
Mineral Abbreviations: ASP = Arsenopyrite, BOUL = Boulangerite, CPY = Chalcopyrite, ELEC = Electrum, JAM = Jamesonite, PY = Pyrite, PYRR = Pyrrhotite, SPHAL = Sphalerite.



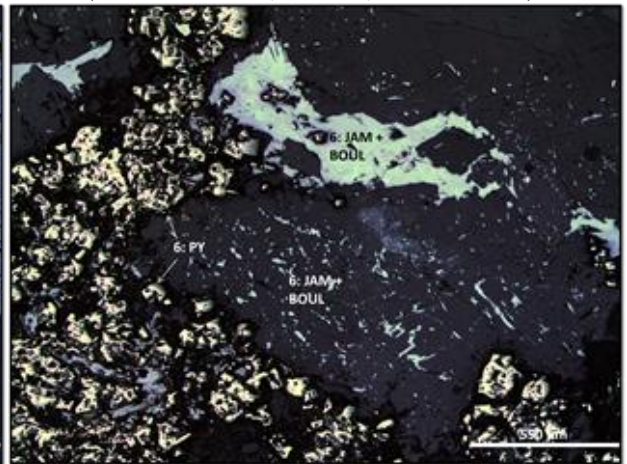
FK-066 (DDH DG10-377C, 199.70m, Shamrock zone)



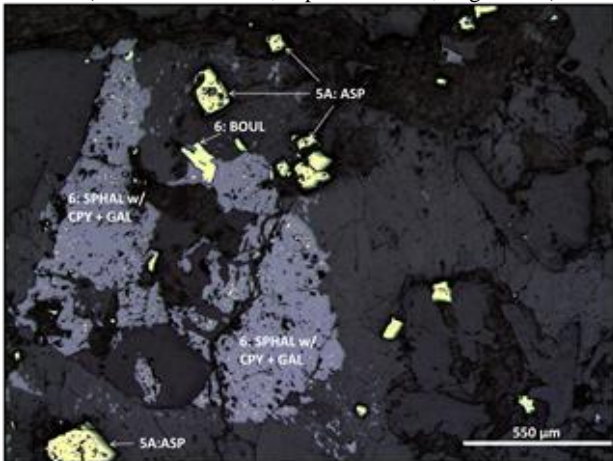
FK-066(DDH DG10-377C, 199.70m, Shamrock zone)



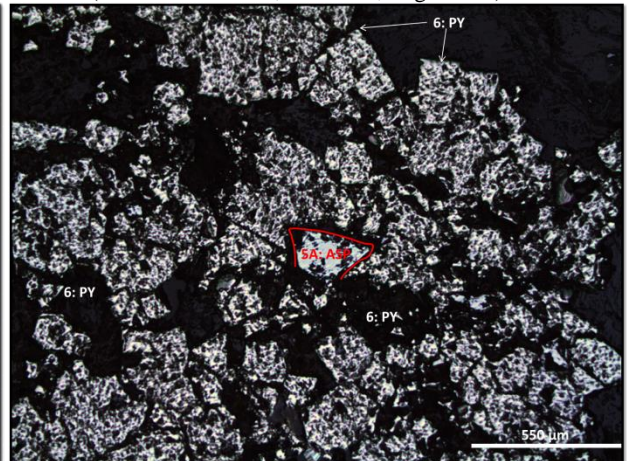
FK-144 (DDH DG10-409C, depth 167.42 m, Eagle zone)



FK-184 (DDH DG10-419C, 114.86 m, Eagle zone)

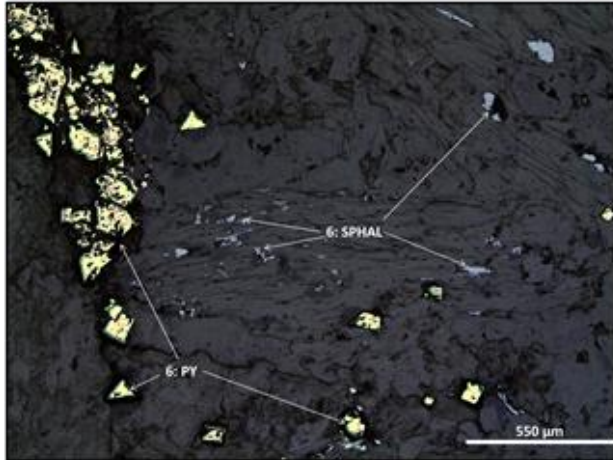


FK-184 (DDH DG10-419C, 114.86 m, Eagle zone)

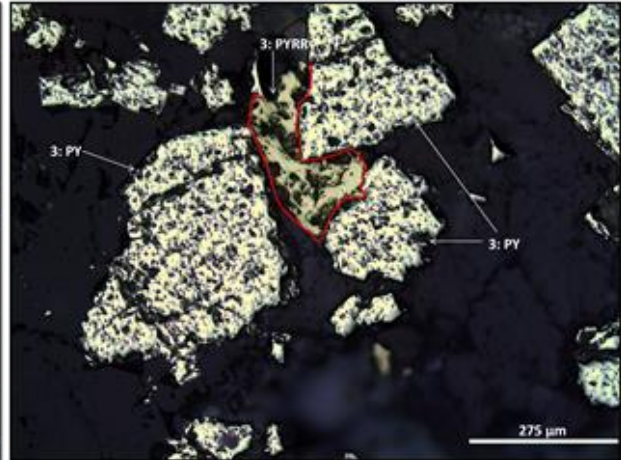


FK-184 (DDH DG10-419C, 114.86 m, Eagle zone)

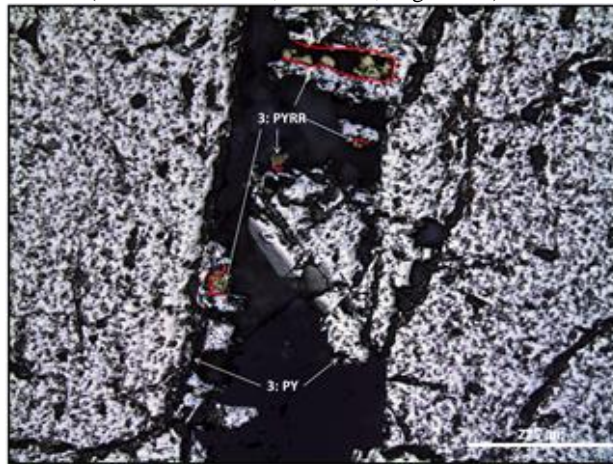
Mineral Abbreviations: ASP = Arsenopyrite, BOUL = Boulangerite, CPY = Chalcopyrite, GAL = Galena, JAM = Jamesonite, PY = Pyrite, SPHAL = Sphalerite, STIB = Stibnite.



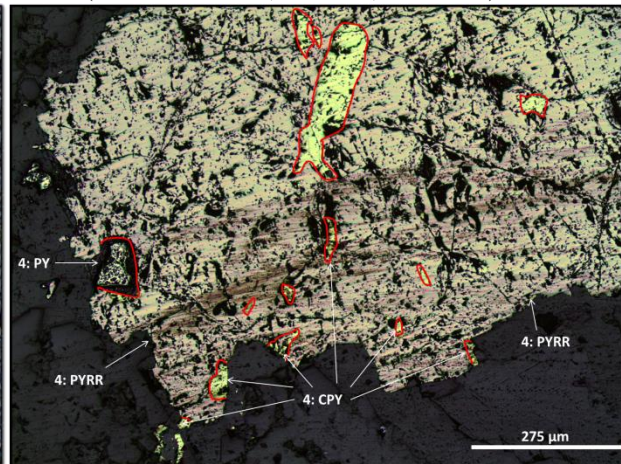
FK-184 (DDH DG10-419C, 114.86 m, Eagle zone)



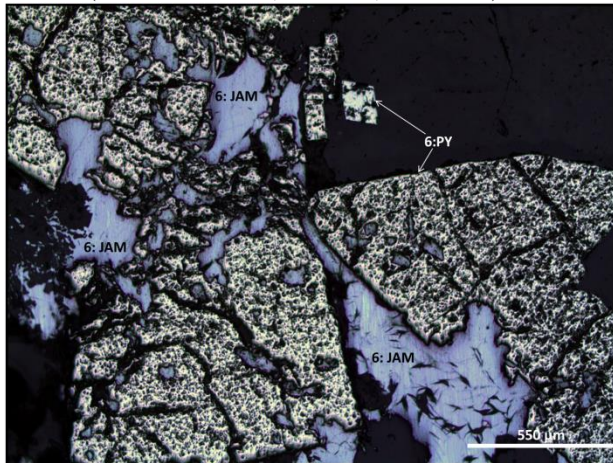
FK-243(DDH DG10-373C, 148.72 m, Olive zone)



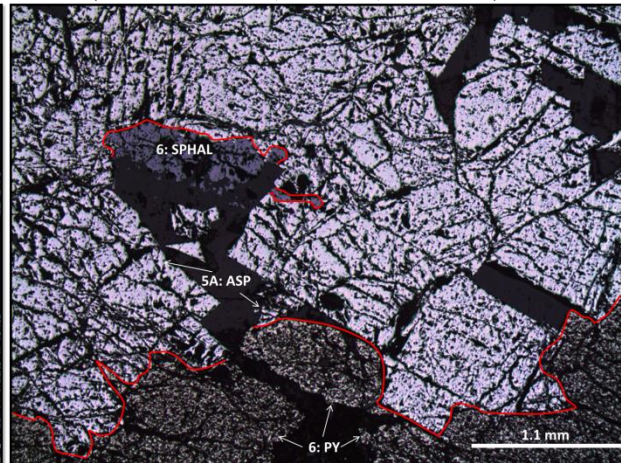
FK-243 (DDH DG10-373C, 148.72 m, Olive zone)



FK-244 (DDH DG10-373C, 149.27 m, Olive zone)

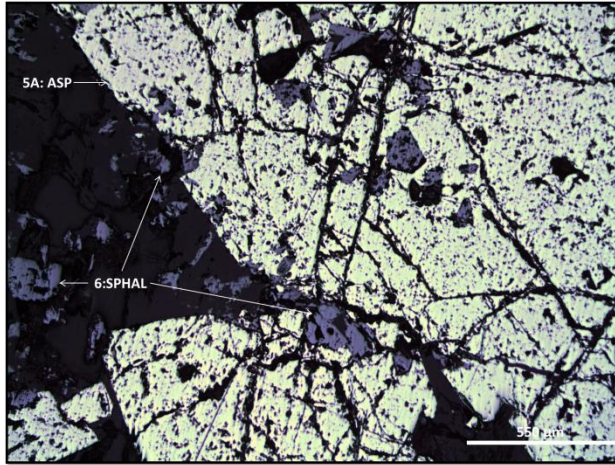


FK-285 (DDH DG10-373C, 277.53 m, Olive zone)

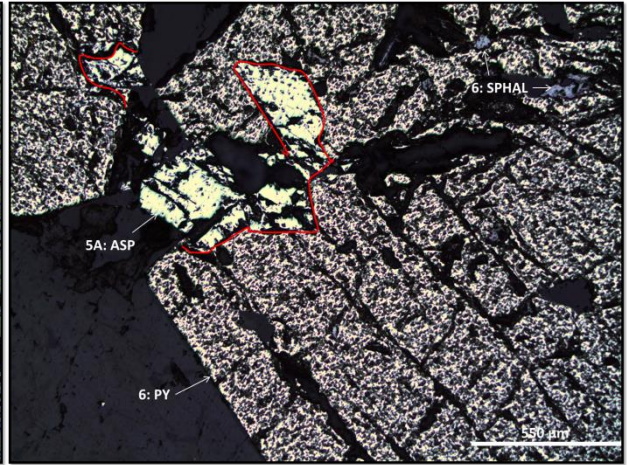


FK-285 (DDH DG10-373C, 277.53 m, Olive zone)

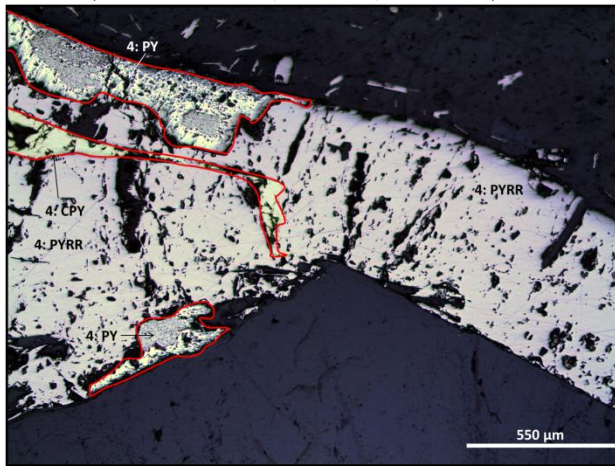
Mineral Abbreviations: ASP = Arsenopyrite, CPY = Chalcopyrite, JAM = Jamesonite, PY = Pyrite, PYRR = Pyrrhotite, SPHAL = Sphalerite.



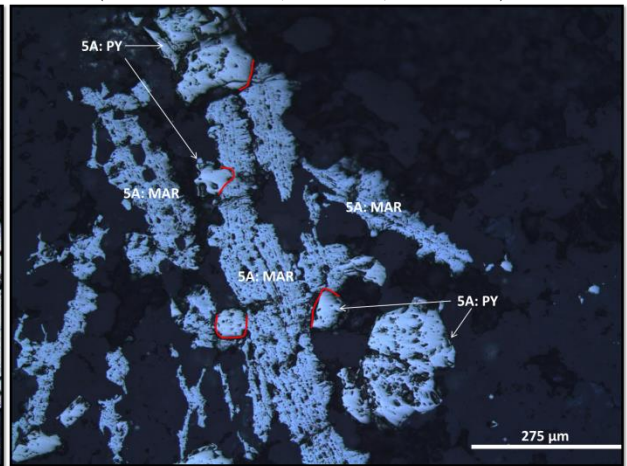
FK-285 (DDH DG10-373C, 277.53 m, Olive zone)



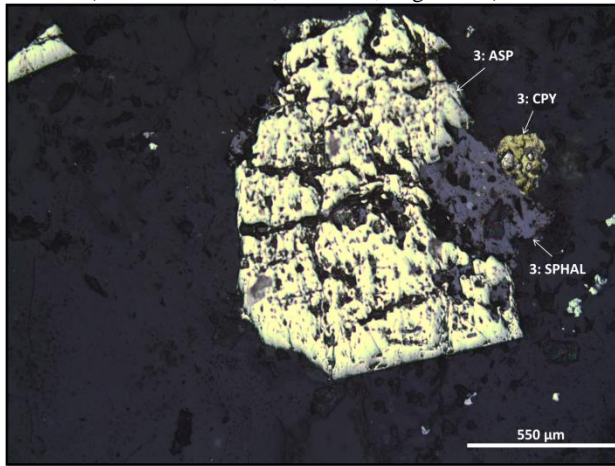
FK-285 (DDH DG10-373C, 277.53 m, Olive zone)



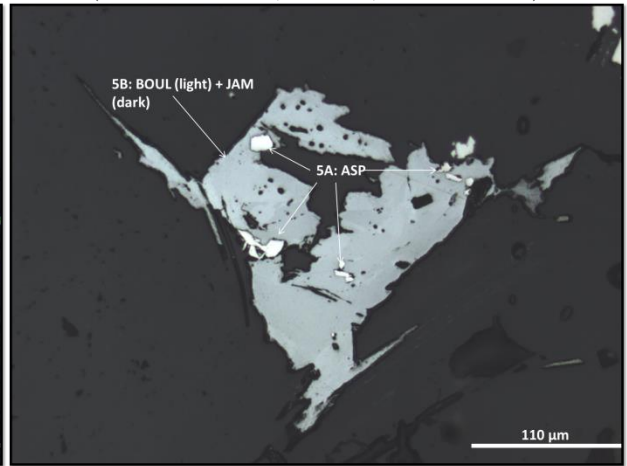
FK-321 (DDH DG11-435C, 235.81 m, Eagle zone)



FK-359 (DDH DG11-465C, 172.52m, Shamrock zone)



FK-359 (DDH DG11-465C, 172.52m, Shamrock zone)



FK-TH12-56 (NAD83 462279 E 7101968 N, Shamrock zone)

Mineral Abbreviations: ASP = Arsenopyrite, BOUL = Boulangerite, CPY = Chalcopyrite, JAM = Jamesonite, MAR = Marcasite, PY = Pyrite, PYRR = Pyrrhotite, SPHAL = Sphalerite.

Appendix C: Limits of Detection for geochemical analyses

C.1 Limits of detection for Chapter 2 Geostatistics and PCA

Element	Package	Lower Limit	Upper Limit	Element	Package	Lower Limit	Upper Limit
Ag	ME-ICP61	0.5 ppm	100 ppm	Mg	ME-ICP61	0.01 %	50 %
	Ag-OG62	1 ppm	1500 ppm	Mn	ME-ICP61	5 ppm	10000 ppm
Al	ME-ICP61	0.01 %	30 %	Mo	ME-ICP61	1 ppm	10000 ppm
As	ME-ICP61	5 ppm	10000 ppm	Na	ME-ICP61	0.01 %	10 %
Au	Au-AA24	0.005 ppm	10 ppm	Ni	ME-ICP61	1 ppm	10000 ppm
	Au-GRA22	0.5 ppm	1000 ppm	P	ME-ICP61	10 ppm	10000 ppm
Ba	ME-ICP61	10 ppm	10000 ppm	Pb	ME-ICP61	2 ppm	10000 ppm
Be	ME-ICP61	0.5 ppm	1000 ppm	S	ME-ICP61	0.01 %	10 %
Bi	ME-ICP61	2 ppm	10000 ppm	Sb	ME-ICP61	5 ppm	10000 ppm
Ca	ME-ICP61	0.01 %	50 %	Sc	ME-ICP61	1 ppm	10000 ppm
Cd	ME-ICP61	0.5 ppm	500 ppm	Sr	ME-ICP61	1 ppm	10000 ppm
Co	ME-ICP61	1 ppm	10000 ppm	Th	ME-ICP61	20 ppm	10000 ppm
Cr	ME-ICP61	1 ppm	10000 ppm	Tl	ME-ICP61	10 ppm	10000 ppm
Cu	ME-ICP61	1 ppm	10000 ppm	U	ME-ICP61	10 ppm	10000 ppm
Fe	ME-ICP61	0.01 %	50 %	V	ME-ICP61	1 ppm	10000 ppm
Ga	ME-ICP61	10 ppm	10000 ppm	W	ME-ICP61	10 ppm	10000 ppm
K	ME-ICP61	0.01 %	10 %	Zn	ME-ICP61	2 ppm	10000 ppm
La	ME-ICP61	10 ppm	10000 ppm				

C.2 Limits of detection for Chapter 4 whole rock geochemistry

The 4Litho package of ActLabs, Ancaster, ON was used to determine the whole rock geochemistry of samples used in Chapter 4. Analyses were obtained using Inductively Coupled Plasma – Mass Spectrometry (ICP-MS).

Element	Lower Detection Limit	Element	Lower Detection Limit
Ag	500 ppb	Na	0.01%
Al	0.01%	Nb	1 ppm
As	5 ppm	Nd	100 ppb
Ba	3 ppm	Ni	20 ppm
Be	1 ppm	P	0.01%
Bi	40 ppb	Pb	5 ppm
Ca	0.01%	Pr	50 ppb
Ce	100 ppb	Rb	2 ppm
Co	1 ppm	Sb	500 ppb
Cr	20 ppm	Sc	1 ppm
Cs	500 ppb	Si	0.01%
Cu	10 ppm	Sm	100 ppb
Dy	100 ppb	Sn	1 ppm
Er	100 ppb	Sr	2 ppm
Eu	50 ppb	Ta	100 ppb
Fe	0.01%	Tb	100 ppb
Ga	1 ppm	Th	100 ppb
Gd	100 ppb	Ti	0.001%
Ge	1 ppm	Tl	100 ppb
Hf	200 ppb	Tm	50 ppb
Ho	100 ppb	U	100 ppb
In	200 ppb	V	5 ppm
K	0.01%	W	1 ppm
La	100 ppb	Y	2 ppm
Lu	40 ppb	Yb	100 ppb
Mg	0.01%	Zn	30 ppm
Mn	0.001%	Zr	4 ppm
Mo	2 ppm		

*Upper detection limit not stated.

Appendix D: Arsenopyrite EPMA Data

D.1 EPMA Arsenopyrite Data

Sample	As (%)	S (%)	Sb (%)	Fe (%)	Bi (%)	Te (%)	Co (%)	Ni (%)	Total
asp200	44.24	21.43	0.03	35.35	0.01	0.00	0.01	0.01	101.08
FK036-asy2-1	44.25	21.43	0.07	34.73	0.03	0.00	0.01	0.01	100.53
FK-036-asy2-2	43.37	21.49	0.06	34.82	0.03	0.01	0.01	0.00	99.78
FK-036-asy2-3	44.97	20.74	0.03	34.30	0.01	0.00	0.00	0.01	100.07
FK-036-asy2-4	41.80	22.72	0.03	34.99	0.00	0.00	0.00	0.01	99.54
FK-036-asy2-5	44.33	21.28	0.04	34.82	0.00	0.00	0.00	0.01	100.49
FK-036-asy3-1	43.69	21.35	0.04	34.88	0.00	0.00	0.01	0.00	99.97
FK-036-asy3-2	44.10	21.23	0.05	34.57	0.00	0.00	0.00	0.00	99.95
FK-036-asy3-3	42.88	21.84	0.12	34.90	0.00	0.00	0.00	0.01	99.75
FK-TH12-56-asy1-1	46.23	19.70	0.03	34.42	0.00	0.00	0.02	0.00	100.41
FK-TH12-56-asy1-2	45.10	20.40	0.01	34.31	0.00	0.01	0.00	0.00	99.84
FK-TH12-56-asy1-3	46.14	19.89	0.04	34.39	0.00	0.00	0.00	0.02	100.49
FK-TH12-56-asy1-4	45.74	19.80	0.00	33.96	0.03	0.00	0.01	0.00	99.54
FK-TH12-56-asy1-5	44.52	20.85	0.01	34.86	0.01	0.00	0.00	0.00	100.26
FK-TH12-56-asy1-6	46.33	19.83	0.03	34.33	0.00	0.00	0.00	0.00	100.52
FK-TH12-56-asy2-1	45.93	20.05	0.00	34.75	0.00	0.00	0.00	0.01	100.74
FK-TH12-56-asy2-2	45.52	20.23	0.04	34.55	0.00	0.01	0.01	0.02	100.37
FK-TH12-56-asy2-3	45.67	20.51	0.02	34.39	0.02	0.00	0.04	0.00	100.64
asy200	44.01	21.09	0.03	34.80	0.00	0.00	0.00	0.00	99.92
FK-313-asy1-1	47.08	18.94	0.02	34.36	0.00	0.00	0.08	0.02	100.50
FK-313-asy1-2	48.12	18.34	0.02	33.93	0.00	0.01	0.03	0.05	100.49
FK-313-asy1-3	48.13	18.29	0.03	33.77	0.03	0.00	0.02	0.07	100.32
FK-313-asy1-4	48.80	17.92	0.02	33.76	0.01	0.00	0.02	0.07	100.59
FK-313-asy1-5	47.94	18.37	0.03	33.88	0.00	0.00	0.02	0.02	100.25
FK-313-asy1-6	48.04	17.90	0.02	33.81	0.00	0.01	0.05	0.05	99.86
FK-313-asy1-7	48.32	18.09	0.01	33.74	0.02	0.00	0.03	0.04	100.24
FK-313-asy1-8	48.36	18.07	0.02	33.88	0.00	0.00	0.03	0.04	100.40

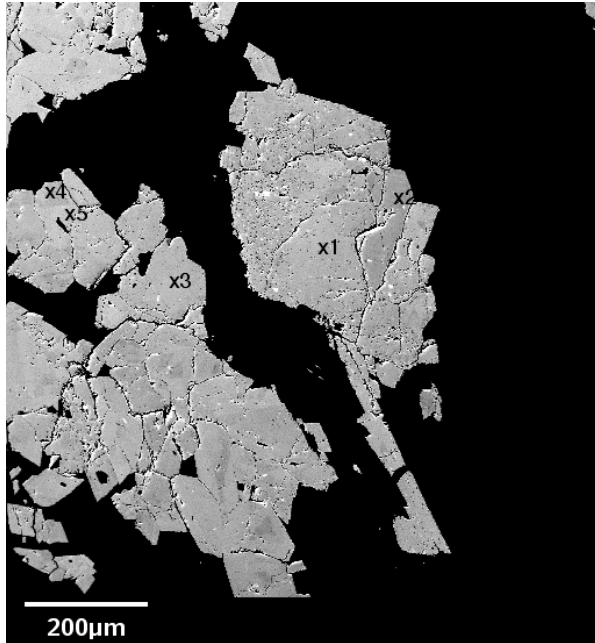
Sample	As (%)	S (%)	Sb (%)	Fe (%)	Bi (%)	Te (%)	Co (%)	Ni (%)	Total
FK-313-asy1-9	47.87	18.28	0.06	33.85	0.00	0.00	0.02	0.03	100.11
FK-313-asy1-10	47.63	18.43	0.04	34.11	0.00	0.00	0.06	0.04	100.31
FK-246-asy1-1	42.92	21.29	0.04	34.89	0.02	0.00	0.03	0.08	99.27
FK-246-asy1-2	44.64	20.83	0.08	34.78	0.00	0.01	0.06	0.03	100.45
FK-246-asy2-1	44.02	21.17	0.04	34.56	0.00	0.00	0.01	0.02	99.82
FK-246-asy2-2	44.20	20.84	0.06	34.70	0.00	0.01	0.00	0.00	99.80
FK-246-asy3-1*	42.79*	19.79*	0.02*	26.46*	0.00*	0.00*	0.02*	0.00*	89.08*
FK-246-asy4-1	44.02	20.20	0.19	32.79	0.00	0.00	0.00	0.01	97.21
asp200	43.84	21.18	0.02	34.65	0.00	0.00	0.00	0.01	99.70
FK-099-asy1-1	49.20	17.46	0.04	27.33	0.00	0.00	5.73	0.56	100.31
FK-099-asy1-2	47.39	18.87	0.02	32.99	0.00	0.00	0.91	0.10	100.27
FK-099-asy1-3	48.21	17.90	0.03	26.87	0.00	0.00	6.30	0.54	99.86
FK-099-asy1-4	47.11	19.09	0.01	33.34	0.00	0.00	0.89	0.16	100.59
FK-099-asy1-5	47.32	19.21	0.01	32.95	0.00	0.02	1.00	0.09	100.59
FK-099-BiTe	0.00	4.31	0.94	0.54	56.51	34.13	0.02	0.01	96.46
asy-cu	45.12	20.30	0.00	34.19	0.03	0.00	0.06	0.01	99.71
asp200	43.76	21.23	0.02	34.61	0.00	0.00	0.02	0.02	99.67
FK-025-asp1-1	45.73	20.21	0.00	33.78	0.00	0.00	0.01	0.01	99.74
FK-025-asp1-2	46.05	19.93	0.00	33.57	0.00	0.00	0.02	0.01	99.58
FK-025-asp1-3	45.41	20.21	0.01	34.29	0.00	0.00	0.00	0.01	99.93
FK-025-asp1-4	43.86	21.27	0.00	34.72	0.04	0.00	0.00	0.00	99.89
FK-025-asp1-5	45.76	20.37	0.01	34.75	0.00	0.00	0.01	0.00	100.90
FK-TH12-41-asp1-1	45.22	20.64	0.03	34.25	0.00	0.00	0.00	0.01	100.15
FK-TH12-41-asp1-2	46.68	20.11	0.05	33.85	0.00	0.01	0.00	0.00	100.70
FK-TH12-41-asp2-1	45.80	20.15	0.00	34.08	0.03	0.00	0.01	0.01	100.09
FK-TH12-41-asp2-2	44.59	20.90	0.00	34.26	0.04	0.00	0.00	0.00	99.79
FK-TH12-41-asp2-3	46.09	19.78	0.01	34.35	0.01	0.00	0.01	0.01	100.26
FK-TH12-41-asp2-4	45.79	19.83	0.03	34.62	0.03	0.00	0.01	0.01	100.32

Sample	As (%)	S (%)	Sb (%)	Fe (%)	Bi (%)	Te (%)	Co (%)	Ni (%)	Total
FK-TH12-02-asy1-1	45.24	20.17	0.04	33.57	0.04	0.02	0.01	0.00	99.09
FK-TH12-02-asy1-2	44.31	20.39	0.01	32.48	0.01	0.01	0.00	0.00	97.21
FK-TH12-02-asy1-3	44.64	20.15	0.01	32.84	0.00	0.02	0.00	0.00	97.67
FK-TH12-02-asy2-1	44.61	20.44	0.03	32.65	0.00	0.01	0.00	0.00	97.73
asy200	43.82	21.08	0.03	34.95	0.00	0.00	0.00	0.02	99.89
FK-TH12-61-asy1-1	46.69	19.89	0.00	34.05	0.00	0.00	0.00	0.01	100.65
FK-TH12-61-asy1-2	42.47	21.80	1.03	34.42	0.00	0.00	0.13	0.00	99.84
FK-TH12-61-asy1-3	40.76	23.41	0.93	35.00	0.02	0.00	0.08	0.03	100.22
FK-TH12-61-asy1-4	46.75	18.96	0.01	33.18	0.01	0.00	0.20	0.01	99.12
FK-TH12-61-asy2-1	48.14	18.11	0.03	33.34	0.00	0.02	0.08	0.01	99.72
FK-TH12-61-asy2-2	45.48	20.14	0.04	34.16	0.00	0.00	0.01	0.00	99.83
FK-TH12-61-asy2-3	45.96	20.16	0.07	33.84	0.00	0.00	0.05	0.00	100.07
FK-TH12-61-asy3-1	46.08	19.42	0.08	33.21	0.01	0.00	0.01	0.01	98.81
FK-TH12-61-asy3-2	48.38	17.94	0.02	33.13	0.00	0.00	0.00	0.02	99.49
FK-TH12-61-asy3-3	45.77	20.16	0.05	33.65	0.03	0.03	0.01	0.01	99.70
FK-TH12-61-asy3-4	46.43	19.60	0.04	33.50	0.00	0.01	0.02	0.00	99.59
FK-TH12-39-asy1-1	46.65	19.50	0.01	34.06	0.01	0.01	0.00	0.02	100.26
FK-TH12-39-asy1-2	46.24	19.93	0.01	34.34	0.00	0.00	0.05	0.05	100.62
FK-TH12-39-asy1-3	44.64	21.10	0.02	34.95	0.01	0.02	0.02	0.00	100.75
FK-TH12-39-asy1-4	45.66	20.00	0.02	34.13	0.00	0.00	0.00	0.02	99.83
FK-TH12-39-asy1-5	46.27	19.76	0.00	34.03	0.06	0.00	0.01	0.00	100.13
FK-TH12-40-asy1-1	45.59	20.07	0.03	34.23	0.00	0.00	0.01	0.00	99.93
FK-TH12-40-asy1-2	46.30	19.56	0.01	34.24	0.02	0.00	0.01	0.04	100.17
FK-TH12-40-asy2-1	46.30	19.51	0.02	34.25	0.00	0.00	0.00	0.02	100.11
FK-TH12-40-asy2-2	45.94	19.81	0.01	34.33	0.00	0.00	0.01	0.00	100.09
FK-TH12-40-asy2-3	45.78	19.62	0.02	34.39	0.02	0.02	0.00	0.01	99.87
FK-TH12-40-asy2-4	45.13	19.98	0.02	34.84	0.01	0.01	0.00	0.01	100.00
FK-TH12-02-asy1-2rep	44.95	20.18	0.00	34.08	0.00	0.02	0.00	0.00	99.24

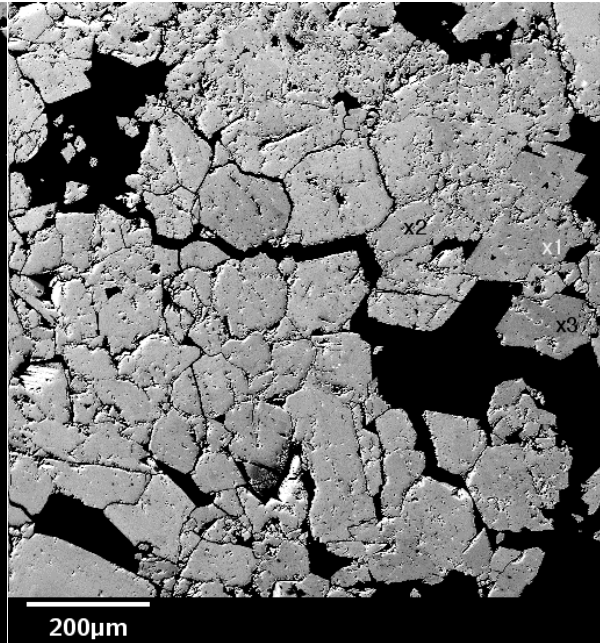
Sample	As (%)	S (%)	Sb (%)	Fe (%)	Bi (%)	Te (%)	Co (%)	Ni (%)	Total
FK-TH12-02-asy1-3rep	44.61	20.15	0.03	34.15	0.00	0.00	0.00	0.00	98.94
FK-TH12-02-asy2-1rep	44.36	20.26	0.02	33.87	0.00	0.01	0.00	0.00	98.52
FK-227-asy1-1	45.02	20.07	0.01	34.59	0.00	0.01	0.00	0.00	99.70
FK-227-asy1-2	46.46	19.29	0.01	34.25	0.00	0.01	0.02	0.00	100.04
FK-227-asy1-3	46.70	19.19	0.00	34.32	0.01	0.01	0.00	0.01	100.24
FK-227-asy1-4	46.17	19.39	0.03	34.29	0.05	0.00	0.00	0.00	99.94
FK-227-asy1-5	45.81	19.30	0.03	34.27	0.00	0.02	0.01	0.01	99.44
FK-227-asy2-1	45.05	20.21	0.01	34.63	0.00	0.00	0.00	0.00	99.90
FK-227-asy2-2	44.53	20.84	0.00	35.09	0.00	0.00	0.00	0.02	100.48
FK-227-asy2-3	45.68	19.72	0.00	34.35	0.00	0.01	0.02	0.01	99.79
FK-227-asy2-4	44.81	20.38	0.00	34.64	0.03	0.00	0.02	0.00	99.88
FK-227-asy2-5	45.88	19.53	0.02	34.34	0.00	0.00	0.00	0.00	99.76
FK-TH12-60-asy1-1*	42.84*	19.58*	0.02*	32.54*	0.00*	0.01*	0.00*	0.00*	94.99*
FK-TH12-60-asy1-2	43.56	21.37	0.09	34.77	0.03	0.00	0.00	0.00	99.82
FK-TH12-60-asy2-1	41.85	22.35	0.03	35.25	0.45	0.01	0.01	0.00	99.95
FK-TH12-60-asy2-2	40.94	23.14	0.03	35.51	0.20	0.01	0.00	0.00	99.83
FK-TH12-60-asy2-3	45.98	19.57	0.02	34.22	0.00	0.00	0.00	0.00	99.79
FK-TH12-60-asy2-4	41.55	22.69	0.02	35.22	0.00	0.00	0.00	0.01	99.50
asp200	44.13	20.48	0.02	34.47	0.00	0.01	0.00	0.03	99.13

* Analyses disregarded due to low totals.

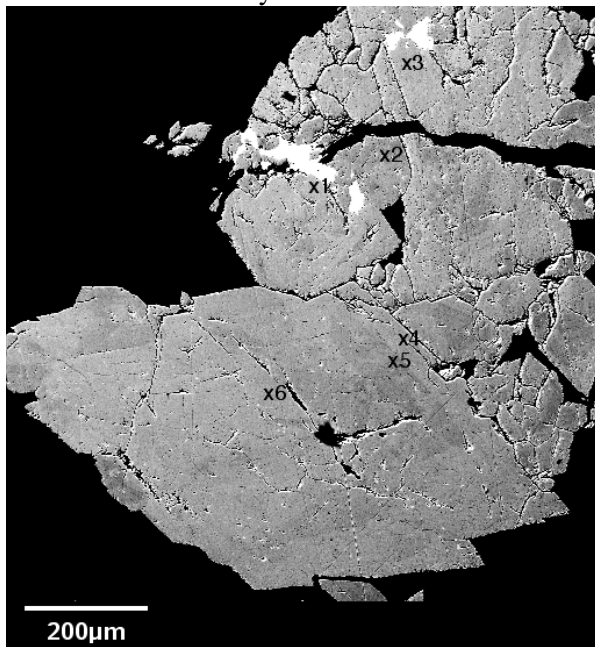
D.2 EPMA Arsenopyrite Analysis Spot Images



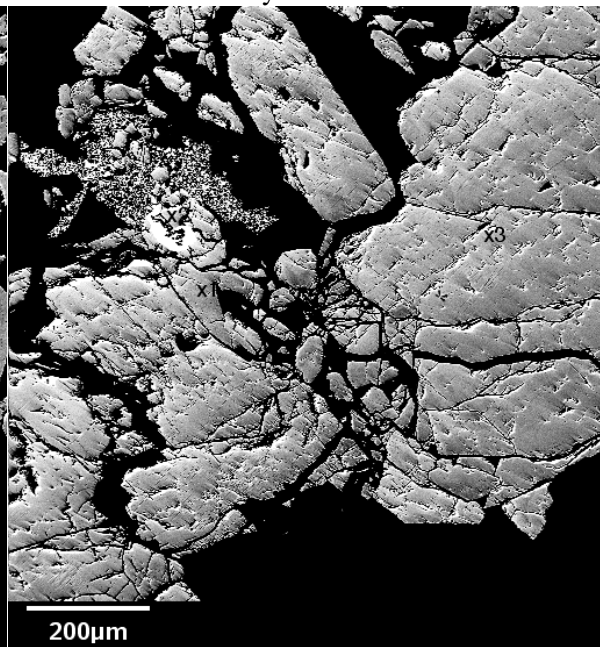
FK-036 ASPY2 Analyses 1 to 5.



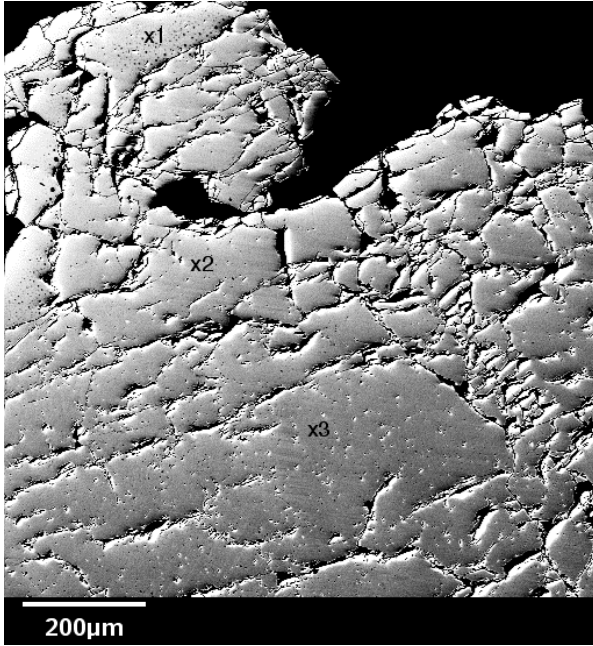
FK-036 APSY3 Analyses 1 to 3.



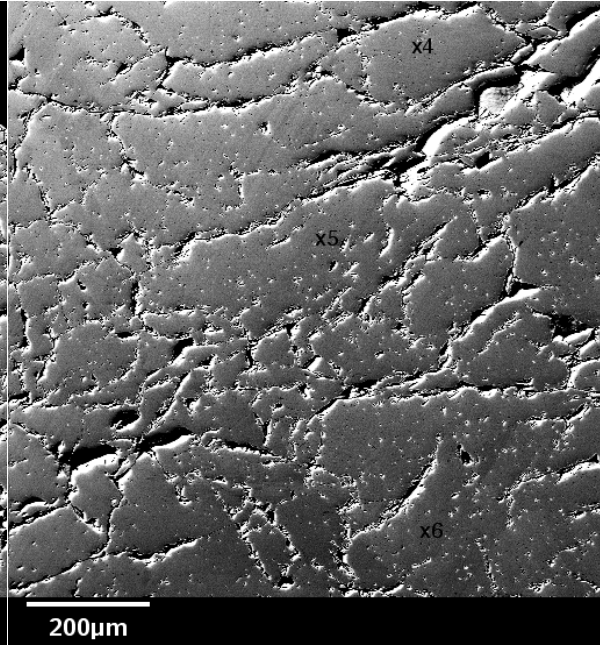
FK-056 ASPY1 Analyses 1 to 6.



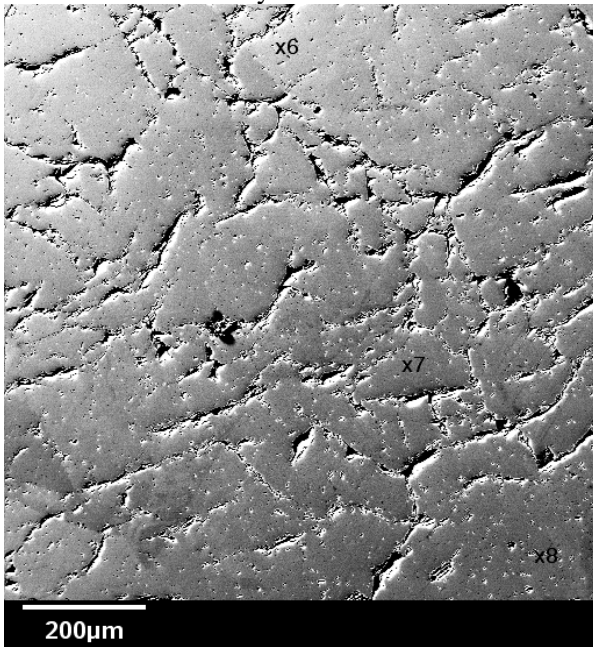
FK-056 ASPY2 Analyses 1 to 3.



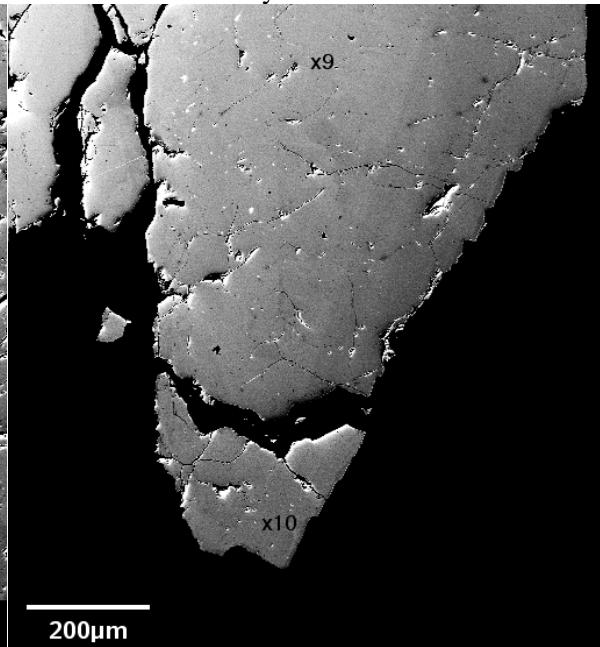
FK-313 ASPY1 Analyses 1 to 3.



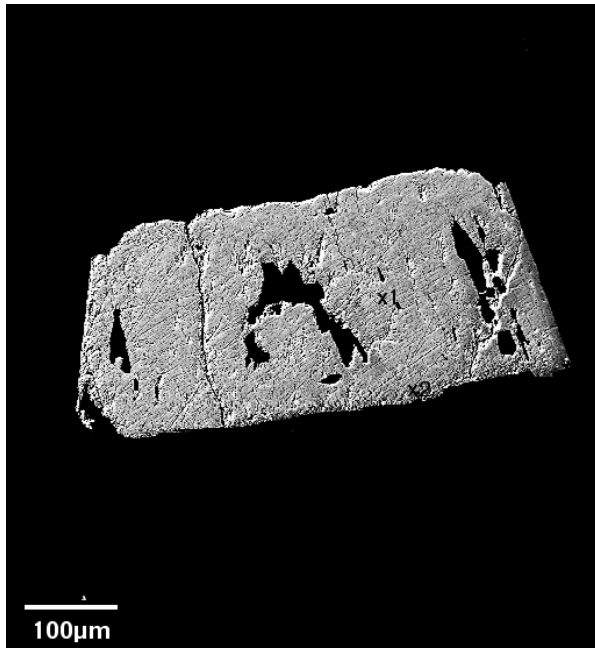
FK-313 ASPY1 Analyses 4 to 6.



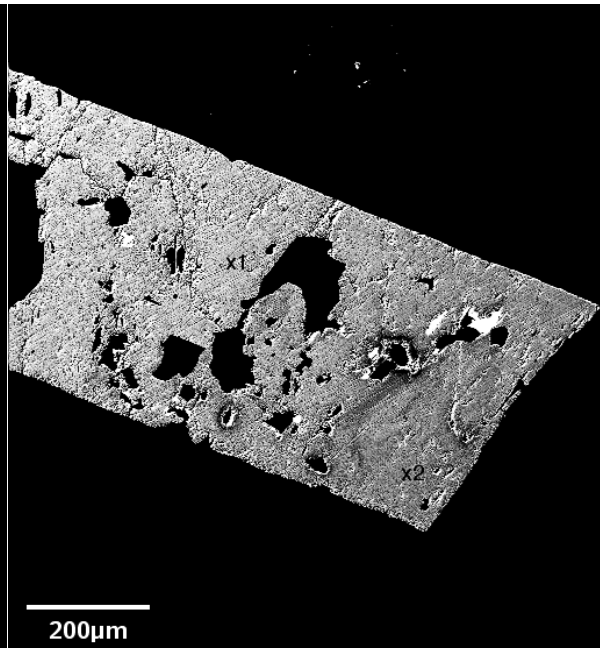
FK-313 ASPY1 Analyses 6 to 8.



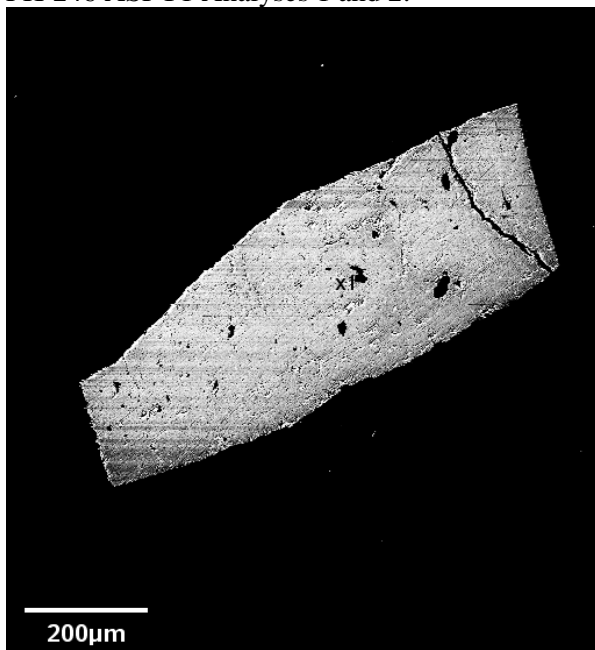
FK-313 ASPY1 Analyses 9 and 10.



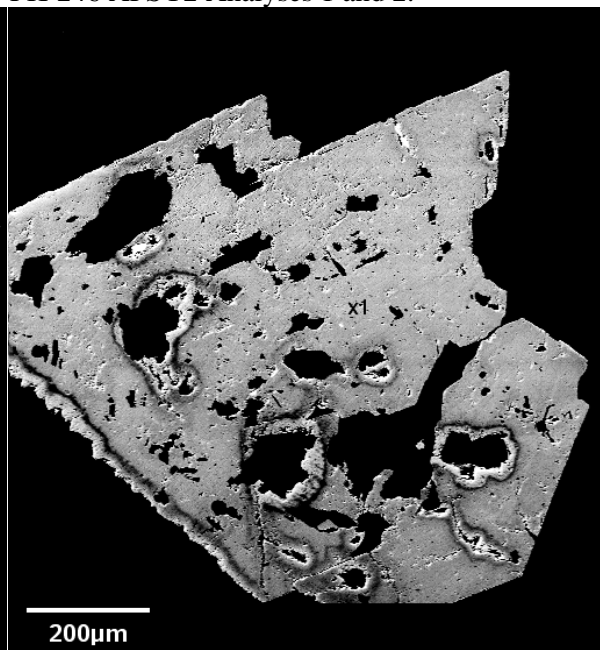
FK-246 ASPY1 Analyses 1 and 2.



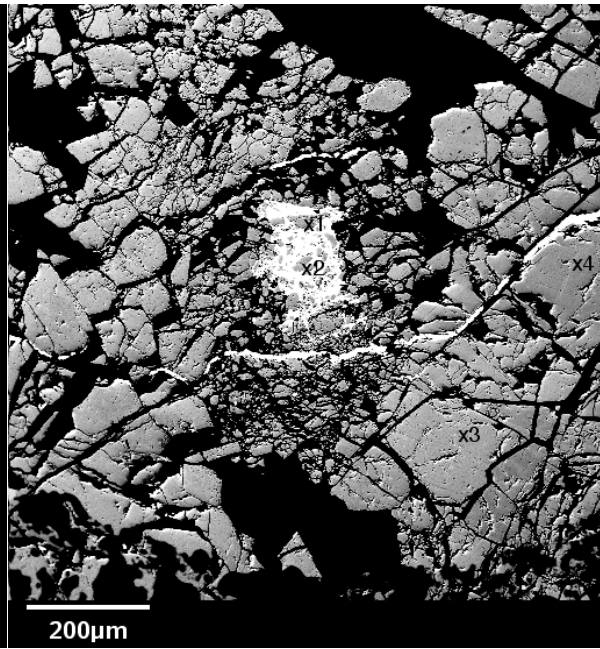
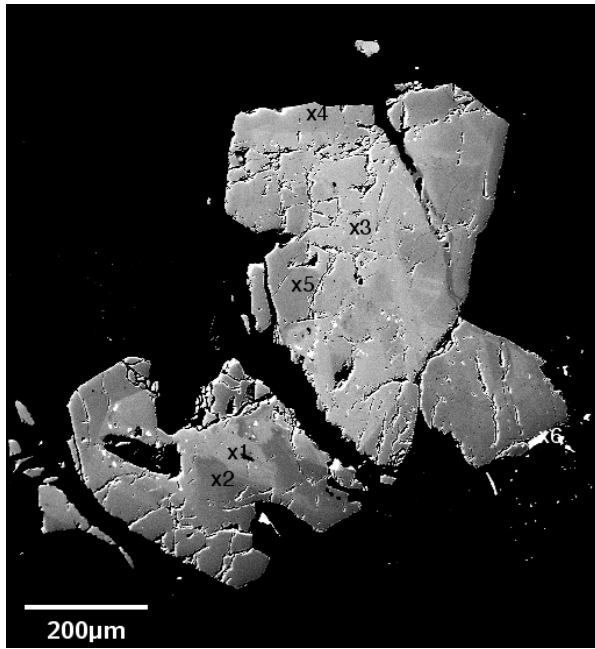
FK-246 APSY2 Analyses 1 and 2.



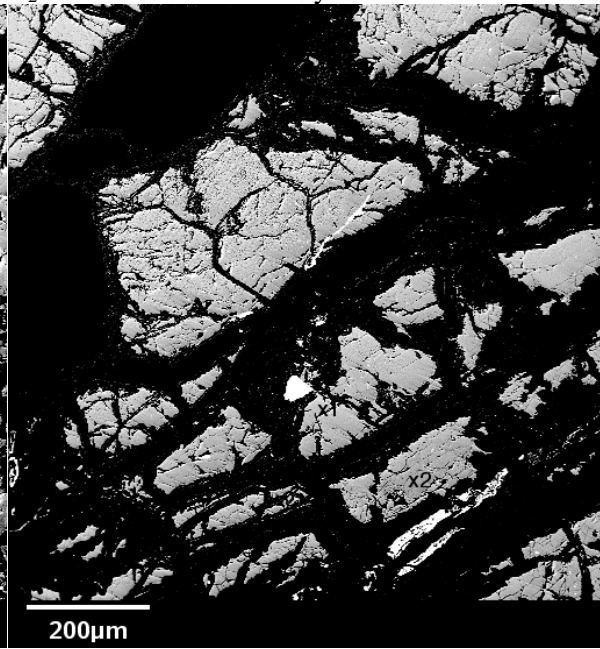
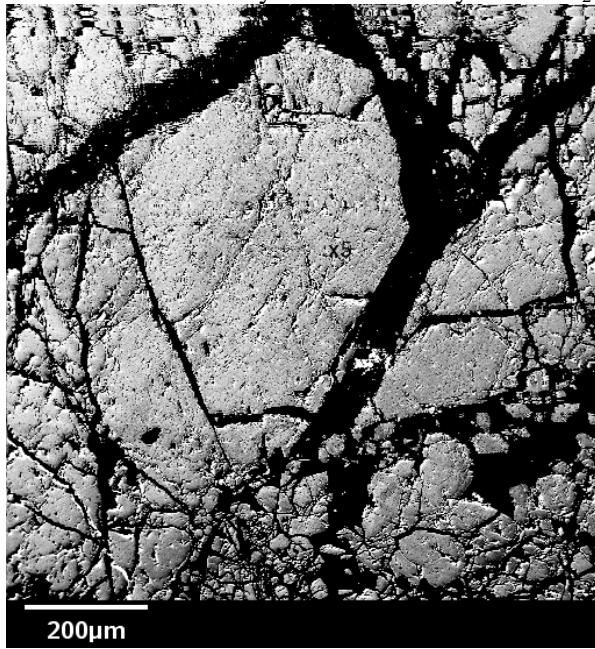
FK-246 ASPY3 Analysis 1.



FK-245 ASPY4 Analysis 1.

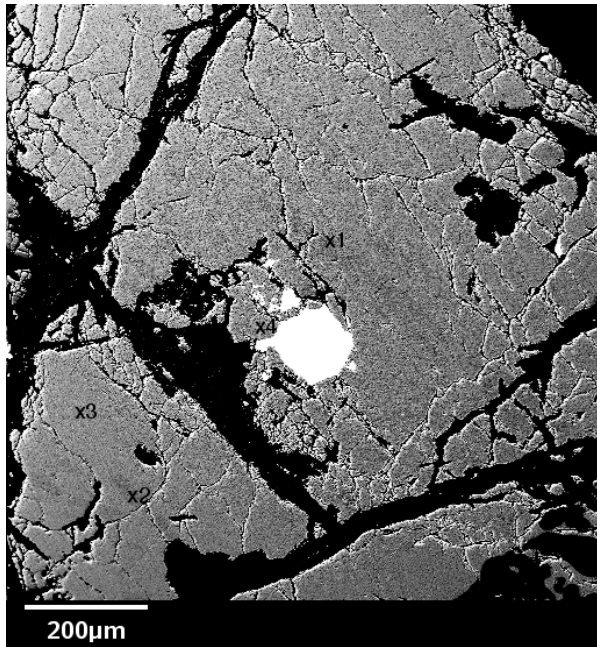


FK-099 APSY1 Analyses 1 to 5. Analysis 6 = $\text{Bi}_2\text{Te}_3\text{S}$ FK-025 APSY1 Analyses 1 to 4.

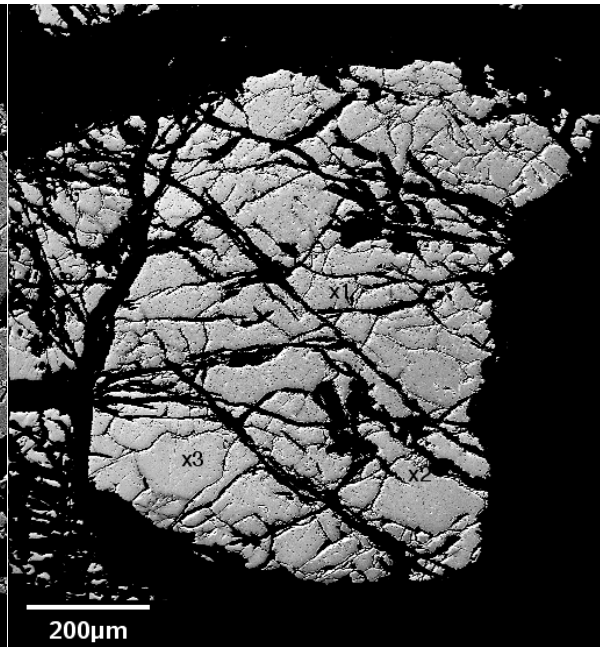


FK-025 APSY1 Analysis 5.

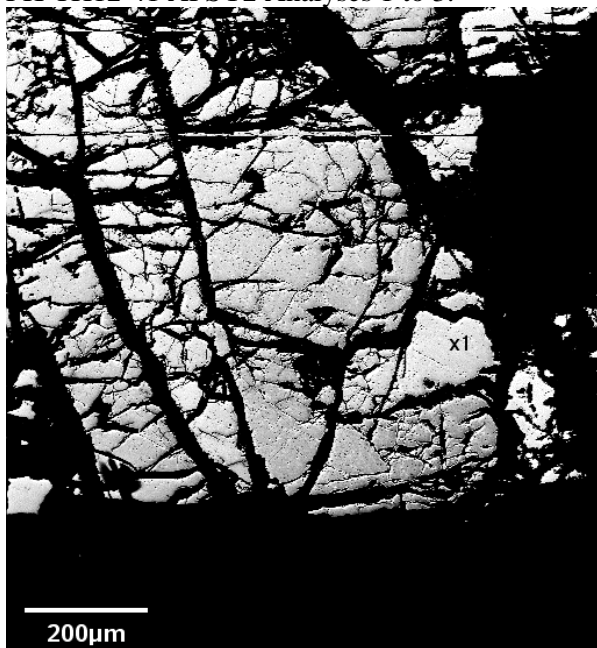
FK-TH12-41 APSY 1 Analyses 1 and 2.



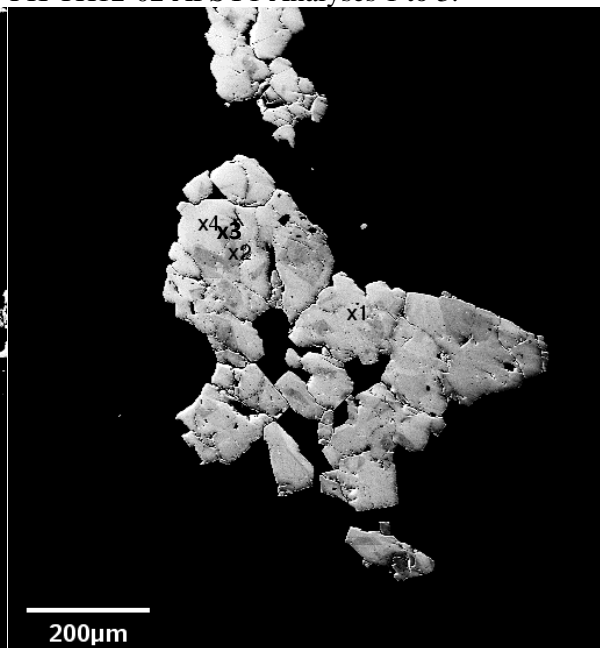
FK-TH12-41 APSY2 Analyses 1 to 3.



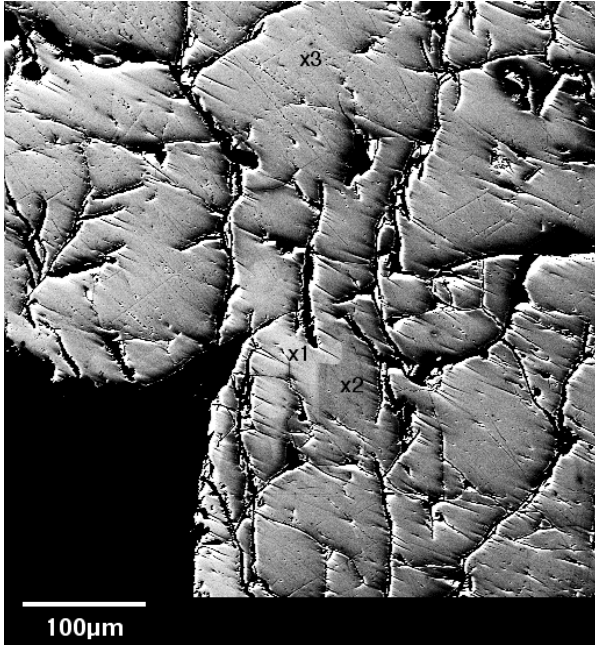
FK-TH12-02 APSY1 Analyses 1 to 3.



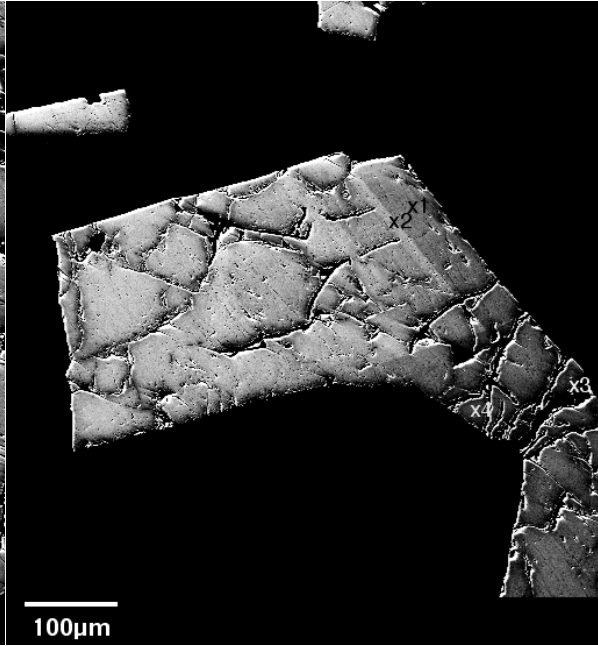
FK-TH12-02 ASPY2 Analysis 1.



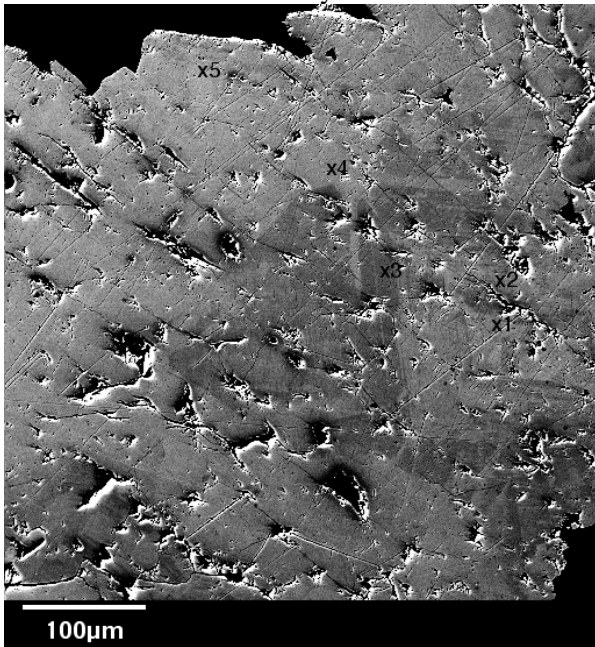
FK-TH12-61 ASPY1 Analyses 1 to 4.



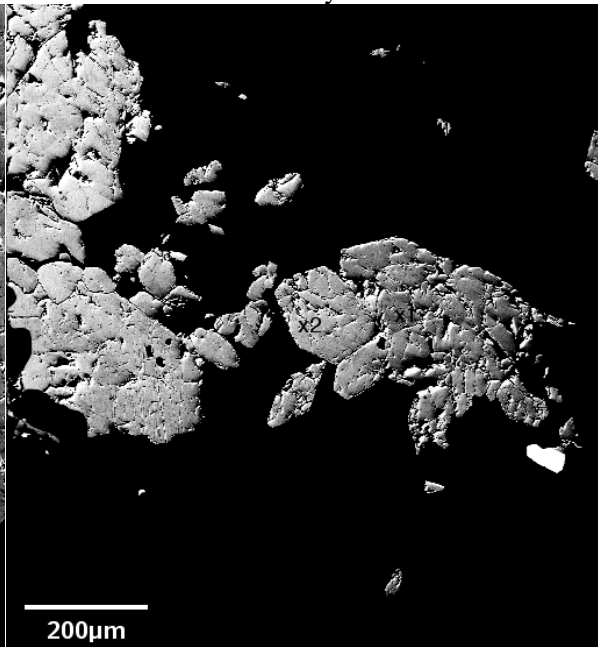
FK-TH12-61 ASPY2 Analyses 1 to 3.



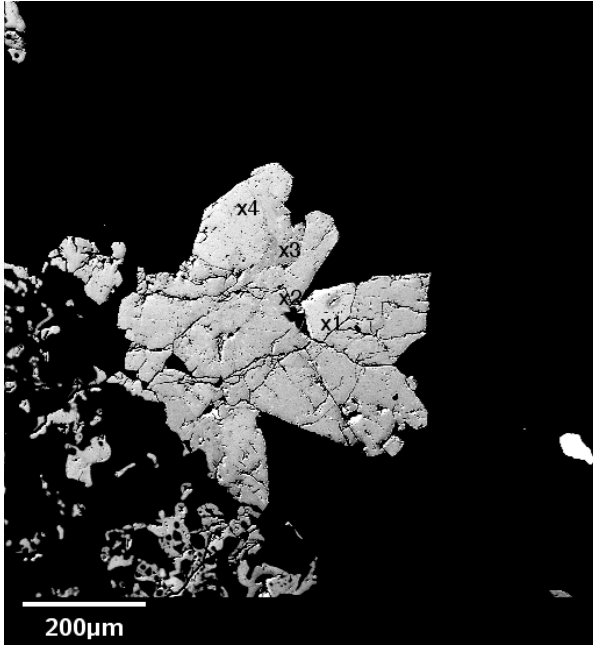
FK-TH12-61 APSY3 Analyses 1 to 3.



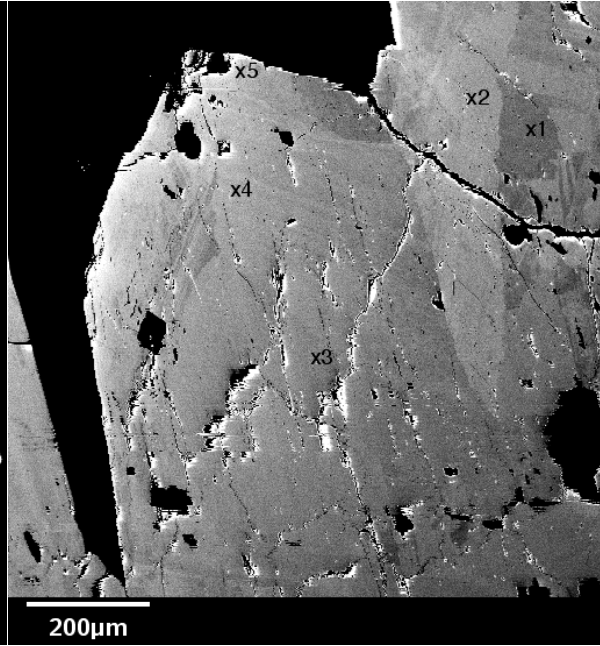
FK-TH12-39 ASPY1 Analyses 1 to 5.



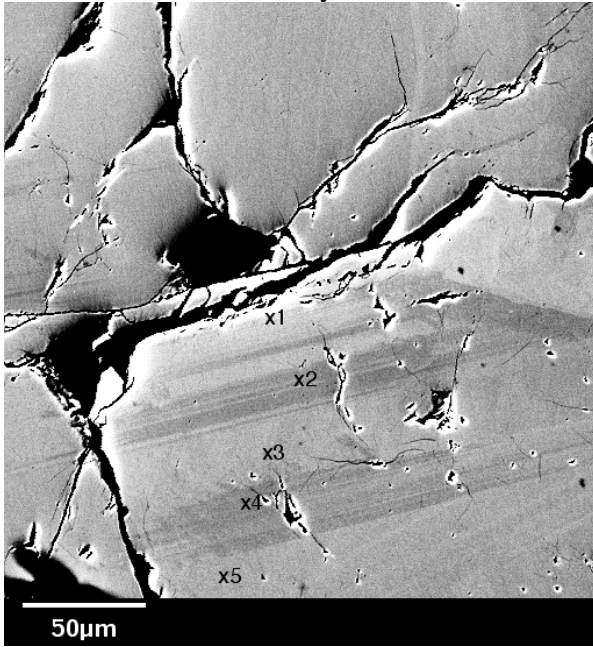
FK-TH12-40 ASPY1 Analyses 1 and 2.



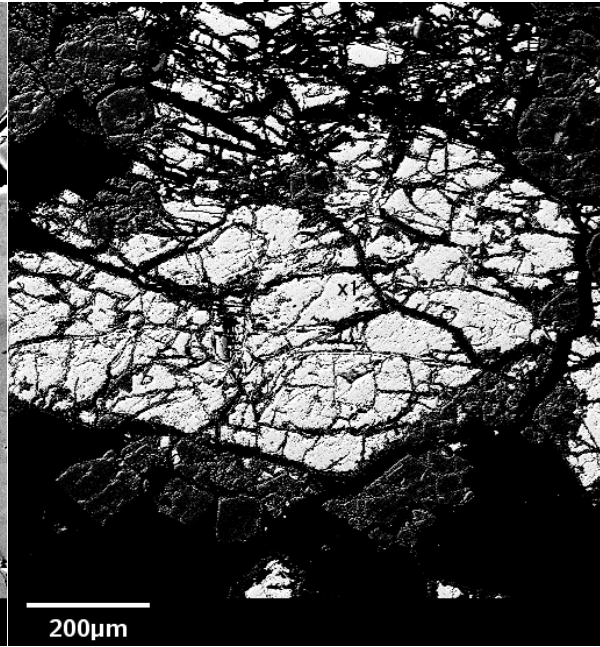
FK-TH12-40 APSY2 Analyses 1 to 4.



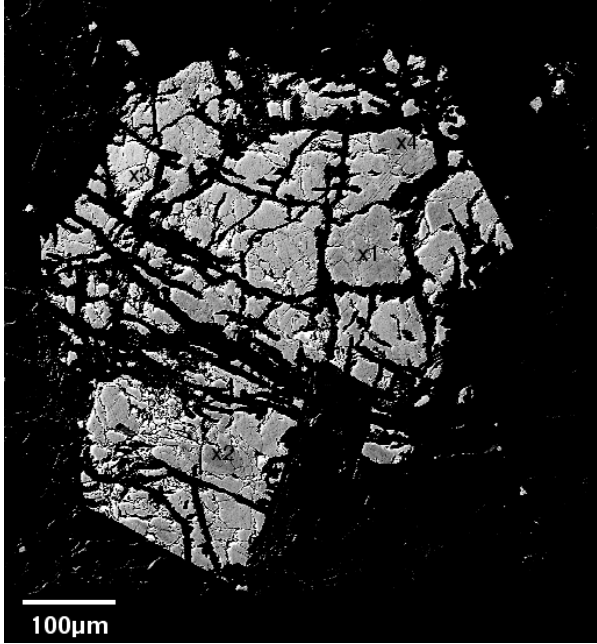
FK-227 APSY1 Analysis 1 to 5.



FK-227 ASPY2 Analysis 1 to 5.



FK-TH12-60 ASPY1 Analysis 1.



FK-TH12-60 ASPY2 Analyses 1 to 4.

Appendix E: Sulfur Isotope Data

E.1 Arsenopyrite Sulfur Isotope Data

A: SIMS Arsenopyrite Sulfur Isotope Data

B: SIMS Arsenopyrite Sulfur Isotope Analysis Spot Images

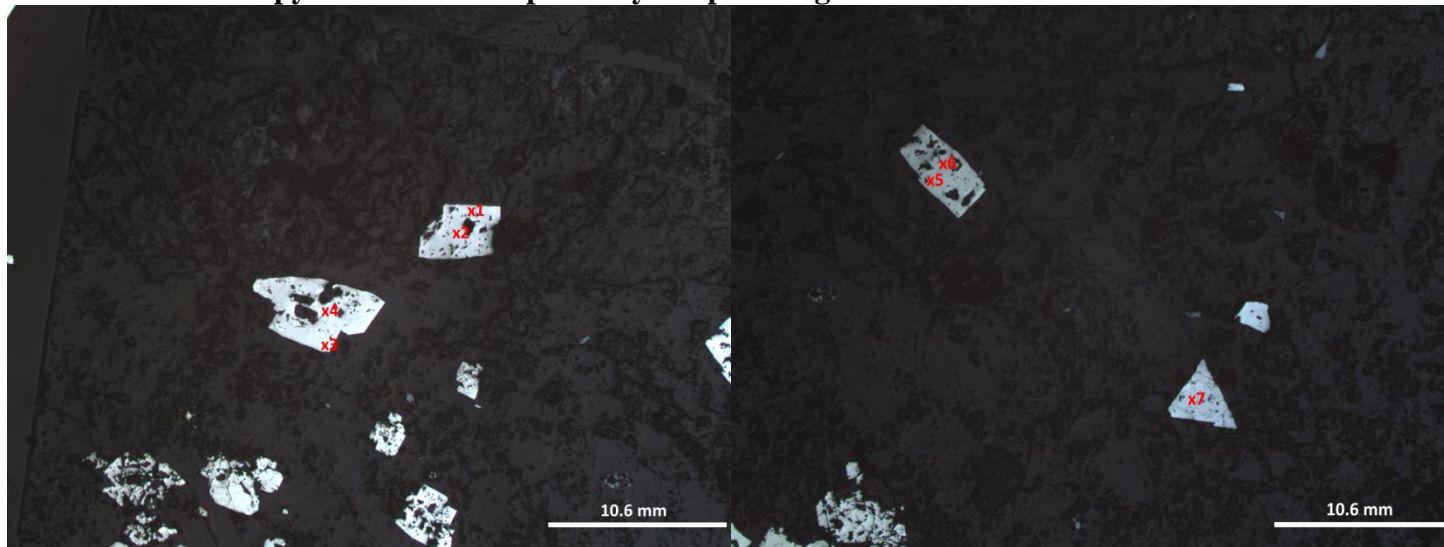
E.1.A SIMS Arsenopyrite Sulfur Isotope Data

Sample	$^{34}\text{S}/^{32}\text{S}$ per mil	SEM	$^{34}\text{S}/^{32}\text{S}$ ratio	2SD	SEM %	Poisson %	N
FK-246 Arspy 1	0.3	0.2	0.043169	0.000153	0.020881	0.028602	72
FK-246 Arspy 2	-0.1	0.2	0.04315	0.000168	0.022752	0.031183	73
FK-246 Arspy 3	-1.3	0.3	0.043099	0.000217	0.029328	0.03048	74
FK-246 Arspy 4	0.9	0.2	0.043193	0.000176	0.023949	0.031378	72
FK-246 Arspy 5	-0.4	0.2	0.043137	0.000175	0.023721	0.029475	73
FK-246 Arspy 6	-1.2	0.2	0.043102	0.000155	0.020994	0.029603	73
FK-246 Arspy 7	-0.9	0.3	0.043118	0.000204	0.027639	0.029718	73
FK-246 Arspy 8	0.9	0.2	0.043196	0.000178	0.024248	0.030635	72
FK-246 Arspy 9	-0.1	0.2	0.043151	0.000158	0.021669	0.030014	71
FK-313 Arspy 1	-11.7	0.4	0.042653	0.000263	0.035864	0.048012	74
FK-313 Arspy 2	-10.8	0.4	0.042694	0.000259	0.035295	0.03889	74
FK-313 Arspy 3	-7.5	0.3	0.042832	0.000197	0.026925	0.03961	73
FK-313 Arspy 4	-7.8	0.3	0.042821	0.000234	0.031349	0.035627	76
FK-313 Arspy 5	-7.7	0.3	0.042823	0.000206	0.027822	0.03533	75
FK-313 Arspy 6	-9.4	0.3	0.042753	0.000186	0.024928	0.03292	76
FK-313 Arspy 7	-9.7	0.3	0.042737	0.000191	0.026114	0.033456	73
FK-099 Arspy 1	-1.3	0.3	0.043101	0.000223	0.030526	0.039209	72
FK-099 Arspy 2	-3.0	0.3	0.043025	0.000196	0.026276	0.038525	75
FK-099 Arspy 3	0.9	0.3	0.043195	0.000225	0.030332	0.03823	74
FK-099 Arspy 4	-3.4	0.3	0.043011	0.000213	0.028547	0.03747	75
FK-099 Arspy 5	-3.5	0.3	0.043004	0.000182	0.024897	0.038592	72
FK-TH12-02 Arspy 1	0.1	0.2	0.043161	0.000182	0.024297	0.033002	75
FK-TH12-02 Arspy 2	0.6	0.3	0.043183	0.000213	0.029112	0.03387	72
FK-TH12-02 Arspy 3	0.5	0.3	0.043178	0.000224	0.030827	0.03481	71
FK-TH12-02 Arspy 4	0.3	0.3	0.043168	0.000183	0.025283	0.034039	70
FK-TH12-02 Arspy 5	0.5	0.2	0.043179	0.000147	0.019671	0.033374	75

Sample	$^{34}\text{S}/^{32}\text{S}$ per mil	SEM	$^{34}\text{S}/^{32}\text{S}$ ratio	2SD	SEM %	Poisson %	N
FK-TH12-02 Arspy 6	-0.7	0.3	0.043123	0.000223	0.03033	0.034884	73
FK-TH12-02 Arspy 7	0.4	0.3	0.043174	0.000246	0.033338	0.033561	73
FK-TH12-02 Arspy 8	0.4	0.2	0.043171	0.000182	0.024329	0.030553	75
FK-TH12-02 Arspy 9	0.7	0.2	0.043187	0.000153	0.021385	0.031559	69
FK-TH12-02 Arspy 10	0.2	0.2	0.043166	0.000157	0.021482	0.030836	72
FK-036 Arspy 1	0.9	0.2	0.043193	0.000162	0.022161	0.033545	72
FK-036 Arspy 2	-0.5	0.3	0.043136	0.00021	0.028491	0.035096	73
FK-036 Arspy 3	1.5	0.3	0.043219	0.000191	0.025915	0.035807	73
FK-036 Arspy 4	2.4	0.2	0.04326	0.000178	0.024183	0.035002	72
FK-036 Arspy 5	0.3	0.3	0.043167	0.000196	0.026584	0.03389	73
FK-TH12-41 Arspy 1	0.1	0.3	0.04316	0.000238	0.032444	0.035953	72
FK-TH12-41 Arspy 2	0.1	0.3	0.043161	0.000206	0.027948	0.034617	73
FK-TH12-41 Arspy 3	0.0	0.3	0.043153	0.000205	0.027627	0.035482	74
FK-TH12-41 Arspy 4	0.1	0.2	0.043159	0.000172	0.023064	0.034789	75
FK-TH12-41 Arspy 5	0.7	0.3	0.043186	0.000189	0.02556	0.029999	73
FK-TH12-41 Arspy 6	1.6	0.3	0.043226	0.000183	0.025062	0.033414	71
FK-025 Arspy 1	-0.8	0.3	0.04312	0.000234	0.030891	0.031562	77
FK-025 Arspy 2	0.3	0.3	0.04317	0.000197	0.026955	0.031455	72
FK-025 Arspy 3	0.5	0.2	0.043176	0.000139	0.018766	0.031196	74
FK-025 Arspy 4	-0.1	0.2	0.043149	0.000165	0.022499	0.031986	72
FK-025 Arspy 5	1.7	0.3	0.043228	0.000215	0.028734	0.028697	75
FK-025 Arspy 6	1.2	0.4	0.043208	0.000284	0.038425	0.030967	73
FK-227 Arspy 1	-0.1	0.3	0.04315	0.000203	0.027655	0.030914	72
FK-227 Arspy 2	-1.0	0.4	0.043111	0.000266	0.03587	0.030712	74
FK-227 Arspy 3	-1.0	0.3	0.043111	0.000232	0.031485	0.030425	73
FK-227 Arspy 4	-0.8	0.3	0.043119	0.000189	0.025431	0.029945	74
FK-227 Arspy 5	-1.7	0.3	0.04308	0.000193	0.026249	0.030454	73

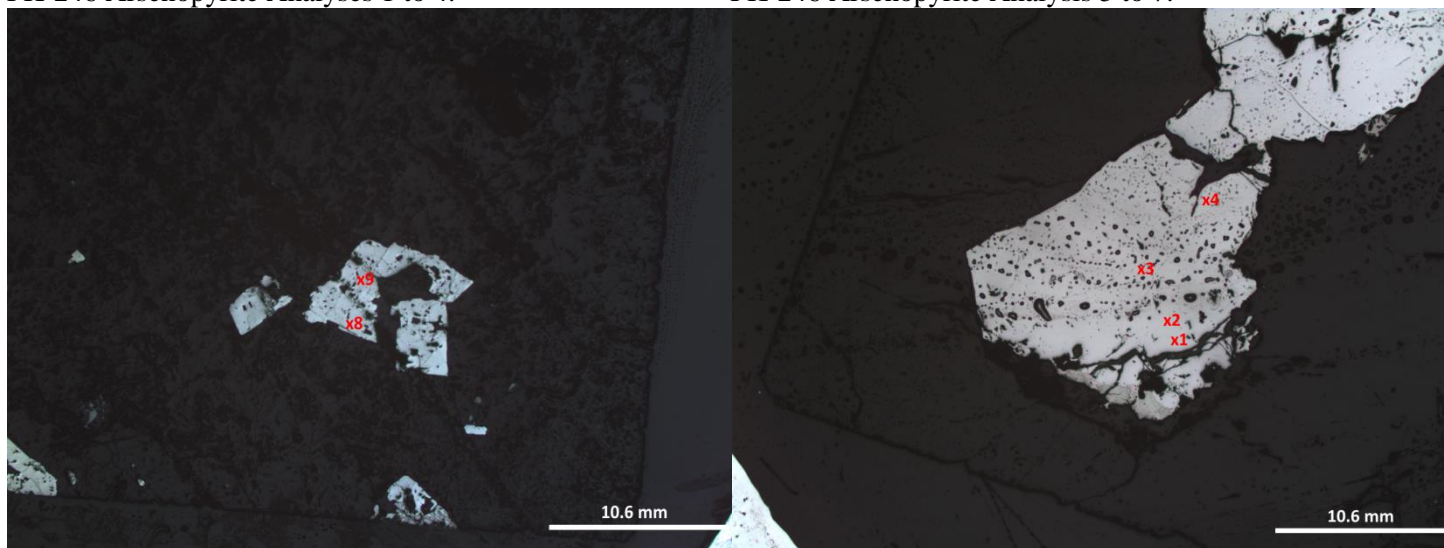
Standards	³⁴S/³²S per mil	SEM	³⁴S/³²S ratio	2SD	SEM %	Poisson %	N
Arspy57 2 Apr 3 2013	3.1	0.3	0.043289	0.000236	0.031498	0.032952	75
Arspy57 3 Apr 3 2013	3.0	0.3	0.043286	0.000186	0.02612	0.033075	68
Arspy57 2 Apr 5 2013	3.0	0.3	0.043285	0.000193	0.026317	0.034453	72
Arspy57 3 Apr 5 2013	3.0	0.3	0.043284	0.000208	0.027702	0.034046	75
Arspy57 3 Apr 8 2013	2.1	0.4	0.043247	0.000276	0.036864	0.032494	75
Arspy57 4 Apr 8 2013	2.6	0.3	0.043267	0.000196	0.026182	0.03357	75
Arspy57 2 Apr 9 2013	3.3	0.2	0.043297	0.000166	0.022338	0.033704	74
Arspy57 3 Apr 9 2013	2.3	0.3	0.043254	0.000191	0.025508	0.031645	75

E.1.B SIMS Arsenopyrite Sulfur Isotope Analysis Spot Images



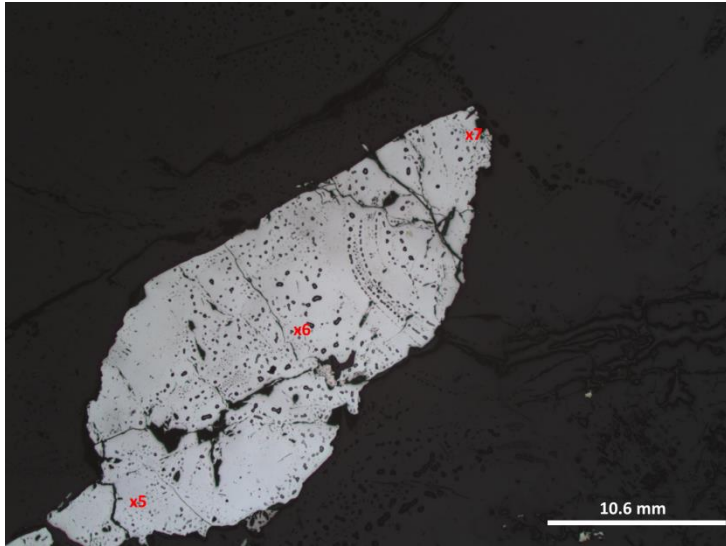
FK-246 Arsenopyrite Analyses 1 to 4.

FK-246 Arsenopyrite Analysis 5 to 7.

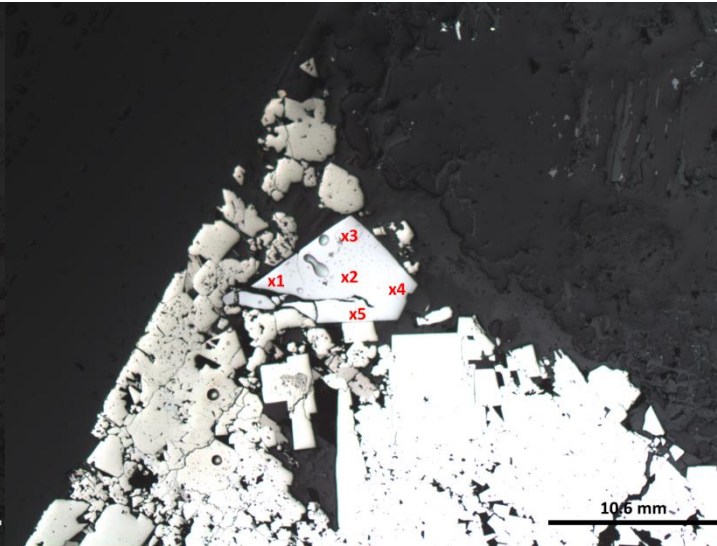


FK-246 Arsenopyrite Analyses 8 and 9.

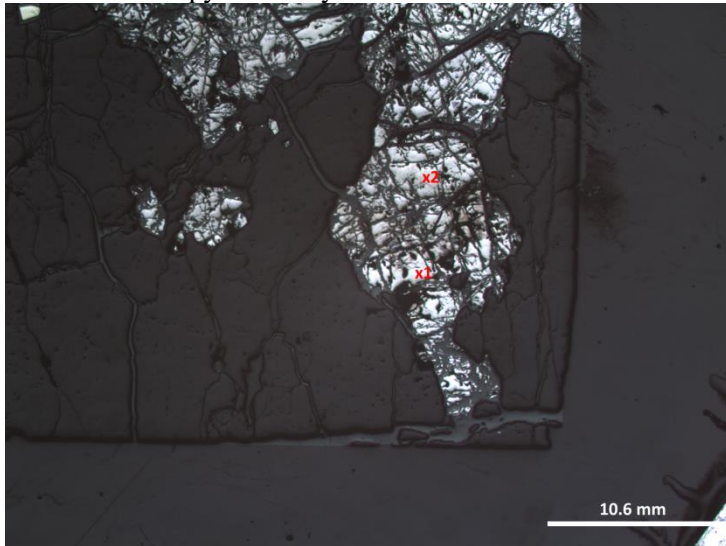
FK-313 Arsenopyrite Analyses 1 to 4.



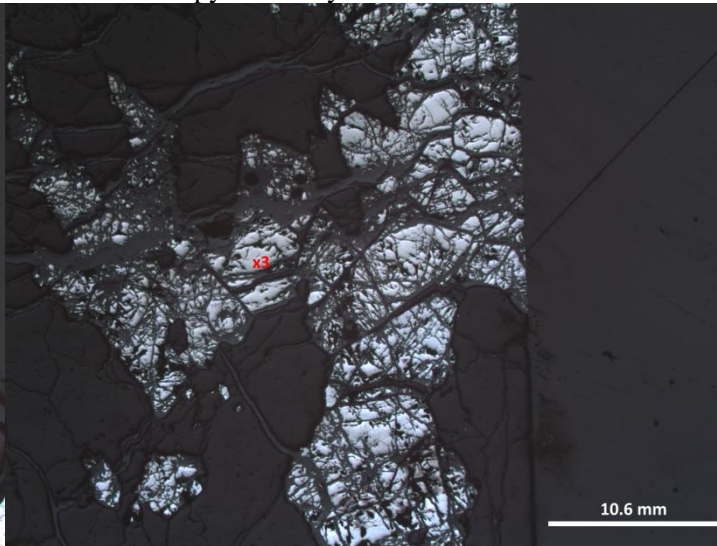
FK-313 Arsenopyrite Analyses 5 to 7.



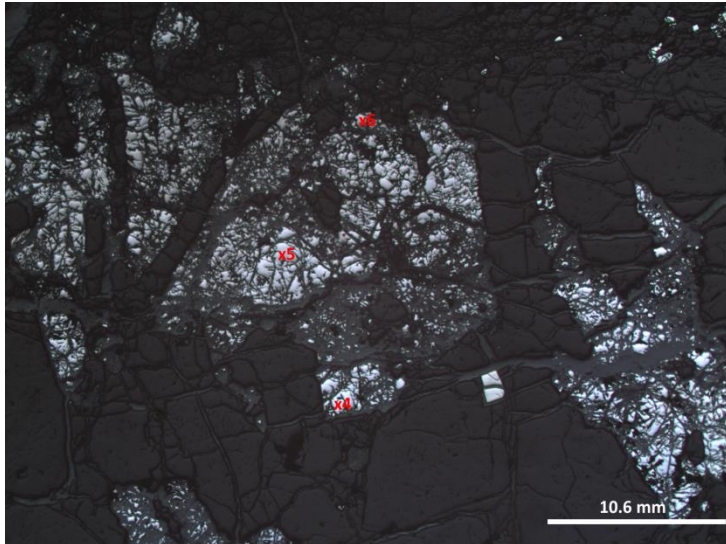
FK-099 Arsenopyrite Analyses 1 to 5.



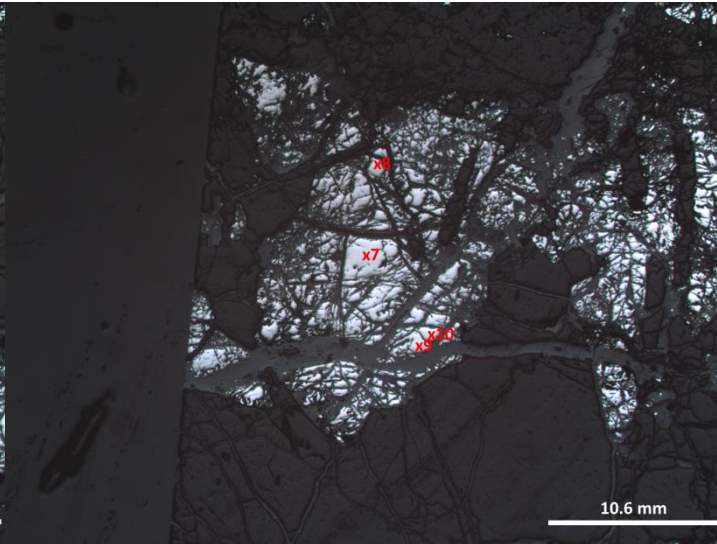
FK-TH12-02 Arsenopyrite Analyses 1 and 2.



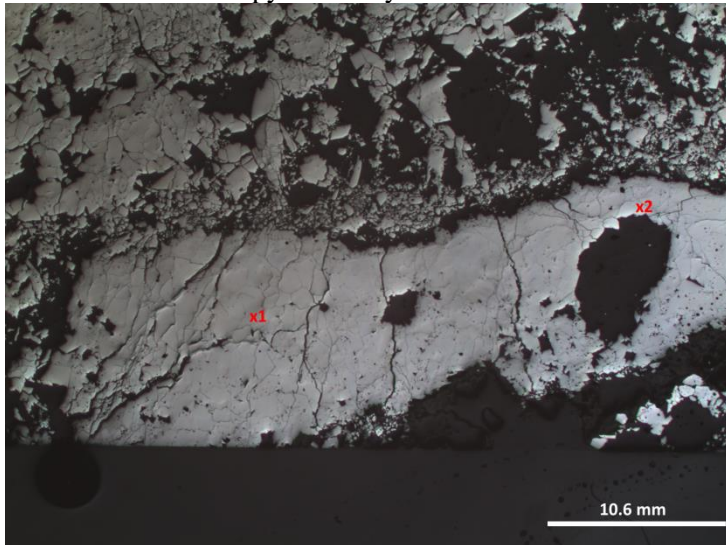
FK-TH12-02 Arsenopyrite Analysis 3.



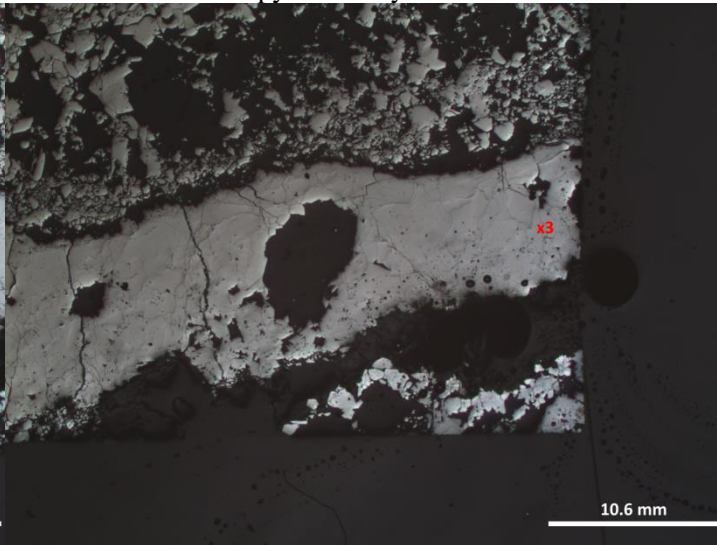
FK-TH12-02 Arsenopyrite Analyses 4 to 6.



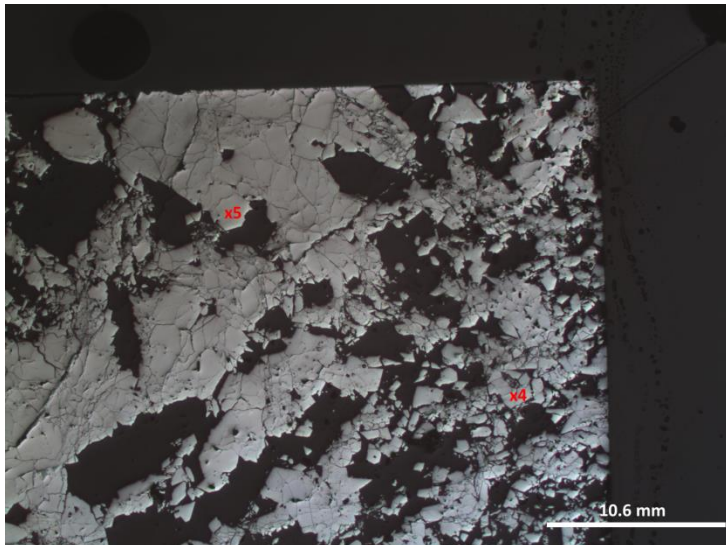
FK-TH12-02 Arsenopyrite Analyses 7 to 10.



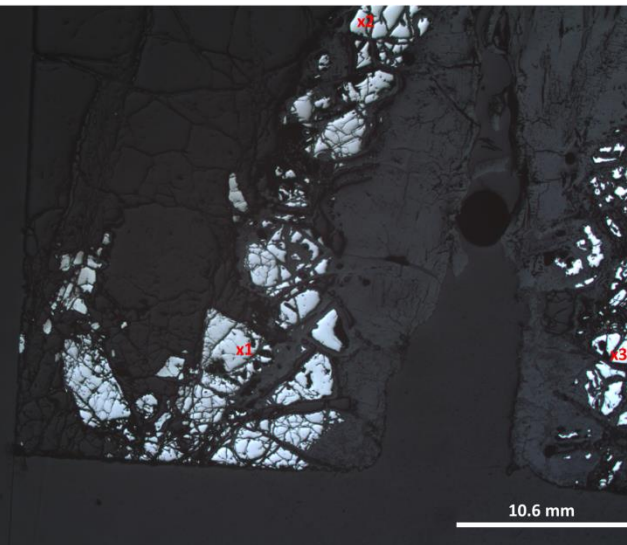
FK-036 Arsenopyrite Analyses 1 and 2.



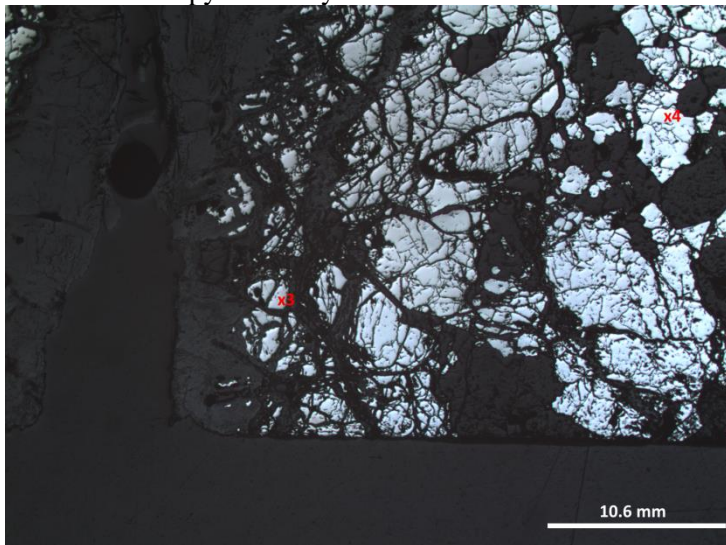
FK-036 Arsenopyrite Analysis 3.



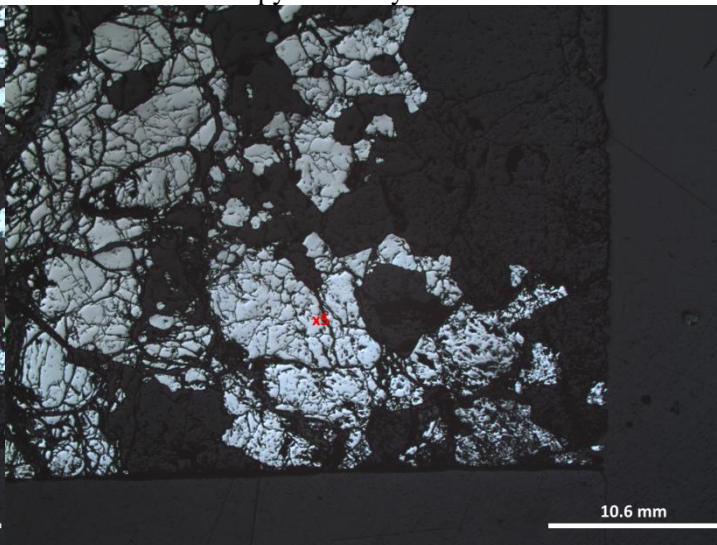
FK-036 Arsenopyrite Analyses 4 and 5.



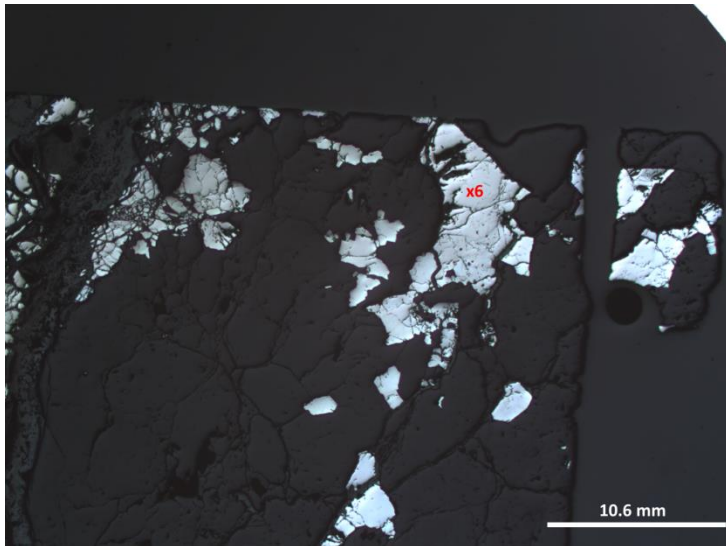
FK-TH12-41 Arsenopyrite Analyses 1 to 3.



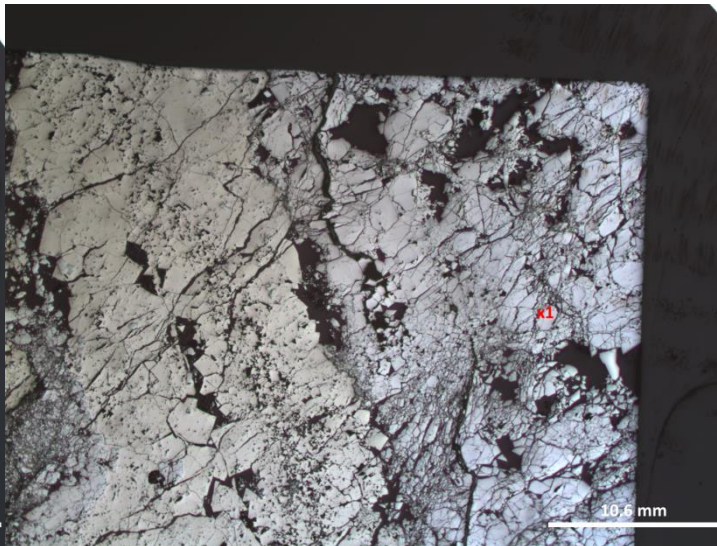
FK-TH12-41 Arsenopyrite Analyses 3 and 4.



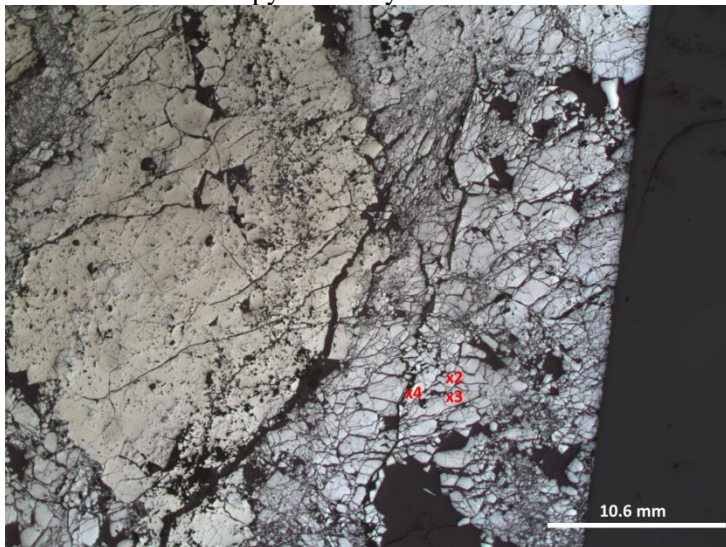
FK-TH12-41 Arsenopyrite Analysis 5.



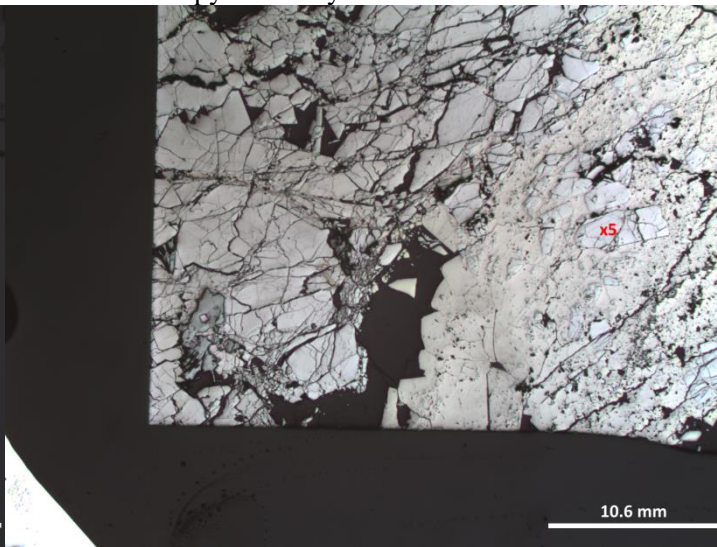
FK-TH12-41 Arsenopyrite Analysis 6.



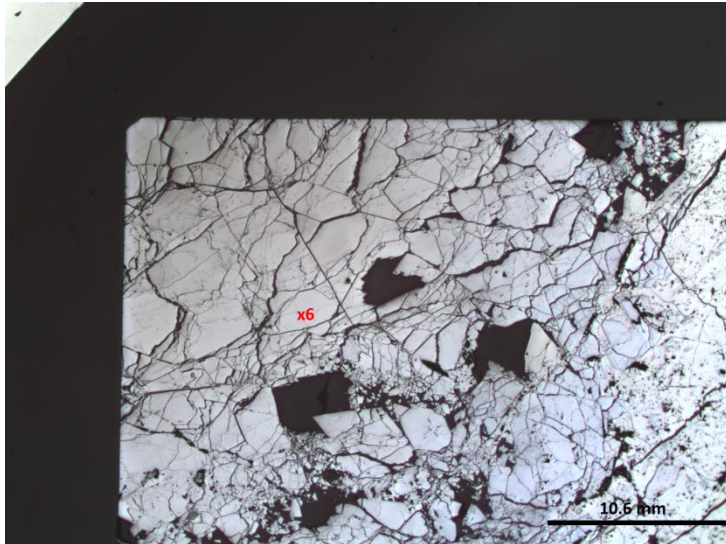
FK-025 Arsenopyrite Analysis 1.



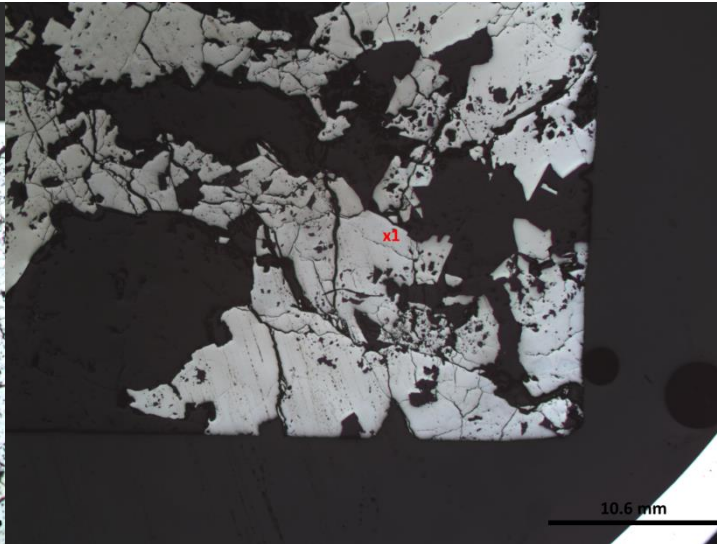
FK-025 Arsenopyrite Analyses 2 to 4.



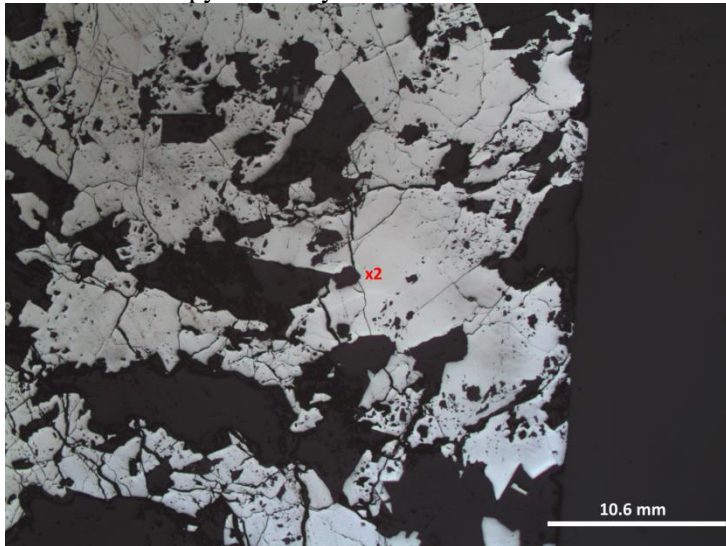
FK-025 Arsenopyrite Analysis 5.



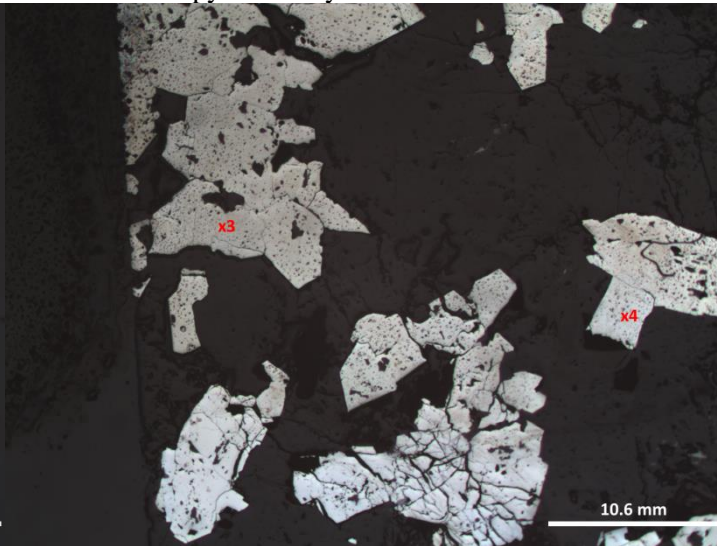
FK-025 Arsenopyrite Analysis 6.



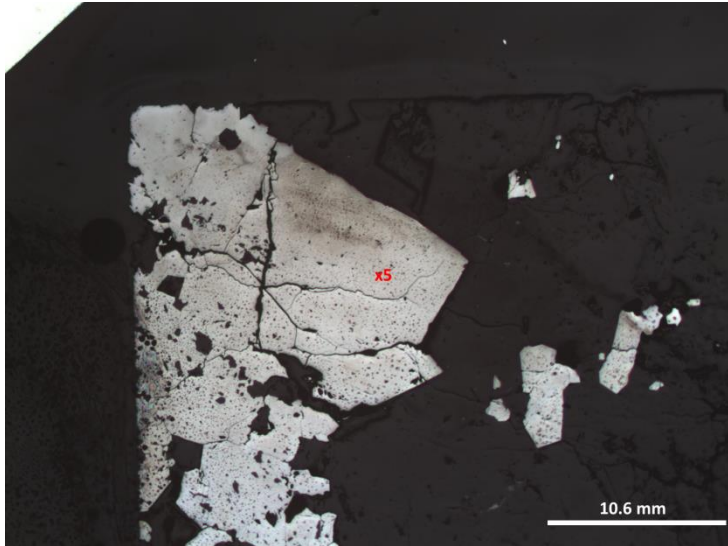
FK-227 Arsenopyrite Analysis 1.



FK-227 Arsenopyrite Analysis 2.



FK-227 Arsenopyrite Analyses 3 and 4.



FK-227 Arsenopyrite Analysis 5.

E.2 Pyrite Sulfur Isotope Data

A: SIMS Pyrite Sulfur Isotope Data

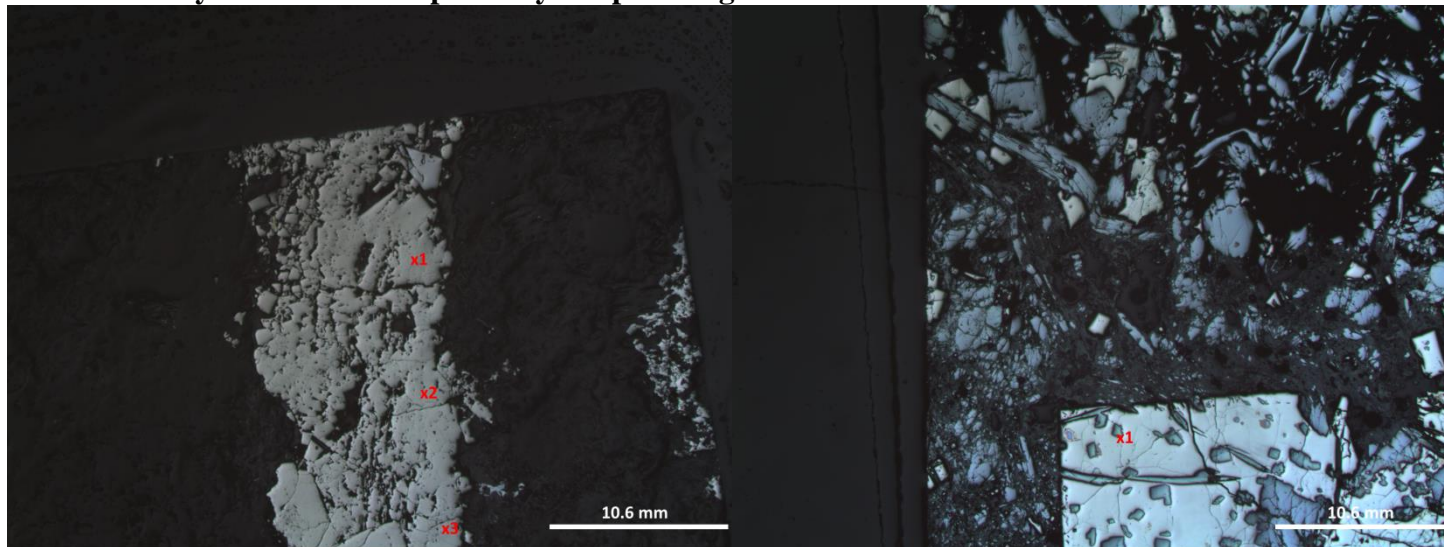
B: SIMS Pyrite Sulfur Isotope Analysis Spot Images

E.2.A SIMS Pyrite Sulfur Isotope Data

Sample	$^{34}\text{S}/^{32}\text{S}$ per mil	SEM	$^{34}\text{S}/^{32}\text{S}$ ratio	2SD	SEM %	Poisson %	N
FK-099 Py 1	-5.3	0.5	0.04291	0.00033	0.047283	0.027557	66
FK-099 Py 2	-4.3	0.2	0.042951	0.000161	0.021698	0.024866	75
FK-099 Py 3	-3.8	0.2	0.042975	0.000171	0.022979	0.024259	75
FK-TH12-03 Py 1	0.2	0.3	0.043146	0.000187	0.025955	0.023844	70
FK-TH12-03 Py 2	1.0	0.3	0.04318	0.000185	0.02539	0.023803	71
FK-TH12-03 Py 3	-1.3	0.4	0.043082	0.000305	0.042301	0.024488	70
FK-TH12-03 Py 4	-0.3	0.3	0.043122	0.000209	0.029406	0.02404	68
FK-TH12-03 Py 5	-0.3	0.2	0.043123	0.000158	0.02136	0.023213	74
FK-TH12-36 Py 1	0.1	0.2	0.043143	0.000164	0.021986	0.022947	75
FK-TH12-36 Py 2	-0.5	0.3	0.043117	0.000203	0.028361	0.02648	69
FK-TH12-36 Py 3	0.3	0.3	0.043151	0.000206	0.028125	0.025196	72
FK-TH12-36 Py 4	1.1	0.3	0.043183	0.000211	0.029406	0.024962	69
FK-TH12-36 Py 5	-1.9	0.3	0.043054	0.000197	0.027163	0.024279	71
FK-TH12-36 Py 6	-3.9	0.2	0.042968	0.000154	0.021099	0.02363	72
FK-025 Py 1	1.1	0.3	0.043182	0.00019	0.0265	0.023364	69
FK-025 Py 2	-0.2	0.1	0.043112	0.000348	0.048229	0.024784	70
FK-025 Py 3	0.7	0.3	0.043159	0.000341	0.04869	0.023427	66
FK-321 Py 1	-6.1	0.2	0.042873	0.000183	0.024747	0.025096	74
FK-321 Py 2	1.2	0.8	0.043188	0.000526	0.077291	0.025897	62
FK-321 Py 3	0.2	0.4	0.043147	0.000306	0.043254	0.025571	67
FK-321 Py 4	2.6	0.3	0.04325	0.000244	0.034018	0.025124	69
FK-321 Py 5	1.8	0.3	0.043214	0.000184	0.026817	0.025621	63
FK-TH12-60 Py 1	1.9	0.7	0.043218	0.000457	0.065039	0.02375	66
FK-TH12-60 Py 2	-1.0	0.5	0.043093	0.000313	0.044985	0.02323	65

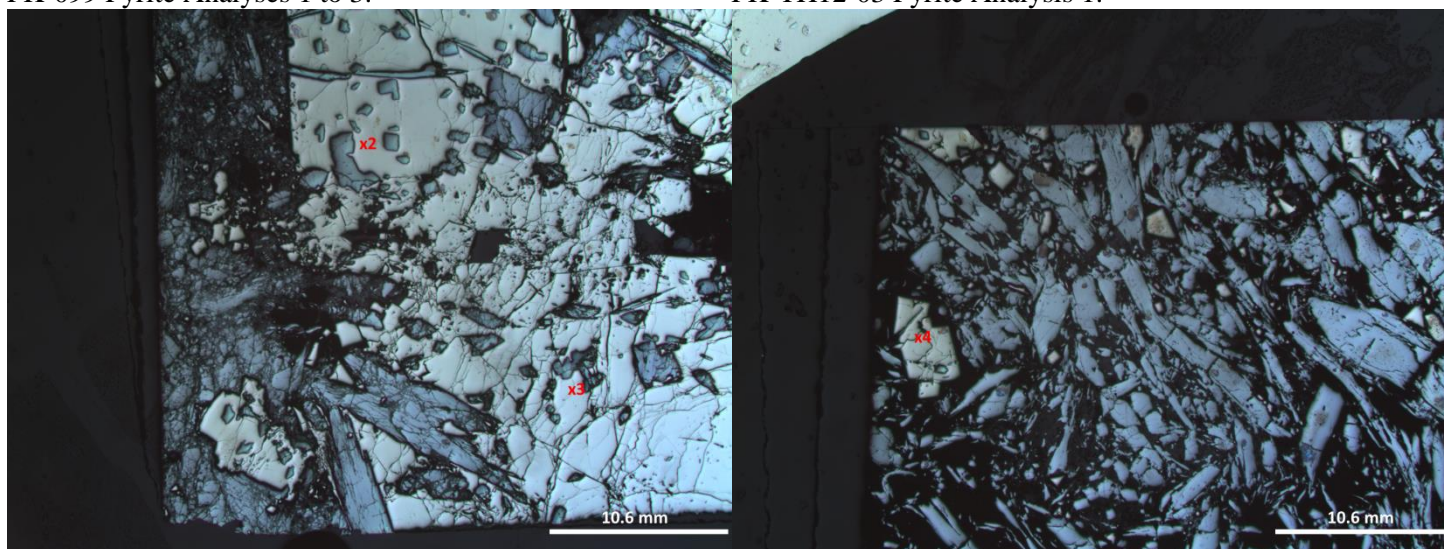
Standards	$^{34}\text{S}/^{32}\text{S}$ per mil	SEM	$^{34}\text{S}/^{32}\text{S}$ ratio	2SD	SEM %	Poisson %	N
UL9 2 Apr 17 2013	15.6	0.3	0.043817	0.000225	0.032302	0.02385	63
UL9 3 Apr 17 2013	15.8	0.2	0.043824	0.00016	0.020953	0.021504	76
UL9 1 Apr 18 2013	15.6	0.4	0.043817	0.000266	0.036336	0.029197	70
UL9 2 Apr 18 2013	16.0	0.3	0.043834	0.000208	0.028153	0.027861	71

E.2.B SIMS Pyrite Sulfur Isotope Analysis Spot Images



FK-099 Pyrite Analyses 1 to 3.

FK-TH12-03 Pyrite Analysis 1.

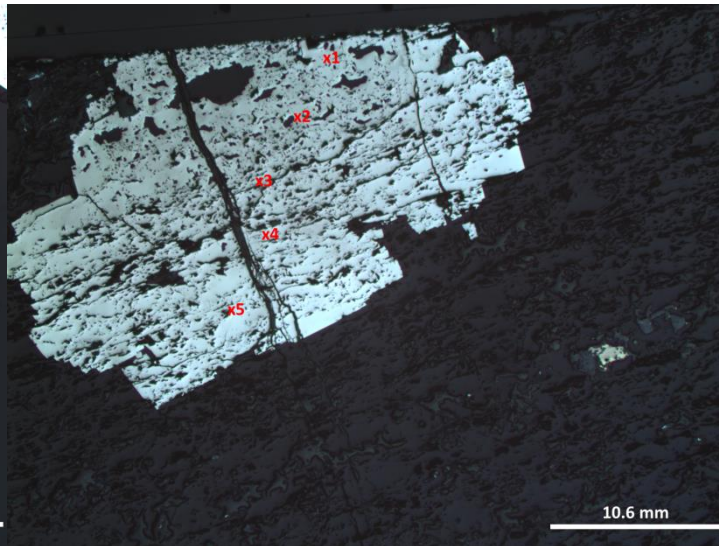


FK-TH12-03 Pyrite Analyses 2 and 3.

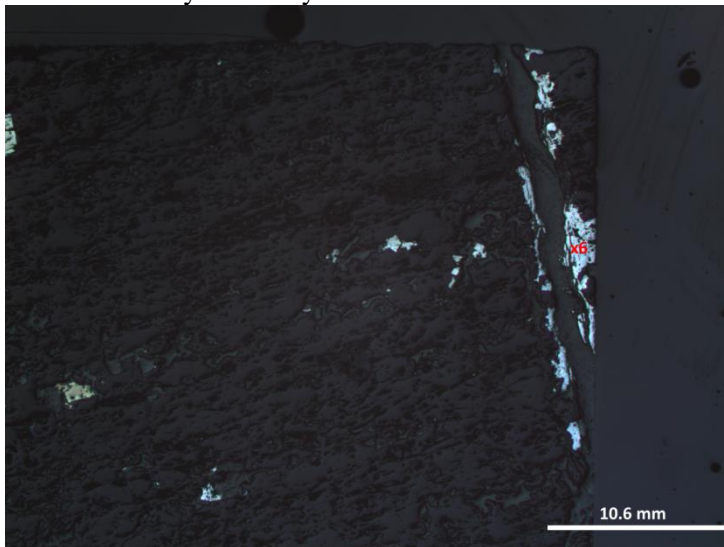
FK-TH12-03 Pyrite Analysis 4.



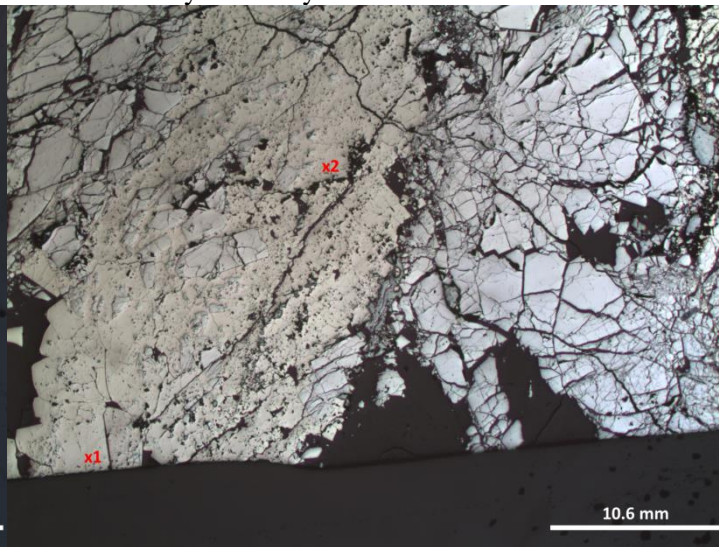
FK-TH12-03 Pyrite Analysis 5.



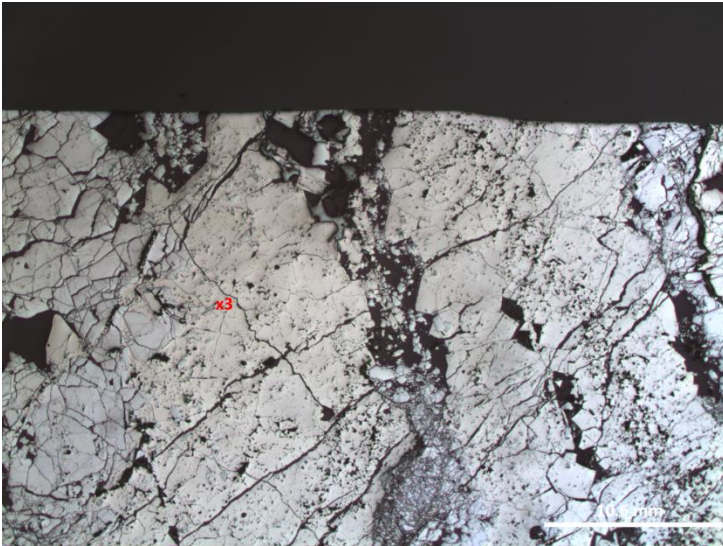
FK-TH12-36 Pyrite Analyses 1 to 5.



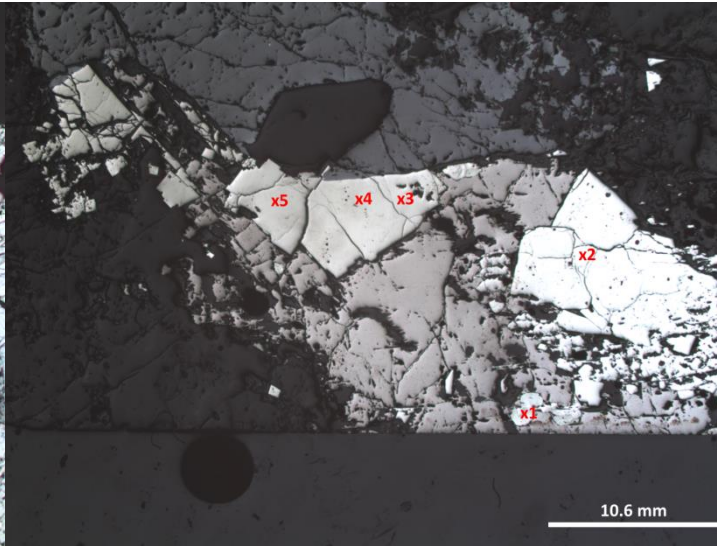
FK-TH12-36 Pyrite Analysis 6.



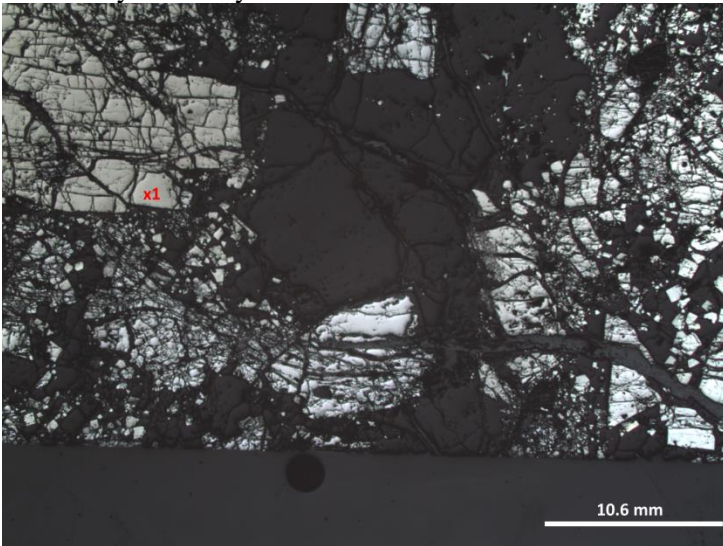
FK-025 Pyrite Analyses 1 and 2.



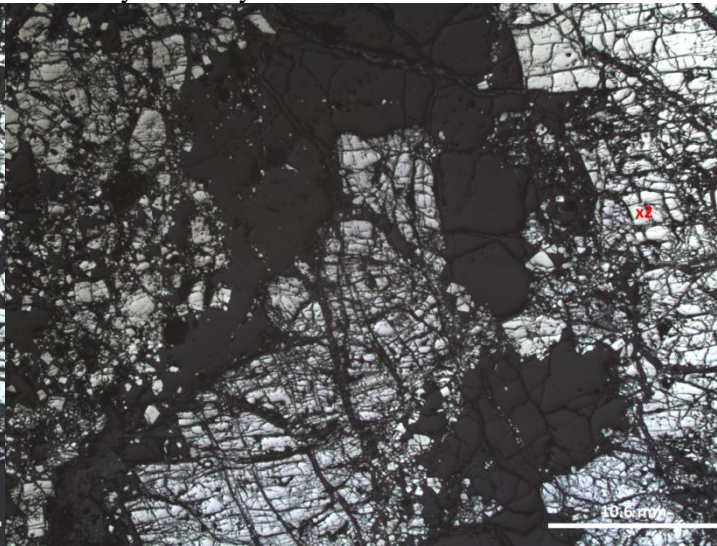
FK-025 Pyrite Analysis 3.



FK-321 Pyrite Analyses 1 to 5.



FK-TH12-60 Pyrite Analysis 1.



FK-TH12-60 Pyrite Analysis 2.

E.3 Pyrrhotite Sulfur Isotope Data

A: SIMS Pyrrhotite Sulfur Isotope Data

B: SIMS Pyrrhotite Sulfur Isotope Analysis Spot Images

E.3.A SIMS Pyrrhotite Sulfur Isotope Data

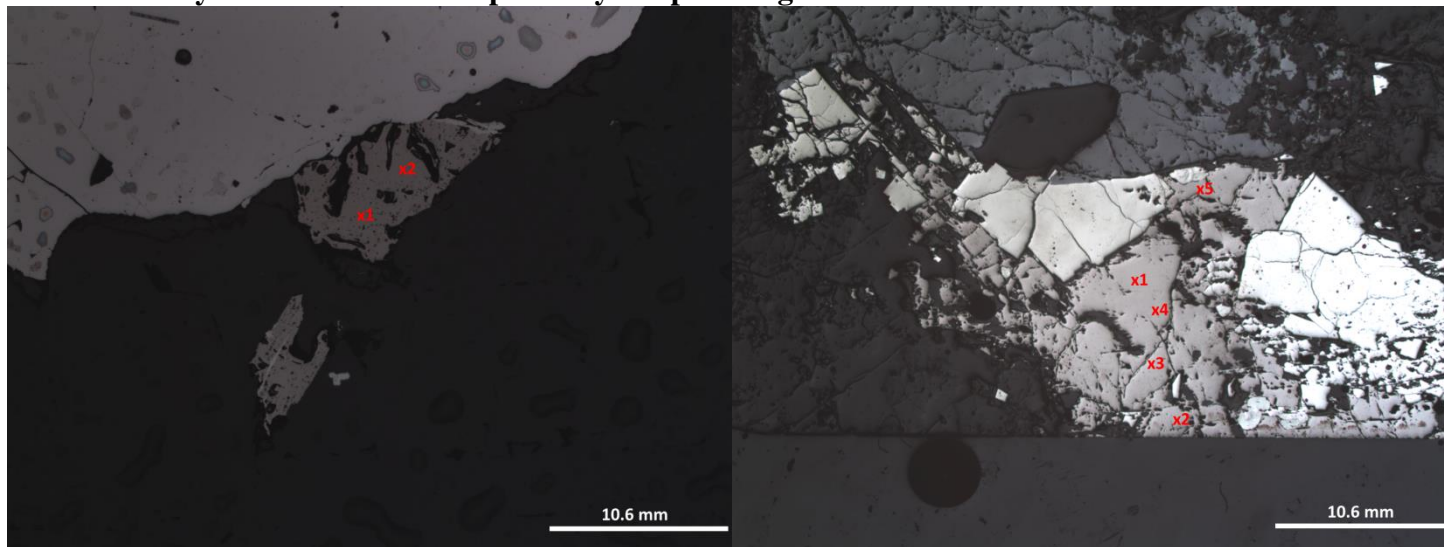
Sample	$^{34}\text{S}/^{32}\text{S}$ per mil	SEM	$^{34}\text{S}/^{32}\text{S}$ ratio	2SD	SEM %	Poisson %	N
FK-313 Po 1	-6.3	0.4	0.042759	0.000302	0.04248	0.029522	69
FK-313 Po 2	-6.4	0.3	0.042755	0.000227	0.033167	0.030104	64
FK-321 Po 1	2.5	0.3	0.043139	0.000214	0.029923	0.026074	69
FK-321 Po 2	2.6	0.2	0.043143	0.00016	0.022261	0.026253	69
FK-321 Po 3	1.2	0.2	0.04308	0.000151	0.020709	0.024972	72
FK-321 Po 4	1.8	0.2	0.043107	0.000153	0.020757	0.024273	73
FK-321 Po 5	1.5	0.2	0.043096	0.000149	0.020425	0.023992	72
FK-358 Po 1	-8.8	0.3	0.042654	0.00022	0.031965	0.028377	65
FK-358 Po 2	-9.1	0.5	0.042641	0.000324	0.04534	0.026907	70
FK-358 Po 3	-11.7	0.2	0.042531	0.000145	0.019749	0.026039	75
FK-358 Po 4	-12.7	0.2	0.042485	0.000149	0.020391	0.025843	74
FK-358 Po 5	-8.7	0.2	0.042656	0.000153	0.020865	0.024801	74
FK-007 Po 1	-6.8	0.2	0.043197	0.000152	0.020432	0.021094	74
FK-007 Po 2	-7.9	0.1	0.043142	0.000203	0.027348	0.022041	74
FK-007 Po 3	-7.4	0.3	0.043168	0.000186	0.024914	0.021843	75
FK-096 Po 1	-3.8	0.2	0.043323	0.000155	0.021216	0.021702	71
FK-096 Po 2	-3.6	0.2	0.043335	0.000171	0.023185	0.021494	72
FK-096 Po 3	-2.6	0.2	0.043376	0.000141	0.019712	0.022201	68
FK-097 Po 1	-2.5	0.4	0.043382	0.000287	0.039035	0.020159	72
FK-097 Po 2	-4.4	0.3	0.043299	0.000191	0.025449	0.021605	75
FK-097 Po 3	0.0	0.2	0.043491	0.00015	0.019808	0.021803	76
FK-097 Po 4	-2.1	0.3	0.0434	0.000236	0.032296	0.022148	71
FK-097 Po 5	-0.6	0.3	0.043462	0.000199	0.026281	0.021761	76
FK-105 Po 5	-5.2	0.2	0.043265	0.000144	0.019579	0.024307	72
FK-105 Po 1	-6.3	0.3	0.043218	0.000208	0.027835	0.023345	75
FK-105 Po 2	-6.5	0.2	0.04321	0.000167	0.022353	0.023413	75
FK-105 Po 3	-5.6	0.4	0.043248	0.000273	0.036379	0.023545	75

Sample	$^{34}\text{S}/^{32}\text{S}$ per mil	SEM	$^{34}\text{S}/^{32}\text{S}$ ratio	2SD	SEM %	Poisson %	N
FK-105 Po 4	-6.9	0.2	0.04319	0.000146	0.019795	0.023899	73
FK-105 Po 6	-5.5	0.2	0.04325	0.000171	0.022965	0.023882	74
FK-146 Po 1	-4.2	0.3	0.043306	0.000196	0.0263	0.02288	74
FK-146 Po 2	-8.4	0.2	0.043128	0.000148	0.019721	0.022498	76
FK-146 Po 3	-7.8	0.3	0.043154	0.000197	0.026675	0.022757	73
FK-146 Po 4	-9.6	0.1	0.043073	0.00012	0.016066	0.022365	75
FK-146 Po 5	-5.5	0.2	0.043252	0.000158	0.021283	0.022403	74
FK-314 Po 1	-2.2	0.2	0.043393	0.00015	0.020483	0.022622	71
FK-314 Po 2	-1.9	0.3	0.043406	0.00019	0.025468	0.022338	74
FK-314 Po 3	-1.8	0.2	0.04341	0.000154	0.021064	0.022789	71
FK-314 Po 4	-3.6	0.3	0.043334	0.000205	0.027642	0.026407	73
FK-314 Po 5	-1.9	0.2	0.043406	0.00015	0.020508	0.022816	71
FK-315A Po 1	-7.4	0.2	0.043171	0.000153	0.02058	0.023225	74
FK-315A Po 2	-4.4	0.2	0.043298	0.00017	0.022952	0.023516	73
FK-315A Po 3	-4.5	0.2	0.043296	0.000145	0.019355	0.023026	75
FK-315A Po 4a	-5.3	0.2	0.043261	0.000172	0.024045	0.024421	68
FK-315A Po 5	-6.8	0.2	0.043195	0.000177	0.02417	0.023752	72
FK-326 Po 1	-8.4	0.2	0.043127	0.000152	0.02039	0.023423	75
FK-326 Po 2	-7.6	0.2	0.043159	0.000141	0.01903	0.023346	74
FK-326 Po 3	-6.8	0.2	0.043195	0.000135	0.018094	0.022846	75
FK-326 Po 4	-6.9	0.2	0.043192	0.000134	0.017822	0.022232	76
FK-346 Po 1	-7.5	0.3	0.043166	0.000228	0.031395	0.023098	71
FK-346 Po 2	-6.9	0.2	0.043191	0.000134	0.018217	0.02285	73
FK-346 Po 3	-6.9	0.2	0.043192	0.00013	0.017432	0.022043	74
FK-346 Po 4	-7.0	0.2	0.043185	0.000147	0.019586	0.021587	75
FK-346 Po 5	-7.4	0.2	0.043171	0.000159	0.021237	0.021744	75
FK-TH12-29 Po 1	3.1	0.2	0.043571	0.000175	0.023686	0.021349	72
FK-TH12-29 Po 2	3.2	0.2	0.043573	0.000175	0.023171	0.020885	75

Sample	$^{34}\text{S}/^{32}\text{S}$ per mil	SEM	$^{34}\text{S}/^{32}\text{S}$ ratio	2SD	SEM %	Poisson %	N
FK-TH12-29 Po 3	2.8	0.3	0.043559	0.000194	0.025524	0.020359	76
FK-TH12-29 Po 4	4.5	0.2	0.043631	0.000165	0.021592	0.020134	77
FK-TH12-29 Po 5	4.9	0.6	0.04365	0.000387	0.054092	0.021294	67
FK-TH12-29 Po 6	4.0	0.3	0.043612	0.000193	0.025414	0.020658	76
FK-348 Po 1	-6.1	0.2	0.043171	0.000157	0.0212	0.025684	74
FK-348 Po 2	-4.1	0.3	0.04326	0.000234	0.03119	0.025176	75
FK-348 Po 3	-5.7	0.2	0.043191	0.000184	0.02464	0.025054	75
FK-348 Po 4	-6.6	0.2	0.043151	0.000164	0.022048	0.024391	74
FK-348 Po 5	-5.5	0.3	0.043196	0.00022	0.030395	0.02515	70

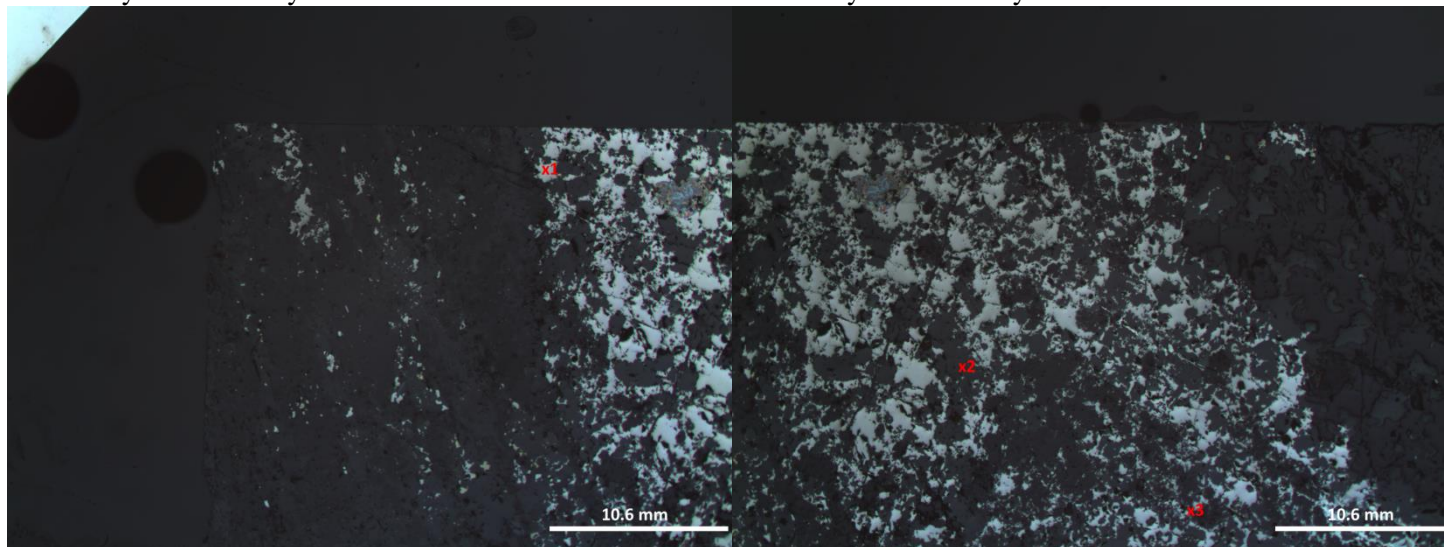
Standards	$^{34}\text{S}/^{32}\text{S}$ per mil	SEM	$^{34}\text{S}/^{32}\text{S}$ ratio	2SD	SEM %	Poisson %	N
PoW1 2 Apr 16 2013	2.3	0.3	0.04313	0.000224	0.031971	0.027709	66
PoW1 Apr 16 2013	2.3	0.3	0.043127	0.000186	0.025831	0.028211	70

E.3.B SIMS Pyrrhotite Sulfur Isotope Analysis Spot Images



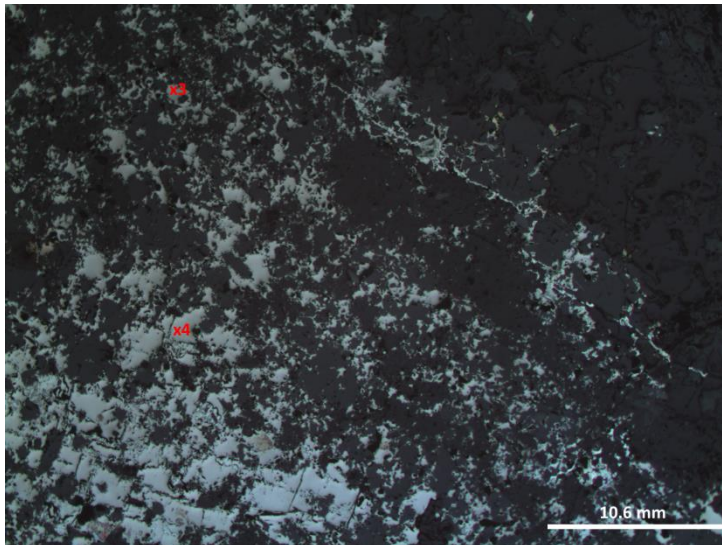
FK-313 Pyrrhotite Analyses 1 and 2.

FK-321 Pyrrhotite Analyses 1 to 5.

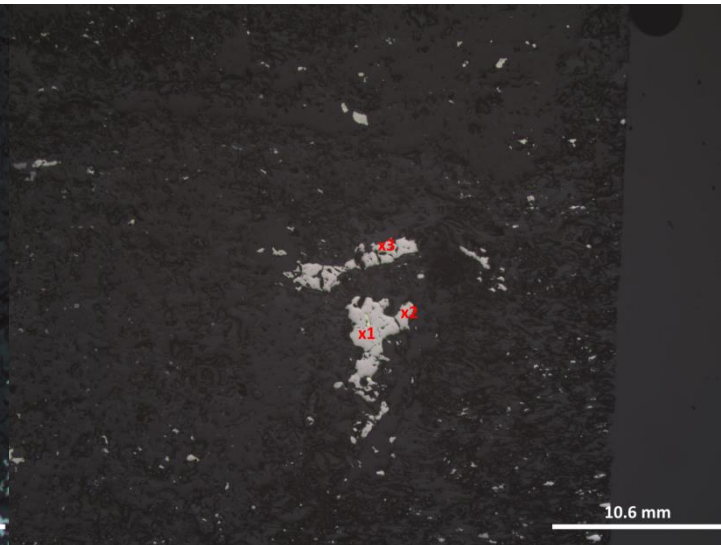


FK-358 Pyrrhotite Analysis 1.

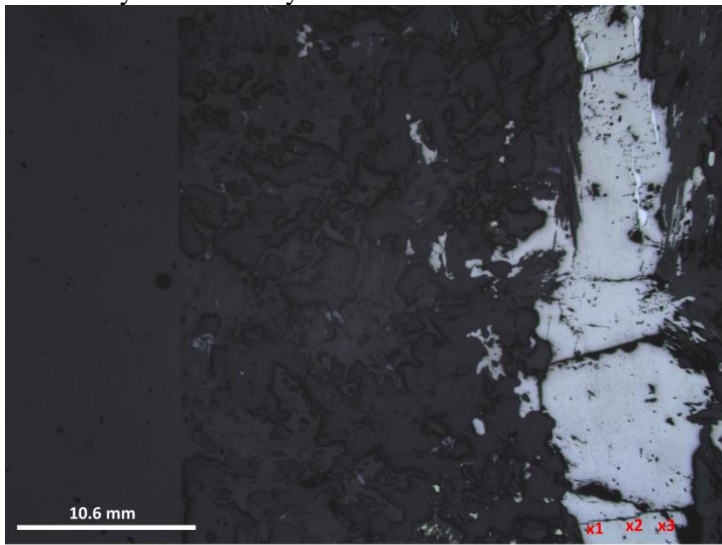
FK-358 Pyrrhotite Analyses 2 and 3.



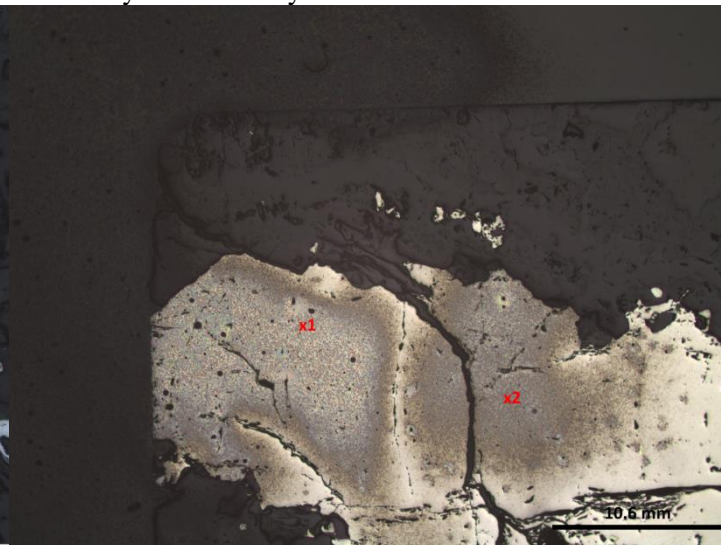
FK-358 Pyrrhotite Analyses 3 and 4.



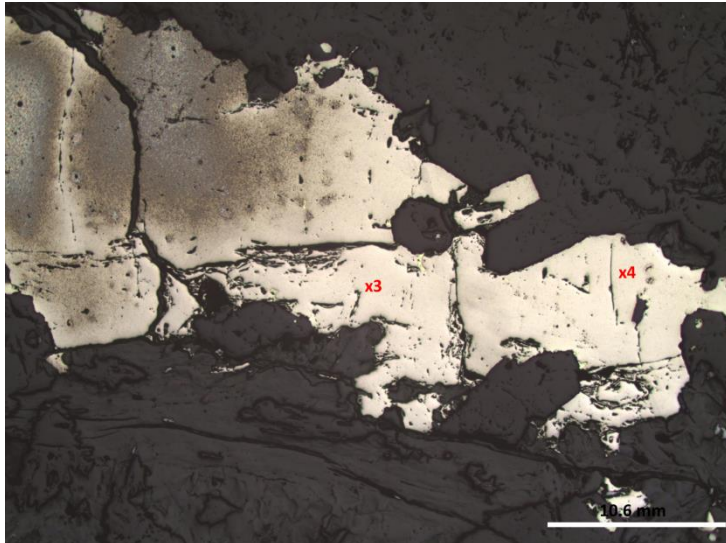
FK-007 Pyrrhotite Analyses 1 to 3.



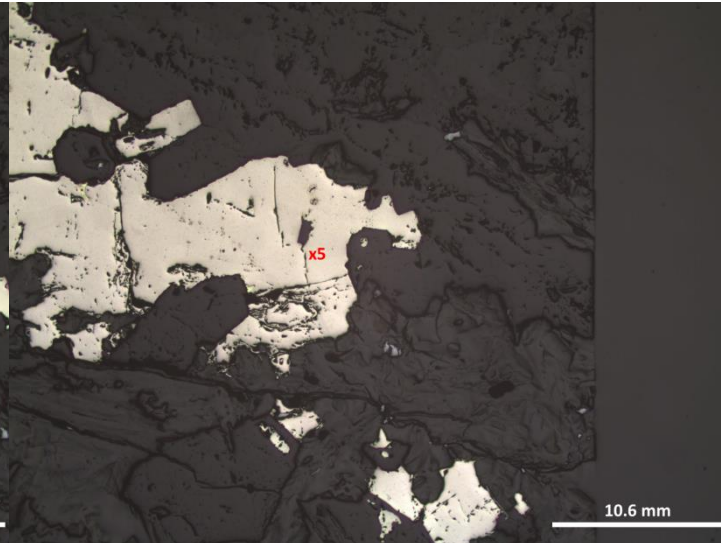
FK-096 Pyrrhotite Analyses 1 to 3.



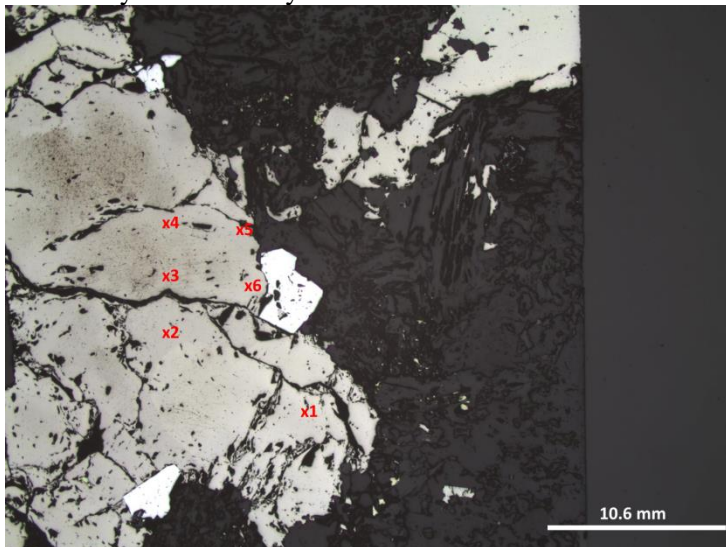
FK-097 Pyrrhotite Analyses 1 and 2.



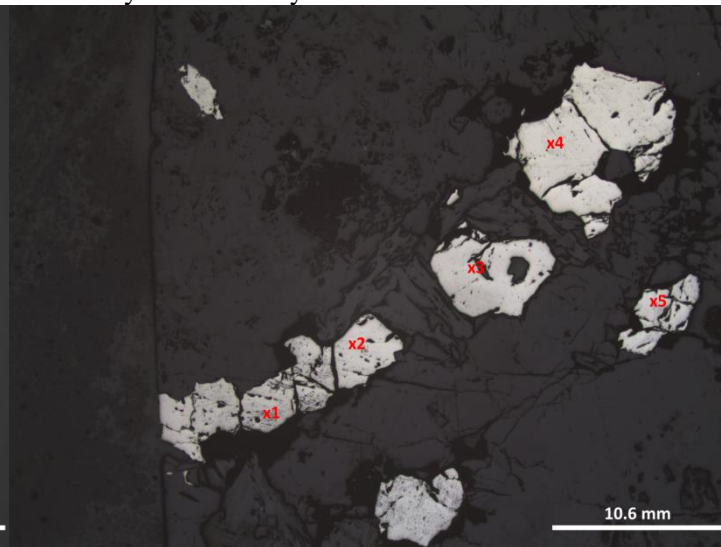
FK-097 Pyrrhotite Analyses 3 and 4.



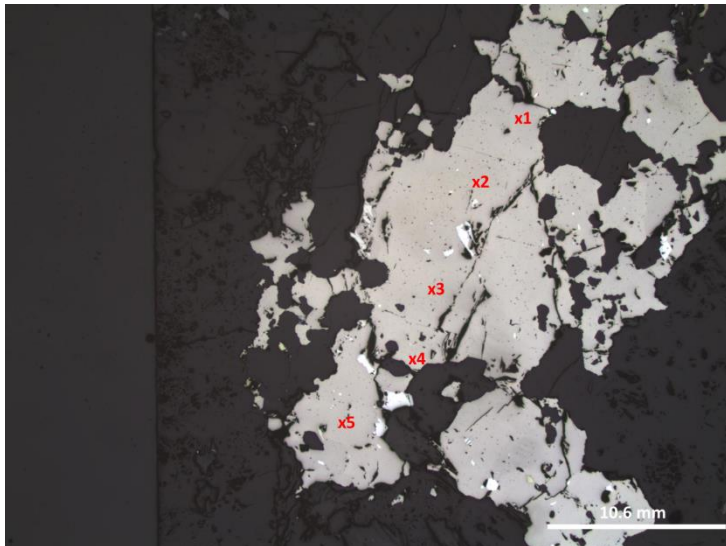
FK-097 Pyrrhotite Analysis 5.



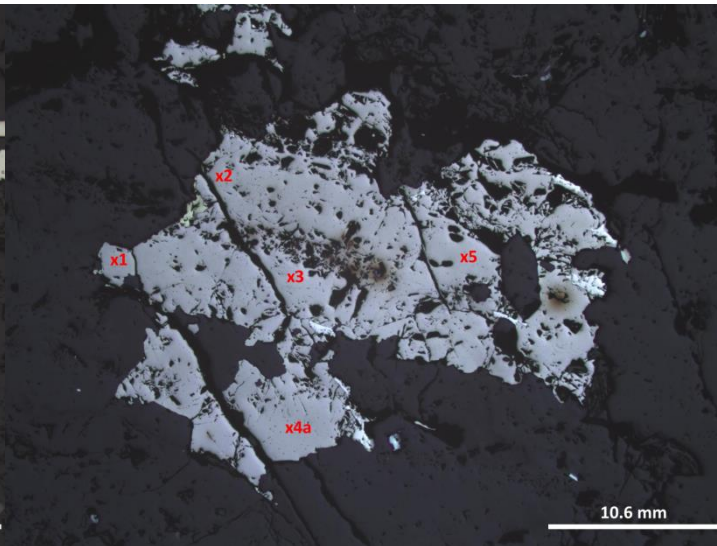
FK-105 Pyrrhotite Analyses 1 to 6.



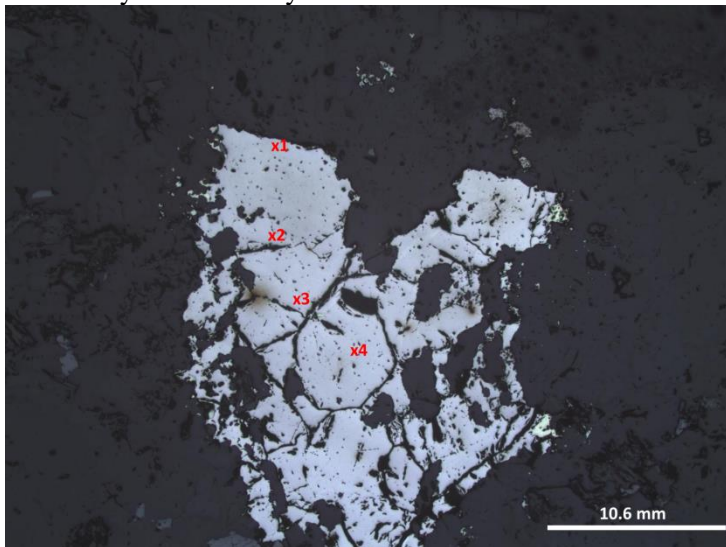
FK-146 Pyrrhotite Analyses 1 to 5.



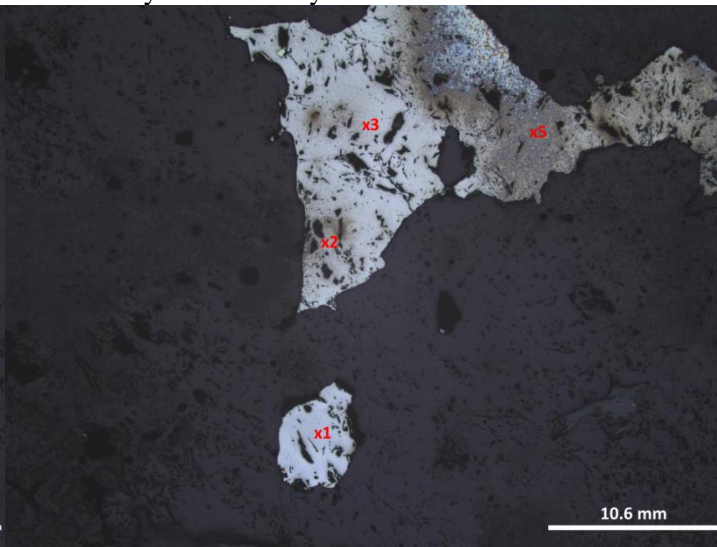
FK-314 Pyrrhotite Analyses 1 to 5.



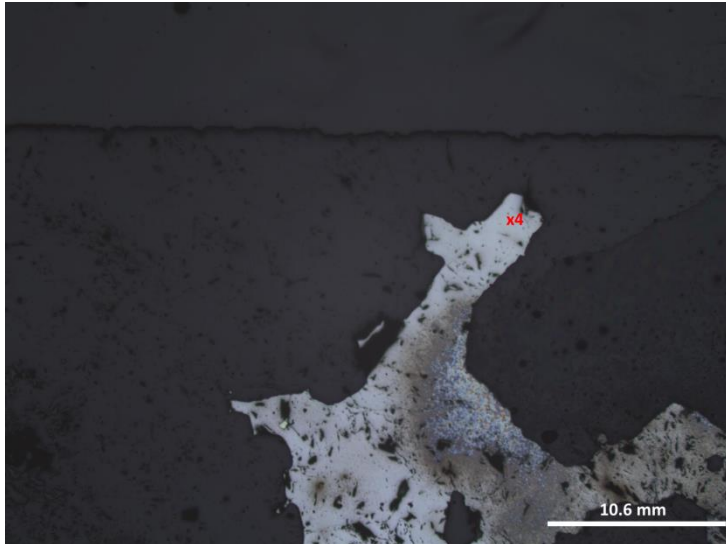
FK-315A Pyrrhotite Analyses 1 to 5.



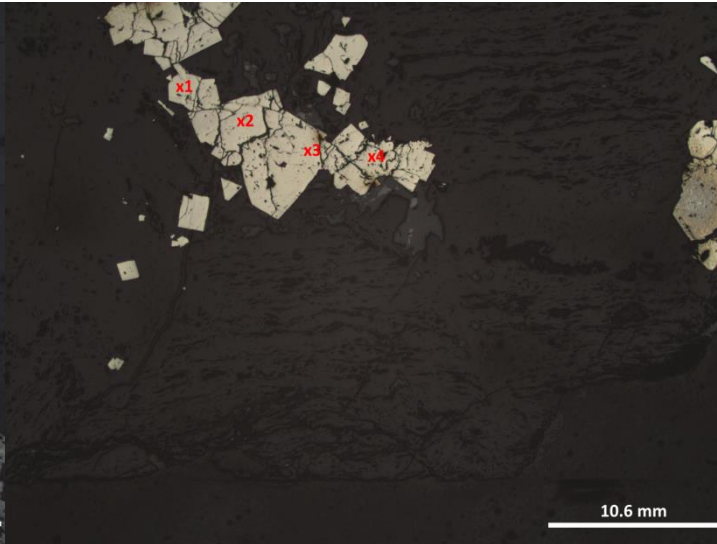
FK-326 Pyrrhotite Analyses 1 to 4.



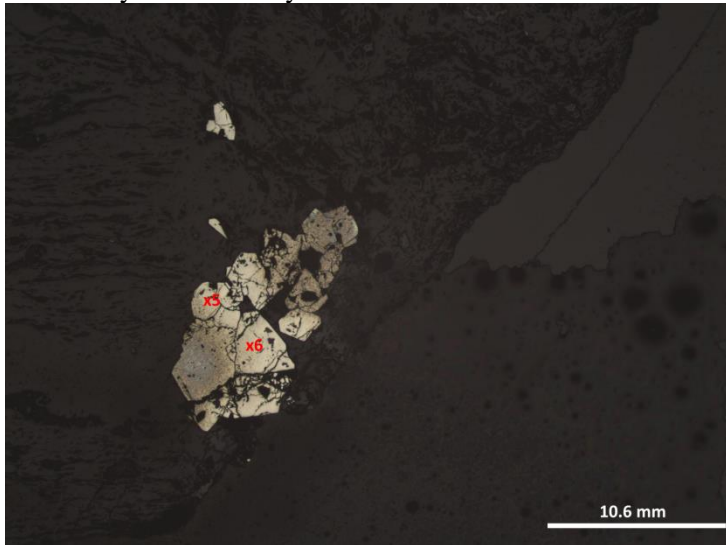
FK-346 Pyrrhotite Analyses 1, 2, 3 and 5.



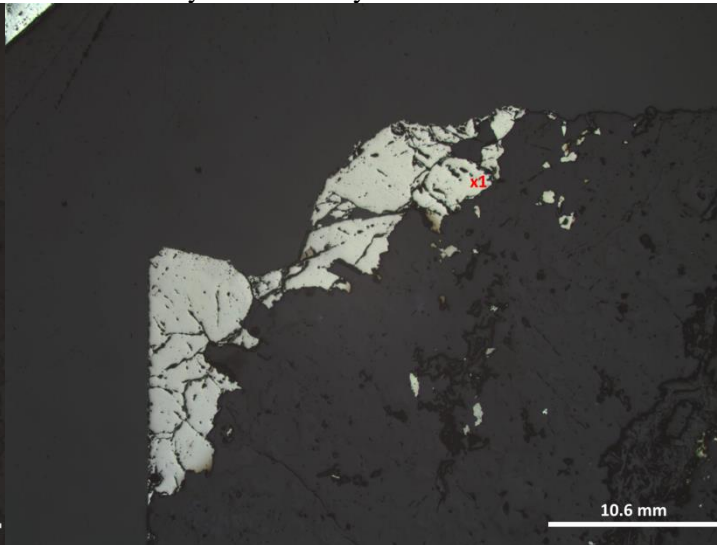
FK-346 Pyrrhotite Analysis 4.



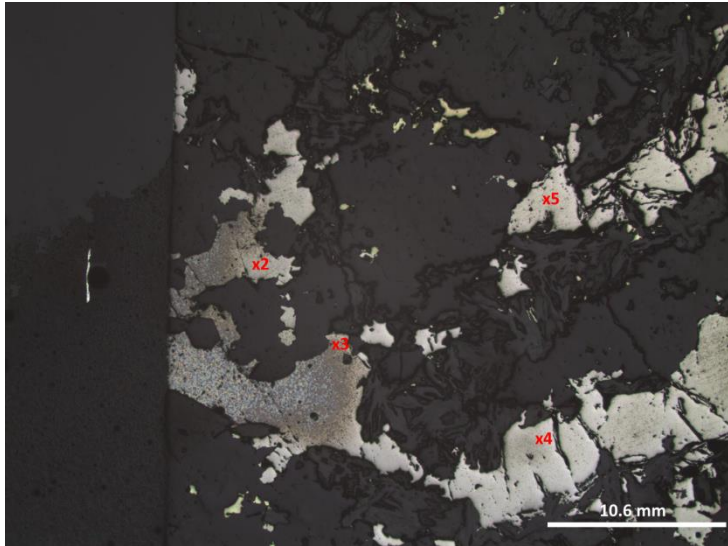
FK-TH12-29 Pyrrhotite Analyses 1 to 4.



FK-TH12-29 Pyrrhotite Analyses 5 and 6.



FK-348 Pyrrhotite Analysis 1.



FK-348 Pyrrhotite Analysis 2 to 5.

Appendix F: Lead Isotope Data

F.1 SIMS Lead Isotope Method

Sample Preparation

Small slabs of sulfide-bearing rock were embedded in two-component epoxy in 25 mm diameter aluminum retaining rings and prepared as flat polished mounts. After lapidary preparation, all samples were sputter coated with 300 Å of Au, to mitigate charging under primary ion bombardment.

Instrumentation

All analyses were performed using the Cameca IMS 4f Secondary Ion Mass Spectrometer at the MAF-IIC Microanalysis Facility of Memorial University. This instrument has been updated with additional source lensing in the primary column, enhancing the ability to deliver more finely focused beams of O⁻, which improves the spatial resolution for Pb isotope analyses. It has also been equipped with modernized ion detection systems that augment precision and reproducibility for stable isotope determinations in general.

Analytical Parameters

Pb isotope determinations were performed by bombarding the sample with a primary ion microbeam of 14-16 nA of O⁻, accelerated through a nominal 10 keV potential, and focused into an ~20 µm diameter spot. To exclude exotic material in the polished surface from analysis, each spot was first pre-sputtered for 120 s with a 25 µm square raster applied to the beam. A smaller square raster (10µm) was applied to the beam during analysis, to improve the homogeneity of primary ion delivery, while maintaining lateral resolution at better than 20-25 µm. The sample was pre-sputtered in this mode for an additional 75 s before data collection began.

Positively charged sputtered secondary ions (Pb⁺) were accelerated into the mass spectrometer of the instrument through a nominal potential of -4.5 keV. The instrument was operated with a medium Contrast Aperture (150 µm), and Entrance and Exit Slits paired to give flat topped peaks at a minimum mass resolving power (MRP) of 300 (10% peak height definition). A sample offset voltage of -60eV and Energy Window of 60eV width were deployed to effectively eliminate minor isobaric interferences through energy filtering. Maximum count rates (²⁰⁸Pb⁺) were generally less than 250,000 cps. Since absolute transmission is not an issue for these determinations, the simple 150 µm Transfer Lens mode was used, along with a large Field Aperture (1800 µm), giving an approximately 125 µm field of view in the mass spectrometer, and enabling easy monitoring of spot and sample centring.

Signals for ²⁰⁴Pb⁺, ²⁰⁶Pb⁺, ²⁰⁷Pb⁺ and ²⁰⁸Pb⁺, and a background position at 203.67 Da, were obtained by cyclical magnetic peak switching. Standard counting times and peak sequence used were; 1.0 s at the background position, 8.0 s on ²⁰⁴Pb⁺ and 4.0 s on each of ²⁰⁶Pb⁺, ²⁰⁷Pb⁺, and ²⁰⁸Pb⁺. Waiting times of 0.4 s (0.5 s for background position) were inserted before each peak counting position to allow for magnet settling. A typical analysis consisted of accumulating 15 of these peak cycles, which takes a total of 9.0 minutes (including pre-sputtering times).

All peak signals were collected with an ETP 133H multiple-dynode electron multiplier (em) and processed through ECL-based pulse-counting electronics with a system dead time of 12 ns. Background measurements at the nominal mass 203.67 Da were taken during each magnetic switching cycle – and were routinely less than 0.05–0.10 counts per second.

Any change in overall peak intensities with time - which is typically monotonic in homogeneous lead-rich sulfide mineral phases (and thus quantitatively minor in its effect on measured Pb ratios) - was compensated for using a standard double interpolation ratio algorithm (an approach adopted from TIMS analysis), with each $^{204,207,208}\text{Pb}^+$ peak ratioed to the time-corrected interpolation of the two immediately adjacent $^{206}\text{Pb}^+$ peaks.

Beyond the excellent spatial resolution, a further advantage of SIMS stems from the gradual nature of material removal by sputtering, with each counting interval producing depth-resolved data on the sample. Inclusions of other sulfide phases, in particular, have the potential to produce excursions in the measured Pb isotope ratios. However, the depth-resolved characteristic of SIMS allows the detection of even small inclusions, or other heterogeneities within the sample, simply by monitoring sharp excursions in signal intensity ($I^{204,206,207,208}\text{Pb}^+$) with time. These signal time intervals can then easily be eliminated from the measured data during processing.

Calibration of Instrumental Fractionation

The production and detection of sputtered secondary ions produces a mass dependent bias between the actual $^{204}\text{Pb}/^{206}\text{Pb}/^{207}\text{Pb}/^{208}\text{Pb}$ of the sample and that measured by the mass spectrometer – termed Instrumental Mass Fractionation (IMF). IMF in SIMS can generally be considered as a combination of mass discrimination effects at the site of sample sputtering with those in the ion detector(s) themselves. Other effects, related to the ion optics of the mass spectrometer, are reduced to comparatively insignificant levels in a properly and consistently aligned instrument.

The magnitude of IMF is modest for heavy elements like Pb – typically 0.05 – 0.15%/Da, depending largely on the age and condition of the em detector. Variation of IMF between galena and other lead-rich sulfides and sulfosalts is relatively insignificant. Pb isotope measurements measured in samples of these minerals were corrected for IMF by comparison to replicate in run measurements of reference materials F19 (galena: $^{204}\text{Pb}/^{206}\text{Pb}$ 16.960; $^{207}\text{Pb}/^{206}\text{Pb}$ 15.535; $^{208}\text{Pb}/^{206}\text{Pb}$ 36.538) and JMBH (galena: $^{204}\text{Pb}/^{206}\text{Pb}$ 16.069; $^{207}\text{Pb}/^{206}\text{Pb}$ 15.451; $^{208}\text{Pb}/^{206}\text{Pb}$ 35.795).

Accuracy and Reproducibility

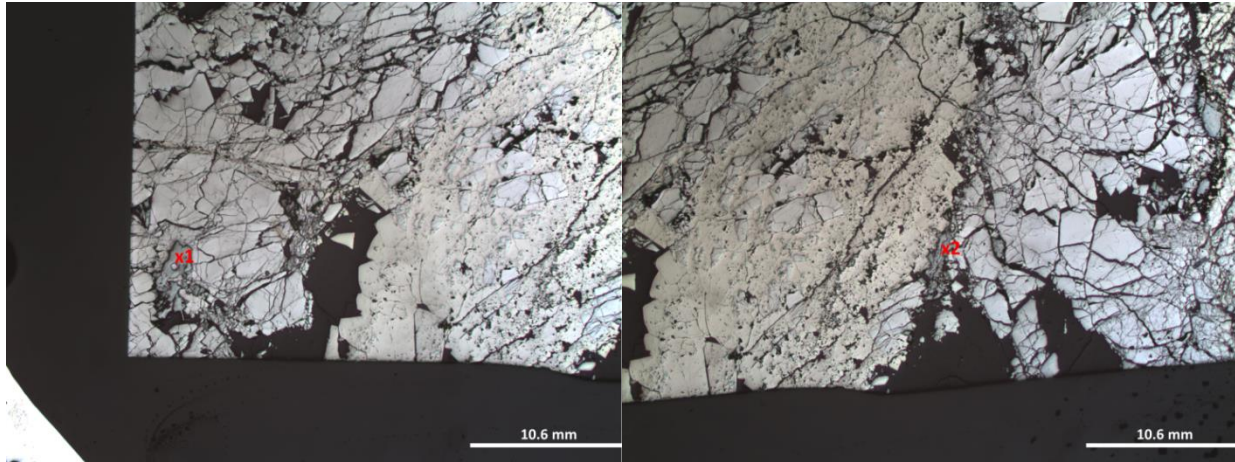
15 cycle analyses accumulated in 9 min routinely yield internal precisions (standard error of the mean) on $^{204}\text{Pb}/^{206}\text{Pb}$, $^{207}\text{Pb}/^{206}\text{Pb}$ and $^{208}\text{Pb}/^{206}\text{Pb}$ determinations of better than ± 0.05 - 0.10% (1σ), while producing sputter craters only a few μm deep. Overall reproducibility, based on replicate analyses of the secondary standard JMBH, is typically better than ± 0.10 – 0.15% for these same ratios.

F.2 Lead Isotope Data

Sample	$^{204}\text{Pb}/^{206}\text{Pb}$	SEM	Poisson	$^{207}\text{Pb}/^{206}\text{Pb}$	SEM	Poisson	$^{208}\text{Pb}/^{206}\text{Pb}$	SEM	Poisson
		%	%		%	%		%	%
FK 025 Pb1	0.04856	0.1	0.2	0.774	0.09	0.05	1.966	0.11	0.04
FK 025 Pb2	0.04856	0.05	0.2	0.7744	0.06	0.05	1.972	0.08	0.04
FK 025 Pb3	0.0486	0.06	0.2	0.7725	0.07	0.05	1.963	0.14	0.04
FK 025 Pb4	0.04861	0.1	0.2	0.7741	0.03	0.05	1.967	0.04	0.04
FK 025 Pb5	0.04864	0.06	0.2	0.7743	0.04	0.05	1.969	0.03	0.04
FK 036 Pb1	0.04883	0.08	0.24	0.7802	0.04	0.07	1.9817	0.05	0.05
FK 036 Pb2	0.04899	0.09	0.19	0.7805	0.04	0.05	1.9833	0.04	0.04
FK 066 Pb1	0.04805	0.1	0.21	0.7681	0.08	0.06	1.97	0.1	0.04
FK 066 Pb2	0.04797	0.07	0.21	0.7671	0.02	0.06	1.967	0.06	0.04
FK 066 Pb3	0.04784	0.11	0.22	0.7661	0.05	0.06	1.96	0.06	0.04
FK 066 Pb4	0.04758	0.1	0.21	0.7619	0.06	0.06	1.956	0.1	0.04
FK 066 Pb5	0.04792	0.09	0.19	0.7677	0.04	0.05	1.968	0.03	0.04
FK 066 Pb6	0.04812	0.16	0.2	0.7676	0.25	0.05	1.97	0.28	0.04
FK 066 Pb7	0.04795	0.06	0.2	0.7679	0.04	0.05	1.966	0.04	0.04
FK 285 Pb1	0.04858	0.08	0.21	0.7754	0.03	0.06	1.9879	0.02	0.04
FK 285 Pb2	0.04863	0.07	0.19	0.7770	0.04	0.05	1.9918	0.02	0.04
FK 285 Pb3	0.04848	0.11	0.21	0.7781	0.08	0.06	1.9931	0.16	0.04
FK 285 Pb4	0.04868	0.08	0.19	0.7781	0.03	0.05	1.9952	0.04	0.04
FK TH12 03 Pb1	0.04608	0.06	0.19	0.7405	0.04	0.05	1.939	0.04	0.04
FK TH12 03 Pb2	0.04607	0.07	0.19	0.7409	0.02	0.05	1.942	0.04	0.03
FK TH12 56 Pb1	0.04795	0.05	0.17	0.7671	0.02	0.05	1.966	0.04	0.03

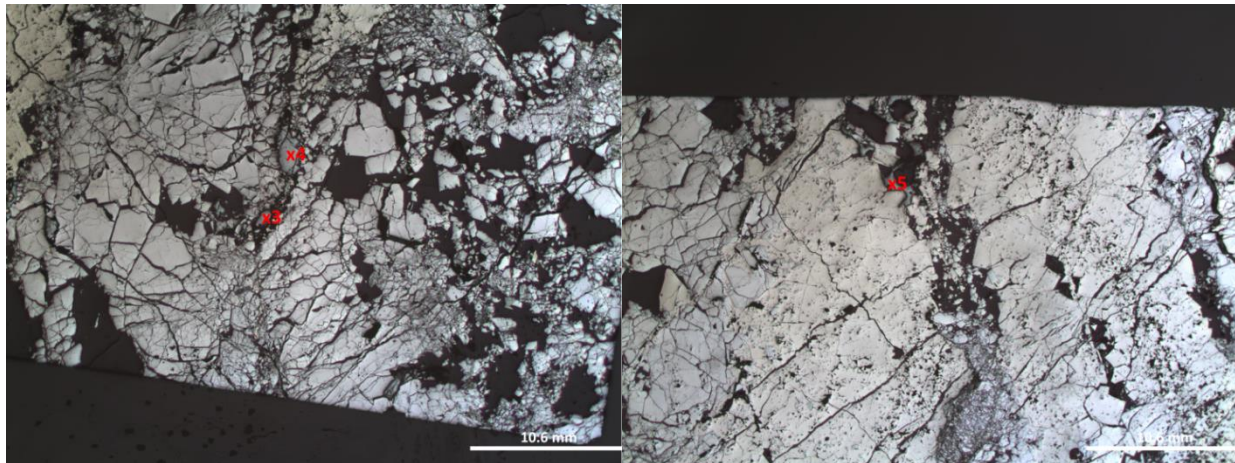
Sample	$^{206}\text{Pb}/^{204}\text{Pb}$	SEM	$^{207}\text{Pb}/^{204}\text{Pb}$	SEM	$^{208}\text{Pb}/^{204}\text{Pb}$	SEM
		%		%		%
FK 025 Pb1	20.59	0.1	15.94	0.13	40.48	0.15
FK 025 Pb2	20.59	0.05	15.95	0.08	40.61	0.09
FK 025 Pb3	20.57	0.06	15.89	0.1	40.39	0.15
FK 025 Pb4	20.57	0.1	15.92	0.1	40.46	0.11
FK 025 Pb5	20.56	0.06	15.92	0.07	40.49	0.07
FK 036 Pb1	20.48	0.08	15.98	0.09	40.58	0.10
FK 036 Pb2	20.41	0.09	15.93	0.10	40.49	0.10
FK 066 Pb1	20.81	0.1	15.98	0.12	40.99	0.14
FK 066 Pb2	20.85	0.07	15.99	0.07	41.01	0.09
FK 066 Pb3	20.9	0.11	16.01	0.12	40.97	0.12
FK 066 Pb4	21.02	0.1	16.01	0.12	41.11	0.14
FK 066 Pb5	20.87	0.09	16.02	0.09	41.08	0.09
FK 066 Pb6	20.78	0.16	15.95	0.3	40.93	0.32
FK 066 Pb7	20.85	0.06	16.01	0.07	41.01	0.07
FK 285 Pb1	20.58	0.08	15.96	0.08	40.92	0.08
FK 285 Pb2	20.56	0.07	15.98	0.08	40.96	0.08
FK 285 Pb3	20.63	0.11	16.05	0.14	41.11	0.19
FK 285 Pb4	20.54	0.08	15.98	0.08	40.99	0.09
FK TH12 03 Pb1	21.7	0.06	16.07	0.07	42.08	0.07
FK TH12 03 Pb2	21.71	0.07	16.08	0.07	42.15	0.08
FK TH12 56 Pb1	20.85	0.05	16	0.06	40.99	0.06

F.3 SIMS Lead Isotope Analysis Spot Images



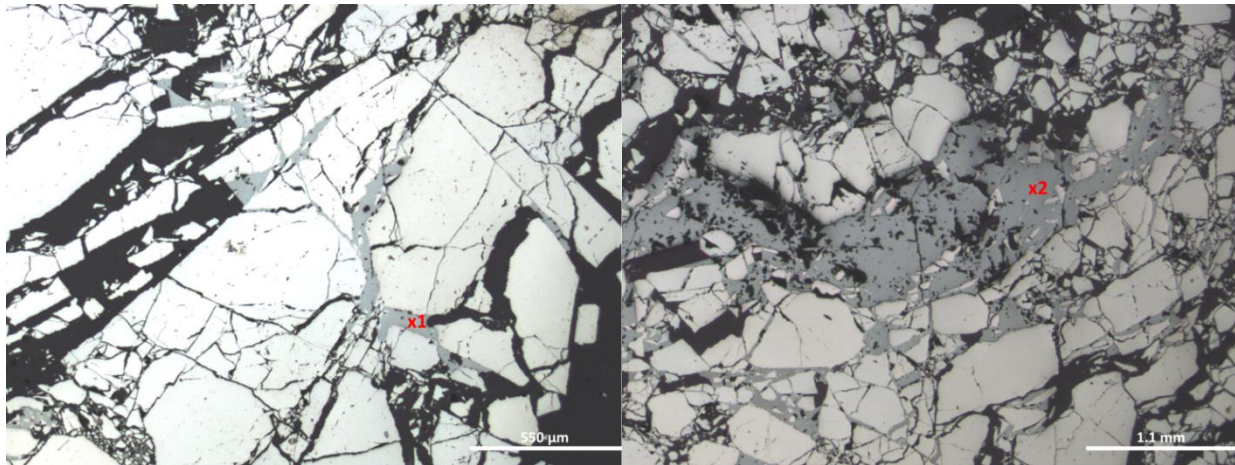
FK-025 Pb1

FK-025 Pb2



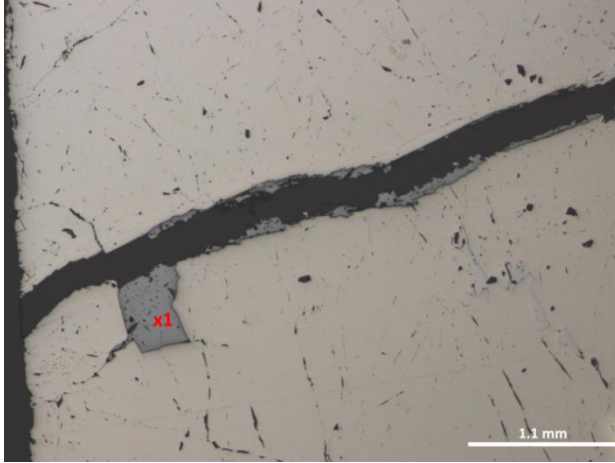
FK-025 Pb3

FK-025 Pb4

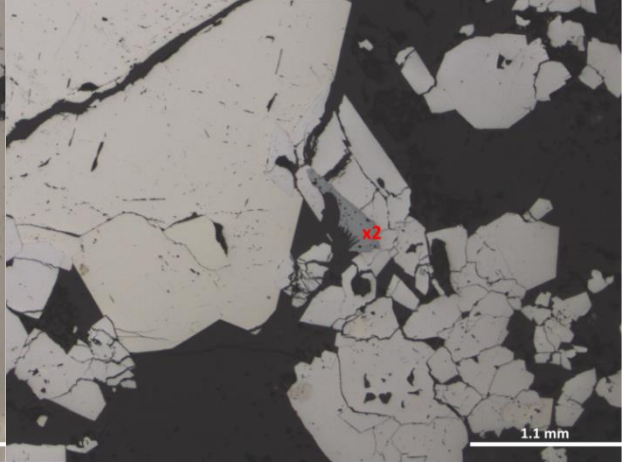


FK-036 Pb1

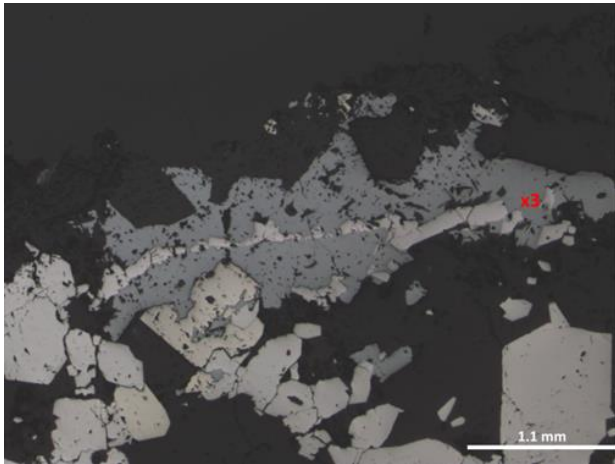
FK-036 Pb2



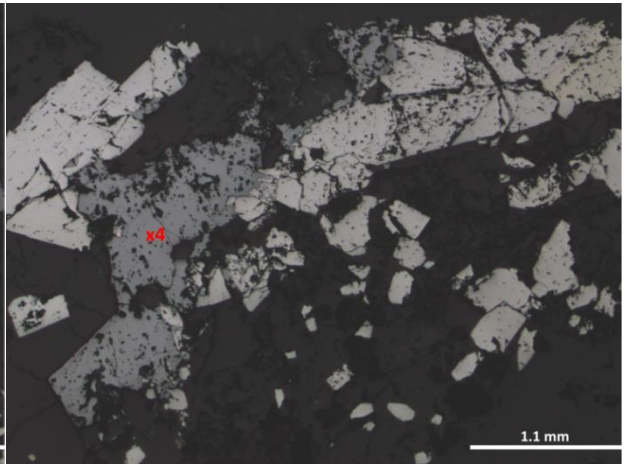
FK-066Pb1



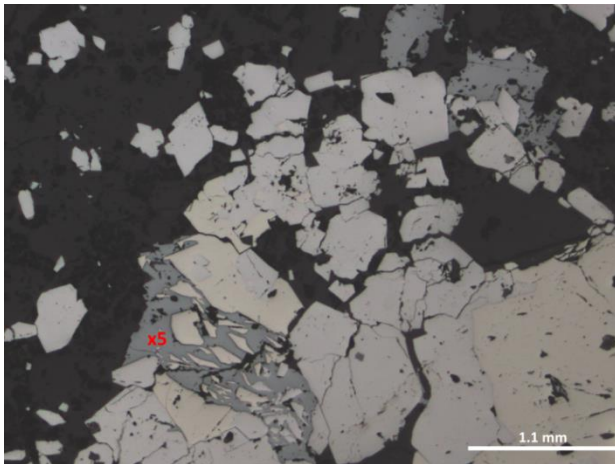
FK-066 Pb2



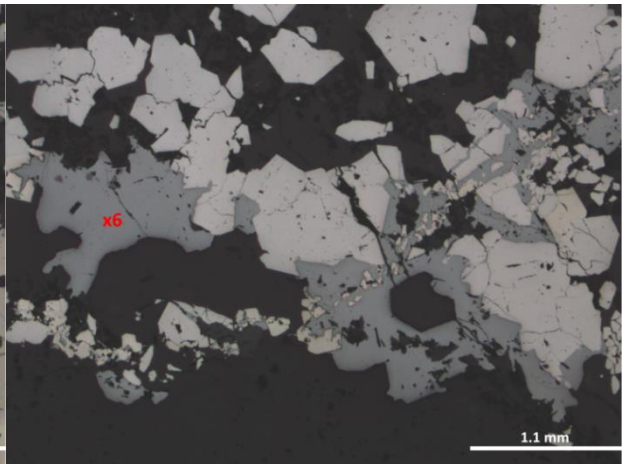
FK-066 Pb3



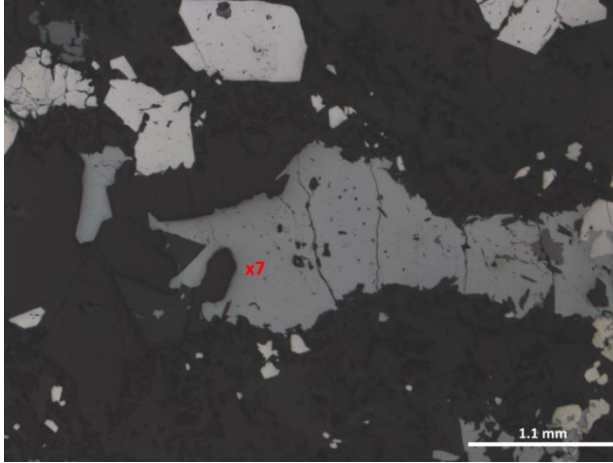
FK-066 Pb4



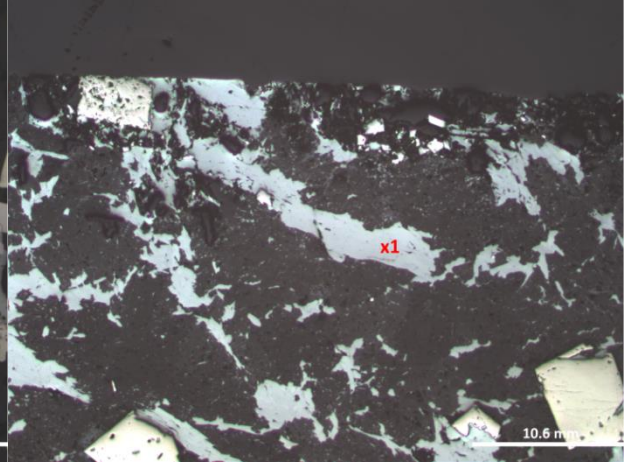
FK-066 Pb5



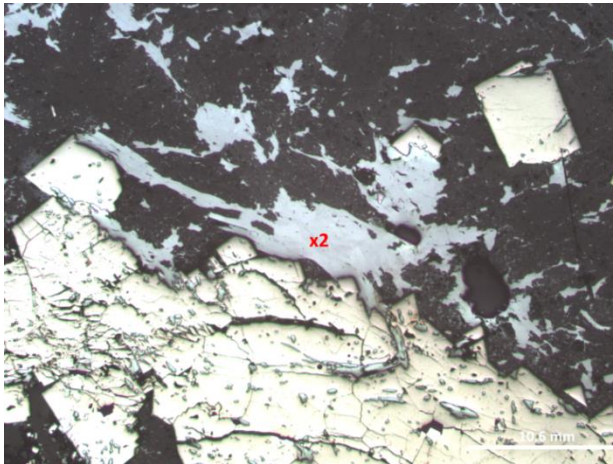
FK-066 Pb6



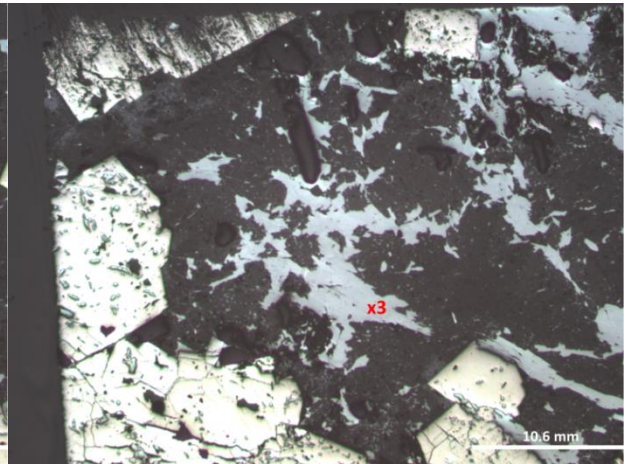
FK-066 Pb7



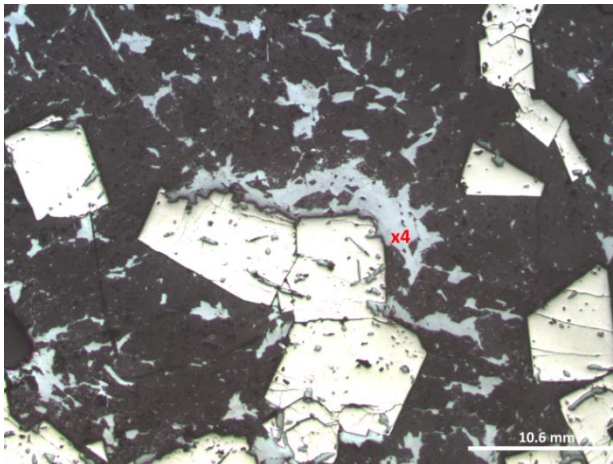
FK-285 Pb1



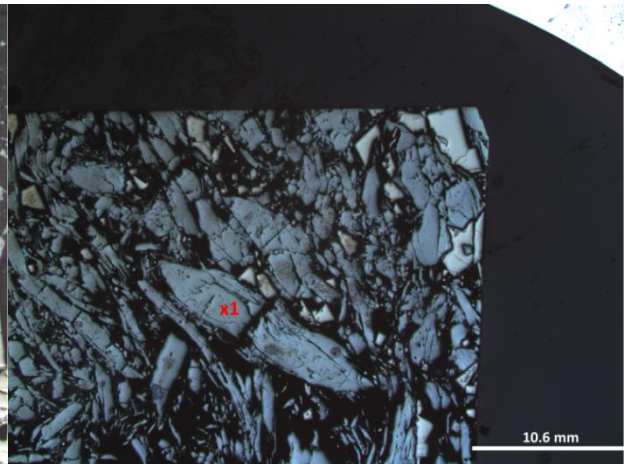
FK-285 Pb2



FK-285 Pb3



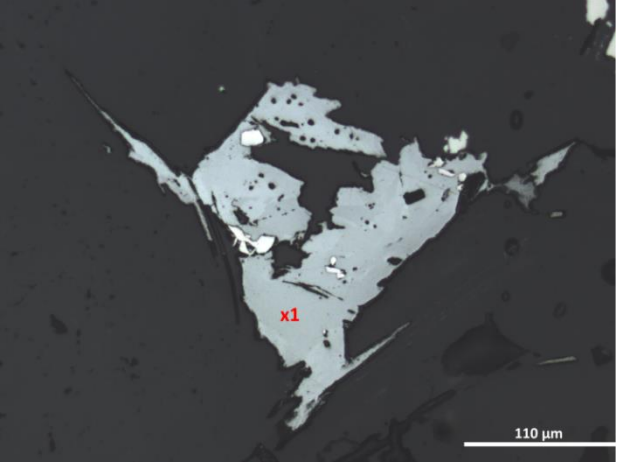
FK-285 Pb4



FK-TH12-03 Pb1



FK-TH12-03 Pb2



FK-TH12-56 Pb1

Appendix G – U-Pb Geochronology Data

FRASER KIRK - YUKON SAMPLES

Fraction	Weight [mg]	Concentration		Measured		Corrected Atomic Ratios						Age [Ma]			
		U	Pb rad [ppm]	total common Pb [pg]	206Pb ----- 204Pb	208Pb ----- 206Pb	206Pb ----- 238U	207Pb ----- 235U	207Pb ----- 206Pb	206Pb ----- 238U	207Pb ----- 235U	207Pb ----- 206Pb			
RPGND-2															
Z1 3 clr euh prm	0.003	784	11.1	4	573	0.0930	0.01449	14	0.0949	22	0.04747	96	93	92	73
Z2 4 clr euh prm	0.004	5492	76.8	4	4929	0.0658	0.01460	22	0.0963	14	0.04783	34	93	93	91
RPGND-3															
Z1 2 sharp needles	0.002	2102	31.2	16	263	0.1190	0.01480	10	0.0979	16	0.04798	74	95	95	98
Z2 2 sharp needles	0.002	4944	71.2	7	1416	0.0905	0.01471	10	0.0972	8	0.04793	32	94	94	96
Z3 1 sharp needle	0.001	2861	42.8	22	139	0.1133	0.01497	10	0.0989	14	0.04790	70	96	96	94
Z4 2 sharp needles	0.002	2375	34.7	18	270	0.0877	0.01495	8	0.0991	14	0.04806	60	96	96	102
PH-D															
Z1 2 med clr euh prm	0.002	3870	53.7	4	1792	0.0515	0.01468	20	0.0966	12	0.04775	42	94	94	87
Z2 2 med clr euh prm	0.002	458	6.7	3	349	0.1136	0.01474	16	0.0959	36	0.04717	170	94	93	58
EAGLE6-1															
Z1 2 prm	0.004	4767	68.4	29	551	0.0875	0.01469	10	0.0973	10	0.04800	36	94	94	99
Z2 1 med prm	0.002	5505	77.9	52	167	0.0589	0.01488	8	0.0978	16	0.04770	74	95	95	85
M384929-31															
Z1 3 sml prm	0.003	3663	51.7	5	1891	0.0693	0.01470	10	0.0971	8	0.04794	28	94	94	96
Z2 4 sml prm	0.004	3872	54.2	5	2675	0.0601	0.01470	12	0.0971	8	0.04793	18	94	94	96

Notes; All zircon was chemically abraded (Mattinson, 2005) prior to dissolution. Z, zircon; 2,4 number of grains in analysis;

prm, prism; sml, small; euh, euhedral; clr, clear; med, medium.

Weights of grains were estimated, with potential uncertainties of 50% for these small samples.

Atomic ratios corrected for fractionation, spike, laboratory blank of 1- 2 picograms (pg) common lead, and initial common lead at the age of the sample calculated from the model of Stacey and Kramers (1975), and 0.3 pg U blank. Two sigma uncertainties are reported after the ratios and refer to the final digits.

Appendix H – Whole Rock Geochemistry Data used in Chapter 4

H.1 Table of Sample Names for Dublin Gulch Samples in Chapter 4.

Original Sample Name	Sample Name in Geochemical Plots
PH-D	DGv-001
RP-GND-2	DGv-002
RP-GND-3	DGv-003
IO-016545	DGv-004
M384929-31	DGv-005
M395914	DGv-006
Eagle 6-1	DGp-001
Eagle 6-2	DGp-002

H.2 Data for Dublin Gulch, Scheelite Dome, and Brewery Creek

Data was compiled and re-calculated for homogeneity. Fe was re-calculated to FeO total. For samples which lacked Zr measurements but contained Hf measurements, the average Zr/Hf ratio for the dataset was used to calculate a value for Zr. For samples with anomalously low Nb/Ta ratios (c. 1-2), the Ta was recalculated using the average Nb/Ta ratio for the dataset.

References used:

- (1) Dublin Gulch - Hart et al. (2004b)
- (2) Scheelite Dome - Mair et al. (2006b)
- (3) Brewery Creek - Lindsay (2006)

Sample	DGp-003	DGp-004	DGpeg-001	DGd-001	DGd-002	SDv-001	SDv-002	SDv-003	SDv-004	SDv-005
Original Sample	DG-mp	DG-qs	DG-peg	DG-d1	DG-d2	M01-min	M02-min	M03-min	M-04-sp	M-05-sp
Reference	1	1	1	1	1	2	2	2	2	2
<i>Major Elements</i>										
SiO₂	68.52	70.87	62.57	61.12	60.71	56.72	56.91	56.60	59.20	60.81
TiO₂	0.47	0.35	0.61	0.57	0.68	1.17	1.06	1.05	0.52	0.52
Al₂O₃	15.50	16.31	17.13	14.56	14.92	14.39	16.03	15.80	12.70	12.16
FeO (Total)	3.13	1.94	1.68	5.25	5.67	7.77	6.78	6.78	6.89	7.48
MnO	0.04	0.02	0.04	0.10	0.10	0.21	0.21	0.21	0.21	0.21
MgO	1.45	0.67	1.65	4.83	4.44	6.29	5.10	4.81	7.24	6.55
CaO	3.53	2.68	4.04	5.63	6.51	6.82	7.33	7.11	8.19	7.59
Na₂O	2.64	2.62	2.05	2.19	2.45	1.07	1.70	1.36	2.41	1.77
K₂O	4.59	4.46	10.06	5.58	4.35	5.01	4.25	5.65	2.52	2.81
P₂O₅	0.13	0.08	0.16	0.16	0.17	0.53	0.64	0.63	0.10	0.10
(LOI)	0.85	1.05	1.80	1.05	1.10	4.00	4.10	3.70	1.30	2.80
<i>Trace Elements</i>										
V	33	21	41	93	84	285	119	134	177	148
Cr	31	n.d.	38	279	181	160	185	200	690	560
Co	7	2	3	18	16	16	12	13	24	16
Ni	21	n.d.	24	62	66	33	22	37	39	27
Cu	n.d.	n.d.	n.d.	n.d.	12	17	11	19	n.d.	n.d.
Pb	16	31	8	23	20	14	13	7	11	3
Zn	60	126	n.d.	87	90	136	128	123	154	116
Ba	1407	2988	3877	1661	1391	2655	1444	2134	2456	1715
Cs	7.65	11.42	8.62	6.77	8.22	43.29	5.10	7.85	15.95	30.67
Ga	20	22	19	19	20	19	17	19	18	19
Rb	202	217	310	244	224	249	210	383	132	158
Sr	474	485	656	479	445	483	448	523	470	405
Y	18	5	33	23	23	38	38	47	20	17
Zr	228	155	304	209	194	195	182	206	111	98
Hf	6.32	4.59	8.62	5.74	5.38	5.33	4.88	5.44	3.25	2.81
Nb	14	14	23	16	14	13	15	16	10	11
Ta	1.22	1.12	1.57	1.27	1.17	0.85	0.96	1.05	0.63	0.62
Th	25.80	13.46	29.85	32.41	26.09	18.34	15.39	19.77	17.63	17.36
U	5.77	7.94	5.34	4.77	6.68	5.44	4.57	5.75	2.94	3.01
La	50.37	22.94	63.70	61.12	52.39	39.24	31.32	37.67	30.23	32.02
Ce	90.14	40.17	113.86	101.94	96.15	81.25	65.19	78.68	58.47	57.17
Pr	9.40	4.17	12.62	10.67	10.03	9.81	8.07	9.52	6.72	6.03

Sample	SDv-006	SDv-007	SDp-001	SDp-002	SDp-003	SDp-004	SDp-005	SDp-006	SDp-007	SDp-008
Original Name	M-06-sp	M-07-lm	M-08-qmd	M-09-qmd	M-10-qm	M-11-qm	M-12-qm	M-13-gd	M-14-gd	M-15-gd
Reference	2	2	2	2	2	2	2	2	2	2
<i>Major Elements</i>										
SiO₂	60.74	59.47	61.36	61.18	62.60	62.67	63.90	63.26	64.43	64.09
TiO₂	0.51	0.71	0.72	0.82	0.82	0.72	0.71	0.72	0.63	0.63
Al₂O₃	12.72	14.46	15.24	13.90	14.57	16.08	15.21	15.33	15.37	15.50
FeO (Total)	6.83	6.32	5.28	6.58	5.08	4.54	4.87	5.37	4.83	4.81
MnO	0.21	0.20	0.10	0.21	0.10	0.10	0.10	0.10	0.11	0.10
MgO	6.57	4.28	3.60	5.05	3.18	2.68	2.65	4.22	3.58	3.56
CaO	7.39	6.41	4.84	5.66	5.03	4.54	4.29	6.07	5.37	5.45
Na₂O	2.15	2.04	2.06	2.06	1.95	2.47	2.25	1.75	2.00	2.09
K₂O	2.77	5.70	6.49	4.22	6.26	5.88	5.61	2.98	3.47	3.56
P₂O₅	0.10	0.41	0.31	0.31	0.41	0.31	0.41	0.21	0.21	0.21
(LOI)	0.90	0.50	1.40	0.80	0.60	0.80	0.60	1.20	4.20	3.00
<i>Trace Elements</i>										
V	159	172	121	159	192	143	163	167	119	119
Cr	621	76	97	246	53	49	50	223	147	145
Co	19	16	8	16	10	9	11	15	10	11
Ni	38	23	23	26	n.d.	36	37	24	32	49
Cu	44	n.d.	n.d.	n.d.	n.d.	n.d.	n.d.	22	25	14
Pb	15	30	18	13	16	66	34	3	26	8
Zn	173	173	96	157	86	101	116	102	138	97
Ba	2411	2749	2162	1741	3068	2917	2858	2314	2527	2094
Cs	18.26	13.14	25.43	19.57	24.53	27.83	22.35	35.28	9.90	14.56
Ga	21	20	21	23	22	23	24	19	20	17
Rb	176	292	305	287	346	316	323	183	135	137
Sr	479	600	543	548	857	843	833	437	496	439
Y	21	41	29	40	46	32	34	28	26	22
Zr	127	173	196	210	284	277	257	181	175	157
Hf	3.49	4.58	5.25	5.77	7.29	7.42	7.04	4.83	4.74	4.19
Nb	12	20	20	21	30	21	24	15	15	14
Ta	0.72	1.22	1.13	1.34	2.57	1.24	1.43	1.03	1.16	0.94
Th	19.70	22.30	26.05	24.20	42.48	36.70	36.44	25.51	25.90	20.63
U	1.95	5.50	6.07	8.96	6.77	6.39	8.37	7.61	6.84	5.55
La	36.12	53.76	64.97	65.40	106.11	95.87	92.48	53.08	54.01	43.77
Ce	61.87	98.67	106.97	116.18	191.48	161.43	152.19	95.45	97.17	78.96
Pr	7.18	11.10	12.66	12.67	20.73	18.66	18.17	10.29	10.42	8.27

Sample	SDp-009	SDp-010	SDp-011	SDp-012	BC-001	BC-002	BC-003	BC-004	BC-005	BC-006
Original Sample Reference	M-16-gdp 2	M-17-gdp 2	M-18-mg 2	M-18-mg 2	SY 3	QBM 3	QBM 3	QBM 3	BM 3	BM 3
<i>Major Elements</i>										
SiO₂	69.43	67.53	68.89	68.35	62.61	66.34	67.82	66.42	58.19	54.51
TiO₂	0.41	0.41	0.41	0.51	0.57	0.60	0.56	0.59	0.91	0.87
Al₂O₃	15.44	15.09	15.27	15.05	16.15	15.25	15.42	15.17	13.95	12.73
FeO (Total)	2.76	3.32	3.23	3.48	4.47	4.25	4.18	4.15	7.23	7.81
MnO	0.10	0.10	0.10	0.10	0.10	0.08	0.09	0.08	0.15	0.16
MgO	1.74	1.33	1.64	1.93	1.27	2.04	1.91	2.09	4.17	5.10
CaO	4.09	3.18	3.49	3.66	2.83	3.50	2.04	3.66	6.21	8.46
Na₂O	2.66	2.77	2.46	2.24	3.50	2.52	2.87	2.81	1.80	1.33
K₂O	3.37	6.06	4.41	4.48	8.29	5.17	4.85	4.77	6.85	8.32
P₂O₅	0.10	0.21	0.10	0.20	0.21	0.26	0.26	0.26	0.53	0.71
(LOI)	0.90	1.00	1.00	0.80	0.44	2.90	2.35	2.74	1.06	0.90
<i>Trace Elements</i>										
V	40	54	57	71	n.d.	n.d.	n.d.	n.d.	n.d.	n.d.
Cr	97	25	40	53	n.d.	n.d.	n.d.	n.d.	n.d.	n.d.
Co	6	5	6	6	n.d.	n.d.	n.d.	n.d.	n.d.	n.d.
Ni	22	22	n.d.	n.d.	n.d.	n.d.	n.d.	n.d.	n.d.	n.d.
Cu	n.d.	11	n.d.	n.d.	n.d.	n.d.	n.d.	n.d.	n.d.	n.d.
Pb	16	36	26	6	n.d.	n.d.	n.d.	n.d.	n.d.	n.d.
Zn	93	66	91	43	n.d.	n.d.	n.d.	n.d.	n.d.	n.d.
Ba	3620	1519	2276	2360	n.d.	n.d.	n.d.	n.d.	n.d.	n.d.
Cs	14.42	10.57	12.92	8.44	n.d.	n.d.	n.d.	n.d.	n.d.	n.d.
Ga	22	23	20	18	n.d.	n.d.	n.d.	n.d.	n.d.	n.d.
Rb	165	291	199	177	n.d.	n.d.	n.d.	n.d.	n.d.	n.d.
Sr	544	802	609	588	n.d.	n.d.	n.d.	n.d.	n.d.	n.d.
Y	11	29	26	23	n.d.	n.d.	n.d.	n.d.	n.d.	n.d.
Zr	192	286	194	164	n.d.	n.d.	n.d.	n.d.	n.d.	n.d.
Hf	5.11	7.90	5.54	4.58	n.d.	n.d.	n.d.	n.d.	n.d.	n.d.
Nb	13	27	23	20	n.d.	n.d.	n.d.	n.d.	n.d.	n.d.
Ta	0.92	1.54	1.33	1.22	n.d.	n.d.	n.d.	n.d.	n.d.	n.d.
Th	22.29	41.97	24.91	26.85	n.d.	n.d.	n.d.	n.d.	n.d.	n.d.
U	5.32	12.93	8.20	10.68	n.d.	n.d.	n.d.	n.d.	n.d.	n.d.
La	62.27	79.64	52.08	58.18	n.d.	n.d.	n.d.	n.d.	n.d.	n.d.
Ce	96.42	140.81	90.93	107.10	n.d.	n.d.	n.d.	n.d.	n.d.	n.d.
Pr	11.76	14.47	9.94	11.49	n.d.	n.d.	n.d.	n.d.	n.d.	n.d.

Sample	BC-007	BC-008	BC-009
Original Sample	BM	HG	MGC 01
Reference	3	3	3
<i>Major Elements</i>			
SiO₂	60.65	46.68	64.71
TiO₂	0.77	1.95	0.64
Al₂O₃	15.25	15.27	15.47
FeO (Total)	6.22	12.42	4.36
MnO	0.12	0.21	0.08
MgO	3.35	11.22	2.58
CaO	5.15	8.45	4.63
Na₂O	2.12	1.95	2.50
K₂O	5.90	1.60	4.74
P₂O₅	0.46	0.27	0.30
(LOI)	1.04	2.28	3.03
<i>Trace Elements</i>			
V	n.d.	n.d.	165
Cr	n.d.	n.d.	n.d.
Co	n.d.	n.d.	n.d.
Ni	n.d.	n.d.	n.d.
Cu	n.d.	n.d.	n.d.
Pb	n.d.	n.d.	n.d.
Zn	n.d.	n.d.	n.d.
Ba	n.d.	n.d.	2938
Cs	n.d.	n.d.	n.d.
Ga	n.d.	n.d.	n.d.
Rb	n.d.	n.d.	n.d.
Sr	n.d.	n.d.	n.d.
Y	n.d.	n.d.	23
Zr	n.d.	n.d.	161
Hf	n.d.	n.d.	n.d.
Nb	n.d.	n.d.	n.d.
Ta	n.d.	n.d.	n.d.
Th	n.d.	n.d.	n.d.
U	n.d.	n.d.	5
La	n.d.	n.d.	50
Ce	n.d.	n.d.	n.d.
Pr	n.d.	n.d.	n.d.

Sample	DGp-003	DGp-004	DGpeg-001	DGd-001	DGd-002	SDv-001	SDv-002	SDv-003	SDv-004	SDv-005
Original Sample Reference	DG-mp 1	DG-qs 1	DG-peg 1	DG-d1 1	DG-d2 1	M01-min 2	M02-min 2	M03-min 2	M-04-sp 2	M-05-sp 2
Nd	32.63	14.58	46.06	37.33	34.72	39.98	31.21	38.71	25.51	21.93
Sm	5.98	2.73	9.42	6.58	6.26	8.64	6.58	8.37	5.04	4.16
Eu	1.31	1.03	1.65	1.37	1.27	2.03	1.59	2.20	1.05	1.04
Gd	4.44	1.58	6.87	4.45	4.65	7.36	6.16	7.64	3.46	2.91
Tb	0.69	0.22	1.16	0.80	0.77	1.28	1.17	1.36	0.63	0.52
Dy	3.38	0.90	5.96	4.09	3.95	6.72	6.05	7.64	3.36	2.91
Ho	0.63	0.13	1.14	0.78	0.77	1.39	1.27	1.57	0.73	0.62
Er	1.62	0.33	3.02	2.06	2.10	3.52	3.50	4.29	1.89	1.56
Tm	0.21	0.04	0.44	0.28	0.29	0.53	0.53	0.63	0.21	0.21
Yb	1.30	0.25	2.82	1.75	1.86	3.20	3.08	3.98	1.68	1.46
Lu	0.19	0.03	0.46	0.26	0.28	0.53	0.53	0.63	0.31	0.21

Sample	SDv-006	SDv-007	SDp-001	SDp-002	SDp-003	SDp-004	SDp-005	SDp-006	SDp-007	SDp-008
Original Sample Reference	M-06-sp 2	M-07-lm 2	M-08-qmd 2	M-09-qmd 2	M-10-qm 2	M-11-qm 2	M-12-qm 2	M-13-gd 2	M-14-gd 2	M-15-gd 2
Nd	25.96	42.05	44.48	45.94	76.25	66.80	64.92	37.24	36.43	29.85
Sm	5.03	8.86	8.13	9.27	14.16	11.75	11.74	6.79	6.63	5.55
Eu	1.23	1.73	1.65	1.54	2.67	2.68	2.65	1.54	1.58	1.36
Gd	3.80	6.62	6.38	7.11	8.93	8.97	9.29	5.14	5.05	4.19
Tb	0.62	1.22	1.03	1.24	1.54	1.24	1.33	0.93	0.84	0.73
Dy	3.39	6.72	4.94	6.90	7.90	5.88	6.23	4.73	4.53	3.77
Ho	0.62	1.32	0.93	1.34	1.54	1.03	1.12	0.93	0.84	0.73
Er	1.85	3.46	2.47	3.50	3.90	2.89	2.96	2.57	2.42	1.99
Tm	0.21	0.51	0.31	0.51	0.51	0.31	0.41	0.31	0.32	0.31
Yb	1.64	3.05	2.16	2.99	3.18	2.37	2.45	2.26	2.11	1.78
Lu	0.21	0.41	0.31	0.41	0.41	0.31	0.41	0.31	0.32	0.31

Sample	SDp-009	SDp-010	SDp-011	SDp-012	BC-001	BC-002	BC-003	BC-004	BC-005	BC-006
Original Sample Reference	M-16-gdp 2	M-17-gdp 2	M-18-mg 2	M-18-mg 2	SY 3	QBM 3	QBM 3	QBM 3	BM 3	BM 3
Nd	41.92	49.47	35.67	41.40	n.d.	n.d.	n.d.	n.d.	n.d.	n.d.
Sm	6.75	8.62	6.66	7.53	n.d.	n.d.	n.d.	n.d.	n.d.	n.d.
Eu	1.43	1.95	1.44	1.63	n.d.	n.d.	n.d.	n.d.	n.d.	n.d.
Gd	4.09	6.16	4.31	4.88	n.d.	n.d.	n.d.	n.d.	n.d.	n.d.
Tb	0.51	0.92	0.82	0.81	n.d.	n.d.	n.d.	n.d.	n.d.	n.d.
Dy	2.05	4.82	4.31	4.17	n.d.	n.d.	n.d.	n.d.	n.d.	n.d.
Ho	0.31	0.92	0.82	0.81	n.d.	n.d.	n.d.	n.d.	n.d.	n.d.
Er	0.72	2.46	2.26	2.03	n.d.	n.d.	n.d.	n.d.	n.d.	n.d.
Tm	0.10	0.31	0.31	0.31	n.d.	n.d.	n.d.	n.d.	n.d.	n.d.
Yb	0.61	2.16	1.95	1.83	n.d.	n.d.	n.d.	n.d.	n.d.	n.d.
Lu	0.10	0.31	0.31	0.31	n.d.	n.d.	n.d.	n.d.	n.d.	n.d.

Sample	BC-007	BC-008	BC-009
Original Sample Reference	BM 3	HG 3	MGC 01 3
Nd	n.d.	n.d.	n.d.
Sm	n.d.	n.d.	n.d.
Eu	n.d.	n.d.	n.d.
Gd	n.d.	n.d.	n.d.
Tb	n.d.	n.d.	n.d.
Dy	n.d.	n.d.	n.d.
Ho	n.d.	n.d.	n.d.
Er	n.d.	n.d.	n.d.
Tm	n.d.	n.d.	n.d.
Yb	n.d.	n.d.	n.d.
Lu	n.d.	n.d.	n.d.

Appendix I – Strontium and Neodymium Isotope Method

Whole rock powders were dissolved in Savillex© Teflon beakers using an 8 ml (4:1) mixture of 29 M HF – 15 M HNO₃. Prior to acid digestion, a mixed 150Nd/149Sm spike was added to each sample, with both sample and spike being weighed on a high-precision balance. After five days of digestion, the solution was evaporated to dryness and then taken back up in 6M HCl for 2-3 days. The sample was finally dried down and then re-dissolved in 2.5 M HCl. Samples were then loaded onto a cation exchange column containing resin (AG-50W-X8, H⁺ form, 200-400 mesh). A Rb-Sr fraction was obtained followed by collection of a fraction containing the rare earth elements (REE). The Rb-Sr fraction was evaporated to dryness, then taken up in 3M HNO₃ and loaded onto a column containing Eichrom© Sr resin to separate out the Sr and remove Rb and other remaining elements. The bulk REE solution is then dried and taken up in 0.18 M HCl and loaded on a second column containing Eichrom© Ln resin (50-100 mesh) to isolate Sm and Nd separately from each other and the other REE.

Sr and Nd isotopic compositions were determined using dynamic mode on a multi-collector Finnigan Mat 262 mass spectrometer. Samarium and Nd concentrations were measured in static mode. Rubidium and Sr concentrations were not determined by isotope dilution and values from the ICP-MS analyses are used for making the age correction to determine the initial Sr isotopic composition.

Samarium and Nd were loaded onto a double rhenium filament assembly, while Sr utilizes a single tungsten filament with 2 µL of Sr activator (tantalum fluoride). Instrumental mass fractionations of Nd and Sm isotopes were corrected using a Raleigh law relative to $^{146}\text{Nd}/^{144}\text{Nd} = 0.7219$ and $^{152}\text{Sm}/^{147}\text{Sm} = 1.783$, respectively. The measured values were adjusted to the JNdi-1 standard ($^{143}\text{Nd}/^{144}\text{Nd} = 0.512115$, Tanaka et al., 2000). Measurement of JNdi-1 yielded a mean $^{143}\text{Nd}/^{144}\text{Nd} = 0.512100 \pm 6$ (1SD, n=21). Strontium ratios were normalized to $^{88}\text{Sr}/^{86}\text{Sr} = 8.375202$ and measured values were adjusted to the NBS-987 standard ($^{87}\text{Sr}/^{86}\text{Sr} = 0.710240$). Measurement of this standard yielded a mean of $^{87}\text{Sr}/^{86}\text{Sr} = 0.710233 \pm 15$ (1SD, n=15).

USGS whole rock reference material BCR-2 was also analyzed in replicate, with each analysis comprising a separate dissolution and thus providing the best estimate of the reproducibility of an individual whole rock analysis. The mean values of BCR-2 are as follows, where the relative two standard deviations of the mean (n= 11) are given in percent in parenthesis; $^{143}\text{Nd}/^{144}\text{Nd} = 0.512636$ (0.0021%); $^{147}\text{Sm}/^{144}\text{Nd} = 0.1383$ (0.389%); Nd ppm=27.7 (0.7%); Sm = 6.33 (0.6%).